Métamatériaux à indice négatif de réfraction : des microondes aux fréquences térahertz

Eric Lheurette

N° d'ordre : H 656

SYNTHÈSE DES ACTIVITÉS POUR L'OBTENTION DE
L'HABILITATION À DIRIGER DES RECHERCHES

en Sciences Physiques

présentée à

L'UNIVERSITÉ DE LILLE 1

par

Éric LHEURETTE

MÉTAMATERIAUX À INDICE NÉGATIF DE RÉFRACTION : DES MICRO-ONDES AUX FRÉQUENCES TÉRAHERTZ

présentée le 11 juin 2009 devant la commission d'examen

Membres du jury :

MM.

A. DE LUSTRAC	Université de Paris-Sud XI	Rapporteur
M. SOROLLA	Université Publique de Navarre (Pampelune)	Rapporteur
S. TOUTAIN	Université de Nantes	Rapporteur
J. L. COUTAZ	Université de Savoie	Examinateur
G. DAMBRINE	Université de Lille1	Examinateur
P. KENNIS	Université de Lille1	Examinateur
J. P. VIGNERON	Facultés Universitaires Notre Dame de la Paix (Namur)	Examinateur
D. LIPPENS	Université de Lille 1	Directeur

Remerciements

Le travail présenté dans ce mémoire a été effectué à l'Institut d'Électronique, de Microélectronique et de Nanotechnologie dirigé par M. Alain CAPPY que je remercie pour m'avoir permis de mener mes recherches au sein du Laboratoire Central. Je lui suis particulièrement reconnaissant pour l'écoute qu'il m'a accordée à l'époque de ma mutation à l'Université de Lille 1.

J'adresse mes plus vifs remerciements à M. Didier LIPPENS, responsable du groupe « Dispositifs Opto et Microélectronique Quantique » pour avoir encadré ce travail qui doit sa concrétisation à son engagement et à son enthousiasme quotidiens. La confiance qu'il m'accorde depuis plus de quinze ans, combinée à sa grande expérience et à son insatiable curiosité, m'ont toujours permis de mener à bien mes différentes études et constitue un moteur pour l'exploration d'idées nouvelles. Je lui suis infiniment reconnaissant pour sa passion communicative qui a contribué à élargir, au fil des années, mon champ d'investigation. Enfin, je n'oublierai jamais le soutien qu'il m'a accordé dans les mois difficiles qui ont précédé ma mutation à l'Université de Lille 1.

Je remercie sincèrement M. André DE LUSTRAC de l'Université de Paris-Sud, M. Mario SOROLLA de l'Université Publique de Navarre et M. Serge TOUTAIN de l'Université de Nantes d'avoir accepté d'évaluer ce travail en qualité de rapporteurs.

Je suis particulièrement reconnaissant à M. Jean-Louis COUTAZ de l'Université de Chambéry, M. Gilles DAMBRINE, M. Patrick KENNIS de l'IEMN ainsi qu'à M. Jean-Pol VIGNERON des Facultés Universitaires Notre Dame de la Paix de Namur qui me font l'honneur de prendre part à ce jury.

Les résultats présentés dans ce mémoire doivent beaucoup aux doctorants, stagiaires de Master et de cycle ingénieur avec qui j'ai été amené à travailler dans une situation de co-encadrement tant formelle qu'informelle. En optant pour un ordre chronologique, je remercie chaleureusement, les docteurs Marta FERNANDEZ DIEGO, Emmanuel DUVAL, Thibaut DECOOPMAN, Sophie FASQUEL, Thomas CRÉPIN, Mouloud BOUZOUAD,

Michel-François FOULON, Nathalie FABRE, futurs docteurs Charles CROENNE, Aurélien MARTEAU, Grégory HOUZET, Fuli ZHANG, Alejandro LUCAS BORJIA, Maxence HOFMAN et les stagiaires Julien CLAY, Baddredine OUAGAGUE et Sylvain POTET.

J'adresse mes remerciements à tous les membres du groupe DOME, passés ou présents, qui ont contribué, chacun à leur manière, à la progression de mon parcours de chercheur de par leurs compétences et leurs qualités humaines. Un grand merci à Patrick MOUNAIX qui m'a initié aux différentes techniques de la salle blanche. Merci également à Olivier VANBÉSIEN qui, peut-être sans le savoir, a certainement motivé mes orientations vers le métier de chercheur. Merci à Hélène LEROUX, Véronique SADAUNE. Merci à Xavier MÉLIQUE dont les efforts en technologie et sur les projets d'enseignement permettent parfois de sauver des situations désespérées.

Merci à Mathias PERRIN, Dmitri YAREHKA et Davy GAILLOT, post-doctorants avec qui j'ai eu le plaisir de partager le bureau 120.

Merci à M. Damien DUCATTEAU et Mmes Élisabeth DELOS et Sylvie LEPILLET pour leur précieuse aide dans la caractérisation fréquentielle des différents dispositifs.

Merci à M. Frédéric GARET pour son engagement dans la caractérisation temporelle aux fréquences térahertz.

Merci à tout le personnel de la centrale de technologie et en particulier à ceux dont les conseils ou la mise en œuvre ont conduit à la finalisation de nos prototypes, à savoir Mmes Karine BLARY, Hermance DESRÉ, Annie FATTORINI, Patricia LEFEBVRE-LEGRY, Christiane LEGRAND et MM. Jean-Louis CODRON, Bertrand GRIMBERT, Jonathan LEMAITRE, Pascal TILMANT, André LEROY et Didier VANDERMORE.

Merci à Anthony TREIZEBRE de m'avoir fait bénéficier, avec une constante bonne humeur, de son expérience dans les procédés BCB.

Merci à M. Christophe BERNARD d'avoir mis en péril son équipement de gravure chimique pour la fabrication des prototypes basse fréquence.

Merci à M. Alex HERMAN pour son concours au développement du banc de caractérisation angulaire.

Merci à Mme Jocelyne LOUCHARD pour la reproduction de ce mémoire.

Merci à Mme Marie-Bénedicte DERNONCOURT pour sa bonne humeur et son mérite dans son soutien administratif.

Merci à Mme Véronique GYSEMBERGH pour son sourire et son aide bibliographique.

Merci à Jorge CARBONELL pour sa précieuse collaboration et pour avoir su si bien agrémenter, avec son épouse Esther, mon séjour à Valencia.

Merci à Marc LE ROY pour le temps de propagation de groupe négatif et pour m'avoir fait découvrir la région de Brest même en compagnie de Claire, Lénaelle et Malo.

Une pensée pour mes collègues rouennais, Serge KOUMETZ, Abdelrafik MALKI, Patrick MARTIN, Marc et Michèle TERRIER.

Un clin d'œil à mes collègues de TELECOM Lille 1 et en particulier MM. Manuel ARDOUIN, Pierre-Marie ALLIOUX, Christophe SÉGUINOT, Kamal LMIMOUNI et Vincent THOMY aux côtés de qui j'enseigne le plus régulièrement.

Je tiens à remercier tous ceux qui, de près ou de loin, ont encouragé mon parcours depuis ma soutenance de thèse avec une pensée particulière pour M. Patrice HESTO.

Merci à Ariane pour sa patience et son précieux concours dans la relecture et la mise en forme de ce mémoire.

Merci enfin à Iris et Aliette pour s'être assises sur mon manuscrit et pour en avoir libéré et mélangé les pages dans le but de provoquer des interprétations nouvelles. Comme le disait Jean Tardieu : « L'impossible est du possible en liberté ».

Table des matières

Curriculum vitae

A.1 État civil, activités professionnelles, formation

Nom : LHEURETTE
Prénom : Éric
Né le 12 mars 1968

Adresse : IEMN-DHS UMR CNRS 8520
Groupe : Dispositifs Optiques et Microélectroniques Quantiques
BP 60069, avenue Poincaré, cité scientifique
59652 Villeneuve d'Ascq Cedex
Téléphone : + 33 (3) 20 19 79 03
Télécopie : + 33 (3) 20 19 78 92
E-mail : Eric.Lheurette@iemn.univ-lille1.fr

Emploi : Maître de conférences depuis le 1er septembre 1999 (titularisé en 2000)

Section CNU :Électronique, Optronique et Systèmes (63e section)

Fonction nominative :Membre suppléant de la Commission de Spécialistes de l'Université de Valenciennes et du Hainaut en 2007 et 2008 Cambrésis (63e section)

Titulaire de la Prime d'Encadrement Doctoral et de Recherche (PEDR) depuis 2005

Activités professionnelles

Depuis 2003 : Maître de conférences à l'USTL, UFR d'IEEA Telecom Lille 1
1999-2003 : Maître de conférences, IUT de Rouen
1998-1999 : Post doc, IEMN
1996-1998 : Attaché Temporaire d'Enseignement et de Recherche, USTL
1993-1996 : Moniteur de l'Enseignement Supérieur, USTL

Formation

1996 : Thèse de doctorat de l'Université, Mention Très Honorable avec Félicitations du jury
Titre : Composants non linéaires à hétérostructures pour la génération aux longueurs d'onde millimétrique et submillimétrique.
Membres du jury :
MM. E. Constant, P. Hesto, J. F. Palmier, G. Beaudin, D. Samson, A. Cappy, D. Lippens
1993-1996 : stages de Monitorat de l'Enseignement Supérieur
1992 : DEA Électromagnétisme et Microondes, mention Bien
1991 : Maîtrise EEA option Microondes
1990 : Licence EEA
1989 : DEUG A Physique Chimie
1988 : BTS Électronique
1986 : Baccalauréat Électronique (F2) mention Bien

A. 2 Enseignement

Mon activité d'enseignement en tant que Maître de conférences peut être divisée en deux parties distinctes qui correspondent à mes affectations à l'IUT de Rouen (septembre 1999 à juillet 2003) et à l'Université des Sciences et Technologies de Lille (USTL) (depuis septembre 2003). Les interventions correspondantes sont regroupées dans deux tableaux.

A. 21 Depuis septembre 2003

Depuis mon recrutement à l'USTL, je suis affecté à l'UFR d'IEEA[1] et j'effectue l'intégralité de mon service d'enseignement à l'école d'ingénieurs Telecom Lille 1.

Années universitaires	**Diplôme, niveau**	**Module**	**Volume horaire moyen équivalent TD**
2003-2004 à 2008-2009	Ingénieur cycle de base 1re année (bac + 1)	Technologie des signaux Coordination du module Cours	130
	Ingénieur cycle de base 1re année (bac + 1)	Technologie de l'électronique numérique Travaux pratiques	30
	Ingénieur cycle de base 2e année (bac + 2)	Champ électromagnétique Coordination du module Travaux dirigés Travaux pratiques	210
	Ingénieur cycle de base 2e année (bac + 2)	Technologie des modulations Travaux dirigés Travaux pratiques	140
	Ingénieur cycle de base 1re année (bac + 1)	Électronique analogique Travaux dirigés	30
	Ingénieur cycle de base 2e année (bac + 2)	Canaux de propagation Travaux dirigés	80
	Ingénieur cycle de base 2e année (bac + 2)	Conception et réalisation d'un système électronique Projets encadrés	280
	Ingénieur cycle d'approfondissement (bac +3)	Technologie des voies de transmission analogiques Travaux pratiques	100
	Ingénieur cycle d'approfondissement (bac +3)	Électronique numérique Travaux dirigés	100
	Formation par apprentissage Formation continue	Électronique numérique Coordination du module Travaux dirigés Enseignement à distance	40

Divers : Suivi de stages ingénieur en 2e année
Encadrement de Travaux d'Étude et de Recherche en Master 1re année
Encadrement de stages de recherche en Master 2e année

A. 22 De septembre 1999 à juillet 2003

Lors de ma nomination à l'IUT de Rouen, j'ai été affecté au département GEII[2] où j'ai effectué la majeure partie de mon service d'enseignement. J'ai également été amené à intervenir au département GTR[3] situé à Elbeuf et j'ai pris part aux enseignements de la formation doctorale dans le cadre du DEA électronique.

Années universitaires	**Diplôme, niveau**	**Module**	**Volume horaire moyen équivalent TD**
1999-2000 à 2002-2003	DUT GEII 2e année (bac + 2)	Électronique Cours Travaux dirigés	200
	DUT GEII 2e (bac + 2)	Télécommunications Travaux pratiques	550
	DUT GTR 2e année site d'Elbeuf (bac + 2)	Technologies du canal Travaux dirigés	20
	DEA (bac + 5)	Capteurs à semi-conducteurs Cours	15

Suivi de stages (DUT 2e année)
Encadrement de projets tutorés (DUT 2e année)
Encadrement d'un stage de recherche en DEA

[1]Informatique Électronique Électrotechnique et Automatique
[2]Génie Électrique et Informatique Industrielle
[3]Génie des Télécommunications et Réseaux

A. 3 Recherche

A. 31 Thèmes développés

Composants pour la microélectronique

Cette activité s'inscrit dans la continuité de ma thèse soutenue en décembre 1996 sur la thématique des composants à hétérostructures III-V pour la génération en bandes millimétrique et submillimètrique. Ce travail a été poursuivi dans le cadre d'un contrat d'Attaché Temporaire d'Enseignement et de Recherche et d'un financement postdoctoral avec une orientation vers les

structures distribuées. Dans ce cadre, une étude a été initiée sur les lignes de propagation non linéaires puis interrompue en raison de ma nomination à l'IUT de Rouen.

Suite à cette prise de fonction, j'ai été amené à travailler sur les composants MOS. La première partie de cette contribution concerne la spectroscopie des défauts à l'interface oxyde – semi-conducteur. La seconde partie est consacrée à l'étude des mécanismes de conduction à travers des hétérostructures de semi-conducteur à haute permittivité destinés à remplacer le SiO_2 dans une perspective de haute intégration. Ces différents travaux sont illustrés par les articles reproduits à la fin de ce mémoire concernant la période comprise entre 1998 et 2003.

Métamatériaux

J'ai débuté cette recherche en septembre 2003 à l'occasion de ma mutation à l'Université des Sciences et Technologies de Lille. Cette activité, menée à l'Institut d'Électronique, Microélectronique et Nanotechnologies, au sein du groupe DOME dirigé par D. Lippens est détaillée dans le volet scientifique de ce mémoire.

A. 32 Encadrement doctoral et jurys de thèse

Encadrement

Thèse de doctorat d'Emmanuel DUVAL soutenue en décembre 2001 à l'Université de Rouen
Co encadrement entre 1999 et 2001

Thèse de doctorat d'Aurélien MARTEAU (soutenance prévue en 2009)
Co encadrement depuis 2004

Thèse de doctorat de Charles CROËNNE (soutenance prévue en 2009)
Co encadrement depuis 2006

Jurys de thèse

Emmanuel DUVAL, Université de Rouen, décembre 2001

Blaise RAVELO, Université de Bretagne Occidentale, décembre 2008

A. 33 Animation scientifique

Implications dans des contrats
Contrat TELEMAC, Programme européen EUREKA, partenaire industriel THALES, 2003-2006

Contrat DGA, Métamatériaux térahertz, 2006-2008

Contrat CNES intitulé : Support de transmission à base de métamatériaux et dispositifs de réfraction négative, 2006-2009

Projets de collaborations
Participation au projet DISPERSION (Réseau Thématique Pluridisciplinaire CNRS nanophotonique), de 2003 à 2005

Participation à l'ACI NANOTHEME (Nanotechnologies pour la texturation et l'hybridation d'ensembles métalliques): IEMN Lille, IEF Orsay, GES Montpellier, animée par O. Vanbésien, de 2003 à 2005

Animation (pôle français) du projet de partenariat EGIDE PICASSO, IEMN Lille, Université Polytechnique de Valence
Intitulé : Métasurfaces pour la réfraction négative et le rayonnement, application au routage par sélection angulaire, 2007-2008

Co animateur du Groupe de Travail GT2 : « Structures à bandes interdites photoniques ou soniques, microcavités, milieux complexes et biologiques », GDR ONDES (CNRS) depuis avril 2009

Divers
Référé pour la revue IEEE Transactions on Antennas and Propagation

A. 4 Liste des publications et communications

A. 41 Revues internationales avec comité de lecture

1 Left handed dispersion of a stack of sub-wavelength hole metal arrays at terahertz frequencies
C. Croënne, F. Garet, É. Lheurette, J. L. Coutaz et D. Lippens, Accepté pour publication dans la revue Applied Physics Letters **94** p. 133112, 2009

2 Ferroelectric tunable balanced right- and left-handed transmission lines
A. Marteau, G. Vélu, G. Houzet, L. Burgnies, É. Lheurette, J. C. Carru et D. Lippens, Applied Physics Letters **94**, p. 023507, 2009

3 Low-loss left-handed metamaterials at millimeter waves
F. Zhang, D. P. Gaillot, C. Croënne, É. Lheurette, X. Mélique et D. Lippens, Applied Physics Letters **93**, p. 083104, 2008

4 Negative-Zero-Positive Refractive Index in a Prism-Like Omega-Type Metamaterial

F. Zhang, S. Potet, J. Carbonell, É. Lheurette, O. Vanbesien, X. Zhao et D. Lippens, Microwave Theory and Techniques, IEEE Transactions on **56**, pp. 2566-2573, 2008

5 Negative-zero-positive metamaterial with Omega-type metal inclusions
F. Zhang, G. Houzet, É. Lheurette, D. Lippens, M. Chaubet et X. Zhao, Journal of Applied Physics **103**, p. 084312, 2008

6 Omega-Type Balanced Composite Negative Refractive Index Materials
É. Lheurette, G. Houzet, J. Carbonell, F. Zhang, O. Vanbesien et D. Lippens, Antennas and Propagation, IEEE Transactions on **56**, pp. 3462-3469, 2008

7 Negative index metamaterial at 100 GHz
C. Croënne, M. F.Foulon, É. Lheurette, X. Mélique, M. Gheudin et D. Lippens, Proceedings of the European Microwave Association **4**, pp. 95-101, 2008

8 Double negative media using interconnected Omeg -type metallic particles
É. Lheurette, O. Vanbésien et D. Lippens, Microwave and Optical Technology Letters **49** pp. 84-90, 2007

9 Left-handed electromagnetics properties of split ring resonator and wire loaded transmission line in a fin-line technology
T. Decoopman, A. Marteau, É. Lheurette, O. Vanbésien et D. Lippens, IEEE transactions on Microwave Theory and Techniques **54**, pp. 1451-57, 2006

10 Left-handed electromagnetism obtained via nanostructured metamaterials : comparison with that from microstructured photonic crystals
M. Perrin, S. Fasquel, T. Decoopman, X. Mélique, O. Vanbésien, E. Lheurette et D. Lippens
Journal of Optics A, 7, pp. S3-11, 2005

11 Wave-mechanical calculations of leakage current through stacked dielectrics for nanotransistor Metal-Oxide-Semiconductor design
M. Le Roy, E. Lheurette, O. Vanbésien et D. Lippens
Journal of Applied Physics, 93, pp. 2966-71, 2003

12 Characterisation of charge trapping at the Si-SiO_2 (100) interface using high-temperature conductance spectroscopy
E. Duval et E. Lheurette
Microelectronic Engineering, 65, pp. 103-112, 2003

13 Determination of slow- and fast-state distribution using high temperature conductance spectroscopy on MOS structures

E. Duval, E. Lheurette, K. Ketata et M. Ketata
Semiconductor Science and Technology, **16**, p. L57, 2001

14 Rapid determination of « slow » and « fast » states densities using thermally stimulated conductance spectroscopy on metal-oxide semiconductor capacitors
E. Duval, L. Soliman, E. Lheurette, K. Ketata, M. Benzohra, C. Duprat et M. Ketata
Material Science in Semiconductor Processing, **4**, pp. 141-143, 2001

15 Improvement of oxide thickness determination on MOS structures using capacitance-voltage measurements at high frequencies
L. Soliman, E. Duval, M. Benzohra, E. Lheurette, K. Ketata et M. Ketata
Material Science in Semiconductor Processing, **4**, pp. 163-166, 2001

16 Step-like heterostructure barrier varactor for high power millimeter-wave applications
R. Havart, E. Lheurette, O. Vanbésien, P. Mounaix, F. Mollot and D. Lippens
IEEE Transactions on Electron Devices, **45**, pp. 2291-2297, 1998

17 Capacitance engineering for InP-based heterostructure barrier varactor
E. Lheurette, X. Mélique, P. Mounaix, F. Mollot, O. Vanbésien and D. Lippens
IEEE Electron Device Letters, **19**, pp. 338-340, 1998

18 High performance InP based heterostructure barrier varactors in single and stack configuration
E. Lheurette, P.Mounaix, P. Salzenstein, F. Mollot and D. Lippens
Electronics Letters, **32**, p. 1417, 1996

19 Coplanar waveguides on dielectric membranes micromachined on a GaAs substrate
P. Salzenstein, O. Dupuis, M. Helal, E. Lheurette, O. Vanbésien, P. Mounaix and D. Lippens
Electronics Letters, **32**, p. 821, 1996

20 Frequency capability of strained AlAs/InGaAs resonant tunnelling diodes
P. Mounaix, E. Lheurette, F. Mollot and D. Lippens
Electronics Letters, **31**, p. 1508, 1995

21 InGaAs/GaAs/AlAs pseudomorphic resonant tunnelling diodes integrated with airbridge
E. Lheurette, B. Grimbert, M. François, P. Tilmant, D. Lippens, J. Nagle and B. Vinter
Electronics Letters, **28**, p. 937, 1992

A. 42 Revue nationale avec comité de lecture

1 Left-handed propagation media via photonic crystal and metamaterials

T. Decoopman, T. Crépin, M. Perrin, S. Fasquel, A. Marteau, X. Mélique, É. Lheurette, O. Vanbésien et D. Lippens, *Comptes Rendus Physique* 6, pp. 683-692, 2005

A. 43 Communication orale invitée

1 Activities on metamaterials at IEMN-CNRS
É. Lheurette, communication invitée, Third workshop on metamaterials special materials for electromagnetic applications and TLC, Rome, Italie, 30-31 mars 2006

A. 44 Communications internationales avec comité de lecture (liste non exhaustive)

1 Left-Handed Metamaterial based on elliptical subwavelength apertures arrays for THz applications
É. Lheurette, J. Carbonell, C. Croënne et D. Lippens
Metamaterial's 2008, communication orale, 22-26 septembre 2008

2 Normal incidence on stacked surfaces of Split Ring Resonators
J. Carbonell, É. Lheurette, A. L. Borja, V. E. Boria et D. Lippens
Metamaterial's 2008, 22-26 septembre 2008

3 Application of Omega-type and related metamaterials for beam steering in X-Ku
F. Zhang, S. Potet, J Carbonell, E. Lheurette, O. Vanbesien, X. Zhao and D. Lippens, EuMc 2007, Communication orale, Munich, 9-12 Oct. 2007

4 Metamaterials-based Routing Devices for Space Applications
F. Zhang, G. Houzet, S. Potet, E. Lheurette, M. Chaubet, and D. Lippens, ISSSE 2007, communication orale, Montréal, 30 juillet – 2 août 2007

5 Voltage-controlled composite metamaterials via the loaded transmission line approach
G. Houzet, E. Lheurette, D. Lippens, G. Velu, L. Burgnies and J.C. Carru, Metamaterials Congress 2007, communication orale, Rome, 22-26 octobre 2007

6 *Left-handed electromagnetic media based on metamaterials*
T. Crépin, X. Mélique, A. Marteau, É. Lheurette, T. Decoopman, O. Vanbésien et D. Lippens, URSI 2005, New Delhi India, 23-29 octobre 2005

7 Metamaterial-based transmission line : the fin-line approach
A. marteau, T. Decoopman, M. F. Foulon, É. Lheurette et D. Lippens, communication orale, EuMC 2005, Paris, 4-6 octobre 2005

8 Pulse Compression with Superluminal Group Velocity In 1-D Photonic Bandgap Coplanar Waveguide

M. Le Roy, E. Lheurette et A. Pérennec, Communication orale, EuMC 2004, Amsterdam, 11-15 octobre 2004

9 Non Linear Transmission Line quintupler loaded by heterostructure barrier varactors
E. Lheurette, M. Fernandez, X. Mélique, P. Mounaix, O. Vanbésien et D. Lippens
29 th European Microwave Conference, Munich Germany
vol 2 pp 217-220, 4–8 octobre 1999

10 Harmonic generation from Non Linear Ttransmission Lines Employing InP based Heterostructure Barrier Varactors
E. Lheurette, X. Mélique, P. Mounaix, O. Vanbésien and D. Lippens
IEEE MTTS International Microwave Symposium, June 12-19 Anaheim, California, USA

A. 45 Communications nationales avec comité de lecture (liste non exhaustive)

1 Réfraction négative dans les métamatériaux
F. Zhang, G. Houzet, C. Croënne, É. Lheurette et D. Lippens
accepté pour communication aux JNM 2009, Grenoble, 26-29 mai 2009

2 Détermination expérimentale des paramètres effectifs des métamatériaux à indice négatif
C. Croënne, F. Zhang, É. Lheurette, X. Mélique et D. Lippens
accepté pour communication aux JNM 2009, Grenoble, 26-29 mai 2009

3 Biocapteurs à base de micro-résonateurs fendus
C. Croënne, G. Houzet, A. L. Borja, X. Mélique, É. Lheurette et D. Lippens
accepté pour communication aux JNM 2009, Grenoble, 26-29 mai 2009

4 Spectroscopie térahertz d'un métamatériau gaucher constitué d'un empilement de réseaux métalliques sous longueur d'onde
C. Croënne, F. Garet, É. Lheurette, J. L Coutaz et D. Lippens
accepté pour communication aux JNM 2009, Grenoble, 26-29 mai 2009

5 Ligne de transmission composite équilibrée fonctionnant en bande Ku et K
G. Houzet, G. Vélu, A. Marteau, L. Burgnies, É. Lheurette, J.C. Carru et D. Lippens
accepté pour communication aux JNM 2009, Grenoble, 26-29 mai 2009

6 Métamatériaux large bande à base de réseaux de motifs Omega interconnectés
Eric Lheurette, Jorge Carbonell, Grégory Houzet, Olivier Vanbésien, Michel Chaubet, Didier Lippens, JNM 2007, Toulouse, 23-25 mai 2007

7 Dispositifs sélectifs en angle à base de métamatériaux gauchers

Grégory Houzet, Eric Lheurette, Véronique Sadaune, Mouloud Bouzouad, Olivier Vanbésien, Michel Chaubet et Didier Lippens, JNM 2007, Toulouse, 23-25 mai 2007

8 Antennes accordables à base de métamatériaux
Mouloud Bouzouad, Badreddine Ouagague, Olivier Vanbésien, Eric Lheurette et Didier Lippens, JNM 2007, Toulouse, 23-25 mai 2007

9 Métamatériaux à indice de réfraction négatif à 100 GHz
Charles Croënne, Michel Foulon, Eric Lheurette, Xavier Mélique, Maurice Gheudin et Didier Lippens, JNM 2007, communication orale, Toulouse, 23-25 mai 2007

10 Lignes de transmission main gauche – main droite accordables par matériaux ferroélectriques
A. Marteau, G. Houzet, K. Blary, E. Lheurette, D. Lippens, G. Vélu, L. Burgnies et J. C. Carru, JNM 2007, communication orale, Toulouse, 23-25 mai 2007

11 Comportement fréquentiel des milieux doublement négatifs : réalisation dans la bande 140-220 GHz
É. Lheurette, Q. Li, X. Mélique, O. Vanbésien et D. Lippens, JNM 2005, communication orale, Nantes, 11-13 mai 2005

12 Lignes de transmission main-gauche en technologie finline
A. Marteau, T. Decoopman, É. Lheurette, X. Mélique, O. Vanbésien et D. Lippens, JNM 2005, communication orale, Nantes, 11-13 mai 2005

13 Compression d'impulsions et vitesse de groupe superluminale dans une structure photonique 1-D coplanaire
M. Le Roy, E. Lheurette, Y. Clavet et A. Pérennec, JNM 2003, communication orale, Lille, 21-23 mai 2003

14 Lignes non linéaires de transmissions chargées par des diodes à hétérostructure varactor en technologie InP
E. Lheurette, X. Mélique, P. Mounaix, O. Vanbésien et D. Lippens
Journées Nationales Micro-ondes 1999, Arcachon

Chapitre I :
Introduction aux métamatériaux

Introduction

Par définition, les métamatériaux sont des matériaux artificiels dont la structuration, à des échelles très inférieures aux longueurs d'onde de travail, permet de les assimiler à des matériaux homogènes. Cette définition, dans son expression la plus générale, montre que le concept de métamatériau peut couvrir tous les domaines de la physique. Cette remarque est illustrée dans la littérature par les différents travaux publiés dans les domaines de l'électromagnétisme incluant l'optique [1, 2], de l'acoustique [3], et de la fluidique [4]. Toutefois, d'un point de vue historique, les premières études ont été consacrées au contrôle des ondes électromagnétiques avec comme principale source d'inspiration, les travaux théoriques publiés dès 1968 par V. G. Veselago [5]. C'est dans ce domaine des ondes électromagnétiques que s'inscrit ce mémoire d'Habilitation à Diriger les Recherches.

L'objectif de ce chapitre introductif est de présenter de façon générale le champ d'étude balayé par les métamatériaux électromagnétiques. Il permettra de situer notre travail dans le contexte de cette thématique afin d'en faire ressortir les originalités.

En électromagnétisme, tout matériau homogène peut être décrit par ses paramètres constitutifs que sont la permittivité et la perméabilité. Dans un premier temps, nous nous appuierons sur une représentation de ces paramètres dans un plan comprenant quatre cadrans afin d'inscrire les métamatériaux dans le prolongement des matériaux disponibles à l'état naturel. Nous décrirons ensuite les différentes voies employées pour travailler sur les ingénieries de la permittivité et de la perméabilité. Enfin dans une dernière partie, nous passerons en revue les applications des métamatériaux électromagnétiques.

I.1 Classification des matériaux en fonction de leurs permittivité et perméabilité

La représentation que nous utilisons est basée sur une description des matériaux par le biais de leurs parties réelles de permittivité et perméabilité relatives, respectivement notées ε_r et μ_r. L'influence des parties imaginaires, qui ne sont pas prises en compte dans ce graphique, sera commentée à partir des cas pratiques présentés dans la suite de ce mémoire.

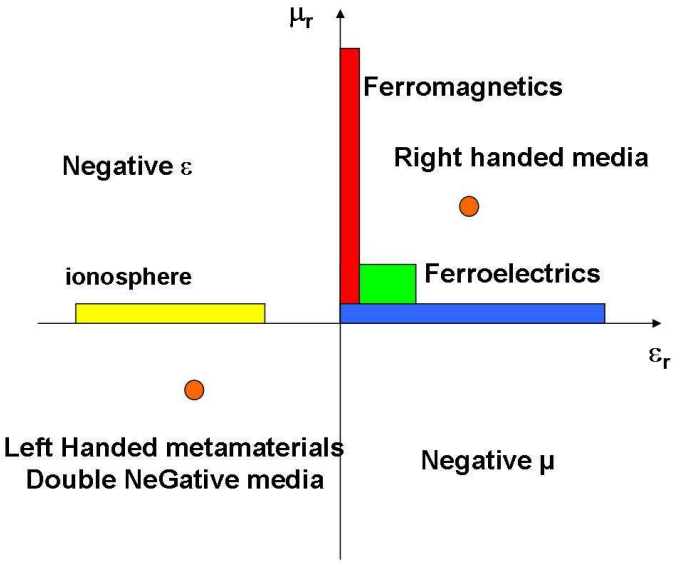

Figure I-1 : Représentation des matériaux en fonction des parties réelles de leurs paramètres constitutifs.

En électromagnétisme classique, les ondes se propagent dans un milieu doublement positif correspondant au premier cadran de la figure I-1. On parle dans ce cas de milieu main droite dans la mesure où la propagation peut être décrite par le trièdre direct avec les vecteurs champs électrique et magnétique et le vecteur d'onde dans le prolongement des trois doigts de la main droite. L'onde qui se propage dans le vide, présente des valeurs de ε_r et μ_r égales à 1 et la plupart des milieux de propagation auront des paramètres constitutifs relatifs du même ordre de grandeur. A titre d'exemple, les polymères fréquemment utilisés comme matériau diélectrique ont des permittivités relatives voisines de 2. En revanche, cette valeur est plus élevée dans le cas des semi-conducteurs non dopés (de l'ordre de 10). Des valeurs de ε_r bien plus importantes, de l'ordre de plusieurs milliers, peuvent être obtenues pour des matériaux ferroélectriques tels que le $BaSrTiO_3$ (BST). La perméabilité des céramiques ferromagnétiques telles que les ferrites vaut quelques unités pour des fréquences supérieures au gigahertz et peut dépasser plusieurs milliers à basse fréquence.

Le quatrième cadran regroupe les milieux à permittivité relative négative. Il est connu que la ionosphère, qui se comporte comme un plasma, présente des valeurs de ε_r inférieures à zéro. De la même manière, le comportement des électrons dans un métal est celui d'un plasma

caractérisé par deux fréquences caractéristiques qui sont la fréquence de collision f_c, associée aux temps de libre parcours moyen et la fréquence plasma f_p. L'évolution de la permittivité d'un métal en fonction de la fréquence suit le modèle de Drude défini par l'expression suivante :

$$\varepsilon(f) = 1 - \frac{{f_p}^2}{f(f + j.f_c)} \quad (1)$$

À titre d'exemple, pour l'or couramment utilisé dans les micro- et nanotechnologies, la fréquence de collision f_c vaut 10,3 THz et la fréquence plasma f_p vaut 2175 THz [6]. L'expression montre que la permittivité du métal tend vers 1 lorsque la fréquence tend vers l'infini. Compte tenu de l'importance de f_p par rapport à f_c, on peut considérer que la fréquence plasma correspond au passage de la permittivité par zéro. En deçà de cette valeur, ε est négatif. Cette évolution de la permittivité peut être mise à profit pour synthétiser un milieu simplement négatif. L'inconvénient du métal réside dans la valeur très élevée de sa fréquence plasma qui se traduit par des perméabilités négatives très importantes, y compris aux longueurs d'onde de l'optique. Par ailleurs, la partie imaginaire de cette permittivité est révélatrice d'un régime de pertes. Afin de pallier ces deux inconvénients, J. B. Pendry a proposé de substituer au métal un réseau de fils métalliques afin d'abaisser la fréquence plasma par effet de dilution [7]. Ceci revient à définir un milieu effectif dont le comportement reste régi par la loi de Drude, avec une valeur de fréquence plasma essentiellement liée aux paramètres géométriques du réseau. Cette possibilité permet de disposer d'une plage fréquentielle de fonctionnement très large associée à un niveau de perte relativement faible jusqu'aux frontières de l'infrarouge. En effet, l'onde se propage entre les fils qui, en micro-ondes, peuvent être assimilés à des conducteurs parfaits. Du point de vue de la transmission, en considérant le champ électrique parallèle à l'orientation des fils, le comportement observé est de type passe-haut [8] avec une fréquence de coupure qui correspond à la fréquence plasma. Cette fréquence est reportée sur la figure I-2. Le spectre en transmission fait également apparaître une bande interdite qui traduit un phénomène de diffraction correspondant à un accord de la demi-longueur d'onde guidée avec la périodicité du réseau. Jusqu'à f_p, la demi-longueur d'onde guidée dans le réseau est très faible, ce qui permet de considérer la structure comme un milieu moyen auquel on associe une valeur de permittivité effective. On parle alors de

régime de métamatériau. En revanche, le mode de fonctionnement en cristal photonique exploite le régime de diffraction situé aux plus hautes fréquences. En raison du caractère passe-haut de la structure, la plage de fonctionnement en permittivité effective négative correspond à un régime d'évanescence, ce qui limite fortement son exploitation en tant que milieu simplement négatif. La première possibilité est d'associer ce réseau à un milieu à perméabilité effective négative. On peut dans ce cas définir une bande passante qui correspond au recouvrement des plages de permittivité et perméabilité effectives négatives. Cette idée constitue la base de l'ingénierie des métamatériaux initiée dès 1999 par les groupes de J. B. Pendry et D. R. Smith [9]. Nous avons conçu plusieurs dispositifs sur ce principe. Un exemple de réalisation sera commenté et analysé au chapitre II de ce mémoire. La seconde possibilité consiste à exploiter les branches de dispersion d'ordre supérieur. Dans ce cas, on peut mettre en évidence un phénomène de réfraction négative qui est la conséquence d'un repliement de bande dans la zone de Brillouin [10]. Toutefois, dans la mesure où les dimensions du réseau métallique sont du même ordre de grandeur que la longueur d'onde guidée, cette structure ne peut pas être décrite comme un milieu moyen par le biais des paramètres constitutifs effectifs. Cette réfraction négative en condition de cristal photonique peut également être observée sur des réseaux diélectriques. Dans ce cas, elle présente un intérêt certain pour les longueurs d'ondes de l'optique où les pertes métalliques et la structuration sous longueur d'onde peuvent être rédhibitoires. Sur ce principe, un phénomène de focalisation à partir d'une lentille plane a été mis en évidence de façon expérimentale, à la longueur d'onde de 1,5 µm [11].

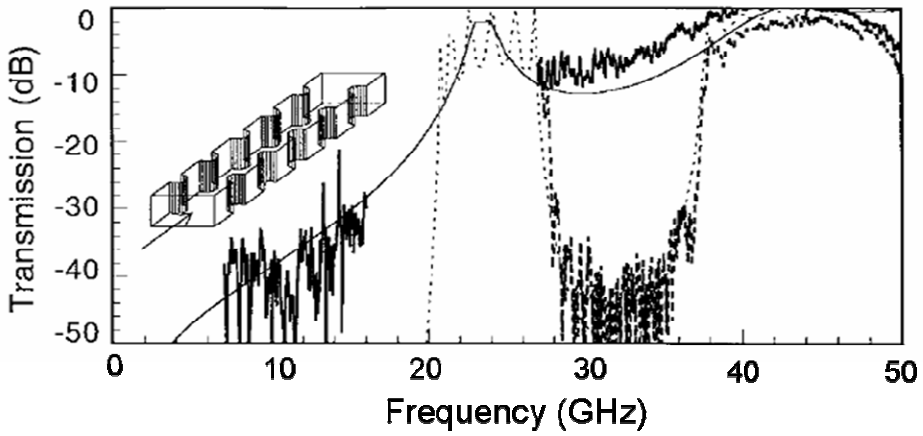

Figure I-2 : Spectre de transmission mesuré (pointillé) et calculé (trait continu) d'un réseau de fils (champ électrique parallèle aux fils). La période du réseau est de 6 mm. Le rayon des fils est de 0,75 mm [8].

Le troisième cadran regroupe les matériaux à perméabilité négative. Des valeurs négatives de perméabilité peuvent être observées dans certains alliages [12]. S'il est possible, en principe, d'exploiter ces propriétés pour la conception de dispositifs, la mise en œuvre pratique peut s'avérer délicate en raison de la disponibilité du matériau considéré, des faibles valeurs de μ_r et des bandes de fréquences limitées. Comme pour les structures à perméabilité effective négative, on va chercher à synthétiser un milieu dont le spectre de perméabilité pourra être accordé en fonction de dimensions géométriques, sur un large domaine spectral. Cependant, à la différence du réseau de fils qui tire parti de la permittivité négative d'un métal, on va tenter de générer du magnétisme de manière artificielle, à partir de matériaux non magnétiques. L'idée proposée par J. B. Pendry en 1999, qui consiste à utiliser des boucles métalliques de faible encombrement au regard de la longueur d'onde, est une exploitation directe du théorème d'Ampère établissant la relation entre le champ magnétique et le courant qui traverse un conducteur. Une résonance de la perméabilité effective peut être observée dans un résonateur en anneau fendu, en anglais Split Ring Resonator (SRR), excité par un champ magnétique parallèle à son axe [13]. La caractéristique typique de ce phénomène en fonction de la fréquence suit une évolution de Lorentz (figure I-3) où ω_0 correspond à la pulsation de résonance de la boucle de courant métallique. À cette pulsation, la valeur de perméabilité effective devient négative et repasse par zéro à la pulsation ω_{mp} désignée comme la pulsation plasma magnétique, par analogie avec la

pulsation plasma électrique. Lorsque l'on s'éloigne de cette résonance, la perméabilité effective tend vers l'unité.

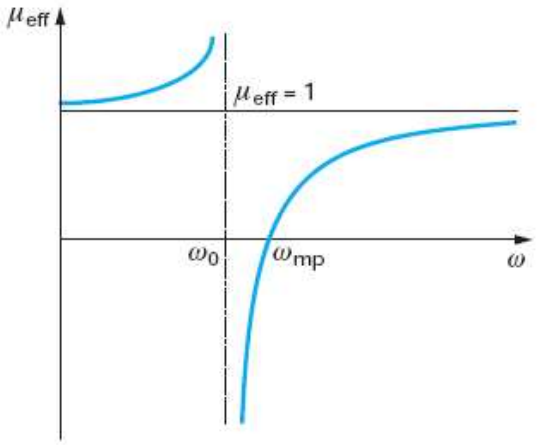

Figure I-3 : Évolution typique de la perméabilité effective (partie réelle) d'un résonateur en anneau fendu (SRR) en fonction de la pulsation.

Si, comme nous l'avons précédemment décrit, l'obtention d'une permittivité effective est la conséquence de l'interaction d'une onde incidente avec un réseau, le magnétisme artificiel est quant à lui un phénomène local. En 2001, le groupe de D. R. Smith a effectué la première démonstration expérimentale d'un phénomène de réfraction négative en superposant des réseaux de fils et de boucle de courant [1]. D'un point de vue fondamental, l'utilisation des résonateurs fendus peut être étendue jusqu'au domaine de l'optique [14]. Toutefois, à ces longueurs d'onde, les dispositifs souffrent de pertes relativement importantes. Par ailleurs, on observe un phénomène d'inertie des porteurs de charge qui entraîne une saturation de la réponse magnétique des résonateurs [15].

L'utilisation de matériaux ferroélectriques ou ferromagnétiques peut constituer une alternative aux structures métamatériaux métalliques. Dans le premier cas, on cherche à tirer parti des fortes valeurs de permittivité pour confiner l'énergie électromagnétique dans un volume dont les dimensions sont faibles devant la longueur d'onde de travail. Dans ce cas, on peut observer des résonances du courant de déplacement, ou résonances de Mie, à même d'inverser la polarisation du champ magnétique [16]. Le groupe DOME a montré que le magnétisme artificiel dans les plots de BST pouvait être mis à profit pour la conception d'une cape d'invisibilité

permettant de masquer un objet pour une onde plane incidente dans le domaine térahertz [17]. Des valeurs négatives de permittivité effective peuvent également être observées par excitation de modes de résonance pairs. En principe, il est possible de superposer les réponses magnétique et électrique afin de définir un milieu doublement négatif correspondant au troisième cadran de la figure I-1 [18]. Dans le second cas, des valeurs de perméabilité négatives peuvent être observées [19] dans un rondin de ferrite en condition de résonance ferromagnétique (FMR) [20]. Récemment, cette propriété a été exploitée pour définir un milieu doublement négatif à partir d'un réseau de microfils ferromagnétiques de CoSiB [21]. Dans ce cas, la permittivité effective négative est attribuée à la nature métallique des microfils. Dans le cadre de cette habilitation, ces matériaux ferroélectriques et ferromagnétiques n'ont pas été exploités en régime dynamique. En revanche, nous avons travaillé sur les possibilités d'agilité offertes par les variations de permittivité d'un film mince soumis à un champ électrique statique. Ce principe a été appliqué à la conception de déphaseurs main gauche accordables présentés au chapitre II.

En conclusion, les récents développements des métamatériaux permettent d'exploiter les quatre cadrans de la figure I-1 par structuration de matériaux métalliques, ferroélectriques ou ferromagnétiques. Par nature, les milieux simplement négatifs, correspondant aux cadrans 2 et 4, sont évanescents. En revanche, les milieux doublement négatifs peuvent être propagatifs au même titre que les milieux doublement positifs. Au paragraphe suivant, nous discuterons des différentes possibilités de synthèse d'un milieu doublement négatif à partir d'inclusions métalliques.

I.2 Ingénierie des métamatériaux métalliques doublement négatifs

I.21 Superposition de deux milieux simplement négatifs

Au paragraphe précédent, nous avons vu qu'il était possible de synthétiser des milieux à permittivité ε_{eff} et perméabilité μ_{eff} effectives négatives à partir de réseaux de fils et de boucles de courant, respectivement. La première idée consiste à superposer ces deux réseaux pour définir un milieu doublement négatif qui sera caractérisé par un indice de réfraction négatif n défini par la relation suivante :

$$n = \sqrt{\mu_{eff} . \varepsilon_{eff}} \quad (2)$$

Du point de vue de la conception, il faut veiller au recouvrement des plages fréquentielles de permittivité et de perméabilités effectives négatives afin de définir une bande passante main gauche, par le choix des dimensions géométriques caractérisant chaque milieu. La figure I-4 représente les fonctions de dispersion de Drude et de Lorentz décrivant respectivement la permittivité effective d'un réseau de fils et la perméabilité effective d'un SRR. En première approximation, la réponse SRR fixe la bande passante du milieu doublement négatif comprise entre la fréquence de résonance et la fréquence plasma magnétique. D'un point de vue pratique, on cherche à minimiser les pertes qui se manifestent par des augmentations des parties imaginaires. Par conséquent, les dimensions géométriques sont optimisées de manière à placer la zone fréquentielle de perméabilité effective négative juste avant la fréquence plasma électrique. Par ailleurs, ce critère de conception permet de travailler avec des valeurs d'indice de réfraction proche de l'unité, condition nécessaire pour les applications en focalisation [22].

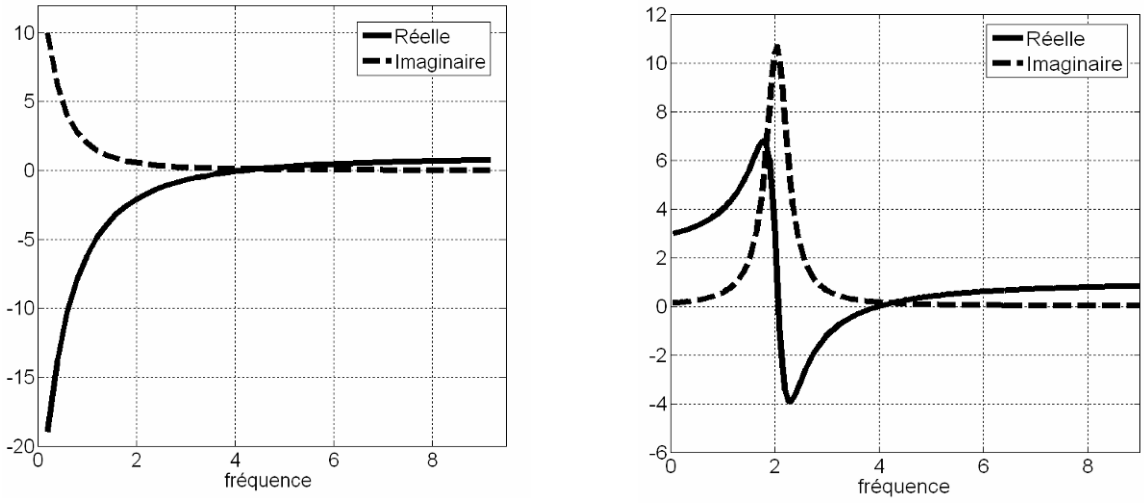

Figure I-4 : Illustration des modèles de dispersion de (a) Drude (permittivité d'un réseau de fils), (b) Lorentz (perméabilité d'un SRR) pour une pulsation plasma $\omega_p = 5$, une pulsation de résonance $\omega_0 = 3$ et une pulsation de perte $\omega_c = 0{,}5$.

Dans la pratique, la réponse fréquentielle du milieu doublement négatif ne correspond pas à la superposition des spectres de chaque milieu simplement négatif. En effet, on peut comprendre que l'imbrication de résonateurs fendus au sein du réseau de fils modifie le facteur

de remplissage, ce qui se traduit par un décalage de la fréquence plasma électrique. En outre, les effets de couplage entre les objets métalliques placés en proximité affectent la réponse globale du système. A priori, on dispose d'une grande marge de manœuvre dans la conception de chaque réseau simplement négatif. Cependant, la nécessité de travailler avec la même périodicité afin de définir le milieu doublement négatif limite les degrés de liberté. Ces difficultés associées au caractère résonant, donc fortement dispersifs des résonateurs fendus se traduisent par un spectre de transmission incluant une bande main gauche relativement étroite d'une part. D'autre part, le niveau de transmission en bande passante main gauche est affecté par l'augmentation des pertes qui accompagne la résonance des SRR.

La première alternative à cette approche résonante du milieu de propagation main gauche est le concept de ligne duale décrit dans la suite de ce paragraphe.

I.22 Concept de ligne duale

Ce concept s'appuie sur la représentation d'une ligne de propagation TEM au moyen d'éléments distribués. Le schéma équivalent d'une cellule unitaire sans pertes fait intervenir un terme d'inductance en série L_s associée à un terme de capacité en parallèle C_p (figure I-5a). La constante de phase est alors donnée par l'expression :

$$\beta = \omega\sqrt{L_s.C_p} \quad (3)$$

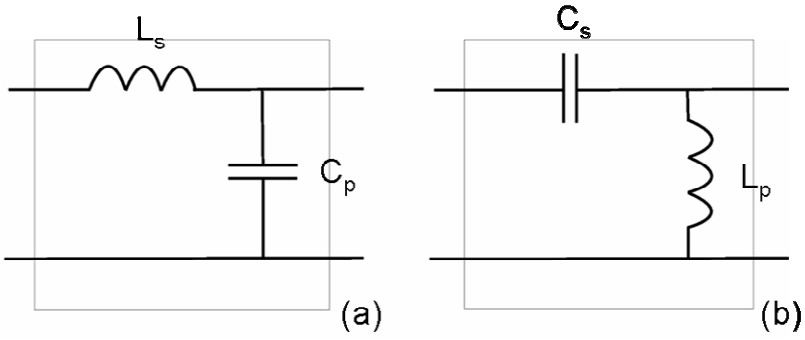

Figure I-5 : Schéma équivalent de la cellule unitaire d'une ligne classique (main droite) et duale (main gauche).

Si l'on permute la position des éléments inductif et capacitif, on obtient le schéma de la figure I-5b. Dans ce cas, on peut montrer que la constante de phase s'écrit :

$$\beta = \pm \frac{1}{\omega \sqrt{L_p . C_s}} \quad (4)$$

Cette expression fait apparaître une solution négative qui signifie une opposition des vitesses de phase et de groupe. Par conséquent, la ligne duale autorise une rétropropagation de la phase. Cette idée, réactualisée dans le contexte des métamatériaux simultanément par les groupes de T. Itoh [23] et G. V. Eleftheriades [24], a conduit à la conception d'un grand nombre de dispositifs tels que des filtres, des coupleurs et des déphaseurs [25-27]. Elle a aussi permis d'aborder la démonstration expérimentale de nouveaux phénomènes physiques tels que la focalisation sous longueur d'onde [28]. Ces études ont bénéficié d'une facilité de mise en œuvre dans le domaine des micro-ondes. En effet, elles s'appuient sur les techniques de fabrication et de caractérisation des circuits plaqués largement répandus tant dans la recherche que dans l'industrie. Nous nous proposons ici de commenter cette approche afin de mieux cerner son champ d'application.

D'un point de vue fondamental, la relation (4) montre que la permutation des termes capacitif et inductif au sein de la cellule unitaire rend le milieu dispersif. Néanmoins, cette dispersion est bien moindre que dans le cas des milieux doublement négatifs qui utilisent des résonateurs. C'est le principal atout du concept de ligne duale. En effet, dans son principe l'obtention d'une bande de transmission main gauche ne repose pas sur un phénomène de résonance. En termes de performance, cela se traduit par une augmentation des niveaux de transmission et un élargissement des bandes passantes. Ce concept apparaît donc prometteur pour le domaine des longueurs d'onde millimétriques et submillimètriques où la contribution des pertes vient inévitablement entacher les performances d'une structure idéale. Notre groupe de recherche a publié en 2005 une démonstration expérimentale de rétropropagation de la phase à la fréquence de 300 GHz à partir d'une structure de propagation conçue sur le modèle d'une ligne duale [29]. Il convient toutefois de noter que la ligne duale idéale telle que schématisée par la figure I-5b est difficile à synthétiser en micro-ondes. En effet, en pratique, on travaille sur la base

d'une ligne de transmission classique correspondant à un milieu de propagation main droit. Cette ligne de transmission est périodiquement chargée par des éléments localisés : inductances en shunt et capacités en série, ce qui se traduit par le schéma équivalent de la figure I-6. Ce circuit équivalent, qui décrit une cellule unitaire, inclut non seulement des termes de capacité en série et d'inductance en shunt mais également des termes d'inductance en série et de capacité en shunt décrivant le milieu hôte. Cela signifie que le comportement fréquentiel d'une ligne duale réelle sera également gouverné par des phénomènes de résonance. Cependant, à la différence des milieux doublement négatifs à base de SRR, la transmission fait intervenir les contributions de deux fréquences de résonance distinctes, l'une correspondant au circuit série ($f_s = \frac{1}{2\pi\sqrt{L_s C_s}}$) et l'autre au circuit parallèle ($f_p = \frac{1}{2\pi\sqrt{L_p C_p}}$) [30]. En cas d'égalité des fréquences de résonance série et parallèle, obtenue pour la condition $L_p C_p = L_s C_s$, le diagramme de dispersion présente une continuité des bandes gauchères et droitières sans bande interdite. On parle dans ce cas de comportement composite équilibré. Le point de croisement caractérisé par une vitesse de phase nulle à vitesse de groupe non nulle est particulièrement intéressant en termes d'applications dans la mesure où il correspond à un régime de longueur d'onde infinie. Par conséquent, pour la conception des structures de propagation ou de rayonnement, il permet de s'affranchir de la limitation liée à la longueur électrique [31].

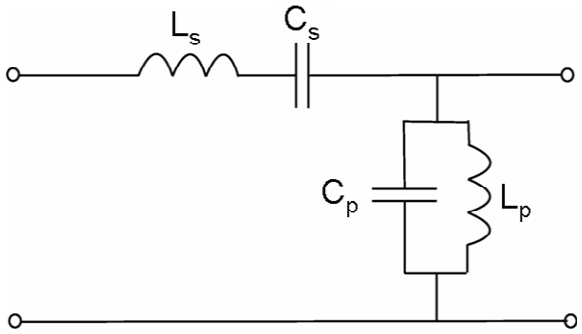

Figure I-6 : Schéma équivalent de la cellule unitaire d'une ligne duale incluant les constantes localisées du milieu hôte.

Par ailleurs, une structure équilibrée peut présenter une avance de phase, un retard de phase ou un déphasage nul en fonction de la fréquence. Inversement, si l'on envisage une possibilité d'accord d'un ou plusieurs éléments du schéma équivalent, on peut alors, à fréquence constante, modifier le signe du déphasage en déplaçant la fenêtre de transmission par rapport à la fréquence centrale. C'est cette possibilité que nous avons exploitée pour la conception d'un déphaseur accordable qui sera présenté au chapitre II [27].

En dépit de tous les avantages présentés par la ligne duale, la généralisation de ce concept aux métamatériaux volumiques n'est pas directe. De plus, sur le plan technologique, si des métasurfaces, notamment sur la base d'un réseau de motifs élémentaires en forme de champignons, ont été proposées, la fabrication de structures tridimensionnelles apparaît délicate. Comme nous l'avons précédemment mentionné, le principal atout de la ligne duale par rapport aux réseaux de fils et SRR réside dans son caractère non résonnant. Or, nous avons montré que le schéma équivalent de la ligne duale idéale devait être complété pour prendre en compte le milieu hôte, incontournable d'un point de vue pratique. Par conséquent, la ligne duale ne peut pas être perçue comme une structure strictement non résonante mais plutôt comme une structure dont le fonctionnement implique la contribution de plusieurs circuits résonnants qui peuvent être accordés par ajustement des constantes localisées. Sur cette base, on peut imaginer une approche hybride entre les milieux doublement négatifs constitués de réseaux de fils et de résonateurs fendus et les lignes duales. C'est dans cette perspective que nous introduisons les réseaux de boucles de courants interconnectées.

I.23 Réseaux de boucles de courant interconnectées

Les forts coefficients de qualité observés dans les résonateurs en anneaux fendus peuvent satisfaire les critères de sélectivité et de compacité de filtres [32]. En revanche, ils ne sont pas favorables en termes de largeur de bande et de niveau de pertes. Ce coefficient de qualité peut être réduit par l'interconnexion de plusieurs résonateurs. C'est l'idée des chaînes infinies de motifs Ω [33, 34] ou S [35] dont les cellules unitaires sont représentées en figure I-7.

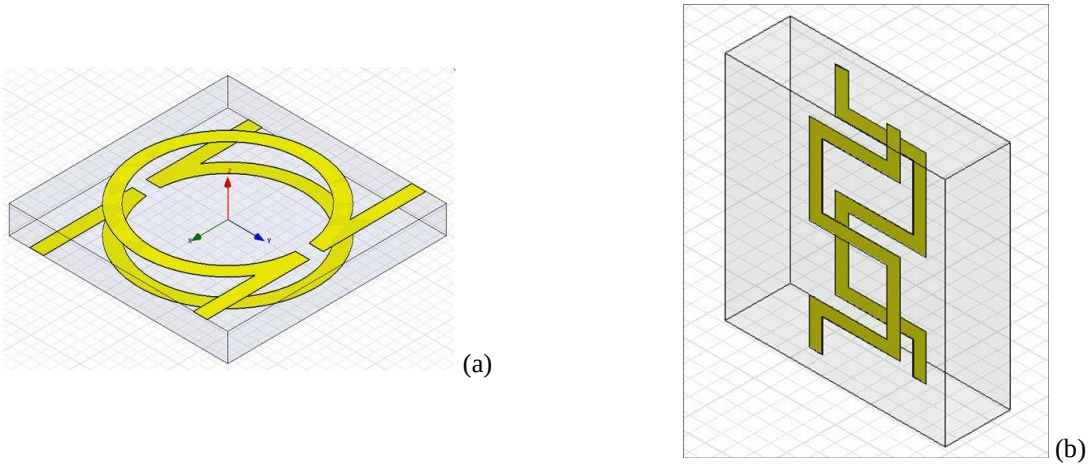

(a) (b)

Figure I-7 : Cellules unitaires d'un réseau de lettres (a) Ω et (b) S interconnectées.

À la base, ce type de motif inclut un dipôle électrique et un dipôle magnétique. Par conséquent, le milieu doublement négatif peut être synthétisé par un seul réseau de particules identiques par opposition à la superposition des réseaux de fils et de résonateurs fendus. Nous avons beaucoup travaillé sur ce type de géométrie. Nos principaux résultats sont détaillés aux second et troisième chapitres.

La modélisation de ces réseaux par éléments localisés permet de mettre en évidence les contributions d'un terme capacitif en série et d'un terme inductif en parallèle [36]. La particule Ω constituée de deux lettres disposées en vis-à-vis afin de compenser les effets de bianisotropie, peut donc être modélisée, en première approximation, par les éléments localisés qui décrivent la cellule unitaire d'une ligne duale. On va donc retrouver le comportement composite incluant des bandes passantes gauchère et droitière relativement larges qui peuvent se rejoindre au point $\beta = 0$,

lorsque la condition d'équilibre est vérifiée. Cette possibilité de travailler à indice de réfraction négatif, nul ou positif dans une approche de métamatériau volumique est très intéressante pour le domaine de la sélection angulaire [37]. Par ailleurs, en raison des caractères large bande et faibles pertes, ces réseaux interconnectés présentent un avantage incontestable sur les métamatériaux composés de plans de fils et de SRR pour les longueurs d'onde millimétriques et submillimétriques [34].

Il convient toutefois de préciser que ces structures, bien que volumiques, restent fondamentalement unidimensionelles. En effet, le régime de paramètres effectifs négatifs n'est atteint que sous certaines conditions de polarisation de l'onde incidente : le vecteur champ magnétique doit être perpendiculaire au plan des motifs afin d'exciter les boucles de courant et le vecteur champ électrique doit être parallèle aux chaînes de motifs interconnectés. L'excitation de ces structures avec différents angles d'incidence nécessite une description des paramètres effectifs au moyen de tenseurs [38]. En dépit des potentialités intrinsèques de ces métamatériaux pour les fréquences élevées, leurs conditions de polarisation vont se traduire par une barrière technologique aux longueurs d'onde submillimétriques. En effet, les dimensions mises en jeu au-delà de quelques dizaines de gigahertz impliquent le recours aux procédés de fabrication de la microélectronique. Or ces procédés sont essentiellement planaires et il semble difficile de fabriquer un empilement suffisamment épais pour exciter le métamatériau par la tranche afin de satisfaire les conditions de polarisation précédemment décrites. Des polarisations alternatives peuvent permettre, sous certaines conditions, de mettre en évidence un régime de réfraction négatif. On perd dans ce cas le bénéfice du caractère large bande et le spectre submillimétrique ne semble accessible qu'au prix d'une technologie très pointue [39].

Cette difficulté a motivé le développement de structures métamatériaux pour l'incidence normale.

I.24 Métamatériaux pour l'incidence normale

Même si les plans de résonateurs fendus peuvent être excités sous incidence normale grâce à la contribution du champ électrique [14], l'activité magnétique dans bon nombre de cas, n'est pas suffisante pour inverser le signe de la perméabilité. Cette difficulté constitue une

barrière pour les applications, aux hautes fréquences notamment, où cette inversion potentielle est inévitablement masquée par les pertes. Les structures spécifiquement définies pour l'incidence normale sont basées sur l'idée de matérialiser des boucles de courant dont l'axe de rotation est parallèle au plan des motifs. La première solution consiste à fabriquer des résonateurs perpendiculairement au substrat. Cette solution reprend le concept du SRR en s'appuyant sur des techniques de fabrication spécifiques telles que la croissance électrolytique ou la définition de via-holes. La seconde solution exploite les contributions des courants de conduction et de déplacement au sein d'une particule composée de deux rubans métalliques séparés par une couche de diélectrique. Il s'agit du concept de nanorod introduit par Shalaev [40]. En travaillant uniquement sur ce nanorod, il apparaît difficile de superposer les réponses magnétiques et électriques pour définir une particule doublement négative. Cette difficulté peut être levée en combinant un réseau de nanorods, autrement dit de dipôles magnétiques, avec un réseau de rubans métalliques continus à même de synthétiser un milieu à perméabilité effective négative. Le concept de structure fishnet [41] reprend cette idée en interconnectant les nanorods suivant la direction du champ électrique. On retrouve ici l'idée des réseaux de boucles de courant interconnectées (cf. paragraphe 2.3) transposée sur un plan normal au vecteur d'onde.

Si l'on souhaite tirer pleinement parti des propriétés de réfraction anormale, il est indispensable de définir une structure en volume, ce qui revient à empiler plusieurs plans de motifs tels que ceux précédemment décrits. Suivant ce principe, le groupe de Zhang a récemment démontré la réfraction négative autour de 1,7 nm à partir d'un prisme défini dans un empilement de plusieurs couches structurées par des réseaux fishnet [2]. Parallèlement, le groupe de M. Sorolla a fait la même démonstration aux longueurs d'onde millimétriques à partir d'un prisme constitué de grilles métalliques percées par des ouvertures sous longueur d'onde [42]. Ce travail s'appuie sur une étude antérieure [43] visant à établir la relation entre la transmission extraordinaire observée dès 1998 par T. Ebbesen [44] et la réropropagation de la phase dans un empilement de réseaux sous longueur d'onde. Il convient ici de souligner la parenté entre les trois structures précédemment décrites. En effet, en vertu du principe de Babinet [45], le réseau de nanorods peut être perçu comme un réseau fishnet complémentaire. De même, en première approximation, le réseau fishnet présente des similitudes avec les réseaux sous longueur d'onde.

Toutefois, en raison de la complexité des phénomènes et des différents régimes observés en fonction des paramètres géométriques, il est difficile, à ce stade de l'étude de parler d'équivalence au sens strict. Nous présenterons au troisième chapitre les premiers résultats obtenus sur des métamatériaux à réseaux sous longueur d'onde pour le spectre térahertz.

I.3 Applications des métamatériaux électromagnétiques

Le choix d'une topologie sera fixé par le type d'application envisagée. Dans ce paragraphe, nous regroupons l'éventail de ces applications sous deux catégories génériques qui sont la sélection fréquentielle et la sélection spatiale.

I.31 Sélection fréquentielle

On distingue ici la propagation guidée de la propagation en espace libre.

I.311 Propagation guidée

Même si plusieurs démonstrations expérimentales ont utilisé un environnement de guide rectangulaire [46-48], en ce qui concerne les applications, on s'intéresse plus particulièrement aux structures plaquées de type coplanaire ou microstrip en raison de leur facilité de mise en œuvre principalement. De plus l'argument de la compacité des structures métamatériaux devient caduc si la structure est insérée dans un guide métallique encombrant. Cette propriété de compacité des filtres à métamatériaux repose sur l'emploi de circuits résonnants. En effet, dans l'approche du réseau doublement négatif, on peut tirer parti des forts coefficients de qualité présentés par les SRR pour obtenir de grandes sélectivés et d'importantes réjections à partir d'un nombre réduit de cellules unitaires [32, 49]. Par ailleurs, dans l'approche de la ligne duale, on peut, à la condition d'équilibre du régime composite équilibré, définir un résonateur d'ordre zéro [31]. En principe, ce résonateur d'ordre zéro qui exploite un régime de longueur d'onde infinie peut être infiniment petit. Toutefois, sa mise en œuvre repose sur l'utilisation d'éléments localisés qui présentent un certain encombrement. Dans la pratique, on peut cependant admettre un encombrement plus faible que la demi-longueur d'onde correspondant au résonateur d'ordre 1. Il convient de préciser que cette condition d'équilibre qui repose sur une stricte égalité des

fréquences de résonance série et parallèle peut être difficile à maîtriser compte tenu des tolérances de fabrication. Indépendamment de la compacité, les structures métamatériaux offrent de nouveaux degrés de liberté pour l'optimisation des gabarits de filtrage. Dans ce contexte, les différentes études menées à bases de SRR et de SRR complémentés (CSRR), par le groupe de F. Martin notamment, offrent un large éventail des différentes possibilités [50]. Il faut néanmoins reconnaître que l'optimisation des topologies de filtres plus classiques est bien maîtrisée grâce au recours à des méthodes de synthèse. Or ces méthodes, souvent basées sur la théorie des lignes, ne peuvent pas forcément être transposées aux structures métamatériaux qui sont généralement très dispersives. En termes de fonctionnalité, le principal apport des métamatériaux réside dans la possibilité d'obtenir un milieu de propagation doublement négatif. Or, dans le contexte d'une structure de propagation, cela se traduit par une rétropropagation de la phase de l'onde. Cette propriété est de second ordre dans le cadre du filtrage fréquentiel où le principal critère porte sur l'amplitude du signal transmis. En revanche, la possibilité de travailler avec un déphasage positif, négatif ou nul peut s'avérer très intéressante pour le domaine du routage de l'information. C'est ce qui motive l'emploi des métamatériaux dans les circuits coupleurs et déphaseurs [26, 27] notamment.

I.312 Propagation en espace libre

Les structures métamatériaux pour la sélection fréquentielle en espace libre s'appuient sur le concept de surface sélective en fréquence, en anglais Frequency Selective Surface (FSS), largement exploré depuis la seconde moitié du XX^{ème} siècle [51-54]. Les dispositifs de bases sont des surfaces partiellement masquées par des motifs métalliques. La transmission d'une onde, en incidence normale ou oblique, à travers ces surfaces, est fonction de la fréquence. Les FSS sont très utilisées aux longueurs d'onde millimétriques et submillimétriques dès lors que l'on privilégie la propagation en espace libre [53]. En première approximation, le comportement d'une FSS peut être décrit par un schéma équivalent. Ainsi, la structuration la plus simple consiste à définir un réseau de rubans métalliques. Suivant la polarisation de l'onde incidence, on pourra observer un comportement inductif si le vecteur champ électrique est parallèle aux rubans ou capacitif s'il est perpendiculaire. En termes de filtrage, ces réseaux inductifs et capacitifs sont

à l'origine de comportements passe-haut ou passe-bas, respectivement. La combinaison des ouvertures parallèle et perpendiculaire sur un même plan permet de définir un réseau de trous carrés ou de patchs. De tels réseaux présenteront plusieurs fréquences de coupure. Sur ces bases de conception, plusieurs motifs résonnants tels que des boucles de courant [55] ou des croix de Jérusalem [56] ont été proposés en vue d'une ingénierie de la réponse fréquentielle. Il est évident que ces structures dont les dimensions de motifs peuvent être inférieures à la longueur d'onde s'apparentent avec ce que l'on désigne sous le terme de métamatériau depuis environ 10 ans. Néanmoins, la terminologie métamatériau est associée à la notion de milieu moyen. Or, dans la mesure où la FSS se limite à un plan, on ne peut pas véritablement parler de propagation et cette structure ne peut pas être décrite par des paramètres constitutifs effectifs. Ces dernières années, plusieurs groupes de recherche dont celui de N. Engheta ont replacé les FSS dans le contexte des métamatériaux en proposant des aspects nouveaux quant à l'analyse et à la conception de ces structures. En particulier, la notion de propagation est introduite par le biais de deux surfaces structurées placées en regard définissant une lame, ou « slab » [57, 58].

Cette définition de « slab » permet d'introduire des aspects volumiques. La dispersion de la constante de propagation à l'origine de la sélection fréquentielle dans les structures unidimensionnelles se traduit par une dispersion de l'indice de réfraction qui peut être exploitée pour des applications de sélection spatiale.

I.32 Sélection spatiale

Les applications en sélection spatiale sont regroupées sous trois grandes catégories qui sont la réfraction, la focalisation et le contournement d'un obstacle plus communément désigné par le terme anglais de cloaking qui signifie revêtir ou masquer.

I.321 Réfraction

Le travail précurseur de V. G. Veselago, publié en 1968, a montré qu'un milieu doublement négatif pouvait être décrit par un indice de réfraction négatif [5]. Cette hypothèse a été vérifiée, environ 30 ans plus tard, par la démonstration expérimentale de D. R. Smith [1]. Cette première expérience de réfraction a été largement reprise par différents groupes de

recherche comme outil de description qualitatif et quantitatif [2, 38, 59]. D'un point de vue théorique, la réfraction négative est décrite par la loi de Snell-Descartes énoncée par la relation suivante :

$$n_1.\sin\theta_1 = n_2.\sin\theta_2 \quad (5)$$

où n_1 et n_2 sont les indices de réfraction des milieux 1 et 2 respectivement et θ_1, θ_2, l'angle de réfraction par rapport à la normale de leur plan de jonction. Par conséquent, la mesure de l'angle de réfraction en fonction de la fréquence permet de déduire l'évolution de l'indice donc de reconstituer le diagramme de dispersion. En termes d'application, la possibilité de faire varier l'indice de réfraction d'un matériau effectif peut être mise à profit pour le routage de l'information [60] ou pour contrôler le diagramme de rayonnement d'une antenne [61]. Il convient de rappeler que beaucoup de structures, notamment celles constituées de réseaux de fils et de SRR sont fortement anisotropes. C'est la raison pour laquelle la plupart des expériences de réfraction sont menées sur des prismes, ce qui permet de conserver une direction de propagation parallèle à la normale à l'intérieur de la structure métamatériau. L'angle de réfraction est alors mesuré dans l'air lorsque l'onde traverse la face inclinée du prisme. Cette difficulté n'est pas insurmontable, mais si l'on veut dépasser le stade de cette simple démonstration expérimentale, il est nécessaire de prendre en compte la variation des paramètres effectifs en fonction de l'angle d'incidence qui peut être décrite par des tenseurs de permittivité et de perméabilité [38]. Les expériences de réfraction sont menées en condition d'onde incidente plane. Si l'on considère à présent l'émission d'une onde par une source ponctuelle, donc divergente, la réfraction négative se traduit par un phénomène de focalisation.

I.322 Focalisation

La possibilité de réfracter une onde avec un angle négatif signifie que l'on peut également focaliser une onde à l'aide d'une lentille plane (figure I-8a). De plus, J. B. Pendry a montré qu'il était envisageable de descendre sous la limite de diffraction de Rayleigh, autrement dit de focaliser une image avec une résolution inférieure à la demi-longueur d'onde. Ce phénomène est justifié par l'amplification des ondes évanescentes à l'intérieur du milieu doublement négatif (figures I-8b et I-8c) [22]. De cette démonstration théorique est né le concept de superlentille.

Malgré le grand intérêt suscité par cette découverte, on relève à ce jour peu de démonstrations expérimentales en raison des contraintes qu'implique sa mise en œuvre pratique [28, 62]. Tout d'abord, le principe de focalisation tel qu'illustré par la figure I-8a sous-entend de travailler avec un indice de réfraction à l'intérieur de la lentille exactement opposé à celui de l'environnement extérieur. Si ces indices ne sont pas égaux en valeur absolue, on n'obtient pas de point focal à l'intérieur de la lentille. Concrètement, si la lentille est interfacée avec l'air, son indice de réfraction doit être égal à -1. De plus, pour limiter les réflexions aux interfaces, il est impératif de respecter la condition d'adaptation d'impédance. Par conséquent, les paramètres effectifs de la lentille doivent respecter les deux équations suivantes :

$$n = -\sqrt{\mu_{eff}\,\varepsilon_{eff}} = -1 \quad \text{et} \quad z = \sqrt{\frac{\mu_{eff}}{\varepsilon_{eff}}} = 1$$

où z est l'impédance réduite. Cela implique que les permittivité et perméabilité effectives valent toutes deux -1. Enfin, pour les applications en focalisation, la condition d'anisotropie du milieu est primordiale. Ces difficultés expliquent pourquoi, jusqu'à présent, la plupart des démonstrations expérimentales de superlentille utilisent des cristaux photoniques, qui à défaut de travailler en régime de métamatériau, offrent certaines facilités de conception notamment au niveau du critère d'isotropie. Cette voix a été explorée avec succès dans notre groupe de recherche pour la longueur d'onde de 1,5 µm [11].

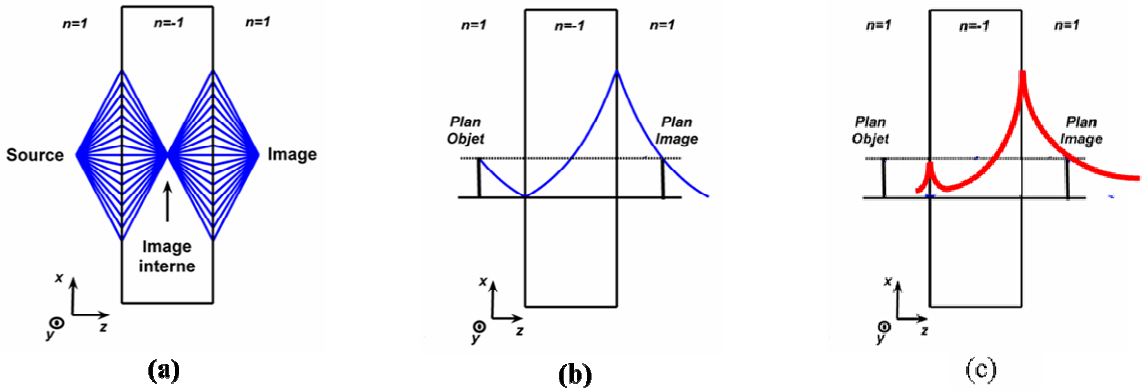

Figure I-8 : Illustrations des propriétés de la superlentille (a) focalisation, (b) et (c) amplification des ondes évanescentes.

Cependant, il est possible de relaxer ces contraintes en travaillant à partir d'un milieu simplement négatif. Cette situation implique nécessairement de travailler en champ proche dans la mesure où, comme nous l'avons déjà mentionné, le métamatériau simplement négatif n'est pas propagatif. Ainsi, la résolution sous longueur d'onde a été démontrée dans le domaine de l'ultraviolet à partir d'une lame d'argent qui présente une permittivité négative jusqu'à sa fréquence plasma [63]. Plus récemment, une lentille à perméabilité négative a été testée par le groupe de R. Marqués dans le contexte de l'imagerie à résonance magnétique, soit à quelques dizaines de mégahertz [64].

Les différents aspects abordés dans ce paragraphe sont révélateurs de l'évolution de la recherche dans le domaine des métamatériaux. En effet, face aux difficultés de mise en œuvre de la lentille parfaite, les efforts se diversifient afin d'explorer d'autres pistes qui permettent de supporter certaines contraintes telles que celles du milieu simplement négatif ou de l'anisotropie. Le meilleur exemple de cette tendance est certainement celui du cloaking qui, indépendamment de l'engouement médiatique suscité par le mot clef d'invisibilité, jette les bases de nouvelles méthodes de travail à partir des métamatériaux.

I.323 Le cloaking

Le cloaking consiste à rendre invisible un objet en l'enrobant d'un métamatériau. Ce concept est particulièrement prometteur en termes d'applications, dans le domaine de la défense notamment. Dans ce contexte, le cloaking se distingue de l'approche classique de la furtivité. En effet, cette dernière repose sur un mécanisme d'absorption. Le signal incident est dans ce cas atténué par un matériau absorbant qui recouvre l'objet qu'on souhaite masquer. En revanche, dans le principe du cloaking, l'onde incidente contourne l'objet sans atténuation. La cloak idéale est donc sans pertes. Le principe du cloaking tel que proposé par J. B. Pendry en 2006 [65] est illustré par la figure I-9.

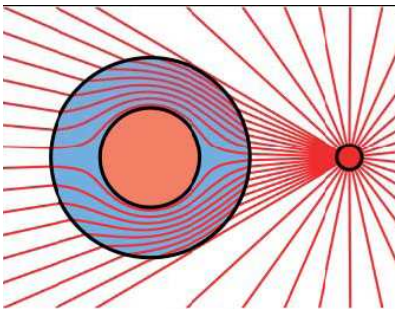

Figure I-9 : Illustration du principe de cloaking ou contournement d'un obstacle à partir d'une source ponctuelle [65].

Cette application emblématique jette les bases d'une nouvelle approche de conception des structures à métamatériaux. En effet, jusqu'à présent les efforts se sont concentrés sur la manière de synthétiser un milieu moyen qui se comporterait comme un matériau homogène présentant des propriétés singulières. C'est le cas notamment pour l'exemple de la superlentille précédemment mentionné. Avec le cloaking, on essaye de tirer parti du caractère globalement inhomogène d'une structure métamatériau pour synthétiser un gradient d'indice. La méthode employée repose sur une transformation conforme de l'espace environnant l'objet à masquer. Cette transformation conforme vise à définir des tenseurs de permittivité et de perméabilité qui vont permettre le guidage de l'onde électromagnétique autour de l'objet et la réduction de la section efficace de diffusion du rayonnement arrivant sur l'objet (figure I-9). Pour une cloak sphérique ou cylindrique les paramètres effectifs du métamatériau s'exprimeront en fonction du rayon. La dernière étape de conception consiste à choisir des géométries d'inclusions métalliques ou diélectriques à même de traduire ces variations. À titre d'exemple, l'énoncé théorique de J. B. Pendry a été immédiatement suivi d'une démonstration expérimentale de masquage d'un cylindre métallique aux longueurs d'ondes centimétriques. Dans cette étude, la cloak traduit une variation de perméabilité réalisée au moyen de plusieurs niveaux de résonateurs en anneau fendus de dimensions différentes. Notre groupe de recherche a proposé une cloak pour le domaine térahertz qui, au lieu de SRR métalliques, exploite les résonances de Mie dans des cubes de BST [17]. Indépendamment des pertes qui dégradent les performances en introduisant des perturbations dans les cartes de champ, ces deux exemples laissent entrevoir la limitation pratique du procédé de cloaking. Dès lors que les variations d'indices sont réalisées par des dispositifs résonants, les

bandes passantes sont forcément très étroites. On mesure la distance qui nous sépare d'une cloak à même de couvrir l'ensemble du spectre visible. En dépit de cette limitation qui freine la quête de l'invisibilité au sens strict, le cloaking présente un intérêt pour bon nombre de systèmes d'émission-réception à porteuse unique. L'approche de conception basée sur la transformation conforme ne se limite pas au cloaking. Elle est employée pour la proposition de plusieurs dispositifs pour l'espace libre tels que les antennes [66] ou les lentilles, et notamment l'hyperlens dont l'objectif est la projection en champ lointain de détails sous longueur d'onde magnifiés [67].

Conclusion

Ce chapitre introductif nous a permis de décrire les grandes évolutions des structures à métamatériau depuis les premières solutions technologiques suggérées il y a environ dix ans.

Dans la première partie, nous avons défini et situé les métamatériaux électromagnétiques dans une classification globale qui s'appuie sur les paramètres constitutifs qui sont la permittivité et la perméabilité.

Dans la seconde partie, nous avons décrit et commenté les différentes solutions permettant de synthétiser un milieu doublement négatif à partir d'éléments métalliques (ε_{eff} et $\mu_{eff} < 0$). Cette analyse a permis de cerner les limitations des deux grandes approches qui sont le réseau composé de SRR et de fils et la ligne duale afin d'introduire des solutions alternatives.

Enfin, nous avons consacré la dernière partie de ce chapitre aux applications qui s'organisent autour des deux dispositifs clefs qui sont la superlentille et le cloaking. Cette étude est à la fois révélatrice des difficultés de synthétiser un milieu doublement négatif parfait (isotrope, large bande et faible pertes) et de la maîtrise conceptuelle et technologique des outils de base qui permettent désormais d'envisager la conception d'une structure à partir d'une répartition donnée des champs dans l'espace (transformation conforme).

La suite de ce mémoire est organisée autour des différentes études que j'ai menées sur les métamatériaux depuis ma prise de fonction à l'Université des Sciences et Technologies de Lille en septembre 2003. Le second chapitre est consacré aux structures unidimensionelles en environnement guidé. Il regroupe les trois approches décrites au paragraphe I. 2, à savoir celle de

la superposition des réseaux de fils et SRR, celle de la ligne duale et l'approche hybride utilisant des anneaux résonnants interconnectés. Le troisième chapitre est dédié aux métamatériaux volumiques. La première partie de ce chapitre est consacrée à l'étude de métamatériaux réalisés à partir de réseaux de lettres Ω interconnectées pour les longueurs d'onde centimétriques et millimétriques. Dans la seconde partie, nous présentons les premiers résultats obtenus sur un métamatériau doublement négatif fonctionnant en incidence normale dans le domaine térahertz.

Références

[1] R. A. Shelby, D. R. Smith, and S. Schultz, "Experimental verification of a negative index of refraction," *Science*, pp. 77-79, 2001.

[2] J. Valentine, S. Zhang, T. Zentgraf, E. Ulin-Avila, D. A. Genov, G. Bartal, and X. Zhang, "Three-dimensional optical metamaterial with a negative refractive index," *Nature*, vol. 455, pp. 376-379, 2008.

[3] C. Huanyang and C. T. Chan, "Acoustic cloaking in three dimensions using acoustic metamaterials," *Applied Physics Letters*, vol. 91, pp. 183518, 2007.

[4] K. J. Morton, K. Loutherback, D. W. Inglis, O. K. Tsui, J. C. Sturm, S. Y. Chou, and R. H. Austin, "Hydrodynamic metamaterials: Microfabricated arrays to steer, refract, and focus streams of biomaterials," *Proceedings of the National Academy of Sciences*, vol. 105, pp. 7434-7438, 2008.

[5] V. G. Veselago, "The electrodynamics of substances with simultaneously negative values of epsilon and mu," *Soviet Physics Uspekhi*, pp. 509, 1968.

[6] P. B. Johnson and R. W. Christy, "Optical Constants of the Noble Metals," *Physical Review B*, vol. 6, pp. 4370, 1972.

[7] J. B. Pendry, A. J. Holden, D. J. Robbins, and W. J. Stewart, "Low frequency plasmons in thin-wire structures," *Journal of Physics: Condensed Matter*, pp. 4785, 1998.

[8] J. M. Lourtioz, A. de Lustrac, F. Gadot, S. Rowson, A. Chelnokov, T. Brillat, A. Ammouche, J. Danglot, O. Vanbesien, and D. Lippens, "Toward controllable photonic crystals for centimeter- and millimeter-wave devices," *Lightwave Technology, Journal of*, vol. 17, pp. 2025-2031, 1999.

[9] D. R. Smith, W. J. Padilla, D. C. Vier, S. C. Nemat-Nasser, and S. Schultz, "Composite Medium with Simultaneously Negative Permeability and Permittivity," *Physical Review Letters*, vol. 84, pp. 4184, 2000.

[10] J. M. Lourtioz and A. d. Lustrac, "Metallic photonic crystals," *Comptes Rendus de Physique* vol. 3, pp. 79-88, 2002.

[11] N. Fabre, L. Lalouat, B. Cluzel, X. Melique, D. Lippens, F. d. Fornel, and O. Vanbesien, "Optical Near-Field Microscopy of Light Focusing through a Photonic Crystal Flat Lens," *Physical Review Letters*, vol. 101, pp. 073901, 2008.

[12] K. Teruhiro, T. Takanori, and H. Kenichi, "Negative permeability spectra in Permalloy granular composite materials," *Applied Physics Letters*, vol. 88, pp. 172502, 2006.

[13] J. B. Pendry, A. J. Holden, D. J. Robbins, and W. J. Stewart, "Magnetism from conductors and enhanced nonlinear phenomena," *Microwave Theory and Techniques, IEEE Transactions on*, vol. 47, pp. 2075-2084, 1999.

[14] S. Linden, C. Enkrich, M. Wegener, J. Zhou, T. Koschny, and C. M. Soukoulis, "Magnetic Response of Metamaterials at 100 Terahertz," *Science*, vol. 306, pp. 1351-1353, 2004.

[15] J. Zhou, K. Th, M. Kafesaki, E. N. Economou, J. B. Pendry, and C. M. Soukoulis, "Saturation of the Magnetic Response of Split-Ring Resonators at Optical Frequencies," *Physical Review Letters*, vol. 95, pp. 223902, 2005.

[16] S. O'Brien and J. B. Pendry, "Photonic band-gap effects and magnetic activity in dielectric composites," *Journal of Physics: Condensed Matter*, pp. 4035, 2002.

[17] D. P. Gaillot, C. Croënne, and D. Lippens, "An all-dielectric route for terahertz cloaking," *Opt. Express*, vol. 16, pp. 3986-3992, 2008.

[18] P. Liang, R. Lixin, C. Hongsheng, Z. Haifei, K. Jin Au, and M. G. Tomasz, "Experimental Observation of Left-Handed Behavior in an Array of Standard Dielectric Resonators," *Physical Review Letters*, vol. 98, pp. 157403, 2007.

[19] L. Kang, Q. Zhao, H. Zhao, and J. Zhou, "Magnetically tunable negative permeability metamaterial composed by split ring resonators and ferrite rods," *Opt. Express*, vol. 16, pp. 8825-8834, 2008.

[20] H. Garcia-Miquel, M. J. Esbri, J. M. Andres, J. M. Garcia, J. M. Garcia-Beneytez, and M. Vazquez, "Power absorption and ferromagnetic resonance in Co-rich metallic glasses," *Magnetics, IEEE Transactions on*, vol. 37, pp. 561-564, 2001.

[21] H. Garcia-Miquel, J. Carbonell, V. E. Boria, and J. Sanchez-Dehesa, "Experimental evidence of left handed transmission through arrays of ferromagnetic microwires," *Applied Physics Letters*, vol. 94, pp. 054103, 2009.

[22] J. B. Pendry, "Negative Refraction Makes a Perfect Lens," *Physical Review Letters*, vol. 85, pp. 3966, 2000.

[23] C. Caloz and T. Itoh, "Application of the transmission line theory of left-handed (LH) materials to the realization of a microstrip "LH line"," *IEEE Antenna and Propagation Society International Symposium*, vol. 2, pp. 412-415, 2002.

[24] A. Grbic and G. V. Eleftheriades, "Experimental verification of backward-wave radiation from a negative refractive index metamaterial," *Journal of Applied Physics*, vol. 92, pp. 5930-5935, 2002.

[25] T. I. Christophe Caloz, "TL Theory of MTMs," in Electromagnetic Metamaterials: Transmission Line Theory and Microwave Applications, 2005, pp. 59-132.

[26] D. Kuylenstierna, A. Vorobiev, P. Linner, and S. Gevorgian, "Composite right/left handed transmission line phase shifter using ferroelectric varactors," *Microwave and Wireless Components Letters, IEEE*, vol. 16, pp. 167-169, 2006.

[27] A. Marteau, G. Vélu, G. Houzet, L. Burgnies, E. Lheurette, J. C. Carru, and D. Lippens, "Ferroelectric tunable balanced right- and left-handed transmission lines," *Applied Physics Letters*, vol. 94, pp. 023507, 2009.

[28] A. Grbic and G. V. Eleftheriades, "Overcoming the Diffraction Limit with a Planar Left-Handed Transmission-Line Lens," *Physical Review Letters*, vol. 92, pp. 117403, 2004.

[29] T. Crepin, J. F. Lampin, T. Decoopman, X. Melique, L. Desplanque, and D. Lippens, "Experimental evidence of backward waves on terahertz left-handed transmission lines," *Applied Physics Letters*, vol. 87, pp. 104105, 2005.

[30] A. Lai, T. Itoh, and C. Caloz, "Composite right/left-handed transmission line metamaterials," *Microwave Magazine, IEEE*, vol. 5, pp. 34-50, 2004.

[31] A. Sanada, C. Caloz, and T. Itoh, "Novel zeroth-order resonance in composite right/left-handed transmission line resonators," *2003 Asia-Pacific Microwave Conference*, 2003.

[32] A. L. Borja, J. Carbonell, V. E. Boria, and D. Lippens, "Symmetrical frequency response in a split ring resonator based transmission line," *Applied Physics Letters*, vol. 93, pp. 203505, 2008.

[33] L. Ran, J. Huangfu, H. Chen, Y. Li, X. Zhang, K. Chen, and J. A. Kong, "Microwave solid-state left-handed material with a broad bandwidth and an ultralow loss," *Physical Review B (Condensed Matter and Materials Physics)*, vol. 70, pp. 073102, 2004.

[34] F. Zhang, D. P. Gaillot, C. Croenne, E. Lheurette, X. Melique, and D. Lippens, "Low-loss left-handed metamaterials at millimeter waves," *Applied Physics Letters*, vol. 93, pp. 083104, 2008.

[35] C. Hongsheng, R. Lixin, H. Jiangtao, Z. Xianmin, C. Kangsheng, M. G. Tomasz, and K. Jin Au, "Left-handed materials composed of only [sans-serif S]-shaped resonators," *Physical Review E (Statistical, Nonlinear, and Soft Matter Physics)*, vol. 70, pp. 057605, 2004.

[36] É. Lheurette, O. Vanbésien, and D. Lippens, "Double negative media using interconnected Omega-type metallic particles," *Microwave and Optical Technology Letters*, vol. 49, pp. 84-90, 2007.

[37] F. Zhang, G. Houzet, E. Lheurette, D. Lippens, M. Chaubet, and X. Zhao, "Negative-zero-positive metamaterial with omega-type metal inclusions," *Journal of Applied Physics*, vol. 103, pp. 084312, 2008.

[38] F. Zhang, S. Potet, J. Carbonell, E. Lheurette, O. Vanbesien, X. Zhao, and D. Lippens, "Negative-Zero-Positive Refractive Index in a Prism-Like Omega-Type Metamaterial," *Microwave Theory and Techniques, IEEE Transactions on*, vol. 56, pp. 2566-2573, 2008.

[39] H. O. Moser, J. A. Kong, L. K. Jian, H. S. Chen, G. Liu, M. Bahou, S. M. P. Kalaiselvi, S. M. Maniam, X. X. Cheng, B. I. Wu, P. D. Gu, A. Chen, S. P. Heussler, S. b. Mahmood, and L. Wen, "Free-standing THz electromagneticmetamaterials," *Opt. Express*, vol. 16, pp. 13773-13780, 2008.

[40] V. M. Shalaev, W. Cai, U. K. Chettiar, H.-K. Yuan, A. K. Sarychev, V. P. Drachev, and A. V. Kildishev, "Negative index of refraction in optical metamaterials," *Opt. Lett.*, vol. 30, pp. 3356-3358, 2005.

[41] S. Zhang, W. Fan, K. J. Malloy, S. R. Brueck, N. C. Panoiu, and R. M. Osgood, "Near-infrared double negative metamaterials," *Opt. Express*, vol. 13, pp. 4922-4930, 2005.

[42] M. Navarro-Cia, M. Beruete, M. Sorolla, and I. Campillo, "Negative refraction in a prism made of stacked subwavelength hole arrays," *Opt. Express*, vol. 16, pp. 560-566, 2008.

[43] M. Beruete, M. Sorolla, and I. Campillo, "Left-handed extraordinary optical transmission through a photonic crystal of subwavelength hole arrays," *Opt. Express*, vol. 14, pp. 5445-5455, 2006.

[44] T. W. Ebbesen, H. J. Lezec, H. F. Ghaemi, T. Thio, and P. A. Wolff, "Extraordinary optical transmission through sub-wavelength hole arrays," *Nature*, vol. 391, pp. 667-669, 1998.

[45] G. Deschamps, "Impedance properties of complementary multiterminal planar structures," *Antennas and Propagation, IRE Transactions on*, vol. 7, pp. 371-378, 1959.

[46] R. Marqués, J. Martel, F. Mesa, and F. Medina, "Left-Handed-Media Simulation and Transmission of EM Waves in Subwavelength Split-Ring-Resonator-Loaded Metallic Waveguides," *Physical Review Letters*, vol. 89, pp. 183901, 2002.

[47] T. Decoopman, O. Vanbesien, and D. Lippens, "Demonstration of a backward wave in a single split ring resonator and wire loaded finline," *Microwave and Wireless Components Letters, IEEE*, vol. 14, pp. 507-509, 2004.

[48] J. Carbonell, L. J. Rogla, V. E. Boria, and D. Lippens, "Design and experimental verification of backward-wave propagation in periodic waveguide structures," *Microwave Theory and Techniques, IEEE Transactions on*, vol. 54, pp. 1527-1533, 2006.

[49] J. Garcia-Garcia, J. Bonache, I. Gil, F. Martin, M. C. Velazquez-Ahumada, and J. Martel, "Miniaturized microstrip and CPW filters using coupled metamaterial resonators," *Microwave Theory and Techniques, IEEE Transactions on*, vol. 54, pp. 2628-2635, 2006.

[50] R. Marqués, F. Martin, and M. Sorolla, *Metamaterials with negative parameters*: Wiley interscience, 2008.

[51] R. Kieburtz and A. Ishimaru, "Scattering by a periodically apertured conducting screen," *Antennas and Propagation, IRE Transactions on*, vol. 9, pp. 506-514, 1961.

[52] C. Chao-Chun, "Scattering by a two-dimensional periodic array of conducting plates," *Antennas and Propagation, IEEE Transactions on*, vol. 18, pp. 660-665, 1970.

[53] A. Saleh and R. Semplak, "A quasi-optical polarization-independent diplexer for use in the beam feed system of millimeter-wave antennas," *Antennas and Propagation, IEEE Transactions on*, vol. 24, pp. 780-785, 1976.

[54] V. Agrawal and W. Imbriale, "Design of a dichroic Cassegrain subreflector," *Antennas and Propagation, IEEE Transactions on*, vol. 27, pp. 466-473, 1979.

[55] R. J. Langley and E. A. Parker, "Double-square frequency-selective surfaces and their equivalent circuit," *Electronics Letters*, vol. 19, pp. 675-677, 1983.

[56] T. Chich-Hsing and R. Mittra, "Spectral-domain analysis of frequency selective surfaces comprised of periodic arrays of cross dipoles and Jerusalem crosses," *Antennas and Propagation, IEEE Transactions on*, vol. 32, pp. 478-486, 1984.

[57] M. Caiazzo, S. Maci, and N. Engheta, "A metamaterial surface for compact cavity resonators," *Antennas and Wireless Propagation Letters, IEEE*, vol. 3, pp. 261-264, 2004.

[58] A. Andrea, E. Nader, and W. Z. Richard, "Finite-difference time-domain analysis of the tunneling and growing exponential in a pair of epsilon-negative and mu-negative slabs," *Physical Review E (Statistical, Nonlinear, and Soft Matter Physics)*, vol. 74, pp. 016604, 2006.

[59] C. Hongsheng, R. Lixin, H. Jiangtao, Z. Xianmin, C. Kangsheng, M. G. Tomasz, and K. Jin Au, "Negative refraction of a combined double S-shaped metamaterial," *Applied Physics Letters*, vol. 86, pp. 151909, 2005.

[60] F. Zhang, G. Houzet, S. Potet, E. Lheurette, M. Chaubet, and D. Lippens, "Metamaterials-based Routing Devices for Space Applications," presented at Signals, Systems and Electronics, 2007. ISSSE '07. International Symposium on, 2007.

[61] A. Ourir, S. N. Burokur, and A. d. Lustrac, "Phase-varying metamaterial for compact steerable directive antennas," *Electronics Letters*, vol. 43, pp. 493-494, 2007.

[62] A. Koray, B. Irfan, and O. Ekmel, "Subwavelength resolution with a negative-index metamaterial superlens," *Applied Physics Letters*, vol. 90, pp. 254102, 2007.

[63] N. Fang, H. Lee, C. Sun, and X. Zhang, "Sub-Diffraction-Limited Optical Imaging with a Silver Superlens," *Science*, vol. 308, pp. 534-537, 2005.

[64] J. F. Manuel, M. Ricardo, and J. Lukas, "Experimental demonstration of a mu = -1 metamaterial lens for magnetic resonance imaging," *Applied Physics Letters*, vol. 93, pp. 231108, 2008.

[65] J. B. Pendry, D. Schurig, and D. R. Smith, "Controlling Electromagnetic Fields," *Science*, pp. 1125907, 2006.

[66] K. Fanmin, W. Bae-Ian, K. Jin Au, H. Jiangtao, X. Sheng, and C. Hongsheng, "Planar focusing antenna design by using coordinate transformation technology," *Applied Physics Letters*, vol. 91, pp. 253509, 2007.

[67] Z. Jacob, L. V. Alekseyev, and E. Narimanov, "Optical Hyperlens: Far-field imaging beyond the diffraction limit," *Opt. Express*, vol. 14, pp. 8247-8256, 2006.

Chapitre II :

Métamatériaux pour les structures guidées

Introduction

À l'occasion du chapitre I, nous avons décrit trois approches permettant de synthétiser un milieu artificiel à permittivité et perméabilité effectives négatives à partir d'inclusions métalliques. Dans le présent chapitre, nous présentons trois exemples de structures unidimensionnelles illustrant chacun de ces concepts. Le premier utilise un réseau de fils et un réseau de résonateurs en anneaux fendus imbriqués dans un environnement de guide finline. Le second s'appuie sur l'approche de ligne duale pour la réalisation d'un déphaseur composite équilibré accordable en technologie coplanaire. Enfin, l'approche hybride, que nous avons définie comme un stade intermédiaire entre la superposition des réseaux simplement négatifs et la ligne de transmission duale, est illustrée par l'analyse d'un métamatériau à base de lettres Ω connectées aux parois d'un guide d'onde rectangulaire. Le choix de dispositifs unidimensionnels permet, dans un premier temps, de mettre l'accent sur le phénomène de rétropropagation de la phase. Les aspects de réfraction sont étudiés au troisième chapitre à partir de métamatériaux volumiques.

II.1 Métamatériau 1D à réseaux imbriqués

II.11 Choix du milieu à permittivité effective négative

En 2002, R. Marqués a publié une première étude expérimentale de métamatériau doublement négatif à partir d'un guide rectangulaire métallique [1]. L'originalité de ce travail est l'utilisation du guide d'onde sous sa fréquence de coupure dans le but de synthétiser le milieu à permittivité effective négative. En effet, on peut montrer que la zone d'évanescence située sous la coupure du guide correspond à un régime de permittivité négative. Le milieu à perméabilité effective est, quant à lui, constitué d'un réseau de SRR (figure II-1).

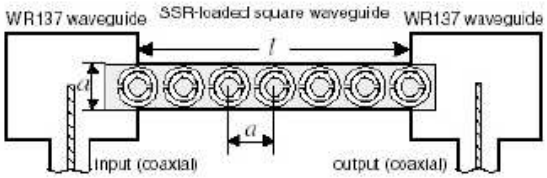

Figure II-1 : Structure métamatériau doublement négative de R. Marqués [1]

Les caractéristiques expérimentales obtenues révèlent un niveau de transmission maximal relativement faible, de l'ordre de -20 dB. Comme le montre la figure II-2, ce niveau varie peu en fonction du nombre de résonateurs insérés dans le guide. Par conséquent, on peut penser que cette structure souffre d'un faible couplage au niveau des accès au guide sous-dimensionné.

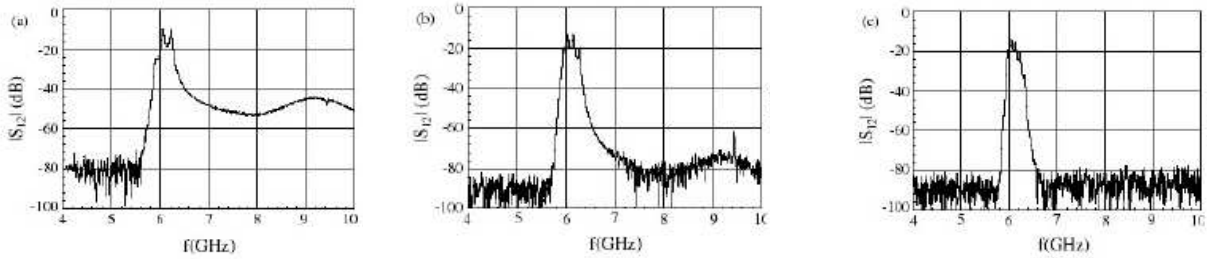

Figure II-2 : Transmission expérimentale de la structure de R. Marqués pour (a) 12, (b) 24 et (c) 36 cellules unitaires [1].

Cette étude constitue une étape importante sur le plan de la physique. Néanmoins, en termes d'utilisation, la forte atténuation est rédhibitoire. Plusieurs solutions ont été proposées pour améliorer le couplage aux accès du guide sous-dimensionné [2]. Une alternative consiste à localiser le rétrécissement du guide sous la forme d'iris qui se comportent comme des fenêtres inductives [3]. Ces fenêtres inductives sont placées au même niveau que les SRR. On retrouve alors une situation analogue à la superposition de deux réseaux simplement négatifs, le réseau de fenêtres inductives jouant le rôle du réseau de fils. Ces études montrent qu'il semble plus favorable de travailler avec un milieu distribué afin de favoriser le couplage de l'onde incidente. C'est à partir de ce constat que le choix s'est porté sur l'utilisation d'un réseau de fils. Dans notre cas, ce réseau est inscrit sur une structure de propagation finline insérée dans un guide rectangulaire WR-62, monomode de 9,5 à 19 GHz. Cette structure, qui permet de bénéficier d'un

mode de propagation quasi-TEM, a fait l'objet d'une étude détaillée dans le cadre de la thèse de Thibaut Decoopman [4, 5]. Comme nous l'avons énoncé au paragraphe précédent, la permittivité effective d'un réseau volumique de fils, donnée par l'équation (1), répond à la loi de Drude. La fréquence plasma du milieu dilué augmente avec le facteur de remplissage défini par le quotient du volume de métal sur le volume total de la cellule unitaire. Ce comportement général se retrouve au niveau d'une structure planaire unidimensionnelle comme le montre le graphe de la figure II-3. En effet, on peut vérifier que la fréquence plasma augmente avec le facteur de remplissage.

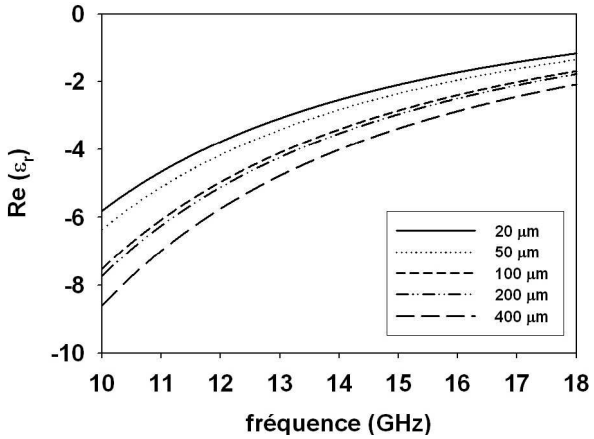

Figure II-3 : Permittivité effective du réseau de fils en fonction de la fréquence pour différentes valeurs de la largeur de métallisation *l* [6].

Ce graphe a été déduit de la simulation des paramètres S_{ij} d'une cellule unitaire par une méthode d'inversion des relations de Fresnel [7]. La cellule unitaire est représentée sur la figure II-8 avec ses dimensions. Pour l'étude du réseau à permittivité négative, le motif se limite au fil court-circuitant les deux demi-plans du guide finline séparés de 200 µm. Pour la fabrication du prototype, une largeur de fil de 200 µm a été retenue par souci de compatibilité avec la résolution du procédé de gravure mécanique. Cette dimension donne une valeur de permittivité effective voisine de -5 à la fréquence de 12 GHz. Il est à noter que cette valeur est modifiée lorsque l'on insère le résonateur dans la cellule unitaire.

II.12 Choix du milieu à perméabilité effective négative

Comme nous l'avons montré au chapitre I, le changement de signe de la perméabilité peut s'observer au voisinage de la fréquence de résonance d'une boucle de courant fendue. Sur cette base, plusieurs géométries ont été proposées mais le motif de doubles résonateurs imbriqués, initialement introduit par J. B. Pendry en 1999, a été très largement repris [8]. Ce dispositif est représenté sur la figure II-4. Pour des aspects liés à la conception ou à la fabrication, on peut être amené à préférer des boucles de courant carrées plutôt que circulaires ; ce choix n'affecte pas le comportement du résonateur dans son principe.

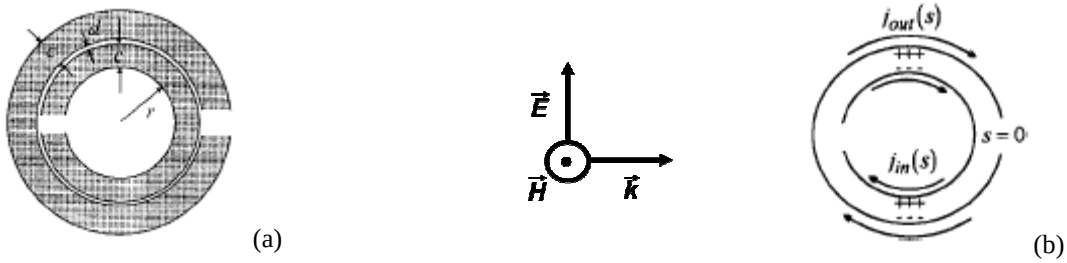

(a) (b)

Figure II-4 : Résonateurs imbriqués : (a) géométrie de base, (b) circulation des courants sous l'effet de la polarisation [8].

Sous l'effet de la polarisation par le champ magnétique, on observe un mode de résonance symétrique caractérisé par des courants parcourant les deux conducteurs dans le même sens. En vertu du théorème d'Ampère, ce courant induit un champ magnétique à l'intérieur des anneaux. À la résonance, la direction de ce champ s'inverse par rapport à celle du champ excitateur. Sur une structure à résonateur unique, cette résonance du champ magnétique pourrait également résulter de la contribution du champ électrique qui crée une différence de potentiel au niveau de la fente de l'anneau. Or, avec la configuration imbriquée, le champ électrique excite un mode de résonance antisymétrique.

Dans ce cas, la résultante des courants qui circulent en sens opposé s'annule. Ce mode antisymétrique est donc sans effet sur l'excitation du champ magnétique. On dit que la structure imbriquée élimine les effets de bianistropie. Elle constitue donc, en première approximation, un dipôle purement magnétique. On retrouve cette propriété dans la particule composée de deux anneaux en vis-à-vis proposée par R. Marqués [9]. Cette géométrie est intéressante pour la

compensation des courants dans la mesure où les deux anneaux ont des géométries rigoureusement identiques. En revanche, elle est plus difficile à intégrer dans une topologie purement planaire. L'autre avantage du motif à résonateur imbriqué est la diminution de sa fréquence de résonance à dimension constante qui contribue à renforcer le caractère homogène du réseau à perméabilité négative. Cette diminution de la fréquence de résonance s'explique par une augmentation de la capacité équivalente de ce dipôle magnétique principalement localisée entre les deux anneaux fortement couplés. Si l'on considère un motif à anneau unique, l'effet capacitif, localisé au niveau de la fente, est bien moindre, ce qui tend à augmenter la fréquence de résonance. Toutefois, cette remarque n'est valable que dans le cas de SRR isolés ou suffisamment découplés de leurs voisins et de tout environnement électromagnétique. À titre d'exemple, en considérant le cas qui nous intéresse, le résonateur est imprimé en face arrière d'un substrat supportant un guide finline.

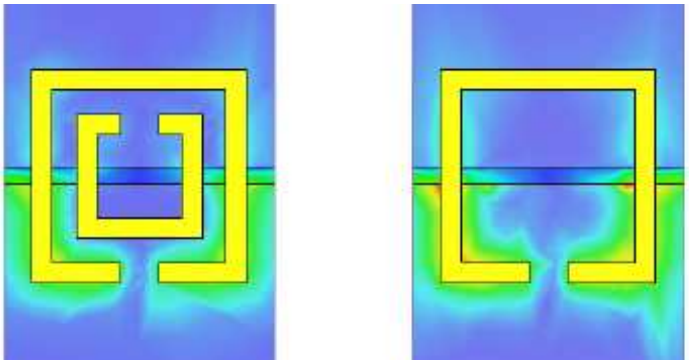

Figure II-5 : Comparaison de l'amplitude du champ électrique à la résonance, résonateur double à gauche, résonateur simple à droite.

La figure II-5 montre une répartition similaire de l'amplitude du champ électrique pour les simple et double résonateurs avec un fort effet de couplage entre la partie inférieure du grand anneau et la ligne. Le diagramme de dispersion de la structure complète décrivant le milieu doublement négatif infini (figure II-6) ne permet pas de percevoir une différence de comportement suivant que l'on considère un milieu à simple ou à double résonateur. Par conséquent, la structure simple anneau a été retenue pour la conception de ce prototype pour des raisons de facilité de fabrication.

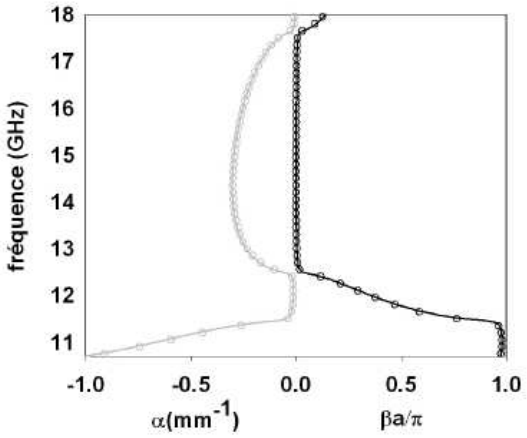

Figure II-6 : Diagramme de dispersion. Traits pleins : simple anneau, symboles ronds : double anneau.

Pour les mêmes raisons, on privilégie généralement les géométries à simple anneau pour les longueurs d'onde de l'optique [10]. De façon générale, cet exemple montre que le comportement de dipôle magnétique est facilement altéré par les effets de couplage avec l'environnement extérieur. Cette tendance participe notamment à la difficulté de prévoir, sur le plan quantitatif, le comportement du milieu doublement négatif à partir de la superposition des deux milieux simplement négatifs.

II.13 Structure métamatériau doublement négative

La structure a été définie sur un substrat de Duroïd 5880 (ε_r = 2,2 ; tanδ = 9.10^{-4}) d'épaisseur 254 µm. Ce substrat est métallisé sur ses deux faces par un film de cuivre d'épaisseur 200 µm et de conductivité $\sigma_{Cu} = 5{,}8.10^7$ S/m. La fabrication est détaillée dans les références [5, 6, 11-13]. Dans son principe, la structure finline utilise un guide d'onde rectangulaire. Par conséquent, il s'agit d'un environnement électromagnétique fermé approprié à la quantification des pertes métalliques et diélectriques.

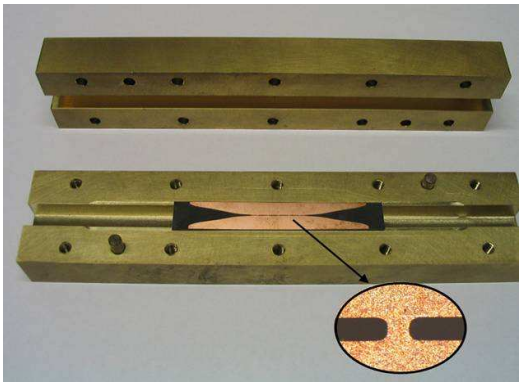

(a)

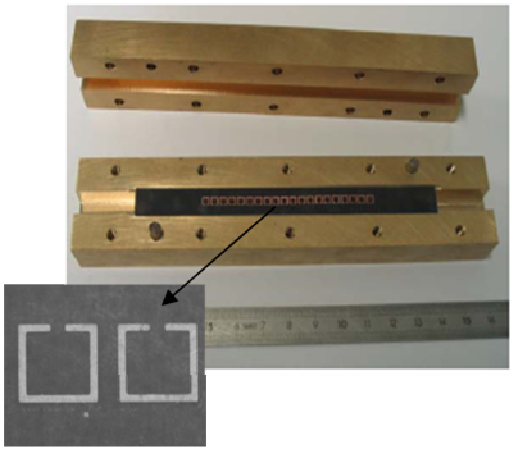

(b)

Figure II-7 : Structure métamatériau insérée dans le guide rectangulaire WR-62 d'ouverture 7,9 x 16 mm^2 : (a) finline périodiquement court-circuitée (face inférieure), (b) réseaux d'anneaux fendus (face supérieure).

La structure étudiée est décrite par une photographie (figure II-7) et par la figure II-8 qui regroupe une vue en perspective de la ligne finline insérée dans le guide (sans les tapers) et une vue de dessus de la cellule unitaire avec ses dimensions caractéristiques.

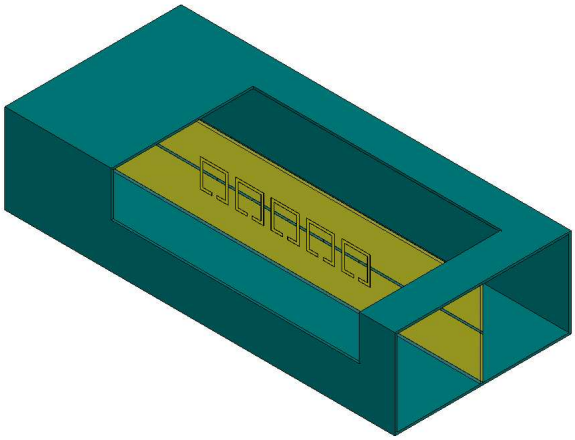

(a)

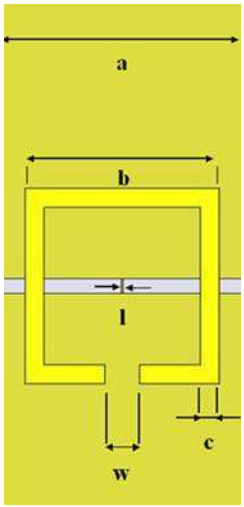

a = 3,3 mm

b = 2,62 mm

c = 250 µm

w = 460 µm

l = 200 µm

(b)

Figure II-8 : Vue en perspective de la structure finline insérée dans le guide rectangulaire (a), vue de dessus d'une cellule unitaire (b).

Plusieurs substrats incluant des nombres de motifs différents ont été fabriqués. Ces structures ont été caractérisées à l'analyseur de réseaux vectoriel *Hewlett-Packard HP 8510*. La

figure II-9 donne les spectres de transmission mesurés pour des structures à une, trois et dix cellules unitaires. Ce premier résultat, qui montre une diminution du niveau de transmission avec le nombre de motifs, préfigure le rôle joué par les résonateurs dans les pertes d'insertion. Le caractère main gauche de la transmission peut être démontré de manière expérimentale à partir de la mesure du relevé de la phase du paramètre S_{21}.

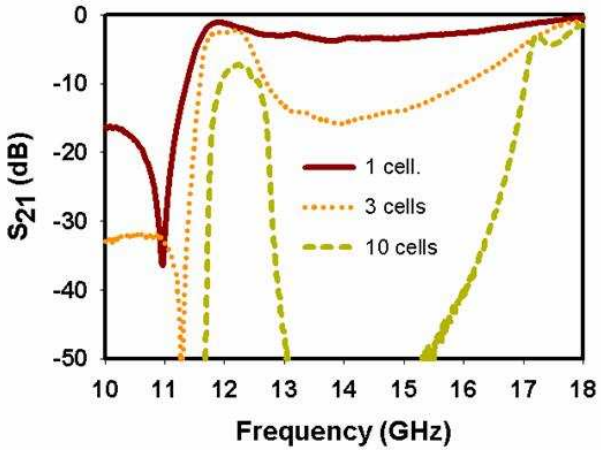

Figure II-9 : Spectres de transmission mesurés pour différents nombres de cellules unitaires

Afin de s'affranchir de l'indétermination de la phase à l'origine, on a recours à une méthode différentielle qui s'appuie sur la mesure de phase pour deux structures de longueurs différentes. En effet, on peut montrer qu'une différence de phase positive ($\Delta\phi = \phi_{S21long} - \phi_{S21court}$) correspond à un régime de transmission gaucher. Au contraire, une différence de phase négative correspond à un régime de transmission droitier [14]. Les différences de phase mesurée et simulée sont données sur la figure II-10. La lecture des figures II-9 et II-10 montre, dans le cas de trois cellules unitaires, la succession d'une bande passante fondamentale main gauche (de 11,5 à 12,5 GHz), d'une bande interdite puis d'une seconde bande passante main droite (à partir de 17 GHz). La bande passante main gauche est relativement étroite ($\frac{\Delta f}{f_0}$ de l'ordre de 10 %). C'est la conséquence de l'emploi des résonateurs pour synthétiser la perméabilité négative. Par ailleurs, la figure II-9 montre un léger décalage de la bande fondamentale en fonction du nombre de cellules unitaires. Enfin, on peut constater une diminution de la fréquence plasma, confirmée par la

simulation [12], par rapport à celle du milieu simplement négatif (figure II-3). Ces deux derniers points illustrent l'importance des effets de couplage à l'intérieur du milieu complet et la difficulté de prévoir quantitativement son comportement à partir de la superposition des spectres des deux milieux simplement négatifs.

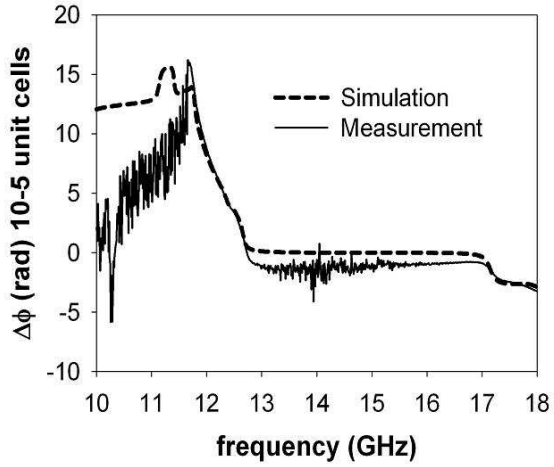

Figure II-10 : Différence de phase simulée et mesurée entre deux structures incluant 10 et 5 cellules unitaires.

La propagation de l'onde s'effectuant dans un environnement électromagnétique fermé, il est possible, à partir du relevé des paramètres S_{ij}, de remonter à la valeur des pertes métalliques et diélectriques. En effet, cette contribution globale correspond à la différence $1-S_{21}{}^{2}-S_{11}{}^{2}$. L'évolution de ces pertes en fonction de la fréquence est donnée sur la figure II-11 pour un nombre de cellules unitaires variant de 1 à 10. Cette représentation illustre l'accroissement des pertes en fonction du nombre de cellules qui sont une autre conséquence néfaste de l'utilisation de particules fortement résonantes.

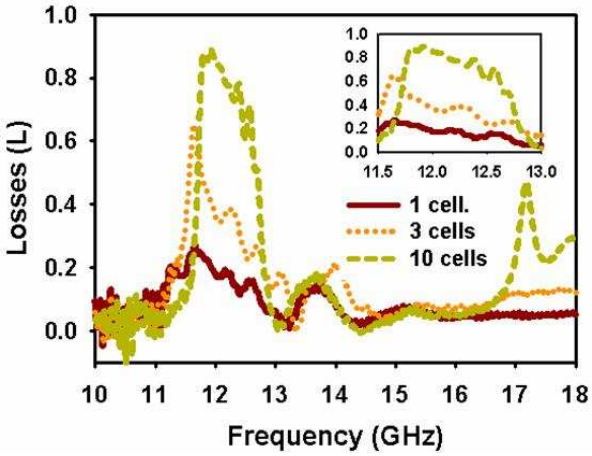

Figure II-11 : Évolution des pertes en fonction de la fréquence pour différents nombres de cellules unitaires.

Par simulation à l'aide du logiciel *HFSS*, il est possible de déterminer l'importance relative des termes de perte métallique et diélectrique en considérant l'un ou l'autre des matériaux comme parfait. Le résultat de ce calcul effectué sur une structure comportant 10 cellules, présenté sur la figure II-12, illustre la prépondérance des pertes métalliques.

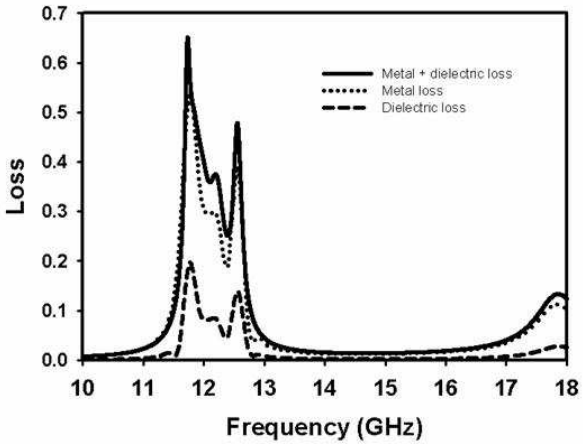

Figure II-12 : Contributions séparées des pertes métalliques et diélectriques en fonction de la fréquence obtenues par simulation d'une structure de 10 cellules unitaires.

Ce problème des pertes est rédhibitoire en termes d'application, notamment aux fréquences élevées. Toutefois, en raison du fort niveau de réjection présenté par un seul résonateur, il n'est pas toujours nécessaire de travailler avec un nombre de résonateurs élevé. La plupart des filtres hyperfréquences qui utilisent des SRR tirent partie de cette propriété [15, 16].

En conclusion, les métamatériaux basés sur l'imbrication de réseaux de fils et de résonateurs métalliques sont caractérisés par des bandes passantes relativement étroites associées à des pertes d'insertion par cellule unitaire élevées. Au paragraphe suivant, nous présentons une structure basée sur le concept de ligne duale qui, par le biais d'une approche non résonante dans son principe, permet d'obtenir des bandes passantes sensiblement plus larges et de réduire les niveaux de pertes.

II.2 Réalisation d'un déphaseur composite accordable

Cette étude a fait l'objet du travail de thèse d'Aurélien Marteau. Elle consiste à tirer partie de la variation de permittivité d'un matériau ferroélectrique pour accorder un déphaseur main gauche / main droite au moyen d'une tension de commande continue. Ce travail concrétise une collaboration avec le laboratoire LEMCEL de l'Université du Littoral. L'accordabilité est obtenue par l'insertion d'une couche de $BaSrTiO_3$ (BST) déposée par la technique sol-gel élaborée au LEMCEL [17].

La caractéristique expérimentale capacité-tension relevée sur un film de BST de 0,3 µm à la fréquence de 20 GHz est représentée sur la figure II-13. Des détails sur la méthode et la géométrie utilisées sont reportés dans la référence [18]. On peut déduire de ce relevé une accordabilité d'environ 50 % pour un champ électrique de 300 kV/cm à température ambiante.

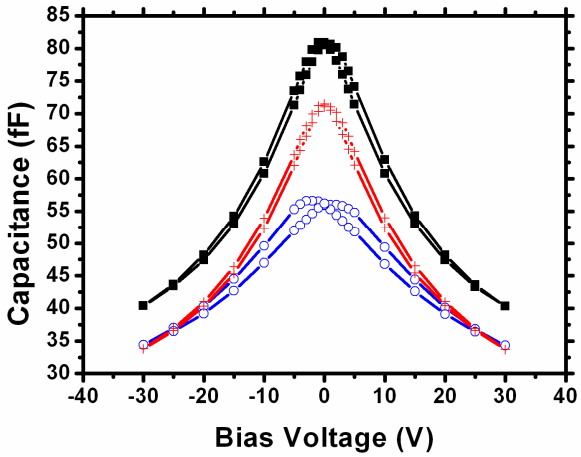

Figure II-13 : Caractéristique capacité-tension d'un film de BST de 0,3 µm relevé à la fréquence de 20 GHz pour des températures de 77 K (ronds bleus), 223 K (carrés noirs), 297 K (croix rouges) [18].

II.21 Choix du circuit équivalent

Le déphaseur utilise le principe de la ligne duale décrit au chapitre I. Rappelons que cette approche permet d'obtenir une continuité des bandes gauchère et droitière à la condition d'équilibre entre les fréquences de résonance des circuits équivalents série et parallèle [19]. Le prototype a été conçu en privilégiant cette propriété afin de pouvoir passer d'un régime d'avance de phase à un régime de retard de phase sans annulation de la vitesse de groupe. Par conséquent, le schéma équivalent (figure II-14a) inclut un terme d'inductance en court-circuit noté L_L et un terme de capacité série noté C_L. La commande, qui exploite la variation de permittivité du film de BST, s'exerce au niveau de cette capacité C_L.

La capacité parallèle C_{RH} est constituée de la capacité intrinsèque du support de propagation hôte associée à un élément localisé repéré C_R. Ce choix permet de contrôler simultanément la valeur des fréquences de résonance série et parallèle lorsque l'on applique la tension continue sur le film de BST.

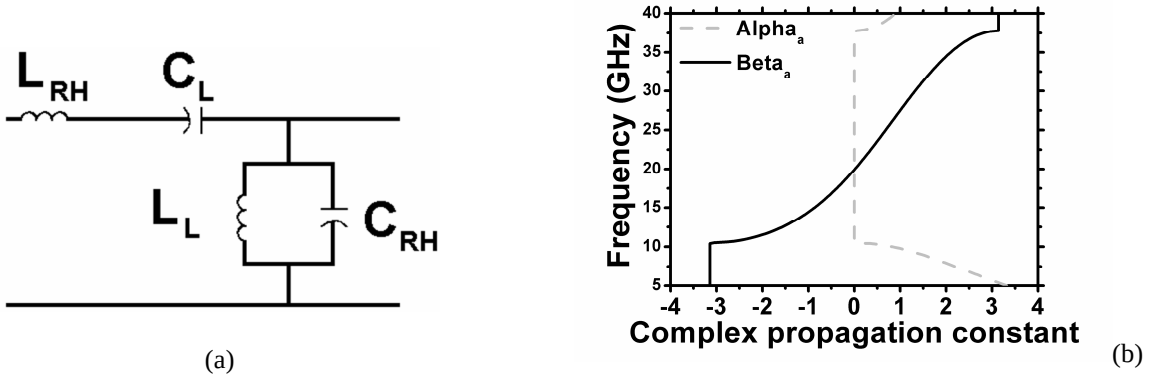

(a) (b)

Figure II-14 : Schéma de la cellule unitaire du déphaseur main gauche (a), diagramme de dispersion simulé (b).

Les valeurs des éléments localisés sont résumées dans le tableau II-1. Ces valeurs ont été déterminées par simulation à l'aide du logiciel *ADS* de la société *Agilent* en considérant les critères de la condition d'équilibre du régime composite (figure II-14b) et d'une valeur d'impédance caractéristique Z_c de 55 Ω. Cette valeur représente un compromis permettant de limiter la désadaptation lorsque l'on applique la tension de commande continue V_{DC}.

Impédance caractéristique (à 0 V_{DC}) Z_c	55 Ω
Inductance linéique intrinsèque L_{RH}	$6{,}24.10^{-7}$ H/m
Inductance shunt L_L	500 pH
Capacité linéique intrinsèque C_{int}	$9{,}08.10^{-11}$ F/m
Capacité série C_L (à 0 V_{DC})	120 fF
Capacité parallèle C_R (à 0 V_{DC})	50 fF

Tableau II-1 : Valeurs des constantes localisées d'une cellule unitaire du déphaseur.

Les valeurs des éléments intrinsèques L_{RH} et C_{int} ont été déterminées à partir d'expressions approchées en considérant la structure du support de propagation coplanaire [20]. Le choix de ce support est commenté au paragraphe suivant.

II.22 Choix de la topologie du déphaseur

Le déphaseur est basé sur une configuration de ligne coplanaire. D'un point de vue électromagnétique, cette structure propage un mode quasi-TEM qui autorise sa modélisation par un schéma équivalent incluant des éléments distribués. Par ailleurs, le champ électrique est majoritairement concentré au niveau des fentes qui séparent le conducteur central des plans de masse. Cette configuration assure une interaction forte avec la couche mince de BST située juste au-dessous du niveau des métallisations. Enfin, du point de vue de la caractérisation, l'emploi de cette configuration est favorable car les stations de mesure que nous utilisons sont équipées de systèmes de pointes coplanaires. La figure II-15 représente le masque employé pour l'étape de métallisation d'une structure qui comprend quatre cellules unitaires de longueur 850 µm.

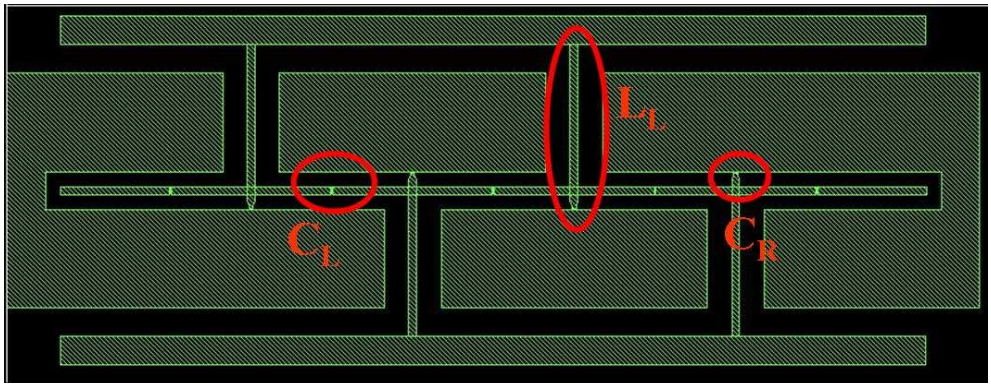

Figure II-15 : Masque du niveau de métallisation d'un déphaseur à 4 cellules unitaires.

Les prototypes sont fabriqués à partir d'un substrat de saphir sur lequel a été élaboré un film de BST par la technique de dépôt sol-gel [21]. Cette première étape conditionne la suite du process. En effet, les éléments d'accord doivent nécessairement adopter une configuration planaire dans la mesure où le film de BST recouvre toute la surface du substrat. Dans cette optique, les capacités C_L et C_R utilisent des motifs interdigités reportés sur la figure II-16.

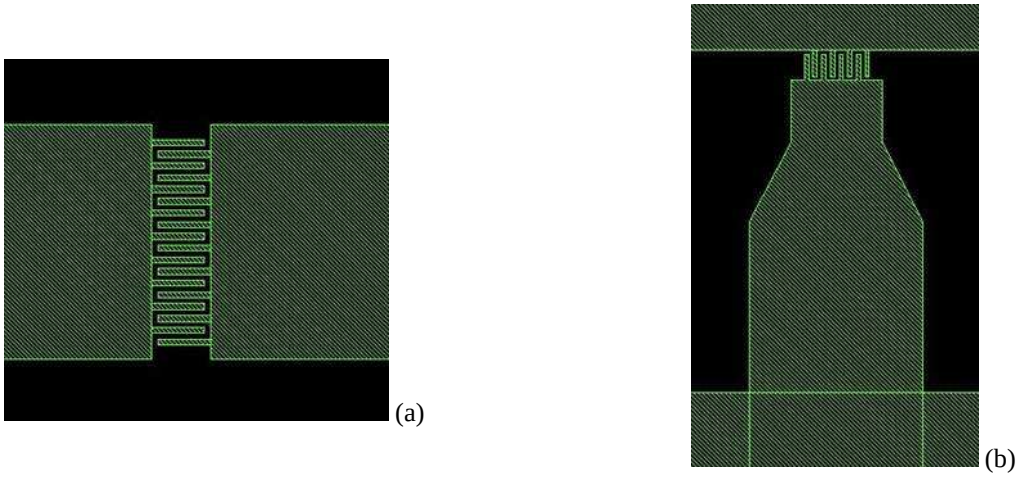

(a) (b)

Figure II-16 : Géométrie des capacités interdigitées : (a) C_L, (b) C_R

L'utilisation de motifs interdigités de petites dimensions présente un réel avantage en terme d'agilité dans la mesure où elle induit une importante concentration du champ électrique dans la couche de BST, ce qui contribue à diminuer la valeur de la tension de commande. Dans le cas présent, avec une largeur de doigt avoisinant le micron, l'accordabilité de 50 % à 300 kV/cm peut être obtenue avec une tension de polarisation d'environ 30 V. La géométrie des capacités est déterminée à l'aide d'une technique de transformation conforme qui permet d'établir l'équivalence entre la structure interdigitée et une capacité plan [22].

II.23 Fabrication du déphaseur

Compte tenu de la résolution nécessaire pour définir les motifs interdigités, le niveau de métallisation est inscrit au masqueur électronique. L'étape de métallisation utilise un procédé de lift-off. La séquence métallique est composée d'une couche d'accrochage en titane d'épaisseur 1000 Å et d'un épaississement d'or de 4000 Å déposés par évaporation sous vide. La continuité

électrique du plan de masse est réalisée au moyen de fils d'or thermocompressés. Par ailleurs, des capacités « chip » de 5 pF sont insérées afin d'assurer le découplage entre le signal RF et la tension de polarisation continue. Cette polarisation est distribuée à partir des deux plots métalliques parallèles à la structure coplanaire. La vue de dessus au microscope optique (figure II-17) montre un prototype fini incluant deux cellules élémentaires.

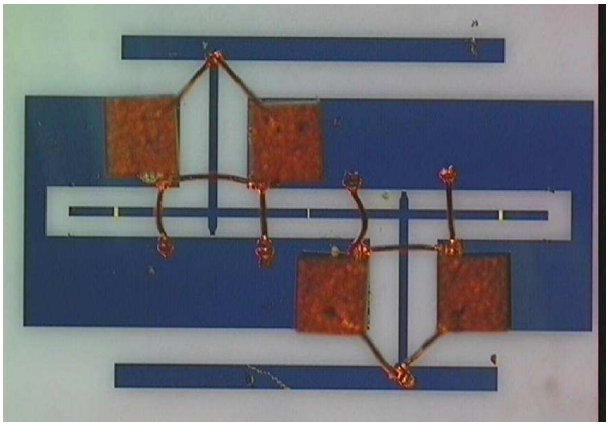

Figure II-17 : Vue au microscope optique d'un déphaseur incluant deux cellules unitaires.

Les dimensions en fin de process de la capacité interdigitée sont reportées sur la vue au microscope électronique à balayage (figure II-18).

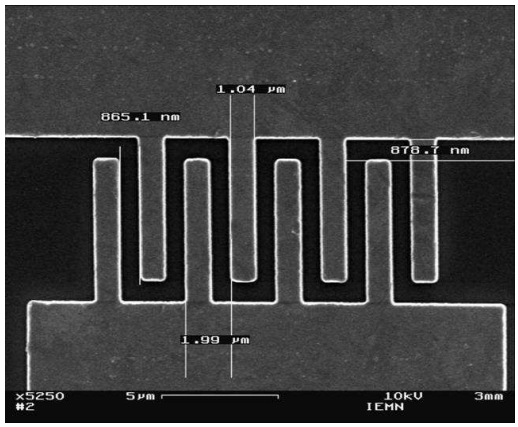

Figure II-18 : Vue au microscope électronique à balayage d'une capacité d'accord C_R.

II.24 Caractérisation du déphaseur

Les circuits ont été caractérisés à l'analyseur de réseau *HP 8510* calibré à partir d'une méthode TRL jusqu'à la fréquence de 75 GHz. Les paramètres S_{ij} obtenus pour différentes tensions de polarisation continue sont reportés sur la figure II-19 pour un déphaseur à deux cellules unitaires. À polarisation nulle, la diminution du paramètre S_{21}, associée à la remontée du coefficient de réflexion, n'apparaît qu'autour de 40 GHz. Par conséquent, la bande passante du déphaseur s'étend sur environ 30 GHz. Cette large bande passante est caractéristique des structures qui utilisent une approche de ligne duale dans la mesure où leur principe de fonctionnement ne repose pas sur l'exploitation d'un phénomène de résonance par opposition aux structures incluant des réseaux de SRR, comme nous l'avons mentionné au chapitre I. Toutefois, il est à noter que les pertes d'insertion restent relativement élevées. Des études complémentaires sur les fils minces de BST ont permis de mettre en évidence des tangentes de pertes voisines de 10^{-2}, ce qui contribue notablement à l'affaiblissement du coefficient de transmission dans la bande passante. Par ailleurs, il convient de rappeler que, par souci de compromis, la structure n'est pas rigoureusement adaptée à l'impédance du système de mesure puisque la valeur théorique de Z_c est de 55 Ω à V_{DC} nulle.

Lorsqu'une tension de polarisation est appliquée à la structure, on assiste à une remontée du coefficient de réflexion, de l'ordre de 10 dB en début de bande pour V_{DC} = 30 V. Cette dégradation est la conséquence directe de la désadaptation d'impédance. En effet, les valeurs des capacités C_L et C_R données dans le tableau II-1 pour une polarisation nulle, diminuent conformément à la variation reportée sur la figure II-13. Or la valeur de Z_c, fonction des constantes localisées, est inévitablement affectée cette variation, ce qui se traduit par une désadaptation importante pour des fortes valeurs de V_{DC}. La plus grande sensibilité à la polarisation est observée en début de bande qui correspond au régime gaucher (figure II-14b). Ce comportement peut s'expliquer par la dispersion importante dans cette plage de fréquence. En effet, le diagramme de dispersion présente, en première approximation, une branche main gauche hyperbolique décrite par l'équation suivante :

$$\beta = -\frac{1}{\omega\sqrt{L_L.C_L}} \qquad (1)$$

En revanche, la transmission au voisinage de la fréquence de transition ne semble pas affectée. En effet, l'augmentation de la tension de polarisation ne se traduit pas par l'ouverture d'une bande interdite entre les branches main gauche et main droite directement observable sur l'évolution du paramètre S_{21}. Les valeurs de V_{bias} indiquées sur la figure II-19 correspondent à la tension de polarisation globale appliquée entre les deux pads encadrant la structure coplanaire (figure II-17). En raison de la continuité électrique assurée par les accès aux capacités, cette tension globale est équivalente à V_{DC}.

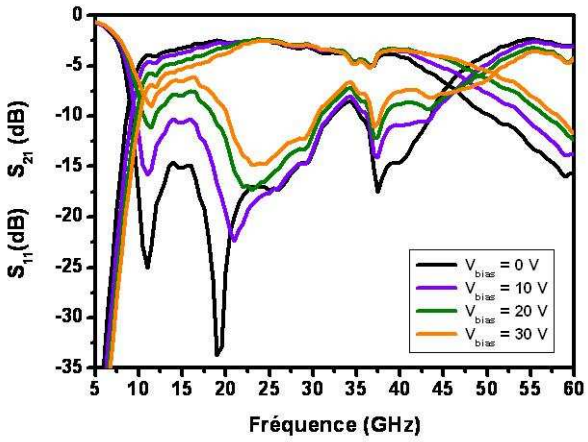

Figure II-19 : Amplitude des paramètres S_{ij} en fonction de la fréquence pour différentes valeurs de la tension de polarisation globale (V_{bias}).

Sur la figure II-20, nous avons reporté l'évolution de la phase du paramètre S_{21} en fonction de V_{bias} pour un déphaseur incluant deux cellules unitaires. Le décalage de phase obtenu est d'environ 18° par cellule unitaire pour une tension de polarisation de 30 V.

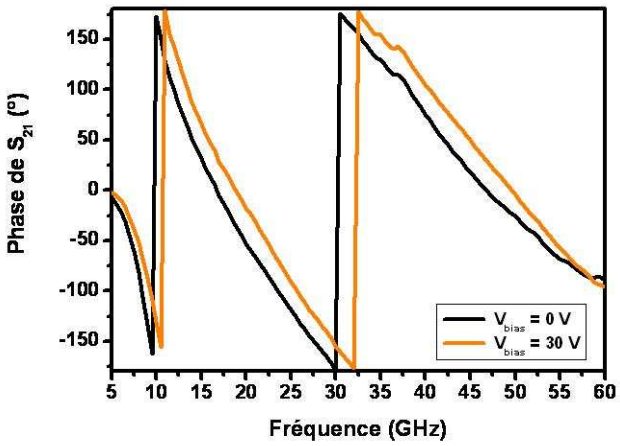

Figure II-20 : Phase de la transmission en fonction de la fréquence pour deux tensions de commande.

Cette description fonctionnelle du déphaseur peut être complétée par une interprétation physique qui conduit à une analyse plus fine de ses paramètres de dispersion sous l'effet de la tension de polarisation. L'inversion des relations de Fresnel [7] permet d'extraire un diagramme de dispersion (figure II-21) et une impédance réduite (figure II-22) à partir des paramètres S_{ij} relevés pour différentes tensions de polarisation. À polarisation nulle, on observe l'évolution continue des bandes passantes droitière et gauchère avec une fréquence de transition autour de 17 GHz. Ce diagramme montre un décalage vers les basses fréquences d'environ 20 % par rapport à la dispersion calculée à partir du schéma équivalent théorique (figure II-14). Le déséquilibre observé lorsque l'on augmente la tension de polarisation se traduit par une discontinuité de la constante de phase autour de l'origine et par une augmentation de la constante d'atténuation. Ce déséquilibre est révélateur d'une compensation imparfaite des termes capacitifs C_L et C_{RH}. En effet, avec une longueur de cellule unitaire de 850 µm, la contribution théorique de C_{int} est de 77 fF contre 50 fF pour C_R. Ces valeurs montrent que la capacité d'accord, associée à la capacité intrinsèque fixe, n'est pas à même de compenser la variation de la capacité C_L en fonction de V_{DC}. Elle ne peut que limiter le déséquilibre du diagramme de dispersion composite pour des tensions de commande modérées. Pour des tensions plus importantes, une bande interdite apparaît entre les bandes passantes gauchère et droitière en raison de la non-équivalence des fréquences de résonance série et parallèle.

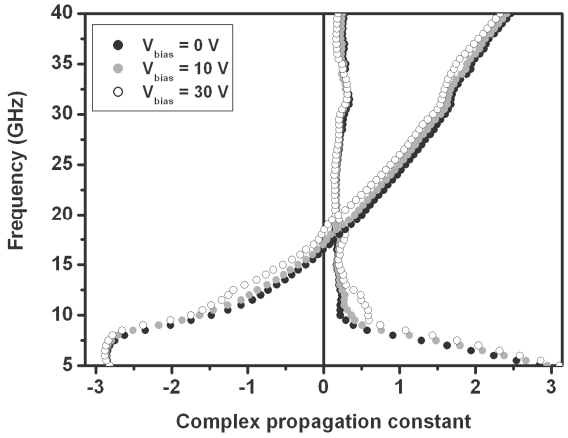

Figure II-21 : Évolution du diagramme de dispersion expérimental en fonction de la tension de commande.

L'évolution de l'impédance réduite montre une forte discontinuité autour de 17 GHz qui correspond à la jonction entre les bandes passantes. Par ailleurs, le plateau observé en bande main droite s'éloigne de l'unité pour de fortes tensions de polarisation. Cette diminution du niveau d'impédance explique l'augmentation du coefficient de réflexion observé sur la figure II-19.

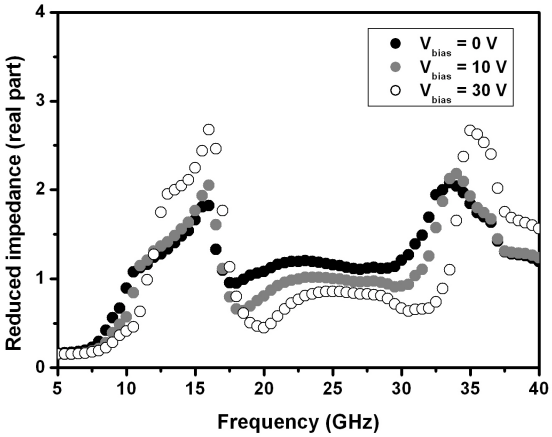

Figure II-22 : Évolution de l'impédance réduite en fonction de la fréquence pour différentes valeurs de la tension de commande.

Par analogie avec l'interaction d'une onde plane et d'un matériau volumique, l'interaction d'un mode TEM avec une structure unidimensionelle peut être décrite par des paramètres constitutifs effectifs [23]. Nous avons représenté sur les figures II-23 et II-24 les parties réelles de

la permittivité et de la perméabilité effectives respectivement. Leur dispersion suit une évolution continue entre les bandes main gauche et main droite avec un croisement à l'origine autour de 17 GHz pour une tension de polarisation de 0 V. Lorsque l'on augmente cette tension de commande, les deux caractéristiques se décalent vers les fréquences élevées. Toutefois, cette tendance est nettement plus prononcée dans le cas de la perméabilité effective. À titre d'exemple, la variation du zéro de permittivité n'excède pas 1 GHz tandis que le zéro de perméabilité varie d'environ 3 GHz lorsque V_{bias} est augmentée de 0 à 30 V.

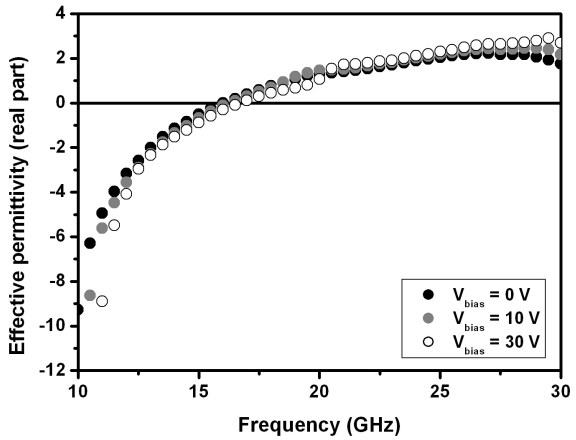

Figure II-23 : Évolution de la permittivité effective en fonction de la fréquence pour différentes valeurs de la tension de commande.

Ce phénomène se traduit par l'ouverture d'une bande interdite pour des tensions de polarisation importantes. Pour comprendre cette différence de comportement entre les permittivité et perméabilité effectives, il faut évoquer les facteurs physiques dominants pour chacun de ces deux paramètres. La permittivité négative est synthétisée par les inductances en shunt qui jouent le rôle du réseau de fils dans la situation des métamatériaux volumiques (zéros de tension). Or, la valeur de cette inductance n'est que peu affectée par la variation de permittivité de la couche de BST sous l'effet d'une tension de polarisation. En revanche, la perméabilité négative est obtenue par les capacités série qui imposent des zéros de courant le long de la ligne de propagation. Or, ces capacités ont été conçues pour être très sensibles aux variations de permittivité par l'adoption d'une structure interdigitée. Comme mentionné précédemment, cette variation de capacité série ne peut être totalement compensée par la

variation de capacité parallèle dans la mesure où cette dernière inclut, en plus de l'élément localisé C_R, la capacité distribuée intrinsèque de la ligne, relativement peu sensible à la variation de V_{bias}.

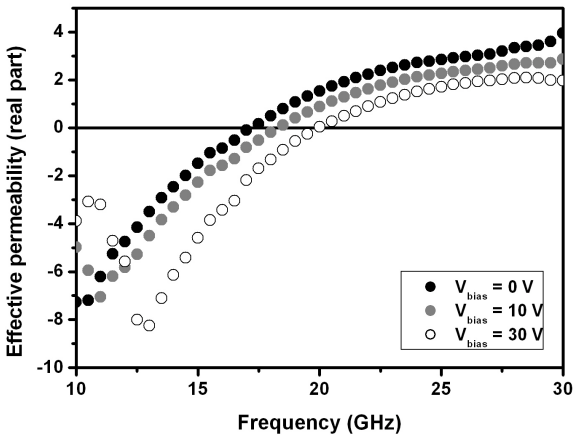

Figure II-24 : Évolution de la perméabilité effective en fonction de la fréquence pour différentes valeurs de la tension de commande.

L'étude menée sur ces déphaseurs conçus à partir d'un film élaboré par technique sol-gel est comparable aux travaux publiés dans la littérature utilisant des techniques de dépôt sous vide [24]. L'extension de ce concept de déphaseur aux fréquences plus élevées se heurte au problème des pertes. En effet, l'évolution de la constante diélectrique complexe reportée sur la figure II-25 montre que la tangente de pertes qui reste inférieure à 10^{-1} autour de 1 GHz augmente jusqu'à la valeur typique de 0,25 à 100 GHz. Cette dégradation a deux conséquences principales sur les performances du déphaseur : du point de vue des caractéristiques hyperfréquences, l'augmentation des pertes diélectriques se traduit par une augmentation des pertes d'insertion. Ces dernières peuvent toutefois être limitées dans le cas de structures relativement courtes comme c'est le cas de celles décrites dans ce paragraphe. Du point de vue de l'agilité, l'augmentation de la partie imaginaire de la permittivité associée à la diminution de sa partie réelle a tendance à décaler la caractéristique *C(V)* vers des valeurs de capacité plus élevées. Cela a pour conséquence de diminuer le rapport C_{max}/C_{min} et ainsi de réduire l'agilité du dispositif. Toutefois, dans le cas de nos structures, l'augmentation de la tangente de pertes est en partie

compensée par les effets inductifs liés à la structure interdigitée [18]. Cette compensation explique en partie la préservation du rapport C_{max}/C_{min} relevé à la fréquence de 20 GHz (figure II-1). L'étude des caractéristiques diélectriques du film BST fait partie du travail de thèse mené par G. Houzet. Les résultats présentés sur la figure II-25 ont été extraits de données mesurées en utilisant la méthode Cole-Cole [25].

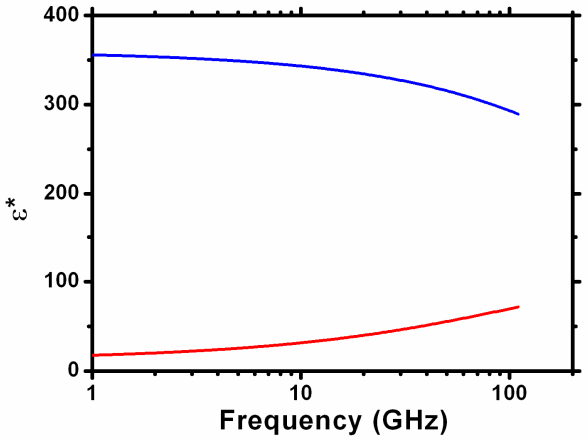

Figure II-25 : Permittivité complexe du film de BST en fonction de la fréquence : partie réelle (courbe du haut en bleu), partie imaginaire (courbe du bas en rouge).

Nous avons montré que l'approche de ligne duale caractérisée par des bandes passantes larges associées à des niveaux de pertes relativement faibles permettait en outre de travailler en régime composite équilibré, propriété intéressante en vue des applications. En dépit de ces avantages, cette approche peut difficilement être étendue à la conception de métamatériaux volumiques. Par ailleurs, la limitation fréquentielle des lignes de propagation constitue une barrière pour les longueurs d'onde de l'optique.

Dans le cadre de cette étude, le BST, élaboré en couche mince, est utilisé en tant que matériau agile, afin d'apporter la fonction d'accordabilité à un circuit déphaseur. Parallèlement à cette application, les valeurs de permittivité relatives très importantes observées dans le BST en font un matériau de choix pour la conception de métamatériaux basés sur la résonance de Mie. Dans ce cas, des volumes élementaires de BST peuvent être utilisés pour la conception de nouvelles structures à base de résonateurs diélectriques [26]. Au paragraphe suivant, nous

présentons l'étude d'un métamatériau 1D basée sur l'utilisation d'un réseau de lettres Ω interconnectées. Cette approche est qualifiée d'hybride dans la mesure où elle conduit à des propriétés de dispersion proches de celles des lignes duales tout en utilisant des résonateurs en boucles de courant.

II.3 Métamatériau 1D à réseau de lettre Ω

Le motif de lettre Ω a été introduit par N. Engheta [27], initialement pour la conception de structures chirales. Plus récemment, dans le contexte des métamatériaux, cette particule a été utilisée pour synthétiser un milieu effectif doublement négatif [28, 29]. Son premier intérêt est celui de la simplification de conception. En effet, la lettre Ω associe un dipôle électrique, matérialisé par ses bras, et un dipôle magnétique matérialisé par sa boucle. Par conséquent, cette particule présente à la fois une réponse électrique et une réponse magnétique. D'un point de vue pratique, un milieu doublement négatif peut donc être synthétisé à partir d'un unique réseau de motifs métalliques.

Le groupe de Kong a démontré de manière expérimentale l'intérêt que pouvaient présenter les réseaux de particules Ω en termes de pertes et de largeur de bande [30]. Dans cette étude, les lettres Ω sont interconnectées par leurs bras pour former des chaînes infinies. Cette configuration revient à coupler des résonateurs matérialisés par les boucles de courant. Ce couplage contribue à diminuer le coefficient de qualité de la résonance, ce qui se traduit par un élargissement de la bande passante et une remontée du niveau de transmission. Il s'agit de l'approche hybride présentée au paragraphe 2.3 du chapitre précédent.

Pour notre première analyse expérimentale des réseaux de lettres Ω [31], nous avons repris le guide rectangulaire WR-62 décrit au paragraphe précédent. Dans ce cas, nous n'avons pas essayé de définir une structure finline. Par conséquent, nous travaillons à partir du mode de propagation TE_{10} qui correspond au mode fondamental du guide dans la bande de fréquence considérée (10-18 GHz). Ce choix a été motivé par le souci d'accéder directement aux paramètres intrinsèques de la structure métamatériau. En contrepartie, nous ne travaillons pas dans des conditions d'excitation par une onde plane. Par conséquent, en raison de la variation du champ

magnétique suivant l'axe de propagation, on peut s'attendre à une relative importance des effets de couplage sur les structures qui incluent plusieurs motifs dans cette direction.

Comme nous l'avons commenté au paragraphe II.13, le guide rectangulaire qui constitue un environnement électromagnétique fermé est favorable pour quantifier les pertes intrinsèques du métamatériau. Concernant les réseaux de particules Ω, nous avons insisté sur le rôle joué par l'interconnexion des motifs sur ces pertes et sur la bande passante. Dans le cas de la structure étudiée, la situation d'interconnexion d'une chaîne infinie est obtenue par effet miroir, en tirant partie des conditions de symétrie du champ électrique imposé par les parois métalliques du guide. La vue en perspective de la figure II-26 décrit une cellule unitaire.

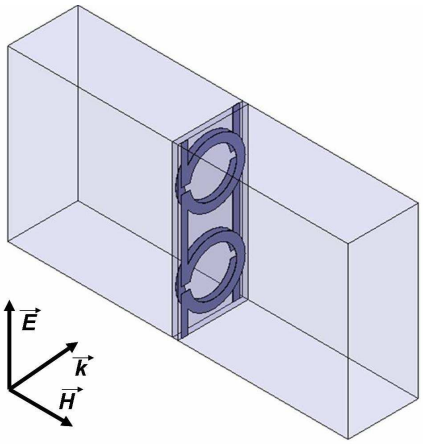

Figure II-26 : Vue en perspective d'une cellule unitaire insérée dans le guide métallique rectangulaire WR-62.

Les motifs Ω sont superposés en un arrangement antisymétrique de part et d'autre d'un substrat Duroïd Rodgers de permittivité relative 2,2 et d'épaisseur 254 µm. De même que pour les anneaux imbriqués [8] ou couplés par superposition [9], cette situation permet de s'affranchir des effets de bianisotropie [29]. Par ailleurs, la cellule inclut deux lettres dans la direction transverse de manière à définir un métamatériau dont la fréquence de fonctionnement soit située dans le domaine de propagation du mode TE_{10}. En effet, la réponse de la lettre Ω est fixée par ses dimensions reportées sur la figure II-27. Par conséquent, l'ouverture du guide, égale à 7,9 mm, permet l'inclusion de deux lettres. Des rubans métalliques ont été insérés de part et d'autre des motifs afin d'assurer le contact électrique avec les parois du guide reproduisant les conditions

d'interconnexion. Sur le plan pratique, le contact électrique est assuré par compression du substrat entre les deux demi-coques du guide WR-62.

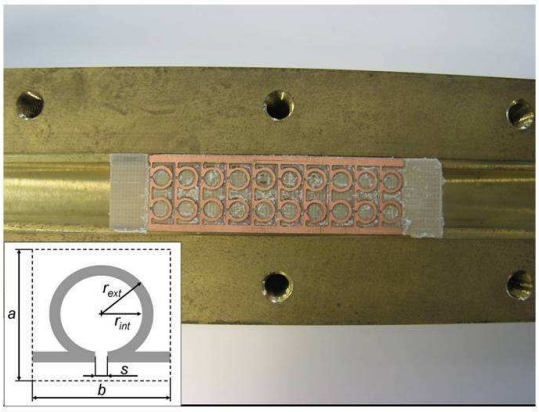

a = 3,3 mm
b = 4,1 mm
s = 0,3 mm
r_{ext} = 1,5 mm
r_{int} = 1,2 mm

Figure II-27 : Vue de dessus d'une demi-coque du guide WR-62 incluant la structure métamatériau. Représentation schématique et dimensionnement de la lettre Ω.

Les mesures de paramètres S_{ij} (figures II-28 et II-29) ont permis de mettre en évidence une première bande de transmission comprise entre 12,5 et 15 GHz suivie d'une bande interdite puis d'une seconde bande passante à partir de 18 GHz. L'analyseur de réseau *HP 8510* a été calibré par une méthode TRL pour la bande Ku (12-18 GHz). Nous avons choisi d'étendre le domaine de mesure jusque 19 GHz afin de visualiser la formation de cette seconde bande passante. Cependant, il est évident que les points situés en dehors de la plage de calibration ne fournissent qu'une information qualitative. La figure II-28 montre les spectres de transmission obtenus pour une structure incluant 5 cellules suivant la direction de propagation. Ce premier résultat montre une bande passante élargie par rapport à la structure précédente. En effet, le quotient $\frac{\Delta f}{f_0}$ est de l'ordre de 20 % contre 10 % pour le métamatériau composé de réseaux de fils et d'anneaux fendus imbriqués. Cet élargissement de la bande passante s'accompagne d'une augmentation du niveau de transmission qui vaut typiquement -5 dB pour 10 cellules (figure II-29).

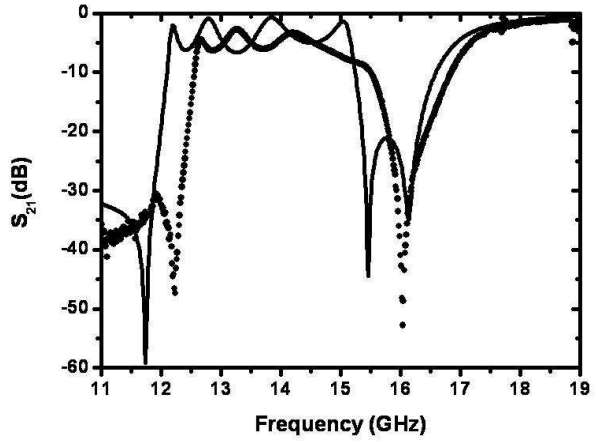

Figure II-28 : Spectres de transmission mesuré (points) et simulé (trait plein) pour une structure incluant 5 cellules unitaires.

Sur la figure II-29, nous avons superposé les relevés du spectre de transmission pour un réseau de 10 cellules et de la différence de phase pour des réseaux à 10 et 5 cellules qui permet de vérifier le comportement gaucher de la bande passante fondamentale.

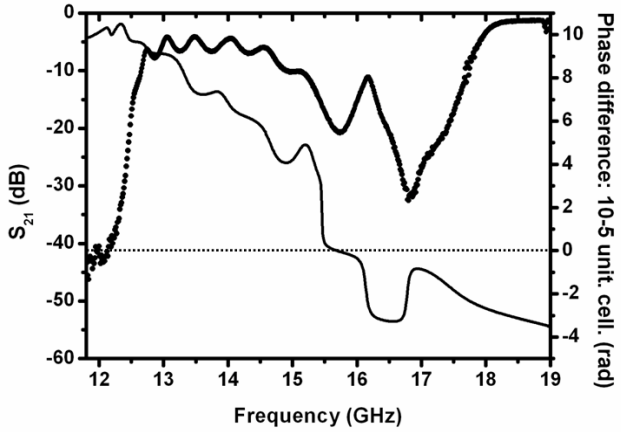

Figure II-29 : Spectre de transmission mesuré sur une structure à 10 cellules (points), différence de phase relevée entre les structures à 10 et 5 cellules (trait plein).

On peut remarquer, sur la figure II-28, un décalage entre les courbes expérimentales et simulées d'environ 500 MHz. Ce décalage peut être attribué à l'imprécision de profondeur de gravure des substrats de Duroïd. En effet, les motifs sont définis par un procédé de gravure mécanique à l'aide d'un système *LPKF Protomat* dont la précision annoncée par le constructeur est de 20 µm. Sur la figure II-30, nous avons représenté les paramètres S_{ij} simulés pour une

structure incluant une seule cellule unitaire en considérant l'épaisseur de substrat nominale d'une part et une épaisseur prenant en compte une tolérance maximale de 20 µm d'autre part. Les caractéristiques expérimentales se situent entre ces deux courbes théoriques, ce qui accrédite l'hypothèse de la surgravure.

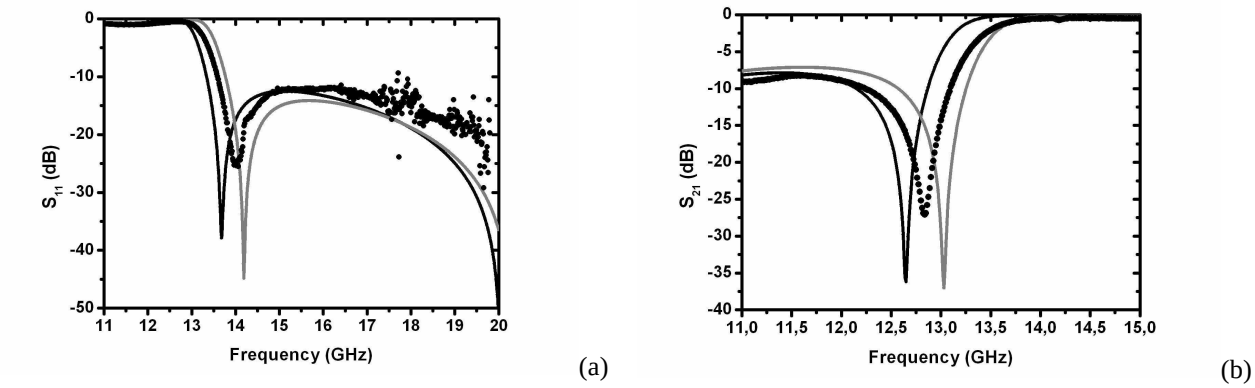

Figure II-30 : Paramètres S_{ij} relevés (points) et simulés (traits pleins) pour une cellule unitaire avec l'épaisseur nominale de substrat (trait noir) et comprenant une tolérance de gravure de 20 µm (trait gris) : (a) S_{11}(dB), (b) S_{21}(dB).

À partir du relevé expérimental de la matrice de répartition sur une structure incluant une seule cellule, nous avons pu extraire des valeurs de permittivité et de perméabilité effectives par la méthode d'inversion des relations de Fresnel [7]. Le relevé des parties réelles présenté sur la figure II-31 montre une zone de recouvrement des valeurs négatives comprise entre 13 et 16 GHz. Bien que cette analyse ne prenne pas en compte les phénomènes de couplage suivant la direction de propagation, ce domaine de fréquence est comparable à la bande passante présentée par les structures de dimension finie intégrant plusieurs cellules unitaires (figures II-28 et II-29). La perméabilité effective suit une évolution lorentzienne caractéristique des boucles de courant résonantes. En revanche, la permittivité effective suit majoritairement une progression de Drude, caractéristique d'un réseau de fils continus parallèles à la direction du vecteur champ électrique. On remarque toutefois l'incidence de la résonance du courant sur cette croissance sous la forme d'une antirésonance au voisinage de 13 GHz. L'affichage des parties imaginaires des paramètres constitutifs effectifs nous permet de vérifier le principe de passivité [32]. En effet, ces parties

imaginaires ne prennent des valeurs négatives que lorsque l'on se trouve en présence d'une antirésonance.

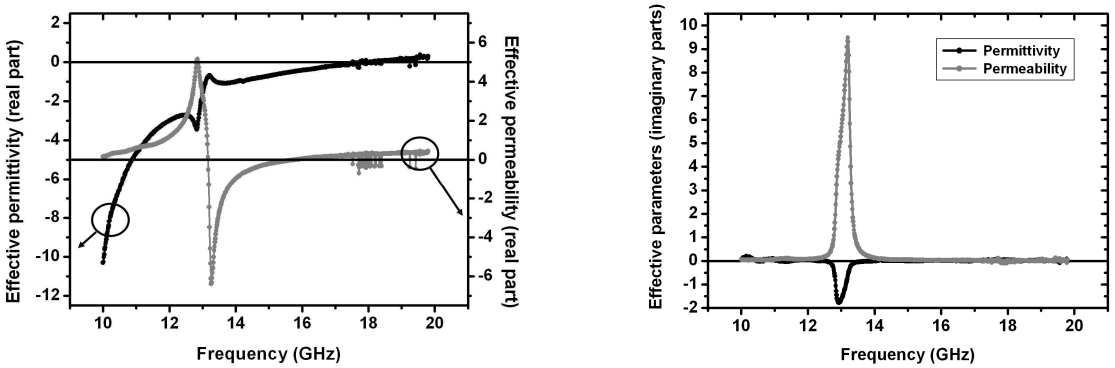

Figure II-31 : Permittivité et perméabilité effectives obtenues par inversion des relations de Fresnel à partir des relevés S_{ij} expérimentaux sur une cellule unitaire : (a) parties réelles , (b) parties imaginaires.

La figure II-32 compare les évolutions obtenues pour des chaînes de motifs interconnectés et des chaînes formées de lettres Ω isolées. Sur le plan qualitatif, le graphe de droite décrit le cas observé en pratique. En revanche, lorsque les motifs sont déconnectés, l'évolution de la permittivité devient résonnante avec un décalage des valeurs négatives vers les hautes fréquences, à partir de 15 GHz. Ce phénomène a déjà été décrit dans le cas de structures à cristaux photoniques qui utilisent des réseaux de fils métalliques [33, 34].

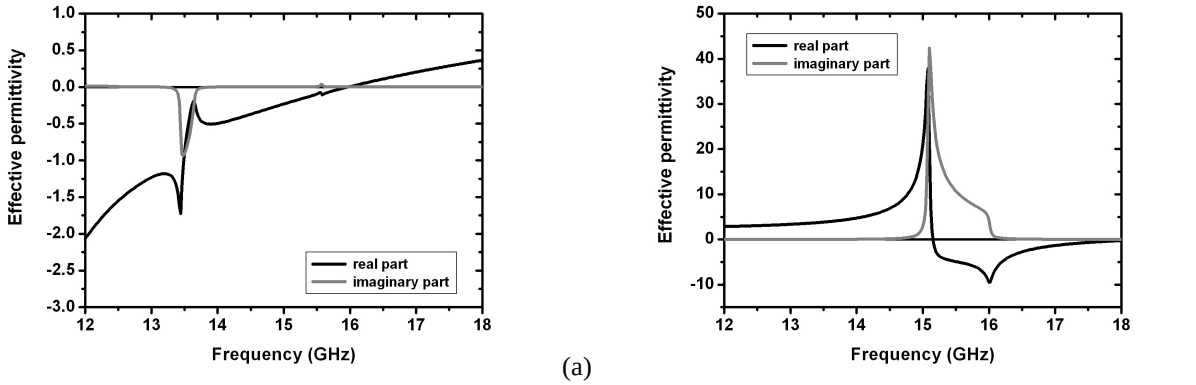

Figure II-32 : Comparaison des permittivités complexes simulées dans le cas de lettres Ω interconnectées (a) et isolées (b).

Les propriétés de dispersion de chaînes de motifs Ω interconnectés sont plus longuement commentées au chapitre III à partir de l'analyse de métamatériaux volumiques.

Conclusion

Nous avons présenté l'analyse de trois structures doublement négatives unidimensionelles, dans un environnement guidé. Cette étude, relativement simple à mettre en œuvre par comparaison à la fabrication et à la caractérisation de structures en espace libre permet de tirer des conclusions qui peuvent être généralisées aux métamatériaux volumiques, même si l'interaction par couplage avec le support de propagation n'est pas négligeable.

Ainsi, nous avons pu mettre en évidence, par des mesures de phase, le phénomène de rétropropagation. De plus, l'inversion de Fresnel à partir de la matrice de répartition complexe a permis d'extraire la dispersion des permittivité et perméabilité effectives.

Par ailleurs, grâce à l'utilisation d'un environnement électromagnétique fermé, nous avons mis en évidence l'importance des termes de pertes dans les structures basées sur des réseaux de boucles de courant isolées qui présentent également des bandes passantes relativement étroites.

En restant dans une approche unidimensionelle, afin de s'affranchir du caractère résonant des boucles de courant, on peut adopter une topologie de ligne de propagation duale. Ce concept, présenté au chapitre I, est mis en application à partir de l'exemple d'un déphaseur main gauche accordable.

Enfin, nous avons démontré expérimentalement l'avantage des réseaux composés de chaînes de motifs Ω interconnectés qui permettent de tirer parti de certaines propriétés de dispersion des lignes duales en s'affranchissant des contraintes de conception relatives aux lignes de transmission. Cette propriété est confortée par l'étude de structures volumiques développée au chapitre III.

Références

[1] R. Marqués, J. Martel, F. Mesa, and F. Medina, "Left-Handed-Media Simulation and Transmission of EM Waves in Subwavelength Split-Ring-Resonator-Loaded Metallic Waveguides," *Physical Review Letters*, vol. 89, pp. 183901, 2002.

[2] J. Carbonell, L. J. Rogla, V. E. Boria, and R. Marques, "Enhanced backward wave propagation in evanescent waveguides loaded with split ring resonators," *Journal of Applied Physics*, vol. 102, pp. 044902, 2007.

[3] J. Carbonell, L. J. Rogla, V. E. Boria, and D. Lippens, "Design and experimental verification of backward-wave propagation in periodic waveguide structures," *Microwave Theory and Techniques, IEEE Transactions on*, vol. 54, pp. 1527-1533, 2006.

[4] T. Decoopman, X. Melique, O. Vanbesien, and D. Lippens, "A taper filtering finline at millimeter wavelengths for broadband harmonic multiplication," *Microwave and Wireless Components Letters, IEEE*, vol. 13, pp. 172-174, 2003.

[5] T. Decoopman, O. Vanbesien, and D. Lippens, "Demonstration of a backward wave in a single split ring resonator and wire loaded finline," *Microwave and Wireless Components Letters, IEEE*, vol. 14, pp. 507-509, 2004.

[6] T. Decoopman, "Mutiplicateurs de fréquence et métamatériaux en technologie finline," in *Microondes et microtechnologies*, vol. Doctorat. Lille: Université des Sciences et Technologies de Lille, 2004.

[7] W. B. Weir, "Automatic measurement of complex dielectric constant and permeability at microwave frequencies," *Proceedings of the IEEE*, vol. 62, pp. 33-36, 1974.

[8] J. B. Pendry, A. J. Holden, D. J. Robbins, and W. J. Stewart, "Magnetism from conductors and enhanced nonlinear phenomena," *Microwave Theory and Techniques, IEEE Transactions on*, vol. 47, pp. 2075-2084, 1999.

[9] R. Marques, F. Mesa, J. Martel, and F. Medina, "Comparative analysis of edge- and broadside- coupled split ring resonators for metamaterial design - theory and experiments," *Antennas and Propagation, IEEE Transactions on*, vol. 51, pp. 2572-2581, 2003.

[10] S. Linden, C. Enkrich, M. Wegener, J. Zhou, T. Koschny, and C. M. Soukoulis, "Magnetic Response of Metamaterials at 100 Terahertz," *Science*, vol. 306, pp. 1351-1353, 2004.

[11] T. Decoopman, T. Crepin, M. Perrin, S. Fasquel, A. Marteau, X. Mélique, E. Lheurette, O. Vanbésien, and D. Lippens, "Left-handed propagation media via photonic crystal and metamaterials," *Comptes Rendus Physique*, vol. 6, pp. 683-692, 2005.

[12] T. Decoopman, A. Marteau, E. Lheurette, O. Vanbesien, and D. Lippens, "Left-handed electromagnetic properties of split-ring resonator and wire loaded transmission line in a fin-line technology," *Microwave Theory and Techniques, IEEE Transactions on*, vol. 54, pp. 1451-1457, 2006.

[13] M. Perrin, S. Fasquel, T. Decoopman, X. Mélique, O. Vanbésien, E. Lheurette, and D. Lippens, "Left-handed electromagnetism obtained via nanostructured metamaterials:

comparison with that from microstructured photonic crystals," *Journal of Optics A: Pure and Applied Optics*, pp. S3, 2005.

[14] O. F. Siddiqui, M. Mojahedi, and G. V. Eleftheriades, "Periodically loaded transmission line with effective negative refractive index and negative group velocity," *Antennas and Propagation, IEEE Transactions on*, vol. 51, pp. 2619-2625, 2003.

[15] J. Garcia-Garcia, J. Bonache, I. Gil, F. Martin, M. C. Velazquez-Ahumada, and J. Martel, "Miniaturized microstrip and CPW filters using coupled metamaterial resonators," *Microwave Theory and Techniques, IEEE Transactions on*, vol. 54, pp. 2628-2635, 2006.

[16] A. L. Borja, J. Carbonell, V. E. Boria, and D. Lippens, "Symmetrical frequency response in a split ring resonator based transmission line," *Applied Physics Letters*, vol. 93, pp. 203505-3, 2008.

[17] G. Velu, J. C. Carru, E. Cattan, D. Remiens, X. Melique, and D. Lippens, "Deposition of Ferroelectric BST Thin Films by Sol Gel Route in View of Electronic Applications," *Ferroelectrics*, vol. 288, pp. 59 - 69, 2003.

[18] G. Houzet, L. Burgnies, G. Velu, J. C. Carru, and D. Lippens, "Dispersion and loss of ferroelectric Ba[sub 0.5]Sr[sub 0.5]TiO[sub 3] thin films up to 110 GHz," *Applied Physics Letters*, vol. 93, pp. 053507, 2008.

[19] A. Lai, T. Itoh, and C. Caloz, "Composite right/left-handed transmission line metamaterials," *Microwave Magazine, IEEE*, vol. 5, pp. 34-50, 2004.

[20] P. F. Combes, Micro-ondes. Vol.1 Lignes, guides et cavités, Dunod ed, 1996.

[21] G. Velu, K. Blary, L. Burgnies, J. C. Carru, E. Delos, A. Marteau, and D. Lippens, "A 310/spl deg//3.6-dB K-band phaseshifter using paraelectric BST thin films," *Microwave and Wireless Components Letters, IEEE [see also IEEE Microwave and Guided Wave Letters]*, vol. 16, pp. 87-89, 2006.

[22] S. S. Gevorgian, T. Martinsson, P. L. J. Linner, and E. L. Kollberg, "CAD models for multilayered substrate interdigital capacitors," *Microwave Theory and Techniques, IEEE Transactions on*, vol. 44, pp. 896-904, 1996.

[23] T. I. Christophe Caloz, "TL Theory of MTMs," in Electromagnetic Metamaterials: Transmission Line Theory and Microwave Applications, 2005, pp. 59-132.

[24] D. Kuylenstierna, A. Vorobiev, P. Linner, and S. Gevorgian, "Composite right/left handed transmission line phase shifter using ferroelectric varactors," *Microwave and Wireless Components Letters, IEEE*, vol. 16, pp. 167-169, 2006.

[25] C. B. James, T. Ichiro, and C. Kao-Shuo, "Microwave-frequency loss and dispersion in ferroelectric Ba[sub 0.3]Sr[sub 0.7]TiO[sub 3] thin films," *Applied Physics Letters*, vol. 87, pp. 082908, 2005.

[26] D. P. Gaillot, C. Croënne, and D. Lippens, "An all-dielectric route for terahertz cloaking," *Opt. Express*, vol. 16, pp. 3986-3992, 2008.

[27] M. M. I. Saadoun and N. Engheta, "A reciprocical phase shifter using novel pseudochiral or Ω medium," *Microwave and Optical Technology Letters*, vol. 5, pp. 184-188, 1992.

[28] C. R. Simovski and S. He, "Frequency range and explicit expressions for negative permittivity and permeability for an isotropic medium formed by a lattice of perfectly conducting [Omega] particles," *Physics Letters A*, vol. 311, pp. 254-263, 2003.

[29] H. Jiangtao, R. Lixin, C. Hongsheng, Z. Xian-min, C. Kangsheng, M. G. Tomasz, and K. Jin Au, "Experimental confirmation of negative refractive index of a metamaterial composed of Omega-like metallic patterns," *Applied Physics Letters*, vol. 84, pp. 1537-1539, 2004.

[30] L. Ran, J. Huangfu, H. Chen, Y. Li, X. Zhang, K. Chen, and J. A. Kong, "Microwave solid-state left-handed material with a broad bandwidth and an ultralow loss," *Physical Review B (Condensed Matter and Materials Physics)*, vol. 70, pp. 073102, 2004.

[31] E. Lheurette, G. Houzet, J. Carbonell, F. Zhang, O. Vanbesien, and D. Lippens, "Omega-Type Balanced Composite Negative Refractive Index Materials," *Antennas and Propagation, IEEE Transactions on*, vol. 56, pp. 3462-3469, 2008.

[32] T. Koschny, P. Markos, E. N. Economou, D. R. Smith, D. C. Vier, and C. M. Soukoulis, "Impact of inherent periodic structure on effective medium description of left-handed and related metamaterials," *Physical Review B (Condensed Matter and Materials Physics)*, vol. 71, pp. 245105-22, 2005.

[33] J. Danglot, O. Vanbesien, and D. Lippens, "Active waveguides patterned in mixed 2D-3D metallic photonic crystal," *Electronics Letters*, vol. 35, pp. 475-477, 1999.

[34] M. M. Sigalas, C. T. Chan, K. M. Ho, and C. M. Soukoulis, "Metallic photonic band-gap materials," *Physical Review B*, vol. 52, pp. 11744, 1995.

Chapitre III :
Métamatériaux pour l'espace libre

Introduction

Le chapitre précédent a permis de mettre en évidence les limitations des deux approches les plus courantes pour la conception des métamatériaux. La première voie qui consiste à superposer un réseau de fils et de résonateurs fendus souffre de bandes passantes étroites et de pertes importantes. La seconde voie, inspirée du concept de ligne duale, ne peut pas être directement appliquée à la définition d'un métamatériau volumique. En raison de sa facilité de mise en œuvre et de ses propriétés de dispersion, l'approche hybride, qui repose sur l'interconnexion de boucles de courant, nous semble appropriée pour la réalisation de métamatériaux volumique aux longueurs d'onde centimétriques et millimétriques. À l'issue d'un premier travail de simulation destiné à mieux comprendre les propriétés de ces réseaux, nous proposons la caractérisation de prototypes en réfraction aux longueurs d'onde centimétriques et en transmission dans la bande 75-110 GHz.

Pour le spectre térahertz, nous proposons les premiers résultats expérimentaux sur une structure composée de l'empilement de réseaux de trous sous longueur d'onde.

III.1 Motifs Ω interconnectés

Leurs caractères large bande et faibles pertes rendent les motifs Ω attrayants pour les longueurs d'onde millimétriques et submillimétriques. Nous proposons une comparaison des spectres de transmission présentés par des réseaux imbriqués classiques (SRR et fils) et par des réseaux de motifs Ω interconnectés [1]. Ce travail constitue une étude préliminaire pour le spectre millimétrique. Par conséquent, les structures sont conçues en vue d'une technologie d'intégration millimétrique utilisant le benzocyclobuthène BCB pour ses propriétés de diélectrique faibles pertes [2]. Les cellules élémentaires sont représentées sur la figure III-1 avec leurs dimensions respectives destinées à obtenir un recouvrement de leurs bandes passantes. Chaque particule inclut deux boucles de courant superposées de manière à éliminer les effets de bianisotropie [3]. Les structures simulées à l'aide du logiciel *HFSS* de *Ansoft* incluent 5 cellules élémentaires dans la direction de propagation. Le motif est répété à l'infini suivant les directions des champs

électrique et magnétique incidents par l'emploi de plans de symétrie de type Perfect E (PEC) suivant *Ox* et Perfect H (PMC) suivant *Oz*. Une valeur de conductivité de l'or ($\sigma = 4{,}1.10^7$ S/m) est prise en compte dans le modèle des motifs métalliques. Le BCB est assimilé à un diélectrique sans perte de permittivité relative 2,6.

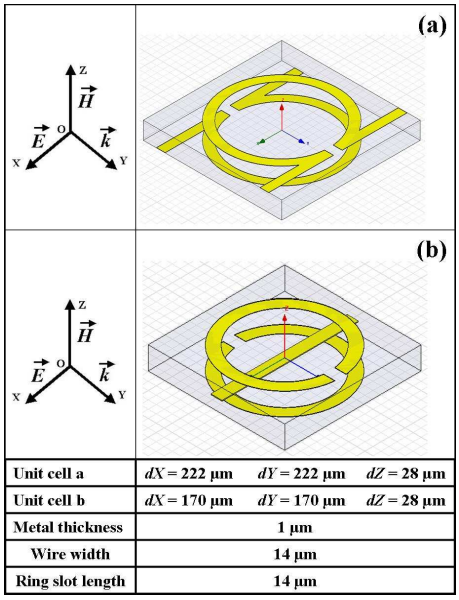

Unit cell a	*dX* = 222 µm	*dY* = 222 µm	*dZ* = 28 µm
Unit cell b	*dX* = 170 µm	*dY* = 170 µm	*dZ* = 28 µm
Metal thickness	1 µm		
Wire width	14 µm		
Ring slot length	14 µm		

Figure III-1 : Vue en perspective des cellules unitaires simulées par *HFSS* : (a) motif Ω, (b) motif fil et broadside coupled SRR [4]. Les métallisations sont noyées dans le BCB.

Les résultats de simulation présentés sur la figure III-2 montrent que la bande passante du réseau de motifs Ω interconnectés est bien plus étendue que pour les réseaux imbriqués conventionnels et ce quelle que soit l'orientation de la boucle de courant par rapport au champ électrique incident. Ces bandes passantes relatives sont de l'ordre de 50 % contre 14 % respectivement. Le réseau de motifs Ω présente un niveau de pertes d'insertion d'environ 0,5 dB par cellule élémentaire.

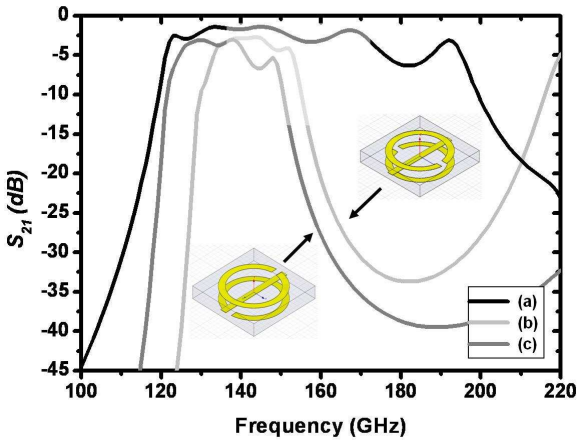

Figure III-2 : Spectres de transmission simulés pour les deux métamatériaux composés de 5 cellules unitaires : (a) motif Ω, (b) et (c) motif broadside coupled SRR.

Afin de mieux comprendre le rôle joué par l'interconnexion des motifs Ω, nous considérons, plusieurs configurations de réseau qui diffèrent par leur degré d'interconnexion (figure III-3). Les diagrammes de dispersion correspondant aux configurations (b) et (c) sont reportés sur la figure III-4.

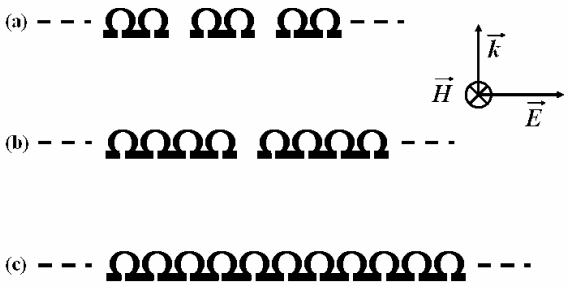

Figure III-3 : Configurations de chaînes Ω différant par leur degré d'interconnexion des motifs élémentaires.

Le diagramme de dispersion de la figure III-4 montre que la largeur de bande la plus importante est obtenue pour la situation de chaîne infinie décrite sur la figure III-3c.

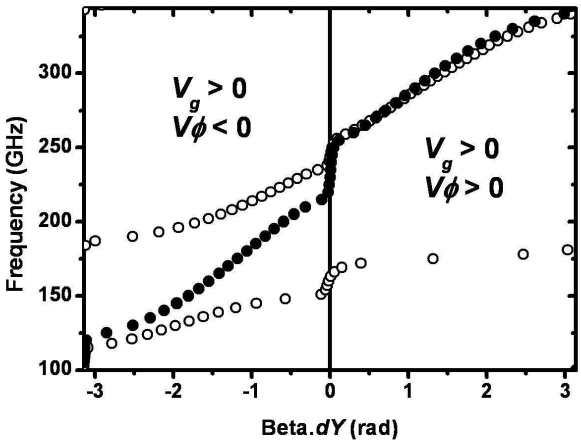

Figure III-4 : Diagrammes de dispersion simulés pour les chaînes 3b (○) et 3c (●).

En comparaison, le réseau périodique formé par des groupes isolés de quatre particules (figure III-3b) fait apparaître plusieurs bandes interdites qui ont pour conséquence de réduire considérablement l'étendue de la bande main gauche fondamentale. C'est sur cette base des chaînes de motifs interconnectés que nous avons fabriqué puis caractérisé plusieurs métamatériaux volumiques.

III.12 Métamatériaux pour la bande W

À l'issue de cette étude préliminaire, qui a permis de mettre en évidence des performances prometteuses pour les longueurs d'onde millimétriques et submillimétriques, un prototype a été réalisé puis caractérisé dans la bande 75-110 GHz [5]. Pour ce travail, nous avons bénéficié du concours de D. P. Gaillot, alors post-doctorant dans notre groupe de recherche. Ce prototype est schématisé sur la figure III-5.

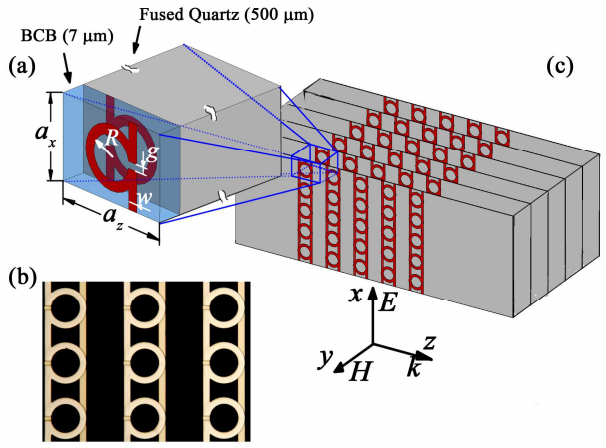

Figure III-5 : Métamatériau volumique réalisé pour la bande W, (a) cellule unitaire incluant le substrat, (b) vue de dessus au microscope optique de l'échantillon réalisé, (c) vue en perspective du métamatériau.

Il est constitué par l'empilement de plusieurs réseaux de particules Ω interconnectées réalisés sur substrat de quartz. Chaque cellule élémentaire inclut deux motifs Ω placés en vis-à-vis et séparés par une couche de BCB de 7 µm. La plus petite dimension mise en jeu (g) est de l'ordre de 30 µm. Par conséquent, les structures ont pu être définies au moyen d'une lithographie optique. Les métallisations sont constituées d'une séquence de 500 Å de titane et 4000 Å d'or évaporée sous vide. La fabrication a été menée à partir de substrats de quartz de 500 µm d'épaisseur et de 2 pouces de diamètre qui ont été ensuite découpés en carrés de 20 mm de côté puis empilés pour définir un métamatériau volumique d'épaisseur 15 mm. La figure III-6 montre le premier niveau de métallisation d'un substrat incluant 10 cellules suivant la direction de propagation.

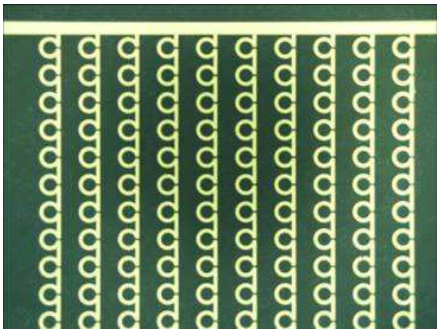

Figure III-6 : Vue au microscope optique du premier niveau de métallisation d'un métamatériau incluant 10 cellules dans la direction de propagation.

Dans le but d'extraire une phase différentielle, deux structurations élémentaires sont définies incluant 10 (figure III-7a) puis 14 cellules élémentaires (figure III-7b) suivant la direction de propagation.

(a) (b)

Figure III-7 : Lames de quartz recouvertes de BCB et métallisées avec les motifs de lettres Ω : (a) lame à 10 motifs, (b) lame à 14 motifs.

Chaque prototype est formé par l'empilement de 30 lames de quartz. Nous avons vu que pour obtenir un effet de magnétisme artificiel, le vecteur champ magnétique devait être parallèle à l'axe des boucles de courant et le vecteur champ électrique, parallèle au plan des motifs. Afin de respecter ces conditions de polarisation, les substrats empilés doivent être excités par la tranche. Cette contrainte implique un bon alignement des substrats de manière à s'affranchir d'une forte rugosité à l'interface avec l'onde plane. Par ailleurs, en dépit des performances de cette topologie en termes de bande passante et de pertes, elle constitue un frein pour le développement de structures fonctionnant aux longueurs d'onde submillimétriques. Ce dernier point est plus largement commenté à l'issue de ce paragraphe. Sur le plan pratique, afin de réaliser l'alignement et le maintien des substrats empilés, nous avons utilisé une boîte en matière plastique avec des parois d'épaisseur faible de manière à ne pas altérer la réponse intrinsèque du métamatériau (figure III-8).

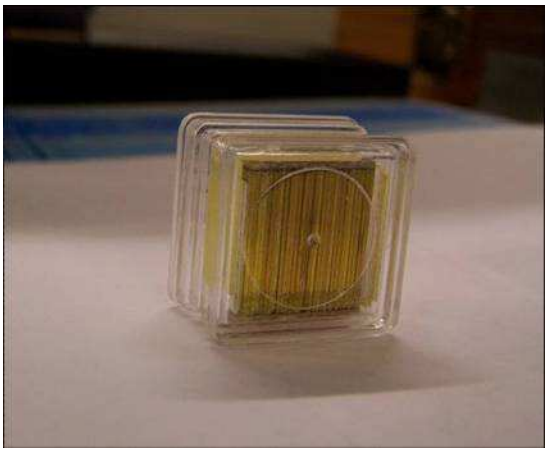

Figure III-8 : Métamatériau volumique constitué par l'empilement de 30 lames (figure III-7).

La caractérisation a été menée en espace libre au moyen d'un analyseur de réseau Hewlett-Packard *HP 8510* calibré dans la bande 75-110 GHz. Les échantillons ont été mesurés en condition de champ proche par Fuli Zhang. Pour ce faire, le métamatériau a été inséré dans une plaque de matériau absorbant Eccosorb AN-75 et placé entre deux cornets scalaires (figure III-9).

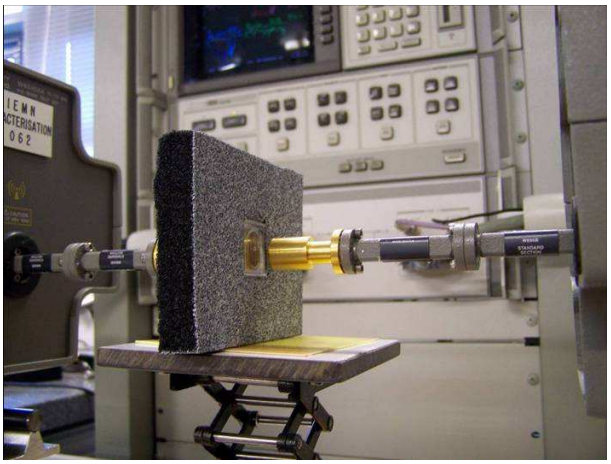

Figure III-9 : Photographie du banc de mesure en espace libre. L'échantillon est inséré dans une plaque de matériau absorbant de manière à limiter l'influence des signaux parasites en réflexion et transmission.

Le spectre de transmission reporté sur la figure III-10 a été obtenu pour un réseau incluant 10 motifs suivant la direction de propagation. Cette caractéristique présente un bon accord avec la transmission simulée à l'aide du logiciel *CST Microwave Studio*. La bande passante, supérieure à

10 %, est plus faible que les prévisions annoncées au paragraphe précédent. Cela peut s'expliquer par la dilution du réseau suivant la direction *Oy* lié à l'insertion des substrats de quartz. Toutefois, il est à noter que les niveaux de pertes de l'ordre de 0,5 dB par cellule confirment les prévisions théoriques. À notre connaissance, le niveau de transmission obtenu se situe à l'état de l'art pour ce domaine de fréquence. Sur le même graphe, nous avons reporté l'indice de réfraction effectif théorique illustrant le caractère main gauche de la première bande passante comprise typiquement entre 75 et 85 GHz.

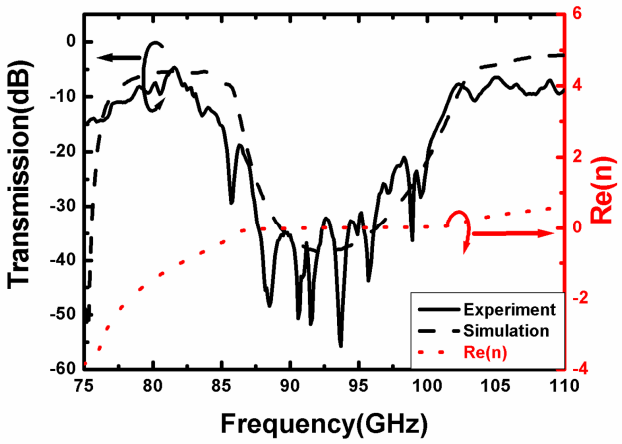

Figure III-10 : Superposition des amplitudes de transmission simulée et mesurée, indice de réfraction extrait de la simulation par inversion des relations de Fresnel [6].

Ces valeurs négatives d'indice ont pu être confirmées par l'expérience au moyen des mesures de phase réalisées sur deux échantillons de longueurs électriques différentes incluant 14 et 10 cellules dans la direction de propagation. Les évolutions correspondantes sont données sur la figure III-11. Ce graphe montre sans ambiguïté une différence de phase positive en bande fondamentale, signature d'un comportement gaucher, et négative en seconde bande illustrant un régime de propagation droitier.

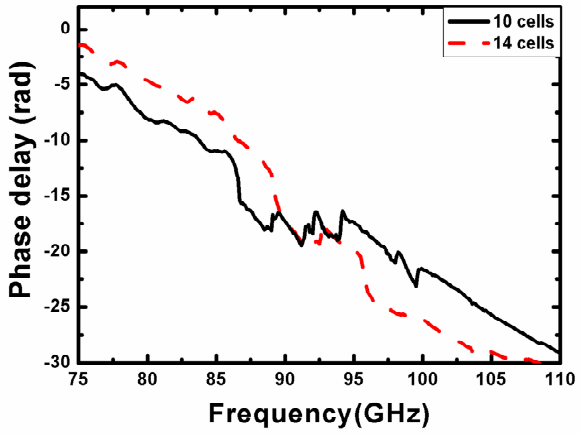

Figure III-11 : Comparaison des phases déroulées mesurées sur les métamatériaux à 14 et 10 cellules unitaires.

La figure III-12 reprend le spectre de transmission de la figure III-10, relevé pour différentes incidences du vecteur d'onde comprises entre 0 et 30°. La première bande passante a tendance à s'éteindre lorsque l'angle d'incidence augmente. Ce phénomène est la conséquence directe de l'affaiblissement de la réponse magnétique des motifs Ω lorsque le vecteur champ magnétique incident n'est plus parallèle à l'axe des boucles de courants. En comparaison, la seconde bande passante est beaucoup moins sensible à l'angle d'incidence. Cette expérience confirme le caractère local de la bande fondamentale qui est obtenue par la superposition des réponses magnétique et électrique des particules Ω.

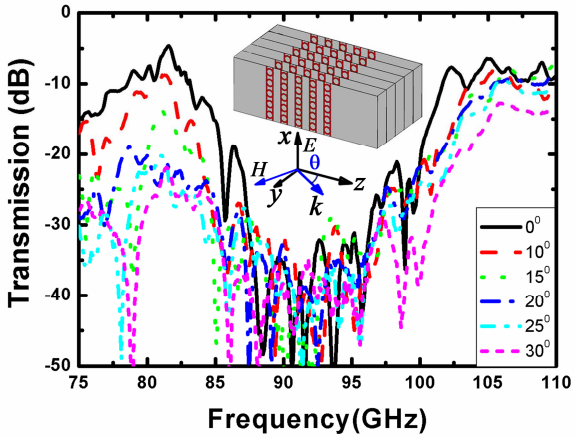

Figure III-12 : Spectres de transmission relevés pour différents angles d'incidence autour de l'axe de rotation *Ox*.

Ce résultat illustre également le caractère fortement anisotrope de ce type de métamatériaux. Ce dernier point est plus largement commenté dans le paragraphe suivant qui présente une étude angulaire effectuée sur un prototype conçu pour le domaine centimétrique.

III.13 Réfraction négative en bandes X et Ku

Cette étude a été menée dans les bandes X et Ku dans le but de démontrer de façon expérimentale les propriétés des réseaux constitués de motifs Ω interconnectés afin de mieux appréhender les phénomènes physiques mis en jeu. Elle s'inscrit dans le cadre des thèses de doctorat suivies par G. Houzet et F. Zhang. Le choix de ce domaine de fréquences permet tout d'abord de s'affranchir des difficultés de la microfabrication. En effet, les deux prototypes utilisés ont été fabriqués par des techniques employées en technologie des circuits imprimés qui autorise une maîtrise des dimensions à une échelle inférieure au millimètre. Par ailleurs, les deux prototypes étudiés, le parallélépipède et le prisme ont pu être caractérisés à l'analyseur de réseau, en espace libre, en bénéficiant de la continuité des bandes X et Ku. La largeur de bande totale du dispositif de mesure, comprise entre 8 et 18 GHz, autorise le balayage des branches de dispersion main gauche et main droite correspondant à des régimes de réfraction négative et positive respectivement.

III.14 Transmission à travers un parallélépipède

Le premier prototype réalisé est un parallélépipède en époxy incrusté de chaînes de motifs Ω en cuivre. Lors de la conception, l'accent a été mis sur l'obtention d'une condition d'équilibre assurant une évolution continue des bandes main gauche et main droite sans bande interdite. Ce comportement, typique des lignes de propagation duales, s'observe dès l'instant où les fréquences de résonance des circuits équivalents série et parallèle sont identiques. Or la particule Ω, qui est employée en technologie MMIC pour définir une self-inductance plaquée, peut être modélisée par une inductance. De plus, la mise en regard de deux plans de motifs illustrée par la figure III-13 est à l'origine d'un couplage capacitif entre les boucles de courant. En effet, de même que dans les anneaux imbriqués (cf. paragraphe II.12), la configuration des deux lettres Ω placées en regard annule le mode de résonance antisymétrique généré par le vecteur champ électrique

parallèle aux bras. Par conséquent, la résonance du champ magnétique à l'origine de la perméabilité effective négative est la conséquence de courants parcourant les boucles dans le même sens. Le couplage entre ces boucles peut donc être modélisé par une capacité distribuée.

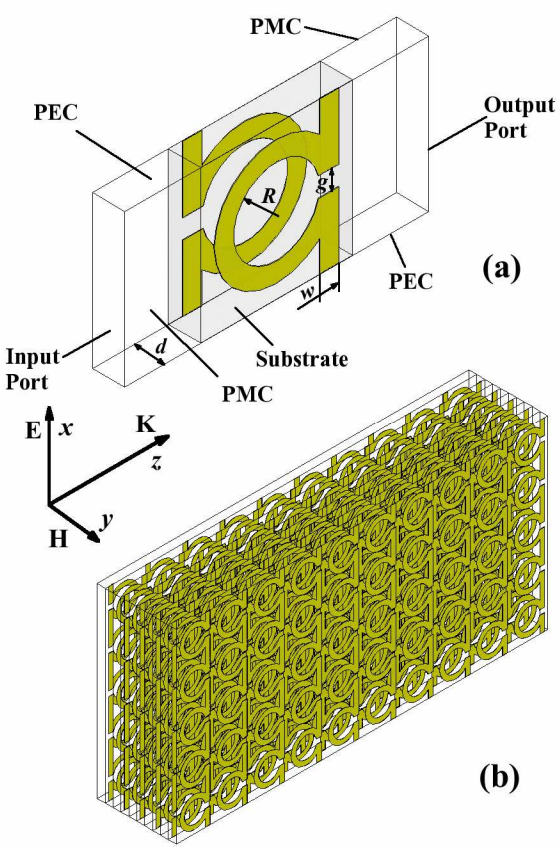

Figure III-13 : Cellule unitaire incluant deux lettres Ω (a), représentation en perspective du métamatériau volumique (b).

Ces comportements permettent de définir un schéma équivalent de la particule Ω (figure III-14) qui met en évidence la contribution d'un terme d'inductance shunt associé à un terme de capacité série. Les inductances L_1 et L_2 décrivent, en première approximation, le comportement inductif des bras et des boucles respectivement. *C* matérialise le couplage capacitif entre les deux boucles. On comprend dès lors que la transmission à travers les réseaux de motifs Ω interconnectés présente des similitudes avec la propagation sur une ligne de transmission duale.

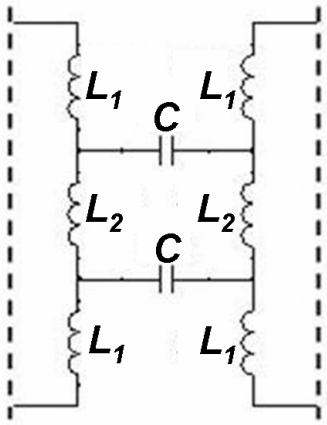

Figure III-14 : Schéma équivalent du motif Ω constitué des deux lettres en regard.

En considérant une permittivité relative du milieu hôte correspondant à celle de l'époxy (ε_r = 4,2), les dimensions des motifs ont été définies de manière à observer la continuité des branches de dispersion gauchère et droitière dans la bande de fréquence comprise entre 8 et 18 GHz. Le diagramme de dispersion théorique présenté sur la figure III-15 illustre la croissance continue de la constante de propagation avec un zéro situé autour de 13 GHz.

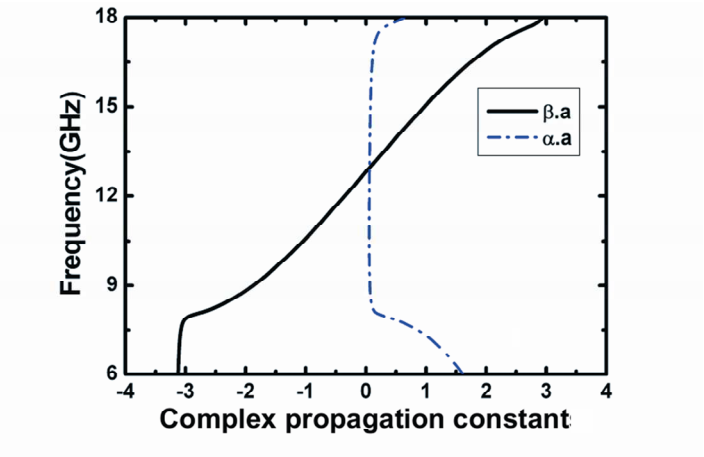

Figure III-15 : Diagramme de dispersion simulé du métamatériau composite équilibré.

Les dimensions retenues, supérieures ou égales à 0,5 mm, permettent d'envisager la définition des motifs par des techniques de fabrication de circuit imprimé conventionnelles. Des chaînes incluant 18 motifs Ω interconnectés sont définies par gravure chimique sur la face métallisée de substrats d'époxy. Ces substrats sont ensuite empilés pour constituer un

parallélépipède en respectant l'orientation des boucles de courant en conformité avec la figure III-13. Le positionnement relatif de chaque substrat est assuré par deux tiges de Teflon qui traversent le parallélépipède de part en part. Un prototype, incluant 10 cellules unitaires dans la direction de propagation, a été réalisé par ce procédé. 120 substrats sont nécessaires de manière à présenter une face d'environ 10 x 7,5 cm^2 en interaction avec l'onde plane incidente (figure III-16). Les faces inférieures et supérieures, qui présentent des irrégularités en raison de l'empilement des nombreux substrats, sont rectifiées à la fraise de manière à favoriser l'insertion du parallélépipède dans l'environnement de mesure décrit ci-après.

(a) (b)

Figure III-16 : Photographie du parallélépipède constitué de l'empilement de 120 substrats : (a) vue globale, (b) détail montrant les chaînes de motifs interconnectés.

La structure a été caractérisée au moyen d'un guide plan parallèle composé de deux plaques d'aluminium entre lesquelles sont insérés deux cornets (figure III-17). La distance entre le dispositif à mesurer et les cornets est d'environ 50 cm, de manière à travailler en condition de champ lointain. L'extension latérale de l'onde incidente est limitée par des couches de matériau absorbant Eccosorb AN-75 afin de s'affranchir des réflexions parasites et d'exciter le métamatériau par un front d'onde quasi plan.

Figure III-17 : Photographie du banc de caractérisation incluant le parallélépipède (sans la plaque supérieure du guide plan parallèle).

Le spectre de transmission mesuré sur une structure incluant 10 cellules suivant la direction de propagation est représenté sur la figure III-18 où figure également la caractéristique simulée. Cette représentation montre un bon accord théorie expérience. L'étendue de la bande passante laisse supposer la contiguïté de deux branches de dispersion main gauche et main droite conformément au diagramme de dispersion de la figure III-15.

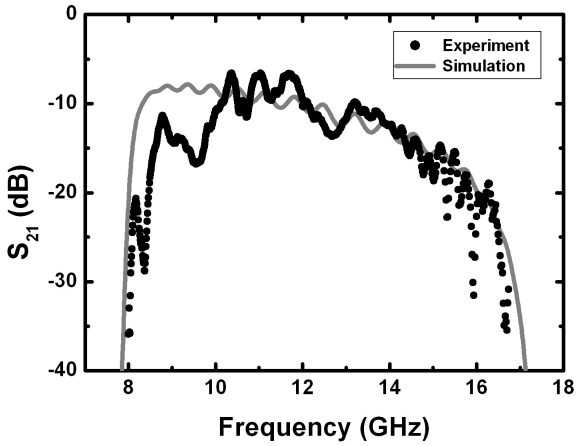

Figure III-18 : Comparaison des spectres de transmission d'un parallélépipède à 10 motifs mesuré et simulé.

Cette situation interprétée précédemment en termes de schéma équivalent correspond à un alignement des fréquences plasma électrique et magnétique illustré par la figure III-19. Les deux graphes du haut correspondent aux indices de réfraction et impédance complexe obtenus, par

inversion de Fresnel [6], à partir de la matrice S_{ij} simulée pour une cellule unitaire. La bande passante exclut la zone hachurée qui correspond à un régime de forte évanescence. La fréquence pour laquelle l'indice de réfraction s'annule, voisine de 13 GHz, correspond à l'alignement des zéros des permittivité et perméabilité effectives. Ainsi, ces grandeurs sont toutes deux négatives entre 8 et 13 GHz, ce qui se traduit par une bande passante main gauche (indice de réfraction négatif) et positives entre 13 et 18 GHz, ce qui correspond à une bande passante main droite (indice de réfraction positif). Il est à noter que l'évolution de la permittivité présentée par les motifs Ω interconnectés est continue, par opposition à la réponse électrique résonante présentée par les particules isolées [1]. La décroissance du niveau de transmission en fonction de la fréquence observée sur le graphe de la figure III-18 s'explique par la diminution de la partie réelle de l'impédance qui tend à augmenter la réflexion à l'interface entre le parallélépipède et l'air. Cette variation d'impédance justifie le fait que les niveaux de transmission observés soient plus importants en bande gauchère qu'en bande droitière.

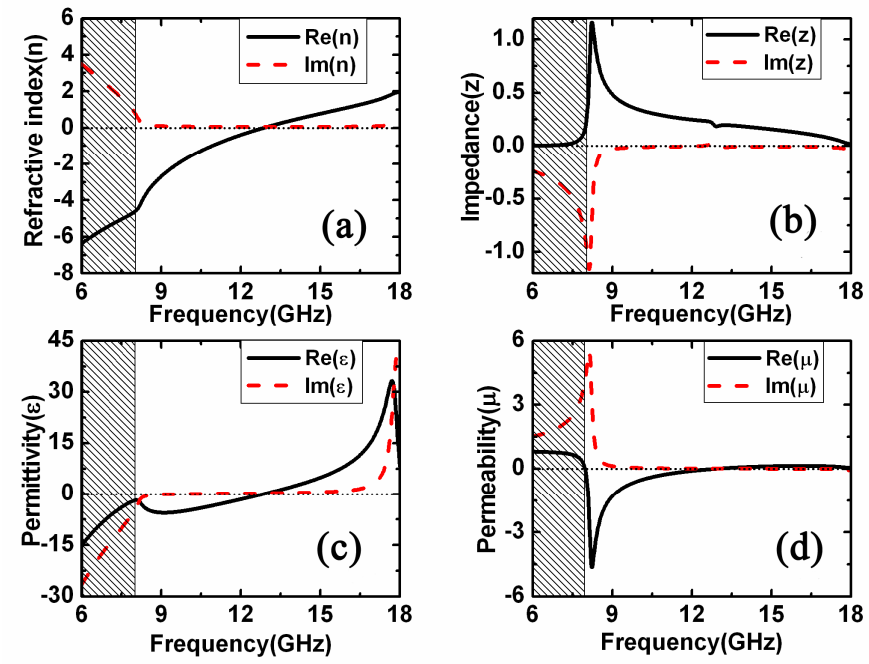

Figure III-19 : Paramètres effectifs obtenus par inversion de Fresnel à partir de la simulation des paramètres S_{ij} sur une cellule unitaire : (a) indice de réfraction, (b) impédance réduite, (c) permittivité, (d) perméabilité.

En complément de l'analyse de la transmission à travers un parallélépipède, au paragraphe suivant, nous proposons une démonstration expérimentale de la réfraction négative au moyen d'un prisme.

III.15 Caractérisation d'un prisme en bandes X et Ku

Deux méthodes peuvent être utilisées pour mettre en évidence, de manière expérimentale, un régime de réfraction négative. La première méthode consiste à caractériser un parallélépipède sous incidence oblique. Dans ce cas, le décalage du faisceau par rapport au point source qui peut être observé à partir de la seconde interface du parallélépipède permet de remonter à l'angle de réfraction à l'intérieur du parallélépipède. Toutefois, cette technique est difficile à mettre en œuvre dans le cas d'un métamatériau structuré car elle suppose une invariance des paramètres constitutifs effectifs en fonction de l'angle d'incidence. Or, dans le cas de milieux basés sur des réseaux de boucles de courant, la perméabilité effective ne peut être obtenue que sous certaines conditions de polarisation de l'onde incidente. En effet, au paragraphe III.12, nous avons montré qu'une incidence oblique se traduisait par une extinction progressive de la bande passante main gauche. La seconde technique consiste à travailler en incidence normale sur un métamatériau en forme de prisme. Cette situation permet une excitation des boucles de courant sous polarisation adéquate et l'angle de réfraction peut être mesuré au niveau de l'interface oblique du prisme. C'est la technique que nous avons mise en œuvre sur la base d'un travail préliminaire de simulation.

La structure simulée est représentée sur la figure III-20. La cellule élémentaire est identique à celle utilisée pour le parallélépipède afin d'établir le lien entre l'angle de réfraction relevé et les différentes régimes de dispersion mis en évidence au paragraphe précédent. De manière à limiter les ressources et le temps de calcul nécessaire, le modèle n'inclut qu'un seul rang de motifs suivant la direction *Ox*. Les conditions d'un milieu infini sont reproduites par l'utilisation de plans de symétrie « perfect E » qui bornent le domaine de simulation suivant cette direction verticale. De manière à éliminer l'influence de la diffusion latérale à l'intérieur de la structure, des parois absorbantes ont été insérées de chaque côté du prisme. Le système est excité par une onde plane injectée dans le port d'entrée. L'interprétation de la réfraction est basée sur

l'observation des cartes de champs en aval du prisme et sur le relevé des diagrammes de rayonnement en conditions de champ lointain. La modélisation des motifs métalliques inclut une valeur de conductivité finie.

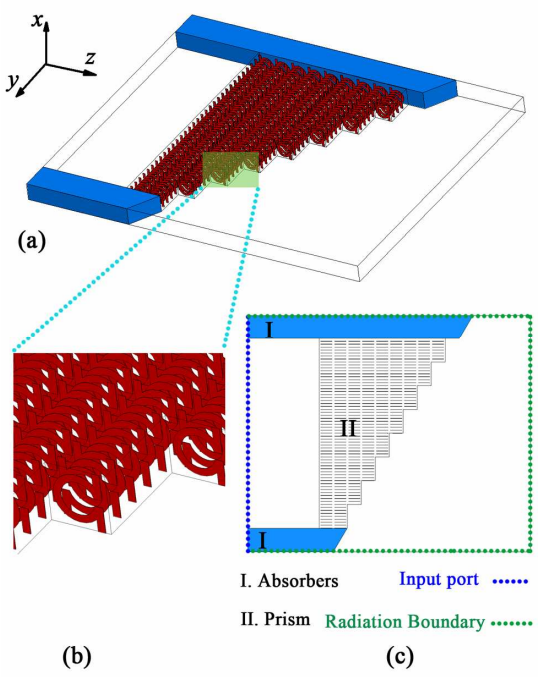

Figure III-20 : Structure de prisme simulée à l'aide du logiciel *CST Microwave Studio* : (a) vue en perspective de l'ensemble, (b) détail représentant les motifs Ω, vue de dessus.

Afin de préserver un nombre entier de cellules élémentaires suivant la direction de propagation, la face inclinée du prisme, qui présente un angle moyen de 30,5° par rapport à la direction *Oy*, adopte un profil en marche d'escalier. Des simulations effectuées en condition de paramètres constitutifs homogènes ont montré que l'influence de cette structuration n'était pas prépondérante.

Comme nous l'avons précédemment mentionné, les métamatériaux qui utilisent des plans de boucles de courant, sont fortement anisotropes. Afin de prendre en compte cette spécificité, nous avons déterminé les tenseurs de permittivité et de perméabilité effectives en appliquant la méthode d'inversion de Fresnel à une cellule unitaire pour différentes polarisations de l'onde incidente. Les données sont résumées dans le tableau III-1. Cette extraction de paramètres a été

effectuée pour les fréquences de 10,9, 12,8 et 15 GHz qui correspondent respectivement à une situation de transmission en bande main gauche, à la fréquence de transition pour laquelle la constante de propagation β s'annule et à une situation de transmission en bande main droite. Conformément aux prédictions, nous pouvons remarquer que lorsque l'indice de réfraction *n* est négatif, pour une fréquence de 10,9 GHz, seules les composantes ε_x de la permittivité et μ_y de la perméabilité sont négatives. Ces deux composantes sont proches de zéro lorsque la constante de propagation s'annule puis deviennent positives en bande main droite.

Frequency (GHz)		10.9	12.8	15.0
n		-1.0052	-0.038	0.777
ε	ε_x (tan ε_x)	-3.49+0.13i (-0.036)	-0.17+0.04i (-0.234)	4.90+0.57i (0.117)
	ε_y (tan ε_y)	4.07+0.08i (0.02)	4.07+0.08i (0.02)	4.07+0.08i (0.02)
	ε_z (tan ε_z)	15.56+0.36i (0.023)	16.66+0.38i (0.02)	15.74+0.24i (0.0153)
μ	μ_x (tan μ_x)	0.99+0.00034i (0.0003)	0.9858+0.0003i (0.0003)	0.9850+0.0003i (0.0003)
	μ_y (tan μ_y)	-0.28+0.03i (-0.091)	-0.0082+0.0002i (-0.022)	0.1232+0.005i (0.04)
	μ_z (tan μ_z)	1.050+0.007i (0.007)	1.055+0.002i (0.002)	0.818+0.002i (0.002)
θ_r (°) (Retrieval value)		-30.6°	-1.10°	23.2°
θ_r (°) Homogenous prism		-28.6°	-2.6°	21.5°
θ_r (°) Microstructured prism		-25.6°	-0.4°	25.4°

Tableau III-1 : Tenseurs de permittivité et perméabilité effectives déterminés par inversion de Fresnel à partir de matrices S_{ij} obtenues par simulation sur une cellule unitaire sous différentes incidences du vecteur d'onde.

Dans les simulations présentées sur les figures III-21, III-22 et III-23. Nous proposons une comparaison entre le matériau structuré et un matériau homogène décrit par ses tenseurs de permittivité et de perméabilité effectives à la fréquence de fonctionnement considérée.

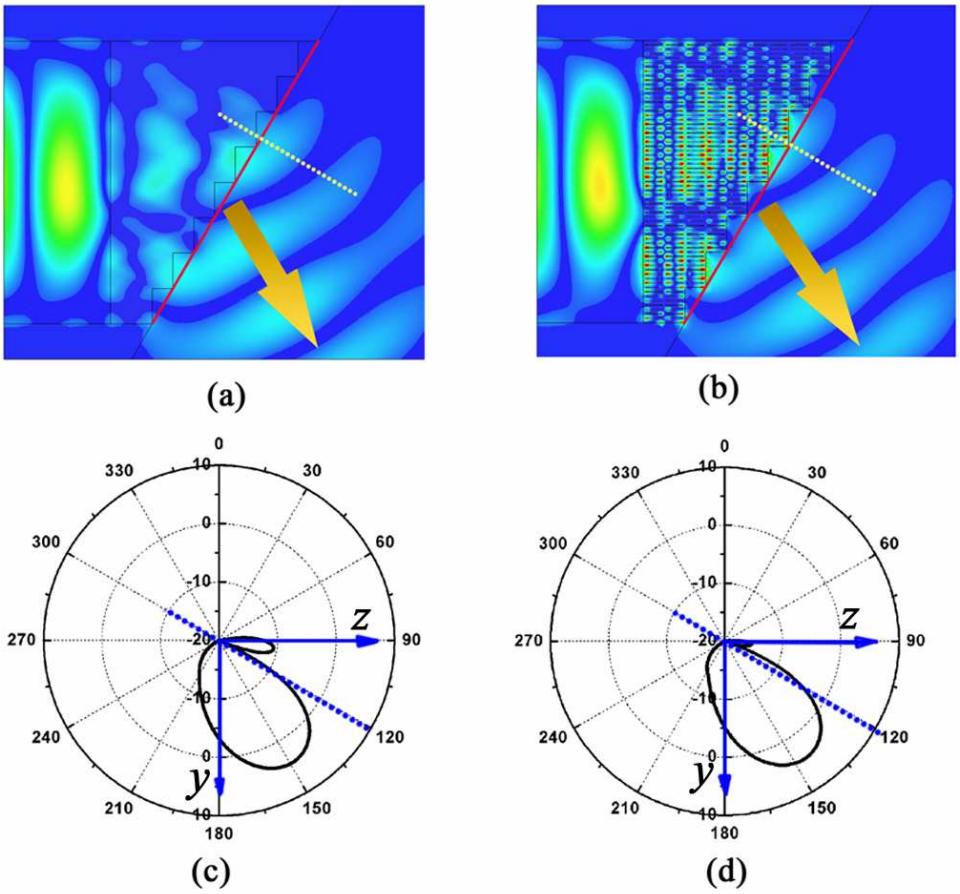

Figure III-21 : Cartographies de l'amplitude du champ électrique à la fréquence de 10,9 GHz et diagrammes de rayonnement correspondants pour le prisme homogène (a), (c) et le prisme structuré (b), (d).

La carte de champ de la figure III-21 (plan *yOz*) a été obtenue pour une fréquence de fonctionnement de 10,9 GHz. Les cartes de champ (figure III-21a et III-21b) montrent clairement une réfraction au niveau du plan incliné situé du même côté de la normale que la direction de l'onde incidente. Le diagramme de rayonnement obtenu dans des conditions de champ lointain indique une valeur d'angle de réfraction de -28,6° pour le matériau homogène et -25,6° pour le matériau structuré. Pour cette fréquence, une animation vidéo permet de visualiser la rétropropagation de la phase à l'intérieur du prisme.

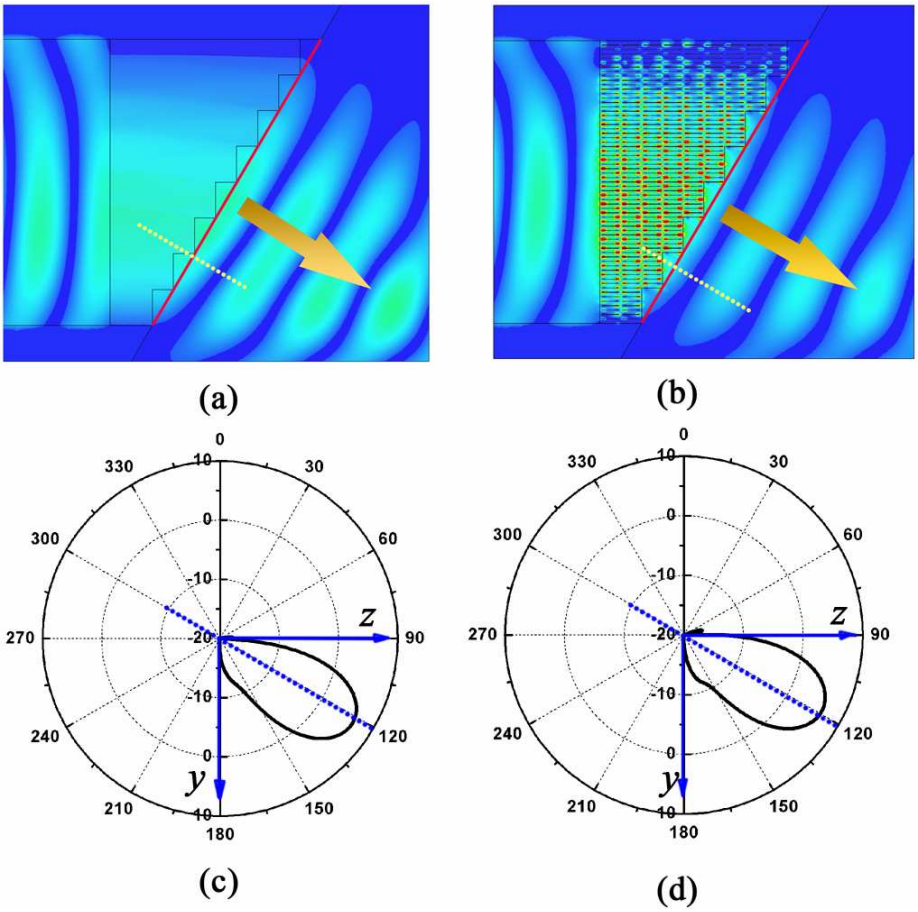

Figure III-22 : Cartographies de l'amplitude du champ électrique à la fréquence de 12,8 GHz et diagrammes de rayonnement correspondants pour le prisme homogène (a), (c) et le prisme structuré (b), (d).

Sur la figure III-22 nous reprenons le même type de représentation pour la fréquence de 12,8 GHz correspondant au raccordement des bandes gauchère et droitière. Les deux cartes de champ montrent que le vecteur d'onde est orthogonal au plan de sortie. Les simulations effectuées en champ lointain confirment l'observation en champ proche avec des valeurs d'angle de réfraction de -0,4° pour le prisme microstructuré et -2,6° pour le prisme homogène. Il convient de noter que le niveau transmis en sortie reste très significatif et du même ordre de grandeur que pour une fréquence localisée en bande main gauche. Comme prévu par les relevés expérimentaux effectués à partir du parallélépipède, l'annulation de la constante de phase β ne se traduit pas par un régime d'évanescence. On parvient ainsi à transmettre une information dont la vitesse de phase tend vers l'infini en conservant une vitesse de groupe positive et non nulle. Cette

particularité est illustrée par les cartes de champ des figures III-22a et III-22b. En effet, à l'intérieur du prisme, on ne distingue ni nœud ni ventre, ce qui signifie que l'on se trouve en régime de très grande longueur d'onde. Cette longueur d'onde tend vers l'infini lorsque la constante de propagation s'annule.

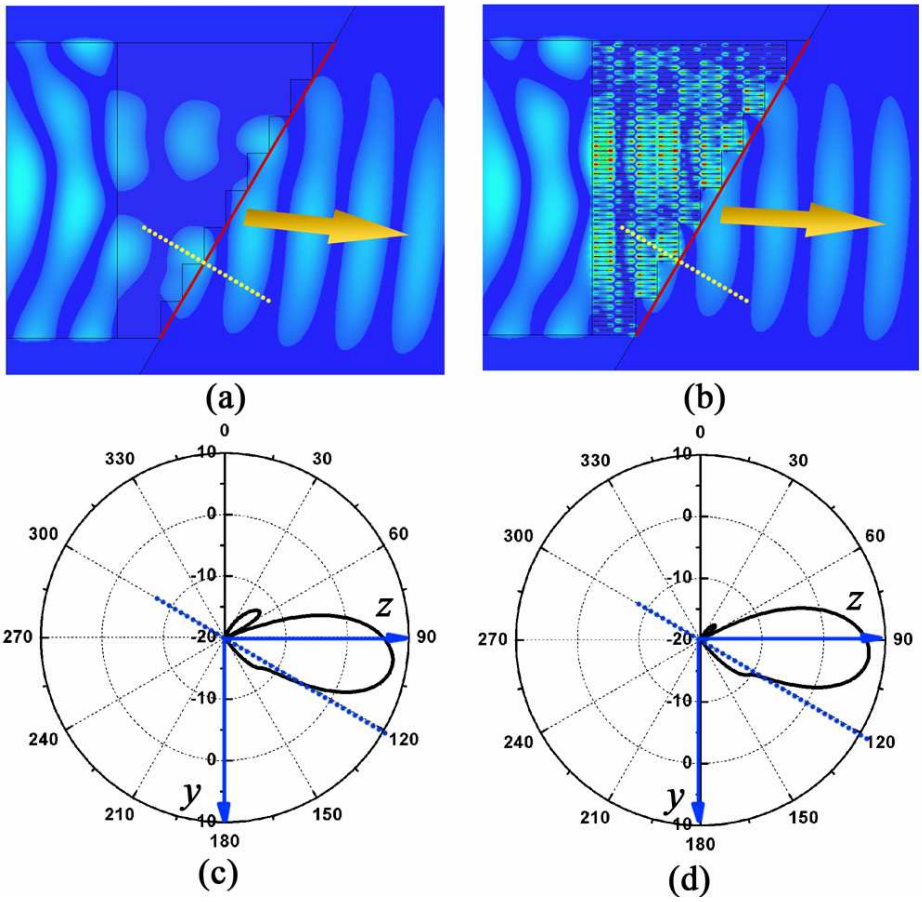

Figure III-23 : Cartographies de l'amplitude du champ électrique à la fréquence de 15 GHz et diagrammes de rayonnement correspondants pour le prisme homogène (a), (c) et le prisme structuré (b), (d).

Enfin, la situation décrite sur la figure III-23, illustre le phénomène de réfraction positive lorsque la fréquence est située au-delà de la fréquence de transition voisine de 12,8 GHz. Dans ce domaine de fréquence, la phase et l'énergie de l'onde se propagent dans le même sens, comme cela peut être confirmé par l'animation de la phase à l'intérieur du prisme. Les angles de réfraction calculés en champ lointain valent 21,5° pour le prisme homogène et 25,4° pour le prisme microstructuré à la fréquence de 15 GHz.

Pour chacun des trois cas de figure précédemment décrits, on remarque une bonne correspondance entre les résultats de simulation des prismes homogène et microstructuré. Cette comparaison, opérée dans une configuration bidimensionnelle, montre la validité des tenseurs de permittivité et perméabilité extraits au moyen d'une méthode d'inversion de Fresnel à partir de la matrice de répartition d'une cellule unitaire. Par ailleurs, ce résultat confirme le caractère de localisation des champs au niveau de la particule Ω. En effet, l'extraction effectuée sur une cellule unitaire ne permet pas de prendre en compte les effets du couplage dans la direction de propagation. Compte tenu de la bonne description apportée par le prisme homogénéisé, ces effets de couplage apparaissent de second ordre. On peut noter sur certains diagrammes de rayonnement l'apparition de lobes secondaires qui peuvent être attribués à la diffraction liée au profil en escalier de l'interface oblique [7]. Toutefois, pour les angles de réfraction que nous avons considérés, compris entre -25° et + 25°, cette diffraction n'est pas prépondérante si l'on se fie à l'importance relative de ce lobe secondaire par rapport au lobe principal.

Un prisme a été réalisé par la même technique que celle employée pour la fabrication du parallélépipède (figure III-24). Les dimensions suivant les directions *Ox* et *Oy* sont sensiblement identiques. Le profil en escalier de l'interface oblique inclut 11 marches, faisant décroître le nombre de cellules suivant la direction de propagation (*Oz*) de 15 à 5.

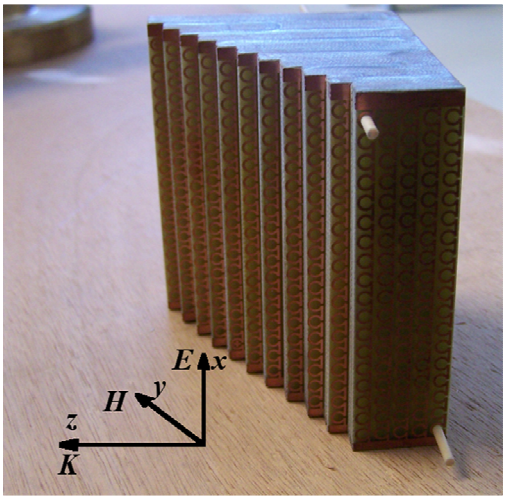

Figure III-24 : Photographie du prisme réalisé pour les mesures de réfraction.

Les mesures ont été effectuées à l'analyseur de réseau vectoriel à l'aide de la structure du guide plan parallèle décrit au paragraphe précédent. Nous travaillons dans des conditions d'incidence normale et le maximum d'amplitude du champ électrique à la sortie du prisme est détecté en condition de champ lointain à l'aide d'un cornet mobile guidé par un rail circulaire (figure III-25).

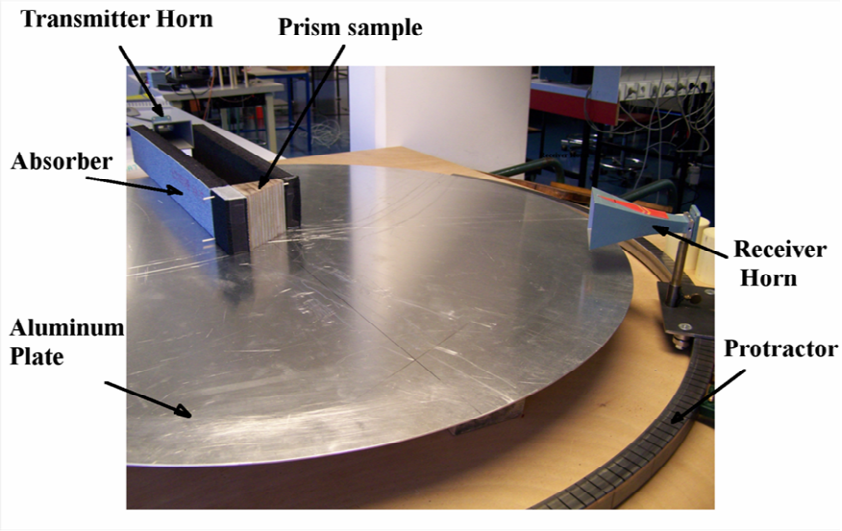

Figure III-25 : Photographie du banc de caractérisation incluant le prisme (sans la plaque supérieure du guide plan parallèle).

La figure III-26 représente l'intensité du champ relevé en fonction de l'angle de réfraction. Alors que bon nombre d'études expérimentales en réfraction emploient des échelles d'unité arbitraire, nous avons préféré indiquer des valeurs d'intensité relative exprimées en dB, en référence à la transmission relevée en absence de prisme pour les deux cornets orientés suivant le même axe. Ce choix permet d'apprécier tout d'abord la faible atténuation présentée par le prisme qui, sans être directement comparable à l'atténuation présentée par le parallélépipède, reste néanmoins du même ordre de grandeur. Par ailleurs, la référence d'intensité permet de mesurer l'importance relative du signal détecté en fonction de l'angle d'incidence. Ainsi, comme indiqué à l'occasion de l'interprétation des mesures en transmission, en régime de réfraction positive, autrement dit en régime de transmission main droite, l'intensité est moins importante qu'en régime de réfraction négative en raison de la diminution de l'impédance présentée par le

métamatériau. À titre d'exemple, la différence entre les intensités relevées aux fréquences de 12 GHz (θ = -22°) et 15 GHz (θ = 13°) est d'environ 6 dB.

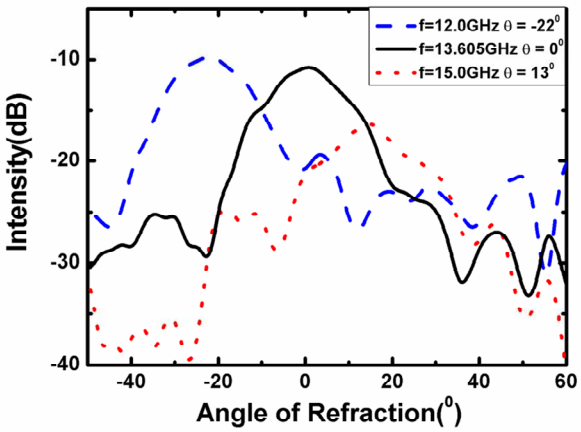

Figure III-26 : Intensité relative du signal relevée en condition de champ lointain en fonction de l'angle de réfraction. Le signal de référence est mesuré en absence de prisme sous incidence normale.

Sur la figure III-27, nous avons reporté les valeurs de la partie réelle de l'indice de réfraction déduites des mesures d'angle de réfraction θ en appliquant la loi de Snell-Descartes. On constate que les valeurs obtenues entre 10 et 16 GHz suivent l'évolution globale de la partie réelle de l'indice déterminée théoriquement par la méthode d'inversion des relations de Fresnel. Toutefois, la caractéristique expérimentale est décalée vers les faibles valeurs d'indice, ce qui se traduit notamment par un décalage du point de croisement n = 0 relevé pour f = 13,6 GHz et déterminé par calcul à f = 12,8 GHz. Cette différence peut s'expliquer par l'incertitude sur la valeur de permittivité de l'époxy. En effet, on peut constater qu'en considérant une permittivité relative de 3,6 au lieu de 4, initialement prise en compte dans les simulations, les points expérimentaux sont alignés sur l'évolution théorique de l'indice de réfraction. Les valeurs de permittivité de l'époxy sont rarement répertoriées au-delà du gigahertz car ce matériau est classiquement réservé aux applications basses fréquences. Cependant, si l'on se réfère aux études publiées dans la littérature, qui montrent la décroissance de ε_r lorsque la fréquence augmente [8], la valeur de 3,6 autour de 10 GHz semble plausible.

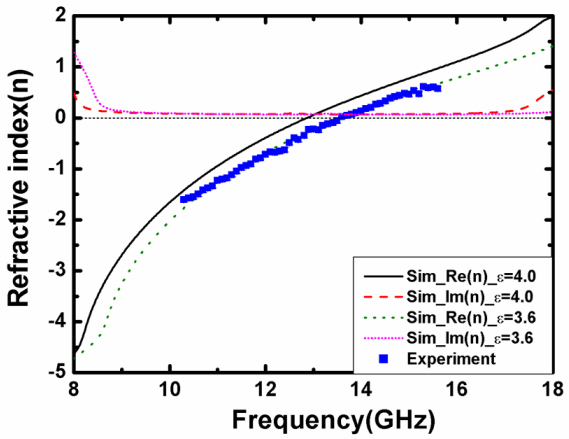

Figure III-27 : Comparaison des évolutions théoriques et expérimentales de l'indice de réfraction en fonction de la fréquence.

Sur la figure III-28, nous avons reporté le diagramme de dispersion présenté par le réseau de motifs Ω pour différentes valeurs de permittivité diélectrique comprises entre 3,4 et 4,2. Il est important de noter que le décalage de la caractéristique affecte les deux branches de dispersion dans des proportions comparables. Par conséquent, cette variation de permittivité ne se traduit pas par l'ouverture d'une bande interdite. On peut donc considérer que la structure reste « composite équilibrée » pour reprendre la terminologie employée dans le cas des lignes duales. Cette propriété est de toute première importance pour l'accordabilité de ces structures. Ainsi, comme nous l'avons proposé au paragraphe précédent dans le cas d'un circuit déphaseur, l'utilisation d'un matériau agile peut permettre d'accorder la caractéristique de sortie par le biais d'une variation de permittivité sous l'effet d'une tension de commande. Or, les simulations de la dispersion en fonction de la fréquence pour différentes valeurs de permittivités de substrat montrent qu'il serait possible de conserver la condition d'équilibre correspondant à un régime d'indice de réfraction nul, autrement dit de longueur d'onde infinie. Pour la mise en œuvre de cette fonction de commande en bande X, l'utilisation de cristaux liquides semble appropriée [9].

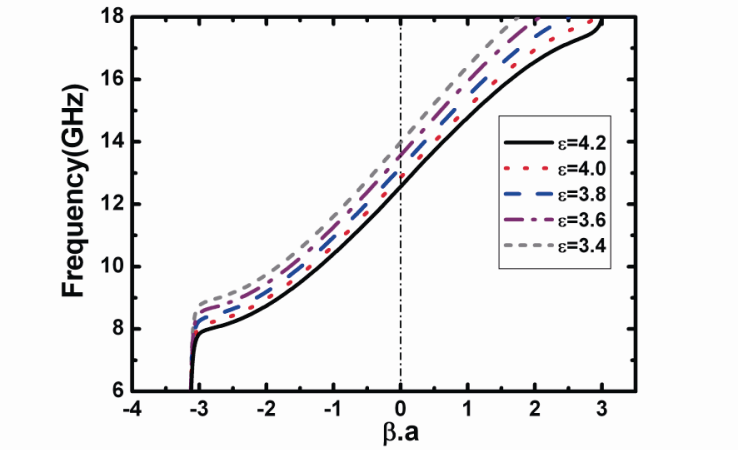

Figure III-28 : Diagramme de dispersion en partie réelle pour différentes valeurs de permittivité du substrat.

En conclusion, nous avons démontré expérimentalement les propriétés de rétropropagation de la phase et de réfraction négative à partir de réseaux de particules Ω interconnectées. Les bandes passantes relativement larges associées à des faibles niveaux de pertes rendent ces structures très attractives pour le domaine des longueurs d'ondes millimétriques en comparaison aux réseaux conventionnels incluant des fils et des boucles de courant déconnectées (SRR). À ce titre, nous avons obtenu des résultats expérimentaux en bande W (75-110 GHz) avec des niveaux de pertes à l'état de l'art (0,5 dB par cellule unitaire). Par ailleurs, nous avons montré que ces structures pouvaient présenter un diagramme de dispersion « composite équilibrée » en référence aux lignes de transmission duales. En effet, nous avons montré qu'il était possible d'aligner les fréquences plasma électrique et magnétique de manière à annuler la bande interdite entre les branches de dispersion main gauche et main droite.

Dans leur principe et compte tenu de leurs performances, l'emploi des réseaux de motifs Ω interconnectés pourrait être étendu aux frontières de l'optique avec comme limitation les effets d'inertie des porteurs de charge dans le métal qui peuvent être modélisés par un terme d'inductance intrinsèque [10]. Cependant, comme nous l'avons décrit au paragraphe I.23, la principale limitation de ces topologies réside dans la mise en œuvre de structures de faible dimension en raison des contraintes de polarisation qui nécessitent des empilements conséquents. C'est la principale motivation au développement de métamatériaux excitables sous incidence normale tels que les réseaux de nanorods [11] et les réseaux de type fishnet [12].

Au paragraphe suivant, nous proposons les premiers résultats d'une étude d'un métamatériau pour l'incidence normale. Cette structure est composée de l'empilement de plans métalliques structurés par des ouvertures de dimension inférieure à la longueur d'onde de travail. Cette étude s'inscrit dans le cadre de la thèse de Charles Croënne.

III.2 Métamatériaux à base de réseaux d'ouvertures sous longueur d'onde

III.21 Introduction

La définition d'un métamatériau pour l'incidence normale sous-entend l'interaction d'une onde plane incidente avec une surface structurée. Comme pour l'approche conventionnelle impliquant l'imbrication d'un réseau de fils et de boucles courant, l'utilisation d'une structure métallo-diélectrique permet de tirer parti d'importants contrastes de permittivité. L'étude proposée dans la dernière partie du présent chapitre est basée sur l'empilement de grilles métalliques qui peuvent être regroupées sous l'acronyme de FSS pour Frequency Selective Surface (cf. paragraphe I.312). Considérons la topologie basique qui correspond à un réseau d'ouvertures pratiquées dans une plaque métallique d'épaisseur finie. Une telle structure va présenter un comportement passe-bande. En effet, la fréquence de coupure basse correspond à la fréquence de coupure du mode guidé dans les ouvertures et la fréquence de coupure haute est attribuée aux anomalies de Wood, phénomène observé pour la première fois en 1902 [13] et expliqué par la redistribution de l'énergie à chaque nouvel ordre de diffraction du réseau planaire [14, 15].

La physique décrivant la transmission à travers les plaques métalliques perforées a connu un nouveau développement en 1998 avec la découverte de T. W. Ebbesen [16]. Pour la première fois, une transmission avec un niveau relatif significatif a été observée dans le domaine de l'optique à travers un film métallique percé de trous de rayon inférieur à la longueur d'onde de travail. En raison des niveaux de transmission observés, nettement supérieurs au rapport entre la surface équivalente des ouvertures et la surface illuminée, le terme de transmission extraordinaire a été introduit. Plusieurs interprétations de ce phénomène ont été proposées [17-19]. Une des théories met en avant la prépondérance de modes propagatifs dans les ouvertures [17]. En

revanche, la théorie proposée par Martin-Moreno *et al* explique la transmission extraordinaire par le couplage à travers les ouvertures d'ondes surfaciques présentes de part et d'autre de la plaque métallique [18]. Alors que la première interprétation suppose la prise en compte de la permittivité diélectrique du métal, la seconde interprétation reste valable en régime de conductivité finie. En effet, des ondes surfaciques peuvent être observées dans un métal parfait structuré périodiquement par des ouvertures. Cette propriété a permis l'extension de l'étude de la transmission extraordinaire, observée initialement dans le domaine de l'optique, aux longueurs d'ondes millimétriques [15]. Le choix d'une topologie sous longueur d'onde présente principalement deux avantages. D'une part, en terme de fabrication, les motifs qui consistent en de simples ouvertures, circulaires par exemple, sont faciles à définir jusqu'aux longueurs d'onde de l'optique. D'autre part, les phénomènes de transmission extraordinaire permettent de compenser les pertes métalliques qui deviennent prépondérantes lorsque la fréquence augmente. Dans la suite, nous décrivons la conception d'une structure qui présente une bande passante autour de 500 GHz, en vue d'une caractérisation temporelle (Time Domain Spectroscopy : TDS).

III.22 Description de la structure

Afin de tirer pleinement parti des effets de volume tels que la réfraction négative qui a été mis en évidence sous incidence rasante, il est impératif de définir un métamatériau incluant la superposition de plusieurs couches dans la direction de propagation. Dans cette perspective, l'intégration monolithique des réseaux métalliques incluant des couches intermédiaires de BCB est intéressante en raison des caractéristiques électromagnétiques de ce diélectrique, à savoir une faible dispersion de la permittivité relative associée à un faible niveau de pertes [2]. Par ailleurs, l'élaboration des couches de BCB utilise une technique classique de dépôt par centrifugation. Ces deux points ont été détaillés à l'occasion du chapitre précédent. Le dimensionnement du réseau d'ouvertures sous longueur d'onde fait l'objet d'une étude paramétrique à l'aide du logiciel *HFSS* décrite au paragraphe suivant. La cellule unitaire dimensionnée pour la fréquence de 500 GHz est représentée sur la figure III-29 avec ses cotes nominales. En raison des contraintes de fabrication, nous nous sommes imposés les épaisseurs de la couche de BCB (*dZ*), déposé par centrifugation, et du film d'or, évaporé sous vide. Nous jouons donc principalement sur la périodicité latérale de

la cellule et sur le diamètre de l'ouverture pour optimiser le niveau de transmission dans la bande de fréquence visée.

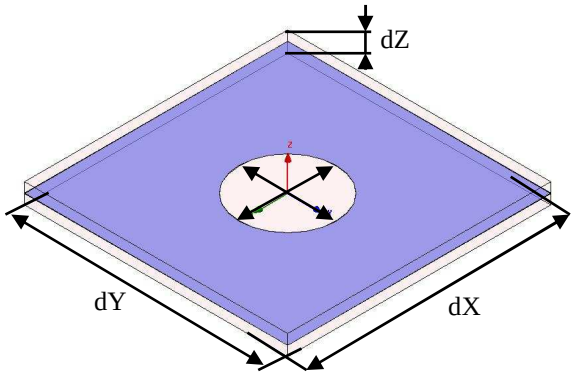

dX = 340 µm

dY = 340 µm

dZ = 26 µm

Diamètre de l'ouverture circulaire : 125 µm

Épaisseur du film d'or : 0.4 µm

Figure III-29 : Représentation en perspective de la cellule unitaire du métamatériau dimensionné pour la fréquence de 500 GHz.

Toutefois, à la différence du prototype réalisé pour la bande 75-110 GHz sur la base de réseaux de motifs Ω, le diélectrique, utilisé ici en dépôt pleine plaque, n'est pas photosensible.

III.23 Simulations

À partir du logiciel commercial *HFSS*, nous avons fait utilisé deux approches complémentaires : dans un premier temps, nous avons décrit les potentialités d'un réseau infini par l'analyse de modes propres à l'intérieur d'une cellule unitaire fermée par des conditions aux limites permettant de traduire la périodicité (master-slave). Dans un second temps, nous avons observé la transmission d'un empilement de plusieurs cellules unitaires décrit par sa matrice de répartition.

On montre que les niveaux de transmission peuvent être améliorés en réduisant la période latérale non critique [20]. En considérant une polarisation du champ électrique suivant l'axe *Oy*, cela revient à diminuer la dimension *dX*. Ce comportement est illustré par la figure III-30 correspondant au spectre de transmission de la structure conçue pour la fréquence de 500 GHz. Il est clair que le niveau de transmission s'approche de l'unité lorsque *dX* évolue de 340 µm, valeur nominale équivalente à *dY*, à 140 µm. Par ailleurs, cette augmentation s'accompagne d'un élargissement de la bande passante.

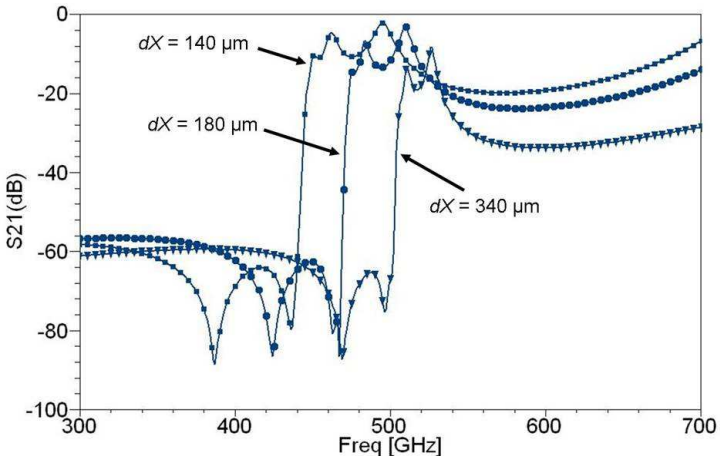

Figure III-30 : Spectres de transmission simulés pour différentes valeurs de périodes définies suivant l'axe *Ox*.

Du point de vue de l'interaction de l'onde incidente avec le plan métallique structuré, cette différenciation des périodicités latérales revient à diminuer le facteur de remplissage suivant la direction non critique. Ce facteur de remplissage, linéique, est défini comme le rapport entre la longueur traversée par le métal et le diamètre total de la surface illuminée. Parallèlement à cette première voix d'optimisation, la diminution de ce facteur peut être obtenue en conservant l'égalité des dimensions *dX* et *dY*. Dans ce cas, on modifie la forme des ouvertures afin de traduire le facteur de remplissage linéique par un rapport d'ellipticité. Ces deux approches ne sont pas rigoureusement équivalentes car la distribution des modes propres dans une ouverture elliptique est différente de celle observée dans une ouverture circulaire. Néanmoins, on retrouve les deux tendances des structures doublement périodiques, à savoir l'augmentation du niveau de transmission et l'élargissement de la bande passante, lorsque l'on observe la transmission à travers un empilement de plans métalliques pourvus d'ouvertures elliptiques (figure III-31). Ces caractéristiques de transmission simulées montrent notamment qu'un niveau proche de l'unité peut être observé pour un rapport d'ellipticité, *EAR* pour Elliptical Aspect Ratio, de 1,8. Au regard de ses potentialités, nous avons choisi, dans un premier temps, de nous focaliser sur cette géométrie particulière en vue d'une démonstration expérimentale.

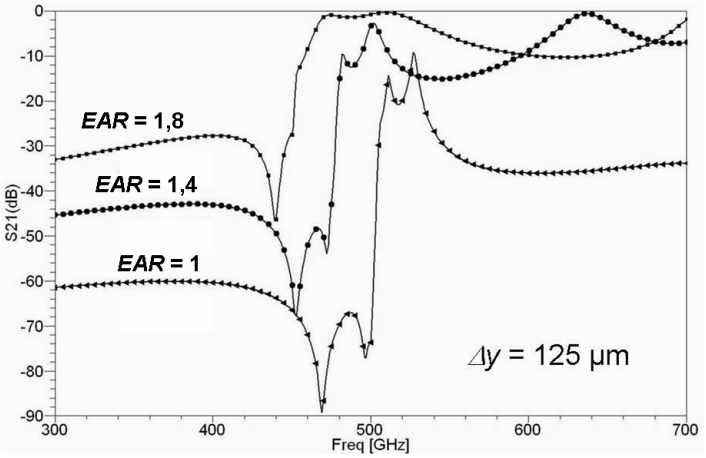

Figure III-31 : Spectres de transmission simulés pour différentes valeurs du rapport d'ellipticité $EAR = \frac{\Delta_x}{\Delta_y}$.

Le diagramme de dispersion simulé en modes propres à partir d'une cellule unitaire est représenté sur la figure III-32. Ce graphe permet de vérifier le caractère main gauche de la bande de transmission fondamentale attesté par l'opposition des vitesses de phase et de groupe. En revanche, la comparaison directe avec le spectre de transmission de la figure III-31 n'est pas directe en raison du nombre de modes présents autour de la bande passante.

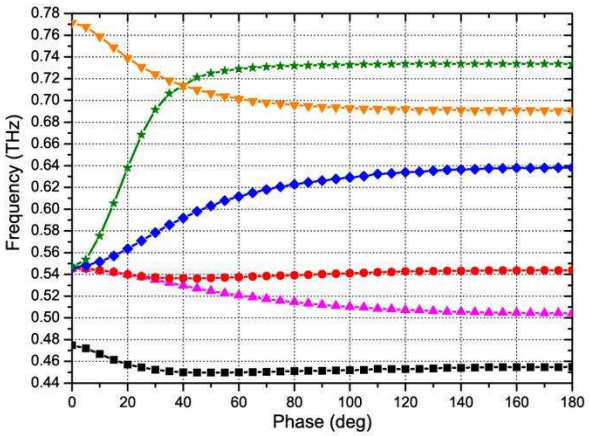

Figure III-32 : Diagramme de dispersion simulé en modes propres à l'aide du logiciel *HFSS* pour un rapport d'ellipticité *EAR* = 1,8.

À partir de spectre de transmission complexe, nous avons extrait la constante de propagation par inversion des relations de Fresnel. Afin d'identifier les modes propres impliqués

dans la transmission pour les conditions de polarisation utilisées (champ électrique suivant *dY* , champ magnétique suivant *dX*), nous avons comparé le diagramme de dispersion de la figure III-32 simplifié à cette constante de propagation (figure III-33).

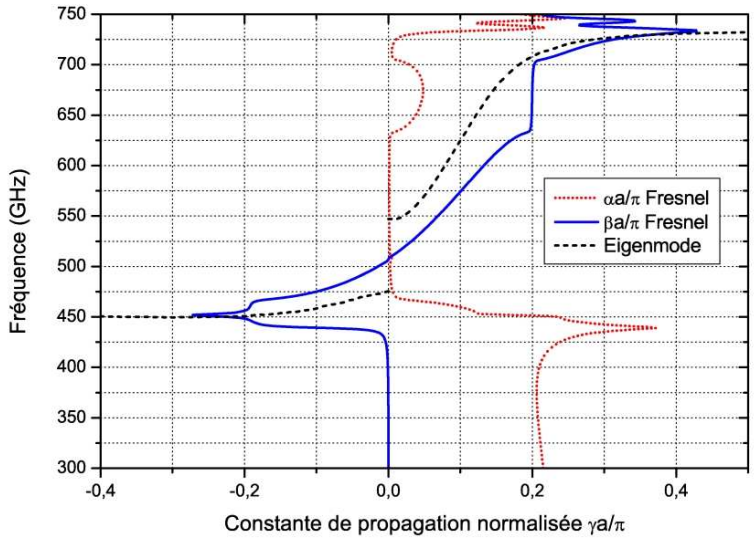

Figure III-33 : Diagramme de dispersion extrait par inversion des relations de Fresnel à partir du spectre de transmission d'une structure à 5 cellules unitaires. Le pointillé noir représente les modes propres dominants autour de la fréquence de 500 GHz.

Cette comparaison montre une superposition de la constante de phase uniquement aux extrémités des bandes gauchère et droitière. Il apparaît évident que la transmission simulée pour une structure incluant cinq cellules ne permet pas de décrire le réseau infini. Toutefois, l'emploi d'une méthode différentielle initialement proposée par Bianco et Parodi pour l'extraction de la constante de propagation d'une ligne de transmission [21], permet de retrouver un diagramme de dispersion proche des évolutions en mode propre (figure III-34).

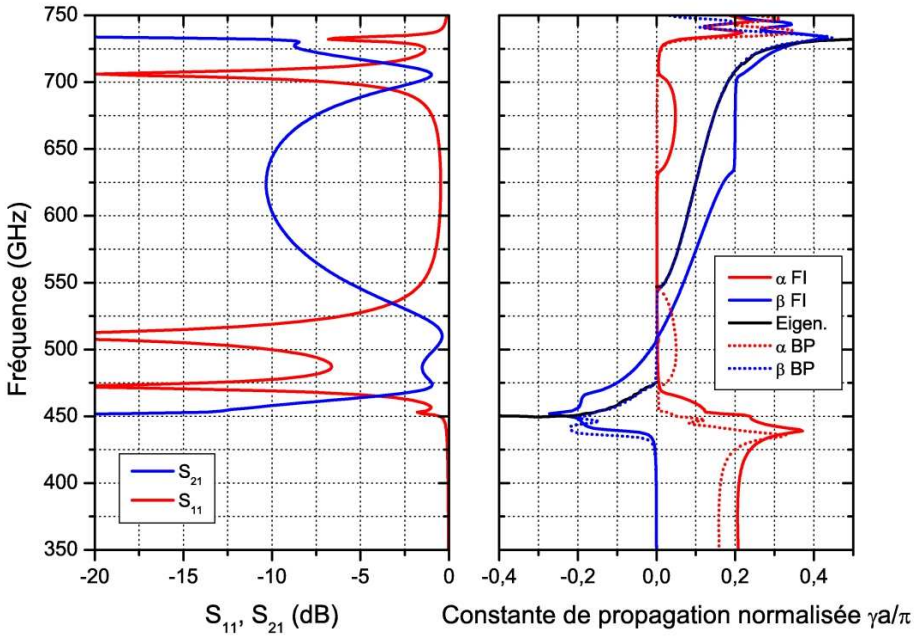

Figure III-34 : Spectre de transmission de la structure incluant 5 cellules unitaires et comparaison des diagrammes de dispersion simulés : modes propres (trait noir), inversion des relations de Fresnel (traits bleu et rouge), méthode différentielle de Bianco et Parodi (pointillés bleu et rouge) appliquée à 2 structures de 7 et 3 cellules unitaires.

En raison de son caractère différentiel, la méthode de Bianco et Parodi s'affranchit de l'interaction de la structure avec son environnement extérieur. En ce sens, elle permet de décrire ses états de cœur. Toutefois, à la différence de l'extraction des modes propres, le diagramme de dispersion est construit sur la base de simulations de structures finies dans la direction de propagation. Or, les simulations effectuées à partir d'un faible nombre de cellules, quatre dans le cas de la figure III-34, sont en très bon accord avec la dispersion calculée en modes propres. Par conséquent, les différences observées sur la figure III-33 illustrent l'importante contribution des états d'interface qui traduisent l'interaction de la structure métamatériau avec l'air.

Cette analyse des diagrammes de dispersion montre l'intérêt de travailler à partir de plusieurs structures de longueurs différentes afin de décrire les états de cœur. Cependant, les méthodes utilisées en simulation reposent sur l'utilisation de la matrice S_{ij} complète incluant les transmission et réflexion complexes. Or, la plupart des techniques de spectroscopie térahertz ne fournissent que la transmission complexe. C'est la raison pour laquelle, en vue de la

caractérisation, nous introduisons une méthode d'inversion des relations de Fresnel simplifiée initialement proposée par D. R. Smith [22]. La dispersion de la structure est décrite par la relation suivante :

$$\cos(nk_0a) = \mathrm{Re}\left(\frac{1}{S_{21}}\right) - \frac{1}{2|S_{21}|^2}(A_1S_{11} + A_2S_{21}) \quad (1)$$

avec n l'indice de réfraction, a l'épaisseur de la structure et k_0 le nombre d'onde dans le vide ($k_0 = \frac{\omega}{c}$).

En régime de faible atténuation $A_1 = A_2 = 0$ et cette relation, qui ne dépend plus que de S_{21}, devient :

$$\cos(nk_0a) = \mathrm{Re}\left(\frac{1}{S_{21}}\right) \quad (2)$$

ou, en considérant la constante de propagation complexe γ

$$\cosh(\gamma a) = \mathrm{Re}\left(\frac{1}{S_{21}}\right) \quad (3)$$

La figure III-35 montre une bonne correspondance entre les deux méthodes, hormis dans les zones de forte atténuation.

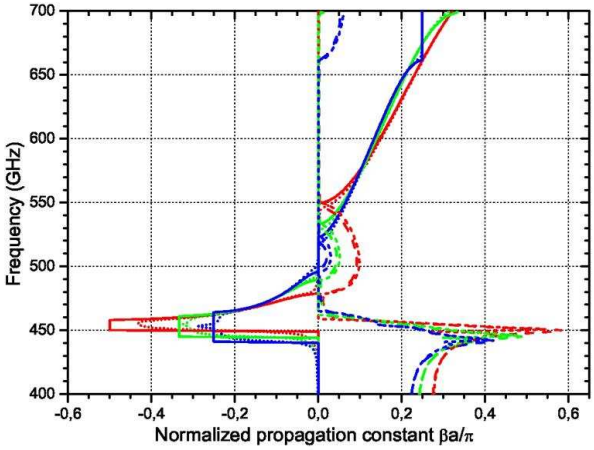

Figure III-35 : Comparaison des diagrammes de dispersion obtenus par inversion des relations de Fresnel (pointillés) et par la méthode simplifiée (trait continu) pour des structures incluant 2 (rouge), 3 (vert) et quatre (bleu) cellules.

En conclusion, cette technique d'inversion simplifiée constitue une première approche pour identifier les domaines de propagation droitier et gaucher à partir d'un spectre de transmission mesuré. Au paragraphe suivant, nous décrivons le procédé de fabrication des prototypes.

III.24 Fabrication

La fabrication d'un prototype implique un procédé d'intégration monolithique décrit par la séquence de la figure III-36. Un premier niveau de BCB est déposé par centrifugation sur un substrat de GaAs de diamètre deux pouces. Les paramètres de dépôt sont définis de manière à obtenir une épaisseur finale de 13 µm qui correspond à une demi-période dans la direction de propagation si l'on néglige l'épaisseur de métallisation. Une fois polymérisé par un traitement thermique sous flux d'azote, cette couche de BCB sert de support à l'étape de lithographie optique qui permet de définir la grille métallique constituée majoritairement d'or évaporé sous vide. L'épaisseur typique de cette métallisation est de 0,45 µm (figure III-36a). On procède ensuite à une nouvelle étape de dépôt de BCB par centrifugation en réduisant la vitesse de rotation de manière à obtenir l'épaisseur nominale de 26 µm correspondant à une période dans la direction de propagation. Ce dépôt est suivi d'une nouvelle étape de métallisation similaire à la première (figure figure III-36b). Cette séquence est reproduite jusqu'à constituer un empilement intégrant le nombre de cellules désiré. Cet empilement est recouvert d'une couche en-tête de BCB d'épaisseur 13 µm afin d'assurer la symétrie de la structure (figure III-36c). Le substrat est ensuite dissous dans une solution acide de manière à libérer une membrane qui constitue le métamatériau. Cette solution, optimisée à l'occasion de travaux antérieurs [23], est réalisée à partir d'une concentration d'eau oxygénée et d'acide sulfurique (H_2SO_4 : 1 / H_2O_2 : 8 / H_2O : 1). La vitesse de gravure obtenue est d'environ 13 µm/min.

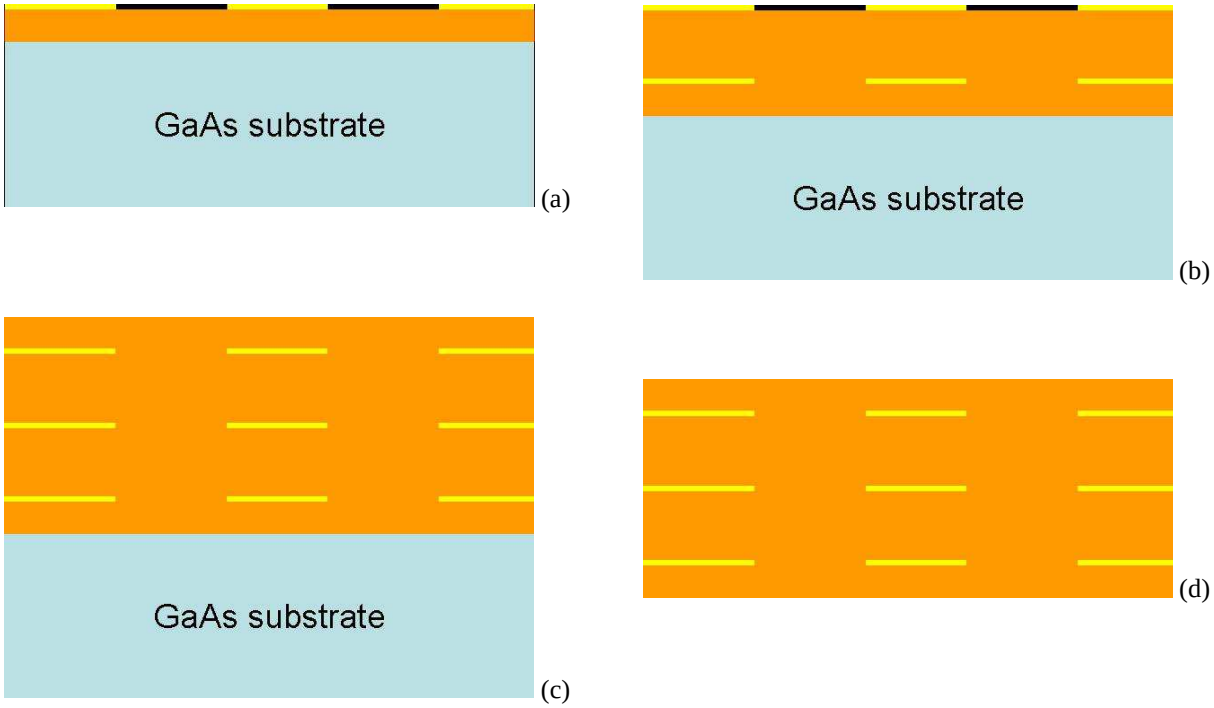

Figure III-36 : Représentation symbolique décrivant les séquences de fabrication du prototype.

La photographie de la figure III-37 regroupe différents clichés du métamatériau au microscope optique (figure III-37a et b) et électronique (figure III-37c). Ce prototype intègre cinq cellules élémentaires. La membrane d'épaisseur supérieure à 100 µm est suffisamment rigide pour être manipulée en vue notamment de sa caractérisation décrite au paragraphe suivant.

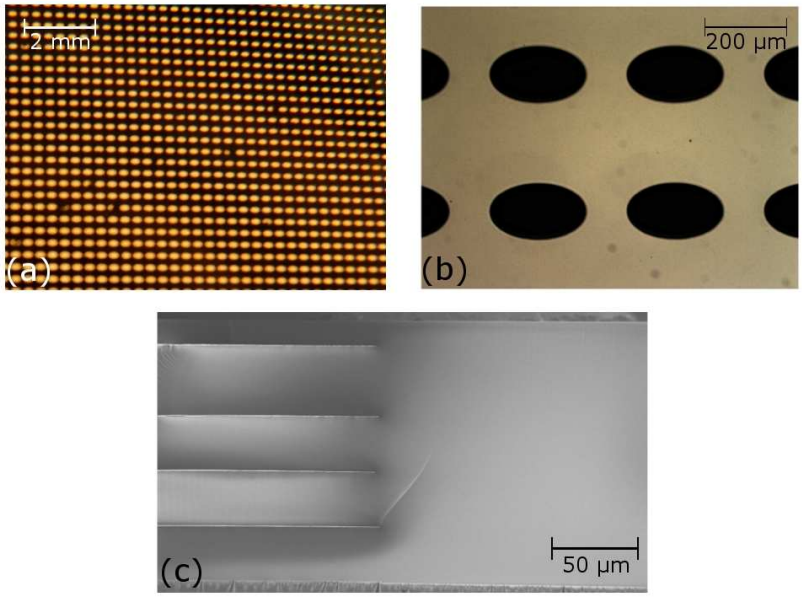

Figure III-37 : Vues au microscope optique du réseau d'ouvertures elliptiques (a) et (b), vue au microscope électronique à balayage de la tranche du métamatériau alternant les couches de métal et de BCB (c).

III.25 Résultats expérimentaux

Les structures métamatériaux ont été caractérisées par une méthode de spectroscopie térahertz dans le domaine temporel en collaboration avec l'IMEP – LAHC localisé à Chambéry. Le banc de caractérisation développé dans le groupe de Jean-Louis Coutaz [24, 25] utilise une technique pompe-sonde qui assure une cohérence entre l'émission et la détection afin de conserver l'information de phase indispensable pour attester de la présence d'une bande de transmission main gauche. Le photocourant généré sous forme d'impulsions picosecondes est rayonné par une antenne dipôle. Un détail du banc de caractérisation montre le prototype disposé sur le trajet du faisceau térahertz focalisé au moyen d'une lentille sphérique placée au contact de l'antenne et de miroirs métalliques (figure III-38). Le diamètre de la tache obtenue à la surface de l'échantillon est de l'ordre du centimètre.

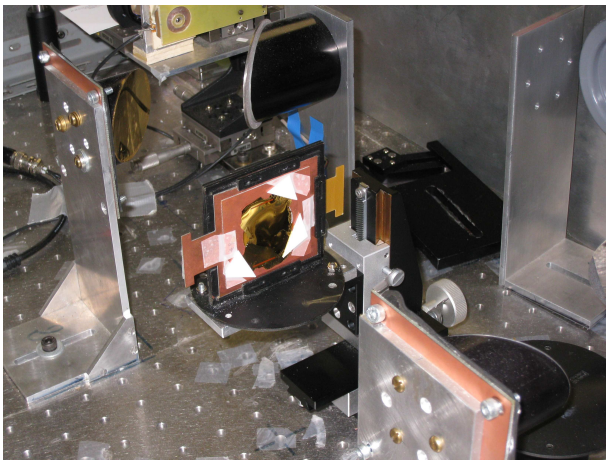

Figure III-38 : Détail du banc de spectroscopie térahertz développé à l'IMEP-LAHC.

Sur la figure III-39, nous donnons le spectre mesuré en comparaison avec la caractéristique simulée pour le métamatériau incluant cinq cellules unitaires. La transmission expérimentale en fonction de la fréquence est obtenue par transformée de Fourier à partir des relevés temporels. L'accord théorie-expérience est très satisfaisant. En outre, le niveau de pertes en bande fondamentale proche de 3 dB place ce résultat à l'état de l'art pour le domaine de fréquence considéré.

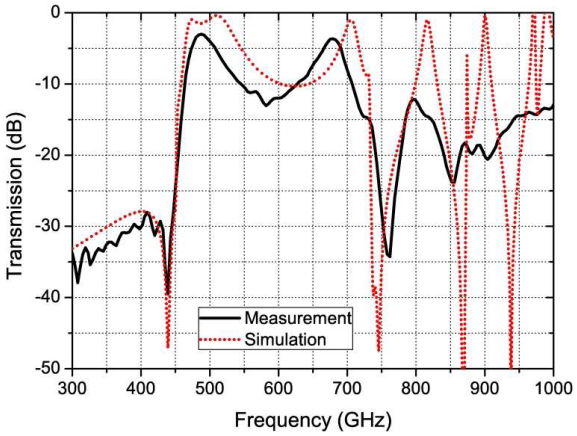

Figure III-39 : Comparaison théorie-expérience des spectres de transmission d'une structure incluant cinq cellules dans la direction de propagation.

Cette comparaison théorie expérience peut être sensiblement améliorée en incluant les pertes diélectriques du BCB et les écarts entre les dimensions du dispositif expérimental et les

dimensions nominales (tableau III-2). Les pertes dans le BCB sont estimées par l'écart suivant [2] : $5.10^{-3} \leq \tan\delta \leq 1.10^{-2}$. L'écart entre l'ouverture réelle et nominale s'explique par le défaut de plaquage lors de la lithographie. Ce défaut est d'autant plus préjudiciable avec l'augmentation du nombre de couches en raison de la déformation de la structure sous l'effet des contraintes dans les films de BCB. Dans le tableau III-2, les épaisseurs repérées en *Zn* avec *n* croissant correspondent à une progression du niveau inférieur vers le niveau supérieur. On peut constater que l'écart d'épaisseur augmente lorsque l'on s'approche de la face supérieure de l'échantillon. Cette tendance peut s'expliquer par la différence des traitements thermiques subis par les différentes couches. En effet, par comparaison avec les niveaux inférieurs, les niveaux supérieurs sont moins recuits, ce qui peut entraîner une polymérisation partielle qui se traduit par une augmentation de l'épaisseur du film correspondant.

	Avant mesure	Après mesure
a	125 µm	140 µm
EAR	1.8	1.7
Épaisseurs des couches de BCB		
Z1	13	13.6
Z2	26	30.9
Z3	26	32.1
Z4	26	32.1
Z5	26	44.1
Z6	13	14.5

Tableau III-2 : Comparaison entre les dimensions nominales et mesurées sur la structure caractérisée.

Lorsque l'on intègre ces différentes données dans la simulation, on obtient un très bon accord avec les caractéristiques mesurées (figure III-40). Deux balayages expérimentaux sont représentés en rouge et noir afin de valider la reproductibilité de la mesure. La figure III-40 inclut également l'évolution de la phase relative obtenue par différence entre la présence et l'absence d'échantillon. Cette représentation permet de vérifier expérimentalement la présence d'une bande gauchère entre 450 et 480 GHz et droitière au-delà de 480 GHz.

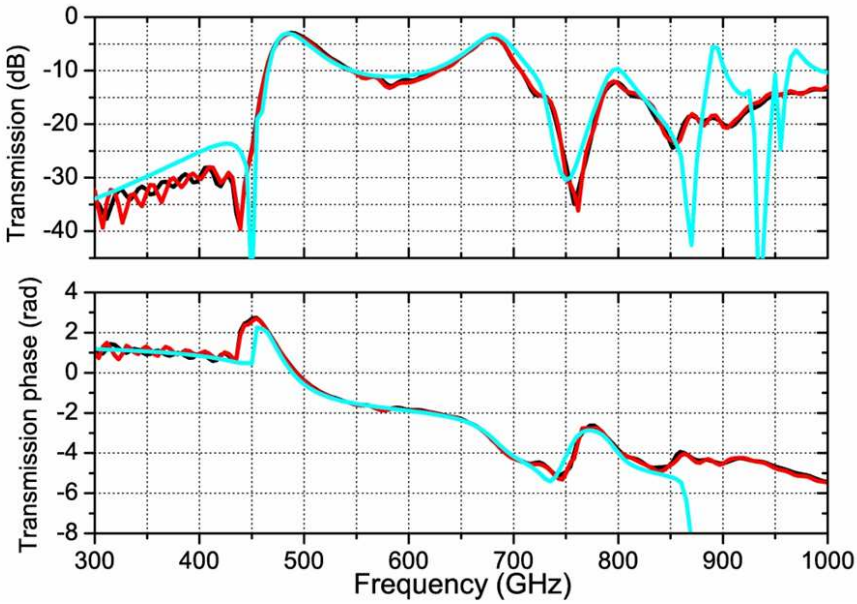

Figure III-40 : Comparaison des spectres de transmission en module et en différence de phase expérimentaux et simulés en incluant les imperfections du dispositif réalisé : mesures (rouge, noir), simulation (bleu).

Ces deux branches de dispersion apparaissent contiguës sur le spectre de phase relative. Cependant, on ne peut pas parler de régime composite équilibré en raison de l'atténuation qui peut être observé en bande main droite sur le spectre d'amplitude.

Ces premiers résultats expérimentaux doivent être complétés de mesure en réflexion afin de pouvoir procéder à une inversion des relations de Fresnel à partir de la matrice S_{ij} complète. Cette procédure est destinée à mieux comprendre les phénomènes électromagnétiques mis en jeu en complément d'une description de la structure au moyen de schémas équivalents. Cette étude est actuellement menée en collaboration avec Jorge Carbonell de l'Université Polytechnique de Valence.

Conclusion

Ce chapitre a permis d'explorer deux voies pour la conception d'un métamatériau volumique. Ces deux approches utilisent un empilement de plusieurs plans de motifs. Dans le premier cas, la structure empilée est excitée par la tranche, parallèlement aux plans des motifs. Cette approche peut être qualifiée de « edge side » en référence à cette contrainte de polarisation.

Dans le second cas, elle est excitée sous incidence normale. On peut alors parler d'approche « front side » par opposition au cas précédent.

Pour l'approche « edge side », nous avons choisi d'utiliser des réseaux de lettres Ω interconnectées. Cette structuration s'avère très performante en termes de largeur de bande et de pertes d'insertion. Par ailleurs, elle offre la possibilité de travailler en régime composite équilibré caractérisée par la jonction des branches de dispersion gauchères et droitières sans bande interdite. Les différents régimes de fonctionnement possibles correspondant à l'indice de réfraction négatif, positif ou nul ont été démontrés par des mesures angulaires. Ce concept a été exploité pour la fabrication et à la caractérisation d'un prototype dans la bande de fréquences comprises entre 75 et 110 GHz. Sur le plan technologique, cette étude a révélé les difficultés de l'approche « edge side » pour les hautes fréquences dans la mesure où il est nécessaire d'empiler un grand nombre de substrats avec une bonne précision d'alignement.

Pour l'approche « front side », nous avons utilisé un empilement de plans métalliques percés par des ouvertures sous longueur d'onde. Le prototype fabriqué comporte cinq niveaux de métallisation afin de définir une structure à cinq cellules unitaires suivant la direction de propagation. Une branche de dispersion main gauche a été mise en évidence expérimentalement autour de la fréquence de 480 GHz par une méthode de spectroscopie dans le domaine temporel. Les faibles niveaux de pertes observés, de l'ordre de 3 dB, illustrent les potentialités de cette approche pour le domaine térahertz. À ce stade, une analyse complémentaire est nécessaire afin de mieux appréhender les mécanismes mis en jeu en vue d'une amélioration des caractéristiques de transmission. Dans cette perspective, les aspects qui nous semblent importants sont la largeur de bande, qui reste relativement faible en comparaison aux structures « edge side », et la possibilité de travailler en régime composite équilibré et notamment à indice de réfraction nul.

Références

[1] É. Lheurette, O. Vanbésien, and D. Lippens, "Double negative media using interconnected Omega-type metallic particles," *Microwave and Optical Technology Letters*, vol. 49, pp. 84-90, 2007.

[2] H. M. Heiliger, M. Nagel, H. G. Roskos, H. Kurz, F. Schnieder, W. Heinrich, R. Hey, and K. Ploog, "Low-dispersion thin-film microstrip lines with cyclotene

(benzocyclobutene) as dielectric medium," *Applied Physics Letters*, vol. 70, pp. 2233-2235, 1997.

[3] H. Jiangtao, R. Lixin, C. Hongsheng, Z. Xian-min, C. Kangsheng, M. G. Tomasz, and K. Jin Au, "Experimental confirmation of negative refractive index of a metamaterial composed of Omega-like metallic patterns," *Applied Physics Letters*, vol. 84, pp. 1537-1539, 2004.

[4] R. Marques, F. Mesa, J. Martel, and F. Medina, "Comparative analysis of edge- and broadside- coupled split ring resonators for metamaterial design - theory and experiments," *Antennas and Propagation, IEEE Transactions on*, vol. 51, pp. 2572-2581, 2003.

[5] F. Zhang, D. P. Gaillot, C. Croenne, E. Lheurette, X. Melique, and D. Lippens, "Low-loss left-handed metamaterials at millimeter waves," *Applied Physics Letters*, vol. 93, pp. 083104, 2008.

[6] W. B. Weir, "Automatic measurement of complex dielectric constant and permeability at microwave frequencies," *Proceedings of the IEEE*, vol. 62, pp. 33-36, 1974.

[7] D. R. Smith, P. M. Rye, J. J. Mock, D. C. Vier, and A. F. Starr, "Enhanced Diffraction from a Grating on the Surface of a Negative-Index Metamaterial," *Physical Review Letters*, vol. 93, pp. 137405, 2004.

[8] A. Namba, O. Wada, Y. Toyota, Y. Fukumoto, W. Zhi Liang, R. Koga, T. Miyashita, and T. Watanabe, "A simple method for measuring the relative permittivity of printed circuit board materials," *Electromagnetic Compatibility, IEEE Transactions on*, vol. 43, pp. 515-519, 2001.

[9] F. Zhang, Q. Zhao, L. Kang, D. P. Gaillot, X. Zhao, J. Zhou, and D. Lippens, "Magnetic control of negative permeability metamaterials based on liquid crystals," *Applied Physics Letters*, vol. 92, pp. 193104, 2008.

[10] J. Zhou, K. Th, M. Kafesaki, E. N. Economou, J. B. Pendry, and C. M. Soukoulis, "Saturation of the Magnetic Response of Split-Ring Resonators at Optical Frequencies," *Physical Review Letters*, vol. 95, pp. 223902, 2005.

[11] V. M. Shalaev, W. Cai, U. K. Chettiar, H.-K. Yuan, A. K. Sarychev, V. P. Drachev, and A. V. Kildishev, "Negative index of refraction in optical metamaterials," *Opt. Lett.*, vol. 30, pp. 3356-3358, 2005.

[12] S. Zhang, W. Fan, K. J. Malloy, S. R. Brueck, N. C. Panoiu, and R. M. Osgood, "Near-infrared double negative metamaterials," *Opt. Express*, vol. 13, pp. 4922-4930, 2005.

[13] R. W. Wood, "On a Remarkable Case of Uneven Distribution of Light in a Diffraction Grating Spectrum," *Proceedings of the Physical Society of London*, pp. 269, 1902.

[14] A. Hessel and A. A. Oliner, "A New Theory of Wood?s Anomalies on Optical Gratings," *Appl. Opt.*, vol. 4, pp. 1275-1297, 1965.

[15] M. Beruete, M. Sorolla, I. Campillo, J. S. Dolado, L. Martin-Moreno, J. Bravo-Abad, and F. J. Garcia-Vidal, "Enhanced millimeter wave transmission through quasioptical subwavelength perforated plates," *Antennas and Propagation, IEEE Transactions on*, vol. 53, pp. 1897-1903, 2005.

[16] T. W. Ebbesen, H. J. Lezec, H. F. Ghaemi, T. Thio, and P. A. Wolff, "Extraordinary optical transmission through sub-wavelength hole arrays," *Nature*, vol. 391, pp. 667-669, 1998.

[17] E. Popov, M. Nevière, S. Enoch, and R. Reinisch, "Theory of light transmission through subwavelength periodic hole arrays," *Physical Review B*, vol. 62, pp. 16100, 2000.

[18] L. Martín-Moreno, F. J. García-Vidal, H. J. Lezec, K. M. Pellerin, T. Thio, J. B. Pendry, and T. W. Ebbesen, "Theory of Extraordinary Optical Transmission through Subwavelength Hole Arrays," *Physical Review Letters*, vol. 86, pp. 1114, 2001.

[19] M. Sarrazin, J.-P. Vigneron, and J.-M. Vigoureux, "Role of Wood anomalies in optical properties of thin metallic films with a bidimensional array of subwavelength holes," *Physical Review B*, vol. 67, pp. 085415, 2003.

[20] M. Beruete, I. Campillo, J. E. Rodriguez-Seco, E. Perea, M. Navarro-Cia, I. J. Nunez-Manrique, and M. Sorolla, "Enhanced Gain by Double-Periodic Stacked Subwavelength Hole Array," *Microwave and Wireless Components Letters, IEEE*, vol. 17, pp. 831-833, 2007.

[21] B. Bianco and M. Parodi, "Determination of the propagation constant of uniform microstrip line," *Alta Frequenza*, vol. 2, pp. 107, 1976.

[22] D. R. Smith, S. Schultz, P. Markos, and C. M. Soukoulis, "Determination of effective permittivity and permeability of metamaterials from reflection and transmission coefficients," *Physical Review B*, vol. 65, pp. 195104, 2002.

[23] P. Salzenstein, O. Dupuis, M. Helal, E. Lheurette, O. Vanbesien, P. Mounaix, and D. Lippens, "Coplanar waveguides on dielectric membranes micromachined on a GaAs substrate," *Electronics Letters*, vol. 32, pp. 821-822, 1996.

[24] F. Aquistapace, L. Duvillaret, F. Garet, J. F. Roux, and J. L. Coutaz, "Photovariation of grating-assisted coupling of terahertz waves into a silicon waveguide," *Journal of Applied Physics*, vol. 94, pp. 7888-7891, 2003.

[25] L. Duvillaret, F. Garet, and J.-L. Coutaz, "Influence of noise on the characterization of materials by terahertz time-domain spectroscopy," *J. Opt. Soc. Am. B*, vol. 17, pp. 452-461, 2000.

Conclusions et perspectives

Ce mémoire d'Habilitation à Diriger les Recherches, centré sur les activités que je mène depuis mon affectation à l'Université des Sciences et Technologie de Lille en septembre 2003, est consacré aux métamatériaux à indice de réfraction négatif, à base de structures métallo-diélectriques. Le principal fil conducteur de cette étude est l'évolution des longueurs d'onde centimétriques vers le spectre térahertz.

Même si certains principes sont directement conservés, cette évolution vers les fréquences élevées ne peut s'opérer par une simple mise à l'échelle des dimensions des dispositifs de base. En effet, l'approche initiale, proposée par J. B Pendry, qui consiste à superposer deux réseaux simplement négatifs, souffre de pertes relativement importantes et de faibles bandes passantes en raison de la contribution de motifs fortement résonnants, nécessaires pour synthétiser la perméabilité effective négative. La démarche alternative qui, en exploitant le concept de ligne de transmission duale, permet de palier ces inconvénients, paraît peu compatible avec la définition d'un métamatériau volumique. En revanche, l'approche qui consiste à tirer parti du caractère doublement négatif de chaînes infinies de boucles de courants interconnectées s'avère très intéressante, tant sur le plan des performances que de la souplesse de conception. Nous avons qualifié cette approche d'hybride dans la mesure où, en intégrant sur une même inclusion des dipôles électrique et magnétique, elle reprend le principe de la superposition des réseaux simplement négatifs tout en bénéficiant de propriétés de dispersion qui s'apparentent à celles des lignes de transmission duales. Ces propriétés sont les caractères large bande et faible perte ainsi que la possibilité de travailler en régime composite équilibré, autrement dit avec une évolution continue des branches de dispersion main gauche et main droite sans bande interdite. Nous avons démontré cette dernière propriété de manière expérimentale par une caractérisation en réfraction. Par ailleurs, l'aspect faible perte est directement illustré par les niveaux de transmission, de l'ordre de -0,5 dB par cellule, que nous avons obtenus sur un prototype conçu pour les fréquences comprises entre 75 et 110 GHz. Toutefois, cette étude a révélé les difficultés de travailler avec les structures « edge side » aux longueurs d'onde millimétriques et submillimétriques. En effet, cette approche exige une excitation du métamatériau parallèlement au plan des motifs, ce qui, en espace libre, implique l'empilement d'un grand nombre de couches élémentaires. En réponse à cette difficulté, nous avons commencé à travailler sur des topologies « front side » qui sont

adaptées à une excitation sous incidence normale. Nous avons obtenu des premiers résultats sur une structure constituée de l'empilement de plusieurs réseaux d'ouvertures sous longueur d'onde à la fréquence de 500 GHz. L'analyse des premières mesures effectuées par une technique de spectroscopie térahertz dans le domaine temporel doit être complétée afin de mieux appréhender les phénomènes. Le premier constat confirme la présence d'une bande de transmission gauchère avec un niveau de transmission élevé, de l'ordre de -3 dB. Cependant, cette branche de dispersion est relativement étroite et sans commune mesure avec les larges bandes obtenues pour les structures « edge side » à boucles de courant interconnectées. À ce stade de notre étude, nous ne pouvons affirmer dans quelle mesure ce paramètre pourrait être amélioré. C'est la raison pour laquelle l'approche « edge side » nous apparaît toujours comme une option à considérer même si les réalisations aux longueurs d'onde submillimétriques sont conditionnées par l'apport de nouvelles solutions technologiques.

Tant au niveau des caractéristiques électriques que des techniques d'élaboration, l'utilisation de couches semi-conductrices constitue une voie intéressante pour les fréquences élevées. En effet, l'alternance de couches métalliques et diélectriques peut être substituée par des hétérostructures alternant des niveaux de dopage très élevés et très faibles. L'élaboration du métamatériau volumique emprunte alors une technique de croissance épitaxiale et la structuration latérale peut être réalisée au moyen de techniques de gravure profonde telles que l'ICP (Inductively Coupled Plasma) ou le FIB (Focus Ion Beam). Cette perspective de travail s'appuie sur l'expérience de l'IEMN dans le domaine des matériaux semi-conducteurs, III-V notamment.

D'un point de vue physique, le point fort des métamatériaux réside dans la localisation de l'énergie électromagnétique au niveau des motifs élémentaires. À titre d'exemple, l'effet de perméabilité effective est la conséquence d'une concentration du champ magnétique à l'intérieur d'une boucle de courant. Si, pour des commodités de conception et de fabrication, on utilise fréquemment des arrangements périodiques, cette caractéristique n'est pas une condition nécessaire pour définir un métamatériau, à l'inverse des cristaux photoniques où tout défaut de périodicité peut se traduire par une dégradation des propriétés de transmission. Compte tenu de cette particularité, il est possible d'élaborer des métamatériaux en utilisant des techniques d'auto-assemblage. Sur le plan théorique tant que sur le plan expérimental, cette perspective ouvre de

nouveaux champs d'investigation. Une première étude est envisagée dans le cadre d'une collaboration avec l'université chinoise de Xian qui possède une expérience dans l'élaboration de structures dendrites.

Liste des articles reproduits

1 Left handed dispersion of a stack of sub-wavelength hole metal arrays at terahertz frequencies
C. Croënne, F. Garet, É. Lheurette, J. L. Coutaz et D. Lippens, accepté pour publication dans la revue Applied Physics Letters **94**, p. 133112, 2009

2 Ferroelectric tunable balanced right- and left-handed transmission lines
A. Marteau, G. Vélu, G. Houzet, L. Burgnies, É. Lheurette, J. C. Carru et D. Lippens, Applied Physics Letters **94**, p. 023507, 2009

3 Low-loss left-handed metamaterials at millimeter waves
F. Zhang, D. P. Gaillot, C. Croënne, É. Lheurette, X. Mélique et D. Lippens, Applied Physics Letters **93**, p. 083104, 2008

4 Negative-Zero-Positive Refractive Index in a Prism-Like Omega-Type Metamaterial
F. Zhang, S. Potet, J. Carbonell, É. Lheurette, O. Vanbesien, X. Zhao et D. Lippens, Microwave Theory and Techniques, IEEE Transactions on **56**, pp. 2566-2573, 2008

5 Negative-zero-positive metamaterial with Omega-type metal inclusions
F. Zhang, G. Houzet, É. Lheurette, D. Lippens, M. Chaubet et X. Zhao, Journal of Applied Physics **103**, p. 084312, 2008

6 Omega-Type Balanced Composite Negative Refractive Index Materials
É. Lheurette, G. Houzet, J. Carbonell, F. Zhang, O. Vanbesien et D. Lippens, Antennas and Propagation, IEEE Transactions on **56**, pp. 3462-3469, 2008

7 Negative index metamaterial at 100 GHz
C. Croënne, M. F.Foulon, É. Lheurette, X. Mélique, M. Gheudin et D. Lippens, Proceedings of the European Microwave Association **4**, pp. 95-101, 2008

8 Double negative media using interconnected Omeg -type metallic particles
É. Lheurette, O. Vanbésien et D. Lippens, Microwave and Optical Technology Letters **49** (1) pp 84-90, 2007

9 Left-handed electromagnetics properties of split ring resonator and wire loaded transmission line in a fin-line technology
T. Decoopman, A. Marteau, É. Lheurette, O. Vanbésien et D. Lippens, IEEE transactions on Microwave Theory and Techniques **54**, pp 1451-57, 2006

10 Left-handed propagation media via photonic crystal and metamaterials
T. Decoopman, T. Crépin, M. Perrin, S. Fasquel, A. Marteau, X. Mélique, É. Lheurette, O. Vanbésien et D. Lippens, *Comptes Rendus Physique* 6, pp. 683-692, 2005

11 left-handed electromagnetism obtained via nanostructured metamaterials : comparison with that from microstructured photonic crystals
M. Perrin, S. Fasquel, T. Decoopman, X. Mélique, O. Vanbésien, E. Lheurette et D. Lippens
Journal of Optics A, 7, pp S3-11, 2005

12 Wave-mechanical calculations of leakage current through stacked dielectrics for nanotransistor Metal-Oxide-Semiconductor design
M. Le Roy, E. Lheurette, O. Vanbésien et D. Lippens
Journal of Applied Physics, 93, pp 2966-71, 2003

13 Characterisation of charge trapping at the Si-SiO_2 (100) interface using high-temperature conductance spectroscopy
E. Duval et E. Lheurette
Microelectronic Engineering, 65, pp 103-112, 2003

14 Determination of slow- and fast-state distribution using high temperature conductance spectroscopy on MOS structures
E. Duval, E. Lheurette, K. Ketata et M. Ketata
Semiconductor Science and Technology, **16**, 2001

15 Rapid determination of « slow » and « fast » states densities using thermally stimulated conductance spectroscopy on metal-oxide semiconductor capacitors
E. Duval, L. Soliman, E. Lheurette, K. Ketata, M. Benzohra, C. Duprat et M. Ketata
Material Science in Semiconductor Processing, **4**, 2001

16 Improvement of oxide thickness determination on MOS structures using capacitance-voltage measurements at high frequencies
L. Soliman, E. Duval, M. Benzohra, E. Lheurette, K. Ketata et M. Ketata
Material Science in Semiconductor Processing, **4**, 2001

17 Step-like heterostructure barrier varactor for high power millimeter-wave applications
R. Havart, E. Lheurette, O. Vanbésien, P. Mounaix, F. Mollot and D. Lippens
IEEE Transactions on Electron Devices, **45**, 1998

18 Capacitance engineering for InP-based heterostructure barrier varactor
E. Lheurette, X. Mélique, P. Mounaix, F. Mollot, O. Vanbésien and D. Lippens
IEEE Electron Device Letters, **19**, 1998

Left handed dispersion of a stack of subwavelength hole metal arrays at terahertz frequencies

Charles Croënne,[1] Frédéric Garet,[2] Éric Lheurette,[1] Jean-Louis Coutaz,[2] and Didier Lippens[1,a)]
[1]*Institut d'Électronique, de Microélectronique et Nanotechnologies, Université des Sciences et Technologies de Lille, Avenue Poincaré BP 60069, 59652 Villeneuve d'Ascq Cedex, France*
[2]*Laboratoire IMEP-LAHC, UMR 5130 du CNRS, Université de Savoie, 73376 Le Bourget du Lac Cedex, France*

(Received 6 February 2009; accepted 13 March 2009; published online 3 April 2009)

We report on the electromagnetic response of a stack of subwavelength hole metal arrays. The samples were designed for exhibiting left handed dispersion branches under normal incidence, and their transmissivities were optimized via the fabrication of elliptical-shaped holes. They are constituted of benzocyclobutene layers with tens of micron thicknesses and submicron-thick gold films patterned by photolithography. Experimental evidence, achieved by time-domain terahertz spectroscopy and supported by full wave simulations, of a ground left handed dispersion branch is found around 0.45 THz. The insertion losses are −3 dB for a five-layer structure, this good level being explained by the matching of the impedance. © *2009 American Institute of Physics*.
[DOI: 10.1063/1.3114411]

After the story of edge-illuminated left handed three dimensional metamaterials fabricated from split ring resonator and wire arrays,[1] operating satisfactorily at least up to 100 GHz,[2] most of the current research effort is now oriented toward the fabrication of metamaterials that can operate in the infrared spectral region under normal incidence. Ideas to reach this goal are numerous, starting from the pioneering work of Podolskiy[3] who proposed to stack two nanoresonators coupled in the direction of wave propagation. Within this scheme, the proper condition of the magnetic field polarization, i.e., perpendicular to the planar resonators, can be fulfilled. The so-called fishnet structure[4–6] is derived from the same idea. On the other hand, subwavelength hole metal arrays have also shown the possibility to observe enhanced transmission.[7–9] *A priori*, their operating principle is based on the effect of extraordinary transmission through a subwavelength hole single grid comparable to a frequency selective surface. In the infrared, the operation of such a grid is based on surface plasmon (SP) physics, and no evidence of negative index was demonstrated for a single array. Recently, the demonstration of the operation of such a grid at millimeter wave shows that the SP propagation condition was not necessary to explain the electromagnetic properties due to the fact that the hole structuring permits to mimic surface wave.[10] More importantly, it was shown by the Navarre University group[11] that a left handed dispersion can also be observed when two grids at least are stacked, which is also the requirement for a fishnet approach. Obviously there are close similarities between the coupled metal rod arrays and the metal structure obtained by taking the complementary arrangement of the staked hole arrays according to the Babinet principle.

In the present paper, we go further with the possibility to induce a negative effective refractive index by means of a stack of hole arrays under normal incidence. This work shows two key originalities with respect to the state of the art in this field. The first original point concerns the frequency of operation, in the terahertz (THz) frequency range and thus one order of magnitude higher than the operating frequency reported in Ref. 11 around 55 GHz. This increase in the operating frequency will not modify the main conclusion drawn at lower frequency, namely, the fact that SPs do not explain the singular electromagnetic properties of these structures, notably a negative value of refractive index. However the aspect ratio between the dielectric layers and the metallic films, which form the stack of subwavelength hole arrays, is strongly modified with values as close to 100. As a consequence, there is a strong unbalance between surface modes in the dielectric layer and guided modes in the holes. The other challenges are (i) in the fabrication of the samples, which requires using microelectronics technologies, and (ii) in the characterization by means of coherent terahertz time domain spectroscopy (THz-TDS) in order to describe the effects of phase advance. The second original issue is the achievement of moderate insertion losses despite the fact that intrinsic losses of both dielectric and metal materials increase at higher operation frequencies. We show that such a result is not connected to the fact that the operation behavior can be compared to a transmission line approach as proposed in the literature.[12]

In our case, it is believed that a matching of the impedance close to the pass band edge is responsible for such a high transmission level at the detriment however of the band width. To achieve such a high transmissivity, an optimization of the hole shape with an elliptical configuration was performed in a manner similar to the width optimization of the strips of fishnet structures.

Figures 1(a) and 1(b) show a large scale photograph and an optical microscope view of the top metal layer. The shape of the hole is elliptical with a ratio of 1.7:1 between the large and small axes. The patterning of holes in the metal film, deposited by evaporation with a Plassys MEB 550S equipment on a GaAs semi-insulating substrate, was achieved by

a)Author to whom correspondence should be addressed: Electronic mail: didier.lippens@iemn.univ-lille1.fr

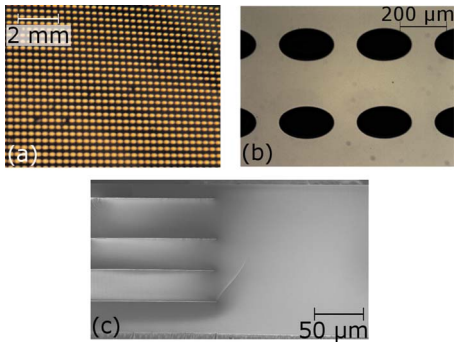

FIG. 1. (Color online) (a) View of one part of the array. (b) Optical microscope view and (c) SEM view of the cross section of the stack of metallic arrays. The homogeneous region on the right corresponds to the cross section of the elliptical holes.

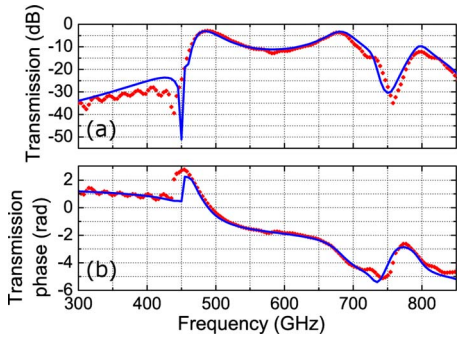

FIG. 2. (Color online) Simulated (solid blue/black lines) and measured (red/gray diamonds) transmission spectra in magnitude (a) and phase (b) for the sample in Fig. 1.

lift-off photolithography using a Clariant AZnLOF 2070 negative resist.

The dielectric spacers are benzocyclobutene (BCB) resist layers. BCB, supplied by the Dow Chemical Co., was chosen for its moderate loss in the terahertz frequency range. Its permittivity constant given by the supplier is 2.6 with a loss tangent ranging from 0.005 to 0.01 at 1 THz. A parametric numerical study of the influence of the BCB thickness on the electromagnetic properties of the device has orientated our choice toward a few tens of micron BCB thickness, hence much thicker than the metal films contrary to the devices fabricated for microwaves applications.[11] The BCB layers were deposited by spin coating and subsequently annealed under nitrogen controlled atmosphere at a temperature of around 300 °C. In practice, we faced two difficulties: (i) the high strain of the BCB layer so that only a limited number of layers (here $n \leq 5$) were deposited with a reasonable bowing of the substrate and (ii) a relatively large dispersion in the BCB thickness measured from the cross section of a peeled sample piece. A scanning electron microscope (SEM) picture of this cross section is shown in Fig. 1(c); the thicknesses range from 30.9 to 44.1 μm. Finally to suppress the substrate effects that introduce an asymmetry in the sample boundaries (interfaced with air on the one side and with a semiconductor on the other side), a membranelike structure was fabricated. This was realized by means of a deep backside wet chemical etching (H_2SO_4:H_2O_2:H_2O), the multilayer playing the role of an etch stop layer.

The transmission measurements were performed with a classical THz-TDS setup using low temperature grown-GaAs photoswitches as antennas, which was already described elsewhere.[13] The frequency spectrum of the signals delivered by this setup, as obtained by a Fourier-transform of the temporal waveforms, ranges from 0.1 to 5 THz. At the top of the spectrum amplitude, i.e., in between 0.5 and 1 THz, the measured dynamics is 60 dB. At the sample location, the THz beam is made almost parallel (3 cm waist at 1 THz) by means of parabolic mirrors. To avoid spurious effect due to diffraction at the sample edges, a 2 cm diameter diaphragm was located in front of the sample, leading to the illumination of about 2700 cells. Despite the fact that the terahertz beam delivered by the photoswitch is almost polarized,[14] a fine control of the polarization state (the *E*-polarization state corresponds to the *E*-field directed along the small axis of the elliptical holes) was realized with grid polarizers. The experimental frequency resolution is 3.75 GHz since the maximum delay of the delay line is 266 ps. The terahertz response presented below is obtained by differential measurement with and without the sample in the terahertz beam path.

Figure 2 shows the frequency dependences of the magnitude and of the phase of the transmission coefficient (T). The key feature in the magnitude of T is the presence of a pass band above 0.45 THz, this frequency corresponding to an antiresonance state (zero of transmission). Below this characteristic frequency, the transmissivity of the sample is extremely weak (of the order of -30 dB) as the hole array is operating below the hole cutoff. From the hole dimensions and taking into account its elliptical shape, as well as the BCB index, one can estimate this cutoff frequency to approximately 483 GHz. This means that the sample exhibits an extraordinary transmission in the sense that a pass band is experimentally evidenced in a frequency band below the conventional Bethe limitation[15] as discussed above. By considering now the unwrapped phase, it can be noticed that the phase offset measured with and without the sample is positive in the first pass band, which indicates that the refractive index is negative.

We also plotted in Fig. 2 the calculated frequency dependence of the transmission in modulus and phase, which can be obtained by a full wave analysis. The calculation was performed by means of the Maxwell equation solver HIGH FREQUENCY STRUCTURE SIMULATOR by Ansoft. In these calculations, the metal losses were taken into account with a conductivity of the gold films of 4.1×10^7 S/m. Losses of the BCB layers, with values of loss tangents ranging from 0.01 to 0.03 at 800 GHz, were also included in the simulation. At last, the dispersion in the BCB layer thickness, evidenced in the cross section displayed in Fig. 1(c), was also taken into account. Under these conditions, it can be noted that there is an excellent fit between the measured and the experimental data. Some discrepancies exist in the upper part above 850 GHz (not shown here) where pronounced dips can be evidenced in the plot of the numerical results but are not reproduced in the experimental trace. They are attributed to Wood anomalies whose analysis is beyond the scope of the present work.

This excellent fit below 850 GHz permitted us to get a deeper insight into the electromagnetism of the structure by the retrieval of the dispersion characteristic and of the frequency dependence of the impedance. The results are reported in Fig. 3. They were obtained by a Fresnel inversion technique, which was applied in our group for describing metamaterials as well as photonic crystals.[16] For the stop

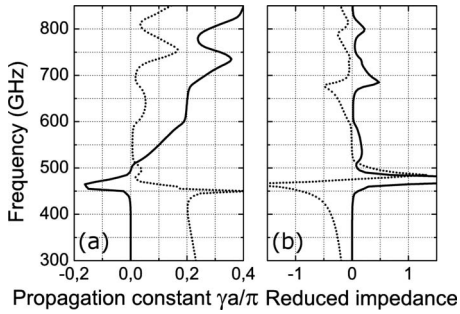

FIG. 3. Dispersion diagram with the real (dotted line) and imaginary (solid line) parts of the propagation constant. (b) Frequency dispersion of the real (solid line) and imaginary (dotted line) parts of the reduced impedance.

band, notably the forbidden band below 450 GHz, the figure of interest is the attenuation constant corresponding to the imaginary part of the wavevector amplitude k. For the left handed branch between 450 and 480 GHz, the dispersion was plotted for the negative value of the real part of k. It can be verified that in this band, the group velocity that corresponds to the slope of the $\omega(k)$ function is positive, while the phase velocity $v_p = \omega/k$ is negative. Above 480 GHz, a narrow gap can be seen before the conventional right handed branch, which starts around 510 GHz. It is believed that a pure balanced composite metamaterial that exhibits negative zero positive index[17] could be achieved by a proper design. With respect to the normalized impedance it can be seen that the matching of the real impedance $(z=1)$ was achieved close to the narrow stop band edge, explaining the high transmissivity peak at a frequency of about 470 GHz.

In conclusion, an experimental evidence of a ground left handed transmission branch, which thus corresponds to a negative refractive index, was demonstrated by a THz-TDS analysis of a stack of subwavelength hole arrays. Despite the fact that the intrinsic dielectric and metal losses lower the maximum of transmission, it appears that the key feature for achieving a high transmission level stems from the characteristic impedance matching, which was obtained here close to the stop band edge.

This work was carried out in the framework of a Délégation Générale pour l'Armement contract.

[1] R. A. Shelby, D. R. Smith, and S. Schultz, Science **292**, 77 (2001).
[2] F. Zhang, D. P. Gaillot, C. Croënne, E. Lheurette, X. Mélique, and D. Lippens, Appl. Phys. Lett. **93**, 083104 (2008).
[3] V. A. Podolskiy, A. K. Sarychev, and V. M. Shalaev, J. Nonlinear Opt. Phys. Mater. **11**, 65 (2002).
[4] S. Zhang, W. Fan, K. J. Malloy, S. R. J. Brueck, N. C. Panoiu, and R. M. Osgood, Opt. Express **13**, 4922 (2005).
[5] S. Zhang, W. Fan, N. C. Panoiu, K. J. Malloy, R. M. Osgood, and S. R. J. Brueck, Phys. Rev. Lett. **95**, 137404 (2005).
[6] G. Dolling, C. Enkrich, M. Wegener, C. M. Soukoulis, and S. Linden, Science **312**, 892 (2006).
[7] J. Rivas, C. Schotsch, P. H. Bolivar, and H. Kurz, Phys. Rev. B **68**, 201306 (2003).
[8] M. Beruete, M. Sorolla, I. Campillo, J. S. Dolado, L. Martin Moreno, J. Bravo-Abad, and F. J. Garcia-Vidal, Opt. Lett. **29**, 2500 (2004).
[9] A. G. Schuchinsky, D. E. Zelenchuk, and A. M. Lerer, J. Opt. A, Pure Appl. Opt. **7**, S102 (2005).
[10] A. Mary, S. G. Rodrigo, F. J. Garcia-Vidal, and L. Martin-Moreno, Phys. Rev. Lett. **101**, 103902 (2008).
[11] M. Beruete, M. Sorolla, and I. Campillo, Opt. Express **14**, 5445 (2006).
[12] F. Medina, F. Mesa, and R. Marqués, IEEE MTT-S Int. Microwave Symp. Dig. **2008**, 213.
[13] F. Aquistapace, L. Duvillaret, F. Garet, J.-F. Roux, and J.-L. Coutaz, J. Appl. Phys. **94**, 7888 (2003).
[14] F. Garet, L. Duvillaret, and J.-L. Coutaz, Proc. SPIE **3617**, 30 (1999).
[15] H. A. Bethe, Phys. Rev. **66**, 163 (1944).
[16] C. Croënne, N. Fabre, D. P. Gaillot, O. Vanbésien, and D. Lippens, Phys. Rev. B **77**, 125333 (2008).
[17] F. Zhang, G. Houzet, E. Lheurette, D. Lippens, M. Chaubet, and X. Zhao, J. Appl. Phys. **103**, 084312 (2008).

Ferroelectric tunable balanced right- and left-handed transmission lines

Aurélien Marteau,[1] Gabriel Velu,[2] Gregory Houzet,[1] Ludovic Burgnies,[2] Eric Lheurette,[1] Jean Claude Carru,[2] and Didier Lippens[1,a)]

[1]*Institut d'Électronique de Microélectronique et Nanotechnologies, Université des Sciences et Technologies de Lille, Avenue Poincaré, BP 60069, 59652 Villeneuve d'Ascq Cedex, France*

[2]*Laboratoire d'Etude des Matériaux et Composants pour l'ELectronique, Université du Littoral Côte d'Opale, 62228 Calais Cedex, France*

(Received 10 November 2008; accepted 17 December 2008; published online 15 January 2009)

The tuning of the dispersion characteristics of a balanced composite right- and left-handed transmission lines is demonstrated at centimeter and millimeter wavelengths. To this aim, coplanar waveguides, periodically loaded by interdigitated capacitances and stublike inductances, were fabricated onto a $Ba_{0.5}Sr_{0.5}TiO_3$ ferroelectric thin film. The scattering parameter measurements show that the lines are left handed from 8 to 18 GHz and right handed above. The results are interpreted by the retrieval of the effective permittivity and permeability, which exhibit Drude-like dispersion characteristics with a magnetic plasma frequency, which can be tuned via the voltage-controlled permittivity variation in the BST thin film. © *2009 American Institute of Physics*.
[DOI: 10.1063/1.3068495]

Metamaterial-based propagation media attract now much interest with the prospect to have further degrees of freedom in the design of novel microwave devices.[1,2] The balanced composite left- and right-handed modes, namely, the fact that the dispersion diagram does not exhibit a gap between the left- and right-handed dispersion branches, were early implemented via a transmission line (TL) approach. More recently, this operating mode was also demonstrated for bulk metamaterials constituted of omega-type inclusion arrays.[3] The key advantage of a balance composite mode is that the effective refractive index can be negative, zero, or positive by shifting the operating frequency across the gapless dispersion diagram. For many practical applications however, the tuning of the dispersion diagram, while maintaining the balance condition, appears preferable with respect to a variation in the operating frequency. So far, various works were reported in literature on the tunability of the metamaterial dispersion characteristics. A first approach is based on the integration of active solid state devices such as varactor diodes.[4,5] The capacitance variations versus voltage change the resonance frequency of the so-called split ring resonator (SRR) or complementary SRR elements. A similar frequency shift is also achieved by taking benefit of a microelectromechanical systems technology.[6] On the other hand, ferroelectric films can be used to tune the relevant frequencies of SRR array[7] or left-handed transmission lines.[8]

In this paper, we consider this latter approach with special attention on the dispersion balance. To this aim, we fabricated coplanar transmission lines loaded by series lumped capacitances and shunt inductances in order to achieve a ground left-handed transmission branch. Indeed by this dual scheme of the conventional transmission line, a high pass filtering response is achieved.[9] The balance condition can be fulfilled provided that the right-handed elements, which result from the interconnecting elements (series inductance and shunt capacitance of a conventional transmission line), are balanced by the lumped elements (series capacitance and shunt inductance) responsible of the left-handed dispersion branch. In terms of circuit analysis, this corresponds to the equality between the resonant frequency of the overall series circuit and of the overall shunt circuit.[10] The difficulty stems from the fact that the distributed shunt capacitance is not tunable under moderate voltage control. A balance condition is demonstrated experimentally in a first stage for unbiased devices. Then, the tunability of the quasigapless dispersion characteristic will be demonstrated in a second stage by voltage controlling the permittivity of interdigitated series and shunt capacitances. At last, the tuning of the balance condition will be discussed on the basis of the experimental retrieval of the effective permittivity and permeability dispersion characteristics.

Figure 1(a) shows the equivalent circuit of a unit cell. The lumped series capacitance is indexed C_{LH} and the shunt inductance L_{LH}, LH stands for left handed. The TL sections,

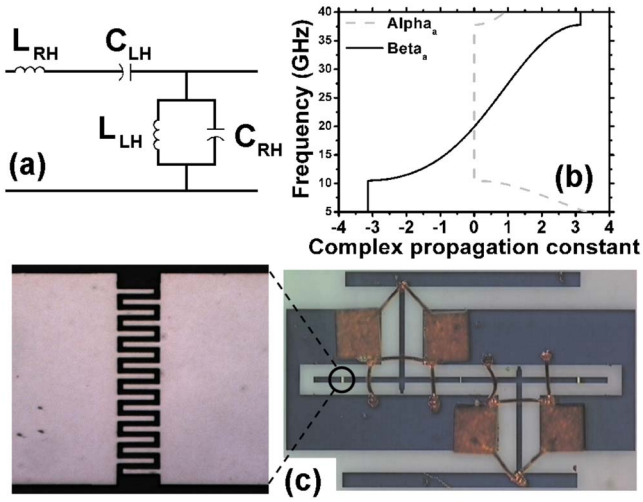

FIG. 1. (Color online) Lumped element circuit (a), dispersion diagram calculated with C_{LH}=120 fF, L_{RH}=0.53 nH, C_{RH}=128 fF, and L_{LH}=0.5 nH (b). Optical view of a two-cell device (c). The inset is an optical view of an interdigitated ferroelectric capacitance.

a)Author to whom correspondence should be addressed: Electronic mail: didier.lippens@iemn.univ-lille1.fr.

which interconnect these elements behave as conventional transmission lines as aforementioned. They can be described in terms of distributed elements with the index RH standing for right handed. L_{RH} is placed in series, whereas C_{RH} is in parallel. In terms of circuit the balance condition is

$$\omega_r = (L_{RH} \cdot C_{LH})^{-1/2} = (L_{LH} \cdot C_{RH})^{-1/2}. \quad (1)$$

It results from this relation that any variation in C_{LH} has to be compensated by a right-handed capacitor put in parallel in the circuit in order to preserve the balance composite regime. This explains why in practice the right-handed capacitance (C_{RH}) will consist in a distributed fixed element and an additional tunable capacitor. The voltage-controlled capacitors were fabricated using an interdigitated (IDC) scheme. Figure 1(c) shows an optical view of a device with 18 finger-shaped electrodes. The finger width (L_w) as well as their spacing (L_s) are on a micron scale yielding a pitch (L_w+L_s) around 2 μm. Under this condition, a moderate voltage is required for controlling the permittivity of the underlying thin ferroelectric $Ba_{0.5}Sr_{0.5}TiO_3$ film. For the dispersion characteristics of material parameters, we took advantage of a broadband characterization of dielectric properties of thin BST films using a TL-like de-embedding technique, which combines the measurements of discrete devices and bare transmission lines.[11] In the frequency band of interest (5–40 GHz), the relative permittivity of a 300 nm thick film is quite constant as a function of frequency $\varepsilon_{rBST} \sim 330$. IDCs were designed using conformal mapping techniques.[12] Further details about the fabrication technology of the $Ba_{0.5}Sr_{0.5}TiO_3$ ferroelectric film deposited by a sol-gel technique and of IDCs can be found in Ref. 13.

An optical view of a completed two-cell device is shown in Fig. 1(c). It consists of a coplanar waveguide (CPW) whose propagation properties can be assessed on wafer, owing to the probe foot prints apparent on both sides of the CPW. Stublike inductances (the long metal strips transverse to the propagation direction) are placed in a shunt configuration. They also serve for biasing the capacitors by means of narrow bias lines on each side of the CPW. Decoupling capacitances (metallized large area ceramic cubes) are soldered on the ground planes and wire bonding, which interconnect the side ground planes. The series capacitors appear as narrow slits in the central conductor. The voltage-controlled additional capacitance, which contributes to C_{RH} in order to preserve the balance condition under bias is also apparent at the junction of stubs.

Figure 1(b) shows the dispersion characteristic, which can be calculated with the following elements: C_{LH} =120 fF, L_{RH}=0.53 nH, C_{RH}=128 fF, and L_{LH}=0.5 nH. They were fine tuned by comparing full wave and circuit analysis. The group and phase velocities exhibit opposite signs from 10 to 18 GHz and thus the propagation medium is left handed in this frequency range. There is no gap in the vicinity of k=0 and hence the group velocity is nonvanishing. Above 18 GHz, the loaded transmission line exhibits a right-handed transmission branch.

Figure 2 shows the frequency dependence of the magnitudes S_{11} and S_{12} for two devices, which consist of two and four cells, respectively, measured by means of an Agilent Vectorial Network Analyzer (10 MHz–40 GHz). As expected, the lines show a high-pass filtering characteristic with a frequency cutoff of around 10 GHz. Also, an almost flat transmission window ranging from 10 GHz up to at least 35 GHz is noticed. The insertion losses are around 1.5 dB/cell for a return loss better than 10 dB. It can be shown that the losses are dominated by the dielectric loss of the BST film.

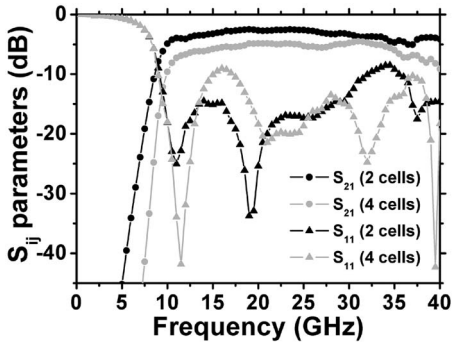

FIG. 2. Scattering parameter measurements vs frequency at zero bias with a two-cell and a four-cell prototype, respectively. The widths of the slot and central strip of the CPW are 80 and 40 μm, respectively. The unit cell length is 850 μm.

A direct experimental measurement of the dispersion characteristic can be achieved by the retrieval technique we recently developed on the basis of a Fresnel inversion technique.[14] The results are plotted in Fig. 3. The overall agreement between the calculated dispersion characteristic and the measured wave vector/angular frequency relation is good with no gap between the left-handed branch and the right-handed branch. The corner frequency between the left- and right-handed dispersion branches is 18 GHz.

By applying a voltage across the capacitance terminals, the dielectric constant of BST film decreases. As a consequence, the resonance frequencies of series and shunt resonant circuits shift to higher frequencies, notably in the range $ka = \pm 0.8$ rd. This frequency blueshift is illustrated in the k vector range of interest (long wavelength operation mode), in Fig. 3, for V_{bias}=10 V and 30 V, respectively. In order to have a deeper insight in the tuning of the dispersion characteristic, we plotted in Fig. 4 the real and imaginary parts of the effective permittivity ε_{eff} and permeability μ_{eff}, respectively. The frequency dependence of ε_{eff} and μ_{eff} was determined from the frequency dependence of the effective index $n=(\varepsilon_{eff} \cdot \mu_{eff})^{1/2}$ and of the impedance $Z=(\mu_{eff}/\varepsilon_{eff})^{1/2}$. Both effective parameters exhibit quasi-Drude dispersion characteristics in contrast to SRR-based transmission line showing Lorentz-type dispersion.[13] This nonresonant characteristic is

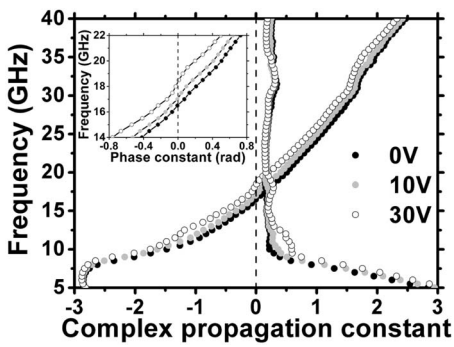

FIG. 3. Bias dependence of the dispersion characteristics measured between 5 and 40 GHz. The inset is a zoomed view in the long wavelength regime defined in the vicinity of k=0.

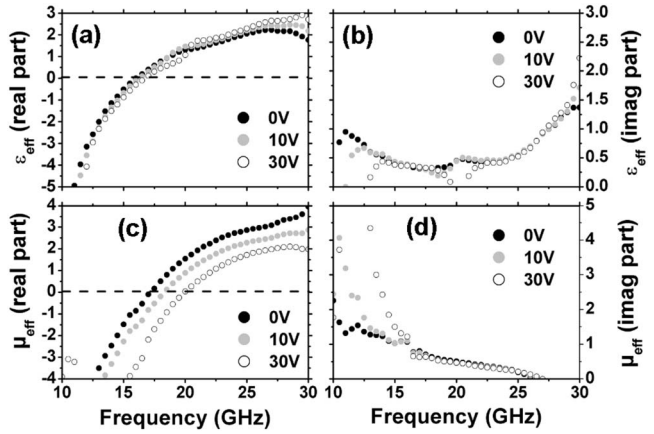

FIG. 4. Dispersion of the effective complex permittivity and permeability at various bias voltages. Frequency dependence of the real (a) and imaginary part (b) of the effective permittivity. Frequency dependence of the real (c) and imaginary part (d) of the effective permeability.

primarily responsible of the broad left-handed dispersion branch. Also, it can be noticed that the equality between the electric and magnetic plasma frequencies is only valid for unbiased conditions for which the slight difference between these relevant frequencies results from the imaginary part of the effective index. Under bias, the discrepancy between the two characteristic frequencies increases in agreement with the aforementioned arguments in connection with the difficulty to the voltage controlling of the distributed capacitance. The change in the values of the lumped capacitance, via the BST permittivity tuning, more significantly affects the dispersion of the effective permeability. In contrast, ε_{eff} is less affected by the voltage control of the BST film permittivity. It is worth mentioning that the stublike elements are responsible for the electrical activity. Indeed, the role of these elements can be compared to that of the shunt wires in the SRR/wire configuration.[15] On the contrary, the magnetic activity stems from the series capacitance. Their tuning by decreasing the capacitance level, via the decrease in the permittivity of BST films, explains the shift toward higher frequencies of the transition between negative and positive values of μ_{eff}.

The composite left- and right-handed transmission lines, loaded by lumped ferroelectric varactors, designed and assessed at centimeter and millimeter frequency bands, show that a near balance condition (gapless dispersion characteristic) can be achieved and tuned continuously. The use however of the zero-index operating mode at $k=0$ appears, however, very sensitive to the voltage control with a balance, which appears more and more difficult to fulfill at increasing tuning voltage, pointing out in the present work by the opening of a slight gap. From the application side, this work gives a deeper insight into the electromagnetic phenomena, which takes place in devices whose operation relies on an infinite wavelength, achieved at the center of the dispersion diagram at $k=0$ with $\omega \neq 0$.

This study was performed in the framework a Centre National d'Etudes Spatiales (CNES) contract. The authors would like to thank K. Blary at IEMN for her help in the device fabrication.

[1]C. Caloz and T. Itoh, *Electromagnetic Metamaterials* (Wiley, New Jersey, 2006).
[2]G. V. Eleftheriades and K. G. Balmain, *Negative Refraction Metamaterials* (Wiley, New Jersey, 2006).
[3]F. Zhang, G. Houzet, E. Lheurette, D. Lippens, M. Chaubet, and X. Zhao, J. Appl. Phys. **103**, 084312 (2008).
[4]I. Gil, J. Bonache, J. García-García, and F. Martin, IEEE Trans. Microwave Theory Tech. **54**, 2665 (2006).
[5]A. Vélez, J. Bonache, and F. Martín, IEEE Microw. Wirel. Compon. Lett. **18**, 28 (2008).
[6]T. Hand and S. Cummer, IEEE Trans. Antennas Propag. **6**, 401 (2007).
[7]T. H. Hand and S. A. Cummer, J. Appl. Phys. **103**, 066105 (2008).
[8]D. Kuylenstierna, A. Vorobiev, P. Linner, and S. Gevorgian, IEEE Microw. Wirel. Compon. Lett. **16**, 167 (2006).
[9]L. Brillouin, *Wave Propagation in Periodic Structures* (Dover, New York, 1946).
[10]A. Lai, T. Itoh, and C. Caloz, IEEE Microw. Mag. **5**, 34 (2004).
[11]G. Houzet, L. Burgnies, G. Velu, J. C. Carru, and D. Lippens, Appl. Phys. Lett. **93**, 053507 (2008).
[12]S. Gevorgian, T. Martinsson, P. L. J. Linner, and E. L. Kollberg, IEEE Trans. Microwave Theory Tech. **44**, 896 (1996).
[13]G. Vélu, J. C. Carru, E. Cattan, D. Remiens, X. Melique, and D. Lippens, Ferroelectrics **288**, 59 (2003).
[14]C. Croenne, N. Fabre, D. P. Gaillot, O. Vanbesien, and D. Lippens, Phys. Rev. B **77**, 125333 (2008).
[15]A. L. Borja, J. Carbonell, V. E. Boria, and D. Lippens, Appl. Phys. Lett. **93**, 203505 (2008).

Low-loss left-handed metamaterials at millimeter waves

Fuli Zhang,[1,2] Davy P. Gaillot,[1] Charles Croënne,[1] Eric Lheurette,[1] Xavier Mélique,[1] and Didier Lippens[1,a)]

[1]*Institut d'Électronique de Microélectronique et Nanotechnologies, Université des Sciences et Technologies de Lille, Avenue Poincaré BP 60069, 59652 Villeneuve d'Ascq Cedex, France*

[2]*Department of Applied Physics, Northwestern Polytechnical University, Xi'an 710072, People's Republic of China*

(Received 2 July 2008; accepted 3 August 2008; published online 26 August 2008)

An omega-type multilayered metamaterial aimed at operating at millimeter wavelengths was characterized between 75 and 110 GHz (*W*-band). The fabrication involves a monolithic integration of planar arrays of broad-side coupled microresonators with a benzocyclobutene spacing layer printed onto quartz substrates. The frequency dependence of the transmittance shows a well-resolved transmission window centered around 80 GHz with a 10% fractional bandwidth and another one starting from 100 GHz, both displaying comparable high transmission levels. The left- or right-handed behavior is assessed by the comparison of the phase delay between two devices of different lengths and by tilted-incidence transmission experiments. © *2008 American Institute of Physics*. [DOI: 10.1063/1.2975187]

Split ring resonator (SRR) arrays, as proposed in the seminal work of Pendry *et al.*,[1] have been used for designing and fabricating single negative magnetic media along with double negative media[2,3] when they are associated with wire arrays.[4] At centimeter wavelengths, demonstrations were reported in the literature not only with proof-of-principle experiments but also with practical applications such as negative refractive index lens[5] and artificial magnetic conductors.[6] The extension of such studies to higher frequencies, notably at millimeter wave and submillimeter wavelengths (terahertz frequencies), was addressed by several groups.[7–11] For all these studies, the main difficulty stems from the requirement of **H**-field polarization normal to the SRR planar pattern, a necessary condition for inducing a significant artificial magnetic polarization. As a consequence, many of these studies take benefit of the *electric* polarization of the resonant particles in a single layer arrangement and a front illumination. However, the problem of extending the concept of artificial magnetism with an edge illumination (grazing incidence) at ultrahigh frequencies was addressed in Ref. 12. The difficulty to blueshift the electric plasma frequency was solved by a proper design of the wire array. Indeed, the plasma frequency $\omega_p \sim (n_{\mathrm{eff}}/m_{\mathrm{eff}})^{1/2}$ (effective electron density n_{eff} and electron mass m_{eff}) (Ref. 4) was engineered by keeping thin wire arrays in order to benefit from the increase in the effective mass while the effective electron density was adjusted via the metal filling factor.

Promising results were reported on this basis with the comparison between closed and split ring patterns. Thus, an experimental evidence of the left-handed behavior of the transmission window was pointed out around 100 GHz. However, a direct application of this proof-of-principle experiment appears problematic at this stage because the loss per cell is as high as −2.5 dB. Under this condition, it seems difficult to envisage real applications with a sizable thickness of metamaterials such as those required for the fabrication of prism or lens devices.

In this paper, we considered the problem of the fabrication of low-loss left-handed metamaterials aimed at operating at millimeter wavelengths. With respect to previous works in this field, notably those aforementioned, the originality stems from an omega-type approach with a broad-side coupling scheme.[13–16] This permits one to decrease the loaded quality factor of the microresonator array and, hence, to broaden their operating band while maintaining low intrinsic losses per basic unit cell. The experimental verification of the left-handedness will be carried out by two different approaches: (i) the normal incidence measurement and the retrieval of the effective parameters from the theoretical side and (ii) the measurements of the phase offset between two prototypes of different lengths and the transmittance measurements by varying the incidence angle.

Figure 1(a) shows the basic unit cell, which consists of

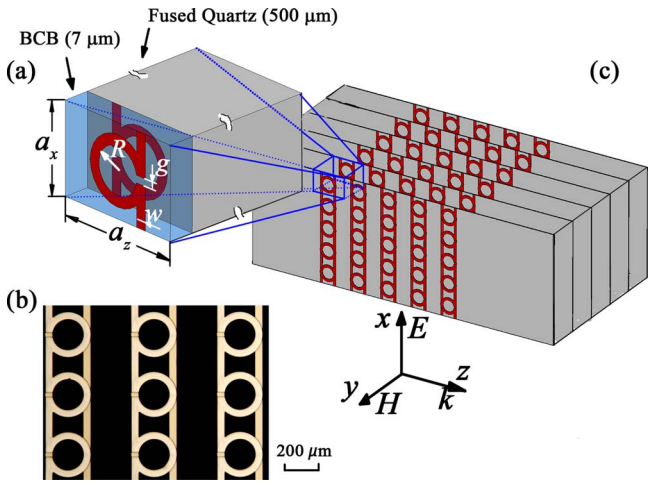

FIG. 1. (Color online) (a) Schematic diagram of the basic unit cell. The dimensions of the basic unit cell are as follows: R=90, g=27.5, and w=42.0 μm. The periodicities along the x and z directions are 350 and 500 μm, respectively. (b) Photomicrograph of the omega patterns. (c) Schematic of the bulk metamaterial.

a)Author to whom correspondence should be addressed. Electronic mail: didier.lippens@iemn.univ-lille1.fr.

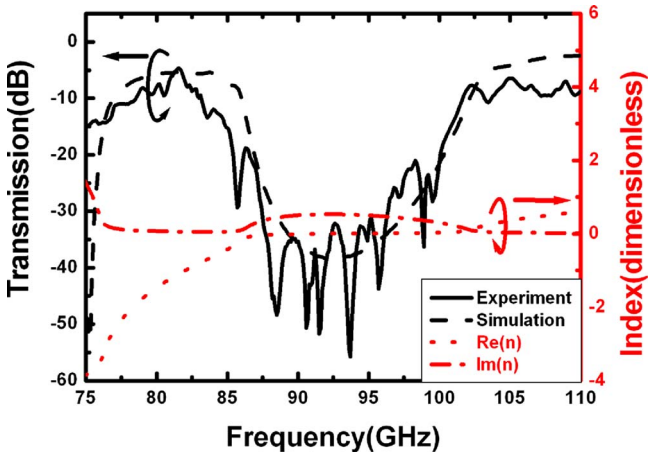

FIG. 2. (Color online) Left axis: experimental (solid black) and simulation (dashed black) transmission spectra of the metamaterial with ten cells stacked along the propagation direction. Right axis: the real (dotted red) and imaginary (dash dotted red) parts of the effective index are also presented.

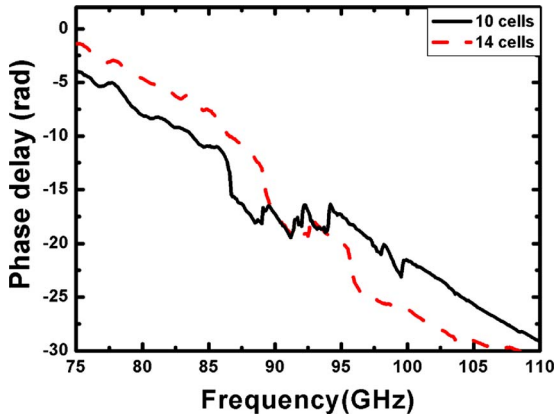

FIG. 3. (Color online) The phase delay for the metamaterials with ten (solid black) and 14 cells (dashed red) stacked along the propagation direction, respectively.

two reversed omega patterns on fused quartz substrates, and illustrates the fabrication process. Here, a thin dielectric film is sandwiched between omega patterns with standard photolithography techniques. This is different from the previous fabrication approaches such as the standard printed circuit board technology employed in the microwave frequencies. Indeed, by increasing the operation frequency, the relevant dimensions have to be shrunk, and it is no longer possible to sustain the desired effects with the omegas printed on both faces of a thick substrate. On the other hand, the microstructured layer (metal+dielectric+substrate) ensures a structural rigidity, which also enables the monolithic assembling of a sizeable volumetric prototype with multiple layers.

On each of the wafers, six individual layers ($20.0 \times 15.0 \times 0.5$ mm^3) were fabricated with 42 omega cells along the x direction. Three of them have ten cells along the z direction and the other three have 14 cells with a view to measure the phase offset.

The first omega layer was patterned with a metal thickness of 500 Å Ti/4000 Å Au onto a 2-in. 500-μm-thick double-sided polished fused quartz wafer. The second stage was the spin coating of a 7-μm-thick benzocyclobutene (BCB) layer. BCB was used owing to its moderate dielectric constant and low-loss tangent in the millimeter wave and terahertz range along with its planarizing properties. Then, the second omega pattern with a reverse orientation was deposited onto the surface of the BCB layer. Figure 1(b) presents a close-up view of the fabricated layered pattern. Finally, the quartz wafer was carefully diced into individual pieces with well-defined dimensions. As illustrated in Fig. 1(c), a "bulk" metamaterial was assembled with 30 layers and stacked via the edge alignment, leaving no air gap between the layers. Thus, the metamaterial bulk has a width (y) of about 15.0 mm and a height (x) of 20.0 mm.

The ten-cell-long metamaterial sample was placed inside the aperture of an absorbing layer similar to the method used in Ref. 17. In the first stage, the sample was illuminated under normal incidence with polarization for the electric field along the x direction and magnetic field along the y direction. The measurements of the S parameters as a function of frequency were performed by using an Agilent 8510C vector network analyzer. Figure 2 shows the transmission spectra of the ten-cell-long device. As seen in Fig. 2, the metamaterial structure exhibits two clear passbands with high transmission levels; one is from around 76.5 to 85 GHz (fractional bandwidth ~10%) and the other one occurs above 100 GHz, with a band gap in between. In order to distinguish the properties of these two passbands, simulations were performed by employing the commercial software CST MICROWAVE STUDIO, which uses the finite integration technique. The millimeter wave dielectric properties for BCB ($\varepsilon_{(\mathrm{BCB})} = 2.6 + 0.002i$) (Ref. 18) and fused quartz ($\varepsilon_{(\text{fused quartz})} = 3.794 + 0.003i$) (Ref. 19) can be readily found in the literature. In addition to the transmission response of multicells repeated along the propagation direction, the S parameters of the basic unit cell were used to obtain the effective parameters, notably the effective refractive index by retrieval methods.[20,21] From Fig. 2, it can be seen that the simulation transmission spectrum shows a good agreement with the experimental result. Furthermore, the real part of the retrieved effective index exhibits negative values for the first passband below 87.0 GHz, indicating a left-handed dispersion characteristic. For this passband, it is noticed that there is a transmission peak as high as −4.6 dB at 81.6 GHz for a ten-cell prototype, which is the lowest loss level for SRR-based metamaterials in this frequency range. This can be attributed to the use of interconnected omega structures, which exhibit better performances than SRR/wire prototypes reported in previous works at microwaves.[13–15]

In order to further confirm the left-handed properties of the first passband, we measured the frequency dependence of the phase delay for the 10- and 14-cell prototypes, as presented in Fig. 3. The phase offset $\Delta\Phi = \Phi_{14} - \Phi_{10}$ is positive below 89 GHz corresponding to a negative refractive index, whereas it becomes negative above 95 GHz, indicating a positive index material.

Figure 4 shows the oblique transmission response of the ten-cell-long metamaterial structure. As shown in the inset of Fig. 4, the incidence direction is rotated around the x axis by an angle of θ with respect to the initial incident route along the z direction. This results in a changing magnetic field polarization while the electric field polarization remains. In Fig. 4, when the oblique incidence angle is increased from 0° to 25°, the transmission peak of the first passband decreases to −20.2 dB, with a narrower bandwidth. By contrast, the second transmission window is much less sensitive to the

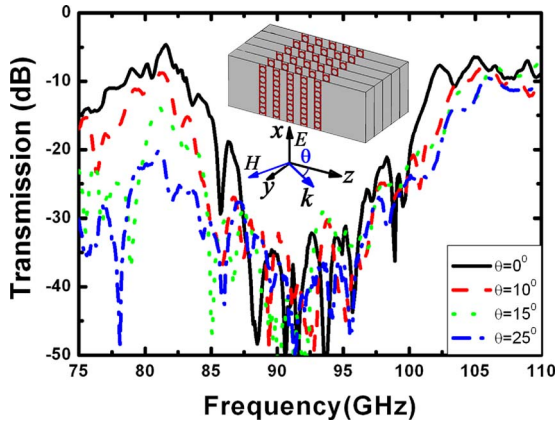

FIG. 4. (Color online) Oblique transmission spectra of the ten-cell prototype for incident angle values ranging from 10° to 25°. Inset: the incident polarization orientation.

angle of incidence. As the incidence angle is increased, the magnetic field component perpendicular to the omega pattern plane decreases and the artificial magnetic resonance strength is weakened.[8,11] As a consequence, the transmission level, which corresponds to a left-handed dispersion branch, decreases accordingly. On the other hand, the electric plasma frequency is hardly affected by the oblique incidence since the electric field remains polarized along the same direction. This sensitivity to an oblique incidence permits us to conclude about the left-handed behavior of the first transmission window.

In summary, a low-loss metamaterial was fabricated via BCB technology at millimeter waves. The left-handedness of the transmission window was confirmed by phase delay measurements under normal incidence and by the sensitivity of transmission levels to the oblique incidence. In order to have a figure of merit independent of the number of cells, we assumed that the intrinsic losses are the dominant contribution close to the resonances. Under this assumption, the insertion loss is below −0.5 dB per cell and thus becomes comparable to that reported for a nonresonant transmission line approach at millimeter wavelengths.[22]

This work was carried out in the framework of the Centre National d'Etudes Spatiales and the Délegation Générale pour l'Armement contracts. F.Z. would like to acknowledge the China Scholarship Council and Northwestern Polytechnical University for his fellowship. The authors would like to thank E. Delos for her help with scattering parameters measurements and D. Vandermoere for sample dicing.

[1] J. B. Pendry, A. J. Holden, D. J. Robbins, and W. J. Stewart, IEEE Trans. Microwave Theory Tech. **47**, 2075 (1999).
[2] V. G. Veselago, Sov. Phys. Usp. **10**, 509 (1968).
[3] R. A. Shelby, D. R. Smith, and S. Schultz, Science **292**, 77 (2001).
[4] J. B. Pendry, A. J. Holden, W. J. Stewart, and I. Youngs, Phys. Rev. Lett. **76**, 4773 (1996).
[5] C. G. Parazzoli, R. B. Greegor, J. A. Nielsen, M. A. Thompson, K. Li, A. M. Vetter, M. H. Tanielian, and D. C. Vier, Appl. Phys. Lett. **84**, 3232 (2004).
[6] A. Erentok, P. L. Luljak, and R. W. Ziolkowski, IEEE Trans. Antennas Propag. **53**, 160 (2005).
[7] H.-T. Chen, J. F. O'harai, A. K. Azadi, A. J. Taylor, R. D. Averitt, D. B. Shrekenhamer, and W. J. Padilla, Nat. Photonics **2**, 295 (2008).
[8] W. J. Padilla, A. J. Taylor, C. Highstrete, M. Lee, and R. D. Averitt, Phys. Rev. Lett. **96**, 107401 (2006).
[9] T. Driscoll, G. O. Andreev, D. N. Basov, S. Palit, T. Ren, J. Mock, S.-Y. Cho, N. M. Jokerst, and D. R. Smith, Appl. Phys. Lett. **90**, 092508 (2007).
[10] S. Linden, C. Enkrich, M. Wegener, J. Zhou, T. Koschny, and C. M. Soukoulis, Science **306**, 1351 (2004).
[11] T. F. Gundogdu, I. Tsiapa, A. Kostopoulos, G. Konstantinidis, N. Katsarakis, R. S. Penciu, M. Kafesaki, E. N. Economou, Th. Koschny, and C. M. Soukoulis, Appl. Phys. Lett. **89**, 084103 (2006).
[12] M. Gokkavas, K. Guven, I. Bulu, K. Aydin, R. S. Penciu, M. Kafesaki, C. M. Soukoulis, and E. Ozbay, Phys. Rev. B **73**, 193103 (2006).
[13] J. Huangfu, L. Ran, H. Chen, X. Zhang, K. Chen, T. M. Grzegorczyk, and J. A. Kong, Appl. Phys. Lett. **84**, 1537 (2004).
[14] F. Zhang, G. Houzet, E. Lheurette, D. Lippens, M. Chaubet, and X. Zhao, J. Appl. Phys. **103**, 084312 (2008).
[15] L. Ran, J. Huangfu, H. Chen, Y. Li, X. Zhang, K. Chen, and J. A. Kong, Phys. Rev. B **70**, 073102 (2004).
[16] E. Lheurette, O. Vanbésien, and D. Lippens, Microwave Opt. Technol. Lett. **49**, 84 (2007).
[17] D. Vier, D. R. Fredkin, A. Simic, S. Schultz, and M. Tanielian, Appl. Phys. Lett. **86**, 241908 (2005).
[18] Dow Chemicals Product datasheet: http://www.dow.com/cyclotene/solution/highfreq.htm
[19] M. N. Afsar and H. Ding, IEEE Trans. Instrum. Meas. **50**, 402 (2001).
[20] C. Croënne, B. Fabre, D. Gaillot, O. Vanbésien, and D. Lippens, Phys. Rev. B **77**, 125333 (2008).
[21] D. R. Smith, S. Schultz, P. Markoš, and C. M. Soukoulis, Phys. Rev. B **65**, 195104 (2002).
[22] T. Crépin, J. F. Lampin, T. Decoopman, X. Mélique, L. Desplanque, and D. Lippens, Appl. Phys. Lett. **87**, 104105 (2005).

Negative-Zero-Positive Refractive Index in a Prism-Like Omega-Type Metamaterial

Fuli Zhang, Sylvain Potet, Jorge Carbonell, *Member, IEEE*, Eric Lheurette, Olivier Vanbésien, Xiaopeng Zhao, and Didier Lippens

***Abstract*—Negative-zero-positive index refraction was demonstrated numerically on the basis of full-wave analysis of a microstructured omega-type array and experimentally via angle resolved transmission measurement of a prism-type prototype. The experimental results are interpreted in terms of characteristic impedance and refractive index retrieved by a Fresnel inversion technique. The possibility to balance the dispersion characteristics with a negative-zero-positive index is demonstrated over X- and Ku-bands.**

***Index Terms*—Composite right/left-handed metamaterial, negative index materials, negative refraction, retrieval technique.**

I. Introduction

NEGATIVE refraction in backward wave media was demonstrated at microwaves frequencies by using split ring resonator (SRR)/wire and omega-type arrays either by taking advantage of negative refraction in a metamaterial isotropic slab or in a prism-type microstructure [1]–[14]. Positive refraction was often used as a reference experiment by using a conventional homogenous material such as Plexiglas, and the zero refraction was assessed by studying the collimating beam of a point source embedded in a zero index medium [15]–[17].

In this paper, we investigate the possibility to combine all the refractive situations, namely, negative, zero, and positive index refraction by using the same sample, which does not exhibit any forbidden gap between the left-handed dispersion branch and the right-handed one. The absence of a forbidden gap in the propagation of waves in a metamaterial-based structure was already shown in the so-called balanced composite transmission lines [18]–[20]. However, to the best of our knowledge, this is the first time that such a property is demonstrated for a metamaterial based on an SRR and wire technology.

The basic idea was first to replace the dual SRR and wire array by an inclusion that simultaneously exhibits an electric and magnetic dipole. This idea was developed in [8]. For this purpose, we chose an omega-type pattern whose magnetic and electric responses were already demonstrated in [8]–[14] and were experimentally characterized in a hollow waveguide in [21]. It can also be shown that an interconnected omega array intrinsically possesses a relatively broad left-handed transmission branch due notably to the Drude-like response of the effective permittivity resulting from the transverse interconnections [14]. The necessary condition for a balanced composite dispersion characteristic is the equality of the electric and magnetic plasma frequencies. Let us recall that these characteristic frequencies govern the dispersion properties of the effective permittivity and permeability as the transition frequency between the negative and positive values of the effective parameters in the upper part of the spectrum. This equality avoids facing the situation of a single negative medium between the double negative condition (left-handed branch) and the double positive one (right-handed branch). Any single negative medium corresponds to a forbidden gap, which we try here to avoid between the backward and forward wave transmission windows. With respect to the transmission line approach, the balance of the plasma frequencies would correspond to the equality between the resonance frequencies of the series and the shunt equivalent resonant circuits. The second goal of the paper will be to demonstrate, by full wave modeling and by angle resolved vectorial analysis, that the design of a balanced composite current loop/wire array was successful. This fact will be confirmed by several methods including the derivation of the refractive index via a refractive experiment (numerical and real world) and by a Fresnel inversion retrieval technique.

In this paper, Section II deals with the design rules, while we will consider the numerical and modeling experiments in Sections III and IV, respectively. Concluding remarks and prospects are considered in Section V.

II. Design Rules

Fig. 1(a) shows a schematic of the basic cell, while Fig. 1(b) illustrates the interconnection arrangement along the x-axis,

Manuscript received March 10, 2008; revised June 12, 2008. First published October 24, 2008; current version published November 07, 2008. This work was supported by the Centre National d'Etudes Spatiales (CNES). This work was supported in part under Bilateral Project EGIDE/PICASSO-MEC (Spain). The work of F. Zhang was supported by the China Scholarship Council under a fellowship.

F. Zhang is with the Institut d'Électronique de Microélectronique et Nanotechnologies (IEMN), Unite Mixte de Recherche (UMR), Centre National de la Recherche Scientifique (CNRS) 8520, Université des Sciences et Technologies de Lille 1, 59652 Villeneuve d'Ascq, France, and also with the Department of Applied Physics, Northwestern Polytechnical University, 710072 Xi'an, China.

S. Potet was with the Institut d'Électronique de Microélectronique et Nanotechnologies (IEMN), Unite Mixte de Recherche (UMR), Centre National de la Recherche Scientifique (CNRS) 8520, Université des Sciences et Technologies de Lille 1, 59652 Villeneuve d'Ascq, France. He is now with Temex, 10150 Pont Sainte Marie, France.

J. Carbonell is with the Instituto de Telecomunicaciones y Aplicaciones Multimedia, Universidad Politécnica de Valencia, E-46022 Valencia, Spain.

E. Lheurette, O. Vanbésien, and D. Lippens are with the Institute of Electronics Microelectronics and Nanotechnologies, Unite Mixte de Recherche (UMR), Centre National de la Recherche Scientifique (CNRS) 8520, Université des Sciences et Technologies de Lille 1, 59652 Villeneuve d'Ascq, France (e-mail: didier.lippens@iemn.univ-lille1.fr).

X. Zhao is with the Department of Applied Physics, Northwestern Polytechnical University, Xi'an 710072, China.

Color versions of one or more of the figures in this paper are available at http://ieeexplore.ieee.org.

Digital Object Identifier 10.1109/TMTT.2008.2005891

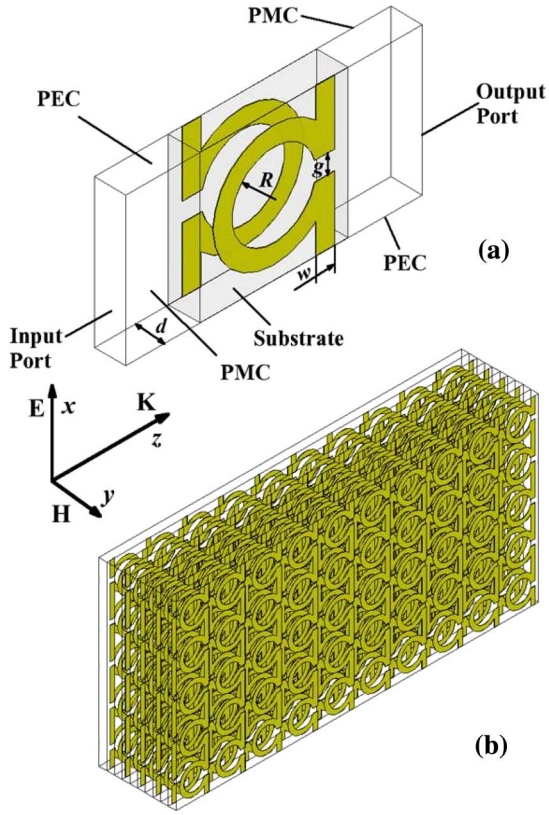

Fig. 1. (a) Schematic of omega unit cell. (b) Schematic of omega pattern array with an edge illumination by a plane wave. The dimension parameters are as follows: $r = 1.1$ mm, $w = g = 0.5$ mm, $d = 0.8$ mm. Both the periodicities along the x- and z-directions are 3.9 mm. The substrate is chosen as epoxy glass with an assumption of relative permittivity of 4.0 ($\tan\delta = 0.02$).

transverse to the propagation direction along z. The basic unit cell consists of two back-to-back omega metal inclusions. The core of the pattern is responsible for a magnetic dipole through current loops via an H-field excitation along the y-axis. It is imperative to satisfy this H-field polarization condition in order to achieve a pure magnetic response, namely, $B = -\mu\mathrm{H}$ [22]. The two arms of the omega pattern are responsible for the electric response when the electric field is polarized along the x-axis. One can compare the omega patterns with the combination of SRRs (the central current loops) and wires (the arms of omega patterns). The back-to-back configuration suppresses the magneto-electric response according to the basic ideas developed in broadside-coupled SRRs [23].

The fact of combining in one motif the magnetic and electric responses means that there exists an interdependence of phenomena. However, as for distinct SRR and wire array, a first optimization of the electromagnetic properties can be carried out by considering separately the dispersion of the magnetic and of the electric dipoles.

The frequency dependence of the effective permeability is governed by the two characteristic frequencies of a Lorentz-like response, namely, the resonant frequency of the current loop (ω_0) and the magnetic plasma frequency (ω_{mp}). The latter corresponds to the transition frequency between negative and positive values of μ_{eff} in the upper part of the spectrum [3]. Many experimental and theoretical studies have addressed the derivation of the resonant frequencies of C- or U-shaped microresonators either on the basis of full-wave analysis or by a lumped-element approach. The latter is particularly useful in an optimization procedure, notably through adjustments of the permittivity and thickness of the substrate and of the width of the metal strips that tune the coupling capacitance between the opposite omega motifs.

For the current loops, the magnetic angular resonance frequency ω_0 can be predicted by an LC resonance in which $L = \mu_0(\pi r^2/d)$ is the inductance of the current loops and $C = (1/2)(\varepsilon_0\varepsilon_r w/d)(\pi((2r + w)/2) - (g/2))$ is the total capacitance between the broadside-coupled SRRs [13] (here, ε_0 and ε_r are the permittivity of vacuum and substrate, respectively. μ_0 is the permeability of vacuum, w is the wire width, r is the inner radius, g is the gap of omega pattern, and d is the thickness of the substrate). The so-called magnetic plasma frequency ω_{mp}, is directly related to the magnetic resonant frequency ω_o and the filling factor $F = \pi r^2/S$, the area ratio occupied by the interior ring with respect to the area of basic unit cell in the x–z-plane [see Fig. 1(a)], according to the following approximation [3]:

$$\begin{aligned}\omega_{\mathrm{mp}} &= \frac{\omega_0}{\sqrt{1-F}} \\ &= \frac{1}{\sqrt{(1-F)(LC)}} \\ &= \frac{1}{\sqrt{(1-F)}\sqrt{\left(\mu_0\dfrac{\pi r^2}{d}\right)\cdot\dfrac{1}{2}\dfrac{\varepsilon_0\varepsilon_r w}{d}\left(\pi\dfrac{2r+w}{2}-\dfrac{g}{2}\right)}}.\end{aligned} \tag{1}$$

For the electrical response, which can be compared to that of an array of infinite metal wire, the effective permittivity follows a Drude-like model. Under this assumption, the frequency dependence of the permittivity exhibits negative values below the plasma frequency ω_p, which can be considered as a characteristic frequency. An estimate of ω_p can be found in the seminal work of Pendry *et al.* [2]

$$\omega_p^2 = \frac{2\pi c_0^2}{a^2\ln(a/r)} \tag{2}$$

where a and r are the periodicity of the wire array and radius of the wire, respectively. The cross section of the wire, considered here, is rectangular instead of circular, as in Pendry's model. However, the plasma frequency has an analogous dependence as a function of the wire width (w), i.e., increasing with w [24].

As outlined in the introduction, a balanced condition can be achieved when $\omega_{\mathrm{mp}} = \omega_p$. To this aim, the degrees of freedom for a given permittivity of a substrate are the width of the metallization and the substrate thickness.

As aforementioned, the dielectric and magnetic responses are not strictly independent and a resonant feature is superimposed onto the frequency dependence of the electric response. This spurious response is, however, weak and the simple rule that insists on saying that the effective permittivity is negative below the plasma frequency and positive above still holds.

In practice, the fine tuning of the balanced condition between ω_{mp} and ω_p was performed by full-wave analysis (via the commercial package High Frequency Structure Simulator (HFSS)

simulation code) of the electromagnetic behavior of the basic cell by applying the Bloch–Floquet theorem. The boundary conditions are displayed in Fig. 1(a). Perfect electrical conductors are placed along the x-direction, while perfect magnetic conductors are imposed along the y-direction. A plane wave with the electric field polarized along x was assumed to illuminate along the z-direction. Two ports according to Fig. 1(a) allow the calculation of the scattering parameters.

In the following, we derive the effective index n and the characteristic impedance z. This derivation was carried out according to the procedure we already used in [25] and [26] for SRRs integrated in a hollow waveguide. In short, the scattering matrix is transformed into a chain or $ABCD$ matrix. On the other hand, the chain matrix of a homogeneous propagation medium is

$$M = \begin{bmatrix} A & B \\ C & D \end{bmatrix} = \begin{bmatrix} ch(\gamma a) & z \cdot sh(\gamma a) \\ \frac{1}{z} \cdot sh(\gamma a) & ch(\gamma a) \end{bmatrix} \tag{3}$$

where $\gamma = \alpha + j\beta$ is the propagation constant, and α and β denote the evanescence of the wave and the phase constant, respectively. a is the unit cell size in the propagation direction. By comparison, we obtain

$$n = \frac{c\gamma}{i\omega} \tag{4}$$

for

$$\beta a = \angle\left(A \pm \sqrt{A^2 - 1}\right) + 2k\pi, \qquad k \in Z \tag{5}$$

$$z = \pm\sqrt{\frac{B}{C}}. \tag{6}$$

It is worth mentioning that the experimental demonstration reported in the following will be carried out by using a parallel-plate waveguide and not a hollow waveguide. By means of the former, it is possible to mimic the free-space conditions, which are assumed here in the retrieval of the effective parameters.

Another important issue is the fact that the effective index of refraction and the characteristic impedance should not depend on the periodicity of the material. This is the case in the so-called long wavelength regime, namely, when the wavelength is much larger than the periodicity. This assumption is correct in the vicinity of the center of the Brillouin zone ($k = 0$, thus corresponding to an infinite wavelength). The balance composite behavior that we address here corresponds to this condition. In this case, the parameter extraction does not depend on the periodicity of the material and it makes sense to define an effective index of refraction and characteristic impedance. In addition, it was verified that the Fresnel inversion method used here does not depend on the number of cells [27].

After careful consideration of the determination of the impedance z square root and the propagation constant β determining the sign of n, which have been discussed in detail in [28], we obtained the same results of n and z as when using the methods proposed in [29] and [30].

Fig. 2 shows the frequency dependence of refractive index n. As shown in Fig. 2, the real part of the refractive index retrieved from simulation (solid line) exhibits a smooth transition between the negative band (8.0–12.8 GHz) and positive band

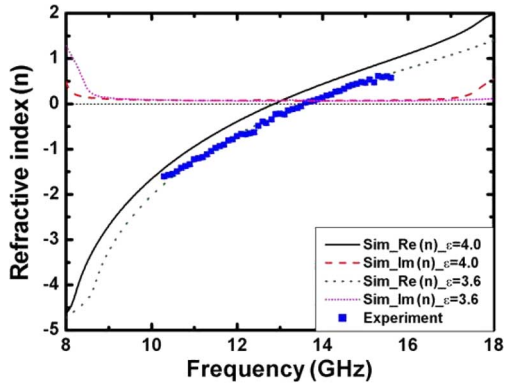

Fig. 2. Simulated and measured refractive indices n as a function of frequency. The solid and dotted lines represent the real parts, while the dashed and short dotted lines show the imaginary parts of n when the substrate is assumed to have relative permittivity of 4.0 and 3.6, respectively. The rectangular symbol denotes the experimental refractive index, which was plotted from 10.2 to 15.0 GHz with a step of 0.1 GHz.

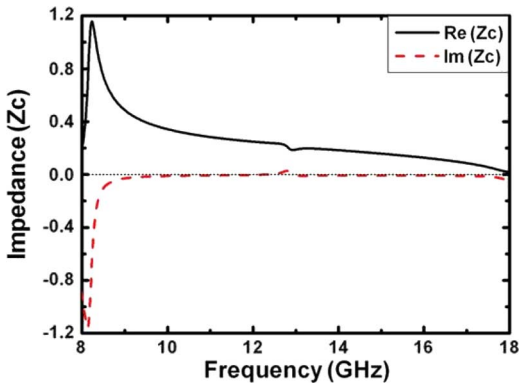

Fig. 3. Frequency dependence of the characteristic impedance. The real part and imaginary parts are represented by a solid and dashed line, respectively.

(12.8 GHz–16.0 GHz) with a transition frequency at 12.8 GHz where the refractive index value is zero.

Let us now consider the frequency variations of the complex characteristics impedance z plotted in Fig. 3 between 8.0–18.0 GHz for one basic cell. It can be noticed that the real part of z peaks at a frequency close to 8.0 GHz. Below this frequency, the metamaterial under consideration exhibits a forbidden gap in which the meaning of the effective parameters is questionable and would not be considered here. The impedance is rapidly varying across the left- and right-handed bands as a consequence of the high dispersion of the electromagnetic system. Let us recall, however, that the calculations are carried out here with a single cell device along the propagation direction. It is noted that the characteristic impedance decreases steeply towards zero as the frequency increases to 18.0 GHz, resulting in a high mismatch and return loss.

III. Modeling of Prism

While the refracted index and characteristic impedance were plotted under a Bloch wave condition (unit cell of an infinite medium), the demonstration of the negative-zero-positive index requires designing a prototype where n can be assessed by the

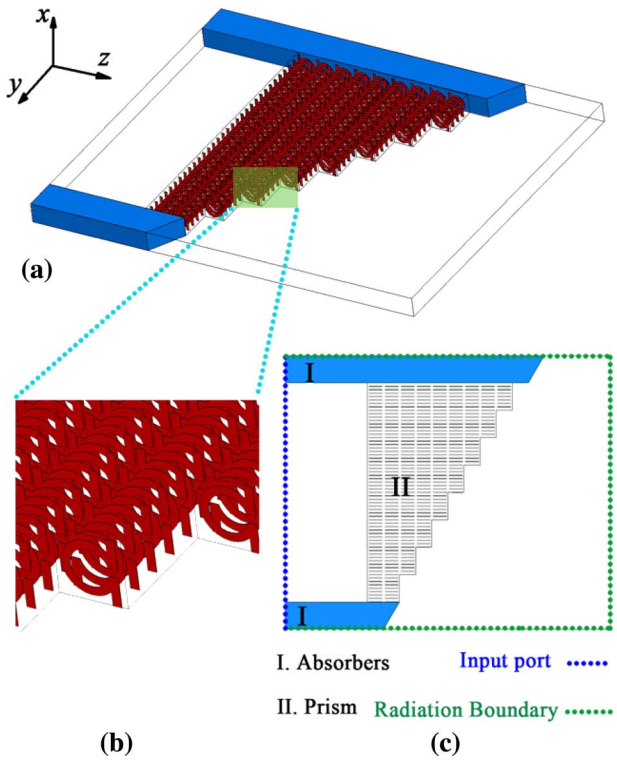

Fig. 4. Illustration of the prism configuration for refraction simulation. (a) 3-D view of the prism model, which consists of eight stairs. (b) Close up view of one step, which consists of four cells along the y-direction and one cell along the x-direction. (c) Top view of the prism model indicating the boundaries.

TABLE I
ANISOTROPIC EFFECTIVE PARAMETERS AT SPECIFIED FREQUENCIES

Frequency (GHz)		10.9	12.8	15.0
n		-1.0052	-0.038	0.777
ε	ε_x (tan ε_x)	-3.49+0.13i (-0.036)	-0.17+0.04i (-0.234)	4.90+0.57i (0.117)
	ε_y (tan ε_y)	4.07+0.08i (0.02)	4.07+0.08i (0.02)	4.07+0.08i (0.02)
	ε_z (tan ε_z)	15.56+0.36i (0.023)	16.66+0.38i (0.02)	15.74+0.24i (0.0153)
μ	μ_x (tan μ_x)	0.99+0.00034i (0.0003)	0.9858+0.0003i (0.0003)	0.9850+0.0003i (0.0003)
	μ_y (tan μ_y)	-0.28+0.03i (-0.091)	-0.0082+0.0002i (-0.022)	0.1232+0.005i (0.04)
	μ_z (tan μ_z)	1.050+0.007i (0.007)	1.055+0.002i (0.002)	0.818+0.002i (0.002)
θ_r (°) (Retrieval value)		-30.6°	-1.10°	23.2°
θ_r (°) Homogenous prism		-28.6°	-2.6°	21.5°
θ_r (°) Microstructured prism		-25.6°	-0.4°	25.4°

Snell–Descartes Law. To this aim, the slab schematically described in Fig. 1(b) cannot be used for inducing a double refraction under tilted incidence and subsequent measurement of the beam shift at it was performed in [12]. Indeed, the artificial medium made of a stacked omega array is highly anisotropic with a negative value of n *only* in the propagation direction. Such a difficulty can be alleviated by using a prism-type prototype, as illustrated in Fig. 4.

This structure also has to be illuminated by a plane wave under normal incidence in order to avoid refraction on the first interface, especially with a limited lateral extent. Ideally, this would require a plane wave, which can be shaped by the absorbing cladding layers on each side of the feeding port. In addition, we performed ab-initio calculations by a proper representation of the microstructure, as illustrated in Fig. 4(b), as well as assuming that the prism behaves as an effective homogenous medium. At last, the prism is realized through a stair-like configuration, as illustrated in Fig. 4(c). The variation in the number of cells, each with a unit size of 3.9 mm, is discrete with an addition of one cell every four staked layers. This corresponds to an average angle of 30.5° at the output side of the prism.

In addition, we also performed a comparative analysis of the refraction by treating the prism as a homogenous medium. To this aim, we used a permittivity and permeability tensor approach, which is much more rigorous, compared to the isotropic homogenous analysis used in several previous publications [7], [21], [31]. In order to obtain the permittivity and permeability tensor components, the incident beam direction, as well as the electric and magnetic fields polarizations, may be changed accordingly. For instance, only the component of ε_x and μ_y can be retrieved in the configuration, as shown in Fig. 1. However, as the polarizations of the electric and magnetic fields are reversed and the incidence direction remains, the tensor components of ε_y and μ_x can be calculated. Table I shows the permittivity and permeability tensor components at three specified frequencies with different characteristic indices, namely, at 10.9 GHz (negative index), 12.8 GHz (zero index), and 15.0 GHz (positive index).

Fig. 5 shows the magnitude map of the electric field component along the x-axis at the mid-plane between the top and bottom perfect electric conductors at 10.9 GHz with an index value extremely close to -1. The structure is illuminated from the left side according to the layout displayed in Fig. 4(a). In Fig. 5(a) and (b), the arrow and dotted lines represent the direction of refracted wave and the surface normal, respectively. For the homogenous prism [see Fig. 5(a)], it can be noticed that the wave is not diffracted when impinging on the first interface so that a quasi-plane wave is preserved within the negative index medium. This wave interacts with the second interface where it experiences a negative refraction, as it can be pointed by tracing the direction of the transmitted beam with respect to the surface normal. The field distribution inside the microstructured prism is comparable to that of the homogenous one at the same phase [see Fig. 5(b)]. Some high field regions inside the microstructured prism can also be noticed, which gives an insight into the local field in the vicinity of the omega patterns. Furthermore, it can be interesting to confirm the direction of refraction by calculating the far field patterns in the y–z-plane, which is displayed in Fig. 5(c) and (d) for the homogenous and microstructured prisms, respectively. The far-field pattern is plotted with

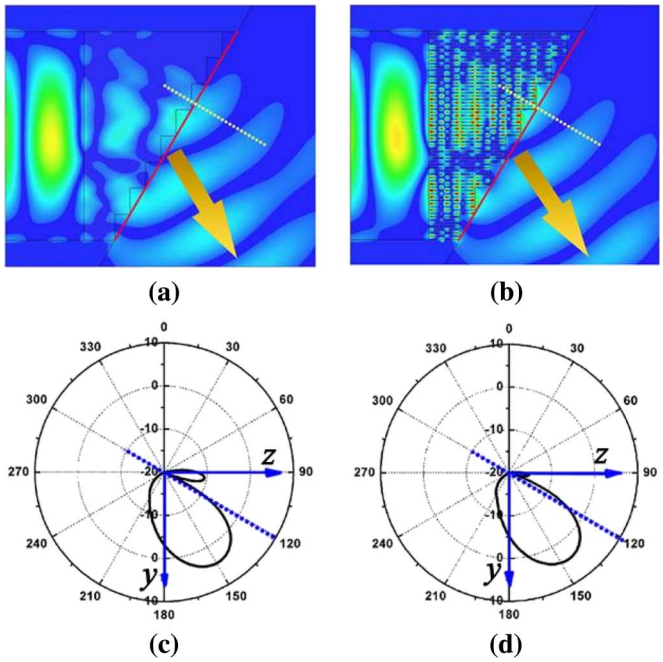

Fig. 5. Numerical evidence of negative refraction at 10.9 GHz. Electric field intensity of: (a) homogenous and (b) microstructured prisms at the same input phase. Refractive angle plotted in far field for: (c) homogenous and (d) microstructured prisms.

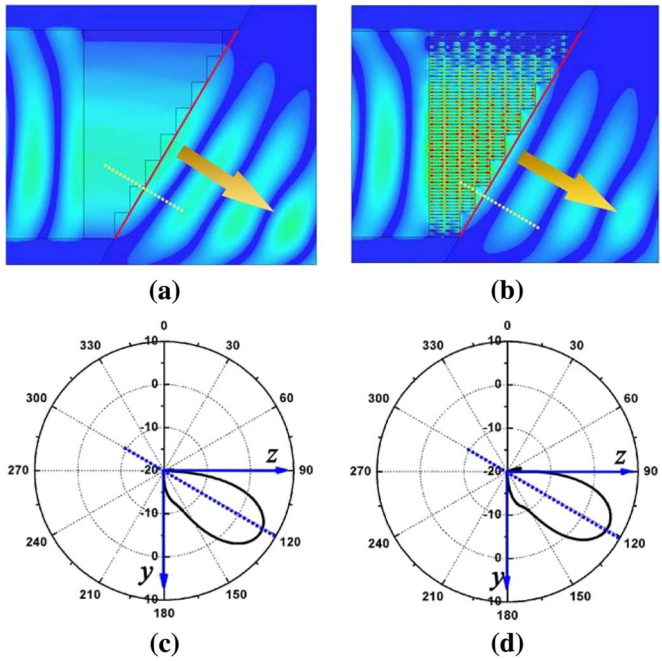

Fig. 6. Numerical evidence of zero-index refraction at 12.8 GHz. Electric field intensity of: (a) homogenous and (b) microstructured prisms at the same input phase. Refractive angle plotted in far field for: (c) homogenous and (d) microstructured prisms.

the angle calculated with respect to the $-y$-axis. For the frequency of interest, the refractive angles are -28.6° and -25.6° for the homogenous and microstructured prisms, respectively. These values are in a relative good agreement with the retrieved values listed in Table I. It is believed that the slight discrepancy is mainly due to the staircase interface rather than a smooth one. The small sidelobe that occurs at the positive direction with respect to the surface normal is due to the diffraction effect investigated by Smith *et al.* [31].

The same kind of numerical refraction experiment was conducted at a frequency of 12.8 GHz, which is expected to be near-zero index condition (Fig. 2). At Table I, the effective index of -0.038 was calculated at 12.8 GHz The map of the magnitude of the E_x component is displayed in Fig. 6. As shown in Fig. 6(a) and (b), the refracted beam is oriented parallel to the surface normal, indicating that the refraction index is extremely close to zero. This is confirmed by the refractive angles of -2.6° and -0.4° retrieved from the far field pattern [see Fig. 6(c) and (d)] for the homogenous and microstructured prisms. The wavelength inside the prism is seen extremely huge, which is consistent with the zero-index properties. Furthermore, the magnitude of the refracted beam at 12.8 GHz is comparable to that of 10.9 GHz, indicating a high transmission level with a nonvanishing group velocity. At last, Fig. 7 shows the results of the calculation performed for a frequency of 15.0 GHz. It can be seen that the transmitted beam is refracted positively with respect to the surface normal, as it is confirmed by the far-field angle-resolved transmissivity.

From the comparison between the homogenous and microstructured prisms shown in Figs. 5–7, good agreements can be observed, not only for the electric field distribution, but also for the far-field pattern. A satisfactory agreement is also

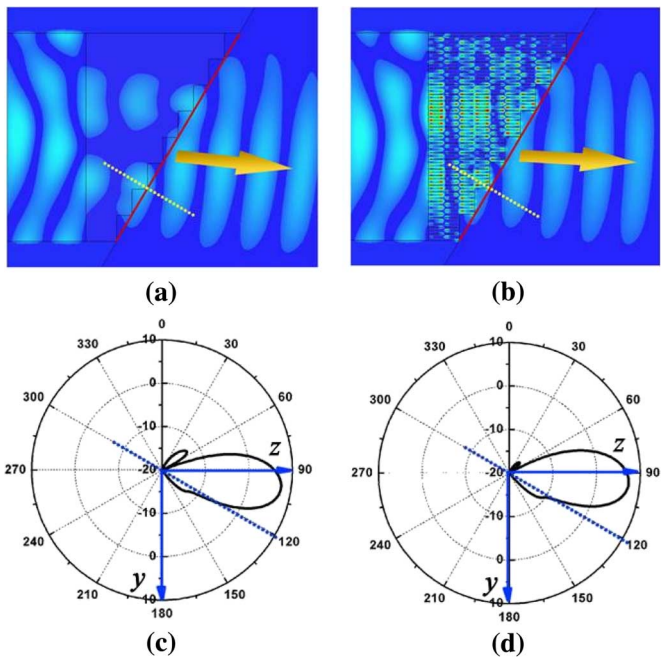

Fig. 7. Numerical evidence of positive refraction at 15.0 GHz. Electric field intensity of: (a) homogenous and (b) microstructured prisms at the same input phase. Refractive angle plotted in far field for: (c) homogenous and (d) microstructured prisms.

achieved between the retrieved values and those deduced from the far-field pattern. Let us now consider the experiments.

IV. Experimental Results of Prism

The prism sample, composed of eleven steps rather than eight for the simulation prototype, is shown in Fig. 8. The

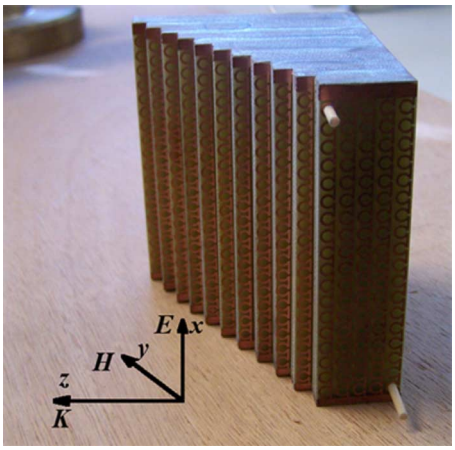

Fig. 8. Prism-type sample.

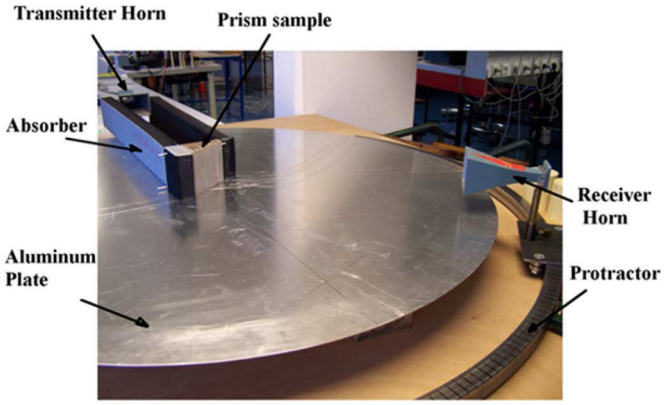

Fig. 9. Angle resolved measurement setup (the upper metal aluminium plate was removed for clarity).

prism sample was fabricated using printed circuit board technology. In practice, 0.8-mm-thick epoxy substrates coated with a 35-μm copper layer ($\sigma = 5.8\ 10^7$ S/m) were assembled according to the layout shown in Fig. 1. Owing to the large dimension of the completed prism-type prototype, we preferred to use a chemical-etching technique by Ion Peroxide rather than micromilling, as in our previous studies on microwave metamaterial [21]. The number of unit cells of each layer along the propagation direction at the first and last steps was increased from five to 15, respectively. Each layer consists of 18 unit cells along the x-direction with a periodicity of 3.9 mm.

The prism refraction experimental setup is shown in Fig. 9. Two absorbing layers (Eccosorb AN-75) are used in the input section for shaping the incident beam with a quasi-plane phase front. Absorber layers were also placed around the prototype for avoiding cavity effects, which could result from the reflected beams. The angle resolved measurements of the transmitted field are carried out by means of a rotating detector whose angular position is recorded via a homemade large scale circular protractor with a step of 1.25°, as shown in Fig. 9. With respect to the similar scattering chamber, which can be found in the literature, most notably in [13], the emission, as well as the detection of electromagnetic waves was performed via two horn antennas rather than by using waveguides flanges. For covering all the bands, two sets of horn pairs were used (Nadar

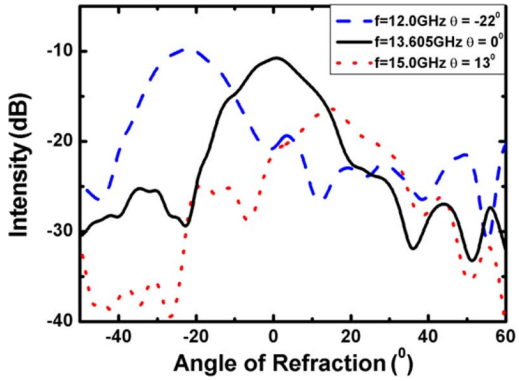

Fig. 10. Angle dependence of the detected signal at three characteristic frequencies: at the negative index band @12.0 GHz (dashed line), zero index @13.6 GHz (solid line) and positive index @15 GHz (dotted line).

640 for operating in the X-band and Nadar 639 for covering the Ku-band). The two horns were placed at the periphery of the 96-cm-diameter aluminium plates in order to satisfy the far-field condition. The refraction measurement was performed by an HP 85107A vector network analyzer.

Fig. 10 shows the angle dependence of the detected signal, which was measured for three representative frequencies of the negative index band (@12.0 GHz), zero index characteristic frequency (@13.6 GHz), and the positive index band (@15.0 GHz). For positive and zero indices, the maximum transmitted signal levels are quite comparable around -10 dB. As aforementioned, the impedance matching to the embedding air medium is more favorable for the lower frequencies of the spectrum. On the contrary, there is an important mismatch in the upper part (Fig. 3), which explains the weaker level of the transmitted wave. In order to clarify the main contribution to the insertion losses, we performed a further simulation as described in [32] via changing the metallic and substrate dielectric properties so as to compare the separate influence on the variation of the transmission magnitude. The resulting comparison indicated that the loss per cell could be reduced greatly to -0.1 dB from -0.8 dB for epoxy used here (not shown here), which confirms that dielectric loss is the dominant contributions.

By applying the Snell–Descartes Law, it is possible to experimentally retrieve the frequency dependence of the effective refractive index. In the equation of the refraction, the incident angle is the angle of the tilted interface (30.5°) and the refraction angle is drawn from the maximum of transmitted power at each measured frequency. The experimental results are reported in Fig. 2. It can be seen that the refractive index is negative from 10.2 to 13.6 GHz with a minimum value of -1.7. Above 13.6 GHz, n becomes positive with values ranging from 0 to 0.5. Thus, the experimental result demonstrates that the proposed structure indeed exhibits a balanced property with a negative-zero-positive behavior. The frequencies shift of the transition frequency between experimental and retrieval results is mainly due to a smaller permittivity value of the substrate than that employed in simulation. An excellent agreement between the simulation and experimental results can be obtained when the permittivity of epoxy glass is assumed to be 3.6. It is noted

that the balanced condition is also achieved when the permittivity of the substrate is lowered from 4.0 to 3.6. Indeed, the electric plasma frequency is found to be proportional to the square root of the background material relative permittivity [33], which has the same substrate permittivity dependence of the magnetic plasma frequency, as shown in (1). As a consequence, the balanced condition is independent of the substrate permittivity.

V. Conclusions

The electromagnetic properties of an omega-type metamaterial were investigated via the calculations and measurements of a prism-like prototype. The possibility to balance the dispersion characteristic with a negative-zero-positive index behavior by a proper engineering of magnetic and electric plasma frequencies was shown. Beyond the proof-of-principle demonstrated here by varying the operation frequency, it is believed that the concept can be extended to the case of a modulated carrier frequency by introducing some tunability of the system, notably via liquid-crystal technology [34]. The concept of the negative-zero-positive index is quite general and could be applied in particular to the steering of antenna beams avoiding by metamaterial technology the complex development of antenna feeding arrays.

References

[1] V. G. Veselago, "The electrodynamics of substances with simultaneously negative values of ε and μ," *Sov. Phys.—Usp.*, vol. 10, pp. 509–514, Jan.–Feb. 1968.

[2] J. B. Pendry, A. J. Holden, W. J. Stewart, and I. Youngs, "Extremely low frequency plasmons in metallic microstructures," *Phys. Rev. Lett.*, vol. 76, pp. 4773–4776, Jun. 1996.

[3] J. B. Pendry, A. J. Holden, D. J. Robbins, and W. J. Stewart, "Magnetism from conductors and enhanced nonlinear phenomena," *IEEE Trans. Microw. Theory Tech.*, vol. 47, no. 11, pp. 2075–2084, Nov. 1999.

[4] D. R. Smith and N. Kroll, "Negative refractive index in left-handed materials," *Phys. Rev. Lett.*, vol. 85, pp. 2933–2936, Oct. 2000.

[5] R. A. Shelby, D. R. Smith, and S. Schultz, "Experimental verification of a negative index refraction," *Science*, vol. 292, pp. 77–79, Apr. 2001.

[6] C. G. Parazzoli, R. B. Greegor, K. Li, B. E. C. Koltenbah, and M. Tanielian, "Experimental verification and simulation of negative index of refraction using Snell's Law," *Phys. Rev. Lett.*, vol. 90, pp. 107401-1–107401-4, Mar. 2003.

[7] R. B. Greegor, C. G. Parazzoli, K. Li, B. E. C. Koltenbah, and M. Tanielian, "Experimental determination and numerical simulation of the properties of negative index of refraction materials," *Opt. Exp.*, vol. 11, pp. 688–695, Apr. 2003.

[8] M. M. I. Saadoun and N. Engheta, "A reciprocal phase shifter using novel pseudochiral or Ω medium," *Microw. Opt. Technol. Lett.*, vol. 5, pp. 184–188, Apr. 1992.

[9] M. M. I. Saadoun and N. Engheta, "Theoretical study of the electromagnetic properties of no local Ω medium," *Progr. Electromagn. Res.*, vol. PIER 9, pp. 351–397, Dec. 1994.

[10] C. R. Simovski and S. He, "Frequency range and explicit expressions for negative permittivity and permeability for an isotropic medium formed by a lattice of perfectly conducting Ω particles," *Phys. Lett. A*, vol. 311, pp. 254–263, Mar. 2003.

[11] J. Huangfu, L. Ran, H. Chen, X. Zhang, K. Chen, T. Grzegorczyk, and J. A. Kong, "Experimental confirmation of negative refractive index of a metamaterial composed of Ω-like metallic patterns," *Appl. Phys. Lett.*, vol. 84, pp. 1537–1539, Mar. 2004.

[12] L. Ran, J. Huangfu, H. Chen, Y. Li, X. Zhang, K. Chen, and J. A. Kong, "Microwave solid-state left-handed material with a broad bandwidth and an ultralow loss," *Phys. Rev. B, Condens. Matter*, vol. 70, pp. 073102-1–073102-3, Aug. 2004.

[13] L. Ran, J. Huangfu, H. Chen, X. Zhang, K. Cheng, T. M. Grzegorczyk, and J. A. Kong, "Experimental study on several left-handed metamaterials," *Progr. Electromagn. Res.*, vol. PIER 51, pp. 249–279, Aug. 2005.

[14] E. Lheurette, O. Vanbésien, and D. Lippens, "Double negative media using interconnected omega-type metallic particles," *Microw. Opt. Technol. Lett.*, vol. 49, pp. 84–89, Jan. 2007.

[15] S. Enoch, G. Tayeb, P. Sabouroux, N. Guérin, and P. Vincent, "A metamaterial for directive emission," *Phys. Rev. Lett.*, vol. 89, pp. 213902-1–213902-4, Nov. 2002.

[16] R. W. Ziolkowski, "Propagation in and scattering from a matched metamaterial having a zero index of refraction," *Phys. Rev. E, Stat. Phys. Plasmas Fluids Relat. Interdiscip. Top.*, vol. 70, p. 046608, Oct. 2004.

[17] A. Alù, M. G. Silveirinha, A. Salandrino, and N. Engheta, "Epsilon-near-zero metamaterials and electromagnetic sources: Tailoring the radiation," *Phys. Rev. B, Condens. Matter*, vol. 75, p. 155410, Apr. 2007.

[18] A. Lai, C. Caloz, and T. Itoh, "Composite right/left-handed transmission line metamaterials," *IEEE Micro*, vol. 5, no. 3, pp. 35–50, Sep. 2004.

[19] S. Lim, C. Caloz, and T. Itoh, "Metamaterial-based electronically controlled transmission-line structure as a novel leaky-wave antenna with tunable radiation angle and beamwidth," *IEEE Trans. Microw. Theory Tech.*, vol. 53, no. 1, pp. 161–173, Jan. 2004.

[20] A. Lai, C. Caloz, and T. Itoh, "Characteristics of the composite right/left-handed transmission lines," *IEEE Microw. Wireless Compon. Lett.*, vol. 14, no. 2, pp. 68–70, Feb. 2004.

[21] F. Zhang, S. Potet, J. Carbonell, E. Lheurette, O. Vanbésien, X. Zhao, and D. Lippens, "Application of omega-type and related metamaterials for beam steering in X–Ku," in *Proc. 37th Eur. Microw. Conf.*, Munich, Germany, 2007, pp. 909–912.

[22] D. Lippens, "Metamaterials and infra-red applications," *Comptes Rendus Phys.*, vol. 9, pp. 184–196, Feb. 2008.

[23] R. Marqués, F. Mesa, J. Martel, and F. Medina, "Comparative analysis of edge-and broadside-coupled split ring resonators for metamaterial design-theory and experiments," *IEEE Trans. Antennas Propag.*, vol. 51, no. 10, pp. 2572–2581, Oct. 2003.

[24] I. Bulu, H. Caglayan, and E. Ozbay, "Designing materials with desired electromagnetic properties," *Microw. Opt. Technol. Lett.*, vol. 48, pp. 2611–2615, Dec. 2006.

[25] T. Crepin, J. F. Lampin, T. Decoopman, X. Melique, L. Desplanque, and D. Lippens, "Experimental evidence of backward waves on terahertz left-handed transmission lines," *Appl. Phys. Lett.*, vol. 87, Sep. 2005, Art. ID 104105.

[26] T. Decoopman, O. Vanbesien, and D. Lippens, "Demonstration of a backward wave in a single split ring resonator and wire loaded finline," *IEEE Microw. Wireless Compon. Lett.*, vol. 14, no. 11, pp. 507–509, Nov. 2004.

[27] C. Croënne, B. Fabre, D. Gaillot, O. Vanbésien, and D. Lippens, "Bloch impedance in negative index photonic crystals," *Phys. Rev. B, Condens. Matter*, vol. 77, pp. 125333-1–125333-6, Mar. 2008.

[28] C. Croënne, M.-F. Foulou, E. Lheurette, X. Mélique, M. Gheudin, and D. Lippens, "Negative index metamaterial at 100 GHz," in *Proc. Eur. Microw. Assoc.*, Jun. 2008, vol. 4, pp. 95–101.

[29] D. R. Smith, S. Schultz, P. Markoš, and C. M. Soukoulis, "Determination of effective permittivity and permeability of metamaterials from reflection and transmission coefficients," *Phys. Rev. B, Condens. Matter*, vol. 65, pp. 195104-1–195104-5, Apr. 2002.

[30] X. Chen, T. M. Grzegorczyk, B.-I. Wu, J. Pacheco, and J. A. Kong, "Robust method to retrieve the constitutive effective parameters of metamaterials," *Phys. Rev. E, Stat. Phys. Plasmas Fluids Relat. Interdiscip. Top.*, vol. 70, pp. 016608-1–016608-7, Jul. 2004.

[31] D. R. Smith, P. M. Rye, J. J. Mock, D. C. Vier, and A. F. Starr, "Enhanced diffraction from a grating on the surface of a negative-index metamaterials," *Phys. Rev. Lett.*, vol. 93, pp. 137405-1–137405-4, Sep. 2004.

[32] J. Carbonell, L. J. Rogla, V. E. Boria, and D. Lippens, "Design and verification of backward wave propagation in periodic waveguides structures," *IEEE Trans. Microw. Theory Tech.*, vol. 54, no. 4, pp. 1527–1533, Apr. 2006.

[33] P. Markoš and C. M. Soukoulis, "Transmission studies of left-handed materials," *Phys. Rev. B, Condens. Matter*, vol. 65, pp. 033401-1–033401-4, Dec. 2001.

[34] Q. Zhao, L. Kang, B. D, B. Li, J. Zhou, H. Tang, X. Liang, and B. Zhang, "Electrically tunable negative permeability metamaterials based on nematic liquid crystals," *Appl. Phys. Lett.*, vol. 90, Jan. 2007, Art. ID 011112.

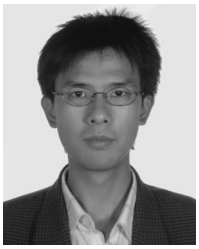

Fuli Zhang was born in Xinxiang, China, on October 19, 1982. He received the B.S. degree in materials science and engineering and M.S. degree in optical engineering from Northwestern Polytechnical University, Xi'an, China, in 2003 and 2006, respectively, and is currently working toward the Ph.D. degree at the Institut d'Électronique de Microélectronique et Nanotechnologies (IEMN), Unite Mixte de Recherche (UMR), Centre National de la Recherche Scientifique (CNRS) 8520, Université des Sciences et Technologies de Lille 1, Villeneuve d'Ascq, France.

His main research interests include the metamaterials of millimeter waves and terahertz and their applications.

Sylvain Potet was born in Reims, France, on March 14, 1984. He received the Ingineer degree from the Ecole Nationale d'Ingénieur de Brest (ENIB), Brest, France, in 2007.

He then joined the Institut d'Électronique de Microélectronique et Nanotechnologies (IEMN), Unite Mixte de Recherche (UMR), Centre National de la Recherche Scientifique (CNRS) 8520, Université des Sciences et Technologies de Lille 1, Villeneuve d'Ascq, France, for engineer training on negative-zero-positive refraction in a prism-like omega-type metamaterial. He is currently a Quality Engineer with Temex, Pont Sainte Marie, France, where he is involved with the Space Socillator Department.

Jorge Carbonell (S'94–M'05) was born in Valencia, Spain, in 1971. He received the Ingeniero de Telecomunicación degree from the Universidad Politécnica de Valencia, Valencia, Spain, in 1995, and the Ph.D. degree in electrical engineering (European label with honors) from the Université de Lille, Lille, France, in 1998.

From 1996 to 1998, he was with the Institut d'Electronique et de Microélectronique du Nord (IEMN), Université de Lille, where his research included electromagnetic (EM) analysis of active and passive devices for space applications, and in particular, photonic-bandgap materials. From 1999 to 2003, he worked within the wireless industry with Ericsson, Siemens, Retevisión Móvil, and Telefónica Móviles. During that period, he was involved in the design and deployment of second- and third-generation wireless communication systems and networks, and mainly focused on radio engineering. Since January 2004, he has held a Ramón y Cajal tenure-track research position with the Universidad Politécnica de Valencia, Valencia, Spain. His current research activity concerns the analysis and design of passive periodic structures and metamaterials.

Dr. Carbonell was the recipient of a Human Capital and Mobility Fellowship.

Eric Lheurette received the Ph.D. degree in microwave electronics from the Université des Sciences et Technologies de Lille, Lille, France, in 1996. His doctoral thesis concerned the technology of resonant tunneling devices and, more generally, of heterostructure devices.

Following a post-doctoral position with the Institut D'Électronique de Microélectronique et de Nanotechnologie (IEMN), with main emphasis on electromagnetic simulation, he became an Assistant Professor with the University of Rouen. In September 2003, he joined the Quantum Opto and Micro Electronic (DOME) Device Group, IEMN, as an Assistant Professor with the prospect to further develop the DOME's terahertz technology program. His current interests concern nonlinear electronics and electromagnetism of complex propagation media.

Olivier Vanbésien was born in Armentières, France, on November 11, 1964. He received the Engineer degree from the Institut Supérieur d'Electronique du Nord (ISEN), Lille, France, in 1987, and the Third Cycle Thesis on quantum devices from the Université de Lille, Lille, France, in 1991.

He then joined the High Frequency Department, Institut d'Electronique, de Microélectronique et de Nanotechnologie (IEMN), as a Chargé de Recherches Centre National de la Recherche Scientifique (CNRS). In November 2000, he became a Professor of Electronics with the Université des Sciences et Technologies de Lille. His current interests concern metamaterials and photonic crystals, exploring both dielectric and metallic routes for applications of abnormal refraction from the terahertz region down to optics.

Xiaopeng Zhao received the B.S. degree in metal physics and M.S. degree in solid-state physics from Lanzhou University, Lanzhou, China, in 1979 and 1982, respectively, and the Ph.D. degree in material physics from the Institute of Metal Research Chinese Academy of Sciences, Shenyang, China, in 1995.

He is currently a Professor with the Department of Applied Physics, Northwestern Polytechnical University, Xi'an, China. He has authored or coauthored 160 international journal papers and 108 Chinese patents. He has served as a reviewer for various leading journals. His current research interests include biomimetical materials, intelligent materials and structure, nanotechnology, left-handed metamaterials, and their applications.

Didier Lippens received the Ph.D. degree in liquid crystal technology and Doctorat d'état' degree in semiconductor physics from the Université de Lille, Lille, France, in 1975 and 1984, respectively.

In 1980, he joined the Centre National de la Recherche Scientifique (CNRS). He is currently a Professor with the Université des Sciences et Technologies de Lille in connection with metamaterial technology. He is currently the Head of the Quantum Opto and Micro Electronic (DOME) Device Group, Institut d'Electronique, de Microélectronique et de Nanotechnologie (IEMN). He has authored or coauthored over 130 journal papers and has supervised 30 Ph.D. students. Over the past few years, he has been a member of several scientific boards of National and European networks, including advanced electronics and nanophotonics networks depending on CNRS, training mobility research (TMR) programs, and future emergent technology (FET) of the European Commission. His current interests include photonic crystals and metamaterials and their tunability via ferroelectrics and liquid-crystal technologies. The targeting applications are cloaking, or more generally, electromagnetic wave control, through optics transformations along with super-lenses and hyper-lenses operating at terahertz frequencies and in the infrared spectral regions.

Negative-zero-positive metamaterial with omega-type metal inclusions

Fuli Zhang,[1,3] Gregory Houzet,[1] Eric Lheurette,[1] Didier Lippens,[1,a)]
Michel Chaubet,[2] and Xiaopeng Zhao[3]
[1]*Institut d'Electronique de Micro-électronique et de Nanotechnologie, UMR CNRS 8520, University of Lille1, 59652, Villeneuve d'Ascq Cedex, France*
[2]*Centre National d'Etudes Spatiales, 18 Avenue Edouard Belin, 31000, Toulouse, France*
[3]*Department of Applied Physics, Northwestern Polytechnical University, Xi'an, 710072, People's Republic of China*

(Received 4 December 2007; accepted 2 March 2008; published online 28 April 2008)

We report on a negative-zero-positive metamaterial based on an omega-type microstructure with special attention on the nonvanishing group velocity for a zero refractive index. We first investigate the dispersion characteristics by full wave analysis, by stressing the necessary conditions of equality between the electric and magnetic plasma frequencies which are characteristic of the dispersion of the effective permittivity and permeability. Also, tuning of the gapless transition frequency between the left and right-handed dispersion branches was analyzed when the permittivity of the host substrate is changed. Last, we demonstrate experimentally the balanced composite character of the dispersion by frequency and angle-resolved transmission measurements, carried out at centimeter wavelengths on slabs and wedge-type prototypes, respectively.
 [DOI: 10.1063/1.2910831]

I. INTRODUCTION

The left-handed materials (LHMs), introduced by Veselago in 1968,[1] are now extensively studied to take benefit of unusual electromagnetic properties not found in natural materials. Basically, backward wave media can be synthesized either by introducing split ring resonator (SRR)/wire structures[2–5] or other related particles such as omega-type arrays[6–10] or by periodically loaded phase advance transmission lines,[11–15] as proposed in the pioneering book of Brillouin.[16] For most LHMs, the left-handed (LH) passband is separated from the right-handed (RH) one by a band gap. At the edges of this passband, the group velocity vanishes. It was recently shown that a zero-gap dispersion characteristic can be achieved in LH transmission lines[12–14] so that an infinite wavelength condition can be met at the wave vector $k=0$ with a nonvanishing group velocity. Such a structure was termed composite right and left-handed (CRLH) material, with an equality criterion between the series and parallel resonant frequencies of the lumped circuit elements. CRLH waveguides were used successfully at microwaves for subwavelength resonators and leaky wave antennas notably. The extension of the concept of balanced composite transmission lines to high-dimensionality devices such as metasurfaces and bulk metamaterials is a difficult task despite the encouraging results published recently.[17,18]

In this paper, we investigate how the SRR/wire technology, which exhibits basically a narrow LH band separated by a forbidden gap from the RH one, can be used to realize a negative-zero-positive index material. To this aim, we based our analysis on an omega-type metal inclusion, which can be considered as a related compound of broadside coupled SRR/wire arrays so that the electric and magnetic responses can be treated as a whole. First, we show that under the condition of interconnecting the omega-shaped particles, a broader band can be achieved, as demonstrated before by Kong's group.[7–9] In a second stage, we identify the key geometrical parameters to balance the dielectric and magnetic plasma frequencies, and demonstrate the balanced composite character of the structure by the retrieval of the effective permittivity and permeability. These conclusions are then assessed experimentally by carrying out frequency and angle-resolved transmission measurements on slab and wedge-type prototypes operating at centimeter wavelengths.

The paper is organized as follows: In Sec. II, we analyze the guidelines to obtain a balanced composite metamaterial on the basis of plasma frequency analytical functions. The fitting of omega geometries is then performed by full-wave simulations, which permits us to deduce the complex k dispersion characteristics and to retrieve the refractive index, the Bloch impedance, along with the effective permittivity and permeability. In this section, we also consider the tunability of the dispersion characteristics. The properties of the microstructured slab and prismlike devices were numerically assessed using full-wave simulations and experimentally characterized by frequency and angle-resolved transmission measurements; the comparison is provided in Sec. III.

II. BALANCED STRUCTURE

A. Mode analysis

Figure 1 illustrates the typical dispersion of the effective permittivity and permeability of an edge-coupled split ring resonator/infinite wire and transmission response of one array whose basic cell is shown in the inset. In fact, an infinite wire array yields a quasi-Drude-type dependence for the dispersion of the effective permittivity, whereas the effective permittivity of SRRs exhibits a Lorentz-type dispersion characteristic. It can be concluded that the material behaves as a

a)Electronic mail: didier.lippens@iemn.univ-lille1.fr.

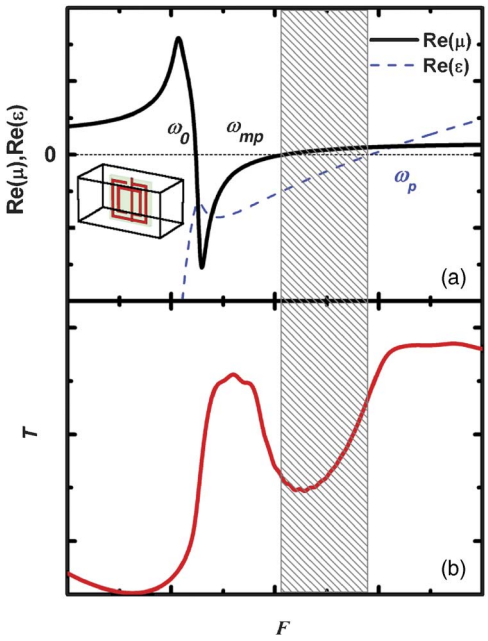

FIG. 1. (Color online) Characteristics of an edge-coupled SRR /wire (basic cell is shown in inset). (a) Real parts of permeability (solid) and permittivity (dash). (b) Frequency dependence of the transmission of an array. The band gap (gray region) ranging from ω_p and ω_{mp} is caused by a single negative effective parameter, i.e., negative permittivity.

single negative medium in the grayed frequency band between the magnetic plasma frequency ω_{mp} and the electric plasma frequency ω_p , within which the waves are evanescent. In contrast, the propagation is backward between the resonance frequency ω_0 (the magnetic resonance frequency of SRRs) and ω_{mp} and forward above ω_p.

Let us now consider an omega-type metal inclusion as depicted in Fig. 2. The basic unit cell [Fig. 2(a)] is composed of two Ω-patterns in a back-to-back configuration to avoid chiral effects.[6] For pure magnetic excitation, namely for a magnetic dipole induced by the incident magnetic field (**H**), the polarization of **H** has to be along a direction normal to the surface on which the current loops (the C shape of the omega inclusion) are implemented. In addition, in order to induce an electrical activity, the *E* field polarization has to be oriented parallel to the arms of the omega patterns. Under these polarization considerations, the array was implemented according to the scheme shown in Fig. 2(b). A volumetric prototype is achieved by stacking several substrates with omega-shaped metal inclusions printed on one side of each layer. In order to alleviate a resonant characteristic in the dielectric response (quasi Drude-type dispersion), the omega arms are interconnected along the direction of the *E* field. As seen above, the plasma frequency ω_p is usually higher than the magnetic plasma frequency ω_{mp} for an unbalanced metamaterial. As a consequence, the condition of a balanced composite structure, achieved when $\omega_p = \omega_{mp}$, requires an increase of ω_{mp} or a decrease of ω_p.

In order to satisfy this criterion for omega-type arrays, we first considered a lumped-element circuit description of the magnetic response of the current loops[9,10,19] and focused on some guidelines to achieve a balanced structure with negative-zero-positive behavior.

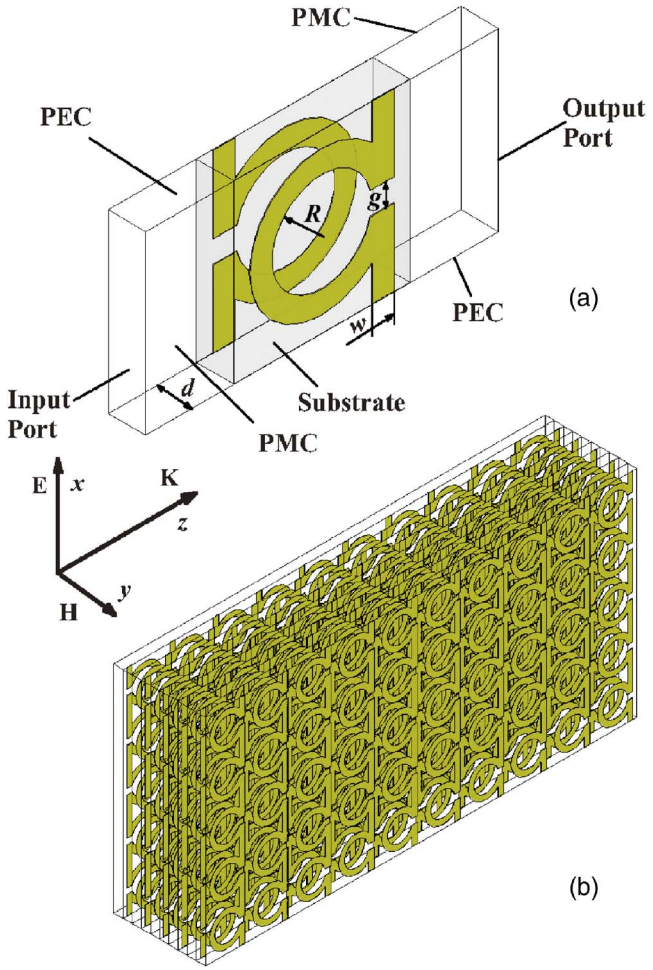

FIG. 2. (Color online) (a) Schematic of the omega unit cell. (b) Schematic of omega pattern array with an edge illumination by a plane wave.

For the current loops, the magnetic angular resonance frequency ω_0 can be described by the equation

$$\omega_0 = \frac{1}{\sqrt{LC}}, \tag{1}$$

where *L* is the inductance of the current loops and *C* is the total capacitance between the broadside coupled split ring resonators. Using a parallel-plate model, the total capacitance *C* (the fringing effect is not considered) is approximated by

$$C = \frac{1}{2}C_g = \frac{1}{2}\frac{\varepsilon_0\varepsilon_r w}{d}\left(\pi\frac{2R+w}{2} - \frac{g}{2}\right), \tag{2}$$

where C_g is the capacitance between two half-circular rings of current loops, ε_0 and ε_r are the effective permittivity of the vacuum and substrate, respectively. *w* is the wire width, *R* is the inner radius, *g* is the gap of the omega pattern, and *d* is the thickness of the substrate. The inductance *L* of the omega pattern is given by

$$L = \mu_0\pi R^2/d. \tag{3}$$

The relation between the magnetic plasma frequency ω_{mp} and the resonant frequency ω_0 can be expressed as[3,4]

$$\omega_{mp} = \frac{\omega_0}{\sqrt{1-F}}, \tag{4}$$

where $F=\pi R^2/S$ is the fraction occupied by the interior ring of the omega pattern in the xz plane and S is the area of the basic unit cell in the xz plane. On the other hand, the electric plasma frequency ω_p can be described in a first approximation by Pendry's formula as follows:[20]

$$\omega_p{}^2 = \frac{2\pi c_0^2}{a^2 \ln(a/r)}, \tag{5}$$

where a and r are the periodicity of the wire array and wire radius, respectively. It can be seen that the plasma frequency ω_p increases with the wire radius r. The cross section of wire considered here is rectangular whereas it was originally circular in Pendry's model, but the plasma frequency has an analogous function, i.e., increasing with the wire width w.[21] Therefore, we see that reducing the strip width will cause an increase of ω_{mp} and a decrease of ω_p simultaneously, which could be employed as a rather simple method to achieve a balanced condition.

The aforementioned arguments can be used not only as a first estimate of the relevant geometry of the omega inclusions but also as guidelines to tune ω_{mp} and ω_p. However, because the magnetic and electric responses are not strictly separated, a finer optimization has to be conducted by means of a full-wave analysis. In practice, this procedure was performed with the HIGH FREQUENCY STRUCTURE SIMULATOR (HFSS) by Ansoft, a finite-element commercial software package. With respect to the numerical simulations reported below, it was found that the approximation of ω_{mp} by means of Eq. (4) is quite good (within a few percent), whereas Eq. (5) gives a more crude assumption of the plasma frequency due mainly to the difference in the wire array geometry. The dimensions of the basic unit cell were chosen as follows: $R=1.1$, $w=g=0.5$ (unit: millimeters). For these simulations, we assumed a substrate with the following dielectric characteristics at centimeter wavelength ($\varepsilon_r=4.0, \tan\delta=0.02$) and a thickness of 0.8 mm. The basic cell dimensions are 3.9 mm along the x and z directions and 0.8 mm along y.

B. Balanced condition

The first clue for a zero-gap CRLH metamaterial is a broad transmission window which is assessed by the magnitude of the scattering parameter S_{21}. It is however difficult to conclude on the left-handedness or right-handedness of the dispersion characteristics. As a consequence, we calculated in the second stage the dispersion characteristics (Fig. 3) according to the method we used in Ref. 22 based on the Bloch-Floquet theorem. Note that this approach is similar to the retrieval method reported in Refs. 23 and 24. For this calculation, only one cell was considered along the propagation direction, whereas an infinitely long periodic array was mimicked along the transverse directions with proper boundary conditions [see Fig. 2(a)]. Perfect E conditions were applied for the surfaces normal to the omega arms, and perfect H boundaries to the surface parallels to the omega plane. In short, the solved scattering matrix is converted into the corresponding transfer matrix M, which is also termed an $ABCD$ or chain matrix. On the other hand, the chain matrix of a homogeneous propagation medium can also be written as a function of a complex propagation constant $\gamma=\alpha+j\beta$, where α and β depict the evanescence of the wave and the phase constant. z is the reduced impedance of the propagation medium with respect to its surrounding environment,

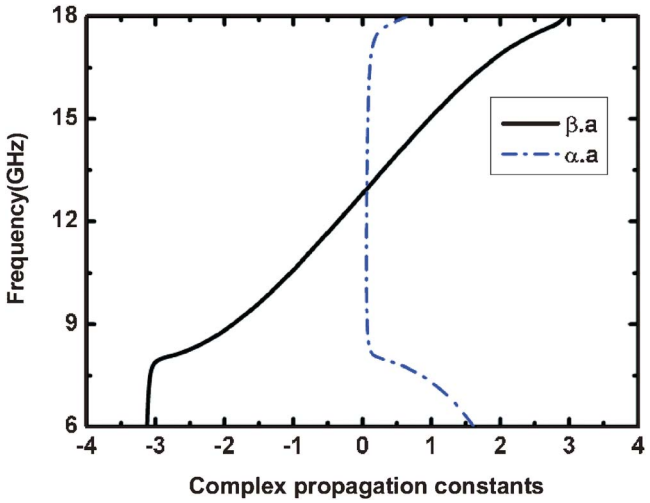

FIG. 3. (Color online) Dispersion characteristics of the negative-zero-positive index structure depicted in Fig. 2(b).

$$M = \begin{bmatrix} A & B \\ C & D \end{bmatrix} = \begin{bmatrix} ch(\gamma a) & z \cdot sh(\gamma a) \\ \frac{1}{z} \cdot sh(\gamma a) & ch(\gamma a) \end{bmatrix}. \tag{6}$$

By equating the various matrix elements of the microstructured and homogeneous media term by term, it can be shown that

$$\alpha = \frac{1}{a} \ln\left|A \pm \sqrt{A^2-1}\right|, \tag{7}$$

$$\beta a = \angle\left(A \pm \sqrt{A^2-1}\right) + 2k\pi, \quad k \in Z, \tag{8}$$

$$z = \pm \sqrt{\frac{B}{C}}. \tag{9}$$

The information about the index is implicitly present in the complex propagation constant since

$$n = \frac{c\gamma}{i\omega}. \tag{10}$$

The dispersion characteristics of the real and imaginary parts of the propagation constant are displayed as a function of $\alpha \cdot a$ and $\beta \cdot a$ (a is the periodicity along the propagation direction; Fig. 2). It can be noted that the phase constant β is negative in the frequency domain in the 8.0–12.8 GHz frequency domain with a positive group velocity v_g ($\partial\omega/\partial\beta$). Hence, the group velocity and phase velocities of the propagating wave are antiparallel and therefore it supports a backward wave (LH mode). On the other hand, it supports a forward wave (RH mode) above 12.8 GHz. The corner frequency between the two modes is at 12.8 GHz, where the

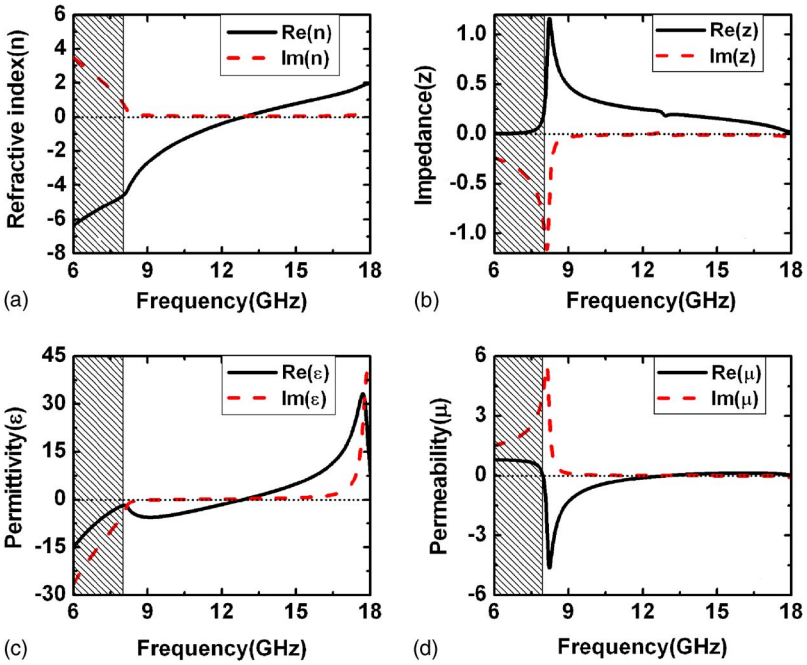

FIG. 4. (Color online) Effective parameters of negative-zero-positive structure retrieved from the scattering parameters of one unit cell. (a) Refractive index. (b) Impedance. (c) Permittivity. (d) Permeability.

phase constant is zero (infinite wavelength). In contrast with the conventional split ring resonator array (see Fig. 1), here the group velocity ($\partial\omega/\partial\beta$) does not vanish and presents a value close to 5.5×10^7 m s^{-1} by taking an estimate of the slope at $k=0$. Below the resonant frequency of the current loops, corresponding to a forbidden gap, the evanescence of the waves is directly related to the decay length α^{-1}.

The variations of the Bloch impedance and of the refractive index, which can be determined from Eqs. (9) and (10), are plotted in Fig. 4. The physical meaning of n below ω_0 (gray region) is doubtful since the incident wave is evanescent. Just above ω_0, a spike can be seen in the impedance resulting from the resonance effect. The refractive index exhibits a smooth transition between the negative band (8.0–12.8 GHz) and the positive band (12.8–16.0 GHz), with thus a transition frequency at 12.8 GHz where the refractive index value is zero. The frequency dependence of the effective permittivity can be described by a Drude model (continuous increase of the negative permittivity up to the electric plasma frequency). Although a slight resonant feature is superimposed at 8.1 GHz, the value of the effective permittivity is always negative. The effective permeability shows a well-defined negative peak at the resonance frequency with an increase in the losses. As a last comment, it can be assessed that the turning frequencies ω_{mp} and ω_p are equal.

C. Tunability of balanced structure

Because balanced structures enable smooth switching from the LH branch to the RH one, this opens the possibility to fabricate tunable balanced composite metamaterials. However, when some tunability is introduced, the magnetic plasma frequency ω_{mp} should always be equal to the plasma frequency ω_p in order to maintain the balanced condition, which considerably increases the difficulties. Basically, tunability can be introduced by changing the value of the capacitance C given by Eq. (2) via the modification of the unit cell geometry for fixed tuning or by varying the permittivity of the substrate. Such a tuning of ω_0 yields a concomitant shift of the magnetic plasma frequency ω_{mp} which varies as the inverse of the square root of the permittivity of the substrate according to Eq. (4).

For the frequency dependence of this artificial permittivity, we learned that the plasma frequency ω_p can also be described as the cutoff frequency of a metal wire array given by[25,26]

$$\omega_p = C_{\text{light}}/2a\sqrt{\varepsilon_r}, \tag{11}$$

where a is the periodicity of the wire array. From Eqs. (4) and (11), we see that both ω_{mp} and ω_p are proportional to $1/\sqrt{\varepsilon_r}$. Therefore, the balanced condition will be independent of the permittivity of the substrate. In order to check this analysis, the influence of the substrate permittivity on the balanced condition was studied numerically. The results of this study in terms of dispersion characteristics are shown in Fig. 5. It is important to note that the balanced criterion is maintained when the permittivity of the substrate varies. The transition frequency increases gradually from 12.5 to 14.0 GHz as the permittivity is decreased from 4.2 to 3.4 with a step of 0.2. In summary, by incorporating some materials which exhibit a tunable permittivity, such as liquid crystals and ferroelectrics, it is possible to realize a reconfigurable balanced composite omega-based metamaterial.

III. EXPERIMENTAL RESULTS

In order to confirm experimentally the main conclusions of the previous theoretical analysis, we carried out two complementary studies. We first performed transmission measurements of a metamaterial slab in order to check the absence of a band gap between the LH and RH transmission window. The second type of transmission experiment was

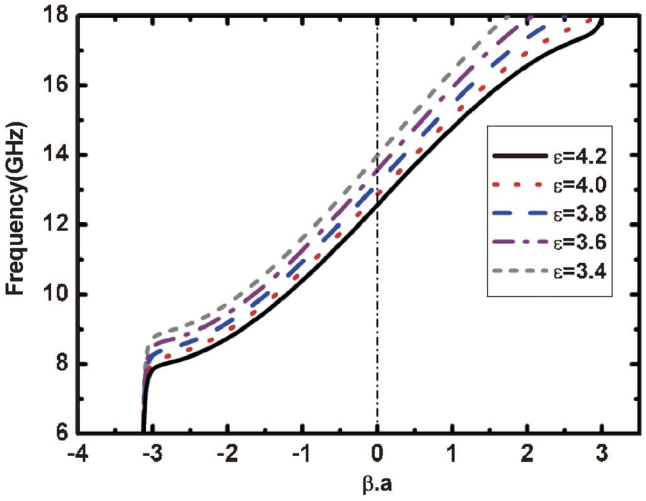

FIG. 5. (Color online) Propagation phase constant as a function of the substrate permittivity.

carried out on a prismlike prototype under angle-resolved conditions, in order to determine the refractive index, via the Snell-Descarte's law.

A. Transmission measurement of the slab device

In practice, the metamaterial slab [Fig. 6(a)] consists of 100 layers of epoxy glass with omega patterns printed on one side by the standard print circuit board (PCB) technology. Each layer consists of 10 unit cells along the z-direction and 18 unit cells along x with the same periodicity of 3.9 mm. Two horizontal strips were printed at the top and bottom edges of each layer to further increase the electrical length of the omega arms in order to avoid the influence of the wire finite length.[27]

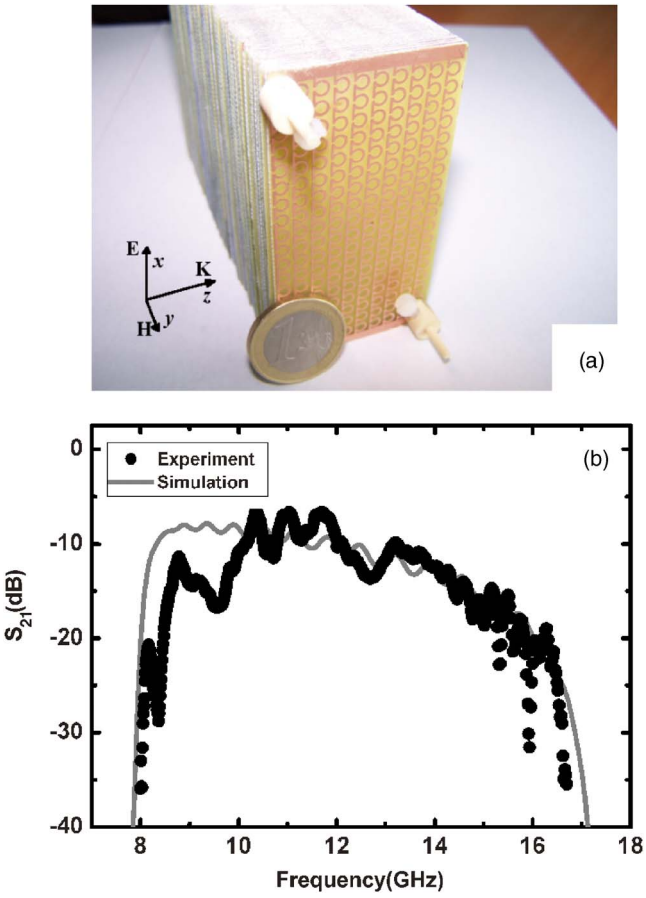

FIG. 6. (Color online) Transmission measurement of the slab. (a) Photograph of slab sample fabricated for transmission measurements. (b) Transmission characteristics of the metamaterial slab.

For the transmission experiment, the metamaterial slab was put between two aluminum plates with microwave absorbers on the side walls. This parallel plate waveguiding setup is similar to the one described in Ref. 28. The spacing between the aluminum plates fits the horn apertures equal to 7.5 cm. Two pairs of horns were used to initiate a Gaussian-shaped electromagnetic excitation at the input and to probe the transmitted signal at the output for the X band and K_u bands, respectively. We recall that the incident wave was set to propagate along the z-direction with the electric field along the x-direction and the magnetic field along y. The transmission spectrum was measured by an HP 85107A vector network analyzer.

Figure 6(b) compares the experimental and simulation transmission results. It can be seen that the slab exhibits a broad passband from 8.3–16.0 GHz, with a good agreement with the simulated transmission window. Despite the ripple resulting from the truncation of the structure, no band gap can be evidenced in the passband, which is consistent with the analysis of the dispersion curve of Fig. 2.

B. Angle-resolved measurement of the prismlike device

For the refraction experiment, we have to ensure that a prismlike structure can be used for the experimental determination of the refractive index n along the propagation direction. In fact, despite the fact that we fabricated a volumetric prototype, the structure properties are anisotropic so that the effective parameters are now described by tensors. This also explains why the previous slab cannot be used in a double-refraction experiment as carried out for isotropic metamaterial.

The model of the prism sample is depicted in Fig. 7. The incident beam impinges onto the sample at normal incidence with a Gaussian intensity profile tailored by side absorbers. For this condition of excitation, the electromagnetic wave undergoes refraction at the second tilted interface. Let us note that the prism model, which exhibits a stairlike pattern with a four-unit cell (eight omega patterns) step along the y-direction and a one-unit-cell along z, can be considered as a wedge of 30.5°. Seven stairs along the y-direction were found to be a good tradeoff between computer resources, accuracy, and reasonable calculation time. The prism was positioned between two perfect electric conductors (PEC), which sandwiched a unit cell in the x direction so that the structure can be considered infinite along this direction.

Figures 8(a)–8(c) shows the maps of the electric field magnitude at various operating frequencies calculated at the midplane between the top and bottom perfect electric conductors. The black arrow and the dash-dot line indicate the direction of the refracted beam and the normal to the second tilted interface, respectively. For a frequency of 10.0 GHz

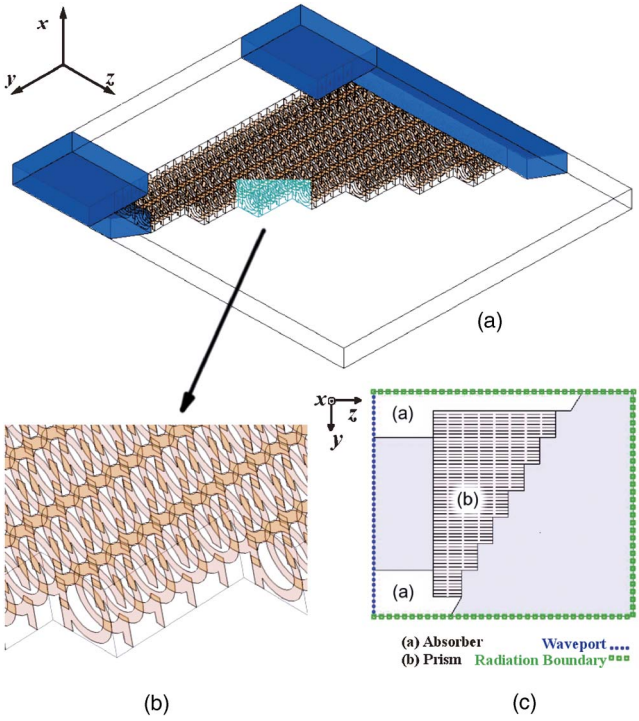

FIG. 7. (Color online) Prism model used in simulation. (a) 3D view of prism sample model. (b) Magnified view of one prism model stair, which consists of four cells along the *y* direction and one cell along the *x* direction. (c) Top view of prism model and applied boundaries.

[Fig. 8(a)], it can be seen that the angle of the refracted beam is in the negative direction with respect to the normal as expected for a LH dispersion branch. At 12.8 GHz [Fig. 8(b)], the refracted beam direction is quasiparallel to the normal, indicating that the refraction index is extremely close to zero. The magnitudes of the refracted beams at 12.8 and 10.0 GHz are comparable, thus in magnitude in agreement with the frequency dependence of the transmission of a slab shown in Fig. 5. Finally, at 15 GHz [Fig. 8(c)] the peak of the refracted beam is directed along a positive angle with respect to the normal and is consistent with the RH branch.

The prism refraction experiment was then carried out in a manner similar to the method reported in Ref. 2. The prism prototype, composed of 11 stairs instead of 7 for the simulation sample, is shown in Fig. 9(a). The number of unit cells along the propagation direction at the first stair and the last stair was increased to 5 and 15 cells, respectively. Figure 9(b) shows the normalized intensity of the refracted beam as a function of angular position of the probing horn antenna for three characteristic frequencies corresponding to a negative, zero, and positive index. By taking the central angle at the full width at half-maximum, the refraction beam peak was found to occur at −38.0°, 0.5°, and 13.0°, at 11.1, 13.6, and 15.0 GHz, respectively. Moreover, half the beamwidth of the refracted beam is only 15.9° at 13.5 GHz, which is smaller than that of 18.2° at 15.0 GHz and 29.2° at 11.1 GHz, consistent with the unique characteristics of a zero-index metamaterial.[29]

The frequency dependence of the refractive index, computed from the Snell-Descartes' law, is plotted in Fig. 10(a). We see that the increase in the refractive index with frequency is continuous throughout the negative index to the positive index region. Thus, the experimental result demonstrates that the proposed structure indeed exhibits a balanced property with a negative-zero-positive behavior. The slight shift of the transition frequency between the experimental and numerical retrieved results is mainly due to the lower substrate permittivity in the simulation. However, it is noted

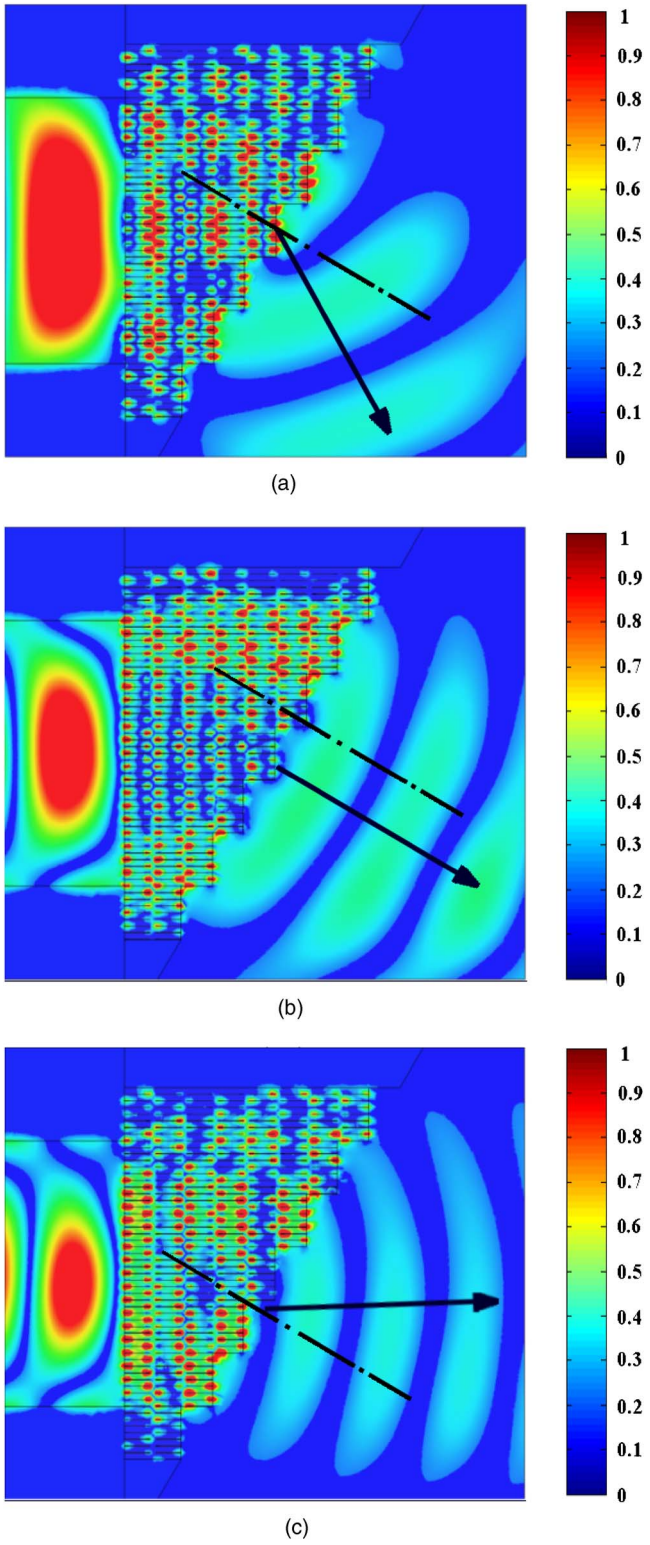

FIG. 8. (Color online) Electric field magnitude of refracted beam at different frequencies, (a) 10.0 GHz; (b) 12.8 GHz; (c) 15.0 GHz.

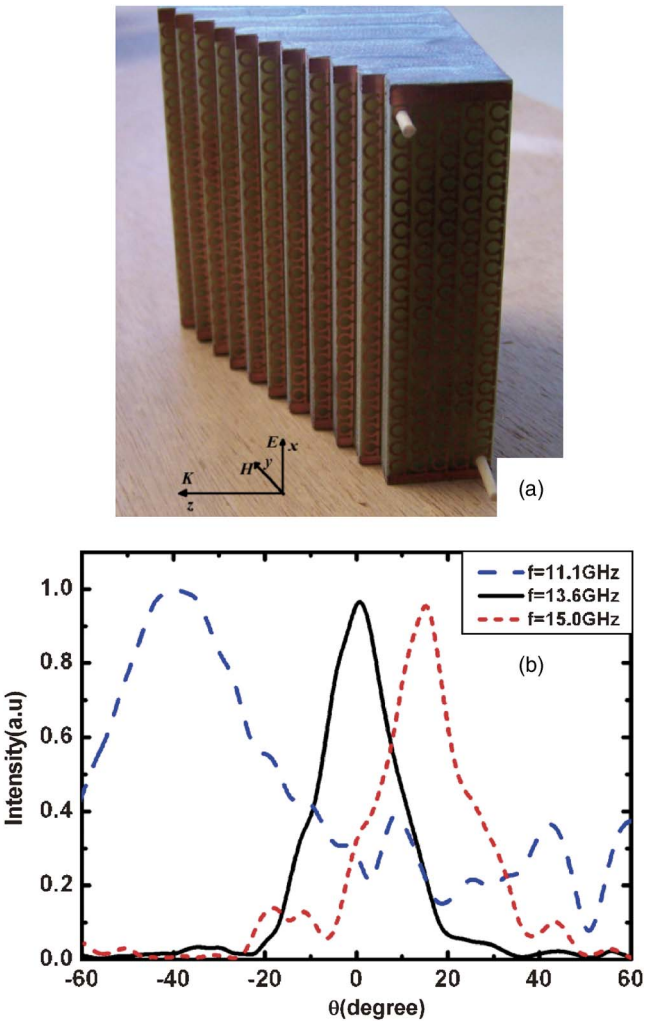

FIG. 9. (Color online) Experimental results of refraction measurement. (a) Photograph of the prismlike prototype. (b) Intensity of the refracted beam as a function of the probing horn angular position.

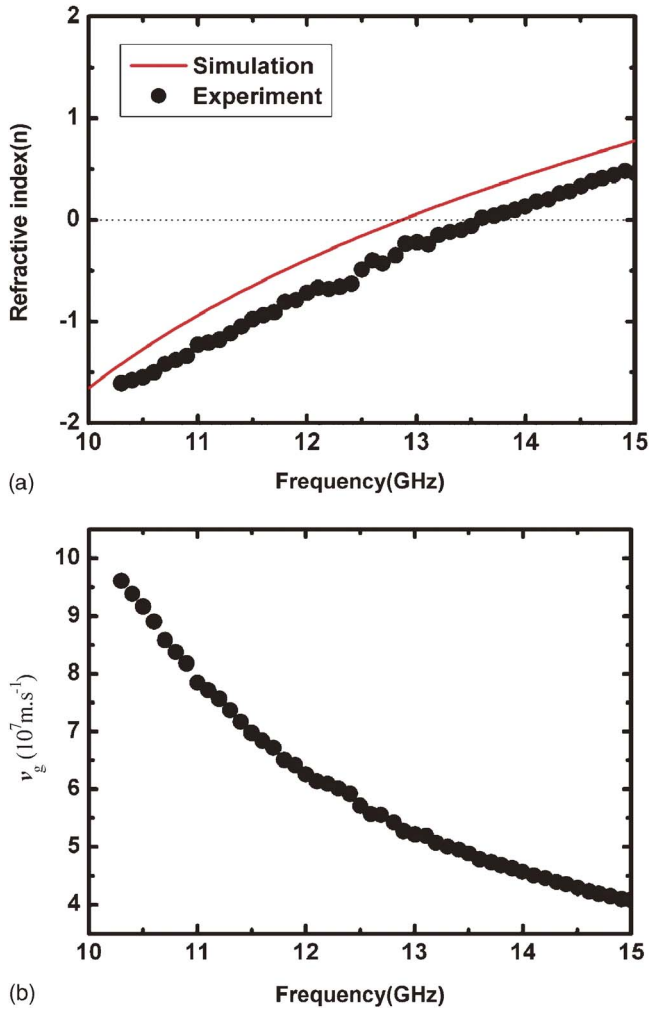

FIG. 10. (Color online) (a) Refractive index as a function of frequency. (b) Frequency dependence of the group velocity.

that the balanced condition is sustained because it does not depend on the substrate permittivity as shown in Fig. 5. Furthermore, the group velocity v_g of this metamaterial can also be obtained from the phase index $\mathrm{Re}(n)$ as follows:[16,30]

$$v_g = \frac{c}{\mathrm{Re}(n) + \omega \dfrac{\partial\, \mathrm{Re}(n)}{\partial \omega}}. \tag{12}$$

As shown in Fig. 10(b), the group velocity continuously decreases as the frequency is increased, indicating that the proposed structure is highly dispersive. For the transition frequency of 13.6 GHz, the group velocity is 4.8×10^7 m s^{-1}, which clearly shows that energy can be transmitted through the device and offers the possibility to make use of the desired frequency point of zero refractive index.

IV. CONCLUSION

In summary, we have proposed a balanced composite LH/RH metamaterial based on omega-type structures. We experimentally and numerically demonstrated that this structure exhibits a broad transmission window from 8.3 to 16.0 GHz with a seamless transition frequency of 13.6 GHz from the LH to the RH dispersion branch. The balanced condition was demonstrated theoretically on the basis of the calculation of the dispersion characteristics and subsequent retrieval of the effective parameters. This was confirmed experimentally by means of frequency and angle-resolved transmission experiments carried out for a slab and prism prototype. The refractive index as well as the group velocity exhibits a continuous frequency dependence, notably at $k=0$ with a nonvanishing group velocity. The insensitivity of the balanced frequency to the tuning of the substrate permittivity makes the proposed architecture an interesting platform for steerable antennas at microwave frequencies.

ACKNOWLEDGMENTS

F. Zhang would like to acknowledge the China Scholarship Council for his fellowship. The authors would like to thank E. Delos and S. Potet for their help in microwave characterization.

[1] V. G. Veselago, Sov. Phys. Usp. **10**, 509 (1968).
[2] R. Shelby, D. R. Smith, and S. Schultz, Science **292**, 77 (2001).
[3] D. R. Smith, W. J. Padila, D. C. Vier, S. C. Nemat-Nasser, and S. Schultz, Phys. Rev. Lett. **84**, 4184 (2000).
[4] J. B. Pendry, A. J. Holden, D. J. Ribbins, and W. J. Stewart, IEEE Trans.

Microwave Theory Tech. **47**, 2075 (1999).
[5]F. Zhang, Q. Zhao, Y. Liu, C. Luo, and X. Zhao, Chin. Phys. Lett. **21**, 1330 (2004).
[6]C. R. Simovski and S. He, Phys. Lett. A **311**, 254 (2003).
[7]J. Huangfu, L. Ran, H. Chen, X. Zhang, K. Chen, T. M. Grzegorczyk, and J. A. Kong, Appl. Phys. Lett. **84**, 1537 (2004).
[8]L. Ran, J. Huangfu, H. Chen, Y. Li, X. Zhang, K. Chen, and J. A. Kong, Phys. Rev. B **70**, 073102 (2004).
[9]L. Ran, J. Huangfu, H. Chen, X. Zhang, K. Cheng, T. M. Grzegorczyk, and J. A. Kong, Prog. Electromagn. Res. **51**, 249 (2005).
[10]E. Lheurette, O. Vanbésien, and D. Lippens, Microw. Opt. Technol. Lett. **49**, 84 (2007).
[11]A. Grbic and G. V. Eleftheriades, Phys. Rev. Lett. **92**, 117403 (2004).
[12]A. Lai, C. Caloz, and T. Itoh, IEEE Microw. Mag. **5**, 34 (2004).
[13]S. Lim, C. Caloz, and T. Itoh, IEEE Trans. Microwave Theory Tech. **53**, 161 (2004).
[14]A. Sanada, C. Caloz, and T. Itoh, IEEE Microw. Wirel. Compon. Lett. **14**, 68 (2004).
[15]T. Crepin, J. F. Lampin, T. Decoopman, X. Mélique, L. Desplanque, and D. Lippens, Appl. Phys. Lett. **87**, 104105 (2005).
[16]L. Brillouin, *Wave Propagation and Group Velocity* (Academic, New York, 1960).
[17]A. Grbic and G. V. Eleftheriades, J. Appl. Phys. **98**, 043106 (2005).
[18]P. Alitalo, S. Maslovski, and S. Tretyakov, J. Appl. Phys. **99**, 064912 (2006).
[19]R. Marques, F. Mesa, J. Martel, and F. Medina, IEEE Trans. Antennas Propag. **51**, 2572 (2003).
[20]J. B. Pendry, A. J. Holden, W. J. Stewart, and I. Youngs, Phys. Rev. Lett. **76**, 4773 (1996).
[21]I. Bulu, H. Caglayan, and E. Ozbay, Microw. Opt. Technol. Lett. **48**, 2611 (2006).
[22]T. Decoopman, O. Vanbesien, and D. Lippens, IEEE Microw. Wirel. Compon. Lett. **14**, 507 (2004).
[23]D. R. Smith, D. C. Vier, T. Koschny, and C. M. Soukoulis, Phys. Rev. E **71**, 036617 (2005).
[24]X. Chen, T. M. Grzegorczyk, B.-I. Wu, J. Pacheco, and J. A. Kong, Phys. Rev. E **70**, 016608 (2004).
[25]P. Markos and C. M. Soukoulis, Phys. Rev. B **65**, 033401 (2001).
[26]X. Xu, Y. Xi, D. Han, X. Liu, J. Zi, and Z. Zhu, Appl. Phys. Lett. **86**, 091112 (2005).
[27]T. Koschny, M. Kafesaki, E. N. Economou, and C. M. Soukoulis, Phys. Rev. Lett. **93**, 107402 (2004).
[28]R. A. Shelby, D. R. Smith, S. C. Nemat-Nasser, and S. Schultz, Appl. Phys. Lett. **78**, 489 (2001).
[29]S. Enoch, G. Tayeb, P. Sabouroux, N. Guérin, and P. Vincent, Phys. Rev. Lett. **89**, 213902 (2002).
[30]J. F. Woodley and M. Mojahedi, Phys. Rev. E **70**, 046603 (2004).

Omega-Type Balanced Composite Negative Refractive Index Materials

Éric Lheurette, Grégory Houzet, Jorge Carbonell, *Member, IEEE*, Fuli Zhang, Olivier Vanbésien, and Didier Lippens

***Abstract*—We report on the theoretical and experimental analysis of Omega-type metamaterials operating in X and Ku-bands. The prototypes are fabricated on the basis of metal waveguide technologies (hollow and TEM parallel plate) loaded with printed boards of interconnected Omega-shaped motifs. This interconnection of particles in the transverse direction leads to a broad left-handed band. Moreover, it is shown that such structures can be designed for a continuous negative-zero-positive index dispersion. This balanced composite behavior, so far known for periodically loaded transmission lines is verified experimentally with left- and right-handed dispersion branches extending from 8 to 12 and 12 to 16 GHz respectively. This zero-gap capability is explained on the basis of effective parameters retrieval.**

***Index Terms*—Composite right/left-handed metamaterial, negative refractive index material, omega-type particle, phase analysis.**

I. Introduction

NEGATIVE index materials (NIMs) are attracting an increasing interest with the prospect of novel functionalities afforded by their left-handed dispersion characteristics. So far, most of the studies published in the literature are devoted to the so-called split ring resonator (SRR) [1]. Such a pattern is equivalent to a current loop with an effective magnetic response achieved from non magnetic materials. In addition, a negative real part of the permittivity can be obtained with sub cut-off metal waveguide [2], wire arrays [3] and slot coupling windows [4]. Due to the high quality factor of the resonant particles, these kinds of structures exhibit a left-handed dispersion branch in a narrow band.

On the other hand, Itoh and Caloz [5] along with Eleftheriades *et al.* [6] suggested synthesizing a left-handed transmission propagation medium by means of one or two dimensional strip arrays loaded by series capacitances and shunt inductances. Such a structure, which is not resonant in its principle, shows broader left-handed passband as well as lower loss levels. This concept has been notably used for the experimental demonstration of sub-wavelength focusing around 1 GHz [7] and for the experimental evidence of backward waves at submillimeter wavelengths [8]. Moreover, it can be shown that the periodically loaded transmission line can operate in the balanced composite regime. This means that the metamaterial based structure exhibits a negative-zero-positive index dispersion diagram. Under such a balance condition, non vanishing group velocity is achieved at the corner frequency between left- and right-handed dispersion branches, a welcome feature for many applications such as routing devices. We study here a hybrid approach by means of an array of interconnected Omega elements. Over the past, the Omega-particle has been employed for the fabrication of chiral materials [9] and more recently its use for the synthesis of a double negative medium (DNG) was demonstrated. In this case, a double negative medium can be achieved with a "one particle" array while conventional NIMs need separate arrays of wires and SRRs. The results presented in [10], [11] and [12] illustrate the capability of such a pattern in terms of bandwidth for the LH dispersion branch. We target here to see whether this kind of structure can be used in the balanced composite regime. Indeed, it is believed that such regime can present a great interest for switching between the left- and right-handed bands in a zero gap scheme. Routing devices could take benefit of such a unique property.

We decided to interconnect the Omega-type particles in the direction transverse to the propagation of wave paying special attention to the cross over of the left- and right-handed dispersion branches. The main goal of this engineering approach is to synthesize a negative permittivity value via a set of continuous wires (Drude dispersion). From the retrieval of the effective parameters some interdependence in the electric and magnetic response will be pointed out. For the experimental verification of electromagnetic properties, two types of prototypes were fabricated. Both are characterized in a waveguide technology with a rectangular waveguide on the one hand, and a TEM parallel-plate waveguide on the other hand. Section II is related to the design rules of the structures on the basis of dispersion curves and transmission calculations. Experimental results are reported in Section III with special attention paid to the phase variations in order to localize the left- and right-handed transmission branches in the measured spectrum. Section IV discusses the balanced composite issue. Finally, Section V gives a summary of conclusions.

II. Design Rules and Fabrication

Basically, the Omega-like pattern combines a wire and a current loop in a single motif and is thus suitable for the design of a double-negative metamaterial, [10], [13]. In addition, the double-sided anti-symmetrical configuration has been chosen

Manuscript received July 09, 2007; revised April 24, 2008. Current version published November 14, 2008. This work was supported by the Centre National d'Études Spatiales, a bilateral "Picasso-Acción Integrada" project and Generalitat Valenciana under project GV/2007/215.

É. Lheurette, G. Houzet, F. Zhang, O. Vanbésien, and D. Lippens are with the Institut d'Électronique de Microélectronique et Nanotechnologies, Université des Sciences et Technologies de Lille, 59652 Villeneuve d'Ascq, Cedex France (e-mail: Eric.Lheurette@iemn.univ-lille1.fr).

J. Carbonell is with the Instituto de Telecommunicaciones y Aplicaciones Multimedia, Universidad Politécnica de Valencia, E-46022 Valencia, Spain (e-mail: jorcarol@dcom.upv.es).

Color versions of one or more of the figures in this paper are available online at http://ieeexplore.ieee.org.

Digital Object Identifier 10.1109/TAP.2008.2005448

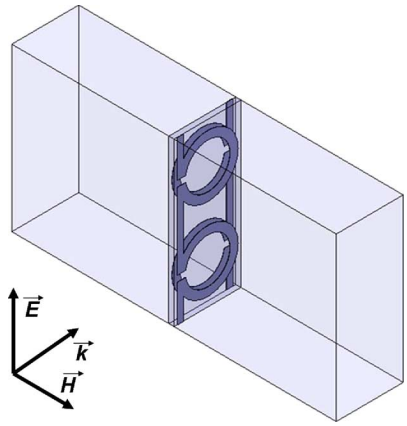

Fig. 1. Sketch view of one single cell structure mounted in a rectangular waveguide (structure I). The trihedron shows the excitation wave polarization.

to avoid bianisotropic effects [10]. Fig. 1 shows a sketch of the structure which will be frequency assessed in a hollow waveguide.

The topology of the Omega pattern has been retained with the constraint of an operation in the Ku-band. The structure includes two vertically interconnected Omega particles centered in the E-plane of the rectangular WR-62 waveguide.

The design procedure is based on a full three-dimensional solution of Maxwell equations using the finite element method. We used the commercial software HFSS developed by Ansoft. The transmission through a unit cell is simulated over a frequency band using the fundamental TE_{10} mode excitation and is quantified by the complex scattering matrix. We notably focused on the transmission spectrum of an elementary cell along the propagation direction which permits us to deduce the dispersion diagram. To this aim we used the procedure successfully applied in [14]. In short, the scattering matrix is converted into the corresponding chain matrix whose first term can be written as $A = \cosh(\gamma a)$ where $\gamma = \alpha + j\beta$ is the complex propagation constant and a the length of the unit cell. Indeed, the solutions obtained for a unit cell correspond to the propagating Bloch modes for an infinite array in the propagation direction as a consequence of the Bloch-Floquet theorem. In practice, the angular frequency (ω) dependence of the phase constant (β) leads to multiple branches. Only the solutions corresponding to a positive value of the group velocity v_g are considered to derive the dispersion diagram. Despite the fact that this approach neglects the mutual effects between adjacent patterns along the propagation direction, this preliminary calculation gives first indications on the composite left- and right-handed character of propagation. The geometrical parameters chosen on the basis of this numerical procedure are reported in Table I.

Initially, for the rectangular waveguide prototype, dimensions are those reported for structure I. For the fabrication, the patterns were etched in 35 μm copper layers on both sides of a Roger's Duroid substrate ($\varepsilon_r = 2.2$, thickness $= 254\ \mu$m) using conventional mechanical milling machine (LPKF Protomat). In order to achieve a reliable electrical connection with the waveguide top and bottom walls, two parallel strips have been added to the pattern. These strips are connected to the walls under pressure when the two shells forming the rectangular waveguide are screwed together. Fig. 2 shows a photo of the split waveguide with a PCB integrating an array of two Omegas along the vertical direction.

A second prototype was fabricated in a parallel plate technology (structure II). The slab-like prototype designed to be inserted in the parallel plate waveguide was fabricated by assembling one hundred Epoxy-Glass wafers ($\varepsilon_r = 4$, thickness $= 800\ \mu$m) (Fig. 3). This kind of structure was designed with special attention to the balance condition of the composite metamaterial. Indeed from the material point of view, a balance composite condition is achieved for an equality of the magnetic and electric plasma frequencies which characterize the dispersions of effective permeability and permittivity. In practice, it was found that such an equality, for the present broadside coupled

TABLE I
DIMENSIONS OF THE EXPERIMENTAL STRUCTURES

Parameter	Structure I	Structure II
a	3.3 mm	3.9 mm
b	4.1 mm	3.9 mm
s	0.3 mm	0.5 mm
r_{ext}	1.5 mm	1.6 mm
r_{int}	1.2 mm	1.1 mm

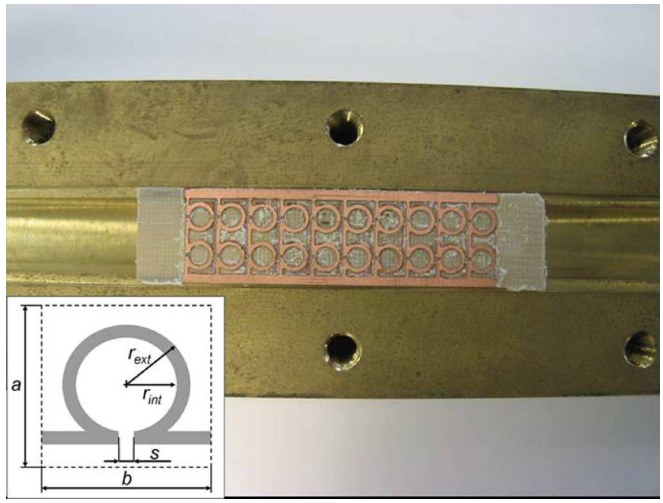

Fig. 2. Photograph of a 10 unit-cell structure included in one shell of the rectangular waveguide. Geometrical parameters are reported in insert.

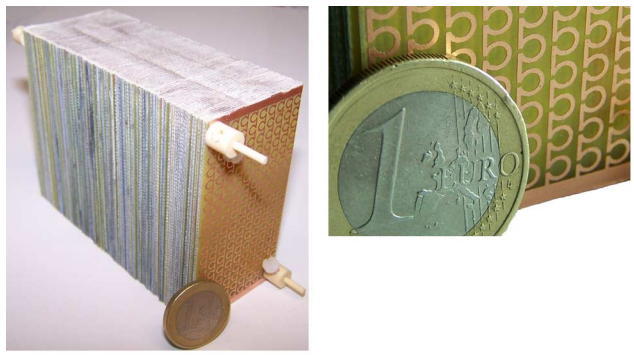

(a) (b)

Fig. 3. Views of the bulk metamaterial prototype.

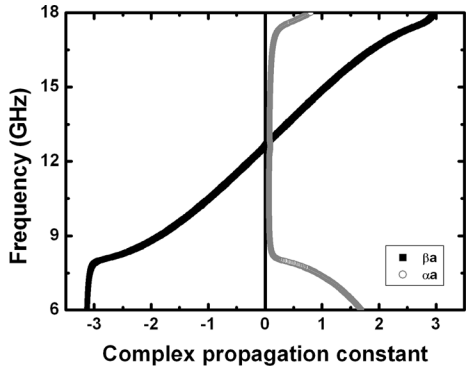

Fig. 4. Dispersion characteristics of structure II (numerical results).

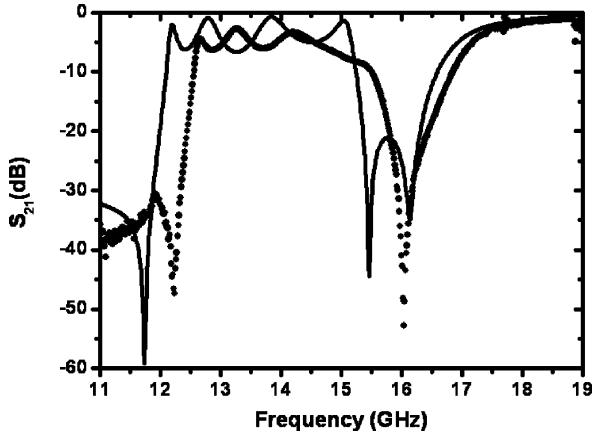

Fig. 5. Transmission parameter for 5 unit-cell structure I, measured (black dots) versus simulated (continuous line) characteristics.

Omega, can be met by properly choosing the coupling capacitance between the two current loops via the substrate permittivity, substrate thickness and strip width. Within the passband corresponding to the minimum value of the attenuation constant (see Fig. 4), the phase constant shows a continuous evolution from negative (from 8 to 12 GHz) to positive values (from 12 to 16 GHz) without any forbidden band in between.

Instead of mechanical milling outlined before, the single-side coppered substrates were chemically etched using ferric chloride solution. This technique was chosen here as regard with the great number of substrates to be processed. Moreover, this chemical method permits to avoid over-etching of the dielectric substrate. The consequence of an over-etched structure in case of mechanical milling will be detailed in the following section. The slab is built by stacking up all the substrates. To this aim, every substrate is drilled using alignment marks patterned on two opposite corners and the slab is held together by Teflon rods [see Fig. 3(a)]. Finally the top and bottom faces of the slab are mechanically milled in order to ensure a planar surface contact for the insertion in the parallel plate measurement setup.

III. Experimental Results

A. Rectangular Waveguide Characterization

For structure I, measurements were carried out on a *Hewlett-Packard* Vectorial Network Analyzer in the 10–18 GHz frequency band where propagation is monomode (in a WR-62 waveguide), using a TRL calibration procedure. In practice however the sweep has been extended above 18 GHz in order to reach the second transmission band. We have to keep in mind that these excursions above the calibration range only provide qualitative information. The wide band character of the interconnected Omega structure is illustrated in Fig. 5 with a transmission bandwidth extending from 12.5 to 15.5 GHz, where a forbidden band appears. The transmitted band also shows oscillations which are due to the finite dimension of the prototype (5 cells in this case), not considered in the Bloch-Floquet approach. It is known that each peak corresponds to the various modes of the envelope which results of the Fabry Pérot resonances within the finite length prototype. However, one can verify that the Bloch-Floquet procedure based on a single cell scattering parameter simulation is able to describe the capability on an array in terms of bandwidth.

Quantitatively, the left-handed bandwidth Δf is about 3 GHz with a central frequency f_0 of 13.7 GHz. The corresponding relative bandwidth defined by the ratio $\Delta f/f_0$ is about 22%. These values can be compared to those obtained in a previous work using conventional SRR and wire arrays in a similar technological context [14] ($\Delta f \sim 1$ GHz, $f_0 \sim 12$ GHz, $\Delta f/f_0 \sim 9.5\%$).

Two main differences can be noted between the measured and simulated characteristics. First, the transmission window is shifted towards the high frequencies with an average offset of 500 MHz. This difference may be attributed to imperfections in the fabrication of the structure. Indeed, the structures are defined on double-side processed Duroid substrates through a mechanical milling technique. As previously reported in [4], the tolerances of the milling process have to be taken into account because a positive frequency shift such as the one observed may be associated to an over-milling situation. This hypothesis is confirmed by Figs. 6 and 7 which compare the measured characteristics to the S_{ij} parameters of a single cell structure simulated for a constant nominal thickness of 0.254 mm and for a maximum milling tolerance of 0.02 mm. The measured frequency response is located between those corresponding to these limit simulated cases. This comment about frequency shifts illustrates the key importance of the substrate thickness in the engineering of the broad side coupled resonators by targeting a balance condition.

The observation of the magnitude of the S_{21} parameter does not permit to definitively conclude about left-handedness. As a complement to this magnitude information which is useful to assess the transmission frequency bands, a phase analysis is necessary to determine the left- or right handedness within these frequency windows. The phase determination of the transmission coefficient determined for prototypes of various lengths permits us to confirm left-handedness by means of a differential phase analysis [15]. Phase variations measured from 1 and 10 cells structure have been superposed to the dispersion diagram calculated from simulated S_{ij} parameters (Fig. 8) using the technique outlined in Section II. In this case, the over milling effect has been taken into account. Despite the difficulty to define accurately the structure length notably owing to the substrate ex-

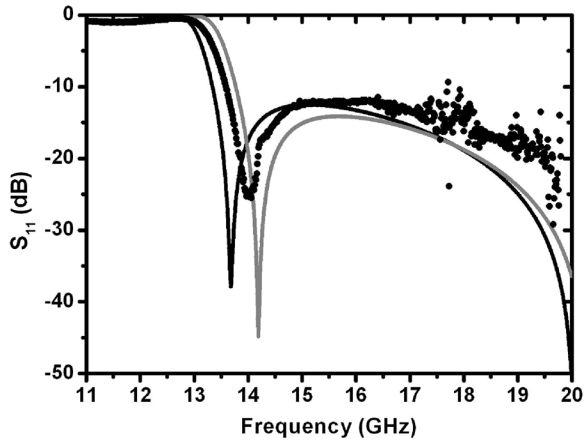

Fig. 6. Reflection parameter of a one unit cell structure of type I: measured (black dots), simulated for the nominal thickness (black solid line), simulated for the maximum milling tolerance (gray solid line).

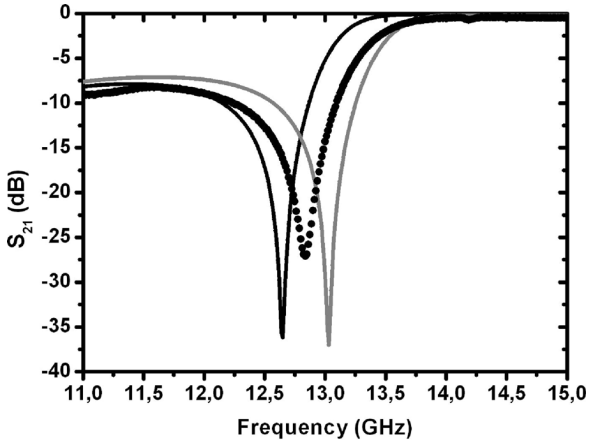

Fig. 7. Transmission parameter of a one unit cell structure of type I: measured (black dots), simulated for the nominal thickness (black solid line), simulated for the maximum milling tolerance (gray solid line).

tension visible in Fig. 2, the agreement between measured and calculated data is good for the one cell prototype. From Fig. 8 it can also be noticed that the 10 unit cell prototype shows a slight broader bandwidth. This illustrates the importance of coupling effects between adjacent cells in the propagation direction for this metamaterial embedded in a rectangular waveguide. These coupling effects are mainly due to the TE_{10} mode which implies a dependence of the magnetic field along the propagation direction. Indeed, these are less important in a TEM configuration as will be verified in the following.

B. Bulk Metamaterial Characterization

Since the prototype has a finite height (7.5 cm in the x-direction) this raises the difficulty of a pure free-space experiment. To alleviate such a problem, we decided to characterize the slab in a dual-plate waveguide as shown in Fig. 9. Indeed, such a waveguide technology mimics free-space condition owing to the top and bottom metal plates which play the role of perfect electric boundaries. By putting absorbing layers on the two other sides, a quasi-TEM mode beam can be fed to propagate through the slab. The incident wave is fed by a horn antenna and guided along the z-direction with the electric field in the x-direction

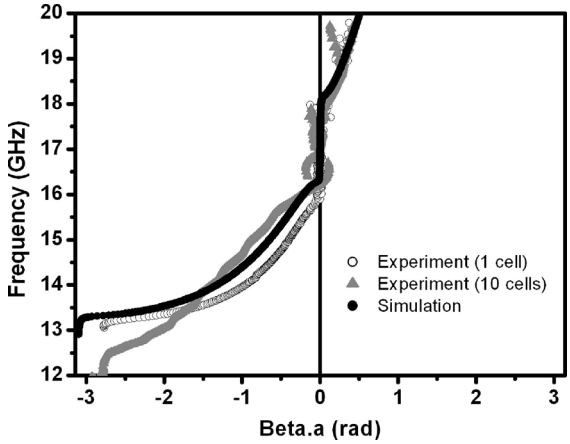

Fig. 8. Dispersion diagram of structure I (from measured and simulated results).

Fig. 9. The experiment setup for transmission measurement. Only the bottom plate is shown, top plate not shown for visibility purposes.

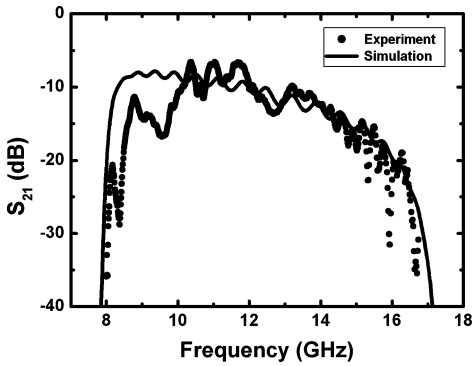

Fig. 10. Transmission parameter versus frequency for a 10-unit cell structure II.

and magnetic field in the y-direction (consequently perpendicular to the Omega pattern).

The transmission curve is plotted in Fig. 10 along with the simulated characteristic. Despite the irregularities depicted on the experimental curve, a transmission band is clearly identified between 8 and 16 GHz. Moreover, as predicted by the dispersion diagram the transition frequency which has been calculated around 12 GHz does not involve any significant attenuation which means that the structure is balanced as a reference to the definition introduced by C. Caloz and coworkers [16]. Moreover, it is important to note that the 10-cell transmission spectrum agrees with the simulated dispersion diagram. This means

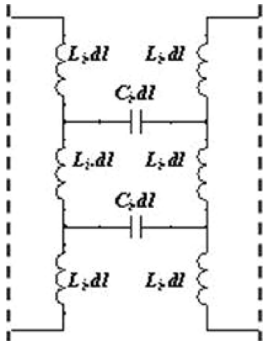

Fig. 11. Equivalent circuit of the broadside coupled Omega particle.

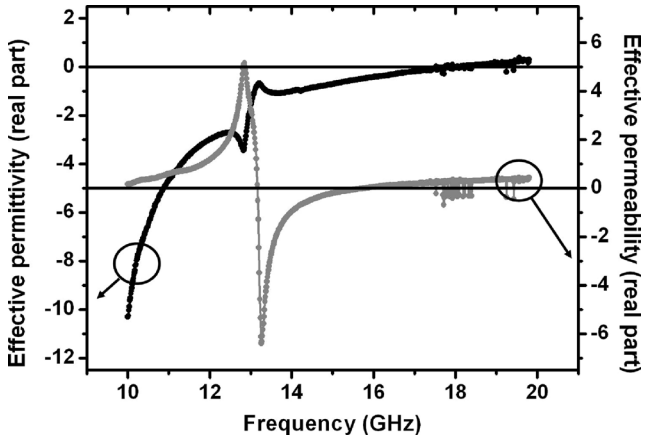

Fig. 12. Real parts of the effective permittivity and permeability extracted from a measured structure I unit cell.

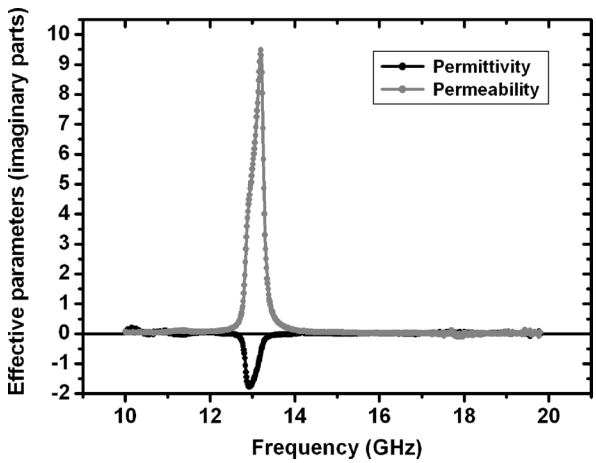

Fig. 13. Imaginary parts of the effective permittivity and permeability extracted from a measured structure I unit cell.

that the coupling effects in the propagation direction are much less important in this TEM environment as a comparison with the hollow waveguide structure which propagates a transverse electric mode. Therefore, both the broadband and balance effects are due to the intrinsic interconnected Omega particle.

For this structure, the total relative bandwidth $\Delta f/f_0$ is about 60%. Considering a transition frequency of 13 GHz, the left-handed branch width is about 40%. The left-handed behavior can be further explained by means of a lumped element model under the assumption of short scale comparing to the propagation wavelength. The Omega particle, which is known as single loop inductor in the framework of MMIC technology, can be modeled by a lumped inductive element. Capacitive elements are included along the propagation direction to model the broadside coupling between Omega layers. This leads to the equivalent circuit of a typical unit cell (Fig. 11) where L_i describes the inductance of a single Omega pattern and C_i the distributed capacitance between the loops of the broadside coupled Omegas. Further details on this lumped element model are given in [17]. To sum up, it can be concluded that the basic cell behaves as circuit element consisting in a series capacitance and a shunt inductance which is the generic representation of backward wave propagation media [18]. As mentioned before such a design is particularly interesting in terms of bandwidth and zero-gap operation capability. In the measured prototypes, 18 unit cells are interconnected between the two metallic planes of the dual-plane waveguide to form an Omega chain.

In the following section, the balance condition, which leads to a zero gap transmission spectrum, will be analyzed in terms of effective permittivity and permeability.

IV. DNG Behavior of the Effective Medium

In the present section, we will describe the electromagnetic behavior in terms of effective material properties. In other words, this means that the structure is approximated by an effective medium characterized by the frequency dependence of its effective permittivity and permeability. In practice we follow the procedure introduced in [19], based on a Fresnel inversion retrieval method. All the retrieval results were achieved by assuming an $e^{-j\omega t}$ time dependence. This procedure is applied to S_{ij} parameters which were measured for a single cell structure of type I. Figs. 12 and 13 show the variation versus frequency of the real and imaginary parts of the effective permittivity and of the effective permeability respectively. For clarity, the baseline was shifted for both variations. The frequency dependence of the effective permeability follows a Lorentz-type dispersion characteristic. The resonance and plasma frequencies are around 12.5 GHz and 15 GHz respectively. The dispersion characteristic of the effective permittivity follows, as a general trend, a Drude model. Namely ε_{eff} is negative below the electric plasma frequency (around 17.5 GHz here). However it can be observed that a small antiresonance is superimposed on this Drude like behavior. This illustrates some interplay between the magnetic and electric responses. However it also appears that the polarization conditions of the electric and magnetic fields are sufficient to minimize this dependence between the two responses which are consequently dominated either by a Lorentz-like or a Drude-like behavior.

It is important to note that this retrieval procedure leads to expected evolutions of the effective parameters on both their real (Fig. 12) and imaginary parts (Fig. 13). Let us note that the imaginary part is positive for a resonant permeability effect while it is negative for an antiresonant permittivity phenomenon. This resonance-antiresonance coupling does not violate the passivity requirement [20]. As aforementioned, the antiresonant effect is weak with respect to the general frequency behavior dominated by the Drude-like variation so that the imaginary part of ε_{eff}

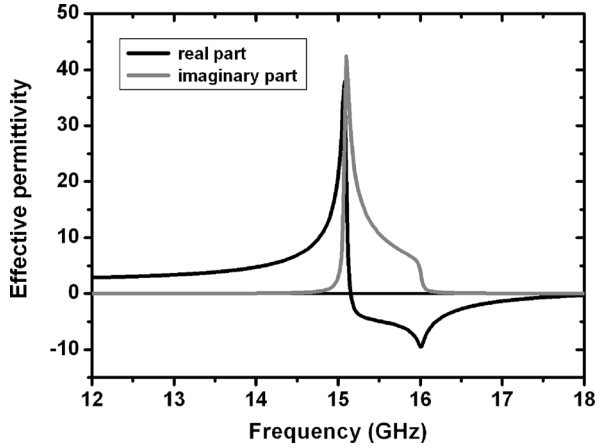

Fig. 14. Real and imaginary parts of the effective permittivity extracted from a simulated structure I unit cell (arms disconnected).

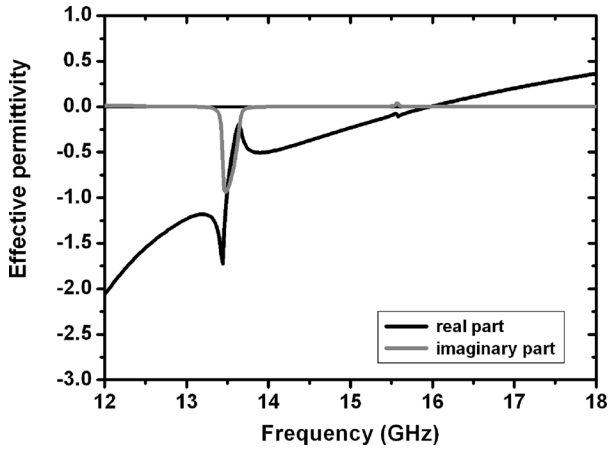

Fig. 15. Real and imaginary parts of the effective permittivity extracted from a simulated structure I unit cell (arms connected).

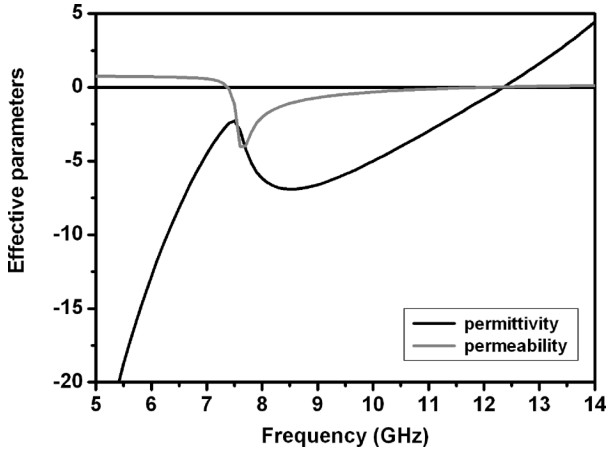

Fig. 16. Effective parameters of the balanced dual-plate structure (structure II), real parts.

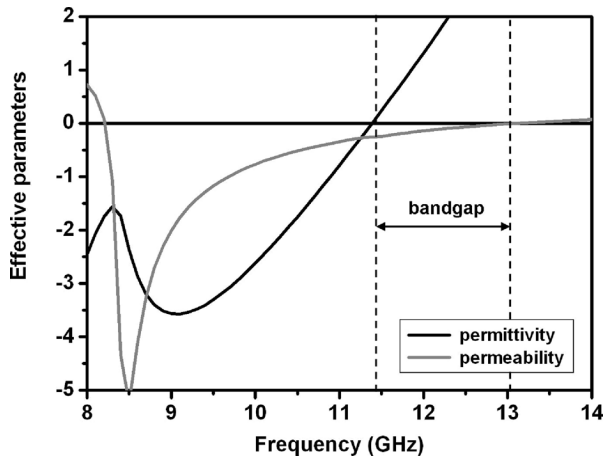

Fig. 17. Effective parameters of an unbalanced dual-plate structure (substrate thickness: 1 mm), real parts.

is much lower than the imaginary part of μ_{eff}. Furthermore, extracted parameters correspond to the whole one-dimensional guiding structure (the waveguide filled with Omega inclusions) and they are in general not exactly equal to the parameters that would be achieved for the plane wave illumination.

The benefit of connecting the Omega particles is illustrated by the Drude like increasing of ε_{eff}. Indeed, previous studies showed that this continuous evolution is lost if the wire is periodically cut, thus implying a resonant characteristic [20]–[22]. This partly explains also the narrow-band character observed in case of disconnected Omega arrays [13]. This hypothesis is confirmed by the direct comparison of retrieved parameters from disconnected and connected simulated structures. In case of isolated particles, the effective permittivity follows a Lorentz type evolution governed by the eigen resonance frequency of the Omega pattern (Fig. 14). In case of connected particles (Fig. 15), only the permeability follows a Lorentz law, whereas the permittivity, starting from a negative value increases according to a Drude function. It should be noted that a discontinuity under the form of antiresonance remains present in this permittivity variation. However, the amplitude of this incidence is much less important that for the disconnected media.

Fig. 16 depicts the real parts of effective permittivity and permeability simulated for the dual plate structure (structure II). For clarity purpose, the imaginary parts are not plotted here but it is important to note that both the passivity and causality requirements are satisfied [20], [23]. First, it is important to note that the bandwidth of the measured slab corresponds to the frequency domain where the effective permittivity and permeability are both negative. These curves retrieved from the single-cell scattering matrix simulations confirm the weak coupling effects between successive unit cells.

Second, the balanced condition is directly illustrated by the fact that the signs of permittivity and permeability change at the same frequency point. This is not the case with Fig. 17 where we simulated a substrate thickness increase of 20%. This close-up view shows a forbidden band between 11.5 and 13 GHz. These values can also be read from the dispersion diagram (Fig. 18).

This property leads to new options in terms of design. Indeed, let us recall that the technological challenges of periodically loaded transmission lines in a 3D configuration, notably at submillimeter wavelengths, are high. On the other hand, SRR based arrays are lossy and narrow band. On this basis, interconnected Omega media, owing to their hybrid concept, appear as

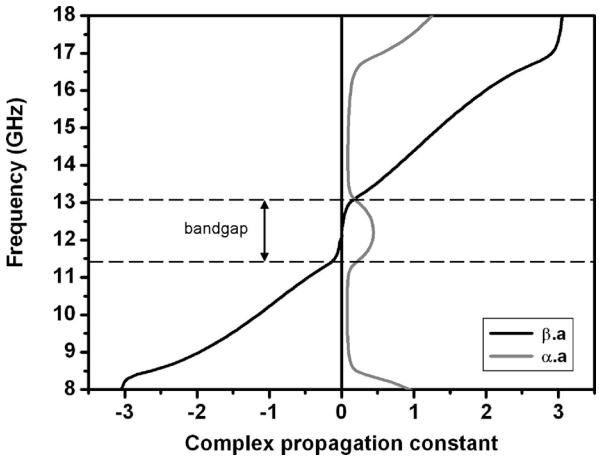

Fig. 18. Dispersion diagram (unbalanced structure).

a promising solution for terahertz technology. First elements of design for the band 140–220 GHz are reported in [17]. Moreover, this simplification of the elementary pattern can also pave new ways for the design of voltage controlled metamaterials.

V. Conclusion

An experimental analysis of Omega-based arrays has been carried out. Dispersion plots as well as relative permittivity and permeability as effective medium parameters have been retrieved from measured and simulated scattering matrix data.

Left-handedness has been discussed on the basis of effective permittivity and permeability characteristics and lumped element model. The broadband character of Omega type arrays has been assessed under the condition of lateral interconnection of the particles. A balance composite condition leading to a zero-gap between left- and right-handed bands has been experimentally demonstrated. These experiments carried out from waveguide and slab measurements, for one direction of the wave vector may be completed by refraction characterization using a prism like structure. Such an experiment leads to a zero-refraction angle corresponding to the crossing point between the left- and right-handed transmission bands as demonstrated in [24].

Acknowledgment

The authors would like to thank B. Bernardo and C. Bernard, for their assistance in the fabrication of the samples, E. Delos for help in the vectorial characterization of the prototypes, and C. Croenne and S. Pottet for fruitful discussions.

References

[1] J. B. Pendry, A. J. Holden, D. J. Robbins, and W. J. Stewart, "Magnetism from conductors and enhanced nonlinear phenomena," *IEEE Trans. Microw. Theory Tech.*, vol. 47, pp. 2075–2084, 1999.

[2] R. Marqués, J. Martel, F. Mesa, and F. Medina, "Left-handed-media simulation and transmission of EM waves in subwavelength split-ring-resonator-loaded metallic waveguides," *Phys. Rev. Lett.*, vol. 89, p. 183901, 2002.

[3] R. A. Shelby, D. R. Smith, and S. Schultz, "Experimental verification of a negative index of refraction," *Science*, pp. 77–79, 2001.

[4] J. Carbonell, L. J. Rogla, V. E. Boria, and D. Lippens, "Design and experimental verification of backward-wave propagation in periodic waveguide structures," *IEEE Trans. Microw. Theory Tech.*, vol. 54, pp. 1527–1533, 2006.

[5] C. Caloz and T. Itoh, "Application of the transmission line theory of left-handed (LH) materials to the realization of a microstrip "LH line"," in *IEEE Antennas and Propa. Society Int. Symp.*, 2002, vol. 2, pp. 412–415.

[6] A. Grbic and G. V. Eleftheriades, "Experimental verification of backward-wave radiation from a negative refractive index metamaterial," *J. Appl. Phys.*, vol. 92, pp. 5930–5935, 2002.

[7] A. Grbic and G. V. Eleftheriades, "Overcoming the diffraction limit with a planar left-handed transmission-line lens," *Phy. Rev. Lett.*, vol. 92, p. 117403, 2004.

[8] T. Crepin, J. F. Lampin, T. Decoopman, X. Melique, L. Desplanque, and D. Lippens, "Experimental evidence of backward waves on terahertz left-handed transmission lines," *Appl. Phys. Lett.*, vol. 87, p. 104105, 2005.

[9] M. M. I. Saadoun and N. Engheta, "A reciprocal phase shifter using novel pseudochiral or Ω medium," *Microw. Opt. Tecnhol. Lett.*, vol. 5, pp. 184–188, 1992.

[10] H. Jiangtao, R. Lixin, C. Hongsheng, Z. Xian-min, C. Kangsheng, M. G. Tomasz, and K. Jin Au, "Experimental confirmation of negative refractive index of a metamaterial composed of Omega-like metallic patterns," *Appl. Phys. Lett.*, vol. 84, pp. 1537–1539, 2004.

[11] L. Ran, J. Huangfu, H. Chen, Y. Li, X. Zhang, K. Chen, and J. A. Kong, "Microwave solid-state left-handed material with a broad bandwidth and an ultralow loss," *Phys. Rev. B: Cond. Matter and Mater. Phys.*, vol. 70, p. 073102, 2004.

[12] L. Ran, J. Huangfu, H. Chen, X. Zhang, K. Cheng, T. M. Grzegorczyk, and J. A. Kong, "Experimental study on several left-handed metamaterials," *Progr. Electromagn. Res.*, vol. PIER 51, pp. 249–279, 2005.

[13] C. R. Simovski, "Plane-wave reflection and transmission by grids of conducting [Omega]-particles and dispersion of [Omega] electromagnetic crystals," *AEU – Int. J. Electron. Commun.*, vol. 57, pp. 358–364, 2003.

[14] T. Decoopman, A. Marteau, E. Lheurette, O. Vanbesien, and D. Lippens, "Left-handed electromagnetic properties of split-ring resonator and wire loaded transmission line in a fin-line technology," *IEEE Trans. Microw. Theory Tech.*, vol. 54, pp. 1451–1457, 2006.

[15] O. F. Siddiqui, M. Mojahedi, and G. V. Eleftheriades, "Periodically loaded transmission line with effective negative refractive index and negative group velocity," *IEEE Trans. Antennas Propag.*, vol. 51, pp. 2619–2625, 2003.

[16] A. Lai, T. Itoh, and C. Caloz, "Composite right/left-handed transmission line metamaterials," *IEEE Microw. Mag.*, vol. 5, pp. 34–50, 2004.

[17] É. Lheurette, O. Vanbésien, and D. Lippens, "Double negative media using interconnected Omega-type metallic particles," *Microw. Opt. Tecnhol. Lett.*, vol. 49, pp. 84–90, 2007.

[18] L. Brillouin, *Wave Propagation in Periodic Structures*. New York: McGraw-Hill, 1946.

[19] W. B. Weir, "Automatic measurement of complex dielectric constant and permeability at microwave frequencies," *Proc. IEEE*, vol. 62, pp. 33–36, 1974.

[20] T. Koschny, P. Markos, E. N. Economou, D. R. Smith, D. C. Vier, and C. M. Soukoulis, "Impact of inherent periodic structure on effective medium description of left-handed and related metamaterials," *Phys. Rev. B: Cond. Matter and Mater. Phys.*, vol. 71, pp. 245105–22, 2005.

[21] J. Danglot, O. Vanbesien, and D. Lippens, "Active waveguides patterned in mixed 2D-3D metallic photonic crystal," *Electron. Lett.*, vol. 35, pp. 475–477, 1999.

[22] M. M. Sigalas, C. T. Chan, K. M. Ho, and C. M. Soukoulis, "Metallic photonic band-gap materials," *Phys. Rev. B*, vol. 52, p. 11744, 1995.

[23] C. R. Simovsky and S. A. Tretyakov, "Local constitutive parameters of metamaterials from an effective-medium perspective," *Phys. Rev. B*, vol. 75, p. 195111, 2007.

[24] F. Zhang, F. Zhang, G. Houzet, S. Potet, E. A. L. E. Lheurette, M. A. C. M. Chaubet, and D. A. L. D. Lippens, "Metamaterials-based routing devices for space applications," presented at the Int. Symp. on Signals, Syst. Electron. ISSSE'07, Montreal, QC, Canada, Jul. 30–Aug. 2 2007.

Éric Lheurette received the Ph.D. degree in microwave electronics from Lille University of Sciences and Technology, Lille, France, in 1996. His doctoral thesis concerned the technology of resonant tunnelling devices and, more generally, of heterostructure devices.

Following a Postdoctoral position with the Institut D'Électronique de Microélectronique et de Nanotechnologie (IEMN), with main emphasis on electromagnetic simulation, he became an Assistant professor with the University of Rouen. In September 2003, he joined the Quantum Opto and Micro Electronic device group (DOME), IEMN, Lille, as an Assistant Professor with the prospect to further develop the DOME group's terahertz technology program. His current interests concern non linear electronics and electromagnetism of complex propagation media.

Grégory Houzet was born in Cambrai, France, on November 21, 1982. He received the Master degree from the Université du Littoral Côte d'Opale (ULCO), Calais, France, in 2006. He is currently working toward the Ph.D. degree at the Institut d'Electronique, de Microélectronique et de Nanotechnologie (IEMN), Université des Sciences et Technologies de Lille (USTL), Lille, France.

His current interests concern the transmission medium with metamaterials, negative refraction devices and tuneability by ferroelectric thin films.

Jorge Carbonell (S'94–M'05) was born in Valencia, Spain, in 1971. He received the "Ingeniero de Telecomunicación" degree from the Universidad Politécnica de Valencia, Spain, in 1995 and the Ph.D. degree in electrical engineering (with Honors) from the University of Lille, Lille, France, in 1998.

From 1996 to 1998, he was with the Institut d'Electronique et de Microélectronique du Nord (IEMN), University of Lille, France, where his research activity included EM analysis of active and passive devices for space applications, and in particular photonic bandgap materials. From 1999 to 2003, he worked within the wireless industry with Ericsson, Siemens, Retevisión Móvil, and Telefónica Móviles. During that period he was involved in the design and deployment of second- and third-generation wireless communication systems and networks, and mainly focused on radio engineering. Since January 2004, he holds a Ramón y Cajal tenure-track research position at the Universidad Politécnica de Valencia,Spain. His current research activity concerns the analysis and design of passive periodic structures and metamaterials.

Dr. Carbonell was the recipient of a Human Capital and Mobility Fellowship.

Fuli Zhang was born in Xinxiang, China, on October 19, 1982. He received the B.S. degree in materials science and engineering and M.S. degree in optical engineering from Northwestern Polytechnical University, Xi'an, China, in 2003 and 2006, respectively. He is currently working towards the Ph.D. degree in the Institut d'Électronique de Microélectronique et Nanotechnologies (IEMN), Université des Sciences et Technologies de Lille, France.

His main research interests include the metamaterials of millimeter wave and Terahertz and its applications.

Olivier Vanbésien was born in Armentières, France, on November 11, 1964. He received the degree of engineer in 1987 from the Institut Supérieur d'Electronique du Nord (ISEN), Lille, France, and the third cycle thesis on quantum devices in 1991 from the university of Lille.

He then joined the High Frequency Department, Institut d'Electronique, de Microélectronique et de Nanotechnologie (IEMN) as a Chargé de Recherches CNRS. In November 2000, he was appointed Professor of Electronics at Lille University. His current interests concern metamaterials and photonic crystals, exploring both dielectric and metallic routes for applications of abnormal refraction from the terahertz region down to optics.

Didier Lippens received the Ph.D. degree in liquid crystal technology and the Doctorat d'état' in semiconductor physics from the University of Lille, Lille, France, in 1975 and 1984, respectively.

In 1980, he joined the Centre National de la Recherche Scientifique (CNRS). He is a Professor at the University of Sciences and technology, Lille, in connection with metamaterial technology and is currently the head of the Opto-and Micro-electronics Quantum Devices Group (DOME), Institute of Electronics Microelectronics and Nanotechnology (IEMN). He has authored and coauthored more than 130 journal papers and supervised 30 Ph.D. students. Over the past few years, he has been a member of several scientific boards of National and European networks including advanced electronics and nanophotonics networks depending on CNRS, TMR programmes and FET's of the European Commission. His current interests include photonic crystals and meta-materials and their tuneability via ferroelectrics and liquid crystals technologies. The targeting applications are cloaking or more generally electro-magnetic wave control through optics transformations along with super-and hyper- lens operating at terahertz frequencies and in the infra red spectral regions.

Negative index metamaterial at 100 GHz

Charles Croënne[1], Michel-François Foulon[1], Eric Lheurette[1], Xavier Mélique[1], Maurice Gheudin[2] and Didier Lippens[1]

Abstract – We present the free space characterization results of a metamaterial made of Split Ring Resonators and metallic wires scaled for an operation at 100 GHz. The interpretation of the measured transmission spectra is performed by means of a three dimensional electromagnetic modelisation which allows us to identify the left-handed band and find the origin of the losses using a parametric study over the number of elementary resonators in the propagation direction. We also extract the effective parameters values in the frequency band where the material behaves as a double negative medium, by means of two complementary methods, namely the Fresnel Inversion and the Field Summation.
Index Terms – Negative index, Metamaterial, Millimeter waves, Split ring resonators, Vectorial analysis.

I. Introduction

The slope reversal of the dispersion branch which allows defining a negative refractive index can be obtained by different means. For example, one can use phase advance propagation supports [1] or periodical arrays of micro resonators (Split Ring Resonators) and metallic wires [2]. Their fabrication and the values of their effective parameters are now sufficiently controlled in the microwave to enable applications ranging from flat lens focalization [3] to invisibility by means of an ultra-refractive cloak [4]. However, these materials must be optimized for operation in the Terahertz gap separating the optical and microwave ranges. In this paper we present the results of a numerical and experimental study of an array of SRR's and wires operating at 100 GHz.

II. Design and fabrication

Figure 1 shows a schematic of the structure of interest, developed by E. Ozbay at the University of Bilkent (Turkey) with dimensions based on [5]. Note that the type of double SRR investigated was originally proposed by J. B. Pendry [6]. The current loop pattern, from which the artificial magnetic dipole arises, is made of two concentric loops with diametrally opposed splits. In such a motif, the currents induced by the incident magnetic field circulate in the same direction in the two concentric loops and give rise to a magnetic response, whereas the currents induced by the electromotive force circulate in opposite directions in the two loops. Therefore they cannot create a significant magnetoelectric response. Another advantage of this design is the increase in capacitance introduced by the gap between the two rings. It allows operation at lower frequencies for a given unit cell size and therefore helps satisfying the metamaterial condition (the unit cell dimension should be very small compared to the wavelength). Taking into account the limitations of the UV-photolithography process, a unit cell size six times smaller than the wavelength in glass at operating frequency can be obtained.

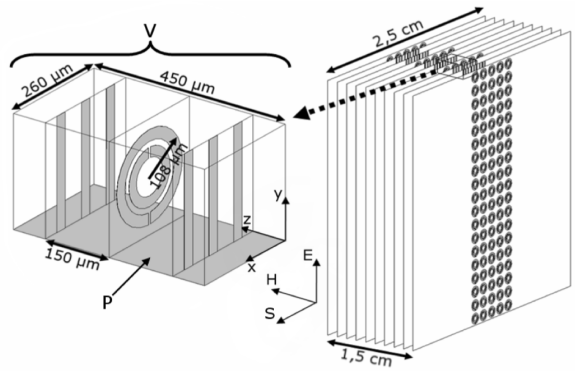

Fig. 1. Schematic of the structure and characteristic dimensions. The directions of the electric field E, magnetic field H and Poynting vector S are given for the incident wave. The V volume and P plane are respectively the volume of one unit cell and one of its boundary planes perpendicular to the incident electric field.

The behaviour of the wire array is primarily determined by its plasma frequency and shows a metallic behaviour below that frequency, or in other words a negative real part of effective permittivity [7]. Let us recall that its shift to the lower frequencies with respect to the bulk metal is not only a consequence of the filling factor but also of the increase of the effective mass due to the wire patterning. In our case, in order to maintain the plasma frequency in the 100 GHz range, the array of metallic wires is weakly diluted with a period smaller than the SRR's. Both SRR and wire patterns are printed on glass substrates by employing UV-photolithography followed by microfabrication with a metal thickness of 100 Å Ti/4500 Å Au. The characteristic dimensions are given in Figure 1. Most of them are micrometric, in particular the gap between the concentric loops and the width of the splits. Figure 2 shows an optical view of the stacking of wire and SRR patterns. The whole prototype is made of a stack of 100 glass substrates. It should be noted that the incident electromagnetic wavevector is parallel to the substrates. Moreover, the polarization must be chosen so that the incident electric field is oriented along

Received September 27th, 2007. Revised December 21th, 2007.

[1]IEMN, Université des Sciences et Technologies de Lille 1, Avenue Poincaré, BP 60069 Villeneuve d'Ascq Cedex, France;
E-mail:charles.croenne@iemn.univ.-lille1.fr;
[2]LERMA, Observatoire de Paris, 61 Avenue de l'Observatoire, 75014 Paris, France.

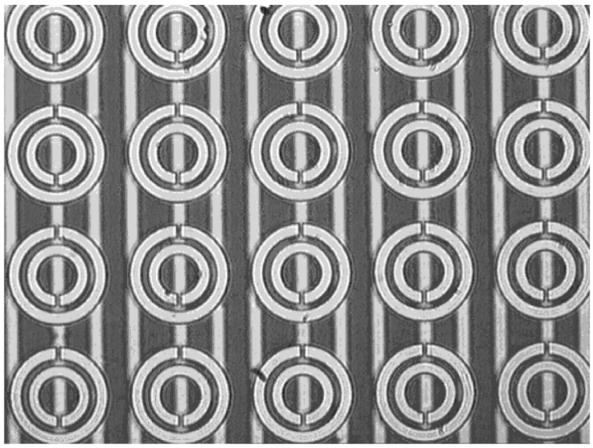

Fig. 2. Optical microscope view of the stack.

the wires whereas the magnetic field is *perpendicular* to the rings.

III. Free space measurements

The objective of the characterization is to deduce the values of refractive index as a function of frequency. Therefore it is imperative to complement the transmission measurement in amplitude performed at the University of Bilkent with vectorial transmission measurements. A first campaign was conducted at the IEMN using the HP 8510 Vector Network Analyser. In practice the prototype ($1.5 \times 2.5 \times 2.5$ cm^3) is inserted between two horn antennas operating in the V band (50-75 GHz). These are connected to the W waveguides (75-110 GHz) of the analyser mixers by means of matching guides. For the sake of simplicity, we used a TRL calibration between the guides without the horn antennas for these measurements. The reference planes are therefore taken at the waveguide flanges. Ideally, a free-space TRL calibration including the horns should be used. The measurements are performed under near field condition. The prototype is placed in the aperture of a baffle made of absorbing material in order to limit the parasitic transmission around.

Figure 3 shows the spectral response in transmission. The sample exhibits a pass band around 100 GHz with a bandwidth of 5%, in agreement with the electromagnetic simulations which were performed to design the structure. The transmission spectrum shown here is not normalized with respect to the transmission spectrum of the absorbing baffle. Its very low level is due in part to the losses in the glass substrates (supplied by Corning Glass) under low-angled incidence which account for 10 dB. The losses in these glass substrates were measured under normal incidence at the University of Bordeaux by means of electro-optical sampling and their absorption coefficient (κ) was reasonable. Therefore it seems that the 10 dB losses measured on a glass stack under low-angled incidence are due to the misalignments of the substrates and the roughness of the sides.

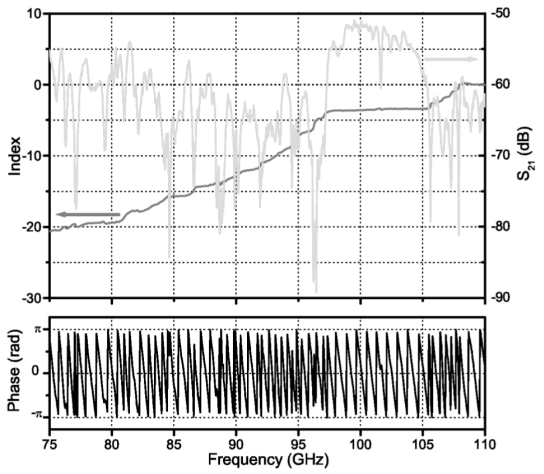

Fig. 3. Characterization results. Top graph : transmission spectrum in amplitude and extracted refractive index. Bottom graph : transmission spectrum in phase.

IV. Interpretation of the transmission in amplitude and phase

First, we tried to get a better understanding of the losses. To this aim, we performed simulations of the transmission levels *as a function of* the number of elementary cells in the propagation direction by using Ansoft HFSS (High Frequency Structure Simulator) software. The boundary conditions for our simulation domain are perfect electric conductors on the upper and lower boundaries and perfect magnetic conductors on the side boundaries. In the polarization and incidence used here they reproduce periodic boundary conditions. For gold, a finite conductivity is used.

Figure 4 illustrates the calculated *modulus* of the transmission for a prototype including 5 elementary cells. The measured (Figure 4) and calculated (Figure 5) scattering parameters versus frequency both show a transmission window around 100 GHz. However the calculated transmission window lies at slightly higher frequencies with re-

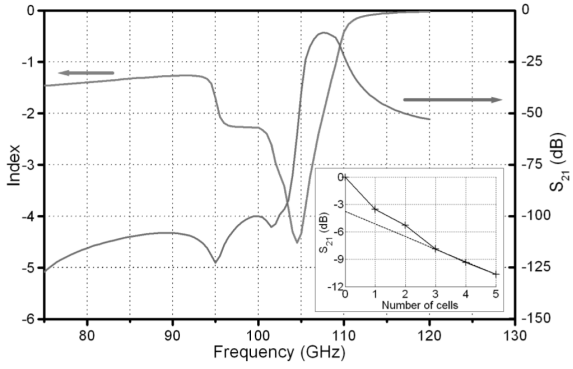

Fig. 4. Transmission and refractive index for 5 elementary cells. Insert: insertion losses as a function of the number of cells.

spect to the experimental one. A posteriori it was checked by a numerical parametric analysis that the resonant frequency of SRR is strongly dependent on the permittivity value of the substrate and on its dispersion. The permittivity of the glass used for the prototype being not known accurately, this uncertainty can explain the discrepancy. We can also notice a low level of transmission of -10 dB for 5 cells (at this number of cells we reach the limit of our calculation tools in terms of memory consumption) which can explain an important part of our measured losses, considering that the prototype has 10 cells in the propagation direction. The parametric study on the number of cells (insert of Figure 4) shows that the insertion losses (expressed in dB) at the center of the passband are not a linear function of the number of cells. This can be attributed to the different environment seen by the different layers. Therefore, a thin prototype (one or two cells in the propagation direction) has more losses per cell than a thick one. Since the simulations for structures thicker than 3 cells give a value of losses per cell of 1.4 dB this can account for about -17.5 dB of losses for the prototype.

Using a Fresnel Inversion method which will be presented in detail in the next section, we can extract the refractive index from the 5-cell simulation. As an illustration, the real part of the index was reported in Figure 4. In the passband the index is negative with a minimum value of -4.5, which shows that this structure is left-handed in this frequency band.

This result is corroborated by the measurement of the transmission phase for the prototype (Figure 3) including the access zones from which we deduce the phase delay inside the material, and therefore the refractive index, also reported in Figure 3. We obtain an almost constant value of index in the transmission band.

V. Retrieval technique and field summation: calculation of the effective permittivity and permeability

In this part we will use the two complementary methods of effective material parameter calculation, namely the Fresnel Inversion (FI) and the Field Summation (FS).

For the FI, the idea is to solve the inverse problem of determining the complex values of permittivity and permeability of an homogenous material which would show the same S parameters as the micro-structured metamaterial. The outputs of this method are the complex values of refractive index and impedance, from which the complex permittivity and permeability are deduced.

More precisely, we first convert the S matrix obtained by simulation into its equivalent chain matrix. Then we can write:

$$\begin{pmatrix} A & B \\ C & D \end{pmatrix} = \begin{pmatrix} \cosh(\gamma a) & z \cdot \sinh(\gamma a) \\ (1/z)\sinh(\gamma a) & \cosh(\gamma a) \end{pmatrix} \quad (1)$$

with γ being the propagation constant, z the normalized impedance and a the length of the simulation domain in the propagation direction. From this we get:

$$\gamma a = \cosh^{-1}(A);\ z = \sqrt{B/C} \quad (2)$$

Both the complex hyperbolic inverse cosinus and square root functions are multibranch functions. For the square root, we just choose the branch that gives a positive value for the real part of z. For $\cosh^{-1}$ the problem is more difficult, in particular when there is more than one cell in the propagation direction. There is an infinity of branches but we can exclude half of them if we require the sign of α (real part of the propagation constant, representing the evanescence inside the material) to be positive. The remaining solutions are then all equal for the real part α and equal modulo $2\pi/a$ for the imaginary part β. However, we can safely make the hypothesis that at very low frequencies the imaginary part is between $-\pi/a$ and π/a. It is equivalent to saying that we cannot have left the first Brillouin zone yet, or that the metamaterial condition is met. As the frequency increases, we choose the branch that allows us to keep both β and $\partial\omega/\partial\beta$ (that is to say both group and phase velocities) continuous. It is important to note that this method makes no assumption on the metamaterial condition at higher frequencies.

Figure 5 shows the permittivity obtained for one cell whereas Figure 6 shows the permeability (lines with crosses). We note that the dispersion of permittivity mostly follows a Drude model whereas a strong resonance is evidenced on the frequency dependence of the permeability. For this last parameter we only get negative values of the real part between 106 and 109 GHz. As a consequence, the refractive index (Figure 7) is negative between these two frequencies, which is in agreement with the index extracted from the experimental phase. Between 98 and 106 GHz, the extracted refractive index shows a plateau with values very close to -5.2. This corresponds to the edge of the first Brillouin zone since, at 100 GHz and for a unit cell of length $a = 262.7\ \mu$m, $\beta = -\pi/a \Leftrightarrow \Re(n) = -5.71$. At this point we are satisfying the Bragg conditions and no

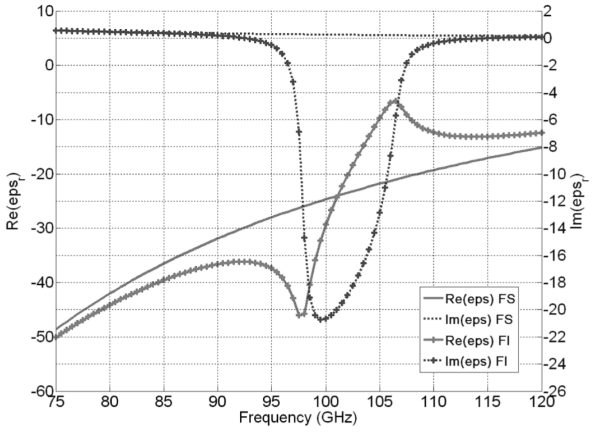

Fig. 5. Complex permittivity obtained by FI and FS as a function of frequency.

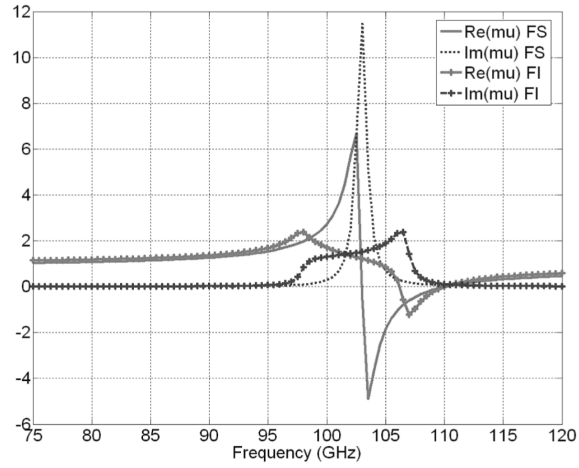

Fig. 6. Complex permeability obtained by FI and FS as a function of frequency.

longer the homogenization conditions. Therefore, it is an effect of the finite length of the structure.

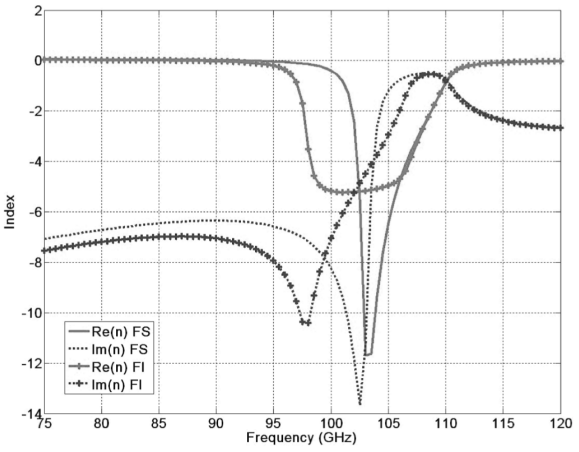

Fig. 7. Index dispersion obtained by FI and FS for one elementary cell.

The FS method relies on the definition of the effective parameters for homogenized materials [9, 10]. When the metamaterial condition is met, it is possible to replace the local values of the fields by their averages over one unit cell as given by equations 3 and 4. By properly chosing the integration domains, we can extract the complex values of permittivity and permeability from the EM field maps given by HFSS. More precisely, we compare the results of the integration of the electromagnetic fields in the volume of a unit cell with that of a boundary plane perpendicular to the electric field to deduce the effect of the cell. The relevant directions for the effective parameters and integration domains are shown in Figure 1.

$$\epsilon_{\text{eff}}^{yy} = \frac{\langle D^y \rangle_P}{\langle E^y \rangle_V} \tag{3}$$

$$\mu_{\text{eff}}^{zz} = \frac{\langle B^z \rangle_V}{\langle H^z \rangle_P} \tag{4}$$

In these expressions, the averaging operator $\langle\,\rangle$ should be taken as

$$\langle K^i \rangle_\Omega = \frac{1}{\Omega} \int_\Omega K^i(\vec{r}) d\vec{r}$$

with K^i the i component of the field quantity K and Ω a spatial integration domain.

However, directly applying these formulas to our structure will not give meaningful results because of the continuous wires placed in the direction of the incident electric field which cross the boundaries between the cells and more precisely the P plane. If we integrate the electric field on this plane, we lose the information carried by the conduction currents that flow between the cell and its neighbors. Therefore, we obtain a constant value of permittivity very close to the one of the glass substrate. In order to describe the effect of the continuous wires, the conduction currents must be converted into displacement currents at the intersection with the P plane. In other terms, we have to cut the wires when they cross the plane, thus creating locally a capacitance. Hence the concentration of the electric field can be integrated.

However, a simple cut of the wires introduces an important perturbation in our structure. Instead of continuous wires we have metallic segments which possess a resonance frequency. To compensate for this effect we have to increase the value of the capacitance such that its resonance is shifted to the lower frequencies. A possibility would be to reduce the gap width. However, applying the FS method on the resulting structure would be much more difficult since all the information about the conduction current would be included in a very limited surface on the P plane. In other words we would have to integrate the most important phenomenon with a very limited number of points. To overcome this difficulty, we have chosen to add at each wire cut a large metallic square parallel to the P plane (and therefore perpendicular to the wires). This way, we can both increase the capacitance and let the field spread over a larger surface. This has to be done until the S parameters remain unchanged. The final structure has 1 µm long cuts with 50 per 50 µm perpendicular metallic plates (which can be seen in Figure 8). With such modifications we can use the FS method on our structure without modifying its behavior.

Since we integrate over the length of the unit cell along the propagation direction, this method neglects the effects of the finite length of our cell. We obtain effective parameters that follow exactly a Drude and a Lorentz-like model, which confirms that our cell behaves as 2 superimposed arrays of SRRs and continuous wires, with an added effect only due to the cell size.

One of the main advantages of the Field Summation method is that we can locally perform the extraction of the effective parameters of individual cells in a multicell simulation domain. For example, we will consider here 3 cells along the propagation direction (Figure 8)and we will use the FS technique to retrieve the effective parameters of

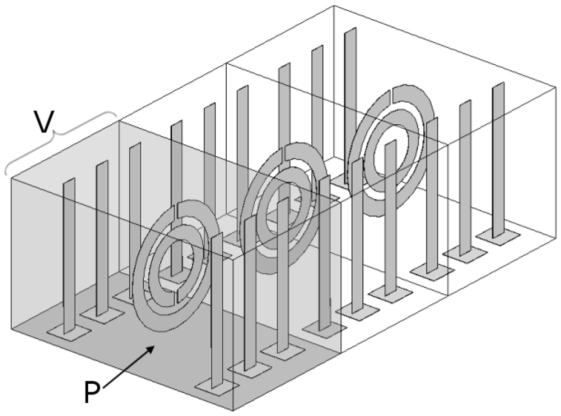

Fig. 8. Schematic of the multicell simulation domain properly modified for the application of the FS technique. The shaded plane and volume are respectively the P and V integration domains for the first interface cell.

each individual cell. Figure 9 and Figure 10 show respectively the permittivity and permeability obtained for the 3 cells. The most visible features here are the very large resonances appearing only in the second and third cells in the propagation direction. They are quite difficult to interpret since they do not correspond to significant features on the transmission spectrum, even in the frequency bands where they predict a double negative behavior with low losses (for example at 92 GHz in the second cell). However, in the frequency band where the metamaterial condition is met according to the FI (that is to say between 106 and 110 GHz) they indicate that the permittivity values are approximately the same in the three consecutive cells because this parameter does not follow a resonant behavior. On the other hand, the permeability values differ significantly. More precisely we can see that the resonances in the first and last cells are stronger but associated with more losses (larger imaginary parts). This corroborates our interpretation of the study of losses as a function of the number of cells.

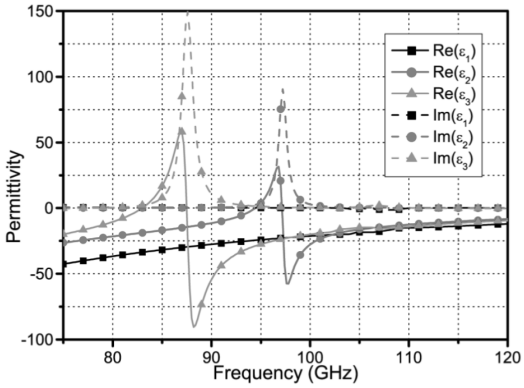

Fig. 9. Permittivity obtained by FS on the elementary cells of a 3-cell simulation domain.

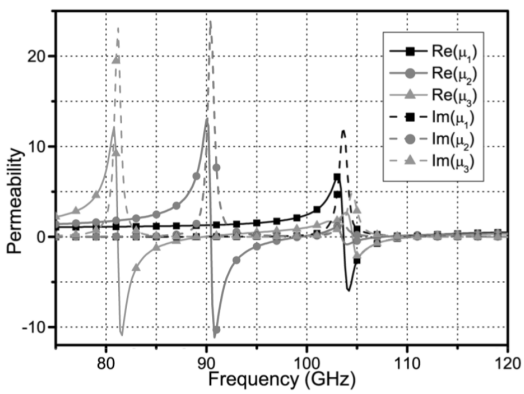

Fig. 10. Permeability obtained by FS on the elementary cells of a 3-cell simulation domain.

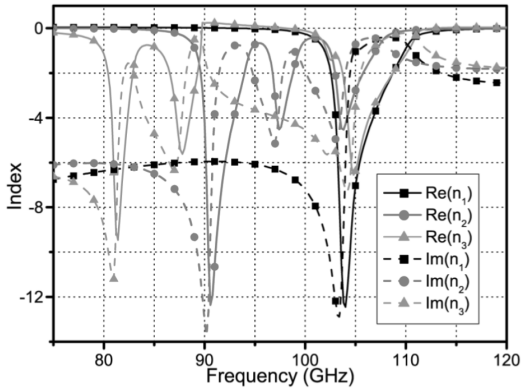

Fig. 11. Refractive index obtained by FS on the elementary cells of a 3-cell simulation domain.

As a direct consequence, the refractive index (Figure 11) in the transmission band is similar in the first and third cells but larger than in the second one. Lastly, the calculation of the average of the three local values of refractive index (Figure 12) is in agreement with the values obtained by FI in the transmission band.

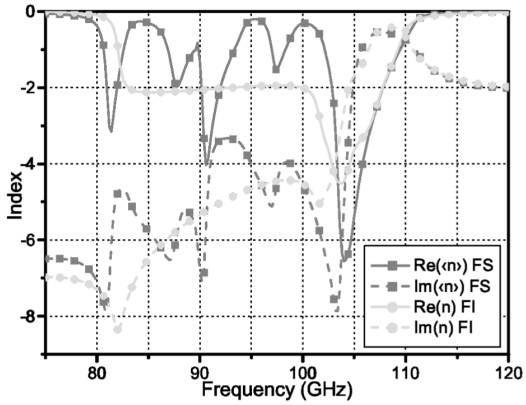

Fig. 12. Comparison of the average of the three local indexes obtained by FS with the index obtained by FI.

VI. Conclusion

By means of a free space vector characterization we have verified, for the first time to our knowledge, the possibility of obtaining a left-handed passband around 100 GHz, fabricating a metamaterial made of continuous wire arrays and micro-resonators. This was demonstrated directly on the phase measurement with limits of validity based on numerical simulations.

Acknowledgements

This work was conducted in the framework of a DGA (Délégation Générale pour l'Armement) contract. C. Croënne and M. Foulon thank the DGA for its financial support. D. Lippens would also like to thank E. Ozbay for lending the prototype.

References

[1] Crépin, T.; Lampin, J.F.; Decoopman, T.; Mélique, X.; Desplanque, L.; Lippens, D.: Experimental evidence of backward waves on terahertz left-handed transmission lines. Appl. Phys. Lett. **87** (2005), 104105.

[2] Gokkavas, M.; Guven, K.; Bulu, I.; Aydin, K.; Penciu, R.S.; Kafesaki, M.; Soukoulis, C.M.; Ozbay, E.: Experimental demonstration of a left-handed metamaterial operating at 100 GHz. Phys. Rev. B **73** (2006), 193103.

[3] Aydin, K.; Bulu, I.; Ozbay, E.: Subswavelength resolution with a negative-index metamaterial superlens. Appl. Phys. Lett. **90** (2007), 254102.

[4] Schurig, D.; Mock, J.J.; Justice, B.J.; Cummer, S.A.; Pendry, J.B.; Starr, A.F.; Smith, D.R.: Metamaterial electromagnetic cloak at microwave frequencies. Science **314** (2006), 977-980.

[5] Penciu, R.; Kafesaki, M.; Gundogdu, T.F.; Economou, E.N.; Soukoulis, C.M.: Theorical study of left-handed behavior of composite metamaterials. Photon. Nanostruct. **4** (2006), 12-16.

[6] Pendry, J.B.; Holden, A.J.; Robbins, D.J.; Stewart, W.J.: Magnetism from conductors and enhanced nonlinear phenomena. IEEE Trans. Microwave Theory and Tech. **47** (1999), 2075-2084.

[7] Pendry, J.B.; Holden, A.J.; Stewart, W.J.; Youngs, I.: Extremely low frequency plasmons in metallic mesostructures. Phys. Rev. Lett. **76** (1996), 4773-4776.

[8] Croënne, C.; Lerat, J.F.; Malléjac, N.; Acher, O.; Lippens, D.: Extraction ab-initio des paramètres effectifs des métamatériaux. Proc. of the Journées Nationales Microondes, 2007.

[9] Acher, O.; Adenot, A.L.; Duverger, F.: Fresnel coefficients at an interface with a lamellar composite material. Phys. Rev. B **62** (2000), 13748-13756.

[10] Smith, D.R.; Pendry, J.B.: Homogenization of metamaterials by field averaging (invited paper). J. Opt. Soc. Am. B **23** (2006), 391-403.

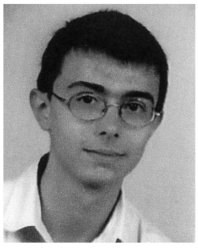

Charles Croënne was born in Arras, France, on April 17, 1983. He received the engineer degree from the Ecole Centrale de Lille (France) and the M.S. degree from Lille University of Sciences and Technology (USTL) in 2006. He is currently working towards the Ph.D. degree within the Quantum Opto and Micro Electronic Device group (DOME) of the Institut d'Electronique de Microélectronique et de Nanotechnologie (IEMN).

Eric Lheurette received the Ph.D. in microwave electronics from USTL in 1996. His doctoral thesis concerned the technology of resonant tunnelling devices and, more generally, of heterostructure devices. Following a post-doctoral position with the IEMN, with main emphasis on electromagnetic simulation, he became an Assistant Professor with the University of Rouen. In September 2003, he joined the IEMN as an Assistant Professor with the prospect to further develop the DOME group's Terahertz technology program. His current interests concern non linear electronics and electromagnetism of complex propagation media.

Michel-Franọise Foulon received the engineering degree from the "Institut Supérieur d'Electronique du Nord" (Lille) in 2003. He spent one year in 2003 at Montreal's "Ecole Polytechnique". He is currently finishing his Ph.D. in microwave electronics from Lille University of Sciences and Technologies (USTL) in the DOME group of the IEMN. His research interests are mainly in simulation and characterisation of passive and active metamaterials and non linear devices such as Hetero Structure Barrier Varactors both in temporal and frequency domains.

Xavier Mélique was born in Tourcoing, France, on April 12, 1972. He received the M.S. and Ph.D. degrees from the USTL in 1994 and 1999, respectively. He is currently an Assistant Professor with the IEMN. His main research interests concern the development and the fabrication of left-handed metamaterials in free space configuration and in waveguiding structures. Dielectric and metallic nanostructuration technologies are developed for artificial media exhibiting backward propagation or negative refraction effects and operating from Terahertz up to optical frequencies.

Didier Lippens received the Master of Science degree in electronics engineering, Ph.D. degree and Doctor ès Sciences degree from Lille University of Sciences and Technology (USTL) in 1975, 1978 and 1984, respectively. From 1980 to 1981 he was Research Engineer at Thomson CSF. He led the Quantum and Terahertz Devices team up to 2001. He currently leads the Quantum Opto and Micro Electronic Device group (DOME), Institut d'Electronique de Microélectronique et de Nanotechnologie (IEMN), USTL. He is currently a Professor of electrical engineering at the USTL where his main interests are nanotechnology and nanosciences. He has been involved with molecular dynamics in liquid crystals and with semiconductor physics, and is currently more involved with non-linear electronics and opto-electronics along with electromagnetism in artificial media. He has undertaken pioneering research on resonant tunnelling devices and more generally on heterostructure semiconductor devices. His current interests are Terahertz sources, most notably quantum cascade laser (QCL's), photomixers and heterostructure barrier varactors, photonic bandgaps and metamaterials-based passive and active devices.

open-loop resonator shown in Figure 1(b), the proposed structure efficiently employs the space inside the loop, resulting in size reduction. The dimensions of the loops in Figure 1(b) are the same with that in Figure 1(a). The resonant frequencies of the two structures are compared as shown in Figure 2. As can be seen in Figure 2, the resonant frequency of the proposed structure is 1.135 GHz, whereas that of the conventional one is 2.050 GHz. This means that 45% size reduction is achieved.

As a demonstration, a filter of this type is designed and fabricated. The substrate with relative dielectric constant of 6.15 and a thickness of 0.635 mm is used for this design. After an optimally design process, the dimensions of the proposed structure are chosen as follows:

$W1 = 0.93$ mm, $W2 = 0.5$ mm, $L1 = 9.85$ mm, $L2 = L3 = 1.5$ mm, $g1 = g2 = 0.2$ mm, $S1 = 0.2$ mm, $S2 = 0.3$ mm, $S3 = 0.5$ mm.

3. SIMULATED AND MEASURED RESULTS

The simulation was accomplished using IE3D simulator, based on the method of moment (MoM). Measurements were carried out on an HP8510 vector network analyzer. Figure 3 shows the simulated and measured results of the proposed bandpass filter, where solid lines denote the measurements and dashed lines denote the simulations. At the center frequency of 1.135 GHz, the fabricated filter has a 3 dB fractional bandwidth of 2.6%, ranging from 1.12 to 1.15 GHz. The insertion loss and return loss are about 2 and −15 dB, respectively. Two transmission zeros are realized at about 1.04 and 1.27 GHz, and the attenuation at these frequencies exceeds 40 dB. The measured results agree well with the simulated ones. The slight shift in frequency between the simulation and measurement is attributed to the fabrication tolerances and the assumption of an infinite dielectric and ground plane in the simulation.

4. CONCLUSION

A compact microstrip bandpass filter using open-loop resonators with captive loading has been presented. The filter has a compact size, which is 45% smaller than the conventional filters using square open loop. The filter shows sharp rejections of outbands owing to the transmission zeros near the passband. The proposed filter has been validated by simulation and experiment. Both the simulated and measured results demonstrate almost identical electrical performances.

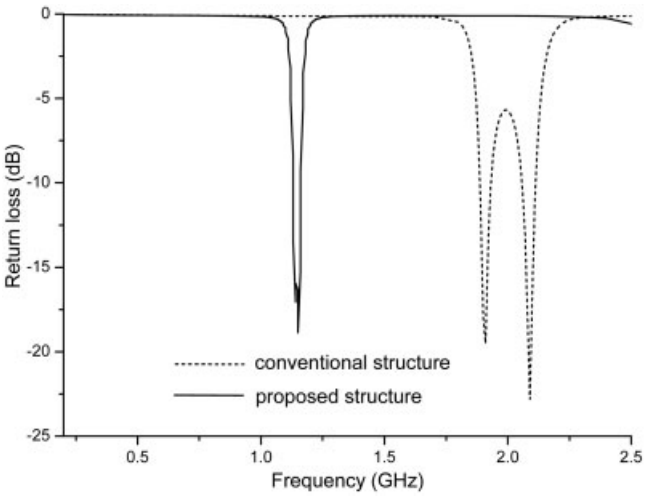

Figure 2 Simulated return loss for different resonator structures

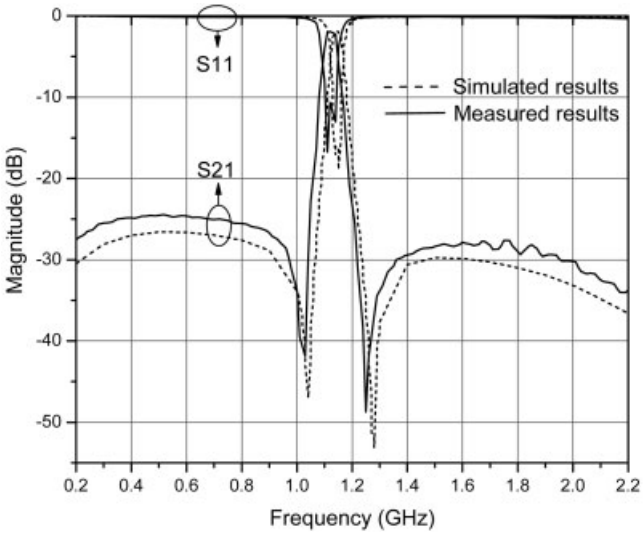

Figure 3 Simulated and measured results

ACKNOWLEDGMENT

The work described in this paper was supported by the Research Grants Council of the Hong Kong SAR under grant no. CityU121905.

REFERENCES

1. J.S. Hong and M.J. Lancaster, Theory and experiment of novel microstrip slow-wave open-loop resonator filters, IEEE Trans Microwave Theory Tech 45 (1997), 2358–2365.
2. C.C. Yu and K. Chang, Novel compact elliptic-function narrow-band bandpass filters using microstrip open-loop resonators with coupled and crossing lines, IEEE Trans Microwave Theory Tech 46 (1998), 952–958.
3. A. Gorur, A novel dual-mode bandpass filter with wide stopband using the properties of microstrip open-loop resonator, IEEE Microwave Wireless Compon Lett 12 (2002), 386–388.
4. J.X. Chen, J. Xu and Q. Xue, A novel compact microstrip bandpass filter using an open loop resonator with radial stub, Microwave Opt Tech Lett 46 (2005), 387–389.
5. M.H. Awida, A.M. E Safwat and H. El-Hennawy, Dual-mode microstrip bandpass filter using ring of arrows resonator, Electron Lett 41 (2005), 1335–1336.

DOUBLE NEGATIVE MEDIA USING INTERCONNECTED Ω-TYPE METALLIC PARTICLES

É. Lheurette, O. Vanbésien, and D. Lippens
Institut d'Électronique
de Microélectronique et de Nanotechnologie
Université des Sciences et Technologies de Lille
59652 Villeneuve d'Ascq Cedex, France

Received 2 June 2006

ABSTRACT: *We report on broadband low-loss properties of Ω-based metamaterials. It is shown that interconnecting elementary current-loops via their arms can yield to a relative bandwidth of around 70% for infinite arrays. Combining interconnected and disconnected sections permits one to engineer the left-handed and right-handed dispersion branches with the prospect of composite artificial media such as those*

initially proposed by Itoh and coworkers (IEEE Microwave Mag 34 (2004) 34–50) in the context of transmission lines. This typical behavior is interpreted through a lumped element model. At last, some guidelines to optimize the transmission properties of Ω-shaped arrays are presented. These results are discussed on the basis of recently published data concerning Ω-shaped and C-shaped particles. © 2006 Wiley Periodicals, Inc. Microwave Opt Technol Lett 49: 84–90, 2007; Published online in Wiley InterScience (www.interscience.wiley.com). DOI 10.1002/mop.22034

Key words: *metamaterial; left-handed; terahertz; omega*

1. INTRODUCTION

The theoretical work of Veselago introduced the left-handed electromagnetism rules early in 1968 [1]. In the 1990s, Pendry et al. showed how a negative effective permittivity could be obtained into the far infrared region and even in Gigahertz band by "diluting" a metal, making use of thin wire periodic arrays. He also suggested the use of the so-called Split Ring Resonator (SRR) arrays made of nonmagnetic conducting sheets which exhibit an effective permeability that can be negative [2]. The combination of these two periodic structures, which thus compose a double negative media, permitted Smith and coworkers to demonstrate for the first time the existence of a negative refractive index [3]. This tremendous result has been obtained under the assumption of a long wavelength regime, namely, when the incident wavelength is much larger than the dimensions of the unit cell, characteristic of the structured media. Since then, many theoretical as well as experimental works have addressed the frequency response of such double arrays of wires and SRRs, also termed left-handed materials, either under free space conditions [4] or integrated in a transmission line [5, 6]. Basically, the SRRs suffer from a narrow left-handed dispersion branch and from high losses. This is inherent to the resonance working principle with high quality factors, which dramatically enhance the dielectric and metallic losses.

On the other hand, Itoh and coworker [7] along with Eleftheriades and coworker [8] suggested synthesizing a left-handed transmission propagation medium by means of one or two dimensional strip arrays loaded by series capacitances and shunt inductances. Such a structure, which is not resonant in its principle, shows broader left-handed passband as well as lower loss levels. This concept has been notably used for the experimental demonstration of sublambda focusing around 1 GHz [9], and more recently for the experimental evidence of backward waves at submillimeter wavelengths [10] with a quality factor of about 6 at 300 GHz. In its present form, this guided approach cannot be easily mimicked for operation under free space conditions. Such a generalization, in the framework of C-L arrays, would imply further development with the conception of a three dimensional prototype. To this issue, the design of lumped elements for submillimeter and optical wavelengths appears as a key challenge. In the framework of MMIC technologies, one of the simplest printed inductor is the single loop one. At the present time, such a pattern holds a great interest for the design of metamaterials [11–13]. In this case, the terminology of Ω-type particle is commonly preferred to the name of single-loop inductor.

In this paper, we propose to take benefit of the interconnection of elementary single-loop inductors to synthesize a distributed inductance for the design of broadband metamaterials. Recent studies were conducted on Ω-based arrays by means of transmission and refraction experiments. For some configurations, promising results in terms of bandwidth and loss figures have been reported [13]. However, to our knowledge, the literature does not provide any interpretation of this typical behavior. Our aim is to establish a parallel with the so-called Complementary Left/Right-Handed Transmission Line on the basis of a lumped element model.

After a brief presentation of the numerical approach employed for dispersion and transmission calculations, we show how the left-handed passband can be tailored by means of interconnected sections with a direct impact on the phase constant β. We then report on the transmission characteristic of finite structures. With the help of differential analysis of phase properties, left-handedness is shown. These transmission spectra are compared with results obtained for Ω-shaped and C-shaped particles-based arrays in terms of left-handed bandwidth and insertion loss level. A lumped element model is then proposed to interpret the broadband behavior reported in case of interconnected Ω-particles. Finally, on the basis of a parametric study, we propose some guidelines for improving the transmission characteristics of the Ω-like media. Special attention is paid to the homogenization criterion and to the bandgap reduction between the left-handed and right-handed regimes with the prospect of balanced composite metamaterials.

2. FULL-WAVE ANALYSIS METHOD

Our procedure is based on a full three-dimensional solution of Maxwell equations using the finite element method. Appropriate symmetry conditions are defined in order to model an infinite structure for the transverse dimensions. Special care is paid to the discretization procedure. In general, for commercial softwares, mesh is automatically generated at wavelength scale, which is inappropriate for our media. Indeed, the structuration is at subwavelength scale for the existence of a negative refraction regime and a strong refinement; at least one order of magnitude in characteristic dimension is required to ensure a well-conditioned problem.

2.1. Dispersion Characteristics

The transmission through the unit cell is simulated over a frequency band using plane wave excitation and is quantified by the complex scattering matrix. It should be noted here that the media is considered infinite in its transverse dimensions by the use of symmetry conditions defined as follows: perfect magnetic boundaries in the Ω-planes, perfect electric boundaries crossing the Ω-branches. This configuration permits one to derive a transmission spectrum through a slab of metamaterial under a plane wave excitation. We notably focus on the transmission spectrum presented by an elementary cell along the propagation direction, which represents the finest pattern of the propagation structure. The scattering matrix is then converted into the corresponding chain matrix whose first term can be written as $A = ch(\gamma a)$, where $\gamma = \alpha + j\beta$ is the complex propagation constant and a is the length of the unit cell. By this way, the quantities α and βa can be deduced as:

$$\alpha = \frac{1}{a}\ln\left|A \pm \sqrt{A^2 - 1}\right| \tag{1}$$

$$\beta a = \angle\left(A \pm \sqrt{A^2 - 1}\right) + 2k\pi, \quad k \in Z. \tag{2}$$

The solutions obtained for a unit cell correspond to the propagating Bloch modes for an infinite array in the propagation direction, as a consequence of the Floquet theorem. Despite the fact that this approach neglects the mutual effects in the propagation direction, it is able to describe the potentiality of arrays in terms of bandwidth and phase figures, as illustrated by the following transmission characteristics of finite structures. The angular

frequency (ω) dependence of the phase constant (β) extracted from the previous equations describes the dispersion diagram of the periodic structure. Such an expression of β leads to multiple branches and only the solutions corresponding to a positive value of the group velocity v_g are considered to derive the dispersion diagram. The amount of published works concerning the homogenization procedures illustrates the difficulty to retrieve the effective complex permittivity and permeability of left-handed metamaterials, with physical meaning of both their real and imaginary parts. In the frame of this work, we focus on the determination of a real effective refraction index n_{eff}. By considering the expression of the phase velocity $v_\phi = \dfrac{c}{n_{\text{eff}}}$, where n_{eff} is the vacuum light velocity, the evolution of n_{eff} as a function of frequency can be deduced unambiguously from the dispersion diagram.

2.2. *Transmission Characteristics*

In this part, the full-wave method is applied to a finite structure, which means a structure composed of several unit-cells in the propagation direction, to deduce scattering parameters. As a complement of the dispersion characteristics, these calculations bring further information such as the transmission levels in the left-handed and right-handed regime, the rejection level of the forbidden band, and the insertion loss level. Moreover, the phase determination of the transmission coefficient calculated for multiple length structures permits us to confirm the left-handedness by means of the differential phase. Indeed, by considering two structures with corresponding propagation length l_a and l_b, the phase difference is given by the expression:

$$\Delta_\phi = -\frac{\omega(l_a - l_b)}{v_\phi} \tag{3}$$

where ω is the angular frequency. Then for $l_a > l_b$, a positive phase difference Δ_Φ is observed in case of negative phase velocity v_Φ. In the following sections, this numerical procedure is applied to a detailed study of Ω-type arrays.

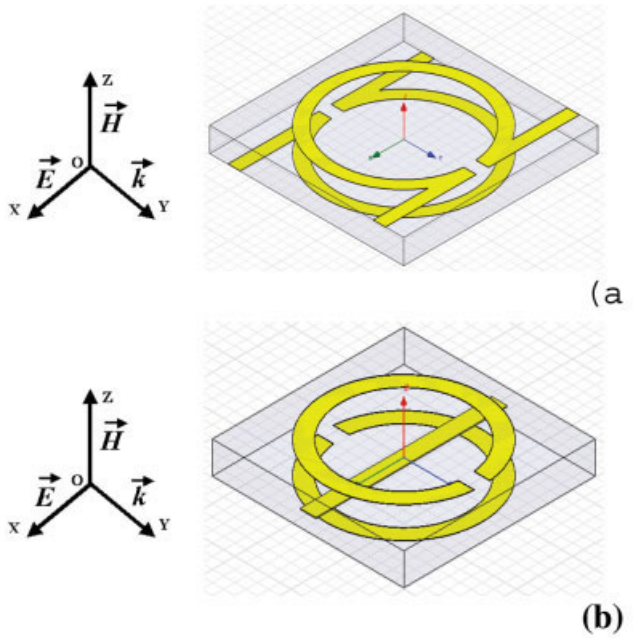

Unit cell a	$dX = 222$ µm	$dY = 222$ µm	$dZ = 28$ µm
Unit cell b	$dX = 170$ µm	$dY = 170$ µm	$dZ = 28$ µm
Metal thickness	1 µm		
Wire width	14 µm		
Ring slot length	14 µm		

Figure 1 Artistic view of the simulated unit cells. Typical Ω unit cell (on top). The bottom unit cell is considered for a comparison of the transmission characteristics. The incident plane wave is oriented as indicated. The dimensions are reported in the table. [Color figure can be viewed in the online issue, which is available at www.interscience.wiley.com]

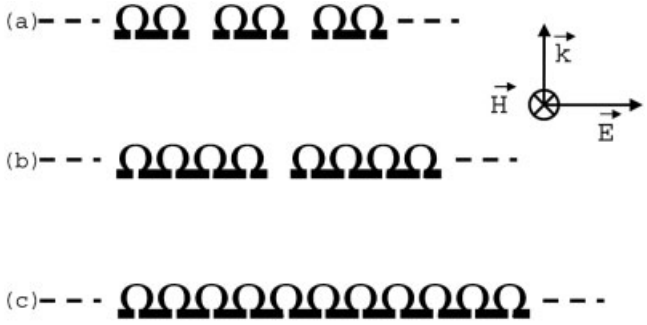

Figure 2 Symbolic representation of the pattern studied showing different multiple Ω (a, b) and the infinitely interconnected Ω structures (c). The incident plane wave is oriented as indicated. The anti-symmetrical layer is not represented on this 2D view

3. DISPERSION CHARACTERISTICS OF THE Ω-PARTICLES MEDIA

With the prospect of an operation in the 140–220 GHz frequency band, we designed artificial media composed of metallic inclusions embedded in a low permittivity host material ($\varepsilon_r = 2.6$) such as benzocyclobutene polymer (BCB). The dielectric properties of this material in terms of permittivity and loss tangent are suitable for a targeted operation in millimeter and submillimeter ranges [14]. The metal is modeled under the approximation of a finite conductivity σ. Value of $\sigma = 4.1 \times 10^{-7}$ S/m, typical of gold conductivity, has been considered. The Ω-like pattern which combines a wire and a current loop on the same particle is suitable for the design of double-negative metamaterial [12, 13]. The double-sided anti-symmetrical configuration [Fig. 1(a)] has been chosen to avoid bianisotropic effects [13]. Different analyses are reported about the ability of synthesizing a double negative medium using such a particle [13, 15]. Indeed, different typical trends, depending on the interconnections of the Ω-like particles described by Figure 2, can be deduced from the dispersion analysis. As stated in Section 2., the dispersion diagram is deduced from *S*-parameter simulations of a single unit-cell along the propagation direction and is here calculated between 100 and 340 GHz.

Figure 3 gives the dispersion diagrams deduced from calculations on unit-cells composed of 4 Ω-particles interconnected along the transverse direction O_x [Fig. 2(b), white dots] and infinitely interconnected [Fig. 2(c), black dots]. These two examples are representative of band structure behavior for all types of cells including one or multiple interconnected Ω particles. First, as previously demonstrated [13], left-handed frequency bands characterized by opposite signs of v_g and v_Φ are present in each case, thus attesting of a left-handed regime. In the case of infinite arrays, this band is about 100 GHz with a center frequency around 175 GHz. It should be noted here that this left-handed passband is very broad when compared with those reported for wires and SRR's double arrays. When the infinite Ω-chain is periodically split, like

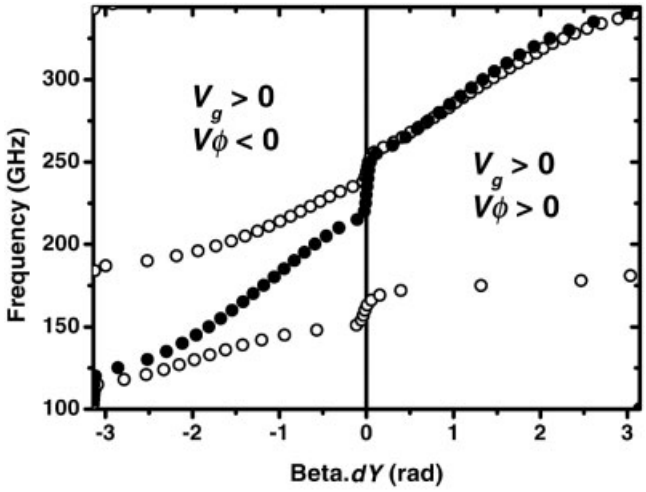

Figure 3 Dispersion diagram for the interconnected Ω structure (black dots) and for 4 Ω-based periodical structures (white dots). *dY* is the array period along the propagation direction *Oy*

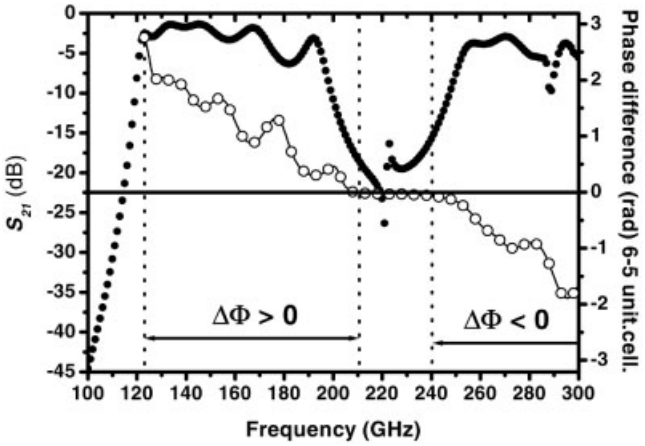

Figure 5 Transmission spectra versus frequency for the interconnected Ω pattern. The S_{21} parameter (black dots) is determined for a 5 unit-cell structure in the propagation direction. The phase difference has been determined from simulation on 6 and 5 unit-cell structures in the propagation direction

for example in Figures 2(a) and 2(b), a right-handed passband appears at low frequency (below 50 GHz). This first passband has already been observed in the transmission of metallic discontinued-wire photonic crystals [16]. This passband is sometimes called valence band using an analogy to a semiconductor band structure [17]. At higher frequencies, alternated left-handed and right-handed branches appear in the limits of the previous left-handed domain.

Considering now an infinite periodic array along O_x and O_z as an effective media, an effective refractive index can be deduced according to the procedure described in Section 2. (Fig. 4). Here, in the propagation direction, the unit length is about λ/5 at 180 GHz, if we consider λ the wavelength calculated in a homogeneous BCB host medium. As a consequence of the frequency dependence of β, only the infinitely interconnected Ω array shows a continuous variation over a broad frequency band with values starting from $n_{\text{eff}} = -6$ at low frequencies and increasing monotonously up to zero when the forbidden band is reached. In this case, the crucial index value $n_{\text{eff}} = -1$ can be reached for a single

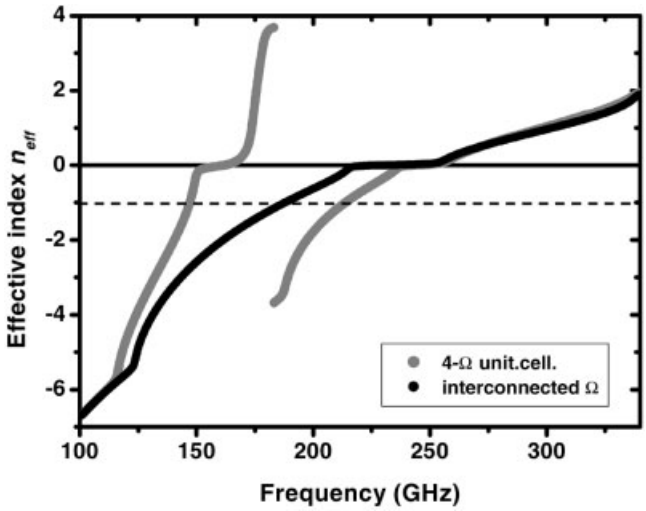

Figure 4 Effective refraction index deduced from the dispersion diagrams for different multiple Ω structures versus frequency. The dashed line indicates the critical value of $n_{\text{eff}} = -1$

frequency around 190 GHz. When the Ω-type current loops are disconnected, several frequencies correspond to $n_{\text{eff}} = -1$. For example, for six interconnected Ω-like patterns, this value of n_{eff} is reached for frequencies around 148, 196, and 204 GHz. However, these multiple branches of n_{eff} are narrow and thus the index variation is sharp around these typical frequencies, evolution that reveals a highly dispersive medium. As a consequence, the infinitely interconnected structure seems preferable because the dispersion of n_{eff} is much less important, especially, around $n_{eff} = -1$. Several authors insist on the importance of this particular value of n_{eff} in terms of applications. For disconnected particles, it is interesting to note that these index variations show negative domains at high frequencies. However, around $f = 400$ GHz, the array period is comparable to λ/2 and the hypothesis of an effective medium becomes questionable.

These first results in terms of effective media are completed in the next section by transmission spectrum analysis when a finite dimension in the propagation direction O_y is assumed.

4. TRANSMISSION CHARACTERISTICS

The broadband potentiality of the interconnected Ω media is confirmed by the transmission spectrum of Figure 5, obtained for a periodical structure of five unit cells in the propagation direction. The first passband is clearly visible between 130 and 210 GHz. This passband is of left-handed type as it is attested by the phase-offset evolution. This curve corresponds to the phase offset calculated from transmission via two structures of different lengths (6 and 5 unit cells). As shown in Section 2., the positive phase-offset corresponds to the left-handed regime. A null phase-offset is recovered at the corner frequencies of the stop band, between 210 and 240 GHz, and a negative phase offset corresponding to a classical right-handed regime is found above 240 GHz. In order to compare this result with the characteristics of a more conventional metamaterial including C-particles and wire array, we also plotted on Figure 6 the transmission spectrum of a five-cell structure based on the pattern proposed in Ref. 18 [Fig. 1(b)]. The unit cell has been scaled down to fit the frequency domain of interest. These evolutions illustrate the advantage of the Ω-type array in terms of relative bandwidth, which is about 50% against 20% for the C-particle-based structure. The relative bandwidth is here defined as the ratio between the left-handed bandwidth Δf and the center

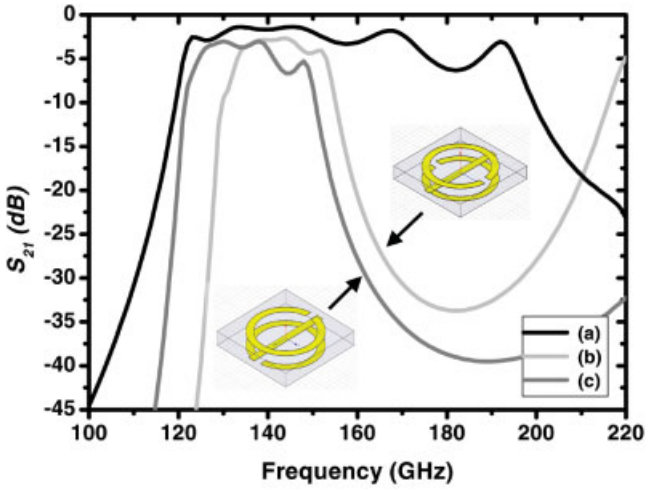

Figure 6 S_{21} parameter versus frequency for 5 unit-cell structures: interconnected Ω (a), wire and ring unit cell with $\theta = 0$ (b), as in Figure 2(b), wire and ring unit cell with $\theta = 90°$ (c), where θ is the orientation of the rings around Oz axis. [Color figure can be viewed in the online issue, which is available at www.interscience.wiley.com]

frequency f_{cent}. In order to investigate the influence of polarization, a different orientation of the current loop has also been considered ($\theta = 90°$ along the z-axis). In both cases, despite a shift of the passband to lower frequencies, the bandwidth remains of the same order. Clearly, only the infinitely interconnected Ω particles allow us to reach bandwidths larger than 50%.

Apart from the bandwidth, as it is often mentioned, the problem of intrinsic losses appears crucial for metamaterials. To assess this contribution, it is necessary to discriminate the various loss terms. Owing to the assumption of an infinite medium in the transverse directions, there is now radiated energy. The reflection losses are directly calculated from the scattering term S_{11} not plotted here. From S_{11} and S_{21}, we can calculate the transmittance and reflectance, respectively, and then deduce the absorbance. For instance, considering the frequency of 140 GHz as a reference, it can be shown that the intrinsic losses are much lower in the case of the Ω-type array with respect to the C-type array. For the latter, the lifetime of the electromagnetic energy trapped within the resonator is much longer, increasing dramatically the effect of metallic losses. In contrast, for the former, the losses are quite reasonable with a value close to 1.5 dB/mm. Similar conclusion in terms of bandwidth and intrinsic losses have also been drawn in Ref. 13 on the basis of an experimental work. The intrinsic behavior of interconnected Ω-particles-array can be understood with the help of a lumped element model, as illustrated in the following.

5. LUMPED ELEMENT MODEL

Due to the boundary conditions described in Section 2., the electric field in the port planes is oriented along the Ω-patterns. Under the assumption of small dimensions when compared with the propagating wavelength, the host medium can be modeled by inductive and capacitive constants in accordance with the transmission line theory. This model applied to the infinite media is reported in Figure 7(a). Typical values of L and C can be deduced from the full-wave simulations, considering the expressions of port impedance $Z_0 = \sqrt{\frac{L}{C}}$ and phase velocity $v_\phi = \frac{1}{\sqrt{LC}}$. The Ω-particle, well known in the MMIC framework under the name of single-loop inductor, can be described by the following analytical formula [19]:

$$L_i\,(\text{nH/cm}) = 2\left(\ln\frac{l}{w+t} - 1.76\right) \tag{4}$$

where w, t, and l are the width, thickness, and length of the wire, respectively. The coupling between facing loops is modeled by a distributed capacitance $C_i\,dl$, thus leading to the equivalent circuit of Figure 7(b). In a first approximation, this distributed capacitance is simplified by two lumped capacitors located at the junction points between the branches and the loop of the Ω-pattern. Considering access planes along the branches of the inductors, the typical unit cell is outlined in Figure 7(c). It is important to note that this model does not include the losses and the coupling effects between adjacent unit cells of the infinite slab. However, it helps to understand the broadband character of the interconnected Ω-particle media. Indeed, the equivalent circuit of Figure 7(c) clearly illustrates the contribution of shunt inductors and series capacitors. The dispersion diagrams plotted in Figure 8 for the host medium [Fig. 8(a)], the distributed loop inductor medium [Fig. 8(b)], and the complete unit cell [Fig. 8(c)] reveals the Composite Left/Right-Handed Transmission Line nature such as described by Caloz and coworkers [20]. As mentioned in the Introduction, such a topology is, especially, favorable in terms of bandwidth and loss.

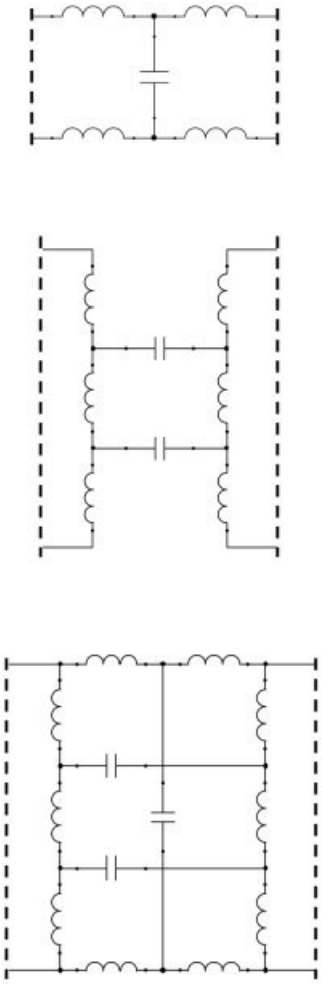

Figure 7 Lumped element circuits describing the Ω-based unit cell: host medium (a), coupled Ω-particles, complete unit-cell (c)

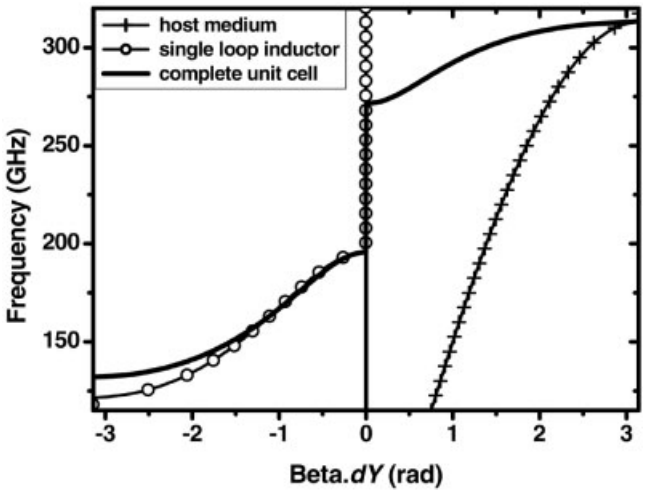

Figure 8 Dispersion diagram of the lumped element circuits

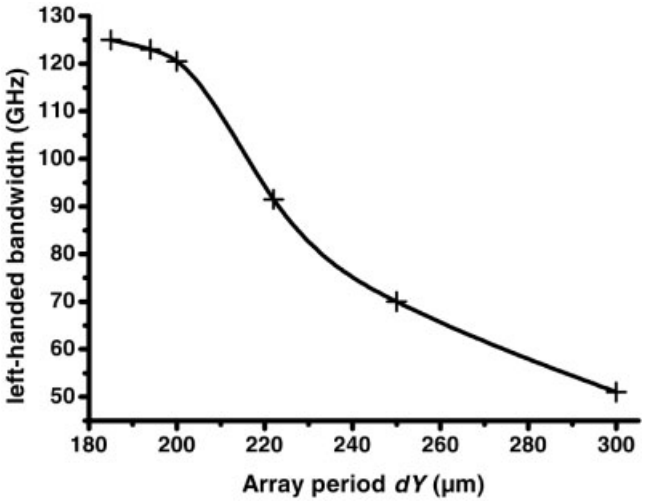

Figure 9 Left-handed bandwidth as a function of the array period *dY*

Moreover, as illustrated by the full-wave simulations, one understands that periodically cutting the Ω-chain degrades the bandwidth by introducing a capacitance in series with the shunt inductor.

In the next section, by focusing on the interconnected Ω structure, we will define some criteria for left-handed band engineering.

6. LEFT-HANDED BAND ENGINEERING

In the following, we address the frequency capability of the interconnected Ω-type arrays by keeping the bandwidth as broad as possible. To this aim, we focus on the influence of the array geometry, which is directly related to the dimensions of the unit cell along O_x, O_y, and O_z (Fig. 2). We started from the unit cell whose dimensions are $dX = 222$ μm, $dY = 222$ μm, and $dZ = 28$ μm and describes the arrays previously simulated. Since the goal of this section is to give guidelines by varying the unit cell dimensions, the metal has been considered perfect and the metallic strip's dimensions remains constant (thickness: 1 μm; width: 14 μm).

Figure 9 shows the bandwidth as a function of the period along O_y. Decreasing this dimension leads to an increase of the left-handed bandwidth from 51 GHz ($dY = 300$ μm) to 125 GHz ($dY = 185$ μm). A saturation effect can be observed below 200 μm. Therefore, the quasi-constant value of 125 GHz can be considered as an optimum for the simulated structure. With a center frequency $f_{cent} = 182$ GHz, the relative bandwidth $\frac{\Delta f}{f_{cent}}$ is about 68%. As O_y is the propagation direction, one has to pay attention to the homogenization criterion. Comparing *dY* with the wavelength at the center frequency gives the variation of the relative period. The boundaries of the plotted variation are λ/4 for $dY = 300$ μm and λ/5.5 for $dY = 185$ μm. This relative period can be reduced as seen in the following. Indeed, in concentric SRR-based metamaterial, the frequency resonance can be decreased through a subsequent increase of the capacitance, by reducing the gap between the two rings while keeping constant the outer ring radius. In the case of Ω-type arrays, the main capacitive contribution, described in Section 5. is relative to the superposed metallic patterns. Therefore, the relative period can be improved by decreasing *dZ* as it can be seen from Figure 10. By considering $dZ = 5$ μm, the center frequency is about 46 GHz, which corresponds to a relative period of λ/20. To this point it is important to note that such a small value of *dZ* is realistic in the context of mutilayer planar microtechnology. Technically, smaller values of *dZ* could be obtained, which means that a high subwavelength regime is achievable with an expected trade-off between the losses and the filling factor. Furthermore, the corresponding relative bandwidth variation plotted on the same graph shows a maximum value, greater than 60%, for the smallest period *dZ*. If we consider both the frequency capability and the width of the left-handed band, an optimum value is obtained around $dZ = 25$ μm.

As a last comment, decreasing the lateral period *dX* induces a narrowing of the forbidden gap between the left-handed and right-handed branches. This gap is typically centered on the frequency of 230 GHz, whose relative variation is negligible. Ideally, a zero-gap structure is interesting with a prospect of fabricating balanced composite metamaterials. To this aim, the stitching of the equivalent circuit passbands can be searched as it is the case for composite backward and forward transmission lines [20].

7. CONCLUSION

A free space metamaterial based on interconnected metallic Ω-particles is proposed. The dispersion diagrams have been calculated and show a relative bandwidth wider than 60%, illustrating the broadband character of such a structure. This is confirmed by the transmission spectrum that also points out low insertion loss levels

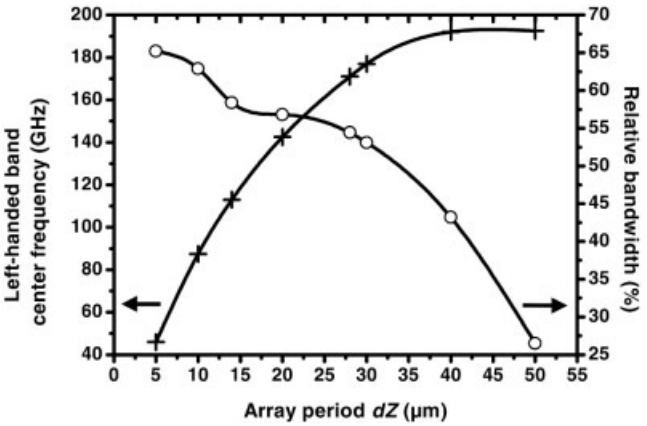

Figure 10 Left-handed band characteristics as a function of the array period *dZ*: center frequency (cross symbols) and relative bandwidth (white dots)

(typically, 1.5 dB/mm at 150 GHz). This spectrum has been compared with those of equivalent scaled wire and C-particle arrays aimed at operating above 100 GHz. These properties, namely, the broadband left-handed character and low insertion loss, of prime importance for applications of metamaterials, are interpreted on the basis of a lumped element approach. The equivalent circuit of a typical unit cell reveals the contribution of both shunt inductors and series capacitances and a comparison with an ideally nonresonant medium employed for the design of transmission line metamaterial was established. A parametric study, carried out to give guidelines for high frequency operation, illustrates the versatility of the interconnected-Ω structure in terms of left-handed band engineering. In addition, it is shown that a high subwavelength condition (typically, λ/20) could be achieved by means of a conventional multilayer planar technology. At last, these structures seems promising for zero-gap operation as a reference to the balanced state of Composite Left/Right-Handed Transmission Lines introduced notably by Caloz and coworkers [20].

ACKNOWLEDGMENTS

The authors acknowledge the funding of the Centre National d'Etudes Spatiales (CNES).

REFERENCES

1. V.G. Veselago, Electrodynamics of substances with simultaneously negative values of permittivity and permeability, Sov Phys Usp 10 (1968), 509–514.
2. J.B. Pendry, A.J. Holden, D.J. Ribbins, and W.J. Stewart, Magnetism from conductors and enhanced nonlinear phenomena, IEEE Trans Microwave Theory Tech 47 (1999), 2075–2084.
3. R.A. Shelby, D.R. Smith, and S. Schultz, Experimental verification of a negative index of refraction, Science 292 (2001), 77–79.
4. C.G. Parazzoli, R.B. Gregor, K. Li, B.E.C. Koltenbah, and M. Tanielian, Experimental verification and simulation of negative index of refraction using Snell's law, Phys Rev Lett 90 (2003), 107401–1-4.
5. R. Marqués, J. Martel, F. Mesa, and F. Medina, Left-handed-media simulation and transmission of EM waves in subwavelength split-ring-resonator-loaded metallic waveguides, Phys Rev Lett 89 (2002), 184901–1-4.
6. T. Decoopman, O. Vanbésien, and D. Lippens, Demonstration of a backward wave in a single split ring resonator and wire loaded finline, IEEE Microwave Wireless Components Lett 14 (2004), 507–509.
7. C. Caloz and T. Itoh, Application of the transmission line theory of left-handed (LH) materials to the realization of a microstrip "LH line," In: IEEE antennas and propagation society international symposium, Vol. 2, 2002, pp. 412–415.
8. A. Grbic and G.V. Eleftheriades, Experimental verification of backward-wave radiation from a negative refractive index metamaterial, J Appl Phys 92 (2002), 5930–5935.
9. A. Grbic and G.V. Eleftheriades, Overcoming the diffraction limit with a planar left-handed transmission-line lens, Phys Rev Lett 92 (2004), 117403–1-4.
10. T. Crépin, J.F. Lampin, T. Decoopman, X. Mélique, L. Desplanque, and D. Lippens, Experimental evidence of backward waves on terahertz left-handed transmission lines, Appl Phys Lett 87 (2005), 104105–1-3.
11. M.M.I. Saadoun and N. Engheta, A reciprocical phase shifter using novel pseudochiral or Ω medium, Microwave Opt Tech Lett 5 (1992), 184–188.
12. C.R. Simovski and S. He, Frequency range and explicit expressions for negative permittivity and permeability for an isotropic medium formed by a lattice of perfectly conducting Ω particles, Phys Lett A 311 (2003), 254–263.
13. J. Huangfu, L. Ran, H. Chen, X. Zhang, K. Chen, T.M. Grzegorczyk, and J.A. Kong, Experimental confirmation of negative refractive index of a metamaterial composed of Ω-like metallic patterns, Appl Phys Lett 84 (2004), 1537–1539.
14. G. Prigent, E. Rius, F. Le Pennec, S. Le Maguer, C. Quendo, G. Six, and H. Happy, Design of narrow-band DBR planar filters in Si-BCB technology for millimeter-wave applications, IEEE Trans Microwave Theory Tech 52 (2004), 1045–1051.
15. C.R. Simovski, Plane-wave reflection and transmission by grids of conducting Ω-particles and dispersion of Ω electromagnetic crystals, AEU Int J Electron Commun 57 (2003), 358–364.
16. J. Danglot, O. Vanbésien, and D. Lippens, Active waveguides patterned in mixed 2D–3D metallic photonic crystal, Electron Lett 35 (1999), 475–477.
17. J.M. Lourtioz, A. de Lustrac, F. Gadot, S. Rowson, A. Chelnokov, T. Brillat, A. Ammouche, J. Danglot, O. Vanbésien, and D. Lippens, Toward controllable photonic crystals for centimeter- and millimeter-wave devices, J Lightwave Technol 17 (1999), 2025–2031.
18. R. Marqués, F. Mesa, J. Martel, and F. Medina, Comparative analysis of edge- and broadside- coupled split ring resonators for metamaterial design—theory and experiments, IEEE Trans Antennas Propag 51 (2003), 2572–2581.
19. M. Caulton, Lumped elements in microwave integrated circuits, In: L. Young (Eds.), Advances in microwave, Vol. 8, Academic Press, New York, 1974, pp. 143–202.
20. A. Lai, T. Itoh, and C. Caloz, Composite right/left-handed transmission line metamaterials, IEEE Microwave Mag 34 (2004), 34–50.

A SMALL-SIZE SEMILUMPED THREE-PORT TUNABLE POWER DIVIDER

A.-L. Perrier,[1] J.-M. Duchamp,[2] and P. Ferrari[2]
[1] LAHC, University of Savoie
73376 Le Bourget-du-Lac
France
[2] IMEP, INP of Grenoble
BP 257, 38016 Grenoble cedex 1
France

Received 6 June 2006

ABSTRACT: *In this paper, a small-size semi-lumped three-port power divider with both power and frequency tune is designed and measured. The proposed topology uses complex impedance transformers in each output branch. A 3D CPW prototype is realized with varactor diodes. It exhibits a wide tunable power, from −1.3 to −17 dB, and a wide working frequency tune, from 0.8 to 1.4 GHz.* © 2006 Wiley Periodicals, Inc. Microwave Opt Technol Lett 49: 90–94, 2007; Published online in Wiley InterScience (www.interscience.wiley.com). DOI 10.1002/mop.22029

Key words: *power divider; tunable device; small-sized device; tuner; varactors*

1. INTRODUCTION

Tunable miniaturized devices constitute a great challenge in the field of modern RF/microwave telecommunications. In the near future, more and more applications will use multiple operating frequencies, with hard miniaturization constraints for MMIC applications. In this context, some researches are carried out to show the feasibility of various tunable devices that can be embedded in RF/microwave telecommunication systems like phase shifters, impedance transformers, filters, couplers, and power dividers. Several technologies can be used to achieve such tunable devices: ferroelectric and ferromagnetic materials, MEMS, piezoelectric devices, optical control, and semiconductors.

Left-Handed Electromagnetic Properties of Split-Ring Resonator and Wire Loaded Transmission Line in a Fin-Line Technology

Thibaut Decoopman, Aurélien Marteau, Eric Lheurette, Olivier Vanbésien, and Didier Lippens

***Abstract*—We report on experiments carried out on a backward transmission line, which consists of a fin-line periodically loaded by split-ring resonators and shunt wires. We first demonstrate the left-handed character of these frequency-selective transmission lines via: 1) dispersion diagram calculations which have been compared to the frequency dependence of measured scattering parameters; 2) the tracking of the phase fronts; and 3) the phase offset between two lines of various lengths. The effective refraction index found experimentally was approximately −4. Taking benefit of the use of a closed electromagnetic system and successful matching, the losses are especially analyzed. The ratio between incident and absorbed energy is 65% for a three-cell prototype and reaches 91% for ten cells.**

***Index Terms*—Fin line, left-handed (LH) materials, metamaterials.**

I. Introduction

METAMERIALS are now attracting much interest with the prospect to synthesize artificial electromagnetic (EM) media of a negative refractive index [1]. As a consequence, the refraction will be negative at the interface separating two media with a positive and negative index, respectively [2]. The propagation of the wave is also backward in the negative refractive index material. These artificial structures are termed "left-handed (LH) materials," as it was proposed by Veselago [3]. With respect to the techniques for fabricating them, there are several routes. The first solution is based on double-negative metallic periodic arrays, which consist of the so-called split-ring resonators (SRRs) proposed by Pendry *et al.* and of wires [4], [5]. The second solution makes use of an EM propagation structure loaded periodically by lumped shunt inductance and series capacitance [6], [7]. In both cases, the EM propagation of waves is backward in the sense that the phase fronts are moving opposite to the direction of energy (the wave vector $\mathbf{k}$ and the Poynting vector $\mathbf{S}$ are antiparallel). From the dispersion characteristic point-of-view, this means that the phase and group velocities are of opposite sign.

In this paper, we report on experimental characterization of a novel backward structure whose modeling was published in [8]. The main goal is to experimentally demonstrate the LH character of the propagation along this line and to extract a negative effective refraction index. The losses, which are of major concern in the filtering and phase shifting applications, are also more specially addressed.

Thus, based on four-port vectorial network analysis, we unambiguously demonstrate that the EM propagation for an X-band prototype, fabricated in a printed circuit board (PCB) technology for the planar circuit, exhibits an LH behavior around 12 GHz. With respect to the overall losses, we first solve the problem of spurious reflection losses by the design and fabrication of a proper tapering section based on a previous work [9]. We then show that the intrinsic losses are dramatically increased as a function of the resonator number leading to some tradeoff in terms of performances.

In Section II, we outlined the guidelines for designing the structures by considering separately the periodic structures that permit us to synthesize the negative permittivity and permeability media. In a first stage, the dispersion characteristics in the passbands and the evanescent lengths in the forbidden bands are computed. Section III deals with the network vectorial measurements with main emphasis on a parametric study as a function of resonator number and, thus, transmission-line lengths. Excellent agreement is found between calculated and measured data with singularities around the resonance frequencies.

II. Design and Fabrication

Basically, this study began by following the proposal published in [10], which makes use of a hollow waveguide designed below the cutoff frequency in order to synthesize a negative permittivity. SRRs, placed in the E-plane of the waveguide, were used for the fabrication of a negative permeability media. The main drawback of the aforementioned structure is the coupling of the EM wave to the sub cutoff waveguide. Therefore, in [10], insertion losses, attributed to reflection losses, as high as 15 dB was measured irrelevant of the number of resonators. Conventional tapering section could, in principle, be designed in order to avoid such mode mismatching, but at the detriment of the simplicity afforded by the sub cutoff waveguide scheme. In order to face this difficulty, it was decided to operate in a propagating mode for the hollow, which facilitates mode matching with the requirement to synthesize a negative permittivity. It is now well

Manuscript received September 5, 2005; revised December 22, 2005. This work was supported by the European project TELEMAC. This work was supported in part by the European Space Agency under fin-line technology.

T. Decoopman was with the Institut d'Electronique de Microélectronique et de Nanotechnologies du Nord, Université des Sciences et Technologies de Lille, 59652 Villeneuve d'Ascq Cedex, France. He is now with Astrium Velizy France, Vélizy 78140, France.

A. Marteau, E. Lheurette, O. Vanbésien, and D. Lippens are with the Institut d'Electronique de Microélectronique et de Nanotechnologies du Nord, Université des Sciences et Technologies de Lille, 59652 Villeneuve d'Ascq Cedex, France (e-mail: didier.lippens@iemn.univ-lille1.fr).

Digital Object Identifier 10.1109/TMTT.2006.871356

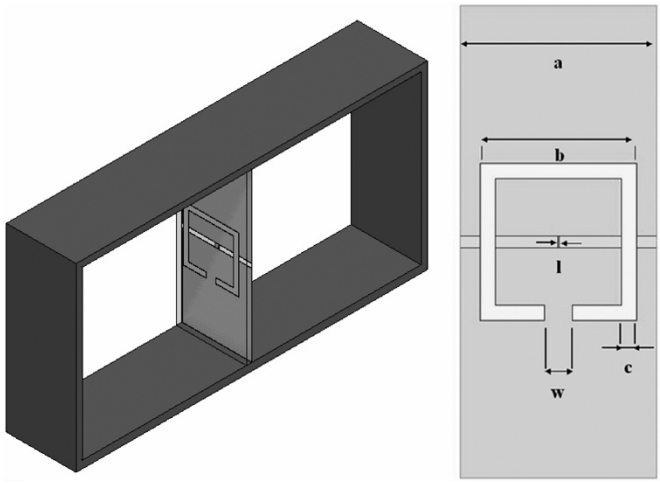

Fig. 1. Schematic of the unit cell of an LH transmission line in a fin-line technology. Unit cell length $a = 3.3$ mm; single SRR dimensions $b = 2.62$ mm, $c = 0.250$ mm, and $w = 0.2$ μm. Wire width $l = 0.2$ mm. Gap of the slot 0.2 mm.

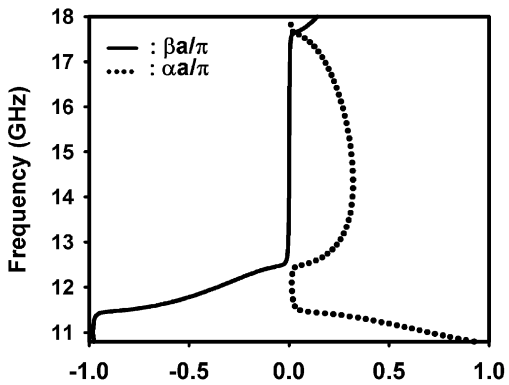

Fig. 2. Dispersion diagram of the unit cell.

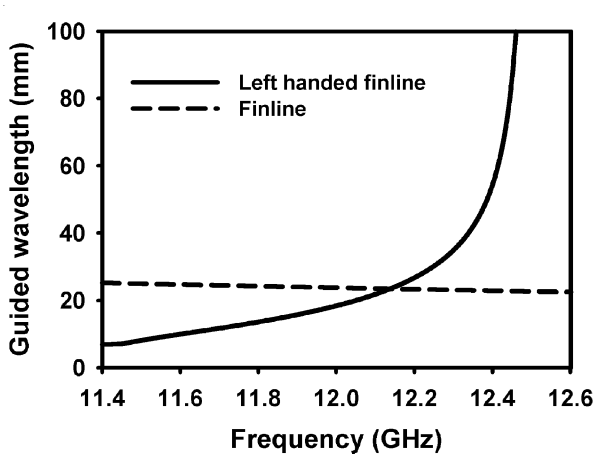

Fig. 3. Frequency dependence of the guided wavelength for a conventional fin line and for the LH section.

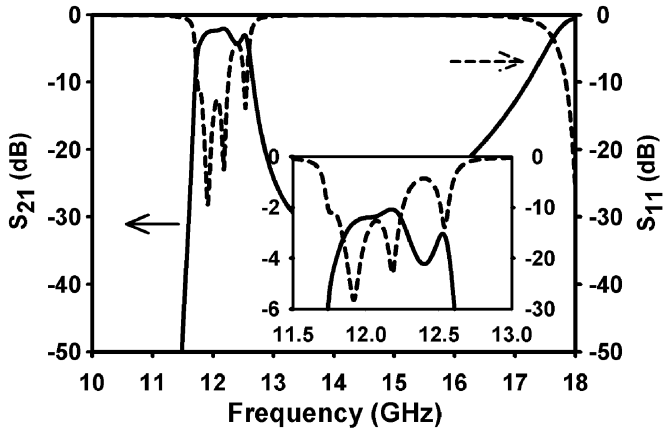

Fig. 4. Scattering parameters S_{21} (solid line) and S_{11} (dashed lines) calculated by full-wave analysis for a five-cell transmission line, including metal and dielectric losses. Inset shows zoom in maximum transmission.

known that a negative permittivity can be achieved via a wire array with a high-pass filter frequency response. The waveguide counterpart of this scheme is a transmission line loaded by shunt narrow wires. At this stage, the high similarity between the solution can be recognized, which takes advantages of transmission lines loaded by shunt inductances (which corresponds to narrow wires) and series capacitance. However, in order to fabricate a negative permeability medium, we have preferred to use SRRs in the same way as proposed in [11] in a coplanar waveguide technology with SRRs patterned on the backside of the substrate.

By combining these guidelines, we obtained the basic cell displayed in Fig. 1. A uniplanar fin line is periodically loaded by 0.2-mm-wide metal strip and SRRs whose relevant dimensions are given in the caption of Fig. 1. The resonance frequency of the SRR is targeted in the X-band, namely, around 10 GHz. The line is periodically loaded by this basic scheme, notably varying the number of resonators.

The band diagram of the unit cell with a single SRR is reported in Fig. 2 for real and imaginary $\mathbf{k}$ vectors. Further details about the numerical procedure, used for calculating these dispersion characteristics, can be found in [8]. On the basis of the calculations, one can expect that the structure is LH between 11.5–12.5 GHz and exhibits a forbidden gap between 12.5–17.5 GHz. A full transmission is recovered above 17.5 GHz, which corresponds to the plasma frequency of the wire array.

Beyond the anomalous properties outlined in Section I based on the reversal of the $\mathbf{k}$ vector with respect to the Poynting vector, the high dispersive nature of the loaded line with respect to the bare fin line with inversion of the curvature in the band structure and, thus, an increase of wavelength at increasing frequency can be noted (Fig. 3).

It is also possible to perform simulations of the EM propagation assuming a finite line length. In practice, the simulations were conducted by full-wave analysis with Ansoft's commercial software High Frequency Structure Simulator (HFSS). An example of results that can be achieved with this simulation tool is given in Fig. 4 with the plot of the frequency dependence of scattering parameters. For these calculations, metallic and dielectric losses have been included with a copper conductivity of $5.8 \cdot 10^7$ S/m, while loss tangent of the substrate is $9 \cdot 10^{-4}$. The maximum of transmission is close to -2 dB over the LH frequency band. The relevant frequency characteristics are in

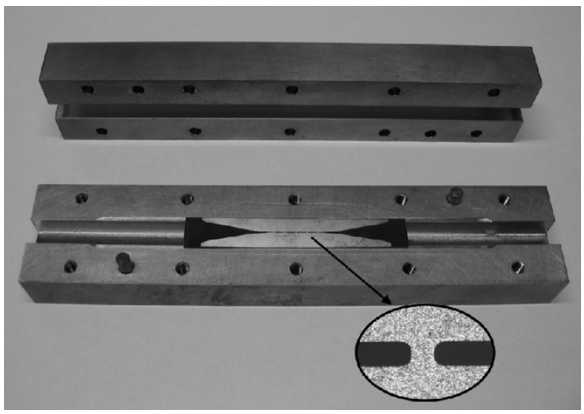

Fig. 5. View of the X-band prototype.

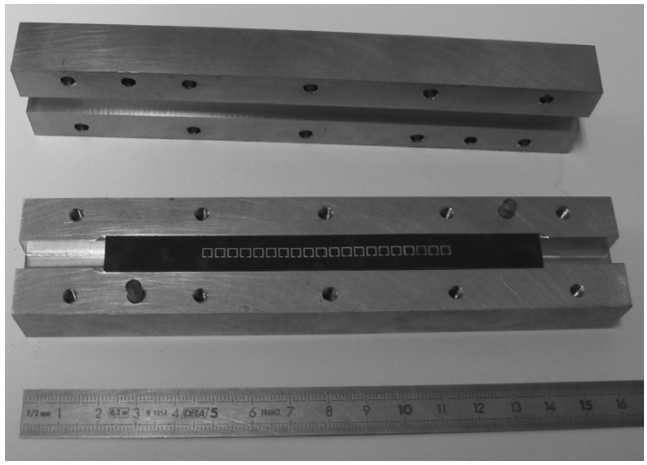

Fig. 6. View of the SRR linear array patterned on the back side of the Duroid substrate.

agreement with the dispersion features, while a high rejection is noted in the forbidden gap. From the application viewpoint, this opens the way of high-performance filters taking advantage of artificial magnetism through a C-shaped metal pattern, as was already pointed out in previous publications [11], [12].

Perhaps more important is the LH character of the propagation that can be demonstrated from *ab-initio* simulations, namely, with the tracking of the phase fronts as a function of time. The calculations, using an HFSS code, are performed in the frequency domain. However, an idea of phase moving can be obtained via initial phase shift of the EM wave impinging onto the device and mapping of the EM fields. [8, Fig. 5] is a numerical demonstration of the existence of a backward wave in the fin-line-based device. By mapping the electric field in a plane perpendicular to the substrate and for a different phase shift at the input, a reversal of the $\mathbf{k}$ vector was pointed out at the interface between the conventional fin-line section and the central one where an LH feature is expected.

For prototyping of the fin-line transmission line, the slot has a width of 200 μm, which corresponds to a characteristic impedance of approximately 120 Ω. Therefore, in order to minimize as far as possible the return loss, avoiding by this way standing wave within the active region and also to measure accurately the intrinsic losses, the LH-based section was clad with two tapering sections whose design principle was published elsewhere [9]. In short, mode matching is achieved via slightly corrugated tapers whose optimization was performed via a homemade code. Such an optimization yields a return loss better than 20 dB over the bandwidth of interest.

At this stage, a prototype including right-handed (RH) access and taper sections and LH transmission structures was fabricated in a printed circuit board (PCB) technology for the planar circuits, while the hollow waveguides were realized using conventional copper machining techniques. Figs. 5 and 6 show two views of the completed device. The dielectric substrate is made from RT Duroid with a relative permittivity of 2.2 and a loss tangent of $9 \cdot 10^{-4}$. The metal patterns, notably the C-shaped resonators, are made of copper with a thickness of 17 μm and were patterned by mechanical milling.

Five types of prototypes have been fabricated and subsequently assessed by vectorial network analysis.

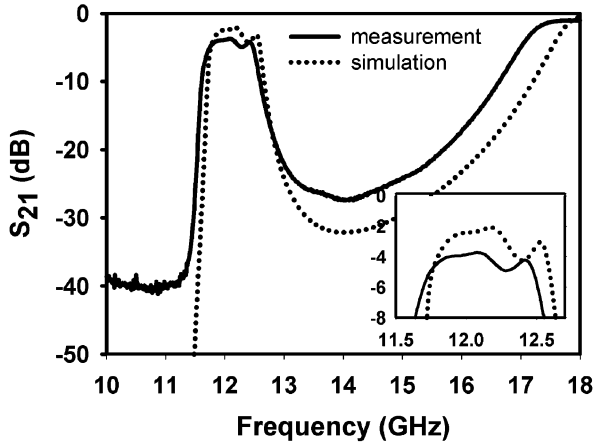

Fig. 7. Frequency dependence of the insertion loss (S_{21}) for a five-cell prototype; calculated data (dotted lines), experimental data (solid line).

III. Experimental Results and Analysis

Measurement of scattering parameters was conducted on an Agilent HP 8510 vectorial network analyzer. A Calset was established including the coaxial-waveguide transitions necessary to RF probe the structure. Fig. 7 gives the variations of the scattering parameters, which were measured and calculated between 10–18 GHz for a five-cell prototype. The agreement between modeling and experiment is good, particularly for the frequency band where an LH behavior was predicted between 11.6–12.5 GHz. With respect to the magnitude of S_{21}, the insertion loss that was measured is a little bit degraded with respect to the calculated ones and could infer a higher value of resistivity than that assumed in the simulation. The features in the transmission window, where the permittivity and permeability are negative simultaneously, are remarkably reproduced in the experiment with a weak ripple. The insertion loss over a frequency band of 10% are close to -4 dB, which compare favorably to the results published thus far in the literature [13], [14].

Fig. 8 displays the variations against frequency of the scattering parameter S_{11}.

Again, a satisfactorily agreement is found between modeling and experiment with a return loss on average better than 10 dB,

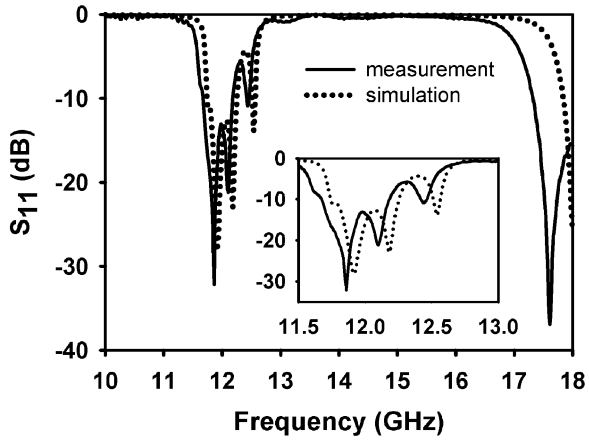

Fig. 8. Comparison of experimental (solid line) and calculated (dotted line) variations of S_{11} as a function of frequency for a five-cell prototype. Inset shows a zoom in the LH window.

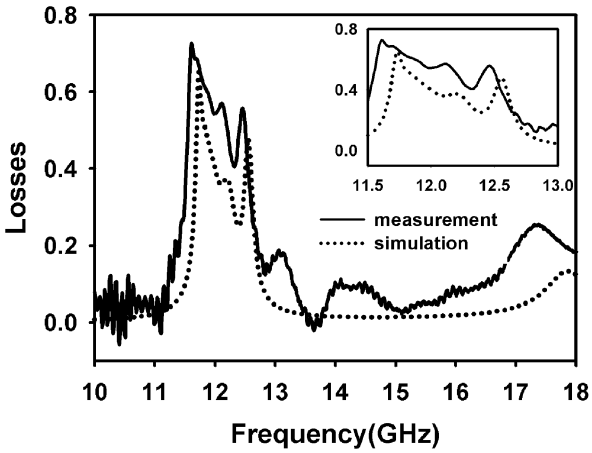

Fig. 9. Intrinsic losses versus frequency, which is computed from (1) for five unit cells.

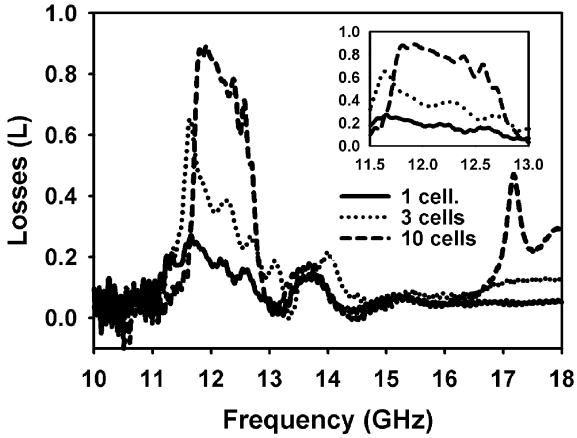

Fig. 10. Comparison of loss level as a function of the number of unit cell.

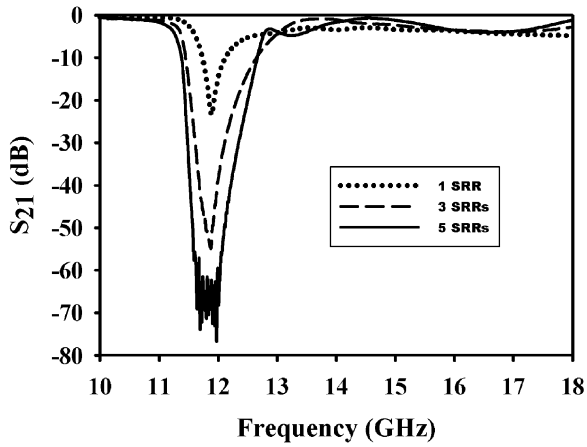

Fig. 11. Measured frequency dependence of the insertion loss (S_{21}) for a one-, three-, and five-cell prototype.

which is especially close to the resonant frequency of the C-shaped resonators around 12 GHz.

Therefore, the origin of the loss has to be further clarified and, to this aim, we plotted in Fig. 9 the loss contribution, which can be computed from (1) as follows:

$$L = 1 - |S_{12}|^2 - |S_{11}|^2. \tag{1}$$

Beyond the excellent agreement in the frequency variations of the intrinsic losses (L), the key result is that more than 50% of the EM wave is lost in the LH transmission line. Assessment of this first conclusion with respect to the loss level can be found from a parametric study of (L) versus the number of resonator and, hence, the length of the LH transmission line. The results of this study are summarized in Fig. 10.

It can be noticed that the loss level is dramatically influenced by the number of unit cell. Therefore, the overall loss level reaches 10 dB (90% of the loss due to absorption) for a ten-cell prototype. It will reach 15 dB for a 20-cell device. As demonstrated before, the loss stems from the resonant nature of the C-shaped patterns. Therefore, for each curve, the loss peaks at a frequency close to the resonant frequency of SRRs depending also on the quality factor of each resonator.

Discrimination between the two arrays can be performed by the characterization of prototypes consisting of only wire or SRR arrays. In this case of single negative media, the waves are evanescent in the frequency band where either the effective permittivity or permeability is negative. Under this condition, a stopband is expected. This permits us to have further information about the quality of the resonance. Figs. 11 and 12 show the variation versus frequency of the scattering parameter S_{21} and of the intrinsic loss term L calculated by means of (1). Here, the number of SRRs was varied between 1–5. As expected, instead of a passband, measured for double negative media (see, for instance, Fig. 8), the frequency dependence of the transmitted wave shows a stopband with two corner frequencies at 11.5 and 13 GHz, respectively. From the metamaterial point-of-view, these two frequencies correspond to the resonance frequency (f_r) of the SRR and to the plasma magnetic frequency of the SRR array. From Fig. 13, it can be seen that the intrinsic losses peaks at these two characteristics frequencies, which is in agreement with simple considerations in connection with an enhancement of losses in a coupled resonator system. This also shows that it could be difficult in practical applications to avoid these intrinsic losses notably by operating much closer to the plasma

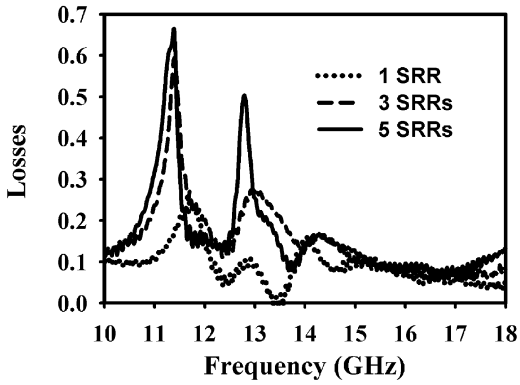

Fig. 12. Intrinsic losses versus frequency for one-, three-, and five-unit cells.

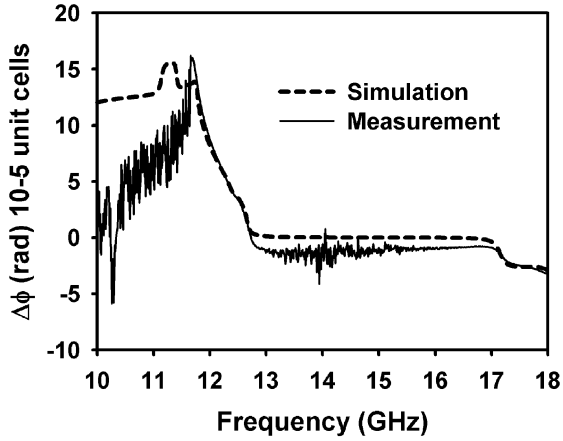

Fig. 14. Phase-shift offset between two lines of ten- and five-unit cells, respectively.

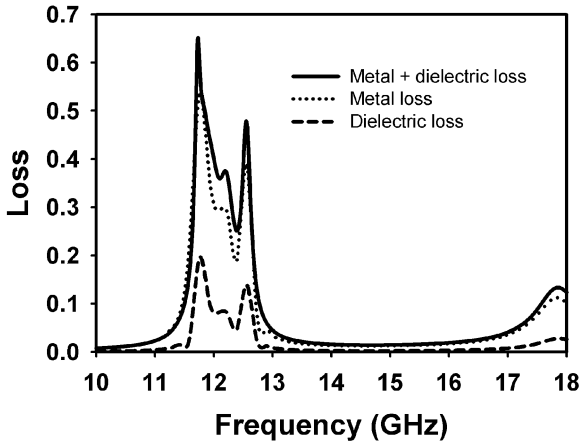

Fig. 13. Study of the various loss contributions for a five-cell prototype.

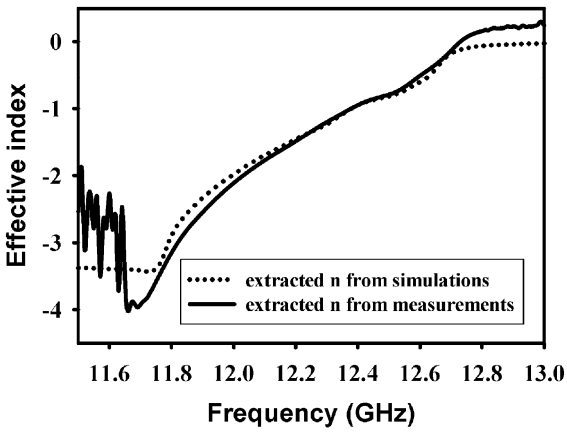

Fig. 15. Extracted effective refraction index, simulated data (dotted line), measured data (solid line).

frequency (f_p). This solution was sometimes proposed on the sole argument of a dramatic increase of the imaginary part of the permeability in the vicinity of f_r.

Therefore, the argument, which proposes to operate a little bit away from the resonant frequencies of the SRRs, does not hold. It remains to better understand the origin of losses with the possibility to have dielectric and metallic losses. In Fig. 13, we compare the frequency variation of the losses for three cases, i.e., dielectric, metallic, and overall losses. The metallic losses are the dominant contribution and are related to the high current flowing in the C-shaped loop at the resonance.

Before concluding, it remains to experimentally demonstrate the left-handedness character of the EM propagation. Some evidence was already obtained via the comparison of band structure and transmission spectrum, but a direct experimental verification is still lacking. As already pointed out in [15], an elegant means to show a reversal in the $\mathbf{k}$ vector direction is to use the phase offset between two lines of different lengths. Under this condition, in the frequency window where the EM waves can propagate, the phase offset is positive if the propagation is backward and negative for conventional lines. Fig. 14 gives the phase offset between two lines, respectively, of ten- and five-unit cells as a function of frequency. It can be seen that $\Delta\Phi$ is positive in the frequency band where the permittivity and permeability are negative simultaneously, while it is negative or vanishing elsewhere.

From the phase offset $(\Delta\Phi)$, it is also possible to extract the values of the effective refraction index using (2) as follows:

$$n = \frac{\lambda_0 \cdot \Delta\Phi}{2 \cdot \pi \cdot \Delta L}. \tag{2}$$

In this expression, λ_0 is the wavelength in free space, and ΔL is the difference of length between the two lines. Fig. 15 shows the results of this extraction procedure using the simulation and experimental data. In the LH window, n is negative with a maximum value of 4 obtained at 11.7 GHz. Again a good agreement between the extracted value from full-wave simulations and measurements is obtained.

IV. Conclusion

Taking advantage of a closed EM system where the propagation properties can be fully characterized, we have assessed the EM properties of a novel backward transmission line based

on a fin-line technology. The LH character of the transmission was demonstrated experimentally with potential application in terms of negative phase shift and inversion of the frequency wavelength relationship (negative curvature in the dispersion diagram). Special attention has to be paid to the loss level resulting from the resonant nature of C-shaped patterns. It is shown by calculating the various loss terms that the high current flowing in the resonant particle are the key contribution. It was also emphasized that a few SRRs are generally sufficient to achieve a highly dispersive EM behavior with unprecedented properties. As a consequence, a tradeoff has to be found with a limited number of cells. In this study, the choice of five cells was a good compromise between a reasonable loss level and the achievement of significant phase-shift effects. Another mean to satisfy the tradeoff between the performance of the LH transmission line notably in terms of bandwidth that is narrow ($\sim$10% here) and the negative index properties would be to decrease the Q factor of the resonators. The asymptotic limit in this decrease would be the transmission-line approach, which, for instance, consists of loading a one-dimensional (1-D) propagation medium with series capacitance and shunt inductance. Thus, in a recent publication, we have shown that such an approach, in the terahertz region [16], permits to work with a Q factor around 5–10 times smaller than the one achieved in the present study for an LH transmission line. With respect to the applications and despite that the fact that here we are using a 1-D system, whereas two-dimensional (2-D) and three-dimensional (3-D) prototypes are already demonstrated for negative refraction, many applications can be foreseen taking profit of the reversal of the phase velocity shown here. One can find in [17] high payoff directions with potential for many years using linear LH transmission lines integrated in composite transmission lines, phase shifters, and multibranch devices, which have been developed thus far with an RH scheme [18]. Also, it seems that the structures shown here could be suitable for nonlinear soliton/shock-wave nonlinear transmission lines. At last it is believed that the concept used here can be generalized to tunable devices notably through the use of ferroelectrics films, which exhibit voltage-controlled permittivity.

ACKNOWLEDGMENT

The authors would like to thank J. Carbonell, University of Valencia, Valencia, Spain, and F. Martin and M. Bonache, both with the University Autonoma of Barcelona, Barcelona, Spain. This study was also a part of the research program of the Institut de Recherche sur les Composants logiciels et matériels pour l'Information et la Communication Avancée (IRCICA) Institute, Villeneuve d'Ascq, France.

REFERENCES

[1] D. R. Smith, W. J. Padilla, D. C. Vier, S. C. Nemat-Nasser, and S. Schultz, "Composite medium with simultaneous negative permeability and permittivity," *Phys. Rev. Lett.*, vol. 84, no. 18, pp. 4184–4187, May 1, 2000.

[2] C. G. Parazolli, R. B. Greegor, K. Li, B. E. C. Koltenbah, and M. Tanielan, "Experimental verification and simulation of negative index of refraction using Snell's law," *Phys. Rev. Lett.*, vol. 90, no. 10, pp. 107 401.1–107 401.4, Mar. 2003.

[3] V. G. Veselago, "The electrodynamics of substances with simultaneously negative values of ε and μ," *Sov. Phys.—Usp.*, vol. 10, no. 4, pp. 509–514, 1968.

[4] J. B. Pendry, A. J. Holden, W. J. Stewart, and I. Youngs, "Extremely low frequency plasmons in metallic meso structures," *Phys. Rev. Lett.*, vol. 76, pp. 4773–4776, Jun. 1996.

[5] J. B. Pendry, A. J. Holden, D. J. Robbins, and W. J. Stewart, "Magnetism from conductors and enhanced nonlinear phenomena," *IEEE Trans. Microw. Theory Tech.*, vol. 47, no. 11, pp. 2075–2084, Nov. 1999.

[6] A. Grbic and G. V. Eleftheriades, "Experimental verification of backward-wave radiation from a negative refractive index metamaterial," *J. Appl. Phys.*, vol. 92, no. 10, pp. 5930–5935, Nov. 2002.

[7] L. Liu, C. Caloz, C. C. Chang, and T. Itoh, "Forward coupling phenomena between artificial left-handed transmission lines," *J. Appl. Phys.*, vol. 92, no. 9, pp. 5560–5565, Nov. 2002.

[8] T. Decoopman, O. Vanbesien, and D. Lippens, "Demonstration of a backward wave in a single split ring resonator and wire loaded fin line," *IEEE Microw. Wireless Compon. Lett.*, vol. 14, no. 11, pp. 507–509, Nov. 2004.

[9] T. Decoopman, X. Melique, O. Vanbésien, and D. Lippens, "A taper filtering finline at millimeter wavelengths for broad-band harmonic multiplication," *IEEE Microw. Wireless Compon. Lett.*, vol. 13, no. 5, pp. 172–174, May 2003.

[10] R. Marqués, J. Martel, F. Mesa, and F. Medina, "Left-handed media simulation and transmission of EM waves in subwavelength split ring resonator loaded metallic waveguides," *Phys. Rev. Lett.*, vol. 89, no. 18, pp. 183 901.1–183 901.4, Oct. 2002.

[11] F. Martin, J. Bonache, F. Falcone, M. Sorolla, and R. Marqués, "Split ring resonator-based left-handed coplanar waveguide," *Appl. Phys. Lett.*, vol. 83, no. 22, pp. 4652–4654, Dec. 1, 2003.

[12] J. Bonache, F. Martin, F. Falcone, J. Garcia-Garcia, I. Gill, T. Lopetegi, M. A. G. Laso, R. Marqués, F. Medina, and M. Sorolla, "Compact coplanar waveguide bandpass filter at the S-band," *Microw. Opt. Technol. Lett.*, vol. 46, no. 1, pp. 33–35, Jul. 2005.

[13] S. Hrabar, J. Bartolic, and Z. Sipus, "Waveguide miniaturization using uniaxial negative permeability metamaterial," *IEEE Trans. Antennas Propag.*, vol. 53, no. 1, pp. 110–119, Jan. 2005.

[14] I. A. Eshrah, A. A. Kishk, A. B. Yakovlev, and A. W. Glisson, "Evanescent rectangular waveguide with corrugated walls: A composite right/left-handed metaguide," in *IEEE MTT-S Int. Microw. Symp. Dig.*, Jun. 12–17, 2005, pp. 1745–1748.

[15] O. F. Siddiqui, M. Mojahedi, and G. V. Eleftheriades, "Periodically loaded transmission line with effective negative refractive index and negative group velocity," *IEEE Trans. Antennas Propag.*, vol. 51, no. 10, pp. 2619–2625, Oct. 2003.

[16] T. Crépin, J. F. Lampin, T. Decoopman, X. Mélique, L. Desplanque, and D. Lippens, "Experimental evidence of backward waves on terahertz left-handed transmission lines," *Appl. Phys. Lett.*, vol. 87, 2005, 104105.

[17] A. Lai, T. Itoh, and C. Caloz, "Composite right/left-handed transmission line metamaterials," *IEEE Micro*, vol. 5, no. 3, pp. 34–50, Sep. 2004.

[18] J.-M. Duchamp, P. Ferrari, M. Fernandez, A. Jrad, X. Melique, T. Junwu, S. Arscott, D. Lippens, and R. G. Harrison, "Comparison of fully distributed and periodically loaded nonlinear transmission lines," *IEEE Trans. Microw. Theory Tech.*, vol. 51, no. 4, pt. 1, pp. 1105–1116, Apr. 2003.

Thibaut Decoopman received the Electrical Engineer degree from the Institut Supérieur d'Electronique du Nord (ISEN), Lille, France, in 2001, and the Master degree from the Institut d'Electronique de Microélectronique et de Nanotechnologies du Nord (IEMN), Université des Sciences et Technologies de Lille, Lille, France, in 2001.

He then joined the Quantum Opto and Micro Electronic Device Group (DOME) Group, IEMN. He is currently with Astrium Velizy France, Vélizy, France. His research concerns ultra-broad-band multipliers aimed at operating in the upper spectrum of millimeter wavelengths and on metamaterials. He is mainly involved in simulation issues in close connection with fabrication.

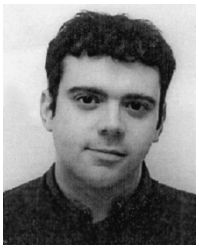

Aurélien Marteau was born in Saint Jean d'Angely, France, in 1979. He received the Engineer degree from the Ecole Nationale Supérieure d'Ingénieurs de Limoges (ENSIL), Limoges, France, in 2003, the Master degree from the DEA Télécommunications Hautes Fréquences et Optiques, University of Limoges, Limoges, France, in 2003, and is currently working toward the Ph.D. degree at the Institut d'Electronique, de Microélectronique et de Nanotechnologie (IEMN), Université des Sciences et Technologies de Lille (USTL), Lille, France.

His current interests concern the modeling of complex EM structures including double-negative media and their characterization.

Eric Lheurette received the Ph.D. degree in microwave electronics from the Université des Sciences et Technologies de Lille, Lille, France, in 1996. His doctoral thesis concerned the technology of resonant tunnelling devices and, more generally, of heterostructure devices.

Following a post-doctoral position with the Institut d'Electronique de Microélectronique et de Nanotechnologies du Nord (IEMN), Université des Sciences et Technologies de Lille, with main emphasis on EM simulation, he became an Assistant Professor with the University of Rouen. In September 2003, he joined the Quantum Opto and Micro Electronic Device Group (DOME) Group, IEMN, as an Assistant Professor with the prospect to further develop the DOME group's terahertz technology program. His current interests concern nonlinear electronics and electromagnetism of complex propagation media.

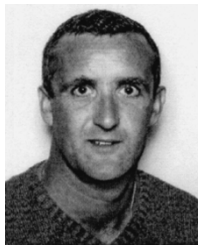

Olivier Vanbésien was born in Armentières, France, on November 11, 1964. He received the Engineer degree from the Institut Supérieur d'Electronique du Nord (ISEN), Lille, France, in 1987, and the Ph.D. degree (third-cycle thesis) in quantum devices from the Université des Sciences et Technologies de Lille, Lille, France, in 1991.

He then joined the High Frequency Department, Institut d'Electronique, de Microélectronique et de Nanotechnologie (IEMN), as a Chargé de Recherches CNRS. In November 2000, he became a Professor of electronics with the Université des Sciences et Technologies de Lille. His current interests concern metamaterials and photonic crystals, exploring both dielectric and metallic routes for applications of abnormal refraction from the terahertz region up to optics.

Didier Lippens received the Master of Science degree in electronics engineering, Ph.D. degree, and Doctor ès Sciences degree from the Université des Sciences et Technologies de Lille, Lille, France, in 1975, 1978, and 1984, respectively.

From 1980 to 1981, he was a Research Engineer with Thomson CSF. He led the Quantum and Terahertz Devices Team until 2001 He currently heads the Quantum Opto and Micro Electronic Device Group (DOME), Institut d'Electronique de Microélectronique et de Nanotechnologie (IEMN), Université des Sciences et Technologies de Lille. He is currently a Professor of electrical engineering with the Université des Sciences et Technologies de Lille, where his main interests are nanotechnology and nanosciences. He has been involved with molecular dynamics in liquid crystals and with semiconductors physics, and is currently more involved with nonlinear electronics and opto-electronics along with electromagnetism in artificial media. He has undertaken pioneering research on resonant tunnelling devices and, more generally, on heterostructure semiconductor devices. His current interests are terahertz sources, most notably quantum cascade lasers (QCLs), photomixers and heterostructure barrier varactors, photonic bandgaps, and metamaterials-based passive and active devices.

Available online at www.sciencedirect.com
SCIENCE DIRECT®
C. R. Physique 6 (2005) 683–692
COMPTES RENDUS PHYSIQUE
http://france.elsevier.com/direct/COMREN/

Interaction of electromagnetic fields with the environment/Interaction du champ électromagnétique avec l'environnement

Left-handed propagation media via photonic crystal and metamaterials

Thibaut Decoopman *, Thomas Crepin, Mathias Perrin, Sophie Fasquel, Aurélien Marteau, Xavier Mélique, Eric Lheurette, Olivier Vanbésien, Didier Lippens

Institut d'électronique de microélectronique et de nanotechnologie, université des sciences et technologies de Lille, avenue Poincaré, BP 60069, 59652 Villeneuve d'Ascq cedex, France

Available online 30 August 2005

Abstract

We review the electromagnetic properties of artificial structures such as photonic band gap materials (Electromagnetic Band Gap at microwaves) and metamaterials with main emphasis on backward (left-handed) propagation media. We consider free space and guiding structures by showing how the interaction of the electromagnetic wave with periodic dielectric (PBGs) and double negative metallic structures (DNGs) yields a negative refractive index. Some of the potential applications in connection with negative index media are briefly discussed such as focusing for a flat lens and phase advance for a left handed transmission line. ***To cite this article: T. Decoopman et al., C. R. Physique 6 (2005).***

Résumé

Propriétés électromagnétiques des milieux artificiels par des cristaux photoniques et des métamatériaux. Nous présentons les propriétés électromagnétiques de milieux artificiels tels que les matériaux à Bande Interdite Photonique (BIP) (ou Bande Interdite Electromagnétique en micro-ondes) et les métamatériaux, en particulier les métamatériaux main-gauche. Nous considérons des dispositifs en espace libre et des structures de guidage, et nous montrons comment l'interaction d'une onde électromagnétique avec des milieux diélectriques périodiques (BIP) et des milieux métalliques doublement négatifs conduit à un indice de réfraction négatif. Quelques-unes des applications potentielles en relation avec les milieux à indice de réfraction négatif sont brièvement présentées, telle que la focalisation par une lentille plane ou l'avance de phase pour une ligne de transmission main-gauche. ***Pour citer cet article : T. Decoopman et al., C. R. Physique 6 (2005).***

1. Introduction

Photonic (Electromagnetic) Band Gaps (PBGs /EBGs) and metamaterials are periodic structures, patterned on a scale comparable or much shorter than the operating wavelength. The relevant dimensions are thus on a nanometer scale if infrared or visible spectra are targeted. Even though they are made of positive index materials, these structures exhibit abnormal dispersion characteristics in the long wavelength regime. The materials can indeed exhibit a strong anisotropy, or behave as a medium of negative index of refraction—associated with negative values of the permittivity and permeability.

* Corresponding author.
E-mail addresses: Thibaut.Decoopman@fresnel.fr (T. Decoopman), Didier.Lippens@iemn.univ-lille1.fr (D. Lippens).

1631-0705/$ – see front matter
doi:10.1016/j.crhy.2005.06.007

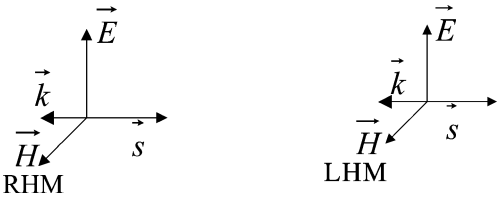

Fig. 1. (E, H, K) trihedrons for Left-Handed (LH) and Right-Handed (RH) materials.

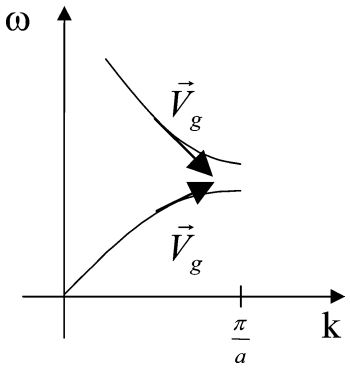

Fig. 2. Illustration of the left-handed character of the second branch.

In such double negative (DNG) media, propagation of light, or generally of electromagnetic (EM) waves can be backwards. The wave vector, **k**, electric field, **E**, and magnetic field, **H**, constitute an indirect trihedron, where **k** and the Poynting vector, **S**, are antiparallel (Fig. 1). In this case, they are termed Left-Handed Materials (LHMs) as proposed by Veselago in 1968 [1].

Beyond this inversion of phase velocity with respect to the direction of energy flow, an impact of a negative refractive index, n, may be found in negative refraction. The incident and refracted beams are then on the same side of the normal to refraction interface, as it is predicted by the Snell–Descartes law, with a negative refractive index. It results in a natural focusing effect with flat lenses (Veselago lens), whose properties are invariant by translation, with the prospect, as proposed recently by Pendry [2], to also avoid the diffraction limit with the so-called 'superlens effect' (ideal lens).

In this paper, we address the general problem of the interaction of an EM wave with such micro and nanostructures, with the main emphasis on the effects in connection with a negative refractive index. First, we show how the lefthandedness can be pointed in DNG media via (i) band structure calculation assuming Bloch waves, and (ii) the comparison of phase shift in finite EM region of various lengths. Then we focus on dielectric periodic structures by considering mainly 2D structures whereas, in the last sections, we address the main issue in connection with metamaterials made of dielectric and metal composites. Technological challenges for fabricating real life prototypes will be shortly discussed when specific technological developments have to be solved.

2. Lefthandedness signature

It is well known that gaps may be open in a periodic structure. The simplest electromagnetic device of this kind is the so-called Bragg reflector made of various alternate layers with different refractive index. The forbidden gap corresponds in this case to the reflectance plateau resulting of the constructive interference of the various components of the reflected wave at the interfaces. The thickness of each layer has to match a quarter of the wavelength in the considered medium and thus the pertinent scale (pitch of this one D-periodic structure) is comparable to the operating wavelength. In the gap, the EM waves are evanescent and thus the propagation is forbidden. Out of this gap, propagation can take place with dispersion effects due to the openness of this gap. For the lower frequency dispersion branch the propagation is right-handed, as illustrated in Fig. 2. The group velocity (v_g) and the phase velocity ($v\varphi$) have the same direction whereas the dispersion branch above the gap is left handed with v_g and v_φ of opposite sign. This is the first signature of the left-handed character of a dispersive propagation media. It is based on the consideration of an infinite propagation medium defined by a unit cell with a characteristic dimension (a) defining by this means the boundary of the Brillouin zone.

Let us consider first a dielectric array of holes etched in a high index dielectric. Fig. 3 shows a Scanning Electron Micrograph (SEM) of such a 2D hole array patterned in a Si_3N_4 thin film which will be used for subsequent deep etching by RIE. This nanostructure, fabricated at IEMN, was patterned by e-beam lithography using conventional PMMA resist, Plasma Enhanced Chemical Vapor deposition (PECVD) for the transfer of a Si_3N_4 layer and Deep Reactive Ion Etching for the dry etching of holes.

Fig. 4 illustrates the etching stage. The structure under test is based on an InP technology with conventional technique to confine the light in the direction perpendicular to the growth axis of semiconductor (namely the use of InGaAsP/InGaAs heterojunction). Despite the high filling factor between air and semiconductor the high degree of anisotropy afforded by the reactive plasma etching technique permitted us to etch holes with a typical diameter around 0.3 μm with comparable period

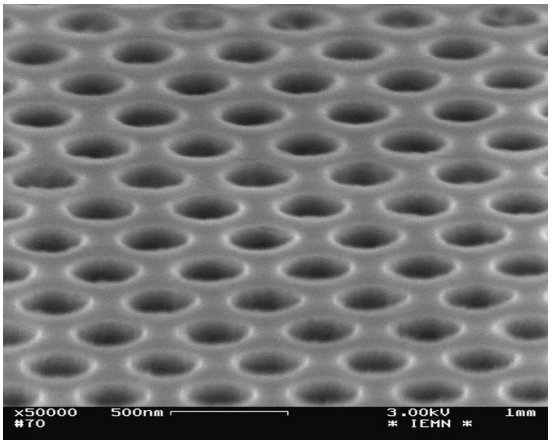

Fig. 3. Scanning electron micrograph of a hole area.

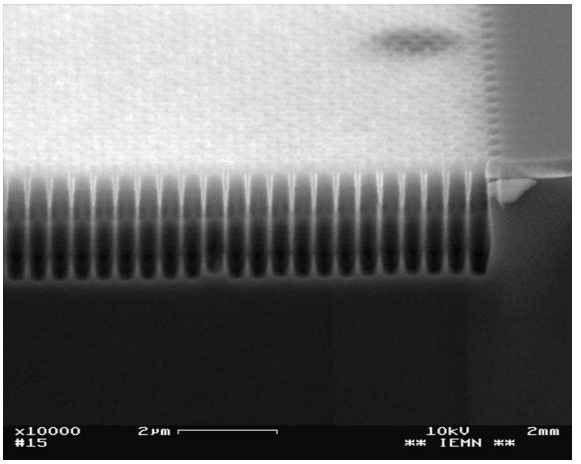

Fig. 4. Scanning Electron Micrograph of a 2D photonic crystal.

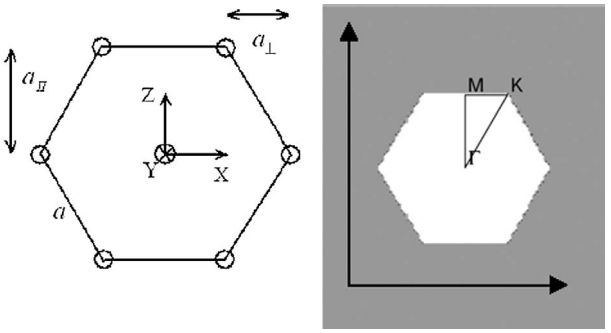

Fig. 5. Schematic of the hexagonal dielectric structure with the definition of main direction in the Brillouin zone.

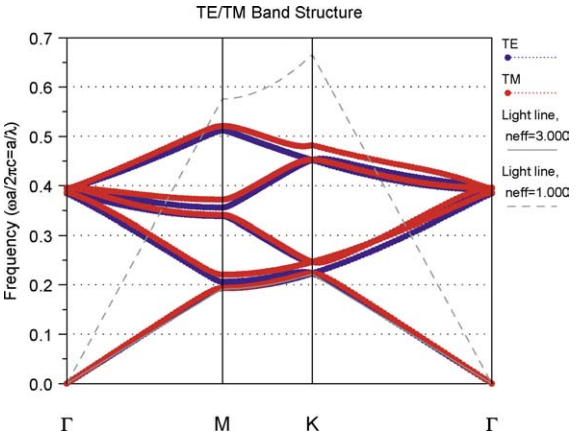

Fig. 6. Dispersion characteristic of a hexagonal hole array for TE and TM polarizations.

and a depth of 3 µm. High aspect ratio nanostructures (10 : 1) are thus successfully fabricated on a deep submicron technology (relevant dimensions around a few hundred of nanometers).

Turning now to a generic hexagonal structure with an index contrast $\Delta n = 2$, whose geometry is schematised in Fig. 5 along the main direction in the Brillouin zone, ΓM, ΓK and KM respectively. The air filling factor we considered in the present example is $f = 0.093$.

The corresponding band structure is shown in Fig. 6, for both TE (field components Hx, Ey, Hz) and TM (field components Ex, Hy, Ez).

The dispersion relation of the photonic structure—band diagram—has been obtained using commercial software, BandSolve, developed by Rsoft. A Matlab code has also been developed, and used for the same purpose. More generally, note that several numerical methods may be used to solve the numerical problem, and find the couple $(\omega, \vec{k})$ to define the dispersion relation of a plane wave propagating in an infinite medium. The core of the problem is the resolution of an eigenvalue equation: $M_k \Phi = \lambda_k \Phi$, where $\lambda_k = (\omega/c)^2$, and,

$$M_k = (\nabla + i\vec{k}) \wedge \left[\left(1/\varepsilon(r)\right)(\nabla + i\vec{k})\right] \wedge,$$

where $\wedge$ is the vectorial product.

We have used a numerical procedure based on Hessenberg decomposition and a QR method to solve the linear system that gives the eigen elements. Such a method requires the computation of all the matrix elements, which is not too serious a problem, provided one avoids 3D simulations. It has been shown that convergence problems may occur with such an algorithm [3]. In that case, one shall use a fine evaluation of the Fourier transform of $1/\varepsilon$ [4], or variational methods [5–7]. However, in our

case, considering around 10^3 plane waves has been enough to model accurately the band structure. We also have carried out time domain simulations: two-dimensional FDTD, using FullWAVE, by Rsoft. This algorithm directly integrates the Maxwell propagation equations using finite difference method.

Due to the small filling factor—small air holes—the first band is very close from the light line of a homogeneous medium of index $n_{\text{hom}} = 2.81$. This corresponds to the average of the permittivity of air and dielectric, weighted by their surfacic fraction. No gap is present here, and thus the higher order bands appear for quite low frequency: $a/\lambda > 0.2$.

The components of group velocity: $Vg_i = \partial\omega/\partial k_i$, with $i = \{x, z\}$, are positive on the first ground band. Conversely, they can take negative values on higher energy bands.

In order to give a more precise look at the prediction concerning propagation in such a bi-dimensional crystal, one has to get out of the 1D-picture and look at the energy contours in the Brillouin zone.

An example of such a mapping of iso-frequency contours is reported in Fig. 7. Close to the Γ point the dispersion properties are quite isotropic circle-like energy contours. In contrast anisotropy effects can be found close to the boundary of the Brillouin zone. For applications in imaging, it will be very important to work in the zones of isotropy, as all the rays coming from one source will experience the same index of refraction. This reasoning is thus different from those invoked for ultra-refraction effects where conversely a high anisotropy is a welcome feature.

Until now, we have presented results valid for infinite structures, where plane waves propagate. Let us now focus on a real device of finite size, where diffraction at the input can occur and be a new origin of anisotropy. Consider here a vacuum wavelength corresponding to $a/\lambda = 0.28$, and compare what happens for directions ΓM (second band), and MK (third band), for TM polarisation. For a hexagonal structure, the step of the grating in both direction MK and ΓM $- a_{\text{II}} = 0.24\lambda$ and $a_{\perp} = 0.14\lambda$, respectively—is not the same.

Thus, a beam coupling from free space will not be diffracted in the same way for both directions. The more intense diffraction in the case of an input along MK will create wavefronts along other directions—cf. Fig. 8(a). On the contrary, Fig. 8(b) shows that the beam propagates with few perturbations. One can conclude that anisotropy effects are twofold: for infinite material, they appear in the band structure (Fig. 6), for finite size systems, diffraction at the entrance/output also plays a role.

If optical devices were made of this material, image limitations due to diffraction would strongly depend on the direction of input, and thus be more complex than what arises with ordinary materials. It is therefore important to work in a frequency range, where the medium behaves isotropically, as if it was homogeneous.

Fig. 9 illustrates the refraction regime for a wave impinging onto a prism like-dielectric array. The feeding of the structure is along the ΓM direction. The frequency of the EM wave is chosen in the Left Handed dispersion branch by taking care to preserve the isotropy, working close to Γ. By analysis of the phase front it can be seen that the—large arrow—beam refracts on the other side of the normal—dashed line—compared to a conventional positive refractive index materials.

Fig. 10 shows the results of a numerical experiment showing focusing of EM waves by means of a flat lens. The source consists in a truncated waveguide on the left hand side of the figure, close to the lens made of the artificial structure. A first focus is apparent within the composite slab and another can also be seen on the other side of the lens. Such a focusing effect, making use of negative refraction, is invariant by translation in contrast to conventional lenses.

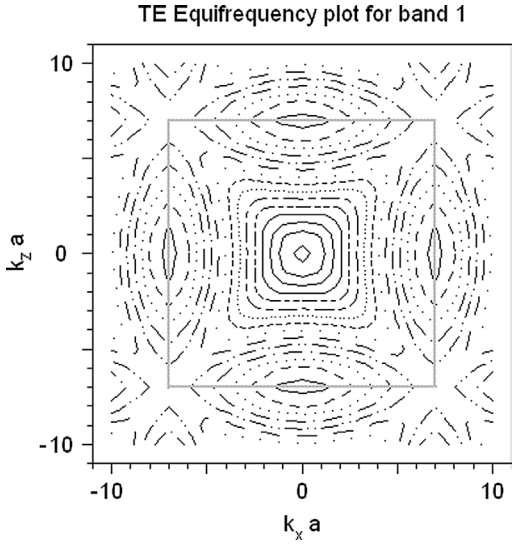

Fig. 7. Iso-frequency (energy plot) in the Brillouin zone.

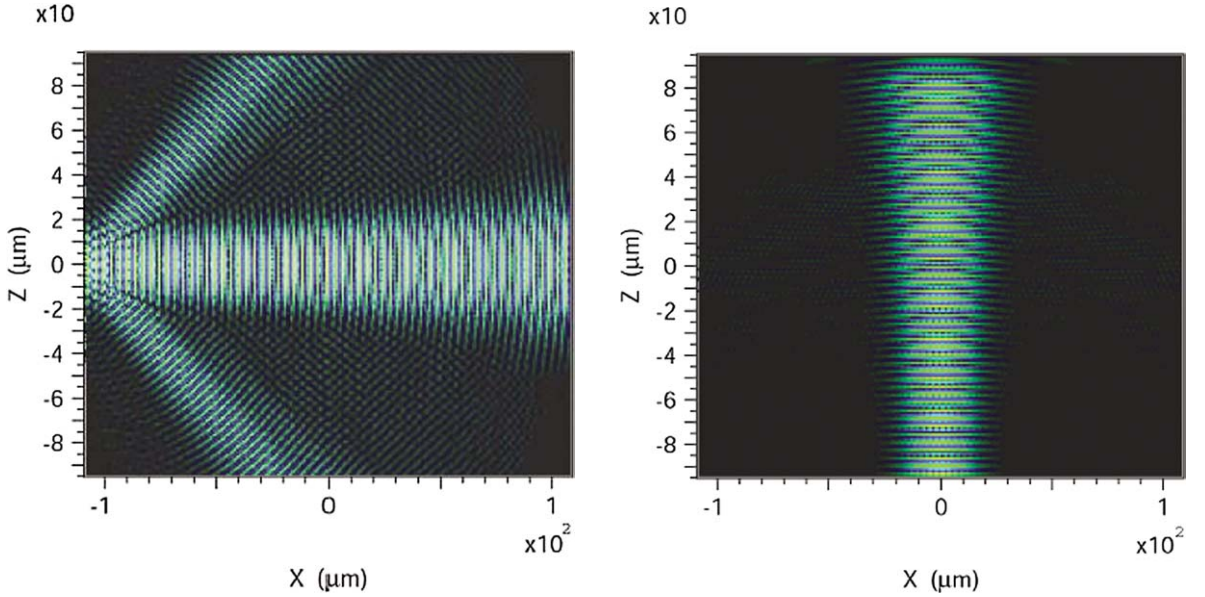

(a) (b)

Fig. 8. (a) Component Hy inside a 2D periodic structure for injection along the MK direction (TM polarization $a/\lambda = 0.28$); (b): Input along the ΓM direction.

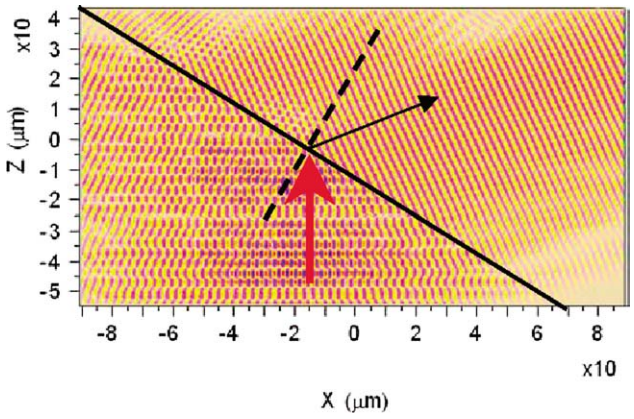

Fig. 9. Numerical modelling of the negative refraction effect.

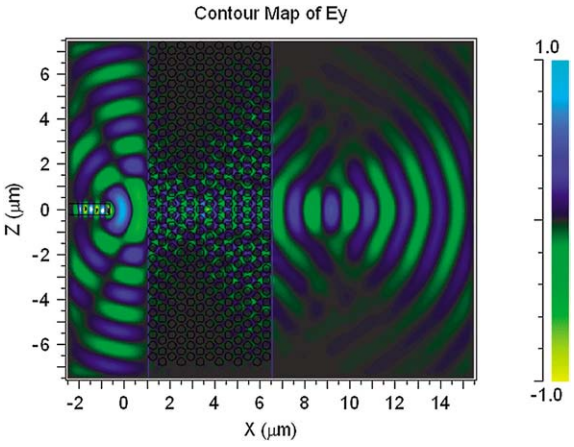

Fig. 10. Illustration of the focusing effect in a 2D flat lens (Veselago lens).

Using the view of the negative refraction of incident beams, it is also possible to have a first estimate of the effective refractive index of the lens. From Snell–Descartes law in the present numerical experiment a value close to unity is thus not far from the ideal situation where perfect matching is obtained.

3. Metamaterials: SRR and wire arrays

The prefix ‘meta’ means beyond. Indeed, by a proper structuring of materials, the possibility to synthesize double negative media can be demonstrated and notably artificial media exhibiting a negative permittivity value, created by wires arrays. This approach was inspired by plasma physics with the key result that a resonant behaviour of free carriers can be obtained at the plasma frequency [8]. Below this frequency, the effective permittivity is negative. For a metal, this frequency is in the UV range, but can be lowered to microwave region by dramatically decreasing the filling factor of wire arrays embedded in a dielectric

host substrate. With this aim, one possibility is to use thin metallic wire grids arranged in a periodic way. In this case, the electron density is strongly decreased, such as the plasma frequency. Fig. 11 shows the scattering parameters (S_{ij}) obtained for Aluminum wires with a radius of 1 µm, separated by 5 mm. This media is excited with a plane wave, electrically polarized along the wires. Below 11 GHz, the permittivity becomes negative and the transmission drops.

To allow EM propagation, permeability has also to be negative, simultaneously. This can be achieved with metallic open rings, such as those first proposed by Pendry and termed as Split Ring Resonators (SRR) [9]. It is worth noting that a magnetic response is thus obtained with current loops made from non magnetic materials. Basically, the principle is to combine inductive and capacitive effects to create a resonance leading to a negative permeability. Fig. 12 is an optical view of various magnetic particles fabricated by e-beam lithography at IEMN. Square- or ring-shaped elements can be designed and their relevant dimensions permit one to tailor the frequency of operation by changing the resonance frequency which is also characterized by a high quality factor.

In conventional operation, in order to properly excite the SRR, the incident magnetic field has to be perpendicular to the plane containing the ring. However, recently it was shown SRRs that can be excited (existence of current loop when the electric field is parallel to a gap bearing arm of the SRR) [10]. The main drawback of the SRR is the limited bandwidth, since the effective permeability is negative in a narrow frequency band between the resonance frequency of the current loops and the magnetic plasma frequency.

To increase the operation frequency range, simple scaling rules can not be applied keeping in mind that other phenomena such as electron inertia and edge effects have also to be considered. Nevertheless, this kind of resonant and metallic ring is expected to operate at least up to mid-infrared. With this aim, other submicronic shapes are investigated to circumvent the aforementioned limitations. Fig. 13 is an optical microscope view of recent structures fabricated at IEMN for infrared operation.

To create a double negative media (DNG), wire and SRR arrays are superimposed [11]. Even if the magnetic and electrical responses are coupled, it is possible to keep the magnetic resonance in a frequency range where the permittivity is negative. Another key point concerns the coupling of this artificial media with free space. Indeed, careful impedance matching has to be achieved to prevent reflection at the interface and thus minimize the return losses. Under these conditions, the transmissivity can be close to unity in the frequency range where both permittivity and permeability are simultaneously negative and the

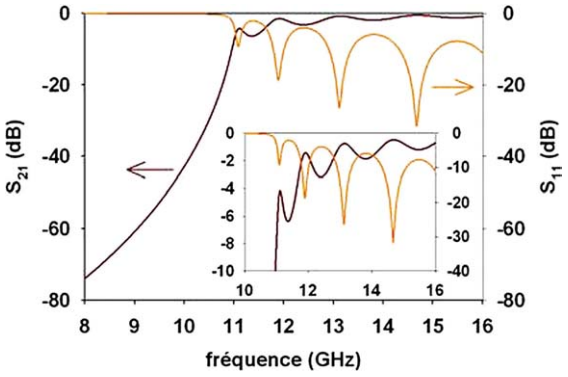

Fig. 11. Electromagnetic response of an aluminum wire array.

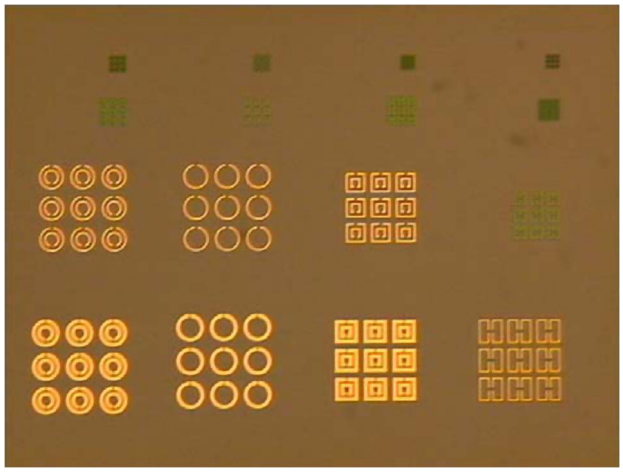

Fig. 12. Optical view of the various SRR (Split Ring Resonators) arrays.

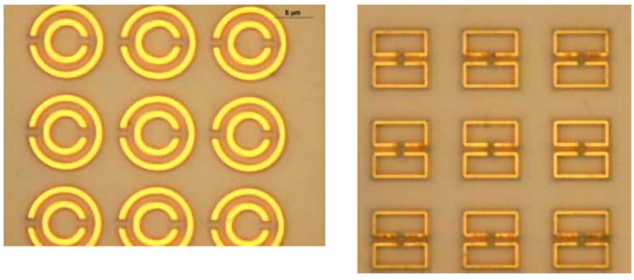

Fig. 13. Enlarged views of two kind of SRRs for operation in infrared.

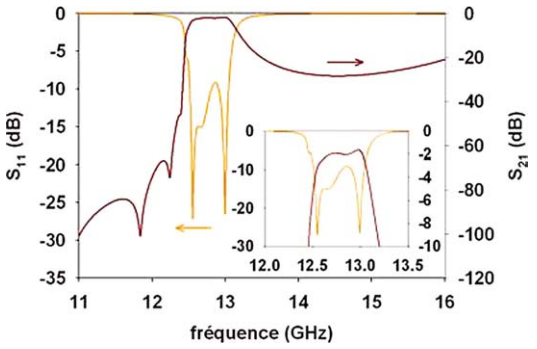

Fig. 14. Full-wave analysis of a DNG array operating in X band.

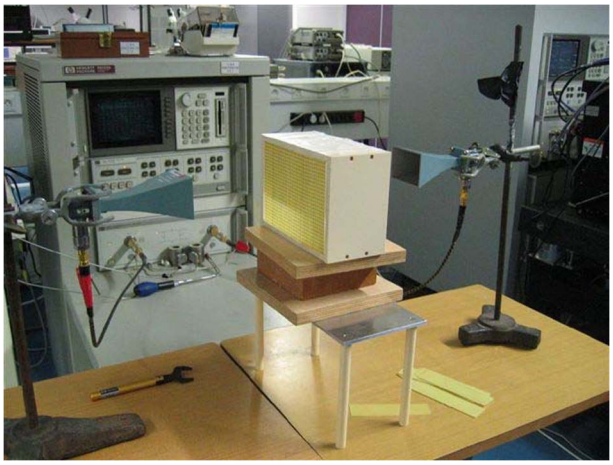

Fig. 15. View of the experimental set up for the frequency assessment of free space prototypes. The SRR array is placed here in order to have the electric field parallel to a gap bearing arm of SRRs.

impedances are equal [12]. Fig. 14 shows the frequency dependence of the scattering of a prototype operating at X band. The device is left-handed between 11.5 and 13.5 GHz with a maximum of transmission around −2 dB.

The free space experimental setup used for the characterization is presented Fig. 15. In the present experiment we assessed the frequency response of a SRR array with the incident electric field parallel to the gap bearing arm. The medium is probed by means of horns, which are used to generate a quasi planar wave. The characterization is conducted by means of vectorial network analysis and we will see in the following section that such experiments allow the experimental assessment of the left handed character.

4. Left-handed transmission lines (finline technology)

For microwave applications, the transmission line approach is more appropriate for circuit design and integration in existing systems. High performance coupling, phase-shifting or filtering devices can be thus fabricated, benefiting from a sub-wavelength structured left-handed medium with the associated benefit of high compactness. In this context, the finline technology is a good candidate and we present in this section the analysis of a novel left-handed composite transmission line that we proposed recently [13].

This one-dimensional propagation structure is based on the dual transmission line configuration. Indeed by inverting reactive elements in order to have a series capacitance and a shunt inductance, it is possible to obtain a highly dispersive left-handed transmission line. Practically, this topology is difficult to realize, but it is possible to load periodically a classical line with discrete elements. In this case, the dispersion diagram is modified and exhibits a frequency bandwidth within the propagation which is left-handed. In this work, the main waveguide is a finline, consisting in a slotline inserted in the E-plane of a metallic hollow waveguide. Such a transmission line is periodically loaded with thin wires in a shunt configuration. Instead of series resistance ring resonators are patterned on the backside of the substrate (Fig. 16). The period and a fortiori the characteristic dimensions of wires and SRR's are small compared to the guided wavelength, in order to allow the homogenisation of the medium. From the modeling side, the band diagram can be deduced from the scattering parameters of an unit cell, calculated

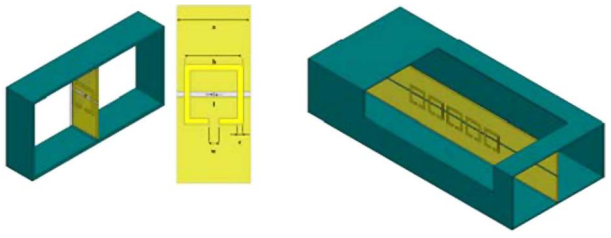

Fig. 16. Basic cell and schematic of a LH transmission line.

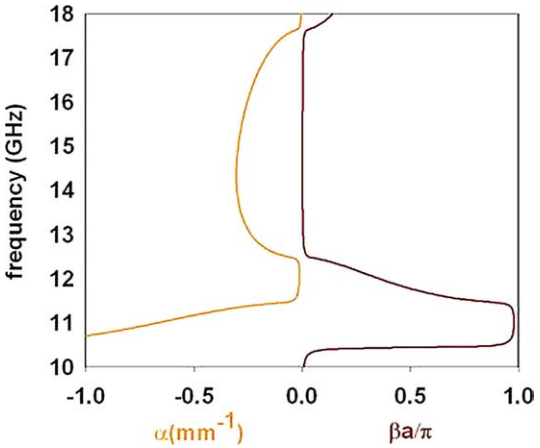

Fig. 17. Band structure of the transmission line in a finline technology.

Fig. 18. Photo of a Ka band LH finline.

with a finite element method (HFSS by Ansoft). This diagram shows a band pass between 11.5 and 12.5 GHz (Fig. 17), with a negative slope, indicating that the wave vector and the Poynting vector are opposite in sign as discussed in introduction. The propagation is thus backward, since the wave front moves in an opposite direction with respect to that of energy. Numerically, this backward propagation can be demonstrated by time domain analysis or by modifying the phase at the origin in order to mimic a temporal analysis. Fig. 18 shows a photo of a Ka band prototype (10–18 GHz), consisting in 20 unit cells. The metallic waveguide is split and machined to allow planar circuit housing inside a groove.

The ring resonators on the picture were fabricated by conventional Printed Circuit Board techniques, and the prototypes were characterized by means of vectorial network analysis. These measurements have shown low insertion losses, indicating a good impedance matching between the composite transmission line and the embedding media (waveguiding section). The metallic shielding afforded by the waveguide prevents any radiation losses. Under this condition the transmission losses can be linked to the use of highly resonant metallic rings and a trade-off has to be found between the level of rejection and the overall losses.

A direct experimental verification of the lefthandedness of this structure can be found from the phase offset between two lines of various lengths. It can be shown that this offset ($\Delta\phi$) is positive when propagation is backward and negative for a right handed behaviour. Fig. 19 shows the variation versus frequency of $\Delta\phi$ measured and calculated for the device under test. In the left handed dispersion branch $\Delta\phi$ is positive in agreement with the band structure calculation.

5. Periodically loaded C–L transmission lines

As shown before LH propagation media can be realized with transmission lines periodically loaded by quasi-lumped elements. In this section we present a coplanar strip (CPS) transmission line approach using Metal Insulator-Metal-capacitors and meander-like inductors. The first originality with respect to the literature is their frequency of operation in the Terahertz range while to the state of the art, works address the microwave range. The second novelty is the characterization method we used which is based on electro-optic sampling experiment.

Fig. 20 is an optical view of the devices which were designed and fabricated following these guide lines. The Coplanar stripline (CPS) is composed of two planar metallic conductors patterned on a substrate. On such a line, with two separate conductors, the propagation mode is quasi-TEM.

With the C–L type scheme loading the line, the electromagnetic wave interacting with the structure will see a series of C–L high-pass sections. It can be shown that the ground dispersion branch is left handed. According to the criterion of metamaterials, the physical dimensions of components have to be small with respect to the wavelength. In practice we chose the following parameters. The width of the strips is 10 μm and the distance between both strips is 25 μm. The capacitors are parallel-plate capacitors with 100 μm^2 area and 300 nm Si_3N_4 dielectric. To extend the inductance value we design a meander strip. This strip has a 200 μm total length and a 200 nm width. The periodicity is about 30 μm. Full wave analysis shows the first transmission band is centered around 200 GHz and the bandwidth is approximately 200 GHz (Fig. 21). From the technological point of view the meander inductances were patterned by e-beam lithography, and the parallel plate capacitors were fabricated by PECVD dielectric deposition.

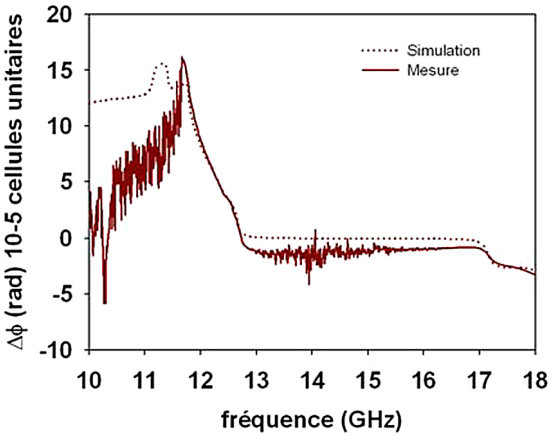

Fig. 19. Experimental evidence of lefthandedness via the phase offset between two lines.

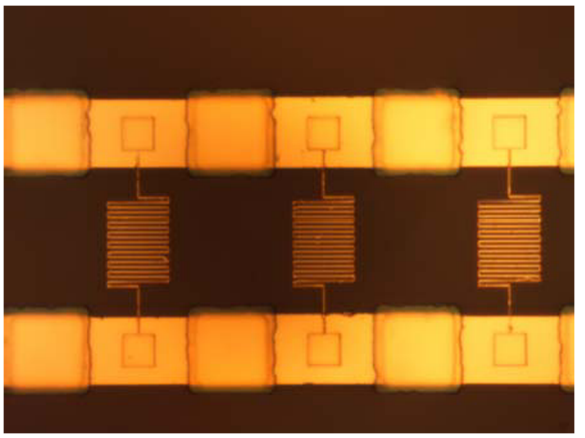

Fig. 20. Photo of the C–L type LH transmission line operation at Terahertz frequencies.

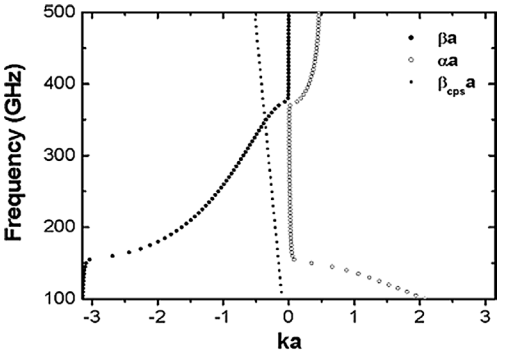

Fig. 21. Band structure calculation of the C–L type LH transmission line.

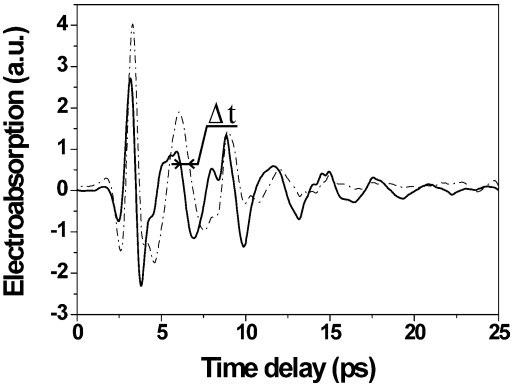

Fig. 22. Time dependence of the transmitted signal through the devices. Experimental evidence of the phase advance (21 cells solid line, 17 cells dashed line).

In order to generate ultra short pulses, the lines are covered with patches of low temperature grown semiconductor. Electro-optic sampling is carried out in a pump probe experiment with GaAs thin film for the generation and AlGaAs ones for the probing of the transmitted and reflected wave. For the latter, we record the variations of electro-absorption by Franz Keldish effect.

Fig. 22 shows the time variation of the transmitted pulse for a 21 cells and 17 cells transmission lines. There is a phase advance for the former resulting from the backward propagation.

6. Conclusion

Left-handedness of various metamaterial-based EM propagation media is now demonstrated theoretically and experimentally. This can be seen through the band structure calculation numerical experiment of the negative refraction and the focusing by flat lenses or by monitoring the phase offset by frequency or time domain analysis. Beyond the improvement of intrinsic performance notably by addressing the losses issue, the next stages are nanostructring of 3D devices and the investigation of new routes for negative permeability.

Acknowledgements

This work has been carried out in the framework of the Network of excellence METAMORPHOSE, the Eureka project TELEMAC and the coordinated research projects in the framework of Nanosciences and Nanotechnology French programme (ACI NANOTHEME and METAPHORE).

References

[1] V.G. Veselago, The electrodynamics of substances with simultaneously negative values of ε and μ, Sov. Phys. Uspekhi 10 (4) (1968).
[2] J.B. Pendry, Negative refraction makes a perfect lens, Phys. Rev. Lett. 85 (18) (2000).
[3] H.S. Sozuer, J.W. Haus, R. Inguva, Photonic Bands: Convergence problems with the plane-wave method, Phys. Rev. B 45 (1992) 13962.
[4] R.D. Meade, A.M. Rappe, K.D. Brommer, J.D. Joannopoulos, O.L. Alerhand, Accurate theoretical analysis of photonic band gap material, Phys. Rev. B 48 (1993) 8434.
[5] S.G. Johnson, J.D. Joannopoulos, Bloch-iterative frequency-domain methods for Maxwell's equations in a planewave basis, Optics Express 8 (2001) 173.
[6] A. Edelman, S.T. Smith, On conjugate gradient-like methods for eigen-like problems, B.I.T. 36 (1996) 494.
[7] M.C. Payne, M.P. Tater, D.C. Allan, T.A. Arias, J.D. Joannopoulos, Iterative minimization technique for ab-initio total-energy calculations: molecular dynamics and conjugate gradients, Rev. Mod. Phys. 64 (1992) 1045.
[8] J.B. Pendry, A.T. Holden, W.J. Stewart, I. Youngs, Extremely low frequency plasmons in metallic mesostructures, Phys. Rev. Lett. 76 (1996) 4773.
[9] J.B. Pendry, A.J. Holden, D.J. Robbins, W.J. Stewart, Magnetism from conductors and enhanced nonlinear phenomena, IEEE Trans. Microwave Theory Tech. 47 (11) (1999).
[10] R. Marques, F. Mesa, J. Martel, F. Medina, Comparative analysis of edge- and broadside-coupled split ring resonators for metamaterial design. Theory and experiments, IEEE Trans. on Antennas and Propagation, in press.
[11] R.A. Shelby, D.R. Smith, S.C. Nemat-Nasser, S. Schultz, Microwave transmission through a two-dimensional, isotropic, left-handed metamaterial, Appl. Phys. Rev. Lett. 78 (2001).
[12] C.G. Parazzoli, R.B. Greegor, K. Li, B.E.C. Koltenbah, M. Tanelian, Experimental verification and simulation of negative index of refraction using Snell's law, Phys. Rev. Lett. 90 (2003) 107401.
[13] T. Decoopman, O. Vanbésien, D. Lippens, Demonstration of a backward wave in a single split ring resonator and wires loaded finline, IEEE Microwave and Wireless Components Lett. 14 (11) (2004).

INSTITUTE OF PHYSICS PUBLISHING JOURNAL OF OPTICS A: PURE AND APPLIED OPTICS
J. Opt. A: Pure Appl. Opt. **7** (2005) S3–S11 doi:10.1088/1464-4258/7/2/R01

REVIEW ARTICLE

Left-handed electromagnetism obtained via nanostructured metamaterials: comparison with that from microstructured photonic crystals

Mathias Perrin, Sophie Fasquel, Thibaut Decoopman, Xavier Mélique, Olivier Vanbésien, E Lheurette and Didier Lippens

Institut d'Electronique, de Microélectronique et de Nanotechnologie, Université des Sciences et Technologies de Lille, 59 652 Villeneuve d'Ascq, Cedex, France

E-mail: Didier.lippens@iemn.univ-lille1.fr

Received 1 June 2004, accepted for publication 10 November 2004
Published 20 January 2005
Online at stacks.iop.org/JOptA/7/S3

Abstract
In this work, we review some of the key issues for designing dielectric and metallic arrays in the diffraction or refraction regimes with main emphasis on left-handed electromagnetism. We first discuss dispersion characteristics of periodic dielectric arrays which are structured on the wavelength scale (photonic crystals for optics and electromagnetic band gaps for microwaves) with special attention paid to propagation and refraction effects. Special attention was also paid to the isotropy properties in the Brillouin zone with the prospects of defining a negative refractive index. Then, we considered metallic structures which permit one to synthesize double-negative media with the goal of pushing their operation frequency into the infrared region. For both classes of microstructures and nanostructures, the technological challenges will be addressed by considering air hole arrays in a high refractive index semiconductor substrate and embedded C-shaped and wire metal arrays patterned on low index substrates.

Keywords: metamaterial, nanostructures, dielectric and metallic structure photonic band gaps, photonic crystals, negative refraction

(Some figures in this article are in colour only in the electronic version)

1. Introduction

Metamaterials are periodic structures, patterned on a scale much shorter than the operating wavelength and thus on a nanometre scale if the infrared or visible spectra are targeted. Though they are made of positive index materials at small length scale, these structures exhibit abnormal dispersion characteristics at large scale. The material can indeed exhibit a strong anisotropy, or behave as a medium of negative index of refraction—associated with negative values of the permittivity and permeability. In such periodic media, propagation of light, or generally of electromagnetic (EM) waves, can be backward. The wavevector, **k**, electric field, **E**, and magnetic field, **H**, then constitute an indirect trihedron, where **k** and the Poynting vector, **S**, are antiparallel. In this case, they are termed left-handed materials (LHMs) as proposed by Veselago in 1968 [1]. Beyond this inversion of the phase velocity with respect to the direction of propagation of energy, the main impact of

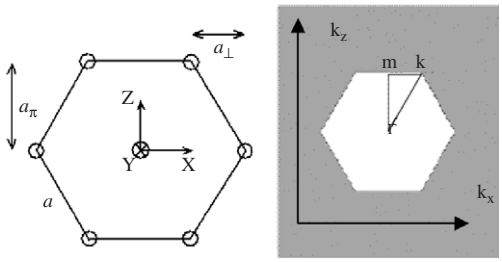

Figure 1. A schematic diagram of the hexagonal dielectric structure with the definition of the main direction in the Brillouin zone.

a negative refractive index, n, may be found in the negative refraction [2–4]. Both the incident and refracted beam are then on the same side of the normal to the refraction interface, as if predicted by Snell's law with a negative refractive index. Under this condition, any radiating source placed in a front of a slab of negative refractive index shows focusing effects within and outside the slab under near field conditions. One can thus build flat lenses (Veselago/Pendry lenses), whose properties are invariant upon translation parallel to their surface. Besides this, as proposed recently by Pendry [5], one prospect is also to avoid the diffraction limit with the so-called 'superlens effect'. In the far field limit, using a vanishing index [5] may also contribute to the collimation of an isotropic radiating source.

This work reviews the study of different types of artificial material, made of dielectric or metallic structures. Section 2 will address anisotropy effects and backward propagation in photonic crystals (PC), which exhibit right-handed and left-handed dispersion branches. On the basis of numerical simulations in the time domain and of band structure calculations over the whole Brillouin zone, we have studied the influence of anisotropy on the diffraction effect, and observed a negative index effect in the second and third bands of dispersion. Section 3 deals with metamaterials, considering the ways to synthesize negative permittivity and negative permeability media, on the basis of microwave prototypes, which can be considered as scaled models. Technological challenges are addressed in section 4, for both kinds of microstructures and nanostructures.

2. Dielectric structures

2.1. Dispersion characteristics

Let us consider first a hexagonal dielectric array of holes etched in a high index dielectric. We present in this section results for a hexagonal structure with an index contrast $\Delta n = 2$, whose geometry is shown figure 1. The air filling factor that we considered is $f = 0.093$.

The dispersion relation for the photonic structure—band diagram—has been obtained using commercial software, BandSolve, developed by Rsoft[1]. A Matlab code has also been developed, and used for the same purpose. More generally, note that several numerical methods may be used to solve the numerical problem, and find the couple—ω, $\vec{k}$—for defining the dispersion relation of a plane wave propagating in an infinite medium. The core of the problem is the resolution

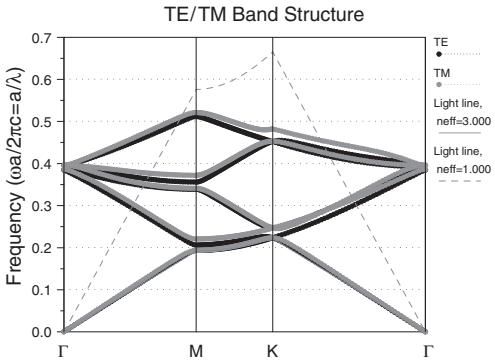

Figure 2. The dispersion characteristic, for TE polarization (black) and TM polarization (grey), for a hexagonal structure of holes; see the text for details.

of an eigenvalue equation: $M_k \Phi = \lambda_k \Phi$, where $\lambda_k = (\omega/c)^2$, and,

$$M_k = (\vec{\nabla} + \mathrm{i}k) \wedge [(1/\varepsilon(r))(\vec{\nabla} + \mathrm{i}k)] \wedge,$$

where $\wedge$ is the vectorial product.

We have used a numerical procedure based on Hessenberg decomposition and a QR method[2] to solve the linear system that gives the eigenelements. Such a method requires the computation of all the matrix elements, which is not too serious a problem, provided that one avoids 3D simulations. It has been shown that convergence problems may occur with such an algorithm [6]. In that case, one should use a fine evaluation of the Fourier transform of $1/\varepsilon$ [7], or variational methods [8–10]. However, in our case, considering around 10^3 plane waves has been enough for modelling the band structure accurately. We have also carried out time domain simulations: bi-dimensional FDTD (finite difference time domain), using FullWAVE, by Rsoft. This algorithm directly integrates the Maxwell propagation equation using the finite difference method.

The results are shown figure 2, for both TE field components, Hx, Ey, Hz polarization, and TM field components, Ex, Hy, Ez polarization. Going towards low frequencies, the dispersion relation of the photonic structure tends to that of a homogeneous medium. Its index is $n_{\mathrm{hom}} = 2.81$, identical for the two polarizations, which corresponds to the averages of indexes of the component materials—air and dielectric—weighted by their respective filling fractions. One also notices that the first band is everywhere 'right handed', i.e., the components of the group velocity, $V_i = \partial\omega/\partial k_i$, with $i = \{x, z\}$, are positive.

Let us now focus on higher energy bands. For the geometry studied, no band gap is present below the line frequency corresponding to $a/\lambda = 0.5$. Higher order bands thus appear for wavelength as large as $a/\lambda < 0.25$, larger than the pattern length scale. One observes that group velocities can take negative values on these higher energy bands. At this point, in order to have a more precise look at the prediction concerning propagation in such a bi-dimensional crystal, one has to get out of the 1D picture (figure 2) and look at the energy contours in the Brillouin zone. This is shown figure 3(a), as a contour plot, for the second and third bands. The change of convexity and relative lack of

[1] http://www.rsoftdesign.com

[2] http://www.nr.com

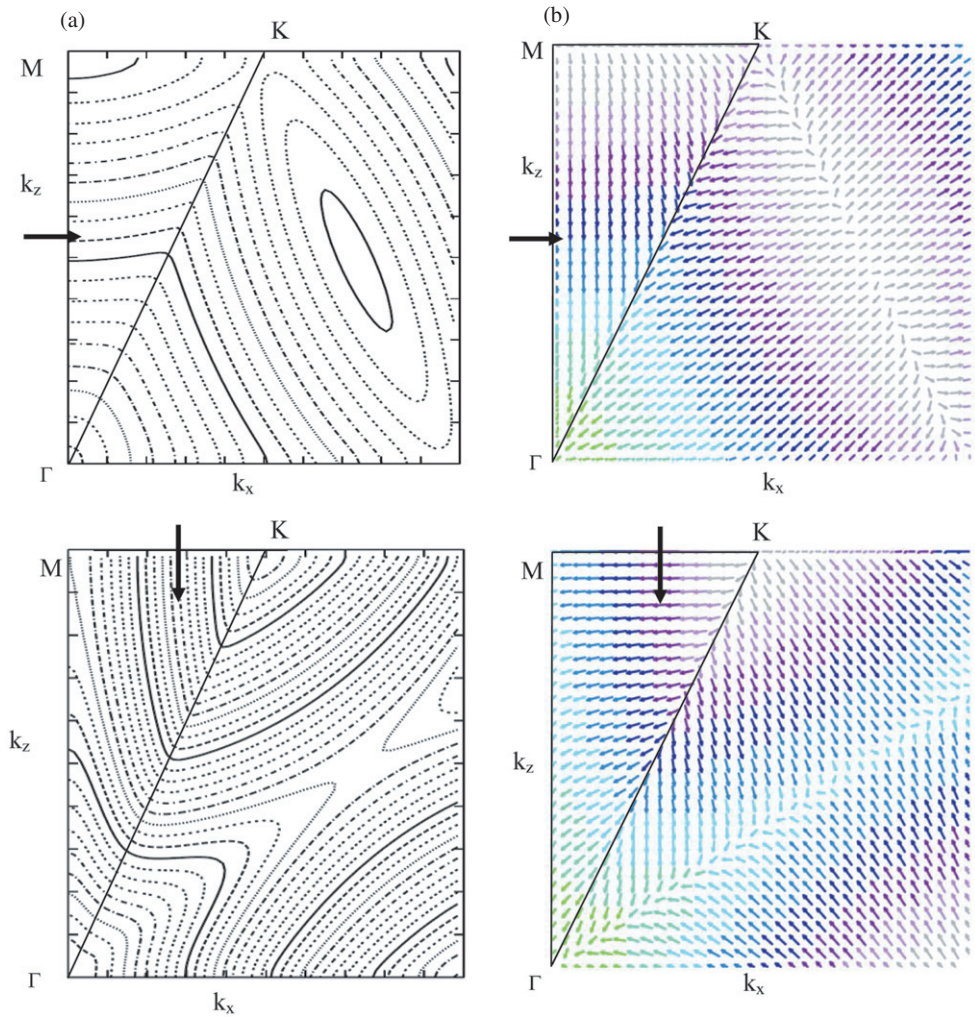

Figure 3. (a) Iso-energy contours for TM polarization and (b) vectorial group velocity in the Brillouin zone, for the second band (upper plots) and third band (lower plots). The shading in (b) corresponds to the frequency contours displayed in (a). Thick arrows indicate the frequency corresponding to $a/\lambda = 0.28$.

symmetry of the energy contours—except in the vicinity of Γ—is observable in figure 3(b), where the (vectorial) group velocities are represented. Due to the underlying crystalline structure, preferred directions exist, and the medium generally exhibits strong anisotropy. This is clearly visible when the iso-energy curves are distorted from the shape corresponding to an isotropic medium, i.e. circles. In some regions of the band diagram, however, the medium is more isotropic. This is the case in the vicinity of the centre of the Brillouin zone—the Γ point. The wavelength inside the crystal then becomes much larger than its structure. The influence of the crystalline structure then disappears, and the iso-energy lines always have a circular shape.

Possible applications in imaging would certainly need to work in the zones of the band diagram where the medium has an isotropic behaviour. Indeed, all the rays coming from one source will experience the same index of refraction. For superprism design, in contrast, one seeks to have a substantial dependence of the refractive index as a function of the direction of incidence, so that two beams separated by a small angle impinging on such a system will come out separated by a larger angle [11].

Until now, we have presented results valid for infinite structures, where plane waves propagate.

Let us now focus on a real device of finite size, where diffraction at the input can occur and be a new cause of anisotropy. Consider here a vacuum wavelength corresponding to $a/\lambda = 0.28$, and compare what happens for directions ΓM (second band) and MK (third band), for TM polarization—see figure 2. For a hexagonal structure, the steps of the grating in the two directions MK and ΓM—respectively $a_{\parallel} = 0.24\lambda$ and $a_{\perp} = 0.14\lambda$—are not the same.

Thus, a beam coupling from free space will not be diffracted in the same way for the two directions. The more intense diffraction in the case of an injection along MK will create wavefronts along other directions—cf figure 4(a). In contrast, figure 4(b) shows that the beam propagates, with few perturbations, along ΓM. One can conclude that anisotropy effects are twofold: for infinite material, they appear in the band structure—figure 3; for finite size systems, diffraction at the entrance/output also plays a role—cf figure 4.

If optical devices were made of this material, image limitations due to diffraction would strongly depend on the direction of injection, and thus be more complex than what

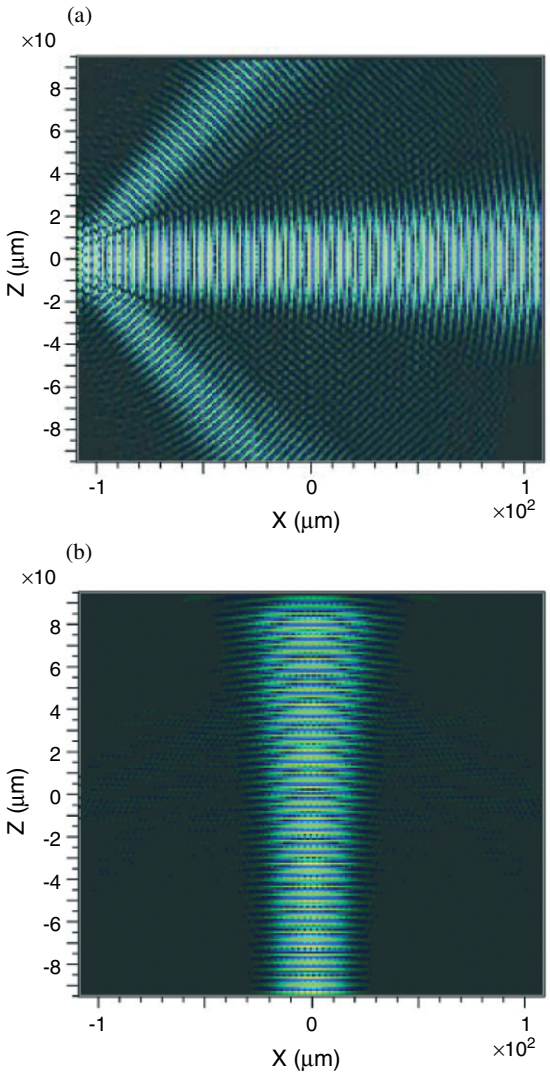

Figure 4. Component Hy inside a photonic crystal for (a) injection along the MK direction and (b) injection along the ΓM direction. TM polarization, $a/\lambda = 0.28$.

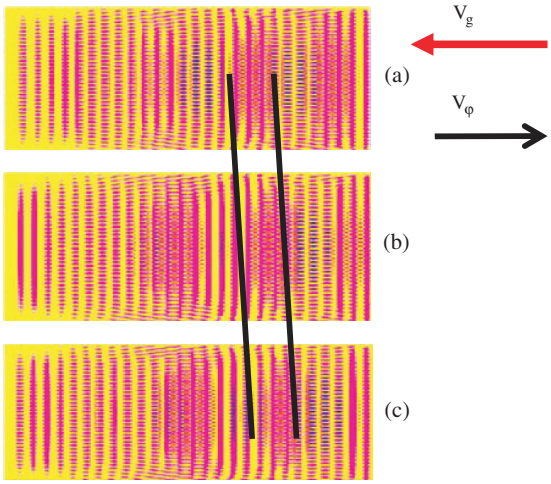

Figure 5. The Hy component inside the crystal, for increasing times (a)–(c). Energy is injected as a plane wave, from right to left, with a group velocity V_g inside the photonic crystal. The phase front (indicated by thick black lines) propagates in the opposite direction, from left to right. Thus, $V_g \cdot V_\varphi < 0$. The simulation has been done for $a/\lambda = 0.37$.

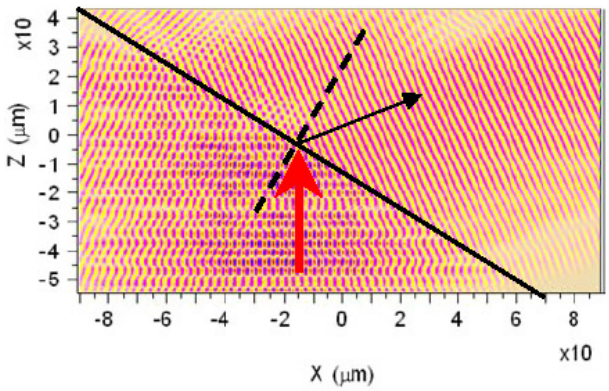

Figure 6. A numerical experiment showing a negative refraction effect at the output of a 30° prism made of a hexagonal structure of holes in a dielectric bulk. The thick arrow represents the incoming wavevector and the thin arrow the outgoing wavevector. The outgoing wave (dashed line) comes out on the 'negative' side of the normal.

arises with ordinary materials. It is therefore important to work in a frequency range where the medium behaves isotropically, as if it were homogeneous.

2.2. *Backward propagation characteristics*

Let us now adjust the ratio λ/a so as to work close enough to the Γ point. The propagation along the second band is characterized by an isotropic behaviour and a negative phase velocity with respect to the group velocity. Figure 5 shows the amplitude of the Hy component at different times. One can see basically two length scales in the space variation of the field—cf figures 5(a)–(c). The smaller one corresponds to the hole size, i.e. the length scale of the permittivity modulation of the photonic crystal. It is visible in both X and Z directions. The larger one is present only along the X direction. It corresponds to the wavelength of the solution of the Maxwell equation, in an infinite medium, for the frequency given by λ/a—cf figure 2, for the ratio $a/\lambda = 0.37$. From the band diagram, figure 2, one remarks that large scale modulation should propagate backward. That is indeed what we observe in the FDTD simulation, performed with FullWave—compare figures 5(a)–(c). One can see that the large scale phase modulation is going backward with respect to the direction of injection of energy.

Until now, we have focused on the behaviour inside a photonic crystal. We will now examine the negative refraction effect, when light passes from the composite material to a homogeneous dielectric medium.

2.3. *Negative refraction*

Figure 6 illustrates the refraction regime for a wave impinging onto a prism-like dielectric array. The feeding of the structure is along the ΓM direction. The frequency is chosen in the left-handed dispersion branch, taking care to preserve the isotropy, working close to Γ. By analysis of the phase front it can be seen that the—large arrow—beam refracts on the other side of the

normal—dashed line—compared to the case for conventional positive refractive index materials.

3. Metamaterials: metallic arrays

The prefix 'meta' means beyond. In order to go beyond the electromagnetic properties of one homogeneous material, one can structure matter into complex heterogeneous media, e.g. using a periodic pattern, which involves different materials. In some cases, the resulting composite structure can be simply described in terms of averaged quantities, e.g., the averaged index of refraction of component materials. This is the homogenization limit [12, 13]. Then, gathering positive index material into a composite would simply lead to a new material of positive index, permittivity and permeability. However, the homogenization limit sometimes fails. This is the case when the injected wavelength is of the order of the size of the pattern structures. In such interesting situations, one can build from media with positive index of refraction, permittivity and permeability a composite medium with negative permittivity, permeability and index of refraction. Electromagnetic properties are then those predicted by conventional rules such as the Snell–Descartes law, but with singularities stemming from the negative refractive index.

Whereas in the periodic dielectric structures addressed in the previous section the negative refractive index stems from the use of high energy dispersion branches, metallic metamaterials take benefit from the fabrication of double-negative media. Such electromagnetic materials are realized from the combination of periodic arrays which allow synthesizing electromagnetic media with negative permittivity and permeability values.

3.1. Negative permittivity media

To our knowledge, there are two main ideas for fabricating negative permittivity media. The first possibility is to use a periodic structure whose frequency spectrum mimics the response of a high pass filter [14–16]. The second possibility uses a waveguiding structure—for example a hollow metallic waveguide—*below* its cut-off frequency[3] [17, 18]. Under this condition, electromagnetic waves are evanescent at low frequencies and propagate in the high frequency region. This evanescence in the low frequency gap can be described in terms of negative permittivity values below some specific frequency: the corner frequency.

For free space prototypes (3D metamaterials), the most popular structures are arrays of thin wires [19–21], which are well known devices, especially in quasi-optics, used as polarization grids. The electromagnetic properties of such metallic arrays have been studied as metallic photonic band gap structures (diffraction regime) but also under long wavelength conditions (refraction regime). For the latter, John Pendry has shown that transmission properties can be understood on the basis of the Drude model for the permittivity of metal where the corner frequency is in this case the plasma frequency of the composite. It is relatively intuitively obvious that on diluting the metal in a composite dielectric the metal array shifts down the plasma frequency to the low frequency region of the electromagnetic spectrum [22].

[3] Let us recall that a hollow waveguide exhibits a high pass behaviour with a cut-off frequency related to its geometry.

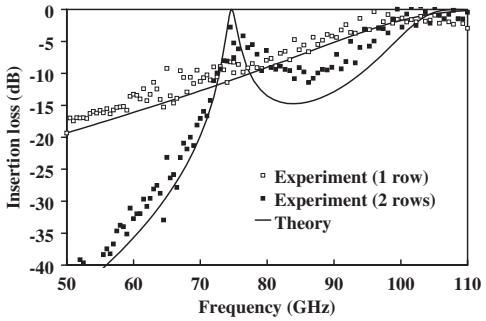

Figure 7. The frequency response of a metallic grid and array.

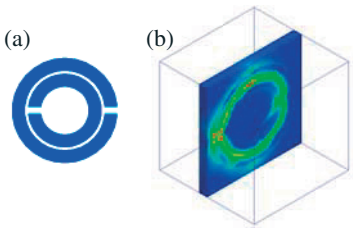

Figure 8. (a) A schematic diagram of split ring resonators. (b) *E* field magnitude mapping.

Quantitatively, various formulae can be found in the literature for predicting the variation of the plasma frequency as a function of the filling factor and, thus, for a wire array, as a function of the ratio between the wire diameter and the pitch of the periodic structure. These formulae show the same trends and slight deviations in the estimates. As shown by Pendry, the frequency shift can be understood not only in terms of a decrease in the electron density but also in terms of an increase of the effective mass of electrons resulting from pronounced inductance effects. So far, to our knowledge, most of the artificial media operate at microwave frequencies [23–25]. For instance, figure 7 shows the frequency response above 50 GHz of a metallic grid and of an array of just two rows fabricated and characterized by vectorial network analysis at the 'Institut d'Electronique de Microélectronique et Nanotechnologies'. The low pass characteristic is verified with a resonant transmission effect under subwavelength conditions which can be compared to the resonant tunnelling effect in a double-barrier semiconductor. If more rows are added a miniband is formed, as in a semiconductor superlattice [26].

3.2. Negative permeability media

The basic idea is to engineer the permeability of the constitutive media via current loops and to introduce some resonance effects, which yield a negative permeability for frequencies close to the resonance. The most popular particle used for the engineering of relative permeability is a C-shaped structure, which is well known from the scientific community working on chirality [27].

At microwave frequencies, split ring resonators (SRRs), also proposed by Pendry, in a back-to-back configuration, have been used. Figure 8(a) shows the basic pattern whereas figure 8(b) is a mapping of the electric field magnitude in the

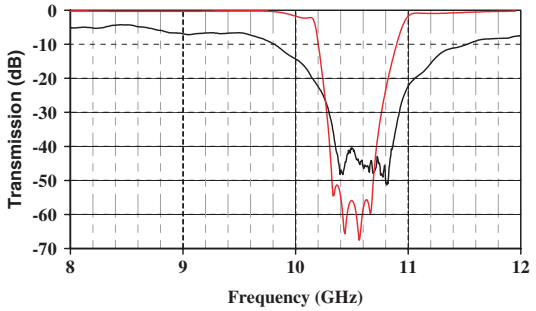

Figure 9. Comparison of the computed transmission (thin curve) and measured transmission (thick curve) as a function of frequency for an array of SRRs.

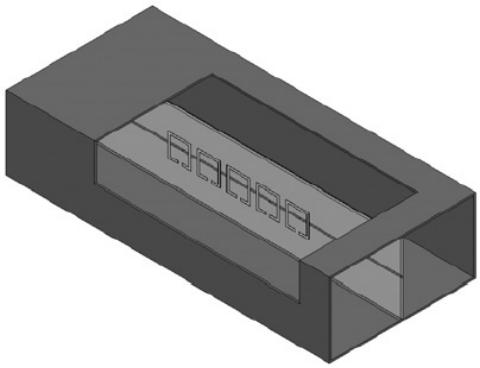

Figure 10. An illustration of a double-negative propagation medium based on single-ring resonators.

plane computed by full wave analysis. As expected, the E field is localized in the slot between the edge-coupled rings. This coupling can be strengthened in practice by conventional guide lines, notably with two resonators separated by a thin dielectric slab.

Figure 9 compares experimental and theoretical predictions as regards the frequency response of the transmission for a microwave prototype consisting of arrays of edge-coupled SRRs. From conventional techniques of extraction of the refractive index impedance and relative permittivity and permeability, it can be demonstrated that the gap apparent in this transmission spectrum is due to a negative permeability value.

3.3. Double-negative media

One can now find in the literature many proposals of double-negative media based on wire and SRR arrays operating under free space conditions [28–34]. Experimental verifications of (i) transmission in a frequency range where both permittivity and permeability are negative and (ii) negative refraction effects have been pointed out. In the following we will illustrate backward propagation, which is a signature of a left-handed behaviour, in a novel waveguide structure whose scheme is given in figure 10: a hollow metallic waveguide loaded with series of split ring resonators and wires. They are patterned on the front and back of a transmission line, which corresponds to the so-called fin line technology.

Figure 11 gives the dispersion characteristics for structures which consist of two embedded or single rings for both the

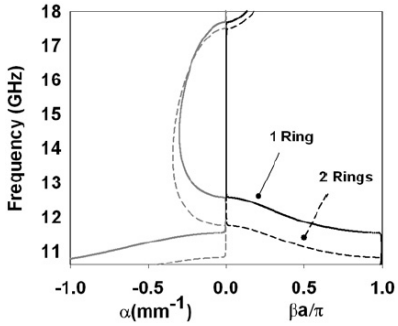

Figure 11. A dispersion diagram for the waveguide structure loaded by SRRs and wires, for single-ring (see figure 10) and two-ring structures. The real (α) and imaginary (β) parts of the wavenumber are represented, respectively, in the intervals $[-1, 0]$ and $[0, 1]$, in units of a/π, where a is the period of the structure.

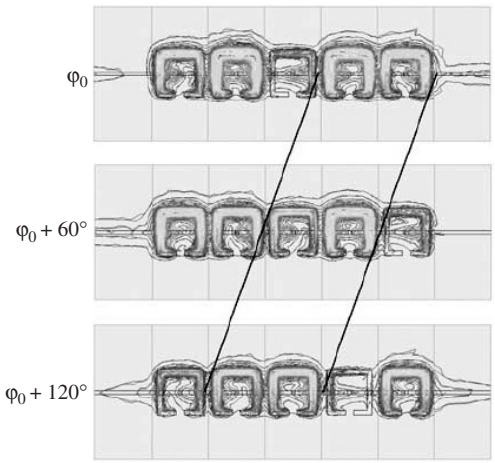

Figure 12. A numerical experiment showing the phase fronts for propagation in a metamaterial line of transmission. Phase fronts are indicated by the black lines. Varying the initial phase in this frequency domain analysis mimics the time evolution in a real (i.e. time domain) situation. One observes that energy propagates from left to right, whereas phase propagates from right to left.

real and imaginary components of the wavevector k. The left-handed branch is here the ground one.

Figure 12 illustrates the backward propagation effect in a five-cell device by showing the mapping of the magnetic field calculated by a frequency domain analysis. The initial phase shift (φ_0) was varied so that the various figures would be equivalent to the different snapshots of time varying simulations. Straight lines track the phase fronts. In the present case, the energy is supplied from the left-hand side and thus determines the direction of the Poynting vector. It can be seen that the propagation directions of the energy (group velocity) and the phase fronts (phase velocity) are opposite.

4. Technological challenges

The technological challenges for the fabrication of photonic crystals and metamaterials aimed at operating in the infrared spectral region are not trivial and special attention is paid here to fabrication issues. Beyond these difficulties in the

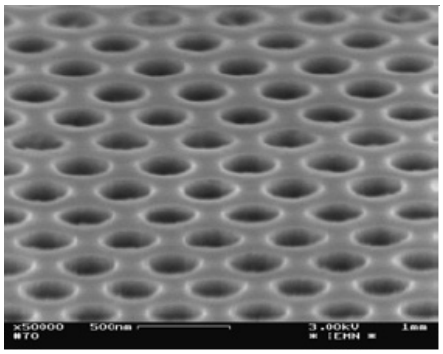

Figure 13. A SEM of a hole array patterned dielectric layer prior to deep etching.

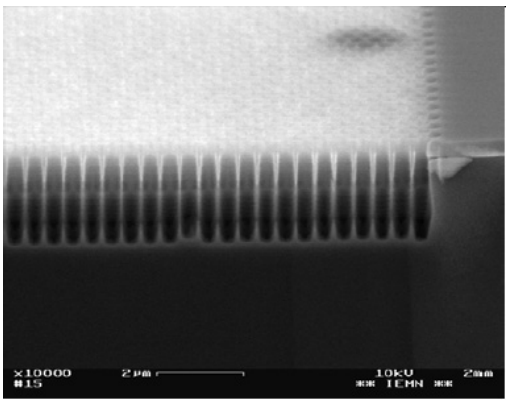

Figure 14. A SEM of a high aspect ratio 2D hole array.

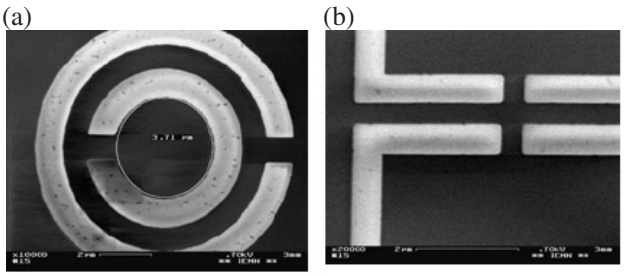

Figure 15. (a) A SEM of embedded split ring resonators. (b) The back-to-back scheme.

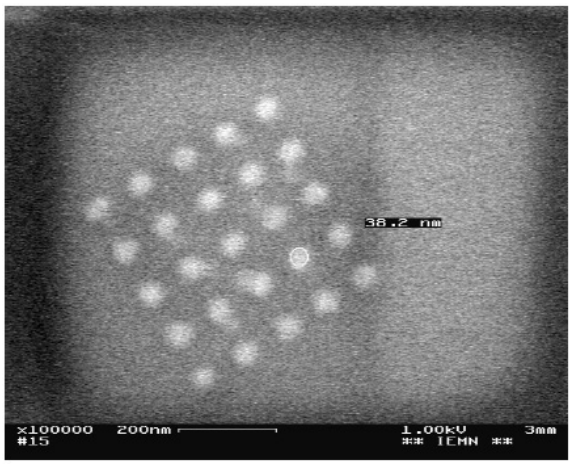

Figure 16. A SEM of a metal dot array patterned by e-beam lithography.

realization, there are still open questions such as the problem of metallic losses.

In contrast to the prototype made of metallic rods, most PCs are made of bi-dimensional hole arrays which are deeply etched in a semiconductor host substrate. In section 2 we saw that a left-handed branch can be found for a higher lying energy band whereas the ground band is right handed. In the case where the pitch of the period is comparable to the wavelength, this means that the relevant dimensions for operation in the near infrared (for example for the 1.5 μm window of telecommunications) have to be on a submicron scale. On the other hand, it can be shown that the band gap is relatively broad provided that the filling factor (the ratio between the semiconductor cell and the air hole) is high. Finally, because the current fabrication techniques are more suited to the fabrication of 2D arrays, the vertical confinement is ensured by semiconductor band gap engineering, namely by varying the composition of the semiconductor alloys and thus the refractive index, as in conventional integrated photonics. Figure 13 shows a scanning electron micrograph of a bi-dimensional array of holes, patterned in a Si_3N_4 thin film which will be used for subsequent deep etching by RIE. This microstructure fabricated at IEMN was patterned by e-beam lithography using a conventional PMMA resist, plasma enhanced chemical vapour deposition (PECVD) for the transfer of the Si_3N_4 layer and deep reactive ion etching for the dry etching of holes.

Figure 14 illustrates the etching stage. The structure under test is based on InP technology with a conventional technique used to confine the light in the direction perpendicular to the growth axis of the semiconductor (namely, the use of a InGaAsP/InP heterojunction). Despite the high filling factor for between the air and semiconductor, the high degree of anisotropy afforded by the reactive plasma etching technique permits us to etch holes with a typical diameter around 0.3 μm with comparable period and a depth of 3 μm. High aspect ratio microstructures (10:1) are thus successfully fabricated using a deep submicron technology (relevant dimensions: around a few hundred nanometres).

Let us now consider the fabrication of metamaterials, which must have, by definition, dimensions much smaller than the wavelength. By analogy with the previous example of a passive dielectric component operating around 1 μm, this means that the overall dimension, for instance the outside diameter of the SRR, should be smaller than $\lambda/10$, namely 100 nm. The fine features within this magnetic particle have again to be much shorter, let us say an order of magnitude less, than the C-shaped pattern. We thus obtain for NIR operation an ultimate limit of 10 nm. Such an ultrafine structure on a nanometre scale could be in principle patterned using one-shot ultrahigh resolution e-beam lithography. The difficulties are relaxed for operation at the mid-infrared ($\sim$10 μm) and obviously at the far infrared ($\sim$100 μm). Figure 15(a) shows a SEM of an embedded SRR designed for operating at the FIR with an inner ring around 4 μm. Other schemes can also be envisaged such as the one displayed in figure 15(b).

In practice, we used lift-off techniques for the metal structuring using gold evaporation. If shorter wavelengths are targeted, it becomes more and more difficult to fabricate

C-shaped patterns. It is believed however that the reasoning still holds with arrays of metal dots. To illustrate such issues, figure 16 shows a SEM of round-shaped pads evaporated onto a host substrate with the diameter of 30 nm. As a last comment, self-assembly techniques could also be envisaged, notably for the fabrication of left-handed metamaterials operating in optics by means of carbon nanotubes in their metallic or semiconductor regimes.

5. Conclusions

One of the main conclusions of this study is that it is possible to use the singular properties of refraction and diffraction by left-handed materials, from microwaves to optics. A number of experimental verifications has been made possible in the microwave range via double-negative EM media based on wire and SRR arrays. The next stage is now to push their frequency of operation by shrinking the dimensions of the SRR and the pitch of the array, to get higher filling factors. The question of losses in connection with the skin depth is still an open problem, although some attempts to address it have already been made [35]. One expects to observe a damping of the resonant effect accompanied by a saturation of the resonant frequency. This should not scale linearly with the characteristic length of the structure. For optics, the utilization of PCs or PBGs in their left-handed regime and not solely using them for their gap properties as in integrated optics seems very promising. Real difficulties still exist however, notably the problems linked to anisotropy, to the leakage radiation above the cone light and to the losses by diffraction. For instance, the latter terms are very important for defected PBGs using confinement by the gap and could preclude any practical use. In the short term, they must be carefully addressed in the high dispersion propagation mode.

Acknowledgment

This work was carried out in the framework of the research programme of IRCICA (CNRS/University of Lille) and of the network of excellence METAMORPHOSE.

References

[1] Veselago V G 1968 The electrodynamics of substances with simultaneously negative values of ε and μ *Sov. Phys.—Usp.* **10** 509
[2] Smith D R, Pendry J B and Wiltshire McK 2004 *Science* **305** 788–92
[3] Shelby R A, Smith D R, Nemat-Nasser S C and Schultz S 2001 Microwave transmission through a two-dimensionnal, isotropic, left-handed metamaterial *Appl. Phys. Rev. Lett.* **78** 489
[4] Shelby R A, Smith D R and Shultz S 2001 Experimental verification of a negative refraction index *Science* **292** 77–9
[5] Pendry J B, Holden A J, Robbins D J and Stewart W J 1999 Magnetism from conductors and enhanced nonlinear phenomena *IEEE Trans. Microw. Theory Tech.* **47** 2075
[6] Sozuer H S, Haus J W and Inguva R 1992 Photonic bands: convergence problems with the plane-wave method *Phys. Rev.* B **45** 13962
[7] Meade R D, Rappe A M, Brommer K D, Joannopoulos J D and Alerhand O L 1993 Accurate theoretical analysis of photonic band gap material *Phys. Rev.* B **48** 8434
[8] Johnson S G and Joannopoulos J D 2001 Bloch-iterative frequency-domain methods for Maxwell's equations in a planewave basis *Opt. Express* **8** 173
[9] Edelman A and Smith S T 1996 On conjugate gradient-like methods for eigen-like problems *BIT Numer. Math.* **36** 494
[10] Payne M C, Teter M P, Allan D C, Arias T A and Joannopoulos J D 1992 Iterative minimization technique for *ab initio* total-energy calculations: molecular dynamics and conjugate gradients *Rev. Mod. Phys.* **64** 1045
[11] Kosaka H *et al* 1998 Superprism phenomena in photonic crystals *Phys. Rev.* B **58** R10096
[12] Felbacq D and Bouchitte G 1997 *Waves Random Media* **7** 245
[13] Poulton C, Guenneau S and Movchan A B 2004 Noncommuting limits and effective properties for oblique propagation of electromagnetic waves through an array of aligned fibres *Phys. Rev.* B **69** 195112
[14] Eleftheriades G V, Iyer A K and Kremer P C 2002 Planar negative refractive index media using periodically L-C loaded transmission lines *IEEE Trans. Microw. Theory Tech.* **50** 2702
[15] Grbic A and Eleftheriades V 2002 Experimental verification of backward-x-wave radiation from negative refractive index metamaterials *J. Appl. Phys.* **92** 5930
[16] Liu L, Caloz C, Chang C C and Itoh T 2002 Forward coupling phenomena between artificial left-handed transmission lines *J. Appl. Phys.* **92** 5560
[17] Marquès R, Martel J, Mesa F and Medina F 2002 Left-handed-media simulation and transmission of EM waves in sub wavelength split-ring-resonator-loaded metallic waveguides *Phys. Rev. Lett.* **89** 183901
[18] Marques R, Mesa F, Martel J and Medina F 2003 Comparative analysis of edge- and broadside-coupled split ring resonators for metamaterial design. Theory and experiments *IEEE Trans. Antennas Propag.* **51** 2572
[19] Danglot J, Vanbésien O and Lippens D 1999 Active waveguides patterned in 2D–3D metallic photonic crystal *Electron. Lett.* **53** 475
[20] Danglot J, Vanbésien O and Lippens D 1999 A 4-port resonant switch patterned in a photonic crystal *IEEE Microw. Guid. Wave Lett.* **9** 274
[21] Lourtioz J M, De Lustrac A, Gadot F, Rowson S L, Chelnokov A, Brillat T, Ammouche A, Danglot J, Vanbésien O and Lippens D 1999 Towards controllable photonic crystals for centimetre and millimetre wave devices *J. Lightwave Technol.* **17** 2025
[22] Pendry J B, Holden A T, Stewart W J and Youngs I 1996 Extremely low frequency plasmons in metallic mesostructures *Phys. Rev. Lett.* **76** 4773
[23] Akalin T, Danglot J, Vanbésien O and Lippens D 2001 Resonant tunnelling in photonic microcavities: design of highly directive radiating system *Superlatt. Microstruct.* **30** 181–8
[24] Martin F, Falcone F, Bonache J, Lopotegi T, Laso M and Sorolla M 2002 New periodic-electromagnetic band gap coplanar waveguide with complete spurious passband suppression *IEEE Microw. Wireless Comp. Lett.* **12** 434
[25] Akalin T, Laso M A G, Lopotegi T, Vanbesien O, Sorolla M and Lippens D 2001 PBG-type microstrip filters with one and two sided pattern *Microw. Opt. Technol. Lett.* **30** 69
[26] Engheta N and Saadoun M 1991 *Proc. PIERS (Cambridge, MA, July 1991)* p 339
[27] Bayindir M, Aydin K, Ozbay E, Markos P and Soukoulis C M 2002 Transmission properties of composite metamaterials in free space *Appl. Phys. Lett.* **78** 489–91
[28] Smith D R, Schultz S, Markos P and Soukoulis C M 2002 Determination of effective permittivity and permeability of metamaterials from reflection and transmission coefficients *Phys. Rev.* B **65** 195104
[29] Loschiolpo P F, Smith D L, Forester D W, Rachford F J and Schelleng J 2003 Electromagnetic waves focused by a negative-index planar lens *Phys. Rev.* E **67** 025602

[30] Houck A, Brock J B and Chuang I L 2003 Experimental observations of a left handed material that obeys Snell's law *Phys. Rev. Lett.* **90** 137401

[31] Parazzoli C G, Greegor R B, Li K, Koltenbah B E C and Tanelian M 2003 Experimental verification and simulation of negative index of refraction using Snell's law *Phys. Rev. Lett.* **90** 107401

[32] Enoch S, Tayeb G, Sabouroux P, Guérin N and Vincent P 2002 A metamaterial for directive emission *Phys. Rev. Lett.* **89** 213902

[33] Akalin T, Danglot J, Vanbésien O and Lippens D 2002 A highly directive antenna embedded in a Fabry Pérot cavity *IEEE Microw. Wireless Comp. Lett.* **12** 48–50

[34] Vanbésien O, Akalin T, Carbonell J, Danglot J and Lippens D 2001 Wave shaping through finite electromagnetic band gap structure *Superlatt. Microstruct.* **30** 321

[35] O'Brien S and Pendry J B 2002 Magnetic activity at infrared frequency in structured metallic photonic crystals *J. Phys.: Condens. Matter* **14** 6383–94

Wave-mechanical calculations of leakage current through stacked dielectrics for nanotransistor metal-oxide-semiconductor design

M. Le Roy and E. Lheurette
Laboratoire Electronique Microtechnologie Instrumentation (LEMI), UPRES-EA 2654, Université de Rouen, Rue Lavoisier, 76821 Mont-Saint-Aignan Cedex, France

O. Vanbésien[a] and D. Lippens
Institut d'Electronique, de Microélectronique et de Nanotechnologie (IEMN), UMR CNRS 8520, Département Hyperfréquences et Semiconducteurs, Université des Sciences et Technologies de Lille, Avenue Poincaré, BP 69, F-59652 Villeneuve d'Ascq Cedex, France

(Received 5 July 2002; accepted 11 December 2002)

Quantum calculations of leakage current through ultrathin dielectric heterostructures are used to propose design criteria for the next generation of metal-oxide-semiconductor devices in a deep submicron technology. By using as input parameters both the dielectric constant and the barrier height of different dielectrics, including at first stage SiO_2, Si_3N_4, TiO_2, and Ta_2O_5, but also such emerging materials as HfO_2 and ZrO_2, we show that, depending on the voltage range investigated, the hierarchy between those dielectrics is not simply given by the increase of their permittivity. Deeper considerations based on resonant tunneling mechanisms, of prime importance when dielectric heterostructures are used for fabrication purposes, must be taken into account especially for the future low-consumption nanotransistors with operating voltages below 1 V. © *2003 American Institute of Physics.* [DOI: 10.1063/1.1544650]

I. INTRODUCTION

As a consequence of very large scale integration, scaling down the gate length in ultimate metal-oxide-semiconductor (MOS) transistors marks the intersection of several research domains, including materials, technology, and modeling techniques. Within this context, the gate dielectric remains one of the main concerns. New high-κ materials, as well as new architectures, have been proposed and tested since classical approaches appear to be unrealistic on a nanometer scale. Indeed, some aspect ratio between gate length and dielectric thickness has to be preserved in order to maintain the control of charge in the device channel. Oxide thickness reduction yields an increase of the gate leakage current and therefore of the static consumption.

According to the *International Technology Roadmap for Semiconductors*,[1] constant adequacy to Moore's law will require oxide thickness of 10 Å around 2010. Now, a maximum in the gate leakage current of 1 $A\,cm^{-2}$, commonly admitted as a consumption criterion for desktop applications, shows the limitation of SiO_2 as an insulator gate.[2] Several solutions have been proposed for the next MOS field-effect transistor (MOSFET) generations. Basically, the use of a high-permittivity dielectric allows the thickness to be increased, while maintaining the same control of charge. However, from a technological point of view, the substitution of silicon dioxide by another higher permittivity material is not easy without degrading interface quality. Moreover, among the different candidates, several dielectrics are not thermally stable on silicon. Thus, in most of the MOSFET processes, a small SiO_2 layer exists on the silicon surface prior to anything else.

Among the different possible solutions to continue downscaling, a first approach consists of a progressive introduction of impurity atoms (e.g., nitrogen) in a thermal dioxide growing process. This can lead to a Si_3N_4 final layer by oxygen substitution.[3] It has been shown that such an oxynitride layer can reduce boron penetration from *p*-type polysilicon gates[4] and thus parasitic currents. Since a greater average permittivity allows us to increase the insulator thickness, the leakage current can be reduced with a constant charge control. Nevertheless, it has been shown that oxynitrides are not able to replace silicon dioxide for thicknesses lower than 13 Å.[5]

A second approach would be the use of high-κ dielectrics in a stacked configuration. Such insulator engineering combines three main advantages. First, the excellent Si/SiO_2 interface properties can be kept. Second, the stacked configuration brings a solution to the problem of thermal instability on silicon. Finally, the multilayer insulator offers another degree of freedom in the design. Several couples of dielectric layers can achieve the same SiO_2 equivalent thickness.[6] Therefore, the reduction of leakage current is based on the choice of permittivities (κ) and barrier heights (ΔE_c) values. Our main topic is to propose some design rules towards an optimized bilayered insulator for future MOSFET generations. Section II describes the quantum model that was developed in order to describe energy states, to perform a transmission energy spectroscopy, and to calculate the current density through stacked dielectrics. A parametric study involving several materials, such as Si_3N_4, Ta_2O_5, and TiO_2, is presented in Sec. III. These materials have been chosen as representative candidates for high-κ dielectrics in terms of

[a]Electronic mail: olivier.vanbesien@iemn.univ-lille1.fr

($\kappa, \Delta E_c$) parameters. Nevertheless, new applicants, such as HfO_2 and ZrO_2, whose dielectric parameters are close to Ta_2O_5, will be also considered. In Sec. IV, a discussion, based on quantum considerations, on the competition between different conduction mechanisms (tunneling, resonant tunneling, thermionic, etc.) is given. Section V contains concluding remarks.

II. NUMERICAL METHOD

The motivation is to give a quantum description of conduction mechanisms through stacked dielectric layers in order to analyze the origins of gate leakage current in nano-MOS transistors. To this aim, we use a one-dimensional code solving jointly Poisson's and Schrödinger's equations. This resolution is applied in the direction perpendicular to the gate. Thus, the simulation domain includes the semiconductor material (here, Si), with or without doping modulation, the different stacked dielectric materials and finally the metal, representing the outer reservoir.

The inputs are the microstructure parameters in terms of thickness, doping concentration in case of semiconductors, dielectric constant, conduction-band edge discontinuities (with reference to a given material) along the operating conditions, notably the applied voltage and the device temperature. The output informations are mainly the current–voltage relationships. In addition, such physical figures as quantum transmissions, envelope wave functions, and current increments can be exploited to analyze more deeply the intrinsic conduction properties.

Compared to other approaches found in literature,[7–11] the numerical tool outlined here does not require any approximation on the potential profile and on energy domains under consideration. Let us mention that it was primarily developed to treat III–V electronic quantum devices as Schottky diodes,[12] HBVs (heterostructure barrier varactors),[13] or RTDs (resonant tunneling diodes).[14] It is a full analysis of the current–voltage relationship, whatever the current origin (tunneling, thermally-assisted tunneling, resonant tunneling, thermionic emission), via the integration over energy of a transmission spectrum times a function describing the balance between filled and empty states in the emitting and collecting regions. Defect-assisted tunneling could be also treated in principle, but will not be considered in the present work.

In practice, our calculation is divided into four steps:

(i) The electrostatic potential is determined in the semiconducting region by solving the Poisson equation under Thomas–Fermi approximation. Any homo- or heterojunction can be simulated. A Dirichlet condition (a fixed potential) is assumed on one side of the simulation domain, which will later be the semiconductor/oxide interface, whereas a Neumann condition (zero electric field) is assumed on the opposite side. The resulting band bending has to be taken into account prior to any current estimation. Besides, in case of accumulation regime, electrons or holes can accumulate in front of the oxide region and form, by space-charge effect, a quasitriangular electrostatic quantum well. The implications of such quantum effects are expected to be comparable to those present in the emitter region of a RTD.[15] At this point, let us note that we have ignored this two-dimensional (2D) gas of electrons to establish the potential using a classical three-dimensional (3D) Fermi distribution. Moreover, using a zero-current Thomas–Fermi approximation, we also neglect the influence of charges responsible for the current on the potential. In previous papers, we have studied in detail the degree of approximation afforded by such assumptions and concluded that, as long as potential is considered (an integrated value), no significant error was made on the potential profile.

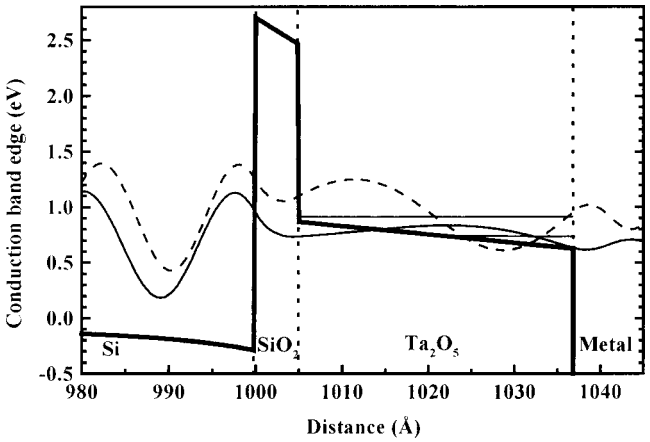

FIG. 1. Potential profile for a SiO_2 (5 Å)/Ta_2O_5 (32 Å) heterostructure at 0.95 V. Also given, the two first wave functions (real part) at $E=0.81$ and 1.01 eV revealing quantum bound states localized in the Ta_2O_5 region bounded on one side by SiO_2 and on the other by the interface Ta_2O_5 metal (virtual confinement wall).

(ii) The potential profile has to be determined throughout the structure. To this aim, the electric field is extracted from the previous step at the Dirichlet boundary. As the insulator layers are supposed to be free of charges, the electric field is assumed to be constant for a given dielectric and thus the potential is easily determined. Finally, as a function of the last oxide/metal discontinuity, the Fermi level within the metal is deduced. Compared to the Fermi level reached in the semiconductor assumed at thermal equilibrium on the opposite side of the structure, bias voltage is finally deduced. Here again, induced by the potential drop within the dielectric heterostructure, quantum effects appear due to the semiconductor/dielectric and dielectric/metal heterointerfaces. The oxide region appears as a ''cavity'' where quasi-bounded states can be evidenced. These energy states induce temporary localization with a sufficient strength to affect dramatically the conduction characteristics as seen in the following.

(iii) The envelope wave functions are calculated for each energy by solving the time independent Schrödinger equation. Different approaches can be used depending on boundary conditions whether open, semi-open, or closed structures are under concern. In our case, we will focus on the ballistic tunnel current issued from the semiconductor region. Thus, we considered an open structure, with the need of plane wave boundaries on each side. As illustrated in Fig. 1, wave functions are calculated at each energy value and can reveal momentary localization within the oxide barrier with a po-

tential form given by the dielectric heterostructure. Here, quantum effects would appear for lower energies than in the pure case of SiO_2, since barrier heights are generally lowered with other dielectrics. Fowler–Nordheim (FN) regimes or other tunneling assisted mechanisms would then affect conduction properties, and bias voltage ranges when they appear have to be carefully studied when the device design is considered.

(iv) The final step, as wave functions are known, is to derive current–voltage characteristics. Assuming a transmission coefficient calculated by the ratio of the incoming and the transmitted particle current (square of the plane wave amplitude weighted by the local wave vector) and Fermi–Dirac distributions on both sides, a global procedure for each energy is used by integrating the transmission spectra times the so-called ''supply function,'' which gives the balance between the filled and empty states in the supplying and collecting regions. Details of the procedure can be found in Ref. 12. Here, it is important to notice that no approximation is made depending on energy domains as often done with pure tunnel (in general Wentzel–Kramer–Brillouin approximation), FN regime (triangular barrier) and thermionic (Richardson-type formula) separations. Some effects such as quantum reflection, even for energies higher than any barrier height, are naturally included in our approach.

As a final comment on the numerical procedure, let us mention that the comparison between the different dielectric stacks is sometimes difficult due to the lack of accuracy of material parameters. Moreover, as often mentioned in III–V or IV–IV electronics, the concept of effective mass for such thin layers (a few angstroms) becomes questionable. Nevertheless, such descriptions are easy to handle and give in general physically meaningful results supported by experiments. In order to limit the number of parameters used in the simulation, our calculations have been tested with classical SiO_2 structures with a satisfactory agreement with experimental or previously published current density values and evolutions as a function of bias voltage. Then, to explore other dielectric candidates, only two parameters are chosen to be characteristic of a given material, namely, the dielectric constant κ (considered as the relative permittivity in this article), and the barrier height ΔE_c compared to the semiconductor (Si). It will be seen in the following that already with these sole two parameters, conception rules can be drawn for ultimate MOS design.

III. PARAMETRIC STUDY: OPTIMIZATION OF STACKED LAYERS GEOMETRY

The properties of the major high permittivity dielectrics, which can candidate in stacked layer gates, are presented in Table I.[2,6] Among these materials, Ta_2O_5 appears like a favorite due to its high-κ and well-known properties for memory applications. TiO_2 seems more advantageous in terms of permittivity, but the drawback is a smaller barrier height. Both TiO_2 and Ta_2O_5 present thermal instability[2] when used directly on Si, which implies the use of a SiO_2 interfacial layer. Recent studies tend to promote the use of HfO_2[16] and ZrO_2[17] mainly in the perspective of a single dielectric layer substitution as these materials are more stable

TABLE I. Reference parameters for gate dielectric materials.

Material	Dielectric constant κ	Band gap E_g (eV)	Barrier height ΔE_c (eV) to Si
SiO_2	3.9	9	3.0
Si_3N_4	7.5	~5	2.0
Ta_2O_5	~25	~4.4	1.4
TiO_2	~40	~3.5	1.1
HfO_2	25	5.7	1.5
ZrO_2	25	7.8	1.4

on Si. Nevertheless, a real monolayer approach does not seem achievable without compromising the dielectric potential. Therefore, a bilayer approach employing interlayered dielectrics such as SiO_2 or Al_2O_3[18] is mostly preferable as stability on Si is not the only criterion. It should be noted that concerning HfO_2 and ZrO_2, barrier height and permittivity are very close to the values reported for Ta_2O_5 (Table I). We can therefore conclude that our model applied to ZrO_2 and HfO_2 would rather give similar current trends and transmission evolutions as for Ta_2O_5. We focused on TiO_2 and Ta_2O_5 because, although these materials exhibit comparable leakage current around 1-V gate bias, their conduction mechanisms are different and illustrate the role of both barrier height and permittivity as design parameters. In our simulations, we consider metal/TiO_2/SiO_2/Si and metal/Ta_2O_5/SiO_2/Si, where the silicon is *n*-type with a doping of 10^{17} A/cm^3. The metal work function is equal to 4.3 eV. Figure 2 depicts the current densities versus voltage $[J(V)]$ evolutions for SiO_2/Ta_2O_5 and SiO_2/TiO_2 heterostructures, which are compared to a conventional SiO_2 monolayer and a SiO_2/Si_3N_4 bilayer. The dielectric thicknesses have been calculated to achieve an equivalent oxide thickness $t_{eq} = 10$ Å following the equation

$$t_{eq} = t_{SiO_2} + \frac{\kappa_{SiO_2}}{\kappa_{high\text{-}\kappa}} \times t_{high\text{-}\kappa}, \tag{1}$$

where t_{SiO_2} and $t_{high\text{-}\kappa}$ are the thicknesses of SiO_2 and the high-κ dielectric respectively and κ_{SiO_2} and $\kappa_{high\text{-}\kappa}$ are the corresponding dielectric constants.

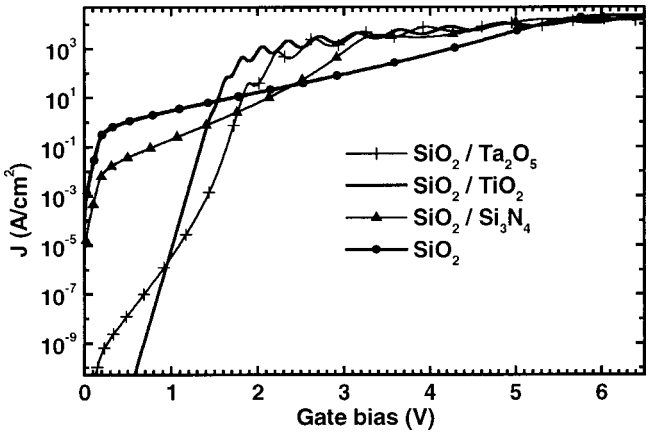

FIG. 2. Tunneling current density as a function of gate voltage for 10 Å pure oxide and for SiO_2/Si_3N_4, SiO_2/TiO_2 and SiO_2/Ta_2O_5 stacked dielectrics (for $t_{eq} = 10$ Å).

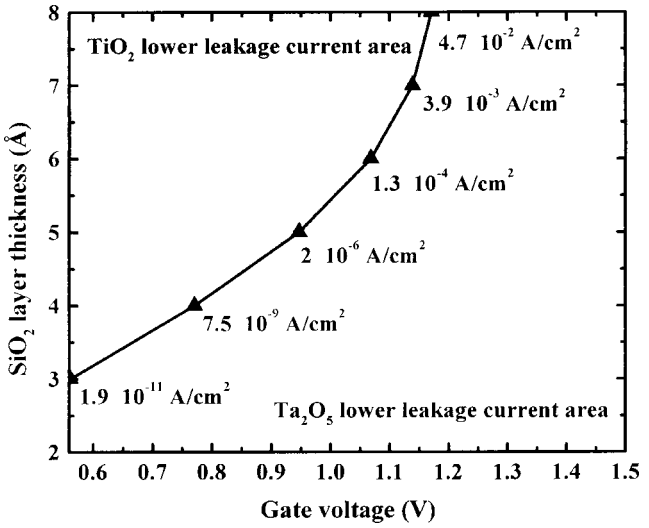

FIG. 3. SiO_2/TiO_2 and SiO_2/Ta_2O_5 stacked-layer tunneling-currents intersections plotted from 2- to 8-Å SiO_2 layer thicknesses (for $t_{eq}=10$ Å) versus gate voltage. This curve separates two distinct areas, indicating the best stacked layer to minimize leakage currents following the initial parameters.

In Fig. 2, the SiO_2 interlayer has been fixed to 5 Å. This choice will be commented later. The SiO_2 monolayer ($t_{ox}=10$ Å) curve confirms that the 1-A/cm^2 leakage current limit recommended for desktop applications is exceeded for low voltages (around 0.5 V). The SiO_2/Si_3N_4 bilayer shows a rather similar evolution with lower current values, typically one order of magnitude lower with respect to the SiO_2 counterpart around 1 V. For higher voltages, the slope slightly increases which leads to a crossing point before 2.5 V. This behavior is the consequence of the low Si_3N_4 barrier height (2 eV) to be compared to the 3 eV of SiO_2. This general phenomenon, common to every stacked structure will be discussed in details in the following section. At first order, all stacked dielectrics chosen here satisfy the roadmap criteria, but because of the weak leakage current margin of Si_3N_4, this dielectric is often presented only as a short term candidate comparing to high-κ materials. At longer term, other options must be considered.

The high-κ based (TiO_2 and Ta_2O_5) stacked $J(V)$ curves depict clearly several typical behaviors. In the following section, the conduction properties associated to each regime will be pointed out. Overall, the Ta_2O_5-based bilayer seems more advantageous above 1 V approximately. However, it can be noted that the $J(V)$ characteristics intersect at 0.95 V and considering the future MOSFET generations scaling parameters, bias voltages below 1 V must be taken into account.[1] Figure 3 shows the evolution of the crossing point as a function of the interlayer thickness. This curve sets a frontier which permits a choice between TiO_2 and Ta_2O_5 by observing the leakage current. The domain below this curve corresponds to the Ta_2O_5 lower leakage current area. Inversely, the area favorable to TiO_2 is located above the curve. As predicted, the current decreases with the interlayer thickness because of the low permittivity of SiO_2. According to the literature, a thickness lower than 5 Å does not seem technically achievable.[2] This means that the TiO_2-based bilayer leads to the lowest leakage current until the 0.95-V bias. Because of the great current margins observed for both materials, it would not be reasonable to make predictions for the future technologies from the sole consumption criterion. Nevertheless, these first calculations show that, considering the leakage current amplitude, the choice of a dielectric heterostructure cannot be valid within the whole 0.5–1.5 V range. Other parameters linked to the technological feasibility have to be clearly analyzed.[2] Nevertheless, in order to bring further informations on the degradation mechanisms, a complete understanding of the way current builds up in such stacked structures is necessary. In the following section, we propose such an analysis from a transmission spectroscopy.

IV. QUANTUM CURRENT CONTRIBUTIONS IN STACKED LAYERS

In Fig. 2, the quite pure tunneling behavior of the oxide and oxide/nitride $J(V)$ characteristics can be noted since no pronounced oscillation appears below a 3-V bias. Nevertheless, tunnel current oscillations caused by quantum wave interferences may appear for ultrathin oxide and oxide/nitride gate but for higher voltages.[19] The measurements of the oscillation quasiperiod have been recently used to estimate oxide parameters as, for example, its thickness.[20,21] On the contrary, the weak barrier height of the high-κ dielectrics causes the current oscillations to occur just above the 1.5-V gate voltage. For a single layer, these quantum interferences can be modeled by the analytical Airy function approximation (single triangular well). Obviously, in its initial formulation, this approach is not valid for stacked layers due to simultaneous multiple current contributions.

In order to interpret the different current slopes at the 0.95-V crossing, we plotted the quantum transmission probability and the supply function as a function of energy in Fig. 4(a) and the variations of the conduction-band edge versus distance in Fig. 4(b). Due to a weaker barrier height, the peaks in the quantum transmission appear at much lower energy levels for the SiO_2/TiO_2 stack than for SiO_2/Ta_2O_5. For both stacked layers, the dominant contributions can be roughly divided in several domains while increasing energy.

For SiO_2/TiO_2, below 400 meV, the current behavior is dominated by the direct tunneling through the total bilayer thickness. Above 400 meV, direct tunneling through the oxide layer is combined with a FN contribution through the second layer. Resonant levels appear in the quasitriangular quantum well delimited by the TiO_2 conduction-band edge. An alignment of these preferential paths with the concentration of free electrons in the emitting region yields the maxima observed on the transmission evolution. Above 570 meV, the tunneling length is equal to the SiO_2 interlayer thickness.

Conduction through the SiO_2/Ta_2O_5 stacked layers is governed by the same mechanisms but FN tunneling appears later since the Ta_2O_5 barrier is higher. Indeed, the first resonant level is located at 800 meV, as illustrated by the first transmission maximum. For such a high energy level, the number of occupied states is low. Thus, we think that the contribution of this level to the total current will be weak at a 0.95-V bias voltage. As expected by comparing the total

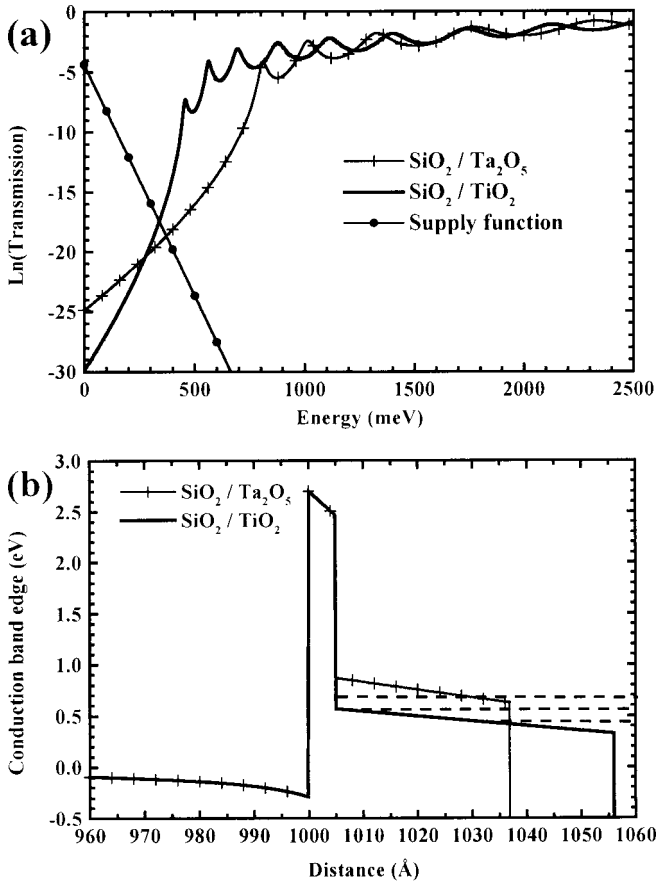

FIG. 4. (a) Quantum transmission probabilities and supply function versus injection energy at 0.95-V bias voltage for SiO_2/TiO_2 and SiO_2/Ta_2O_5 stacked layers and (b) spatial variations of the conduction-band edge for the corresponding stacked gates with the first three quantum bound states for the SiO_2/TiO_2 heterostructure.

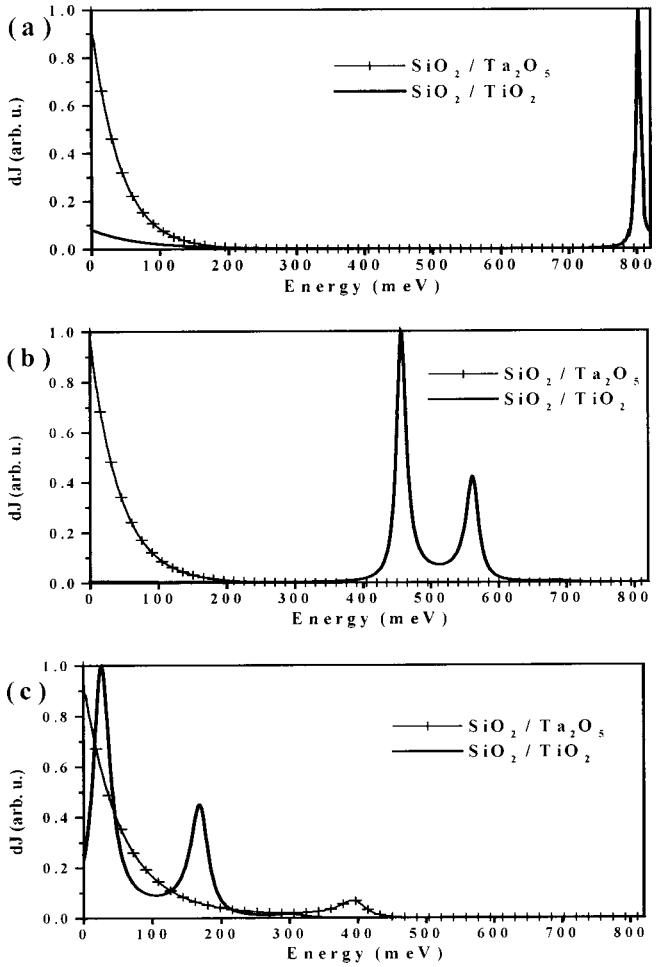

FIG. 5. Current increments of both stacked layers versus energy to illustrate the significant tunneling contributions for increasing bias voltages: (a) $V_g = 0.54$ V, (b) $V_g = 0.95$ V, (c) $V_g = 1.44$ V.

thickness of both high-κ stacked structures, the pure tunneling contribution is higher for Ta_2O_5 below 300 meV.

For both structures, increasing the supply voltage shifts the transmission peaks towards lower energies. As for a single layer dielectric, the positions of the resonant levels and then the energy offsets in the transmission resonances are governed by the quantum well geometry. Therefore, it strongly depends on the thickness and the slope (i.e., bias voltage and permittivity) of the high-κ material triangular barrier.

To quantify the influence of the resonant levels on the total current, we calculated the current increment dJ.[12] This increment is plotted as a function of energy for increasing bias voltages in Fig. 5. For each curve, the current amplitude has been divided by the maximum value to allow a clear insight into the different conduction mechanisms.

For Ta_2O_5, these curves confirm that the pure tunneling is the dominant phenomenon as illustrated by the monotonous decrease of current values. This decrease follows the supply function variation which models the occupation statistics. However, at 1.44 V, the first resonant level contribution around 400 meV is no more insignificant. This tunneling path shift towards low energy explains the first peak appearance on the corresponding $J(V)$ characteristic. For SiO_2/TiO_2 stacked layer, the major current is governed by a resonant mechanism through several preferential tunneling paths. At 0.44 V, the total current involves a conduction mechanism through a single resonant level and a weak contribution of direct tunneling. At the $J(V)$ crossing voltage (0.95 V), the pure tunneling becomes negligible, while the resonant effect contribution is shared among two levels. At this voltage, it can be noticed that the scale proportions between the two curves are respected. For the highest voltage (1.44 V), three levels contribute to the total current. The $J(V)$ oscillations are controlled by the superposition of significant transmission levels with the supply function. For instance, at 1.44 V, we can observe an oscillation in the $J(V)$ curve due to the presence of a resonant level near the Si conduction-band edge. When this resonant level shifts under the occupied injection states, a $J(V)$ minimum appears. When increasing bias, the shift of the resonant levels in the supply function window creates the oscillations on the $J(V)$ characteristic. At this point, it has to be mentioned that from a quantitative point of view, further refinements appear necessary. First of all, even if the conclusions drawn before will remain valid, ideally a 2D treatment of the accumulation layer pronounced effects at increasing voltage should be included. Let us mention also that the optimal parameters deduced for the heterostructure have to be weighted by the fact

that our approach is ballistic. Other contributions induced, particularly by defects, should degrade the calculated current leakage values. Other design criteria including capacitance considerations, which quantum determination is under development, must be added to this first conduction approach.

V. CONCLUSION

In summary, we have used an approach based on the conduction mechanisms through stacked dielectrics to propose design criteria for the ultrathin insulator of future MOS nanotransistors. The natural trend is to invoke the use of high-κ dielectrics to overcome the problem of too thin SiO_2 thicknesses when following the classical downscaling. In the article, we have shown that, the κ value is not a sufficient parameter to decrease the leakage current for a given equivalent barrier width. Among the dielectrics often quoted in the literature, such as TiO_2 or Ta_2O_5, at least two parameters have to be taken into consideration, namely, the permittivity and the barrier height, to define what dielectric heterostructure would lower the leakage current. Moreover, this kind of parametric study is of prime importance since the trade-off, and consequently the choice of a material, stands in the expected operating voltage range (below 1 V) of the future generations of MOS devices.

[1] See *The International Technology Roadmap for Semiconductors* (Semiconductor Industry Association, San Jose, CA, 2002), see also http://public.itrs.net/ for the most recent updates.
[2] G. D. Wilk, R. M. Wallace, and J. M. Anthony, J. Appl. Phys. **89**, 5243 (2001).
[3] X. Guo and T. P. Ma, IEEE Electron Device Lett. **19**, 207 (1998).
[4] T. Ito, T. Nakamura, and H. Ishikawa, IEEE Trans. Electron Devices **29**, 498 (1982).
[5] S. Song, W. S. Kim, J. S. Lee, T. H. Choe, J. K. Choi, M. S. Kang, U. I. Chung, N. I. Lee, K. Fujihara, and H. K. Kang, Tech. Dig. VLSI Symp. **2000**, 190 (2000).
[6] J. Zhang, J. S. Yuan, Y. Ma, and A. S. Oates, Solid-State Electron. **44**, 2165 (2000).
[7] J. Sune, P. Olivo, and B. Ricco, J. Appl. Phys. **70**, 337 (1991).
[8] F. Ranna, S. Tiwari, and D. A. Buchanan, Appl. Phys. Lett. **69**, 1104 (1996).
[9] E. M. Vogel, K. Z. Ahmed, B. Hornung, W. Kirklen Henson, P. K. McLarty, G. Lucovsky, J. R. Hauser, and J. J. Wortman, IEEE Trans. Electron Devices **45**, 1350 (1998).
[10] E. Cassan, J. Appl. Phys. **87**, 7031 (2000).
[11] R. Clerc, G. Ghibaudo, and G. Pannanakis, Solid-State Electron. (in press).
[12] F. Podevin, O. Vanbésien, and D. Lippens, J. Appl. Phys. **89**, 6247 (2001).
[13] E. Lheurette, X. Mélique, P. Mounaix, F. Mollot, O. Vanbésien, and D. Lippens, IEEE Electron Device Lett. **19**, 338 (1998).
[14] L. Burgnies, O. Vanbésien, V. Sadaune, D. Lippens, J. Nagle, and B. Vinter, J. Appl. Phys. **75**, 4527 (1994).
[15] P. Mounaix, O. Vanbésien, and D. Lippens, Appl. Phys. Lett. **57**, 1517 (1990).
[16] Z. Xu, M. Houssa, S. De Gendt, and M. Heyns, Appl. Phys. Lett. **80**, 1975 (2002).
[17] M. Houssa, V. V. Afanas'ev, A. Stesmans, and M. M. Heyns, Appl. Phys. Lett. **79**, 3134 (2001).
[18] C. Zhao, O. Richard, E. Young, H. Bender, G. Roebben, S. Haukka, S. De Gendt, M. Houssa, R. Carter, W. Tsai, O. Van Der Biest, and M. Heyns, J. Non-Cryst. Solids (in press).
[19] G. Lewicki and J. Maserjian, J. Appl. Phys. **46**, 3031 (1975).
[20] L. Mao, C. Tan, and M. Xu, Solid-State Electron. **44**, 1501 (2000).
[21] H. Katto, Solid-State Electron. **45**, 101 (2001).

ELSEVIER

Microelectronic Engineering 65 (2003) 103–112

MICROELECTRONIC ENGINEERING

www.elsevier.com/locate/mee

Characterisation of charge trapping at the Si–SiO_2 (100) interface using high-temperature conductance spectroscopy

E. Duval, E. Lheurette*

LEMI-UPRES.EA2654, Université de Rouen, 76131 Mont-Saint-Aignan Cedex, France

Received 6 February 2002; accepted 25 April 2002

Abstract

We report an experimental study of interface silicon trivalent defects on (100) oriented MOS structures. Considering the surface potential fluctuations, high-temperature conductance spectroscopy is used to detect acceptor and donor trap energy levels on N- and P-type devices, respectively, and to measure their capture cross-sections. The trap levels values are confirmed by a UV-assisted capacitance analysis. The capture cross-sections show very good agreement with published data deduced from different experimental methods. Our results confirm the capability of high-temperature conductance spectroscopy for interface defects characterisation.

Keywords: Trivalent defects; P_b centres; Interface states; Conductance spectroscopy; UV-assisted capacitance measurements

1. Introduction

Defects in MOS structures have been widely studied because of their direct involvement in ULSI systems instabilities [1–6]. During the last 10 years, the oxide thickness has been drastically reduced down to a few nanometers, leading to an increase of the gate leakage current by tunnelling effect [7]. As a consequence, different gate insulators have been proposed in order to replace the classical silicon dioxide. Many approaches, like for example the promising stacked dielectric structure [8], tend to keep a small layer of native or thermally grown SiO_2 in order to preserve interface quality. As a consequence, we can figure out that the Si–SiO_2 interface quality will remain a key factor for the future developments of ULSI technologies. From a crystallographic point of view, the interface states are mostly associated to a silicon trivalent defect which creates a dangling bond oriented to the oxide

*Corresponding author.
E-mail address: eric.lheurette@univ-rouen.fr (E. Lheurette).

0167-9317/03/$ – see front matter
PII: S0167-9317(02)00732-3

[9]. The electrical behaviour of such defects will be discussed in the forthcoming sections. Despite many investigations published on the $Si-SiO_2$ interface, a quantitative study is not easy because both interface and oxide traps have an impact on the measured characteristics [10,11]. The conductance technique developed by Nicollian and Goetzberger [1] is a powerful tool to deduce interface state densities and to study their dynamic behaviour. Moreover, it is well known that temperature can be used as an experimental parameter to enlarge the energy range scanned by the conductance spectroscopy [12]. In a previous work, we used a high-temperature conductance procedure to improve the mid-gap sensitivity [13]. Our $G(\omega,T)$ data lead to the description of 'slow' and 'fast' states within the whole gap width and gives pieces of information on their dynamic behaviour by means of the capture cross-section profiles. Further investigations on the high-temperature conductance data can lead to the identification of silicon trivalent defects on both trap energy levels and capture cross-section profiles.

2. High-temperature conductance spectroscopy

The $G(\omega)$ method is based on the observation of the conductance dispersion as a function of frequency for depletion bias voltages to avoid the interface state capacitance (C_{it}) to be hidden by the semiconductor capacitance. The dispersion variable ($\xi_{n,p}$) is given by Eq. (1):

$$\xi_{n,p} = \omega\tau_{n,p} \tag{1}$$

where ω and $\tau_{n,p}$ are the angular frequency and the major carrier lifetime, respectively. First, the oxide capacitance (C_{ox}) and series resistance (R_s) are deduced from capacitance measurements in the fully accumulated regime. G_p and C_p are the measured parallel conductance (G_m) and capacitance (C_m) corrected by the values of C_{ox} and R_s. A discussion on the conductance model is reported in [13]. For an accurate observation of interface state densities, a statistical model has to be considered. As a matter of fact, such a model is able to describe the large dispersion of interface time constants by taking into account the surface potential fluctuations. According to the statistical model proposed by Nicollian et al. [3], the equivalent parallel conductance is given by Eq. (2):

$$\frac{G_p}{\omega} = \frac{C_{it}}{2\xi_{n,p}\sqrt{2\pi\sigma_s^2}} \int_{-\infty}^{+\infty} \exp\left(-\frac{\eta^2}{2\sigma_s^2} - \eta\right) \ln(1 + \xi_{n,p}^2 \exp(2\eta)) d\eta \tag{2}$$

with $\eta = \upsilon_s - \langle\upsilon_s\rangle$ where where σ_s is the surface potential standard deviation, C_{it} is the interface trap equivalent capacitance and ψ_s is the surface potential. Our main topic is an accurate determination of the capture cross-section ($\sigma_{n,p}$) and lifetime ($\tau_{n,p}$) in order to describe the dynamic behaviour of traps. In our study, these parameters are deduced as functions of energy in band-gap from relations (3) and (4):

$$\sigma_{n,p} = \frac{\omega_{max}}{\upsilon_{th} N_{Dop}} \exp\left(\frac{\mp q\Psi_s}{kT}\right) \tag{3}$$

$$\tau_{n,p} = \frac{\xi_{n,p}}{\omega_{max}} \tag{4}$$

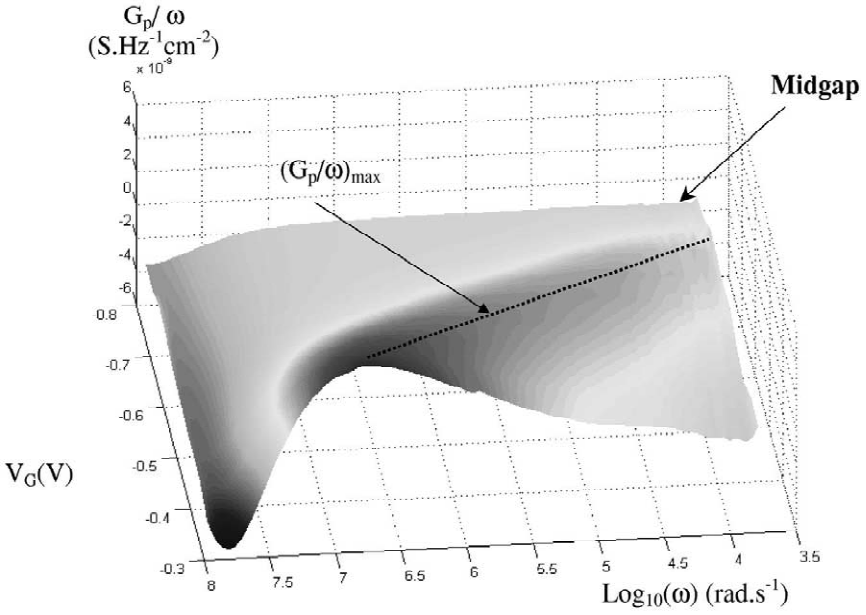

Fig. 1. Measured (G_p/ω (ω,V_G)) in depletion regime, at 300 K on a N-type structure between 1 kHz and 15 MHz.

where ν_{th} is the thermal velocity of majority carriers, N_{Dop} is the doping density and ω_{max} is the maximum angular frequency of the (($G_p/\omega)_{max}$) peak. Increasing the temperature allows a more efficient exploration in the mid-gap region as it is shown on Figs. 1 and 2. These 3D plots illustrate the parallel conductance dispersion as a function of frequency and bias voltage. It can be noted that

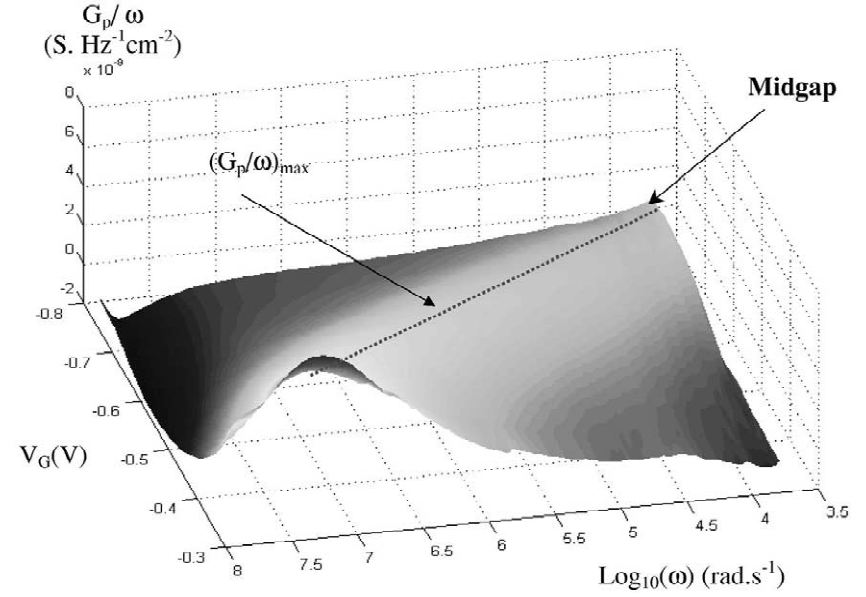

Fig. 2. Measured (G_p/ω (ω,V_G)) in depletion regime, at 350 K on a N-type structure between 1 kHz and 15 MHz.

the $(G_p/\omega)_{max}$ voltage range is more important for the 350 K plot which means the energy domain explored by the conductance technique is enlarged. Further details on the high-conductance spectroscopy procedure are given in Ref. [13].

3. Experimental results

The experiments were performed on MOS capacitors fabricated on (100) N- and P-type substrates. In both the cases, the gate oxide was grown by dry oxidation at 900 °C (N-type) and 1100 °C (P-type) after a standard RCA cleaning. The $C(V)$ measurements were carried out between 1 and 15 MHz [14]. The base characteristics of the MOS capacitors deduced at different temperatures are given in Table 1. The conductance method accuracy is governed by the determination of the transition frequency (F_{max}) associated to the peak conductance. To detect the conductance variations, we used an impedance analyser (HP 4194A) with a 100 Hz–15 MHz frequency sweep. $G(\omega)$ measurements were performed in the depletion regime to alternately fill and empty the interface states with a 50-mV small signal excitation. In order to quantify the silicon trivalent defects contribution, it is essential to separate the 'slow' and 'fast' state distributions. In that aim, the fast state contribution is estimated from the peak conductance and the slow state distribution is deduced from the observation of the 'slow state plateau' in the low frequency domain [15]. Traps distribution profiles show that the slow states density tends to decrease for the high temperatures. As a consequence, the high-temperature conductance measurements can be particularly useful to characterise the silicon trivalent defects contribution which gives rise to fast states. The evolution of interface states density and capture cross-sections measured on a P-type structure are, respectively, reported in Figs. 3 and 4 as a function of energy. Both interface states density and fast states capture cross-section exhibit a peak around 0.38 eV. Besides, this peak does not appear clearly on the capture cross-section profile bellow 400 K, confirming the usefulness of high-temperature exploration. Fig. 4 also depicts the 'slow' states capture cross-sections which typical exponential evolutions have been commented in [13]. The capture cross-section corresponding to the 0.38-eV peak is about $3–4\times10^{-16}$ cm^2. We have reported on the same graph (Fig. 5) the fast state capture cross-sections for P- and N-type capacitors as a function of energy. The N-type curve exhibits a peak of 10^{-14} cm^2 associated to an energy of 0.7 eV. It can be pointed out that the peak previously detected at 0.38 eV on a P-type structure vanishes on the 500-K curve. This can be explained by an annealing effect previously observed between 450 and 500 K [16]. In the following sub-section, we

Table 1
Parameters of characterised structures

Structure parameters	MOS P	MOS N at 300 K	MOS N at 350 K
Surface S (cm^2)	25	9	9
Doping density N_{Dop} (10^{15} at/cm^3)	4.93	1.70	1.74
Series resistance R_s (Ω)	88	148	135
Oxide capacitance C_{ox} (10^{-12} F)	125	226	263
Flat bands voltage V_{fb} (V)	−1.27	−0.26	−0.30
Oxide thickness T_{ox} (10^{-9} m)	68	11	11

All parameters have been evaluated with capacitance–voltage method at high frequencies [14].

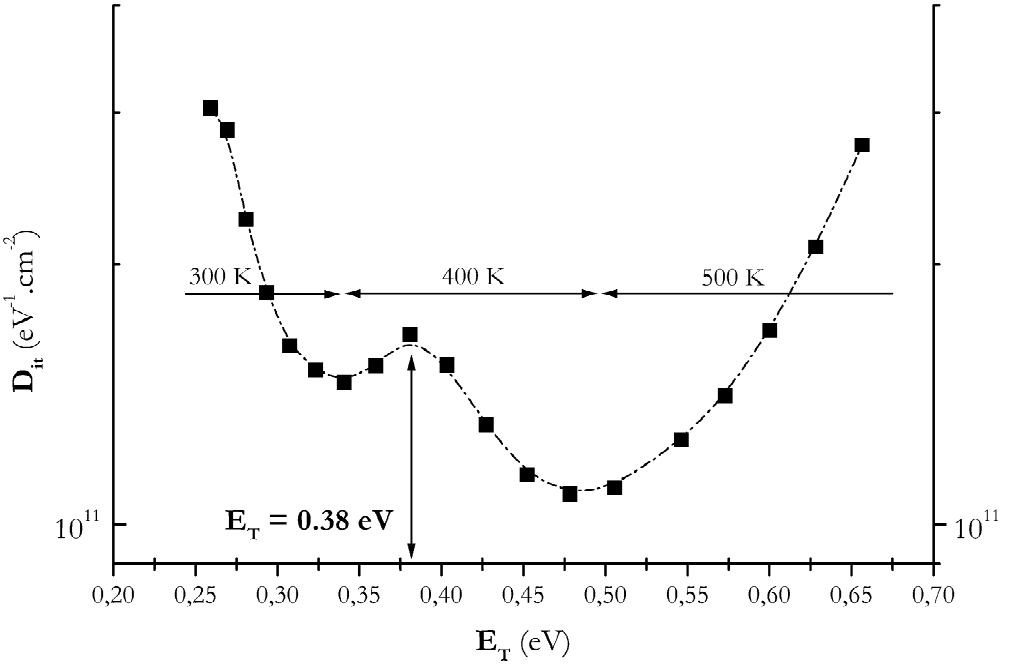

Fig. 3. Interface states density as a function of energy deduced from conductance measurements on a P-type structure.

propose to confirm our analysis by the UV-assisted capacitance method and to compare our data with results published on silicon trivalent defects at the $Si–SiO_2$ interface.

4. Discussion

In order to complete our $G(\omega,T)$ analysis, we first propose a comparison with the $C(V)$ data. The interface state density has been deduced from the well known BF-HF procedure [17]. The D_{it} profiles of Fig. 6 show that the 0.38-eV peak is not detected with the $C(V)$ method. As a matter of fact, the simple $C(V)$ procedure is not sensitive enough because it does not consider the surface potential fluctuation. Therefore, the $G(\omega,T)$ has been validated with the UV-assisted $C(V)$ method first proposed by Ling [18]. The basic principle is to subject capacitors to a UV stress which modifies the charge state at the $Si–SiO_2$ interface. Actually, a 253.7-nm UV irradiation yields a 4.9-eV energy increase, thus allowing interface electrons from the valence band to get over the SiO_2 potential barrier. This mechanism called ultraviolet bleaching has been very well described by Caplan et al. [19]. The trivalent defects trapping energies are extracted from the differential capacitance analysis (without any stress and after UV irradiation). Further details on this method are given in Ref. [18]. On the P-type differential capacitance evolution (Fig. 7), two peaks appear in depletion and weak inversion bias regions. This illustrates the amphoteric behaviour of the silicon trivalent defects. The peak around 0.4 eV previously deduced from the $G(\omega,T)$ spectroscopy is clearly observed. This trap energy level can be attributed to a donor state. An acceptor state is also present near 0.94 eV. Trap energy levels around 0.9 eV on (100) MOS structures have been reported in literature from different characterisation

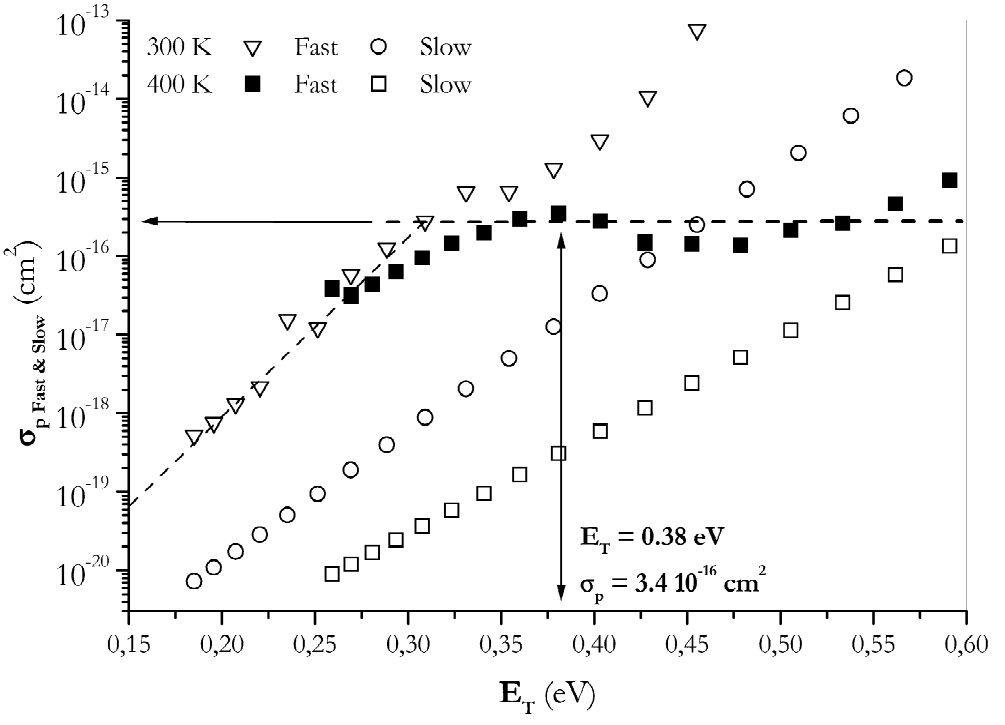

Fig. 4. Capture cross-section of 'fast' and 'slow' states as a function of energy deduced from conductance measurements on a P-type structure.

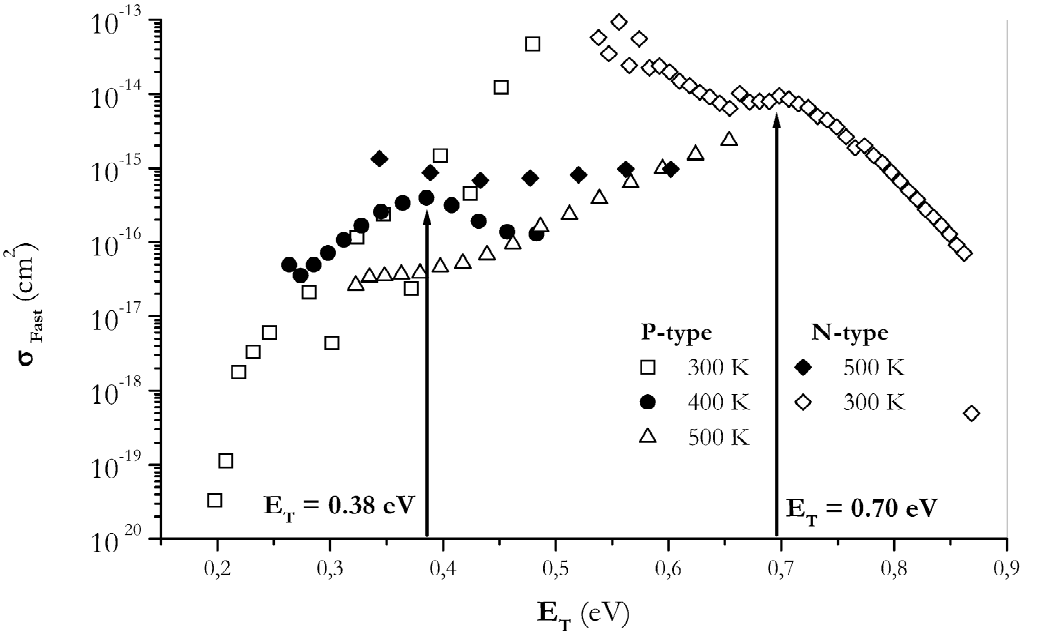

Fig. 5. Capture cross-section of 'slow' states as a function of energy between 300 and 500 K for P- and N-type structures.

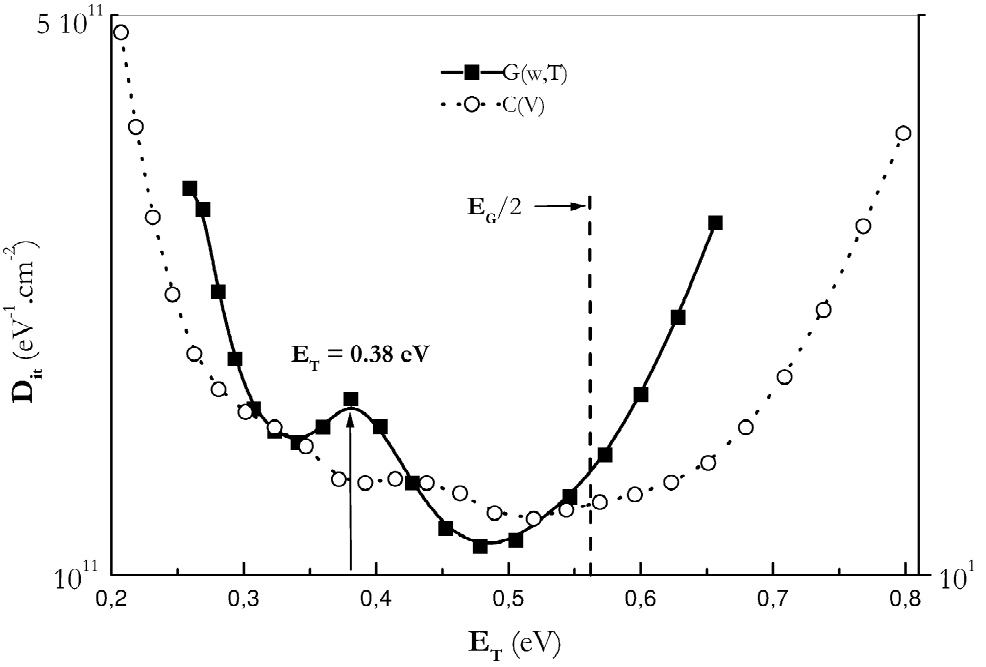

Fig. 6. Interface states density profiles deduced from conductance and capacitance measurements on a P-type structure.

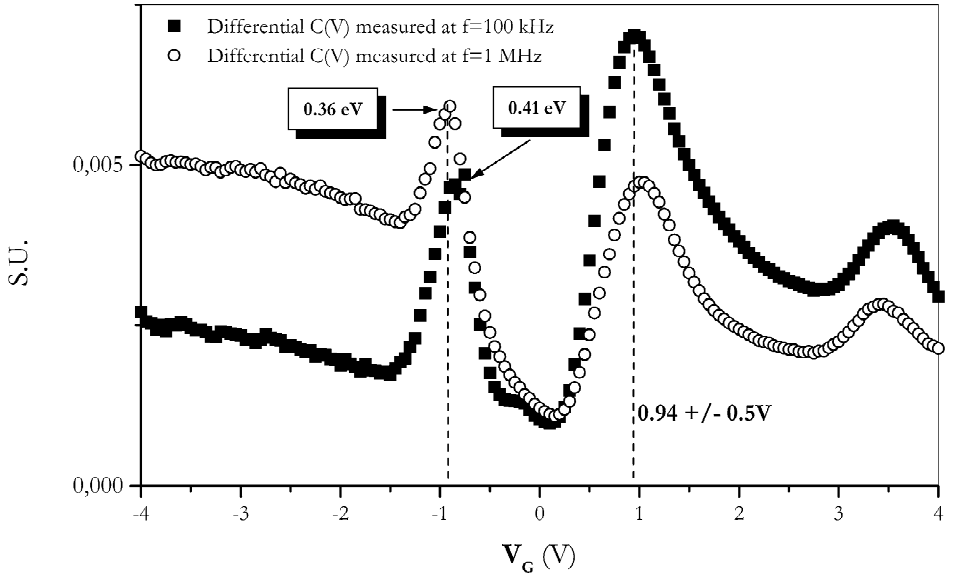

Fig. 7. Differential capacitance profile due to a 300-s UV irradiation on a P-type structure. The differential capacitance is divided by the value of C_{ox}.

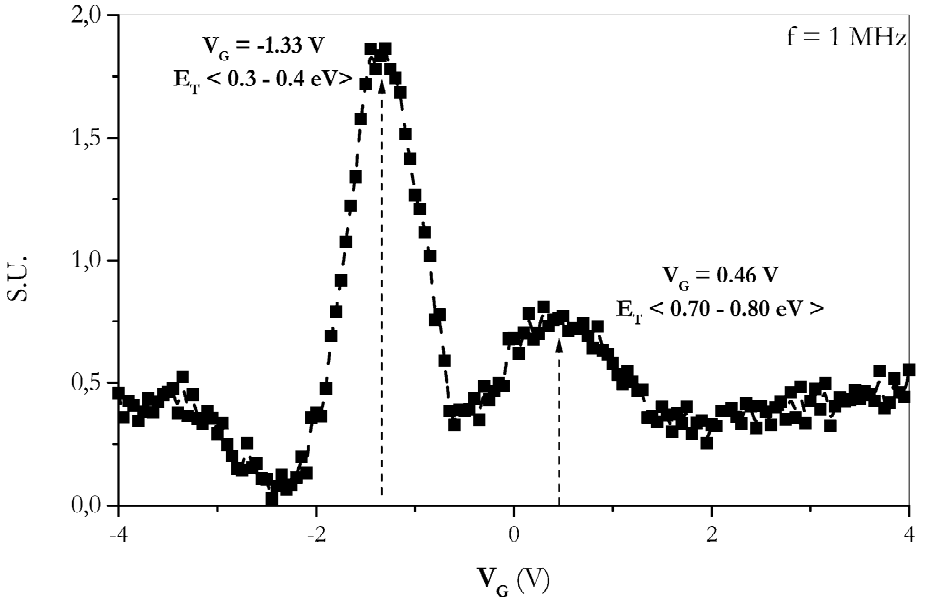

Fig. 8. Differential capacitance profile due to a 300-s UV irradiation on a N-type structure. The differential capacitance is divided by the value of C_{ox}.

methods including conductance [20] and electron spin resonance [21]. The same procedure applied to the N-type capacitors leads to the curve reported in Fig. 8. A peak near 0.4 eV is also present. The 0.7-eV peak previously deduced from the $G(\omega,T)$ spectroscopy on N-type samples is also detected and reveals the presence of an acceptor state. Increase of the interface state density around 0.4 and 0.7 eV appears for many kinds of stresses [22]. The most common trivalent defects of the $Si–SiO_2$ interface are designed as P_b centres in relation with their paramagnetic resonance signature. A lot of results have been published on the (111) interfaces because the P_b centres density is more important than in the case of (100) based devices [16]. On the other hand, two different centres designed as (100) P_{b0} and (100) P_{b1} have been identified on (100) interfaces which complicates the experimental data interpretation. To further investigate the chemical nature of traps, it is necessary to observe their capture cross-section variation. However, according to Uren et al. [20], the conductance spectroscopy is not able to distinguish P_{b0} and P_{b1} contributions on the (100) surface because of the weak differences in their capture cross-sections. As a matter of fact, despite many experimental studies, the trap centres capture cross-section is always under debate especially concerning the (100) interface. The values previously published scatter over several orders of magnitude. This great disparity illustrates both the limitations of the characterisation methods employed and the fact that several types of dangling bonds contribute to the interface states [23]. In Table 2, we tried to gather significant results deduced from different characterisation methods concerning the trap energy levels (E_T) and the capture cross-section (σ) on (100) oriented structures. This selection is very far from being exhaustive. The capture cross-sections deduced from our $G(\omega,T)$ method are very close to previously published data on both conductance [24] and emission time spectroscopies [25]. A recent article by Albohn et al. shows very similar capture cross-profiles measured on different processed (111) and (100) N-type samples. The order of magnitude of 10^{-14} cm^2 extracted from modulated capacitance measurements is in good agreement with our results [23].

Table 2
Comparison between several published results deduced from different characterisation procedures on (100) $Si–SiO_2$ interface

	DLTS Vuillaume et al. [25]		$G(\omega)$ Uren et al. [24]	MCV Albohn et al. [23]	Our results
	P_{b0}	P_{b1}		P_{b0}	
Donor:					
E_T (eV)	0.22	0.42			0.38
σ (cm^2)	8×10^{-15}	5×10^{-16}	$\approx3\times10^{-16}$		3×10^{-16}
Acceptor:					
E_T (eV)					0.7
σ (cm^2)			$\approx1\times10^{-14}$	$\approx1\times10^{-14}$	1×10^{-14}

5. Conclusion

We report silicon trivalent defects characterisation using the high-temperature conductance spectroscopy on (100) MOS structures. Increase in temperature improves the sensitivity near mid-gap thus allowing the detection of trap energy levels and the determination of the associated capture cross-sections. Using a surface potential fluctuation model, we separate 'slow' and 'fast' state contributions in order to observe the trap energy peaks on P- and N-type (100) MOS capacitors. The detected trap energy levels are confirmed by UV-assisted $C(V)$ experiments. Our values are in good agreement with the levels deduced from both ESR [21] and DLTS measurements [25]. Concerning the capture cross-sections, our results are close to published data obtained on (100) devices from DLTS [25] conductance [24] and modulated capacitance measurements [23]. This confirms the capability of high-temperature conductance spectroscopy which allows the separation of 'slow' and 'fast' states, permits a clear detection of silicon trivalent defects at the (100) $Si–SiO_2$ interface and is able to describe the dynamic behaviour of the associated trap centres by means of the capture cross-section.

Acknowledgements

The authors would like to thank G. Sarrabayrouse and L. Jalabert from LAAS–CNRS for fruitful discussions and supplying N-type samples, M. Benzohra and C. Dupras from the Atelier Inter-Universitaire de Microélectronique (AIME Toulouse, France) for supplying P-type samples and A. Pavan for technical help.

References

[1] E.H. Nicollian, A. Goetzberger, MOS conductance technique for measuring surface state parameters, Appl. Phys. Lett. 7 (8) (1965) 216–219.
[2] E.H. Nicollian, J.R. Brews, in: Metal Oxide Semiconductor) Physics and Technology, Wiley, New York, 1982.

[3] E.H. Nicollian, A. Goetzberger, A.D. Lopez, Expedient method of obtaining interface state properties from MIS conductance measurements, Solid-State Electron. 12 (1969) 937–944.
[4] E. Klausmann, W. Fahrner, D. Hand Bräunig, The electronic states of the Si–SiO_2 interface, instabilities in silicon devices, in: G. Barbottin, A. Vapaille (Eds.), Silicon Passivation and Related Instabilities, Vols. 1 and 2, Elsevier, Amsterdam, 1989.
[5] G. Declerck, R. Overstraeten, G. Broux, Measurements of low densities of surface states at the Si–SiO_2 interface, Solid-State Electron. 16 (1973) 1451–1460.
[6] H. Deuling, E. Klausmann, A. Goetzberger, Interface states in SiO_2 interfaces, Solid State Electron. 15 (1972) 559–571.
[7] E.M. Vogel, K.Z. Ahmed, B. Hornung, W.K. Henson, P.K. McLarty, G. Lucovsky, J.R. Hauser, J.J. Wortman, Modeled tunnel currents for high dielectric constant dielectrics, IEEE Trans. Electron Devices 45 (6) (1998) 1350–1355.
[8] J. Zhang, J.S. Yuan, Y. Ma, A.S. Oates, Design optimization of stacked layer dielectrics for minimum gate leakage currents, Solid State Electron. 44 (2000) 2165–2170.
[9] D. Stievenard, D. Vuillaume, Profiling of defects using deep level transient spectroscopy, J. Appl. Phys. 60 (3) (1986) 973.
[10] D.M. Fleetwood, 'Borders traps' in MOS devices, IEEE Trans. Nucl. Sci. 39 (2) (1992) 269–271.
[11] D.M. Fleetwood, P.S. Winokur, J. Reber, T.L. Meisenheimer, Effects of oxide traps, interface traps and 'border traps' on metal-oxide-semiconductor devices, J. Appl. Phys. 73 (10) (1993) 5058–5074.
[12] A. De Dios, E. Castan, L. Baillon, J. Barbolla, Interface state density measurement in MOS structures by analysis of the thermally stimulated conductance, Solid State Electron. 33 (8) (1990) 987–992.
[13] E. Duval, E. Lheurette, K. Ketata, M. Ketata, Determination of slow- and fast-state distributions using high temperature conductance spectroscopy on MOS structures, Semicond. Sci. Technol. 16 (2001) L57–L63.
[14] L. Soliman, E. Duval, E. Lheurette, M. Benzohra, K. Ketata, M. Ketata, Improvement of oxide thickness determination on MOS structures using capacitance-voltage measurements at high frequencies, Mater. Sci. Semicond. Process. 4 (2001) 163–166.
[15] W. Fahrner, A. Goetzberger, Energy dependence of electrical properties of interface states in Si–SiO_2 interfaces, Appl. Phys. Lett. 17 (1) (1970) 16–18.
[16] D. Vuillaume, Physique des défauts induits lors de la dégradation des composants MOS silicium submicroniques, Habilitation à diriger des recherches (1992), 23–26.
[17] R. Castagné, A. Vapaille, Description of the Si–SiO_2 interface properties by means of very low capacitance measurements, Surf. Sci. 28 (1971) 157–193.
[18] C.H. Ling, Trap generation at Si–SiO_2 Interface in submicrometer metal-oxide-semiconductor transistors by 4.9 V ultraviolet irradiation, J. Appl. Phys. 76 (1993) 581–583.
[19] P.J. Caplan, E.H. Poindexter, S.R. Morrison, Ultraviolet bleaching and regeneration of Si–Si_3 centers at the Si–SiO_2 interface of thinly oxidized silicon wafers, J. Appl. Phys. 53 (1) (1982) 541–545.
[20] M.J. Uren, V. Nayar, K.M. Brunson, C.J. Anthony, Interface state capture cross section measurements on vacuum annealed and radiation damaged Si–SiO_2 surfaces, J. Electrochem. Soc. 145 (2) (1998) 683–689.
[21] E.H. Poindexter, MOS interface states: overview and physicochemical perspective, Semicond. Sci. Technol. 4 (1989) 961–969.
[22] M. Itsumi, S. Noboru, M. Shimaya, Si–SiO_2 interface state generation at the surface potential of 0.4 and 0.7 eV, Microelectron. Eng. 28 (1995) 333–336.
[23] J. Albohn, W. Füssel, N.D. Sinh, K. Kliefoth, W. Fuhs, Capture cross sections of defect states at the Si–SiO_2 interface, J. Appl. Phys. 88 (2) (2000) 842–849.
[24] M.J. Uren, K.M. Brunson, A.M. Hodge, Separation of two distinct fast interface state contributions at the (100) Si–SiO_2 interface using the conductance technique, Appl. Phys. Lett. 60 (5) (1992) 624–626.
[25] D. Vuillaume, D. Goguenheim, G. Vincent, New insights on the electronic properties of the trivalent silicon defects at oxidized (100) silicon surfaces, Appl. Phys. Lett. 57 (12) (1990) 1206.

INSTITUTE OF PHYSICS PUBLISHING SEMICONDUCTOR SCIENCE AND TECHNOLOGY
Semicond. Sci. Technol. **16** (2001) L57–L63 PII: S0268-1242(01)25492-3

LETTER TO THE EDITOR

Determination of slow- and fast-state distributions using high-temperature conductance spectroscopy on MOS structures

E Duval, E Lheurette, K Ketata and M Ketata

LEMI-UPRES.EA2654-IUT, Université de Rouen, 76131 Mont-Saint-Aignan Cédex, France

E-mail: Emmanuel.Duval@univ-rouen.fr and Eric.Lheurette@univ-rouen.fr

Received 5 June 2001
Published 28 August 2001
Online at stacks.iop.org/SST/16/L57

Abstract
This letter presents an experimental study of interface trap parameters versus energy. Our method is based on conductance measurements as a function of angular frequency and temperature $G(\omega, T)$. The temperature is swept between 300 and 500 K in order to increase the mid-gap sensitivity. Capacitance as a function of voltage is used to establish the relation between the surface potential and the gate voltage at each temperature value. Then the conductance dispersion as a function of frequency is analysed in order to determine the distribution of the interface states D_{it} and of their capture cross section $\sigma_{n,p}$. Our results are in good agreement with those published on DLTS measurements. This confirms the capability of this technique compared with emission time spectroscopy, which implies a complex treatment of the measured data. Our $G(\omega, T)$ procedure brings an accurate observation of two different populations of traps and we propose a classification of 'slow' and 'fast' states.

(Some figures in this article are in colour only in the electronic version)

1. Introduction

Defects in MOS structures have always been an important source of instabilities in ULSI technology systems [1–6]. During the last decade oxide thickness has been drastically reduced down to a few nanometres. As a consequence different gate insulators have been proposed in order to minimize leakage currents [7–9]. Many approaches, for example the stacked dielectrics, tend to keep a small layer of SiO_2 in order to preserve interface quality [8]. As a consequence, we can figure out that the Si–SiO_2 interface quality will remain a key factor for future metal–insulator–semiconductor technologies. Despite many experimental investigations published on the Si–SiO_2 interface [10–14], quantitative study is difficult because both effects of oxide and interface traps have an impact on the measured characteristics [15, 16]. Among all the different approaches, the conductance technique developed by Nicollian and Goetzberger [1] is a powerful tool to extract interface state parameters of MOS devices. The main improvement of the conductance technique is the thermally stimulated conductance approach [17]. Actually, the temperature can be used as an experimental parameter to enlarge the measured energy domain. Several authors have worked on the low-temperature domain (<300 K) to describe the influence of P_b centres [18]. Our study uses the high-temperature domain (300–500 K) to improve the mid-gap sensitivity. The interface parameter determination is based on the observation of the parallel conductance maximum frequency. Our $G(\omega, T)$ data lead to an accurate determination of interface parameters and gives a description of the traps' behaviour and contributions of 'slow' and 'fast' states within the whole gap width.

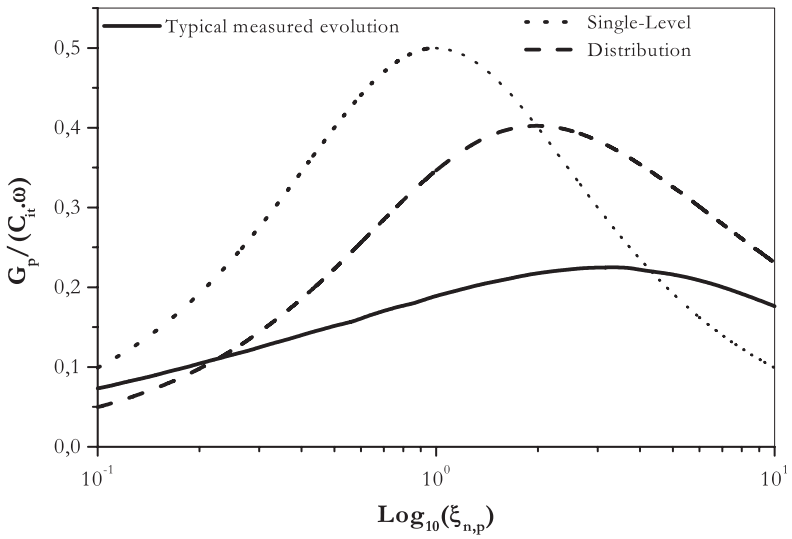

Figure 1. Typical conductance variation as a function of the dispersion variable for the single-level and distribution models (dotted curves) and typical measured evolution (solid curve).

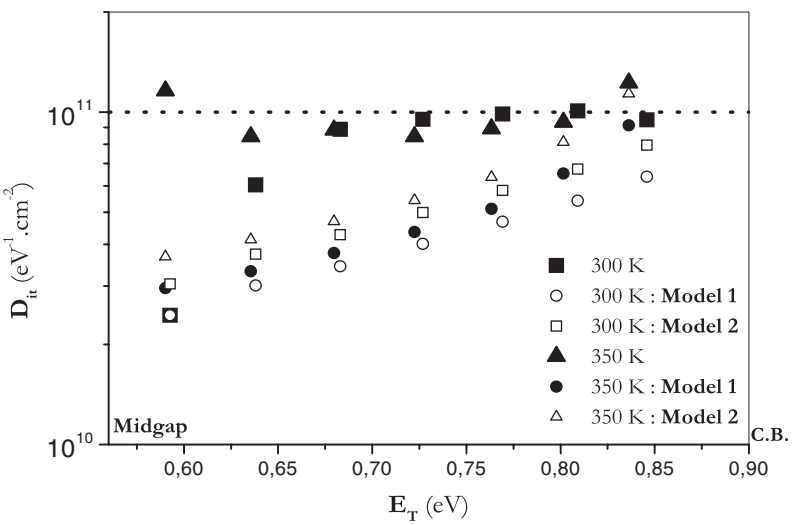

Figure 2. Interface state density as a function of energy at 300 and 350 K. All measurements have been carried out with the conductance method using model 1 (○ at 300 K and ● at 350 K), model 2 (□ at 300 K and ▽ at 350 K), models 1, 2 and the statistical model (■ at 300 K ▲ at 350 K), for a N-type structure described in table 2.

2. Conductance model

The choice of an appropriate model is one of the main conditions for an accurate determination of interface parameters. Therefore, we first describe this primordial step. The three models considered are a single-level model [1], a distribution model [2] and a statistical model [3]. Our choice is based on $G(\omega)$ curve observation and we introduce the dispersion variable ($\xi_{n,p}$) given by equation (1):

$$\xi_{n,p} = \omega\tau_{n,p} \tag{1}$$

where ω and $\tau_{n,p}$ are the angular frequency and the major carrier lifetime respectively. The typical evolution of G_p/ω as a function of $\xi_{n,p}$ for the single-level and distribution conductance models is plotted in figure 1. On the same graph, a typical measured characteristic is depicted. The conductance dispersion can be evaluated by considering the maximum angular frequency (ω_{max}) and the variation between $\omega_{max}/5$ and $5\omega_{max}$. The comparison between the three models is given in table 1 by taking into account these particular frequencies. The comparison of figure 1 and table 1 shows that the statistical model is the most appropriate to our samples. The interface state density for each model at 300 and 350 K represented in figure 2 confirms this conclusion. In fact the statistical model is very helpful in the depletion regime because it can describe the large dispersion of interface state time constants caused by surface potential fluctuations. According to this model, the equivalent parallel conductance (G_p) is given by

$$\frac{G_p}{\omega} = \frac{C_{it}}{2\xi_{n,p}\sqrt{2\pi\sigma_s^2}} \int_{-\infty}^{+\infty} \exp\left(-\frac{\eta^2}{2\sigma_s^2} - \eta\right) \times \ln(1 + \xi_{n,p}^2 \exp(2\eta))\, d\eta$$

$$\text{with} \quad \eta = \nu_s - \langle\nu_s\rangle \qquad \text{where} \quad \nu_s = \frac{q\Psi_s}{kT} \tag{2}$$

Table 1. Comparison of admittance and impedance variables for the different conductance models.

Conductance models	Single level (model 1)	Distribution (model 2)	Statistical (model 3)
$G_p/(\omega C_{it})$	0.500	0.402	<0.402
$(C_p - C_D)/C_{it}$	0.500	0.557	>0.557
$R_{\omega/5}$	0.385	0.457	>0.457
$R_{5\omega}$	0.385	0.576	>0.576
$\xi_{n,p}$	1	1.98	>1.98

Table 2. Parameters of characterized structures. All parameters have been evaluated with the capacitance–voltage method at high frequencies [21].

Structure parameters	MOS P	MOS N at 300 K	MOS N at 350 K
Surface S (cm^2)	25	9	9
Doping density N_{Dop} (10^{15} at cm^{-3})	4.93	1.70	1.74
Series resistance $R_s(\Omega)$	88	148	135
Oxide capacitance C_{ox} (10^{-12} F)	125	226	263
Flatband voltage V_{FB} (V)	−1.27	−0.26	−0.30
Oxide thickness T_{ox} (10^{-9} m)	68	11	11

where σ_s is the surface potential standard deviation, C_{it} is the interface trap equivalent capacitance and ψ_s is the surface potential.

3. Extraction of interface parameters

Our topic is an accurate determination of capture cross section ($\sigma_{n,p}$) because this parameter reveals the dynamic evolution of traps. The interface state parameters are deduced as a function of energy in the bandgap from the relations

$$\sigma_{n,p} = \frac{\omega_{max}}{\nu_{th} N_{Dop} \xi_{n,p}} \exp\left(\frac{\mp q \Psi_s}{kT}\right) \tag{3}$$

$$\tau_{n,p} = \frac{\xi_{n,p}}{\omega_{max}} \tag{4}$$

where ν_{th} is the thermal velocity of majority carriers, N_{Dop} is the doping density and ω_{max} is the maximum frequency of the $((G_p/\omega)_{max})$ peak. We suggest directly linking these measurement parameters by an efficient and accurate procedure, which can be easily computed.

The first step is the determination of the semiconductor capacitance (C_p) and conductance (G_p) by correcting the measured capacitance (C_m) and conductance (G_m) with the values of series resistance (R_s) and oxide capacitance (C_{ox}). R_s and C_{ox} are directly measured by biasing the sample in its fully accumulated regime at high frequencies [21]. The flatband potential (V_{FB}) and doping density (N_{Dop}) are deduced to establish the relation between the surface potential ψ_s and the gate voltage.

The second step is the determination of the dispersion variable following the procedure described in section 2.

Finally, the interface parameters are extracted by means of the conductance or capacitance divided by the interface state capacitance contribution, respectively $G_p/\omega \cdot C_{it}$ or $(C_p - C_D)/C_{it}$, where C_D is the depletion layer capacitance.

4. Experimental procedure

The experiments were performed on different MOS capacitors fabricated on N- and P-type (100)-oriented silicon substrate. Our experimental procedure follows the two steps described in section 3. The $C(V)$ measurements were carried out between 1 and 15 MHz [21]. The flatband voltage (V_{FB}), acceptor density (N_{Dop}), oxide layer capacitance (C_{ox}) and series resistance (R_s) experimental values are summarized in table 2. The conductance method accuracy directly depends on the determination of frequency (f_{max}) associated with the maximum value of the parallel conductance. For this reason we have measured the conductance between 100 Hz and 15 MHz with an impedance analyser (Hewlett–Packard 4194A). $C(V)$ and $G(\omega)$ measurements were carried out with a 0.05 V bias step.

For the $C(V)$ curves, the voltage was swept from accumulation to inversion. $G(\omega)$ measurements were performed in the depletion regime to alternately fill and empty the interface states with a small signal excitation. The procedure was repeated for different temperatures using a Biorad CS8900 cryostat system.

5. Experimental results

The measured value of the oxide capacitance (C_{ox}) as a function of temperature is represented in figure 3. The capacitance deduced from ellipsometry measurements is also plotted on this graph. We can see that increasing the temperature leads to a better determination of C_{ox}, which is a fundamental parameter for the accuracy of the $G(\omega)$ technique. Moreover we observe in figures 4 and 5 that increasing temperature allows a more efficient exploration near the mid-gap. These 3D plots show the parallel conductance ($G_{p/\omega}$) versus frequency for different bias voltages at 300 and 350 K. These curves illustrate the frequency dispersion of parallel conductance with the bias voltage. At 350 K, the bias voltage range is more important, which means the exploration range of interface parameters is enlarged in the bandgap. Therefore, the sensitivity near the mid-gap is improved. As a conclusion, for a given frequency range the energy domain can be enlarged; this is the main advantage of the thermally stimulated conductance spectroscopy.

The interface state density distribution is a very significant parameter concerning the Si–SiO_2 interface quality but it is not able to describe the dynamic behaviour of traps. To understand this dynamic behaviour, it is necessary to evaluate the capture cross section for the two types of structure (N- and P-type) presented in table 2. The procedure proposed by Uren [19,20] leads to a determination of the interface state parameters, and measures in fact the contribution of 'fast' states in MOS devices. Extending this procedure to high temperatures, we have deduced the 'fast'-state density (D_{Fast}) and the associated capture cross section (σ_{Fast}), as a function of the potential surface at 300 and 350 K. The capture cross section is proportional to the frequency response maximum of the parallel conductance, as described by equation (3). The measured capture cross section of 'fast' states is plotted as a function of energy for different temperatures in figure 7. For a given temperature, σ_{Fast}

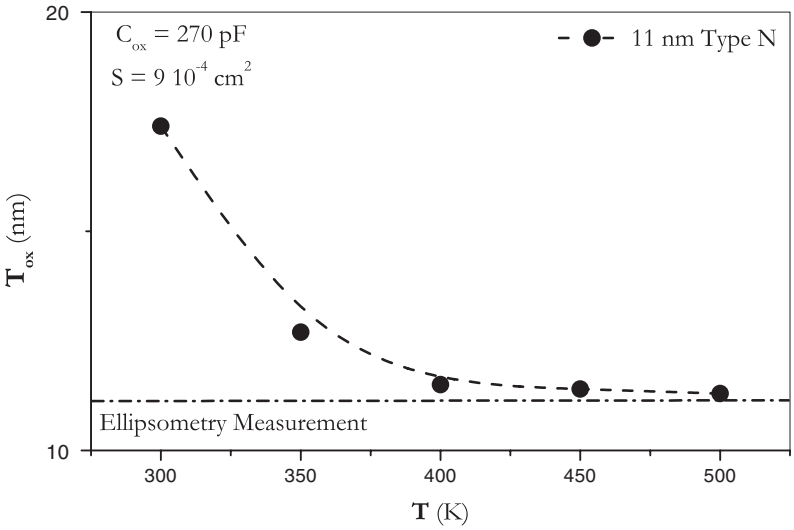

Figure 3. Oxide thickness deduced from conductance measurements as a function of temperature on a N-type structure. The value of C_{ox} is deduced from ellipsometry measurement.

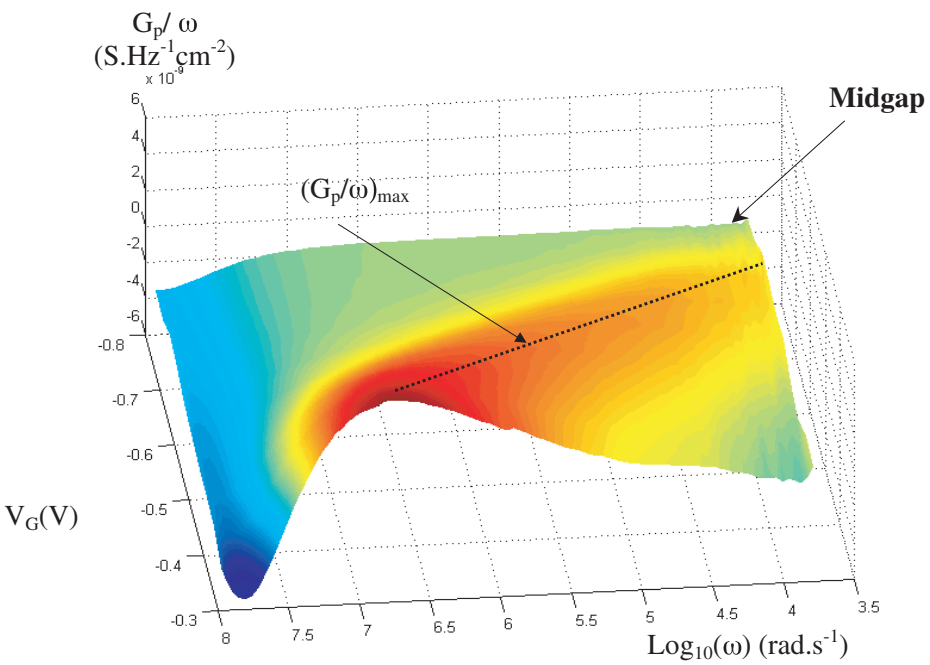

Figure 4. Measured $G_p/\omega(\omega, V_G)$ in the depletion regime, at 300 K on an N-type structure between 1 kHz and 15 MHz.

is quasi-constant and independent of surface potential near the mid-gap. We observe a plateau-like behaviour in good agreement with most of the results previously published [1, 22, 23]. However, the conclusions of Singh and Simmons [26] are different, because in their study the capture cross section of 'fast' states decreases exponentially in the whole bandgap. As a matter of fact, this plateau near mid-gap is directly associated with the exponential evolution of lifetime versus energy frequently observed from different experimental procedures [6, 22, 23]. Therefore, we think that an exponential evolution of capture cross section should be associated with 'slow' states as proposed in figure 8. Figures 6 and 7 also depict a quantitative relation between the capture cross section and the 'quality' of the interface and we can see that the capture cross section average near mid-gap increases while the 'quality' of interface diminishes. These first results confirm the published data on the conductance spectroscopy method [22–25].

The capture cross section behaviour of 'slow' states (σ_{Slow}) in the bandgap is determined at low frequencies by the 'slow'-state plateau [19]. In this case, the curves reported in figure 8 are driven by temperature. This result allows a rapid evaluation of σ_{Slow} as a function of temperature and in figure 9 a meaningful variation of this capture cross section is observed. This kind of graph is representative of capture cross section deduced from DLTS measurements and the sets of curves we obtain are in very good agreement with experimental results published by Katsube [27]. Furthermore, we observe that the variation of 'slow' states capture cross section is very wide in

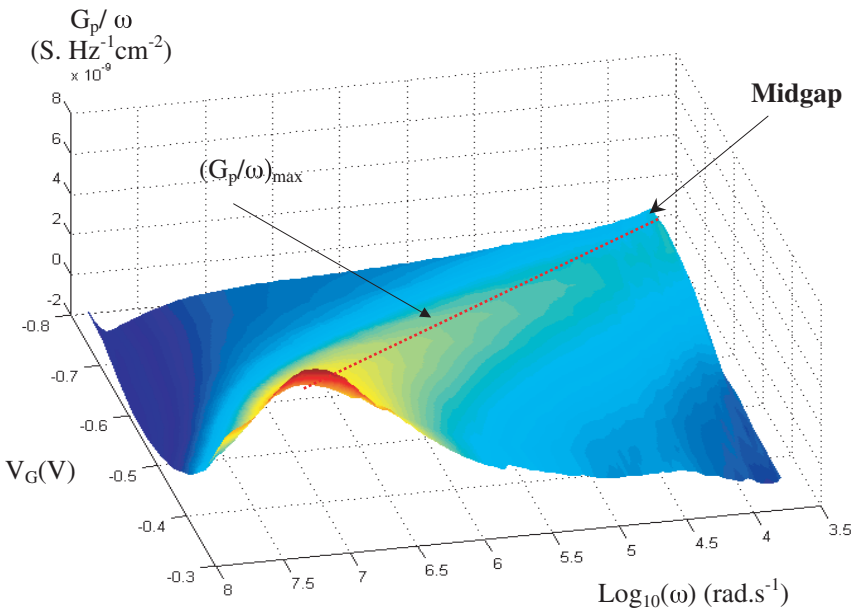

Figure 5. Measured $G_{sc}/\omega(\omega, V_G)$ in the depletion regime, at 350 K on an N-type structure between 1 kHz and 15 MHz.

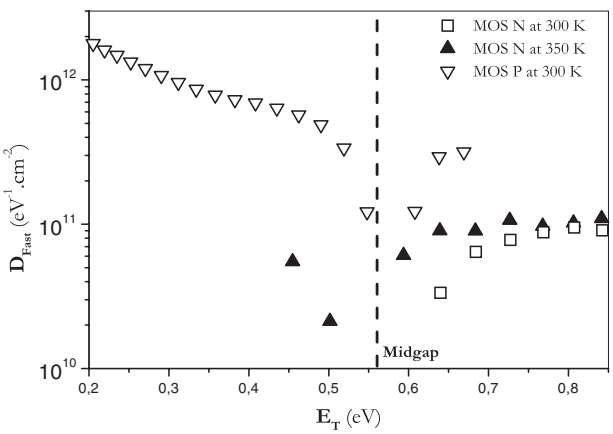

Figure 6. 'Fast'-state density as a function of energy, deduced from conductance measurements with the statistical model.

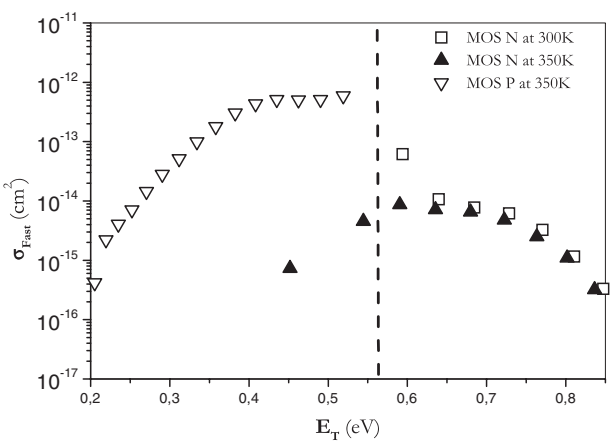

Figure 7. Capture cross section of 'fast' states as a function of energy, deduced from conductance measurements with the statistical model.

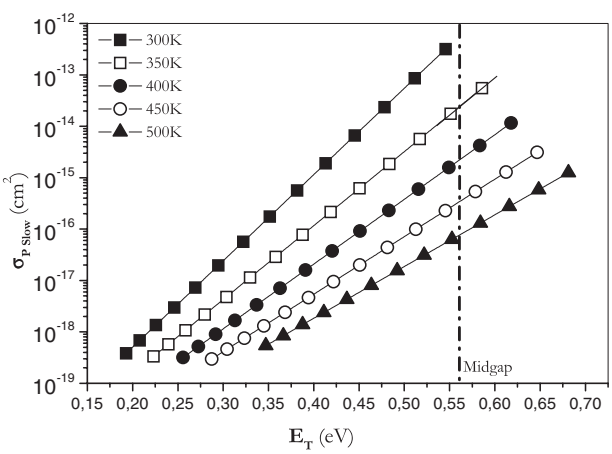

Figure 8. Capture cross section of 'slow' states as a function of energy between 300 and 500 K. Measurements were carried out on P-type MOS structures with $T_{ox} = 350$ Å and $S = 12.5 \times 10^{-4}$ cm^2.

the bandgap, this evolution reveals the importance of 'slow' states in MOS structures.

Finally, it can be noticed that the measurements were performed on rather high-quality structures ($\sim 1 \times 10^{10}$ eV^{-1} cm^{-2} near mid-gap). As a consequence, it is difficult to draw conclusions about the type of trap population near mid-gap as already noticed in our previous work [28]. This uncertainty in determination near mid-gap is not a specific drawback of the conductance method, as shown by charge pumping spectroscopy studies [13, 14].

6. Conclusion

We have presented a determination of 'slow'- and 'fast'-state parameter distribution using high-temperature stimulated conductance spectroscopy on MOS structures. The state

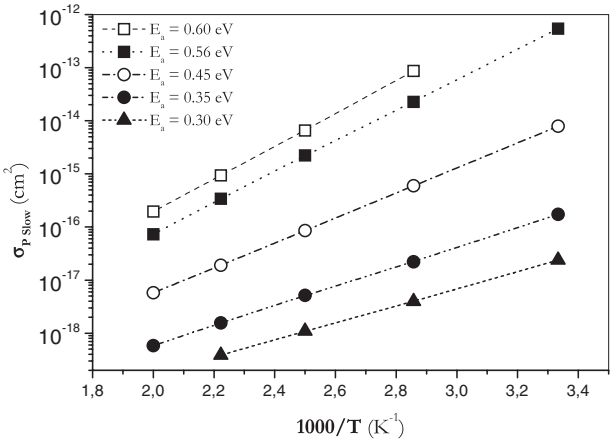

Figure 9. Capture cross section of 'slow' states as a function of temperature at different energy levels.

densities and associated capture cross section can be deduced by this $G(\omega, T)$ technique. We have shown that increasing the temperature enlarges the energy domain and improves the observation of the capture cross section near the mid-gap. Our results are in very good agreement with the previously published data on conductance spectroscopy techniques [22–25]. Moreover, concerning the 'slow'-state parameter characteristics, our curves follow the evolutions deduced from DLTS measurements [27]. Our $G(\omega, T)$ technique allows the simultaneous characterization of two different trap populations with the same measurement procedure.

The authors would like to thank L Soliman for fruitful discussions, Dr G Sarrabayrouse and L Jalabert PhD of LAAS–CNRS for fruitful discussions and supplying type N samples, Professor M Benzohra and Dr C Dupras for supplying type P samples and Dr P Martin, Dr M Masmoudi and M Hanine PhD for $C(V)$ and $G(\omega)$ acquisition programs. This work was partly supported by the Laboratoire d'Architecture et d'Analyse des Systèmes, Centre National de la Recherche Scientifique (LAAS-CNRS Toulouse, France) and the Atelier Inter-Universitaire de Microélectronique (AIME Toulouse, France).

References

[1] Nicollian E H and Goetzberger A 1965 MOS conductance technique for measuring surface state parameters *Appl. Phys. Lett.* **7**

[2] Nicollian E H and Brews J R 1982 *MOS (Metal–Oxide–Semiconductor) Physics and Technology* (New York: Wiley)

[3] Nicollian E H, Goetzberger A and Lopez A D 1969 Expedient method of obtaining interface state properties from MIS conductance measurements *Solid-State Electron.* **12** 937–44

[4] Klausmann E, Fahrner W E and Bräunig D 1989 *The Electronic States of the Si–SiO$_2$ Interface, Instabilities in Silicon Devices, Silicon Passivation and Related Instabilities* vols 1 and 2, ed G Barbottin and A Vapaille (Amsterdam: Elsevier)

[5] Declerck G, Van Overstraeten R and Broux G 1973 Measurements of low densities of surface states at the Si–SiO$_2$ interface *Solid-State Electron.* **16** 1451–60

[6] Deuling H, Klausmann E and Goetzberger A 1972 Interface states in SiO$_2$ interfaces *Solid-State Electron.* **15** 559–71

[7] Vogel E M, Ahmed K Z, Hornung B, Henson W K, McLarty P K, Lucovsky G, Hauser J R and Wortman J J 1998 Modeled tunnel currents for high dielectric constant dielectrics *IEEE Trans. Electron Devices* **45** 1350–5

[8] Zhang J, Yuan J S, Ma Y and Oates A S 2000 Design optimization of stacked layer dielectrics for minimum gate leakage currents *Solid-State Electron.* **44** 2165–70

[9] Campbell S A, Gilmer D C, Whang X C, Hsieh M T, Kim H S, Gladfelter W L and Yan J 1997 MOSFET transistors fabricated with high permitivity TiO$_2$ dielectrics *IEEE Trans. Electron Devices* **44** 104–9

[10] Ma Y M, Li Z, Liu L, Tian L and Yu Z 2000 Effective density of states approach to QM correction in MOS structures *Solid-State Electron.* **44** 401–7

[11] Moragues J-M, Sagnes B, Yckache K, Jérisian R, Oualid J and Vuillaume D 1995 Experiments and modelling to determine trapped holes and slow states in Fowler–Nordheim stressed MOS capacitors *Microelectron. Eng.* **28** 329–32

[12] Vuillaume D, Gogenheim D and Bourgoin J C 1991 Nature of the defects generated by electric field stress at the Si–SiO$_2$ interface *Appl. Phys. Lett.* **58** 490–2

[13] Cilingiroglu U 1990 Charge pumping spectroscopy with pulsed interface probing *IEEE Trans. Electron Devices* **37** 267–72

[14] Groeseneken G, Maes H E, Beltran N and Keersmaecker R D 1984 A reliable approach to charge-pumping measurements in MOS transistors *IEEE Trans. Electron Devices* **31** 42–53

[15] Fleetwood D M 1992 'Borders traps' in MOS devices *IEEE Trans. Nucl. Sci.* **39** 269–71

[16] Fleetwood D M, Winokur P S, Reber J and Meisenheimer T L 1993 Effects of oxide traps, interface traps and 'border traps' on metal–oxide–semiconductor devices *J. Appl. Phys.* **73** 5058–74

[17] De Dios A, Castan E, Baillon L and Barbolla J 1990 Interface state density measurement in MOS structures by analysis of the thermally stimulated conductance *Solid-State Electron.* **33** 987–92

[18] Uren M J, Statis J H and Cartier E 1996 Conductance measurements on P_b centers at the (111) Si:SiO$_2$ interface *J. Appl. Phys.* **80** 3915–22

[19] Uren M J, Collins S and Kirton M J 1989 Observation of 'slow' states in conductance measurements on silicon metal–oxide–semiconductor capacitors *Appl. Phys. Lett.* **54** 1448–50

[20] Uren M J, Brunson K M and Hodge A M 1992 Separation of two distinct fast interface state contributions at the (100) Si/SiO$_2$ interface using the conductance technique *Appl. Phys. Lett.* **60** 624–6

[21] Soliman L, Duval E, Lheurette E, Benzohra M, Ketata K and Ketata M 2001 Improvement of oxide thickness determination on MOS structures using capacitance–voltage measurements at high frequencies *Mater. Sci. Semicond. Process.* **4** 163–6

[22] Fahrner W and Goetzberger A 1970 Energy dependence of electrical properties of interface states in Si–SiO$_2$ interfaces *Appl. Phys. Lett.* **17** 16–8

[23] El-Sayed M, Pananakakis G and Kamarinos G 1985 Complete exploration of the silicon gap at the interface of MIS tunnel diodes using conductance technique at various temperatures and illuminations levels *Solid-State Electron.* **28** 345–57

[24] Papadas C, Morfouli P, Ghibaudo G and Pananakakis G 1992 Extraction of interface state density profile from the maximums of the parallel conductance versus applied gate bias curves $G_p(V_a)$ using the conductance technique *Rev. Sci. Instrum.* **63** 4189–91

[25] Bauza D, Morfouli P and Pananakakis G 1991 Detection of interface and volume traps in very thin oxide MOS structures using DLTS, quasi-static and conductance measurements *Solid-State Electron.* **34** 933–6

[26] Singh A and Simmons J G 1982 Determination of energy density distribution and capture cross section of interface states in the metal–nitride–oxide–semiconductor (MNOS)

structure *Solid-State Electron.* **25** 219–26
[27] Katsube T, Kakimoto K and Ikoma T 1981 Temperature and energy dependencies of capture cross section at surface states in Si metal–oxide–semiconductor diodes measured by deep level transient spectroscopy *J. Appl. Phys.* **52** 3504–8
[28] Duval E, Soliman L, Lheurette E, Ketata K, Benzohra M, Duprat C and Ketata M 2001 Rapid determination of 'slow' and 'fast' states densities using thermally stimulated conductance spectroscopy on metal–oxide–semiconductor capacitors *Mater. Sci. Semicond. Process.* **4** 141–3

PERGAMON

Materials Science in Semiconductor Processing 4 (2001) 141–143

MATERIALS SCIENCE IN SEMICONDUCTOR PROCESSING

Rapid determination of "slow" states and "fast" states densities using thermally stimulated conductance spectroscopy on metal-oxide semiconductor capacitors

E. Duval[a,*], L. Soliman[a], E. Lheurette[a], K. Ketata[a], M. Benzohra[a], C. Duprat[b], M. Ketata[a]

[a] *LEMI-UPRES.EA2654, Université de Rouen, Rue Lavoisier, 76131 Mont-Saint-Aignan, France*
[b] *AIME, 135 Avenue de Rangueil, 31077 Toulouse Cedex, France*

Abstract

Both effects of oxide and interface traps have an impact on $C(V)$ and $G(\omega)$ curves, hence, we propose to estimate the contribution of "slow" states and "fast" states with the conductance technique in order to evaluate their contribution as a function of temperature. Silicon metal-oxide semiconductor (MOS) structures show a frequency dispersion of the equivalent conductance due to carriers recombination at interface states. We have observed on conductance measurements a contribution of "fast states" which correspond to the high-frequency peak, and a low-frequency plateau due to the influence of "slow states" on $G(\omega, V)$ curves. We propose to extract the traps distribution at each temperature, in dissociating the "slow" states and "fast" states as a function of energy in band-gap. We estimate the capture cross-section with this conductance method which is proportional to frequency. The use of the $G(\omega, T)$ technique permits a clear identification of two traps populations. These populations give a better description of "slow" and "fast" states contribution in MOS devices.

Keywords: Interface states; "Slow" states; "Fast" states; Capture cross section and conductance measurements

1. Introduction

The measurement of the interface states density in a metal-oxide semiconductor (MOS) structure is a primordial topic within the characterisation in semiconductor. Interface states at the $Si–SiO_2$ interface have been studied in detail because of their effects on the reliability and quality of MOS structures [1–10]. Many methods have been developed for some specific applications [11–16]. We propose a modification of the Nicollian–Goetzberger technique, which is based on the measurements of conductance as a function of frequency at given temperature. We determine the interface electrical properties, which depends on parallel conductance versus angular frequency. Then, we estimate the influence of "slow" states densities on interface profiles, with "slow" states plateau in low frequency [17]. In this purpose, we have measured the conductance between 100 Hz and 15 MHz, and we deduced the interface parameters. Finally, we have estimated the "fast" and "slow" states distribution and associated capture cross section.

2. Experimental procedure

In practice, we observe random variations of band bending caused by charge nonuniformities. Therefore, a statistic model [1–3] is very useful because it describes the large dispersion of interface states time constant caused by surface potential fluctuations. The experiments were performed on MOS capacitors fabricated on

*Corresponding author. Tel.: +33-235-147179; fax: +33-235-146254.
E-mail address: emmanuel.duval@univ-rouen.fr (E. Duval).

1369-8001/01/$ - see front matter
PII: S1369-8001(00)00154-2

a n-type (1 0 0) oriented silicon substrate of 1–3 Ω cm resistivity. The oxide layer was thermally grown to a thickness of 110 Å. The area of metal gate was 9×10^{-4} cm^2. These standard structure parameters have been determined by $C(V)$ characterisation. The C–V measurements at 1 MHz were performed at each temperature to establish the relation between the surface potential and gate voltage. We have realised a sweep in frequency between 100 Hz and 15 MHz with an Impedance Analyser (Hewlett-Packard 4194A). Conductance and capacitance have been measured with a 50 mV bias step. First, we measure equivalent conductance and capacitance as a function of frequency at different bias voltages. Then, we take into account the influence of series resistance R_s and oxide capacitance C_{ox}. And we determine the interface electrical properties: the interface states density, and capture cross-section distribution of interface states. Finally, we estimate the contribution of "slow" states in low frequency with "slow" states plateau, and we deduce the "fast" states distribution and the capture cross section associated with "fast" and "slow" states.

3. Experimental results

Experimental results are presented to put in evidence; the dynamic behaviour of the capture cross section on band-gap from this conductance method, and to determine the influence and contribution of "slow" and "fast" states. The equivalent conductance versus frequency curves gives us the interface states density calculated with the maximum of G_{sc}/ω peak, using the statistical model [1]. We have obtained experimental curves G_{sc}/ω between 300 and 350 K by step of 10 K, and we have deduced the interface states density D_{it}, "slow" states density in low-frequency D_{Slow} (Fig. 1), and calculated the "fast" states distribution D_{Fast} (Fig. 2) as a function of potential surface. We show in Fig. 1 that "slow" states distribution increases around midgap. In others words, the contribution of "slow" states is primordial in low frequency, and at the origin of deep level in band gap. We also observed that a temperature sweep increases the gap excursion. The "fast" states density is the same as that interface states density near conduction band, but around midgap the "fast" states density decreases.

We have deduced capture cross-section using the method described in Ref. [1]. The measured capture cross section of "fast" states is plotted versus energy at each temperature (Fig. 3). The capture cross section for electrons in depletion regime is quasi-constant and surface potential is independent of energy near midgap at fixed temperature. The behaviour of this parameter is in agreement with previously published data [9,14] of

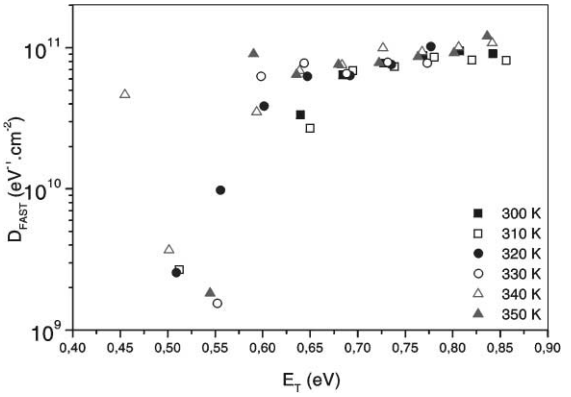

Fig. 2. "Fast" states density distribution as a function of energy between 300 and 350 K.

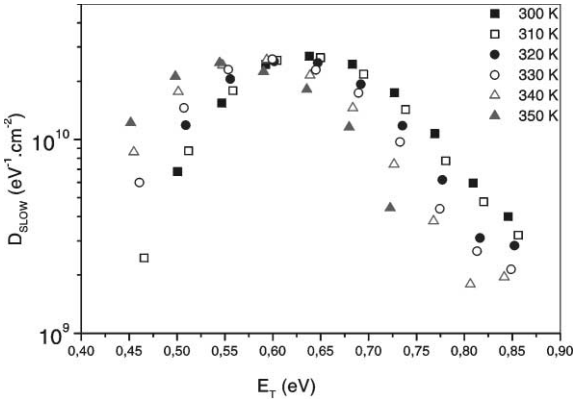

Fig. 1. "Slow" states density distribution as a function of energy between 300 and 350 K.

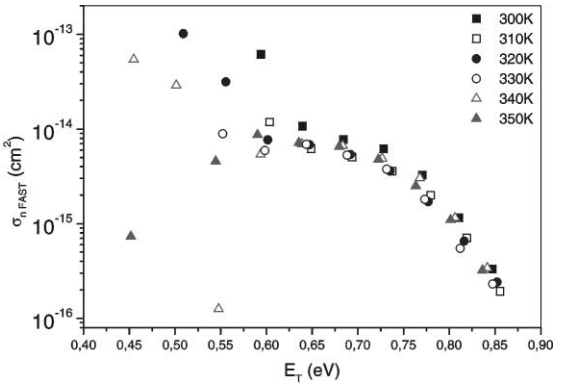

Fig. 3. Capture cross-section distribution of "fast" states as a function of energy between 300 and 350 K.

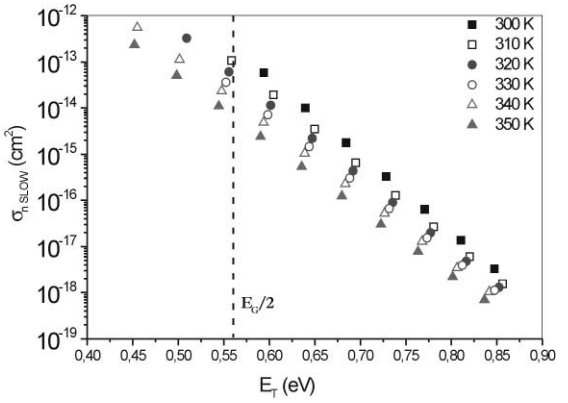

Fig. 4. Capture cross-section distribution of "slow" states as a function of energy between 300 and 350 K.

interface states. We can see that capture cross-section decreases exponentially near valence or conduction band. The behaviour is in agreement with the results published by Deuling [9] and El-Sayed [12]. To resume the above, the determination of capture cross-section behaviour, the equivalent conductance must respond in low frequencies near midgap, and in high frequencies near conduction or valence bands according to the type of semiconductor (N or P). We have deduced the capture cross section of "slow" states, and we show in Fig 4, the real dependence on temperature. Furthermore, we observe that this parameter is largely distributed over the band gap. The appearance of these curves is representative of capture cross-section evolution and contribution of "slow" states near midgap and conduction band . The capture cross section of "slow" states contains both an energy, frequency and temperature dependence.

4. Conclusion

We have presented a modification of Nicollian–Goetzberger technique as a function of frequency at given temperature. From equivalent conductance, we have deduced interface "slow" and "fast" states distribution. The measured capture cross section of "slow" states shows a dependence in energy and temperature. The measured capture cross section of "fast" states shows a weak dependence on energy near the mid gap, and a sharp decrease toward the conduction band edge in good agreement with the data obtained with the DLTS method [16]. The behaviour observed with this conductance method shows a dependence in energy, frequency and temperature. This $G(\omega, T)$ technique improves the dynamic behaviour accuracy of the participation of "slow" and "fast" states, and gives a better description of "slow" and "fast" states contribution of the capture cross-section behaviour in band-gap. The observation of two visible traps population shows the great interest of this conductance technique.

Acknowledgements

The authors would like to thank Dr. Sarrabayrouse and L. Jalabert, Ph.D. for fruitful discussions and also for supplying samples. This work was partly supported by the Laboratoire d'Architecture et d'Analyse des Systèmes, Centre National de la Recherche Scientifique (LAAS-CNRS, Toulouse, France).

References

[1] Nicollian EH, Brews JR. MOS (Metal Oxide Semiconductor) Physics and Technology. New York: Wiley, 1982.
[2] Nicollian EH, Goetzberger A. Appl Phys Lett 1965;7(8):216–9.
[3] Barbottin G, Vapaille A, editors. Instabilities in Silicon Devices, Passivation and Related Instabilities, vol. 1 & 2. Amsterdam: Elsevier, 1989.
[4] Sze SM. Physics of Semiconductor Devices, 2nd ed. New York: Wiley, 1981.
[5] Declerck G, Van Overstraeten R, Broux G. Solid-State Electron 1973;16:1451.
[6] Nicollian EH, Goetzberger A, Lopez AD. Solid-State Electron 1969;12:937.
[7] Brews JR. Solid-State Electron 1983;16(8):711.
[8] Simonne JJ. Solid-State Electron 1973;16:121.
[9] Deuling H, Klausmann E, Goetzberger A. Solid-State Electron 1972;15:559.
[10] Papadas C, Morfouli P, Ghibaudo G, Pananakakis G. Rev Sci Instr 1992;63(9):4189.
[11] Bauza D, Morfouli P, Pananakakis G. Solid-State Electron 1991;34(9):933.
[12] El-Sayed M, Pananakakis G, Kamarinos G. Solid-State Electron 1985;28(4):345.
[13] Singh A, Simmons JG. Solid-State Electron 1982; 25(3):219.
[14] Fahrner W, Goetzberger A. Appl Phys Lett 1970;17(1):16.
[15] De Dios A, Castan E, Baillon L, Barbolla J. Solid-State Electron 1990;33(8):987.
[16] Katsube T, Kakimoto K, Ikoma T. J Appl Phys 1981; 52(5):3504.
[17] Uren MJ, Collins S, Kirton MJ. Appl Phys Lett 1989;54(15):1448.

PERGAMON

Materials Science in Semiconductor Processing 4 (2001) 163–166

MATERIALS SCIENCE IN SEMICONDUCTOR PROCESSING

Improvement of oxide thickness determination on MOS structures using capacitance–voltage measurements at high frequencies

L. Soliman, E. Duval*, M. Benzohra, E. Lheurette, K. Ketata, M. Ketata

LEMI-UPRES.EA2654-IUT, Université de Rouen, 76131 Mont-Saint-Aignan Cedex, France

Abstract

It is well known that capacitance–voltage ($C-V$) measurements provide a simple determination of oxide thickness, but with the scaling down of components the classical method is not appropriated any more. We have observed that for two devices with the same oxide thickness and different surfaces, the classical method is accurate for large area but it is not adapted for the small one. We present a new procedure to make an accurate electrical determination of the oxide thickness on metal-oxide-semiconductor (MOS) structures of low dimensions in U.L.S.I. technology. Our method does not require a measurement in strong accumulation. It is based on $C-V$ measurements at frequencies higher than 1 MHz associated to a non-linear optimisation of the experimental and theoretical band bending versus bias voltage curve ($\Psi_S = f(V_g)$), in the depletion mode. By this way, a corrective factor is estimated with precision in order to make an accurate determination of the oxide thickness value. We show that the frequency associated to the non-linear optimisation of $\Psi_S = f(V_g)$ is function of the MOS device dimensions and is increased when the surface decreases. The experimental results obtained on low-dimension MOS structures and different oxide thickness are precise and in total agreement with those measured by ellipsometry. By using our new procedure the accuracy of oxide thickness determination is improved.

Keywords: MOS; Capacitance; Oxide thickness; Band bending and measure frequency

1. Introduction

The elementary structure used in the majority of electronic devices is the metal/oxide/semiconductor (MOS) structure. Currently, the dimension reduction of this structure involves an oxide thickness lower as well as a surface area lower. Among the optical and electrical existing methods used to characterize MOS structures, the $C-V$ is the most attractive because the test sample can be submitted to all the processing steps, including gate deposition and is consequently representative of the final MOS device. Every one used to talk about the difficulties to measure low oxide thickness but no one took into account the influence of surface contact area on the determination of the structure characteristic. It has already been shown [1–3] that the main reason for the difficulties encountered when determining the insulator thickness D_{ox} (Eq. (1)) from $C-V$ measurements is due to the non-saturation of the $C-V$ curve. Consequently, a large error can be made when identifying the maximum capacitance with the oxide capacitance C_{ox}.

$$D_{ox} = \frac{\varepsilon_0 \varepsilon_{ox}}{C_{ox}}, \tag{1}$$

where C_{ox} is the oxide capacitance, ε_0 the permitivity of vacuum and ε_{ox} the dielectric constant of the oxide. The understanding of electronic behavior of MOS structure is based on the analyses of experimental $C-V$ curves. Until now $C-V$ measurements were made at a maximum frequency of 1 MHz. This frequency was considered as limited frequency from which each defect

*Corresponding author. Tel.: 33-235147179; fax: 33-235146254.

E-mail address: emmanuel.duval@univ-rouen.fr (E. Duval).

1369-8001/01/$ - see front matter
PII: S1369-8001(00)00131-1

in the sample is frozen. This assertion seems not to be verified for small structures as evidenced by the non-supposition in accumulation field of the $C-V$ curve in Fig. 1. The key parameter of $C-V$ analyses is the $\Psi_S = f(V_g)$ relation. However, Ψ_S determination requires to know with a very big precision the value C_{ox} and D_{ox}. We propose to link the ac frequency used to study electrical properties of MOS structures to the structure area and the oxide thickness.

2. Experiment

Experiments were performed on two sets of MOS capacitors. The first set was p-type Si (1 1 0) substrate with contacts areas (A) of $25 \times 10^{-4}\,cm^2$ ($500 \times 500\,\mu m^2$) and $12.5 \times 10^{-4}\,cm^2$ ($146 \times 854\,\mu m^2$); N-doped polycrystalline silicon is used for the gate electrode. The second set was n-type Si (1 1 0) substrate with contacts areas of $9 \times 10^{-4}\,cm^2$ ($300 \times 300\,\mu m^2$) and $1 \times 10^{-4}\,cm^2$ ($10 \times 10\,\mu m^2$). The gate electrode is in aluminum. The oxides layers were processed by thermal oxidation and measured as 636 Å for the first set and 100 Å for the second one by spectroscopic ellipsometry. Capacitance versus voltage measurements were made using a gain phase analyzer HP4194A (Hewlett-Packard) with source and measurement capabilities of ± 40 V and 10^{-1} F–10^{-14} F, respectively. The measuring system can provide a capacitance precision of about 10^{-16} F and an ac modulation frequency from 100 Hz to 40 MHz. For all MOS devices, the contact voltage V_g was applied at the contact area in step of 0.05 V and capacitance measurements were taken at each voltage step. V_g ranged from -4 to 2 V in order to determine the oxide capacitance. The measurement frequency varies from 1 to 30 MHz. For each frequency a corrective factor is estimated and a non linear optimization is used to fit the experimental and theoretical band bending versus bias voltage curve, so the oxide thickness is determined (Fig. 2a and b). Then, a comparison is made between the experimental and ellipsometric values in order to determine the adequate frequency of measurement.

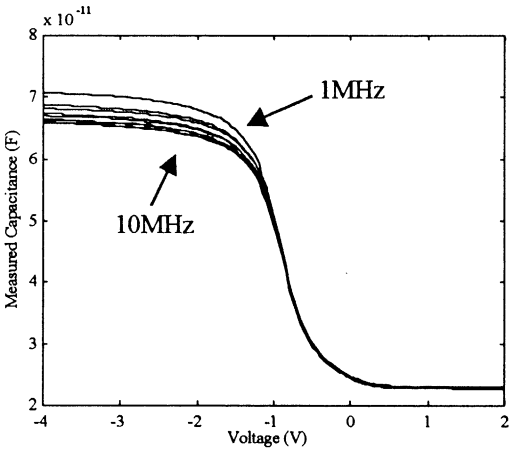

Fig. 1. Capacitance versus voltage curves from 1 MHz to 10 MHz with 1 MHz step; non-superposition in accumulation field; $A = 12.5 \times 10^{-4}\,cm^2$.

3. Results and discussions

The $C-V$ spectroscopies measured at each frequency have been studied and the adequate ac frequency has been determined (Fig. 3). We note that the frequency measurement giving the good value of the oxide thickness seems to follow the same law: for the

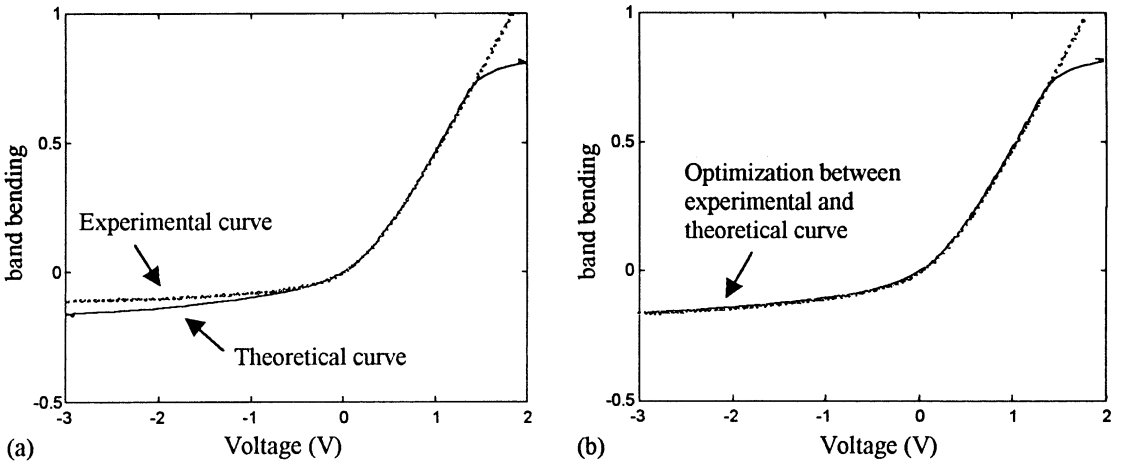

Fig. 2. Optimisation between experimental and theoretical band bending versus bias voltage curve in order to determine the oxide thickness of the MOS structure.

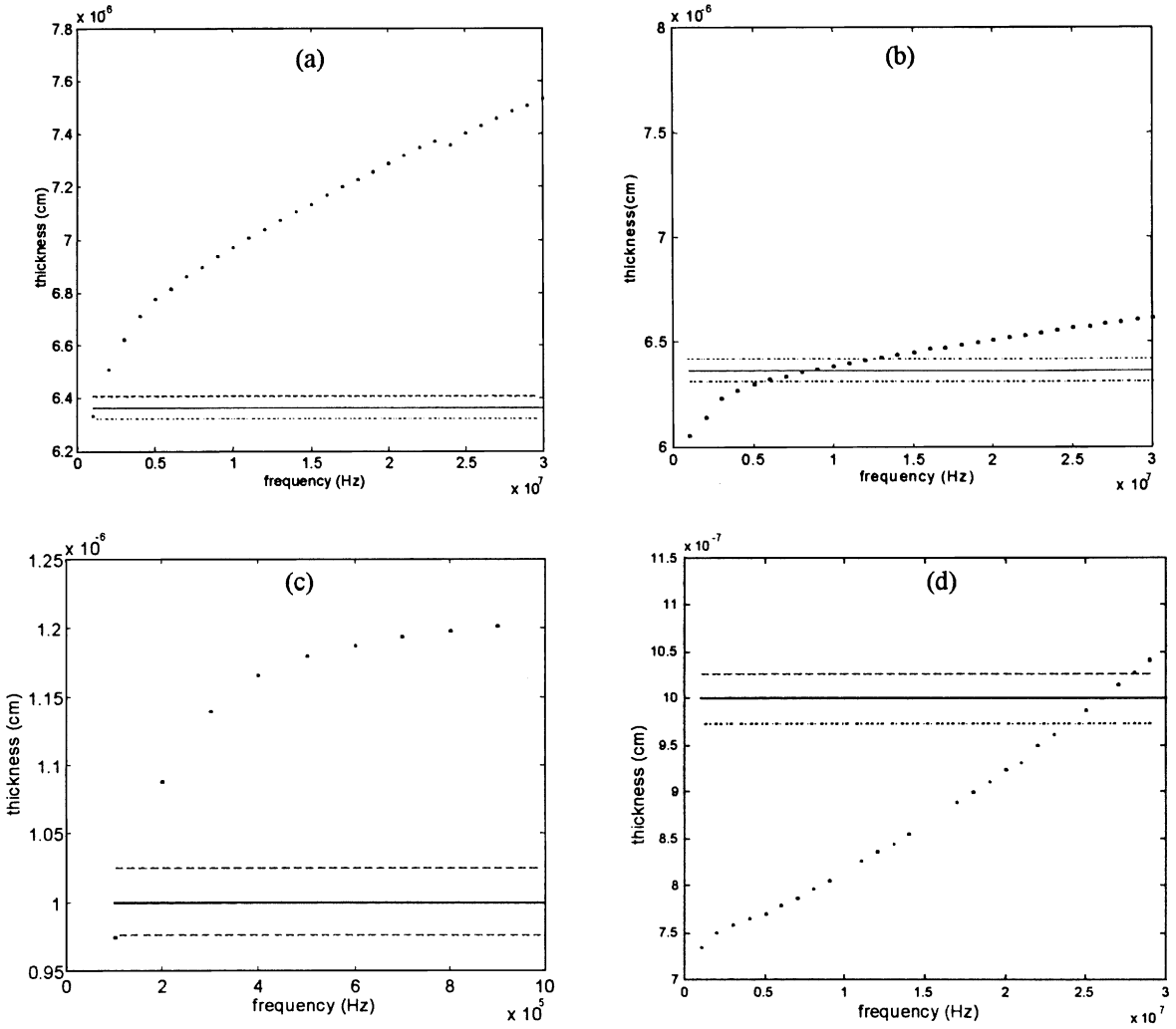

Fig. 3. Experimental values of oxide thickness as a function of frequency for the p-type sample, (a) $A = 25 \times 10^{-4}\,\mathrm{cm}^2$ and (b) $A = 12.5 \times 10^{-4}\,\mathrm{cm}^2$; and for n-type sample, (c) $A = 9 \times 10^{-4}\,\mathrm{cm}^2$ and (d) $A = 1 \times 10^{-4}\,\mathrm{cm}^2$; (- - -) uncertainty on the thickness measured by ellipsometry, (——) ellipsometric value, (· · · ·) experimental measurement.

structures of small surface the frequency measurement is higher than for larger surface. Indeed, for our large surface p-type structures the frequencies of measurements giving the good value of oxide thickness is of 1 MHz whereas it is of 9 MHz for the small surface. By the same way, for our n-type structure the adequate measurement frequency are 1 and 25 MHz. In each case the exact D_{ox} value has been approached within less than 1%. One possible interpretation for the variation of oxide thickness with frequency is that there is only one proper ac frequency for each sample, and this frequency is function of the sample contact area. As it can be seen (Fig. 1) the measured capacitance depends strongly on the applied ac modulation frequency, this can be attributed to interface states in the sample. With increasing ac frequency, the interface states had less time to follow the ac field and contribute to the measured capacitance. For large surfaces the interface states does not influence determination of the oxide thickness from 1 MHz whereas for small surfaces it is necessary to go up higher in frequency to remove their effect.

4. Conclusion

For our small-area samples, the fact of using frequencies higher than 1 MHz enables us to obtain better results for the determination of oxide thickness. This is explained simply by the fact, that the smaller the surface of our sample is, the influence of the impurities present is large. The fact of going up high in frequency is

a means of removing their effect. It then enables us to carry out a good approximation of the real value of the oxide capacitance and thus of oxide thickness which depends directly on it. We suggest that a proper high ac frequency should be selected to study electrical properties of MOS structures using the $C-V$ method so that the influence of interface states can be limited.

References

[1] Sarrabayrouse G, Campabadal F, Prom JL. Private Communication, 1990.

[2] Ricco B, Olivo P, Nguyen TN, Kuan T-S, Ferriani G. IEEE Trans Electron Dev 1988;35(4).

[3] Mcnutt MJ, Sah CT. J Appl Phys 1975;46(9):3909.

Step-Like Heterostructure Barrier Varactor

Reynald Havart, Eric Lheurette, Olivier Vanbésien, Patrick Mounaix, Francis Mollot, and Didier Lippens

***Abstract*—Conduction mechanisms in step-like heterostructure barrier varactor (HBV) have been investigated by means of measurements of current– and capacitance–voltage (C–V) characteristics. For this purpose, $In_{0.53}Ga_{0.47}As/In_{0.52}Al_{0.48}As$/AlAs single barrier varactors have been fabricated and characterized from room temperature up to ~400 K. The devices exhibit state-of-the art results with a breakdown voltage (V_b) of ~6 V for a leakage current of 10 A/cm^2, a C–V ratio of 5 : 1 and a 0 V capacitance of 2 fF/μm^2. By solving the Poisson equation in the Thomas–Fermi approach and the Schrödinger equation, it is shown that the leakage current mechanisms are dominated by a resonant tunneling contribution below the voltage threshold. Subsequently, the results are interpreted in terms of an apparent barrier height equal to 600 meV near equilibrium. Above threshold, we attribute the drastic increase in the current–voltage relationship to impact ionization.**

***Index Terms*— Frequency conversion, heterojunctions, millimeter-wave diode, varactors.**

I. Introduction

VARACTOR multipliers are currently used in local oscillator chains to generate power up to submillimeter wave frequencies [1]. The device uses a nonlinear capacitance to up-convert power at a frequency f_p to power at $n \cdot f_p$. Up to now, the most common type of varactor was the Schottky diode which was biased under reverse conditions [2]–[3]. Recently, new classes of devices have been proposed with symmetrical capacitance–voltage (C–V) characteristics notably heterostructure barrier varactors (HBV's). HBV's, first proposed by Kollberg and Rydberg [4], consists of a wide band gap semiconductor sandwiched between two n-type narrow band gap cladding layers. The potential barrier thus formed in the conduction band should prevent the conduction through the structure and each cladding layer can be depleted according to the bias conditions. Over the past, such devices have been successfully fabricated and RF tested [5]–[11] with promising results in terms of functionality. Indeed, their symmetrical nonlinear C–V relationships make them attractive for tripler and quintupler applications. Up to now however, one of the key limitation of these devices comes from their relatively high leakage current. This is particularly true for GaAs-based devices whose voltage handling is poor with respect to the criterion of a voltage capability limited by impact ionization. Therefore, the breakdown voltage is typically less than two volts for this kind of devices whereas typical avalanche value is about ten Volts. Integration of several devices in series could basically overcome such a drawback but a dramatic degradation of performance with temperature limits the impact of such a solution. This is the purpose of this paper to investigate how the performance of the devices can be improved in terms of voltage handling by investigating the origin of leakage currents, their temperature dependence and the avalanche conditions. To this aim, we fabricated HBV's on InP substrate with special attention on the design of the blocking and cladding layers. The devices are fabricated in a step-like barrier configuration and exhibit state-of-the art results in terms of capacitance nonlinearity, leakage current level, and voltage capability. In order to get an insight into the conduction mechanisms responsible for these good performances, we have calculated theoretically the current–voltage (I–V) and C–V relationships by solving the Poisson equation in the Thomas–Fermi approach along with the Schrödinger equation. For the first time, these calculations permit us to show that the conduction mechanisms in this kind of heterostructures involve a resonant tunneling effect and hence a preferential tunneling energy. On this basis, we studied in details the temperature dependence of conduction characteristics with an estimate of the activation energy for resonant tunneling emission. Section II deals with the device fabrication along with the measurements performed at room temperature. In Section III, we report on I–V and C–V calculations. The experimental data as a function of temperature are reported in Section IV, whereas Section V concerns the impact ionization breakdown. Finally, Section VI gives a general discussion about the voltage handling issue and the impact in terms of device performance.

II. Device Fabrication and Characterization

In order to prevent any significant leakage current over (thermionic emission) and through (tunneling) the barrier, we made use of pseudomorphic AlAs/$Ga_{47}In_{0.53}As$ epilayers. Such a strained material system was previously used for fabricating high breakdown voltage HBV's [13] and more recently high current resonant tunneling diodes [14]. The key advantage afforded by this material system is mainly the very high conduction band offset between AlAs and $Ga_{47}In_{0.53}As$ of ~1.2 eV at Γ conduction band minima. However the use of thick AlAs layers is unfavorable due to the high lattice mismatch between AlAs and $Ga_{0.47}In_{0.53}As$ and the occurrence of conduction mechanisms through the X valley. Therefore, we preferred to insert an AlAs layer with a moderate thickness (3 nm) between two 5-nm thick $In_{0.48}Al_{0.52}As$ layers. The barrier is sandwiched between

Manuscript received March 11, 1998; revised June 29, 1998. This work was supported by ESA under Contract 9777/92/NL/PB. The review of this paper was arranged by Editor W. Weber.

The authors are with the Institut d'Electronique et de Microélectronique du Nord, U.M.R. C.N.R.S. 9929, Université des Sciences et Technologies de Lille, 59652 Villeneuve d'Ascq, France.

Publisher Item Identifier S 0018-9383(98)07834-4.

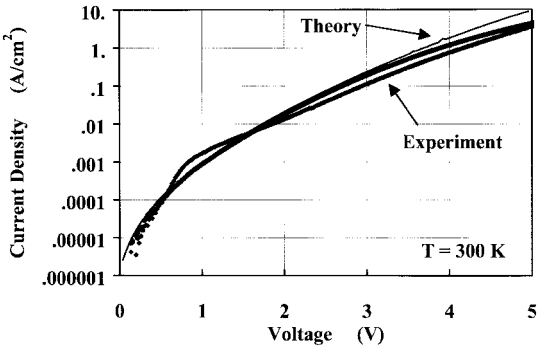

Fig. 1. Comparison between the measured (forward and reverse bias conditions) and calculated I–V characteristics at room temperature.

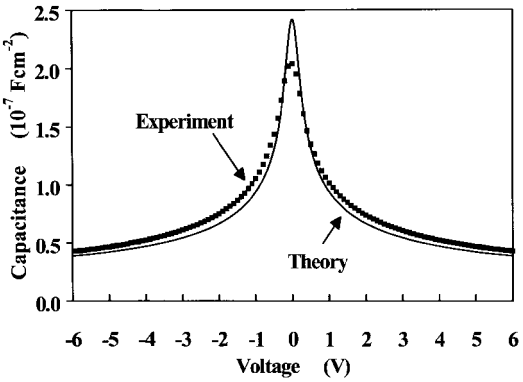

Fig. 2. Comparison between experiment and modeling concerning the C–V relationship under forward and reverse bias conditions at 300 K.

$In_{0.53}Ga_{0.47}As$ 5-nm-thick spacer layers nominally undoped followed by 300-nm-thick cladding layers with a doping concentration of 1×10^{17} cm^{-3} and 500 nm-thick $In_{0.53}Ga_{0.47}As$ contact layers doped to 5×10^{18} cm^{-3}. Starting from a semi-insulating Fe-doped InP substrate, all epilayers were grown in a gas source molecular beam epitaxy (MPE) RIBER machine. Alloy composition and growth rates were deduced from RHEED intensity oscillation measurements on InP (on InP) and of GaAs and AlAs (on GaAs). Silicon doping levels were estimated from Hall measurements of calibration structures. The growth was conducted without interruption at $\sim$ 520 °C for both binary and ternary compounds.

The test structure consists of a mesa-type diode with top and side ohmic contacts in circular pattern configuration with various contact diameters. The samples were fabricated using three photolithography masks. $H_3PO_4/H_20_2/H_2O$ solution was used for mesa etching and sequential Ni/Ge/Au/Ti/Au metallizations were used for the ohmic contacts.

Fig. 1 shows the current density versus bias voltage measured at 300 K, plotted in solid triangles for both bias conditions. Excellent symmetry can be noted between the two bias directions. This high degree of symmetry is quite remarkable and attests to the high quality of epilayers notably to the good morphology of direct and inverse heterointerfaces. It can be seen that the leakage current is as low as 1 A/cm^2 at a bias voltage of 4 V while showing an increase of six orders of magnitude over the bias range considered.

Fig. 2 shows the C–V characteristic (solid square symbols) measured at a frequency of 10 MHz. At zero bias, the normalized capacitance is $\sim 2 \times 10^{-7}$ F/cm^2 and rapidly decreases with a saturation value of about 0.4×10^{-7} F/cm^2 at 6 V. Under these conditions, the capacitance ratio is 5 : 1. Also the symmetry in the C–V variation between the two bias directions is excellent. However, it is worth mentioning that obtaining such a symmetry is less critical to obtain than that of current–voltage (I–V) curves in the sense that the tunneling current is very sensitive to the quality of barrier interface while the capacitance depends mainly of the doping uniformity in the cladding layers. These experimental results in terms of leakage current, capacitance ratio and voltage breakdown compare favorably to the best results published in the literature [6]–[13]. Also plotted in Fig. 1 are the data we calculated theoretically which are explained below.

III. Current– and Capacitance–Voltage Calculations

For the theoretical evaluation of conduction current flowing through the structure, the first stage consists in calculating accurately the conduction band edge across the whole structure. This can be performed by solving self-consistently the Poisson's equation (space charge effect) and the Fermi–Dirac distribution function (carrier density) in the Thomas–Fermi screening approach [15].

In a second stage, starting from the potential profile, it is possible to solve a discretized form of the time-independent Schrödinger equation. Such a procedure permits us to calculate the variation of the envelope wavefunctions versus distance for each value of energy which can be occupied by electrons. From the wave function, the quantum transmission probability can be easily computed along with the resonant energy. Then the current–voltage (I–V) characteristics are directly deduced by integrating over energy the transmission probability times the so-called supply function as it is performed for resonant tunneling diodes [16] and superlattices [17]. It is worth mentioning that the numerical procedure performed here does not require to distinguish between a thermionic emission effect described by a Richardson law and the tunneling contribution often calculated in the WKB approximation [18]. Such a global treatment with accurate calculation of quantum transmission probability is essential for describing the resonant tunnelling effect addressed in the following.

The I–V characteristic calculated by means of this procedure is displayed in solid line in Fig. 1. The agreement with experiment is surprisingly good with a closely fit to the experimental variations. For these calculations carried out at 300 K we used an effective mass of $0.042m_0$ for InGaAs and $0.083m_0$ for AlInAs. Caution is advised to this excellent fit because there is some uncertainty in the material parameters notably in the correct tunneling mass in strained layers. Moreover, there exists a dispersion within 35% for bare HBV's on the whole wafer in the I–V values. More importantly, the trends and magnitudes are well depicted and on this basis, it is believed that the conduction mechanisms are relatively pure. In other words the calculation permits the correct determination of the quantum transmission *through* and *over* the barrier, without involving defect-assisted contributions.

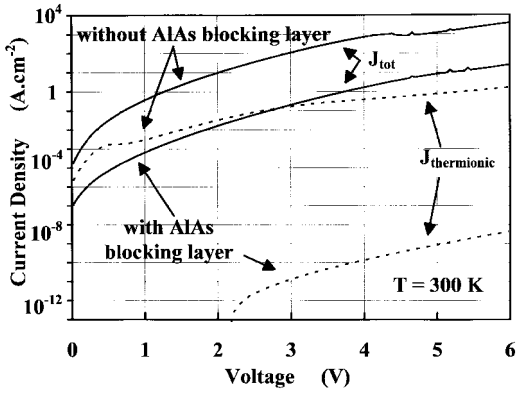

Fig. 3. Calculated current contributions as a function of bias voltage with and without an AlAs blocking layer. Note that the tunneling current through the barrier dominates the leakage current.

Let us consider now to the C–V characteristic displayed by the solid line in Fig. 2. The capacitance is defined as $C = q \cdot \partial n_s / \partial V$ where n_s is the sheet carrier density in the accumulation layer. This procedure is quite similar to that used in [19] except the fact that we used the accumulation layer instead of the depletion layer. The agreement is good excepting at zero bias-voltage where the experimental values are lower. Such a slight discrepancy is a direct consequence of the semi-classical Thomas–Fermi assumption. Indeed, in this case the carrier density peaks at the heterointerface lowering by this means the screening length. In contrast, assuming a quantum distribution permits to push slightly away electron density maxima due to the repelling effect of potential barrier as clearly demonstrated in a full quantum approach notably by using the Wigner distribution function [20] for resonant tunnelling diodes. As a consequence, the capacitance at equilibrium is lower.

In Fig. 3, we illustrate the huge improvement resulting from the insertion of an AlAs blocking layer on the leakage current flowing through the heterostructure. The solid lines show the variations versus voltage of the overall conduction current including both the thermionic and the tunneling contributions. Their relative importance is also investigated with the thermionic contribution plotted in dotted lines. For both cases the tunneling current is the dominant component. Also important is the fact that the use of an AlAs barrier gives rise to a drastic increase in the voltage for which the leakage current becomes significant. The increase in the voltage handling is practically improved by a factor of 3. From the engineering point of view and with respect to previous achievements, it is worth noting that such findings have a direct impact on device performance. It is now well known that GaAs/AlGaAs devices with thick barriers face the problem of cross-over of Γ and X valleys. As a consequence the apparent barrier height is strongly reduced and the voltage capability is poor. Moreover, if the leakage current is dominated by a thermionic emission the unavoidable increase in operating temperature leads to a drastic degradation of conduction blocking properties. With respect to the InGaAs/InAlAs scheme, which is compared in Fig. 3 to the step-like scheme, one can conclude that the insertion of an AlAs thin layer avoids the leakage current through Fowler–Nordheim tunneling emission. Hence in any case, this kind of structure exhibits excellent performance provided that the epitaxial layer is of high quality to avoid any spurious defect-assisted tunnelling current.

In order to have further insight into the origin of such an improvement, let us consider Fig. 4 which shows the potential profile (a) along with the current increment (dJ) and the quantum transmission probability as a function of energy (b). It can be seen that the current distribution is very narrow over energy with a maximum at about 600 meV with respect to the conduction band edge in the emitter region close to the barrier. Such a behavior is characteristic of a resonant tunneling process. This conclusion is supported by plotting the quantum transmission probability also shown in Fig. 4(b), which exhibits as expected a maximum. Moreover, the variations of the envelope wavefunction versus distance show an accumulation in the probability density on the emitter side of the barrier, between the InGaAs/InAlAs and the InAlAs/AlAs heterointerfaces, characteristic of quantum-size effects. Therefore, the role played by the relatively thin strained AlAs barrier is to prevent thermionic emission but also to reject the tunneling contributions at higher energies. On the other hand, by using such a barrier scheme we alleviate the problem related to the triangular shape of the barrier under bias resulting in a Fowler–Nordheim tunneling emission.

In the next section, we are trying to estimate experimentally the relevant energy involved in the tunneling processes. For that purpose, we measured the activation energy in a thermally-assisted conduction process by parametric measurements of I–V characteristics as a function of temperature. Moreover these studies give some practical informations about the degradation of voltage capability at increasing temperature.

IV. Measurements as a Function of Temperature

Fig. 5 shows the current density versus bias voltage taking the temperature θ as a parameter between 343 and 415 K. As expected, the current density increases with temperature as a consequence of the increase of the tail of the carrier distribution function in the emitter region. Analysis of these data gives the plot of the activation energy (E_{rt}) versus voltage reported in Fig. 6. The voltage dependence of E_{rt} are deduced from the variation of the ratio between current density and temperature as a function of $1/\theta$ as it was done for resonant tunneling double barrier structures [21] (typical variations are given in inset for an applied voltage of 2 V). Such an activation energy is equivalent to an apparent tunneling barrier height which is well defined owing to the resonant tunneling process. In Fig. 6, we also plotted the theoretical variations of E_{rt} versus voltage. For this calculation, we computed for each bias the conduction band profile then the eigenstate within the accumulation layer in front the barrier and lastly the preferential energy involved in the resonant tunneling process. The agreement between experiment and modeling is relatively good. At equilibrium the equivalent barrier height which prevents the conduction

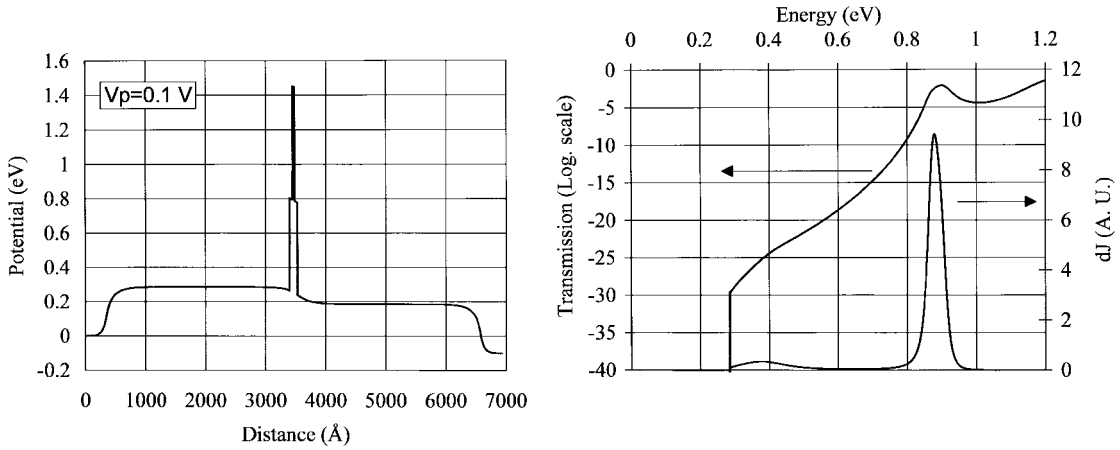

(a) (b)

Fig. 4. Illustration of a resonant tunneling effect through the AlAs 3 nm-thick. Potential profile (a) quantum transmission probabilities in logarithmic scale and current increment dJ in arbitrary unit (b).

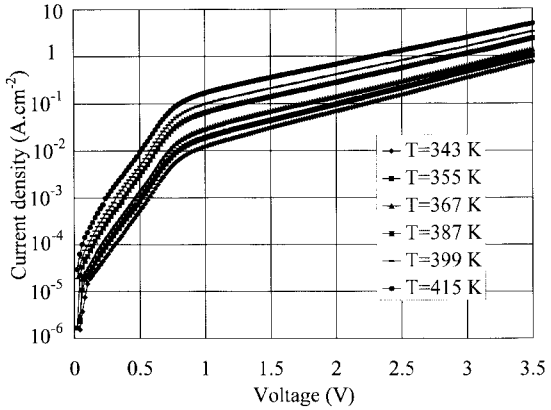

Fig. 5. Current density as a function of bias voltage with temperature as a parameter.

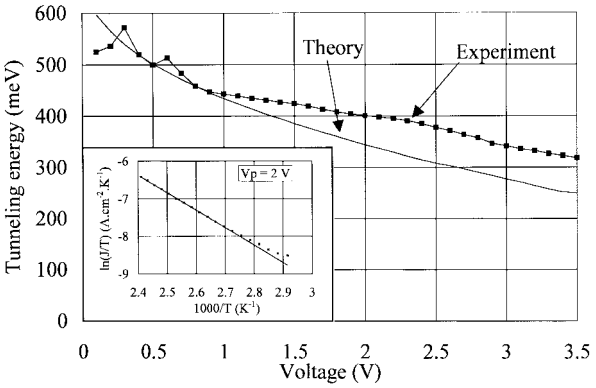

Fig. 6. Comparison between the measured and calculated values of an effective barrier height. The experimental values correspond to the activation energy in an exponential conduction process as a function of $1/\theta$ for a temperature (θ) variation between 330 and 400 K. The calculated values corresponds to the resonant energy in the tunneling probability.

through the barrier is of about 600 meV. At increasing voltage, this figure of merit is decreasing with a value of 300 meV at 3.5 V. At this stage, an ambiguity still subsists about the conduction mechanisms responsible for conduction close to the breakdown voltage. In Kollberg's original paper avalanche breakdown was evoked as a possible limiting factor. By using InP-based material system such as InGaAs layers and hence with narrow gaps we are facing the problem of the onset of avalanche mechanism at moderate voltages. We discuss of such a possibility hereafter.

V. Breakdown Voltage Calculations

First of all, let us mention the assumptions and also the uncertainties which concern the determination of the avalanche breakdown voltage in the present submicron structure. We based the analysis on the computation of the avalanche condition which describes the fact that the multiplication factor resulting from impact ionization becomes infinite. We assumed that impact ionization can only occur within the depleted InGaAs region. In this region, the electric field is high at the heterointerface and at the n/n$^+$ interface. For the latter however its contribution to the ioniazion integral is found negligible. Close to the heterointerface one can expect a ballistic transport following the resonant tunneling injection through the barrier. Under this condition the charge carrier transport is nonstationary and ideally the impact ionization mechanisms should be treated at the microscopic level. For sake of simplicity we have however assumed that the variations of ionization coefficients versus electric field measured by Pearsall [22] with p-n homojunctions were valid for the present n-type heterojunction.

Fig. 7 shows the variations of ionization integral as a function of distance for three values of applied voltage 5.5, 6, and 6.2 V, respectively. Also displayed is the variation of the electric field versus distance at $V = 6.2$ V. It can be seen that the electric field at the heterointerface between the InAlAs and InGaAs materials exceeds 350 kV/cm while the diffusion peak resulting from doping gradient reaches 200 kV/cm. With a doping concentration of 1×10^{17} cm^{-3}, assessed on the other hand by conventional C–V measurements, the

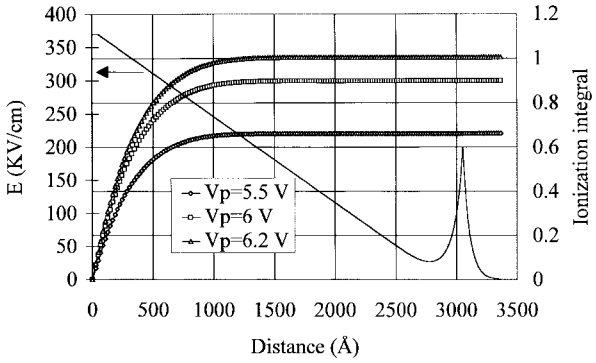

Fig. 7. Illustration of the breakdown voltage mechanisms which take place in the InGaAs cladding layers. The solid line shows the electric field profile whereas the dotted lines gives the variation of the ionization integral versus distance.

depleted zone extends to ∼300 nm which corresponds to the thickness of InGaAs epilayers. The avalanche condition is satisfied, i.e. the ionization integral goes to one, for a bias voltage of about 6.2 V in good agreement with the experimental values. Confidence in the predicted value can also be found by using the work of Sze and Gibbons [23] which permits one to calculate analytically an estimate of the breakdown voltage for abrupt p-n junctions [(5a) in this reference]. We calculated 6.3 V which is quite comparable to the experimental voltage. Therefore, despite the crude assumptions, it is believed that impact ionization is the limiting process for bias voltage close to 6 V. This means that it could be useless to further increase the barrier thickness in order to increase the voltage handling keeping constant the cladding layer parameters. These parameters appear quite optimum for the structure under test since we are under punchthrough condition at the breakdown voltage as seen before. In addition, the doping concentration satisfies the trade-off between the achievement of a low series resistance and of a low capacitance value at saturation.

VI. Discussion

From the above results several guidelines can be proposed for further increase the diode performance in terms of power and frequency capabilities with the goal of a terahertz operation. First of all concerning the voltage handling, we learned that a very low leakage current density let us say $J < 10$ A/cm^2 can be achieved up to 6 V. For a higher bias voltage impact ionization occurs in the narrow gap cladding layer with an injection current supplied by the resonant tunneling process through the strained layer. For further increase in this threshold the doping concentration should be decreased but to the detriment of other limiting mechanisms such as current saturation [24]. On the other hand, one can think to increase the voltage handling of the device by stacking several devices. [25]–[27]. In that case, the overall voltage across the device is increased by a factor n where n is the number of stacked single barrier devices whereas the total capacitance is divided by n. However, it is worth noting that the voltage capability of the basic device is of prime importance. Therefore, if a single structure exhibits poor performance in terms of leakage current, with dramatic degradation at increasing temperature, the impact of such series integration is limited. In fact, it is expected an increase in the junction temperature under large signal degrading drastically the efficiency. When the heterostructure barrier is high enough, the voltage handling is preserved over broad temperature range alleviating this degradation. This opens the way of large power application. With respect to this issue, we succeeded recently to stack two diodes in series with an overall voltage of 12 V which thus scales with epilayer complexity. On the other hand one can find in the literature very encouraging results with ten barriers in series with a total voltage of 22 V [25].

The RF assessment of the devices fabricated in the present work will be reported elsewhere [28]. Nevertheless, some relevant issues can be discussed on the basis of an InP-based technology. The capacitance ratio has a direct consequence on the cutoff frequency related to the elastance $(S = 1/C)$ at equilibrium and at saturation. For the former, the value depends mainly on the screening lengths on each side of the barrier. A first estimate of screening lengths can be obtained in the parallel plate capacitance approximation $C = \varepsilon/L$ where L is the equivalent dielectric thickness. At equilibrium and assuming $L = L_b + 2 \cdot L_s$ (L_b is the barrier thickness equal to 13 nm and L_s the screening length) we thus obtain $L_s \sim 20$ nm. On the other hand, the capacitance at saturation is obtained under punch-through condition ($Cs \sim \varepsilon/L_d$ with $L_d \sim 275$ nm). We are currently investigating various tracks for further improving the capacitance ratio via an increase of the zero bias capacitance [29]. One of the improvement directions is to make use of delta doping layer in order to confine the electric field close to the barrier while maintaining a capacitance modulation. However, it can be demonstrated that the development of such an idea leads to lower the effective barrier height. On the other hand, InAs quantum wells can be grown on each side of the barrier with confinement effects which appears favorable for the electric field localization.

VII. Conclusion

In summary, high voltage InGaAs/InAlAs/AlAs heterostructure barrier varactors have been successfully fabricated. The limiting leakage current mechanisms have been carefully investigated on the basis 1) of the computation of resonant tunneling current through the strained AlAs layer, 2) the derivation of an equivalent resonant tunneling energy which can be compared to an activation energy in a thermally assisted tunneling process, 3) the calculation of impact ionization integral. Moreover, C–V relationships were predicted and compared to experiment showing the importance of the screening length near equilibrium. The devices exhibit high performances in terms of voltage threshold with breakdown voltages as high as 6 V. The lowest capacitance level is 2 fF/μm^2 at zero-bias with a capacitance ratio of ∼5:1.

ACKNOWLEDGMENT

The authors would like to thank E. Delos and D. Vandermoere for technical assistance.

REFERENCES

[1] A. V. Räisänen, "Frequency multipliers for millimeter and submillimeter wavelengths" *Proc. IEEE*, vol. 80, pp. 1842–2852, Nov. 1992, and references therein.
[2] T. W. Crowe, T. C. Grein, R. Zimmermann, and P. Zimmermann, " Progress toward solid state local oscillators at 1 THz," *IEEE Microwave Guided Wave Lett.*, vol. 6, pp. 206–208, May 1996.
[3] K. Hong, P. F. Marsh, G. I. Ng, D. Pavlidis, and C. H. Hong, "Optimization of MOVPE grown $In_xAl_{1-x}As/In_{0.53}Ga_{0.47}As$ planar heteroepitaxial Schottky diodes for terahertz applications," *IEEE Trans. Electron Devices*, vol. 41, pp. 1489–1497, Sept. 1994.
[4] E. L. Kollberg and A. Rydberg, "Quantum barrier varactor diode for high efficiency millimeter-wave multipliers," *Electron. Lett.*, vol. 25, pp. 1696–1698, Dec. 1989.
[5] A. Rydberg, H. Grönqvist, and E. Kollberg, "Millimeter- and submillimeter-wave multipliers using quantum-barrier-varactor (QBV) diodes," *IEEE Electron Device Lett.*, vol. 11, pp. 373–375, Sept. 1990.
[6] S. M. Nilsen, H. Grönqvist, H. Hjelmgren, A. Rydberg, and E. L. Kollberg, "Single barrier varactors for submillimeter wave power generation," *IEEE Trans. Microwave Theory Tech.*, vol. 41, pp. 572–580, Apr. 1993.
[7] D. Choudhury, M. A. Frerking, and P. D. Batelaan, "A 200 GHz tripler using a single barrier varactor," *IEEE Trans. Microwave Theory Tech.*, vol. 41, pp. 595–599, Apr. 1993.
[8] K. Krisnamurthi, S. M. Nilsen, and R. G. Harrison, "GaAs single barrier varactors for millimeter waves triplers: Guidelines for enhanced performance," *IEEE Trans. Microwave Theory Tech.*, vol. 42, pp. 2512–2516, 1994.
[9] A. Rahal, E. Boch, J. Ovey, and R. G. Bosisio, " Planar multistack quantum barrier varactor tripler evaluation at W-band," *Electron. Lett.*, vol. 31, pp. 2022–2023, Nov. 1995.
[10] A. V. Raïsänen, T. J. Tolmunen, M. Natzic, M. Frerking, E. Brown, H. Grönqvist, and S. M. Nilsen, "A single barrier varactor quintupler," *IEEE Trans. Microwave Theory Tech.*, vol. 43, pp. 685–688, Mar. 1995.
[11] J. R. Jones, W. L. Bishop, S. H. Jones, and G. B. Tait, "Planar multibarrier 80/240-GHz heterostructure barrier varactor triplers," *IEEE Trans. Microwave Theory Tech.*, vol. 45, pp. 512–518, Apr. 1997.
[12] L. Dillner, J. Stake, and E. Kollberg, "Modeling of the heterostructure barrier varactor diode," in *Proc. 1997 Int. Semiconductor Device Res. Symp.*, Dec. 10–13.
[13] V. K. Reddy and D. P. Neikirk, "High breakdown voltage AlAs/InGaAs quantum barrier varactor diodes," *Electron. Lett.*, vol. 29, pp. 464–466, Mar. 1993.
[14] P. Mounaix, E. Lheurette, F. Mollot, and D. Lippens, "Frequency capability of strained AlAs/InGaAs resonant tunneling diodes," *Electron. Lett.*, vol. 31, pp. 1508–1510, Aug. 1995.
[15] L. Burgnies, O. Vanbésien, V. Sadaune, D. Lippens, J. Nagle, and B. Vinter, "Resonant tunneling structures with local potential perturbations," *J. Appl. Phys.*, vol. 75, pp. 4527–4531, May 1994.
[16] P. Mounaix, O. Vanbésien, and D. Lippens, "Effect of cathode spacer layer on the current-voltage characteristics of resonant tunneling diodes," *Appl. Phys. Lett.*, vol. 57, pp. 1517–1519, Oct. 1990.
[17] O. Vanbésien, H. Leroux, and D. Lippens, "Maximally flat transmission window in finite superlattices," *Solid State Electron.*, vol. 45, pp. 665–669, 1992.
[18] J. R. Jones, G. B. Tait, S. H. Jones, and D. S. Katzer, "DC and large-signal time dependent electron transport in heterostructures devices: Investigation of heterostructure barrier varactor," *IEEE Trans. Electron Devices*, vol. 42, pp. 1070–1080, June 1995.
[19] J. P. Sun, R. K. Mains, W. L. Chen, J. R. East, and G. I. Haddad, "C-V and I-V characteristics of quantum well varactors," *J. Appl. Phys.*, vol. 72, pp. 2340–2346, Sept. 1992.
[20] W. R. Frensley, "Boundary conditions for open quantum systems driven far from equilibrium," *Rev. Mod. Phys.*, vol. 62, pp. 745–792, July 1990.
[21] O. H. Hughes, M. Henini, E. S. Alves, L. Eaves, M. L. Leadbetter, T. J. Foster, F. W. Sheard, G. A. Toombs, A. Celeste, and J. C. Portal, "Investigations of double barrier resonant tunneling devices based on AlGaAs/GaAs," *J. Vac. Sci. Technol. B*, pp. 1161–1164, July/Aug. 1988.
[22] T. P. Pearsall, "Impact ionization rates for electron and holes in $Ga_{0.47}In_{0.53}As$," *Appl. Phys. Lett.*, vol. 36, pp. 218–220, Feb. 1980.
[23] S. M. Sze and G. Gibbons, "Avalanche breakdown voltages of abrupt and linearly graded *p-n* junctions in Ge, Si, GaAs, and GaP," *Appl. Phys. Lett.*, vol. 8, pp. 111–113, Mar. 1966.
[24] E. Kollberg, T. J. Tolmunen, M. A. Frerking, and J. R. East, "Current saturation in submillimeter wave varactors," *IEEE Trans. Microwave Theory Tech.*, vol. 40, pp. 831–838, May 1992.
[25] A. Rahal, R. G. Bosisio, C. Rogers, J. Ovey, M. Sawan, and M. Missous, "A W-band medium power multi-stack quantum barrier varactor frequency tripler," *IEEE Microwave Guided Wave Lett.*, vol. 5, pp. 368–370, Nov. 1995.
[26] E. Lheurette, P. Mounaix, P. Salzenstein, F. Mollot, and D. Lippens, "High performance InP-based heterostructure barrier varactor in single and stack configuration," *Electron. Lett.*, vol. 32, pp. 1417–1418, July 1996.
[27] K. Krisnamurthi and R. G. Harrison, "Millimeter-wave frequency tripling using stacked heterostructure-barrier varactors on InP," *IEE Proc. Microw. Antennas Propag.*, vol. 143, pp. 272–276, Aug. 1996.
[28] X. Mélique, J. Carbonell, R. Havart, P. Mounaix, O. Vanbésien, and D. Lippens, "InGaAs/InAlAs/AlAs heterostructure barrier varactors for harmonic multiplication," *IEEE Microwave Guided Wave Lett.*, vol. 8, pp. 254–256.
[29] E. Lheurette, X. Mélique, P. Mounaix, F. Mollot, O. Vanbésien, and D. Lippens, "Capacitance engineering for InP-based heterostructure barrier varactor,"*IEEE Electron Device Lett.*, vol. 19, pp. 338–340, Sept. 1998

Reynald Havart was born in France in 1970. He received the M.S. degree in physics from the University of Lille, France, in 1993, where he is currently pursuing the Ph.D. degree.

He works on the physics of millimeter and submillimeter wave frequency multipliers with heterostructure barrier varactors at the Institut d'Electronique et de Microelectronique du Nord (I.E.M.N.), Villeneuve d'Ascq, France.

Eric Lheurette was born in Béthune, France, on March 12, 1968. He received the M.S. degree in 1991 and the Ph.D. degree in 1996 from the Université des Sciences et Technologies de Lille, France.

He is now working in the Quantum and Terahertz Device group at the Institut d'Electronique et de Microélectronique du Nord. His current work involves the development of millimeter and submillimeter wave frequency multiplier arrays. He is also a teacher at the Université des Sciences et Technologies de Lille.

Olivier Vanbésien was born in Armentières, France, on November 11, 1964. He received the Engineer degree in 1987 from the Institut Supérieur d'Etelectronique du Nord (ISEN), Lille, France, and the third cycle thesis (Ph.D.) on quantum devices in 1991 from the University of Lille.

He then joined the High Frequency Department of the Institut d'Electronique et de Micro-électronique du Nord (I.E.M.N.) as a Charge de Recherches C.N.R.S. in the quantum device group. His current interests concern the simulation and the characterization of intraband and interband resonant tunneling diodes as well as quantum waveguide based structures and their optimization for operation at millimeter and submillimeter wavelengths. Recently, he started working on photonic crystals for application in the terahertz frequency range.

Patrick Mounaix received the degree of engineer of Material Science in 1988 from the Ecole Universitaire D'Ingénieur de Lille (EUDIL), France, and the third cycle thesis (Ph.D.) on quantum devices in dipole and tripole configuration in 1992 from the University of Lille.

He then joined the High Frequency Department of the Institut d'Electronique et de Micro-électronique du Nord (I.E.M.N.), as a Charge de Recherches C.N.R.S. in the quantum device group. He is currently interested in various projects such as simulation adn characterization of quantum devices, development of low parasitic technology for millimeter and submillimeter wave components and microtechnology and microsystem on III–V materials.

Francis Mollot was born in Courbevoie, France, on November 1, 1946. He received the Engineer degree from INSA-Toulouse, France. He joined the Groupe de Physique des Solides of ENS, Paris, and received the Docteur es Sciences degree from Université Paris 7 for his work on the metastable optical properties of amorphous chalcogenide semiconductors in 1979.

He participated to the creation of L2M-CNRS Bagneux Laboratory in 1984, where he began an activity in molecular beam epitaxy and physics of III–V semiconductor heterostructures and GaAs–AlAs superlattices. In 1990, he was with Alcatel Alsthom Research, Marcoussis, France, working on quantum effects for optical modulation for fiber communications. Hehas been Directeur de Recherche C.N.R.S. at I.E.M.N., Villeneuve d'Ascq, France, since 1992, where he is in charge of gas source molecular beam epitaxy and physical studies on quantum semiconductor heterostructures. He is concerned with bandgap engineering and growth of structures on InP or GaAs, phosphide-arsenide interfaces and joint use of phosphorous and aluminum for large band offsets.

Didier Lippens was born in 1952 in Lille, France. He received the third cycle thesis (Ph.D.) degree from Lille University in 1978 and the Doctorat ès Sciences Physiques degree from the University of Lille in 1984.

In 1979–1980, he was an Engineer at Thomson Laboratories, Paris, France. From 1981 to 1987, he was Chargé de Recherches for Centre National de la Recherche Scientifique (C.N.R.S.) at Centre Hyperfréquences et Semiconducteurs. Since 1990, Directeur de Recherches and Professor at Institut d'Electronique et de Microélectronique du Nord (I.E.M.N.), Université des Sciences et Technologies de Lille. For the past ten years, he has been heading the quantum device and terahertz application group at I.E.M.N. His current interets concern low dimensional devices notably electron wave guides and high speed heterostructure devices including physics, fabrication technology and high frequency evaluation, micromachining of semiconductor microstructures and photonic band gap materials.

Capacitance Engineering for InP-Based Heterostructure Barrier Varactor

E. Lheurette, X. Mélique, P. Mounaix, F. Mollot, O. Vanbésien, and D. Lippens

***Abstract*— We investigate new schemes of InP-based heterostructure barrier varactors with the aim of enhancing the capacitance nonlinearity of the devices. Starting from a generic step-like InGaAs/InAlAs/AlAs single barrier heterostructure, planar-doped and buried InAs quantum-well barrier heterostructures were successfully fabricated. It is shown that both solutions lead to more efficient screening of electric field near equilibrium and hence to improvement in the capacitance–voltage ratios with values as high as $\sim 7{:}1$. Under bias, the capacitance modulation is governed by an escaping mechanism in contrast to the conventional depletion operation mode observed for conventional varactors.**

I. Introduction

A SINGLE barrier varactor diode, first proposed in 1989 [1], makes use of an heterostructure potential barrier to prevent conduction between anode and cathode and thus allow voltage-dependent depletion regions to develop in the cladding layers. The capacitance non linearity of such a structure is strongly dependent of the capacitance value under full depletion conditions $(C_{\rm sat})$ and at equilibrium (C_0). For the latter to be high requires to strictly control the distance over which the electric field is screened on each side of the heterostructure barrier. For conventional SBV's namely with uniform doping in the cladding layers, this requirement is a relatively challenging issue because large depletion effects and short screening lengths are two opposite goals. As a consequence the capacitance which are measured for these structures are much lower than those expected from the ideal situation given by sheet carrier densities located very close to the potential barrier. In this letter, we investigate in what extent such a tradeoff can be satisfied by means of planar doping and of buried well layers grown on each side of the barrier in close proximity. Over the past there were some attempts toward this goal using delta doping [2]. Unfortunately, the structures fabricated at that time suffer form high leakage currents so that the structures have to be cooled down to be analyzed. In this work, we systematically make use of strained AlAs layers in an InP-based technology [3]. In a previous paper [4], we showed that this kind of barrier scheme was very efficient for improving the voltage threshold of the devices. Starting from this generic structure, we succeed here to greatly enhance the device non linearity specially for the buried InAs quantum well varactor structure which, to the best of our knowledge, is fabricated and analyzed for the first time.

Manuscript received April 13, 1998; revised May 18, 1998. This work was supported by ESA under Contract 9777/92/NL/PB.

The authors are with the Institut d'Electronique et de Microélectronique du Nord, U.M.R. C.N.R.S. 9929, Université des Sciences et Technologies de Lille, 59652 Villeneuve d'Ascq, France.

Publisher Item Identifier S 0741-3106(98)06631-2.

II. Device Structure and Fabrication

The blocking barrier consists of an $In_{0.52}Al_{0.48}As$ 5-nm-thick/AlAs 3-nm-thick/$In_{0.52}Al_{0.48}As$ 5-nm-thick trilayered structure with a pseudomorphic growth of AlAs under tensile strain. The key advantage afforded by this stair-like barrier configuration [4] is mainly the very high conduction band offset between AlAs and $In_{0.53}Ga_{0.47}As$ of about 1.2 eV at Γ points. This barrier configuration permits one notably to avoid parasitic conduction via Fowler-Nordheim tunneling mechanisms which are found to be the primary origin of leakage current. Indeed, for conventional structures, the barrier has to be chosen thick enough for low transmissivity and consequently exhibits a triangular shape under bias. Under these conditions a high conduction current is observed at voltages much lower than the impact ionization threshold which is expected to limit the voltage handling. This blocking structure was sandwiched between two undoped 5-nm-thick spacer layers which contains (δ-SBV) or does not contain (SBV) a planar doping located at 5 nm from heterointerfaces with a sheet doping density equal to 2×10^{12} cm^{-2}. In addition, we designed 5-nm-thick quantum-well heterostructure barrier varactor (QWSBV). The capacitance modulation in the generic SBV's was obtained through the depletion of 300 nm (1×10^{17} cm^{-3}) InGaAs cladding layers. The heavily doped (5×10^{18} cm^{-3}) top and buried InGaAs contact layers allow on the other hand the fabrication of low-resistance ohmic contacts.

Starting from a semi-insulating Fe-doped InP substrate, all epilayers were grown in a Gas Source Molecular Beam Epitaxy RIBER machine. Alloy composition and growth rates were deduced from RHEED intensity oscillation measurements on InP (on InP) and of GaAs and AlAs (on GaAs). Silicon doping levels were estimated from Hall measurements of calibration structures. As a general rule, the growth was conducted at $\sim$520 °C for both binary and ternary compounds. However, the buried 5-nm-thick InAs wells, over the 2.5-nm critical thickness, were grown at lower Temperature ($\sim$400 °C) using the surfactant method [5]. The test structure consists of a mesa-type diode with top and side ohmic contacts in circular pattern configuration with various contact diameters. The samples were fabricated using three photolithography masks. $H_3PO_4/H_2O_2/H_2O$ solution was used for mesa etching and sequential Ni/Ge/Au/Ti/Au metallizations were used for the ohmic contacts.

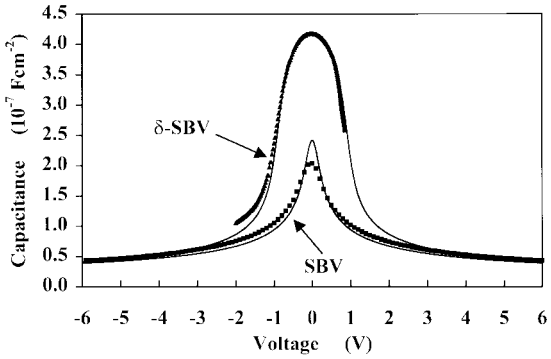

Fig. 1. Comparison of capacitance–voltage characteristics of a δ-doped SBV (triangle symbols) and of a generic SBV (square symbols) measured at 500 MHz. A step like InAlAs/AlAs/InAlAs material scheme is used for the barrier. The calculated voltage–capacitance characteristics are plotted in solid lines.

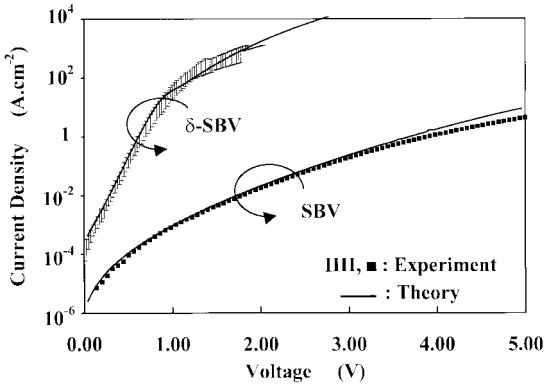

Fig. 2. Comparison between calculated and measured I–V characteristics for Single Barrier Varactors with (δ-SBV) and without planar doping located in the cladding layers close the barrier. For the former error bars are shown.

III. Measurements

Fig. 1 shows a plot of the capacitance–voltage characteristics of the generic structure corresponding to the growth parameters listed above (SBV) and of the planar doped SBV (δ-SBV) measured at 500 MHz. For the former, the voltage handling is high limited by the avalanche breakdown voltage (6 V). At equilibrium the measured capacitance normalized with respect to area is 2×10^{-7} Fcm^{-2}. In fact the capacitance level at zero bias strongly depends on the screening length which are relatively wide as a direct consequence of the repelling effect of the potential barrier. A first estimate of screening lengths can be obtained in the parallel plate capacitance approach $C = \varepsilon/L$ where L is the equivalent dielectric thickness. At equilibrium and assuming $L = L_b + 2 \cdot L_s$ (L_b is the barrier thickness equal to 13 nm and L_s the screening length) we thus obtain $L_s \sim 20$ nm. On the other hand, the capacitance at saturation is obtained under punch-through condition ($C_{\text{sat}} \sim \varepsilon/L_d$ with $L_d \sim 275$ nm). We thus achieved experimentally a ratio of 5:1, which is comparable to the best results published in the literature. The above arguments of large screening lengths are supported by computer simulations of the capacitance relationship by solving self-consistently the Poisson equation and the charge distribution function according to the procedure given in [6] with a fairly good agreement between calculated and measured data.

By means of a planar doping on each side of the heterostructure the zero-bias capacitance is significantly improved with a normalized value about twice higher. At increasing bias voltage it is seen that the C–V curve is monotonously decreasing in contrast to the expectation that the C–V characteristic should exhibit a plateau-like behavior. At saturation, both curves tend to follow the same trends with calculated C_0/C_{sat} ratio as high as 10:1. Experimentally however, the onset of parasitic conduction starting at about 2 V prohibits the measure of the saturation capacitance value.

In order to get insight into the conduction mechanisms, Fig. 2 displays the variations of the current density flowing through the diodes measured at room temperature and estimated theoretically. Generally speaking, the agreement between calculated and experimental data is good for both

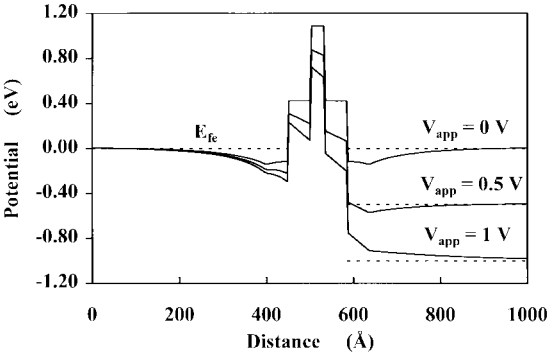

Fig. 3. Conduction band edge profile at various bias voltages. The dip induced by the trapping of a high electron sheet density (2×10^{12} cm^{-2}) close to the heterointerfaces vanishes at increasing voltage.

kind of devices. More interestingly from the application view point is the fact that δ-SBV exhibits two kinds of regime with a well-defined change in the slope at about 1 V. To help clarify this issue Fig. 3 shows a plot of the conduction band edge at 0, 0.5 and 1 V respectively. The salient feature in this figure is the lowering of the barrier at equilibrium with respect to a situation without delta doping. This can be understood by considering the repelling effect of the barrier with tends to break the symmetry in the V-shaped potential profile induced by space charge effect between the sheet doping concentration and the free electron density. Moreover, it can be noted that the sheet carrier density initially trapped on the right hand side of the barrier is progressively escaping as a result of the opening of the V-shaped electrostatic well. At about 1 V there are no more trapped electrons and the C–V characteristic obeys a depletion operation mode of the 10^{17} cm^{-3} doped cladding layer. Also as a consequence there is an increase in the overall voltage due to the voltage drop in the depleted regions.

So far we have discussed structures having δ-doping. Let us now consider the configuration where InAs 5-nm buried quantum wells are placed on each side of the blocking barrier. The device exhibits the measured capacitance–voltage characteristic plotted in Fig. 4. The overall capacitance ratio measured at 500 MHz is of about 7:1 with zero-bias capacitance values as high as 3.5 fF $\cdot$ μm^{-2}. Also interesting is the very steep

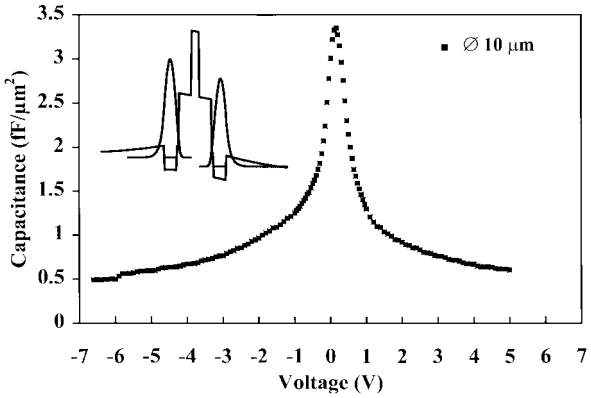

Fig. 4. Capacitance–voltage characteristics for a buried quantum-well structures fabricated from strained InAs epilayers grown prior and after the barrier. The inset shows a conduction band profile calculated at $V = 200$ mV and the corresponding eigenfuctions.

decrease in the C–V variation over about 1 V. At zero-bias, a large number of free carriers coming from the adjacent doped layer is trapped within the quantum well as illustrated in inset of Fig. 4 which displays the conduction band edge and the eigenfunctions. The net effect of this charging process is an increase in the barrier height with benefit for voltage handling. Under bias, the charge trapped on the right-hand-side quantum well is escaping by tunneling effect notably and gives rise to a very abrupt change in the capacitance relationship at moderate voltage. It is believed that such a behavior underlying on supply and escape mechanisms of a quantum well governed by fast capture and escaping time is very promising for harmonic multiplier applications at terahertz frequencies.

IV. Conclusion

High-performance InP-based heterostructure barrier varactors were fabricated with novel structure schemes. By means of planar doping and buried quantum well growth in close proximity to the barrier we succeeded to improve the device nonlinearity in terms of capacitance ratio and capacitance gradient. Further studies are needed to determine the frequency capabilities of this new class of varactor devices involving trapping and escaping mechanisms.

Acknowledgment

The authors would like to thank E. Delos and S. Lepilliet for technical assistance.

References

[1] E. L. Kollberg and A. Rydberg, "Quantum barrier varactor diode for high efficiency millimeter-wave multipliers," *Electron. Lett.*, vol. 25, no. 25, pp. 1696–1697, 1989.

[2] J. P. Sun, R. K. Mains, W. L. Chen, J. R. East, and G. I. Haddad, "C–V and I–V characteristics of quantum well varactors," *J. Appl. Phys.*, vol. 72, pp. 2340–2346, Sept. 1992.

[3] V. K. Reddy and D. P. Neikirk, "High breakdown voltage AlAs/InGaAs quantum barrier varactor diodes," *Electron. Lett.*, vol. 29, no. 5, pp. 464–465, 1993.

[4] E. Lheurette, P. Mounaix, P. Salzenstein, F. Mollot, and D. Lippens, "High performance InP-based heterostructure barrier varactor in single and stack configuration," *Electron. Lett.*, Vol. 32, pp. 1417–1418, July 1996.

[5] E. Tournié and K. H. Ploog, "Virtual-surfactant epitaxy of strained InAs/$Al_{0.48}In_{0.52}As$ quantum wells," *Appl. Phys. Lett.*, vol. 62, pp. 858–860, Feb. 1993.

[6] L. Burgnies, O. Vanbésien, V. Sadaune, D. Lippens, J. Nagle, and B. Vinter, "Resonant tunneling structures with local potential perturbations," *J. Appl. Phys.*, vol. 75, pp. 4527–4531, May 1994.

Résumé

Ce travail s'inscrit dans le contexte général des métamatériaux. Les métamatériaux sont des structures artificielles qui peuvent être décrites comme des milieux moyens en raison de leurs dimensions propres, très inférieures à la longueur d'onde de travail. Les résultats présentés portent plus précisément sur les métamatériaux à indice de réfraction négatif obtenu par le recouvrement de plages fréquentielles de permittivité et de perméabilité effectives négatives. Le fil conducteur de cette étude est l'augmentation des fréquences de fonctionnement : des micro-ondes vers le spectre térahertz.

Sur la base d'une représentation en termes de permittivité et de perméabilité, le premier chapitre propose un inventaire des milieux naturels et artificiels existants, en mettant l'accent sur leurs propriétés de dispersion. Par ailleurs, il fait état des différentes solutions disponibles pour synthétiser un métamatériau à permittivité et à perméabilité négatives. Enfin, il dégage les différentes applications possibles, comptes tenus des technologies mises en œuvre et du domaine de fréquence envisagé.

Le second chapitre concerne les structures unidimensionnelles. La première partie porte sur l'analyse d'un milieu synthétisé à partir de la superposition d'un réseau de fils métalliques et de boucles de courant insérées dans un guide d'ondes rectangulaire. La seconde partie aborde le concept de ligne de propagation duale par l'étude d'un déphaseur gaucher accordable. Enfin, la troisième partie traite des réseaux de particules Ω interconnectées qui constituent une approche hybride permettant de tirer parti des atouts de la ligne duale sans les contraintes propres au support de propagation. Ces atouts sont les caractères large bande, faibles pertes et la possibilité de travailler en régime composite équilibré, autrement dit avec une contiguïté des bandes gauchère et droitière.

Le dernier chapitre est consacré aux métamatériaux pour la propagation en espace libre. Un régime de propagation gaucher, présentant de faibles pertes d'insertion dans la bande de fréquence 75-110 GHz, a pu être démontré à l'aide d'un premier prototype basé sur un réseau de lettres Ω. Un second prototype, conçu pour les bandes X (8-12 GHz) et Ku (12-18 GHz), a permis l'observation de régimes de réfraction positive, négative ou nulle avec une contiguïté des domaines de fréquence. Enfin, la dernière partie de ce chapitre est consacrée à l'analyse expérimentale, aux fréquences térahertz, d'une structure gauchère conçue pour l'incidence perpendiculaire aux plans des motifs. Cette structure est constituée de l'empilement de réseaux métalliques percés par des ouvertures sous-longueur d'onde.